



nature

THE INTERNATIONAL WEEKLY JOURNAL OF SCIENCE

*Recreation of chromothripsis
implicates micronuclei in
chromosomal disruption* **PAGES 162 & 170**

BROKEN BAD

BIOTECHNOLOGY

WHEN DARPA DOES BIOLOGY

*Can peer-reviewless
funding drive innovation?*

PAGE 142

NUCLEAR FUSION

ENERGETIC LEADERSHIP

*ITER director talks tough
to keep the faith*

PAGE 148

REGENERATIVE MEDICINE

STEM CELLS RECRUITED

*Drugs boost reprogramming
in multiple sclerosis model*

PAGE 216

NATUREASIA.COM

11 JUNE 2016

VOL. 537, No. 7555

THIS WEEK

EDITORIALS

CLIMATE Political leaders aim for full phase-out of carbon emissions **p.128**

WORLD VIEW How funders can encourage data sharing **p.129**

EVOLUTION Galapagos genomes reveal secrets of marine iguana **p.131**



Sex and the law

A report from South Africa on the science of human sexuality and its implications for policy-making brings African countries a step closer to confronting laws that criminalize homosexuality.

The motto of the Academy of Science of South Africa is: “Applying scientific thinking in the service of society.” There are many types of scientific thinking, of course, and not all of them serve society particularly well. Scientific thinking on homosexuality, for instance, has a very chequered past.

Until the mid-1970s, the American Psychiatric Association listed homosexuality in its official manual of mental disorders. Academic journals at the time were filled with case reports of psychologists and medics trying to turn gay men straight. A new book, *‘Curing Queers’: Mental Nurses and Their Patients, 1935–74* by Tommy Dickinson, details cases of such ‘aversion therapy’ from the United Kingdom, where behavioural psychologists tried to erase homosexual behaviour by associating it with unpleasant sensations, including pain.

Scientific thinking on homosexuality, and other issues of sex, sexuality and gender, has moved on considerably since then. Thankfully, so too have many societies. Last month, Ireland became the latest country to legalize same-sex marriage. Science played no part in that decision, and why should it have?

Unfortunately, not everyone sees it that way. Science — or, more accurately, a flawed version of scientific thinking — is still used as a cloak for prejudice and persecution of homosexuals in countries across Africa and elsewhere. In February last year, for example, the press office of the Ugandan presidential State House formally announced that President Yoweri Museveni was to sign an “anti-gay bill after experts prove there is no connection between biology and being gay”.

The ‘scientific’ thinking here (and bear with us) is that, because researchers have not found a specific gene that is associated with homosexuality, science cannot say that some people are born gay. And if they are not born that way, the elastic logic goes, homosexuality is a lifestyle choice. And states are within their rights to criminalize some behaviour. “I want a scientific answer,” the president said, “not a political answer.”

As we report on page 135, a scientific answer on this question is now available. The Academy of Science of South Africa has published a comprehensive study on the science of human sexuality and the implications for policy (see go.nature.com/q3rr4k). The report demolishes the political lie that anti-gay laws are supported by scientific evidence. And it shows that, contrary to the public-health claims of politicians who want to criminalize homosexuality, such laws hamper efforts to combat the spread of HIV and other sexually transmitted infections.

What difference will this report make? It would be naive to expect that rational argument — scientific thinking — can draw the poison from the venomous attitudes that drive hatred and prejudice. But the report, if it is distributed widely, can still act as a useful tool for those who have the courage within Africa to oppose unjust laws.

As the report points out, there is precedent here. South Africa under the apartheid regime, and other places, tried to justify laws against mixed-race marriages with references to science and public health. The ‘natural order’ demanded that everyone stick to their own ethnic

and racial groups. Countering such claims alone does not dismantle the regime that produces them, but it offers ammunition to undermine claims to legitimacy that such regimes may make. Science helped to strip away the cloak to reveal the true, ugly motivations for such racial discrimination (and continues to do so, because the argument that ‘mixed’ couples produce more-dysfunctional families than non-mixed ones still rears its head from time to time). And it can do the same for anti-gay rhetoric too.

“The study could find no evidence that homosexuality is anything other than a feature on a spectrum of human sexuality.”

This is not an easy subject for scientists in Africa to cover. The South African academy deserves great credit for taking on this topic, and for producing such an unvarnished account of the true state of the scientific evidence and what that means for evidence-based policy. Credit, too, should go to the Uganda National Academy of Sciences,

which has officially endorsed the findings.

Museveni has the scientific answer he requested. As a phrase used many times in the report reads, the study “could find no evidence that” homosexuality is anything other than a feature on a spectrum of human sexuality. Indeed, the more that scientific thinking is applied to human sex and gender issues, the clearer it becomes that the evidence points towards greater diversity as the norm, not a culturally determined number of select options.

Spread the word. Share the report and its findings. Its conclusions, to those who respect scientific evidence, may be unremarkable. But sometimes stating the obvious again and again until people start to listen can be the best way for scientific thinking to serve society. ■

Undue burdens

Proposed controls on foreign operations in China are a threat to scientific collaboration.

China seems to be cracking down on everything at the moment. Its anti-corruption drive has government officials and businesses in all sectors shaking. The government has tightened its grip on the Internet, and the block on accessing Google and Google Scholar in China has hamstrung researchers’ ability to keep abreast of the latest scientific trends. Some proposed restrictions are so vague that they could be applied to almost anything. What do government officials mean, for example, when they say that ‘Western values’ have no place in Chinese university textbooks?

There are many reasons for these moves. President Xi Jinping is still

consolidating power, in a system rife with corruption. Meanwhile, an increasingly vocal populace complains of rich officials, environmental problems and food safety.

The government wants to stay in charge of efforts to deal with problems and maintain its goal of stability. It is not alone in such efforts. And it is not alone in setting its sights on what it sees as a possible source of dissent and social strife: non-governmental organizations (NGOs). Russia and India in recent months have already set out worrying plans to stifle such operations. Now China is following.

In China, domestic NGOs are, for the most part, government-organized bodies, and so are still under government influence. But foreign NGOs are a concern to the government, and a potential destabilizing force, especially when they try to spread 'Western values'.

Last year, the government surveyed foreign NGOs operating in China and counted about 1,000 permanent operations; when short-term projects are included, NGOs in China number up to 6,000. The government estimates that these groups pour hundreds of millions of dollars into some 20 areas, including health, environmental protection and education. To Chinese officials, these are alarmingly high numbers.

China feels that its grip on these organizations has been too loose. Accordingly, over the past month it has sought comments on a new draft law — the Non-Mainland Non-Governmental Organizations Management Law — that will tighten restrictions on NGOs.

The move may not be a surprise, given the political mood. But the proposed scope of the law is broader than many people expected, and is causing alarm. Its definition of an NGO is so broad — all activities of "not-for-profit, non-governmental social organizations" — that, according to Jia Xijin, a specialist on NGOs in China at Tsinghua University, it covers all organized activities between Chinese nationals and foreigners. Many people, citizens and visitors alike, probably have no idea that the law will apply to them.

The new rules would require individuals or institutions wishing to carry out activities in China to get a sponsor, such as a ministry or other agency of local government. Then they must apply for permission — not to the civil-affairs ministry, as in the existing system, but to the public-security bureau.

What will happen when the public-security bureaus, which are accustomed to operating with a police mindset, start sizing up applications for scientific collaborations? At the very least, the result would be undue, and potentially forbidding, restrictions and red tape. It would

probably, for instance, discourage studies of environmental problems that regional governments are not ready to admit to. At the very worst, it would allow the persecution of institutions or of individuals from blacklisted institutions.

Could a political demonstration at a university overseas mean that researchers from that university would no longer be welcome

"Overseas institutions have already expressed concern."

in China? What if an individual had some other political connection that made officials uncomfortable?

The proposed law is not explicit in how it should be applied to specific collaborations or specific research projects. Those associated with universities or scientific societies in China fear that the decisions will be deferred to officials with little experience of science. What happens when these officials come across a project they do not fully understand? Will they want to take a chance on it? Most probably, observers fear, they would rather just reject it — or, more likely, sit on it — and make things easy for themselves.

Overseas institutions have already expressed concern. One response to the Chinese consultation came from Harvard University in Cambridge, Massachusetts, which said that "universities should not be treated as non-governmental organizations and should not be subject to its provisions which, if implemented, could inadvertently make future transnational faculty and student collaborations more difficult, and therefore less frequent".

In an e-mail to *Nature*, a Harvard spokesperson put it diplomatically: "We would have concern with any law that might inhibit the future ability of faculty and students to work together on common areas of interest by creating new, undue burdens."

Jia says that second- or third-tier universities, and especially local or private universities, are likely to suffer. Whereas prominent government-affiliated universities such as Tsinghua or Peking universities, both in Beijing, would probably be accredited as authorized hosts for foreign NGOs that want to carry out temporary activities in China, smaller and less-well-connected universities are unlikely to get such approval.

Both science and China have benefited from the emphasis that the Chinese government has placed in recent years on research as a driver of growth and development. International links are a key component of that. To weaken such networks could do more than cut useful ties. It could undermine the stability that they help to bring. ■

Tough targets

Concrete goals set out by the G7 nations lay the groundwork for a climate accord.

The Group of 7 (G7) leading industrialized nations this week called for global greenhouse-gas emissions to be reduced by around 70% by 2050, and for the world economy to be decarbonized by the end of the twenty-first century. These twin goals were issued in a communiqué at the conclusion of the group's meeting at Schloss Elmau in Krün, Germany, on 8 June, alongside a suite of promises to help developing nations to provide their citizens with clean energy, jobs, financial security and food.

To the credit of German Chancellor Angela Merkel, leader of the host nation, the commitments surpass all of the G7's previous promises. Most notably, the group has formally acknowledged — and quantified — the scale of the industrial renaissance that will be required to keep global average temperature increase to less than 2°C above pre-industrial levels. It has provided concrete and measurable targets that should help to make clear where precious capital and human resources should be invested — not just for other governments, but also for businesses. It

should also make clear where resources should not be expended. The G7 nations renewed their pledge to end "inefficient" fossil-fuel subsidies.

The nations also reaffirmed a commitment, made in Copenhagen in 2009, to increase climate aid for developing countries to US\$100 billion per year by 2020, including both public and private financing. The communiqué calls for an expansion of renewable energy in developing countries, and further work to help the most vulnerable countries to prepare for climate change. In particular, the G7 pledged to ensure that 400 million people in developing nations have access to climate-risk insurance, to mitigate the effects of disasters such as droughts and storms.

The timing is good. Nations are wrapping up the latest round of climate talks in Bonn this week, with the aim of advancing a climate agreement to be signed in Paris later this year. Policy-makers have their work cut out if they are to sign a meaningful accord, and the G7 meeting represents a small step in the right direction.

But the world is still waiting for action that will give these targets credibility. Countries should adopt the G7 communiqué's emissions targets and look for ways to expand climate-related investment in the developing world, where emissions are poised to rise quickly if no intervention is made. The communiqué rightly points out that engagement by the private sector will be crucial to meeting these goals, but it is up to policy-makers to lay down the rules of the road. ■

➔ NATURE.COM
To comment online,
click on Editorials at:
go.nature.com/xhunqv



Funders must encourage scientists to share

To realize the full potential of large data sets, researchers must agree on better ways to pass data around, says Martin Bobrow.

How can we make best use of the vast amounts of data on genomics, epidemiology and population-level health being collected by researchers? Maximizing the benefits depends on how well we as a scientific community share information.

The Human Genome Project set strong precedents for rapid pre-publication data sharing, and all biological research has benefited enormously from this approach. Most research-funding agencies, and most scientists, now agree that research data should be shared — provided that those who donate their data and samples are protected. This approach is strongly advocated by organizations such as the Global Alliance for Genomics and Health. But data sharing will work well only when it is streamlined, efficient and fair. How can more scientists be encouraged and helped to make their data available, without adding an undue administrative burden?

I chair an expert advisory group on data access that has examined this question. As part of our work, we surveyed current practices and questioned *Nature* readers. We saw plenty of good practice — in the UK social-sciences community, for example — but also significant inefficiencies. Both those who generate data and those who want to use them expressed frustration at the way that data-access processes are frequently opaque.

At present, mechanisms for data sharing are too often an afterthought. Access protocols are set up and managed differently from study to study, and this adds to the administrative burden for both producers and users. No one wins in this scenario, least of all those who donate their personal data.

Today, we publish our recommendations (see www.wellcome.ac.uk/EAGDA). They are aimed at research funders, who are best placed to implement them. But we hope that all researchers will find them useful. A key recommendation is that data-access plans should be integral to the grant-application process. Researchers should set out what they regard as a reasonable process for governing and managing access, including estimates of the costs of making the data visible and available to other researchers. The review process should advise on this and the data-access plan should be an integral, auditable part of the funded grant.

Generally speaking, bigger studies will need more-substantial processes. Small experimental studies may reasonably do no more than make their data available on request, after the time to prepare for publication. Very large studies require a more formal data-access plan from their inception.

Many epidemiological or genomic studies establish data-access committees (DACs) to manage data release. It makes little sense for each to do this in isolation, with individual processes and policies. The information required by DACs,

and the undertakings they ask of potential data users, are usually similar across studies. Where possible, funders should encourage the streamlining and standardization of this process, while allowing for the fact that studies have their own characteristics. It would be helpful, where possible, to introduce common application forms and adjudication processes, and to allow new studies to make use of or consolidate with existing DACs. Access procedures should be made more transparent and straightforward by including an independent appeals process for settling disputes over access requests.

Protecting research participants is sometimes cited as a reason for withholding data. The risk that research participants could be re-identified from shared data must be carefully assessed, particularly when data sets are linked in novel ways. But safeguarding participants' identity should not require a complex or opaque system of data access, as often seems to be the case.

It is easier to protect subjects if researchers build data access into their studies from the beginning. Participant consent forms, for example, should be designed with data sharing in mind — granting permission for de-identified personal information to be shared safely with researchers outside the study group.

It is reasonable for scientists to impose certain conditions or restrictions on the use of their hard-earned data sets, but these should be proportionate and kept to a minimum. Justifiable conditions can range from requiring secondary users to acknowledge the source of the data in publications, to stipulating a fair embargo time on the use of new data releases. Whatever the conditions

imposed, they need to be presented clearly to data users.

Criteria used to judge academic careers still focus heavily on individual publication records and provide little incentive for wider data sharing. Scientists who let others use their data deserve reward too.

To build trust, any significant breaches of data- and material-transfer agreements should be treated seriously, with appropriate sanctions being imposed, such as prevention of future access to data sets, or forcing the withdrawal of a published paper.

Funders should expect that each data set they support will be made accessible unless there are particular, agreed reasons for it not to be. Science is increasingly a joint, international and collaborative enterprise. The emphasis now must be on encouraging scientists, with support and resources from funders, to voluntarily make their data more readily available to others. ■

Martin Bobrow is emeritus professor of medical genetics at the University of Cambridge, UK, and chair of the Expert Advisory Group on Data Access.
e-mail: mb238@cam.ac.uk

**SAFEGUARDING
PARTICIPANTS'
IDENTITY
SHOULD NOT REQUIRE
A COMPLEX OR OPAQUE
SYSTEM OF
DATA ACCESS.**

➔ **NATURE.COM**
Discuss this article
online at:
go.nature.com/wdw9cq

RESEARCH HIGHLIGHTS

Selections from the
scientific literature

MATERIALS

Energy stored inside an aerogel

Researchers have created a promising 3D energy-storage device using a porous aerogel. These 'supercapacitors' could offer much higher power densities than conventional structures.

Mahiar Hamed at the KTH Royal Institute of Technology in Stockholm and his colleagues coated the foamy interior of an aerogel with carbon nanotubes to create an electrode. They covered this with an insulating plastic, followed by another nanotube electrode layer. This formed a supercapacitor that showed stable charging and discharging over 400 cycles, and maintained its performance when the aerogel was compressed by up to 75%.

Aerogels have the largest internal surface area of any synthetic material, so such components could store large amounts of power in a range of electronic devices.

Nature Commun. 6, 7259 (2015)

CELL BIOLOGY

Why human eggs are error-prone

The cellular machinery for separating chromosomes is unusually unstable in human eggs. This makes the eggs prone to having abnormal numbers of chromosomes, which can result in pregnancy loss and genetic disorders.

When cells divide to make eggs or sperm, chromosome pairs separate owing to spindle-shaped cellular machinery. Melina Schuh at the MRC Laboratory of Molecular Biology in Cambridge, UK, and her colleagues observed this process in more than

100 live egg cells from women undergoing fertility treatments. They found that the chromosome segregation period was unusually long, lasting about 16 hours. In many egg cells, the spindles were unstable, causing the chromosomes to lag behind during separation, and increasing the risk that they would not reach the correct side of the spindle before the cells divided.

Science 348, 1143–1147 (2015)



SANJIT DAS/PANOS

AGRICULTURE

The cost of native and GM cotton crops

Native cotton in India can generate similar profits to genetically modified (GM) cotton when both are grown without irrigation.

Carla Romeu-Dalmau, Liam Dolan and their colleagues at the University of Oxford, UK, compared the economic impact of growing native Asiatic cotton (*Gossypium arboreum* L.) with that of growing American Bt cotton (Bt *Gossypium hirsutum*), which has been engineered to contain bacterial genes that make the crop resistant to insect pests. They found that farmers in the Indian state of Maharashtra spent more money to produce Bt cotton than native cotton, even though

Bt cotton generates higher yields.

The authors also looked at farming Bt cotton under different conditions, and found that the GM cotton grown under rain-fed conditions has similar economic benefits to the same cotton grown using irrigation. Although Bt cotton gives higher yields with irrigation than without, growing it under these conditions costs more and eats into profits.

Farmers should bear in mind a range of factors, including expenses and water availability, when choosing which crop to plant, the authors suggest.

Nature Plants 1, 15072 (2015)

CLIMATE CHANGE

Hot storms bring big rainfall swings

As temperatures rise, heavy rainfall during storms becomes even heavier, whereas lighter bursts grow less intense. This could bring storms that are more unpredictable and destructive as the climate warms.

Conrad Wasko and Ashish Sharma at the University of

New South Wales in Sydney, Australia, analysed high-resolution rainfall data from 79 locations across Australia from 1955 to 2005. They found that, at all latitudes, Australian rainfall patterns became less uniform as temperatures rose, and the authors predicted a 5–20% increase in the peak water flow rate during floods at temperatures 5 °C warmer than today.

A warmer climate could lead to short-term floods that

are more intense, the authors suggest.

Nature Geosci. <http://dx.doi.org/10.1038/ngeo2456> (2015)

ANIMAL BEHAVIOUR

Lazy male birds pay a high price

Male songbirds that sleep late risk having their female partners mate with another male.

Mating outside of a monogamous pair in birds normally happens early in the morning. To find out if rising earlier or later would affect reproductive patterns of great tits (*Parus major*), Timothy Greives of North Dakota State University in Fargo and his co-workers captured male birds in Germany and implanted them with a device that releases melatonin.

This hormone is generated mostly at night to set the circadian clock. Male tits that had night-time-like levels of melatonin around the clock began their daily activities on average 10 minutes later than the control group. Their nests also contained more offspring fathered by another male, suggesting that the late-rising males were less able to defend their mates.

The results demonstrate how sexual selection affects circadian rhythms in the wild. *Funct. Ecol.* <http://doi.org/44c> (2015)

EVOLUTIONARY BIOLOGY

Galapagos iguanas share genes

Swimming lizards on one of the Galapagos Islands are evolving into new species, but they also seem to be mating with lizards from neighbouring islands — possibly helping to incorporate adaptations from other populations into their gene pool.

Sebastian Steinfartz at the Technical University of Braunschweig in Germany and his colleagues

analysed the genomes of more than 500 Galapagos marine iguanas (*Amblyrhynchus cristatus*; **pictured**) from the island of San Cristóbal in the Galapagos. They found evidence of ongoing hybridization between lineages from different islands, along with speciation in the San Cristóbal population.

This simultaneous hybridization and speciation could have contributed to the evolutionary success of the marine iguana, the authors say. *Proc. R. Soc. B* 282, 20150425 (2015)

MATERIALS

Tiny robot fuelled by light

A microscopic 'walker' just a few tens of micrometres in size can shuffle, rotate and even jump, powered only by light.

Hao Zeng and Diederik Wiersma at the University of Florence in Italy and their co-workers created their device using materials called liquid crystalline elastomers, which contract and expand like muscles. They added a light-sensitive dye, attached four cone-shaped legs made from acrylic resin and focused a laser beam on the robot. The device walked in a straight line on a patterned surface and even jumped up to 100 times its own body length.

Such a robot could be powered by ambient light alone, and could be modified to perform other actions such as swimming, the authors say. *Adv. Mater.* <http://doi.org/12747b> (2015)

ASTRONOMY

Megaflare seen on star surface

Astronomers have spotted an enormous surge of light and magnetic energy on a nearby star.

A team led by Wouter Vlemmings at Chalmers University of Technology

SOCIAL SELECTION

Popular topics on social media

Unpaid research jobs draw criticism

Volunteer jobs are a rite of passage for many budding ecologists and wildlife biologists, but a website highlighting these unpaid positions calls them "unprofessional" and "exploitative". Alex Bond, a conservation biologist at the RSPB Centre for Conservation Science in Sandy, UK, created the Tumblr page 'Crap Wildlife "Jobs"' on 31 May (<http://crapwildlifevolunteerjobs.tumblr.com>), and it already has supporters on Twitter. "Really cool (and necessary) initiative," tweeted Julie Godbout, an environmental geneticist at Laval University in Quebec City, Canada. "Do what you love AND get paid for it." But Stephanie Stack, an environmental scientist with the Pacific Whale Foundation in Wailuku,

Hawaii, which is featured on the page, says that unpaid internships give young scientists a chance to gain valuable experience and to make connections in the field.

➔ **NATURE.COM**
For more on popular papers:
go.nature.com/pfcw9n

near Gothenburg, Sweden, pointed the ALMA radio telescope in northern Chile at the red giant Mira A, a star 92 parsecs (300 light years) away that was once like our Sun but is now bloated in old age. ALMA's high resolving power was able to pick out features on the stellar surface — a feat unprecedented at these wavelengths. The data revealed a bright hotspot on Mira's surface that is roughly the same size as Mercury's orbit around the Sun.

The star is probably unleashing energy from its magnetic field, similar to what happens on the Sun, suggesting that magnetic fields have a role even when these stars grow old. *Astron. Astrophys.* 577, L4 (2015)

COGNITION

Chimps' mental capacity to cook

Chimpanzees have key cognitive abilities for cooking food — a hint that humans might have developed the capacity for cooking early in evolution.

Felix Warneken at Harvard University in Cambridge, Massachusetts, and Alexandra Rosati at Yale University in New Haven, Connecticut,



studied the cognition of chimps (**pictured**) by presenting them with a specially designed cooking device and raw and cooked foods such as carrots and potatoes. They confirmed that the apes prefer cooked to raw items, and found that chimps are willing to wait longer for cooked food than for raw food. The animals were able to give up their own raw food to cook it, and to save it for later cooking.

The results suggest that the last common ancestor of apes and humans had the cognitive abilities to cook food, long before humans learned to control fire.

Proc. R. Soc. B 282, 20150229 (2015)

➔ **NATURE.COM**
For the latest research published by Nature visit:
www.nature.com/latestresearch



SEVEN DAYS

The news in brief

EVENTS

MERS outbreak

A large outbreak of Middle East respiratory syndrome (MERS) coronavirus in South Korea has caused alarm this week. As *Nature* went to press, the hospital-acquired virus had killed 7 people and infected 94 in the country — the largest outbreak outside the Middle East so far. The latest cases began when a South Korean man returned to Seoul from the Middle East, and visited four health-care facilities before being diagnosed. There is also one case in China, imported from South Korea. The virus could become a greater threat if it acquires mutations that allow it to spread between humans more easily; however, the South Korean health ministry announced on 6 June that sequencing suggests the virus is unchanged. See page 139 for more.

Solar-plane setback

Solar Impulse, the plane that aims to be the first solar-powered craft to circle the world, landed unexpectedly in Nagoya, Japan, on 1 June as it attempted to begin its long trans-Pacific journey. Weather patterns forced the re-routing. On 2 June, wind gusts whipped through the airport at Nagoya and damaged part of Solar Impulse's wing, delaying the

NUMBER CRUNCH

\$400 m

The largest-ever gift donated to Harvard University in Cambridge, Massachusetts, given on 3 June to its School of Engineering and Applied Sciences by alumnus and hedge-fund manager John Paulson.



M. BRICE/CERN

Hopes high as LHC switches on again

Scientists at CERN, Europe's particle-physics laboratory near Geneva, Switzerland, celebrated the official restart of the Large Hadron Collider (LHC) on 3 June. The machine was shut down for two years to undergo upgrades and can now smash protons together at a record energy of 13

teraelectronvolts. Whereas the LHC's first run hunted down the Higgs boson, the second will do a wide-ranging search for discrepancies with the standard model, physicists' best description of particle and force behaviour. See go.nature.com/sglyfm for more.

project for at least another week. The planned round-the-world flight began in March from Abu Dhabi.

Solar sail unfurls

The world's first privately funded solar sail unfurled in orbit on 7 June. The test flight of LightSail, run by the Planetary Society, a space-advocacy group in Pasadena, California, had run into a series of communications and battery problems, but unexpectedly responded to mission control after a three-day silence and deployed its 32-square-metre sail. Solar sails use the pressure from light radiated by the Sun to move through space.

Space partnership

A near-Earth space-weather observatory has been nominated to become the first

official joint mission between the European Space Agency and the Chinese Academy of Sciences. The Solar wind Magnetosphere Ionosphere Link Explorer (SMILE) would study the interaction between Earth's magnetic field and the solar wind, charged particles that stream from the Sun. It is scheduled for launch in 2021. Selected on 4 June from a pool of 13 proposals, SMILE is expected to cost about €100 million (US\$112 million), and will undergo further assessment ahead of a formal selection process later this year.

Chemistry for work showing that proteins marked with a molecular tag called ubiquitin are destined for destruction. This process malfunctions in diseases such as cystic fibrosis and cancer, and Rose's work led to the development of a drug to treat certain blood cancers.

FACILITIES

Mammoth telescope

The Giant Magellan Telescope has been given the go-ahead to start construction at Las Campanas Observatory in Chile, project leaders announced on 3 June. Its ultimate design calls for seven mirrors that together will span 25 metres. When it comes online in 2021, it will have only four of those seven in place, but it will still be the world's largest optical telescope at that point.

PEOPLE

Biochemist dies

Irwin Rose, an American biochemist who co-discovered a cellular recycling system, died on 2 June aged 88. Rose shared the 2004 Nobel Prize in

Eleven international partners have committed more than US\$500 million to the project, just over half of its total expected cost.

RESEARCH

Fracking impacts

Hydraulic-fracturing activities in oil and gas development have not had major effects on drinking-water resources in the United States, the US Environmental Protection Agency reported in a draft assessment on 4 June. The much-anticipated study did document multiple threats to surface and groundwater resources, including poorly constructed wells and the improper disposal of waste water produced during the drilling process. But agency officials said that the number of cases of documented contamination is “relatively low”. Accompanied by more than 20 peer-reviewed reports, the study will be finalized after review by the agency’s Science Advisory Board.

Water-lily discovery

The discovery of a new species of water lily was announced by the Royal Botanic Gardens, Kew, UK, on 5 June. The bloom (pictured), which has yet to be named, was found in Western Australia by Kew tropical-plant specialist



Carlos Magdalena and teams from Kings Park and Botanic Garden and the University of Western Australia, both in Perth. An identical plant had previously been collected in Australia’s Northern Territory, but was thought to be a hybrid. The discovery of this plant in the remote creeks of Kimberley, many hundreds of kilometres away from the previous find, led Magdalena to conclude that it is a new species. DNA analysis will be used to confirm the find.

POLICY

G7 climate pledge

On 8 June, the G7 group of leading industrialized nations adopted a target of reducing global greenhouse-gas emissions to 70% of their 2010 levels by mid-century to achieve climate goals. Issued at the conclusion of the G7 summit at Schloss

Elmau in Krün, Germany, the communiqué goes beyond previous statements. Those had affirmed the goal of limiting the average temperature increase to 2°C above pre-industrial levels, but had not quantified the actual emissions reductions required. The G7 also called for decarbonization of the world economy — ending fossil-fuel use — by the end of the twenty-first century.

Animal experiments

The European Commission has decided not to propose changes to legislation on the use of animals for scientific purposes, after considering a petition to overhaul its laws. A European Citizens’ Initiative called Stop Vivisection, signed by more than one million Europeans and submitted to the commission in March, had called for a complete ban on animal use. The commission said on 3 June that animals are

COMING UP

14–17 JUNE

The latest research on human fertility and reproductive technologies is presented at the European Society of Reproduction and Embryology’s annual conference in Lisbon. www.eshre2015.eu

15–19 JUNE

Interdisciplinary scientists from around the world meet in Chicago, Illinois, for the Astrobiology Science Conference 2015. This year’s theme is Habitability, Habitable Worlds, and Life. go.nature.com/hwhc8z

still required in biomedical research, but it pledged to promote the development of animal-free ways of testing the safety and efficacy of drugs and other chemicals.

AWARDS

Robot contest

A South Korean team won the US\$2-million first prize in the US Defense Advanced Research Projects Agency’s DARPA Robotics Challenge, which took place on 5–6 June in Pomona, California. Twenty-three teams from around the world entered machines into the contest, in which they had to compete at performing tasks that could be useful in a disaster scenario, such as climbing a ladder and shutting down a valve. The winner was DRC-Hubo, a humanoid robot that can switch between walking and moving faster on wheels. It was developed at KAIST, a science and technology research university in Daejeon, South Korea.

► NATURE.COM

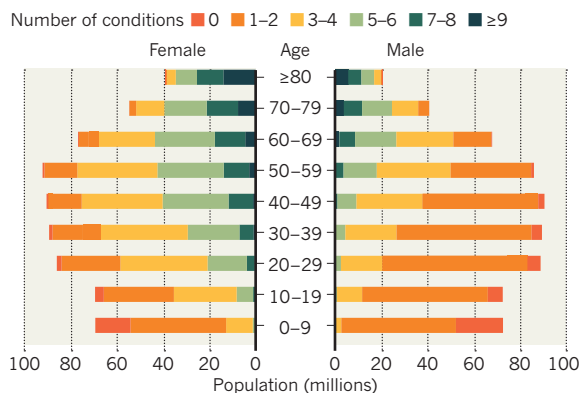
For daily news updates see: www.nature.com/news

TREND WATCH

Although big gains have been made in cutting mortality due to illness, disabilities from illness pose a major problem, warns a study of 188 countries in *The Lancet* (T. Vos *et al.* *Lancet* <http://doi.org/45v>; 2015). It found that the proportion of years of healthy life lost rose from about one-fifth in 1990 to nearly one-third in 2013. The leading causes — including low-back pain and depression — have changed little, but only 1 in 20 people had no problems in 2013, and 1 in 3 had more than 5.

GROWING SICKNESS

Although people are living longer, they are also living with more chronic conditions, as seen here in data for the developed world.



NEWS IN FOCUS

NANOTECHNOLOGY Injectable brain implant paves way for neuroscience revolution **p.137**

BUSINESS Boston biotech hub threatened by soaring rents and influx of giant firms **p.138**

MERS IN SOUTH KOREA Experts urge focus on Middle East to prevent future outbreaks **p.139**



AGRICULTURE Why Africa's super vegetables are on the rise **p.146**

REBECCA VASSIE/AP/PA



A 2014 Ugandan law that punished homosexuality with life imprisonment was later repealed.

HOMOSEXUALITY

African academics challenge homophobic laws

Scientific report demolishes assertions used to back criminalization of homosexuality.

BY LINDA NORDLING

A Western import. Unnatural. Contagious. Un-African. All of these arguments and more have been invoked to support the numerous laws criminalizing homosexuality in Africa. But now African academics have used scientific evidence to argue against such laws and to urge African nations to abandon them.

In a report published on 10 June by the Academy of Science of South Africa (ASSAf), the

academics, most of whom are scientists, make the case that laws criminalizing homosexuality have no basis in science and hamper efforts to prevent and treat HIV and other sexually transmitted infections (see go.nature.com/q3rr4k).

Human-rights activists and many people working in health care welcome the report, which comes in response to a slew of homophobic laws in several African countries, in particular Uganda. "It opens up a new outlook about homosexuality seen through the lens

of science," says Thomas Egwang, a Ugandan immunologist who was not involved in producing the report.

However, activists and health-care workers also warn that it will probably not have a big impact on policy-making — at least in the short term — because homophobic attitudes are deeply entrenched. "I'm not sure the [Ugandan] government is going to listen," says Kent Klindera, programme manager of an initiative at the Foundation for AIDS Research in ►

► New York that promotes HIV prevention for gay men, transgender individuals and men who have sex with men (MSM).

Same-sex relationships are illegal in 38 of Africa's 53 nations and punishable by death in 4. In recent years, anti-gay sentiment has intensified. In February 2014, Uganda, where homosexuality was already illegal, passed a law that made it punishable by life imprisonment and made the 'promotion' of homosexuality a crime. In the same year, Gambia enacted a similar law, and Nigeria passed a law banning same-sex marriage, gay-rights groups and displays of same-sex affection in public.

Although the Ugandan law has since been repealed (a constitutional court declared that there had not been enough members present when parliament passed the act), it prompted an international outcry — and sparked the idea for the report among members of ASSAf. "It had to be Africa-led," says Glenda Gray, co-chair of the report panel. "If it were American-led, African governments would say that it was Western propaganda."

The report's authors, of whom 11 work in South Africa, 1 in Uganda and 1 in the United States, drew on medicine, anthropology, psychology and philosophy to counter arguments used to justify the criminalization of homosexuality.

When signing the Ugandan bill into law, the country's president, Yoweri Museveni, said that it would stop the "social imperialism" of the West, which he said is responsible for promoting homosexuality in Africa. It is an argument also used by many of the continent's faith-leaders. But the report argues that it was missionaries from the West who turned traditional African practices, including same-sex relationships, into problems.

The authors reference a review of literature dating back to the late nineteenth century that documents homosexuality in Africa (see go.nature.com/7un5vx), including woman-to-woman marriage on the Slave Coast (in present-day Togo, Benin and Nigeria), homosexual relations between shepherd boys in Ethiopia, and cross-dressing male prostitutes in Senegal. The authors cite a 2008 review that calculated the prevalence of MSM in Africa

to be at least 2%. This is in line with a global finding that at least 1.5% of men of any given population are exclusively attracted to members of their own sex.

The report also counters the notion that



President Yoweri Museveni signed Uganda's homophobic bill into law.

homosexuality is unnatural, citing evidence for a strong biological role in sexual orientation. And it tears down the ideas that homosexuality is 'socially contagious', promotes the spread of HIV or encourages paedophilia, citing papers that have disproved these, or similar, claims.

The report warns that criminalizing homosexuality is the real threat to public health. This was illustrated in Uganda when a staff member of a US-Ugandan research project at Makerere University was arrested on charges of recruiting homosexuals and carrying out 'unethical research': the US funder suspended the project because of fears about staff safety (see *Nature* **509**, 274–275; 2014).

The authors hope that the report will fare better than an earlier one. Shortly before parliament was to vote on the 2014 bill, the Uganda National Academy of Sciences (UNAS) declined a government request to produce a report on the scientific basis of homosexuality because of insufficient time. But a group of scientists hastily produced one that was later misquoted

by members of parliament who supported the bill.

The UNAS has endorsed the latest report — unlike other African academies invited to do so. "The whole question around homosexuality has become fraught," says Melissa Steyn, an author of the report and a social scientist who holds the South African Research Chair in Critical Diversity Studies at the University of the Witwatersrand in Johannesburg. UNAS president Nelson Sewankambo says that it is the role of the academy to engage with controversial issues, especially where scientific arguments are already being used. However, he does not expect all of his colleagues to support the report's sentiments.

Juliet Kiguli, an anthropologist at Makerere University and the only Ugandan on the expert panel, is hopeful that the report will change views in her country. "The majority of Ugandans think this is not part of our culture. But culture is not static," she says. If policy-makers take a lead in forging a more tolerant society, public opinion will follow, she says.

The report could help human-rights activists across Africa to lobby policy-makers, says Daniel Onyango, executive director of the Nyanza, Rift Valley and Western Kenya Network, which campaigns for gay rights from Kisumu, Kenya. The UNAS's endorsement of the report might ease its acceptance by Kenyans, he adds, given that they see Uganda as culturally closer than South Africa and that ASSAf published the report. Abandoning anti-gay laws would be a major step towards offering good-quality health care and tailored HIV-prevention information to MSM, says Eduard Sanders, an epidemiologist at the University of Oxford, UK, who has done HIV research on MSM in Kenya. "The road is likely to take many years, but there is growing momentum in Africa — and I am proud to be part of it."

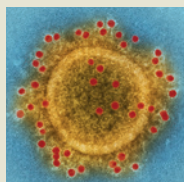
At least one Ugandan activist has no qualms about quoting the report to deter his detractors: "As an activist," says Paul Semugoma, a gay Ugandan physician who lives in exile in South Africa, and who campaigns for gay rights in Uganda, "I plan to get hold of it, and use it akin to how they use the Bible on us." ■

ISAAC KASAMANI/AFP/GETTY



**MORE
ONLINE**

TOP STORY



Five reasons why South Korea's MERS outbreak is not a global threat go.nature.com/9c6ggy

MORE NEWS

- Controversial crystallography tool tries for a comeback go.nature.com/f2jhdw
- Friction of a single atom measured with light go.nature.com/j7369r
- Ultraviolet close-up reveals comet surprise go.nature.com/a9bcc3

NATURE PODCAST



Bronze Age genomes, the prion disease caused by cannibalism, and DARPA's new biology office nature.com/nature/podcast

NANOTECHNOLOGY

Injectable brain implant spies on individual neurons

Electronic mesh has potential to unravel workings of mammalian brain.

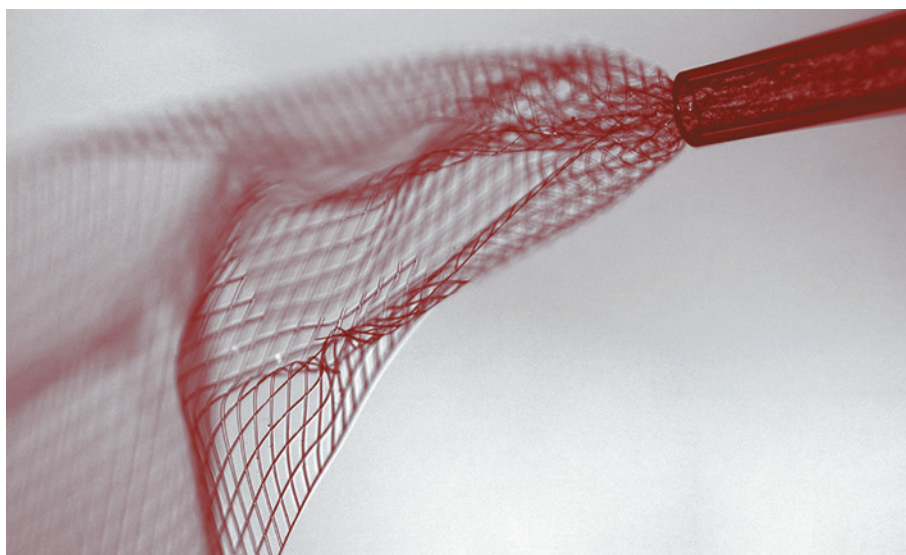
BY ELIZABETH GIBNEY

A simple injection is now all it takes to wire up a brain. A diverse team of physicists, neuroscientists and chemists has implanted mouse brains with a rolled-up, silky mesh studded with tiny electronic devices, and shown that it unfurls to spy on and stimulate individual neurons.

The implant has the potential to unravel the workings of the mammalian brain in unprecedented detail. “I think it’s great, a very creative new approach to the problem of recording from large number of neurons in the brain,” says Rafael Yuste, director of the Neurotechnology Center at Columbia University in New York, who was not involved in the work.

If eventually shown to be safe, the soft mesh might even be used in humans to treat conditions such as Parkinson’s disease, says Charles Lieber, a chemist at Harvard University on Cambridge, Massachusetts, who led the team. The work was published in *Nature Nanotechnology* on 8 June¹.

Neuroscientists still do not understand how the activities of individual brain cells translate to higher cognitive powers such as perception and emotion. The problem has spurred a hunt for technologies that will allow scientists to study thousands, or ideally millions, of neurons at once, but the use of brain implants is currently limited by several disadvantages. So far, even the best technologies have been composed of relatively rigid electronics that act like sandpaper on delicate neurons. They also struggle to track the same neuron over a long period, because individual cells move when an animal breathes or its heart beats.



LIEBER RES. GROUP/HARVARD UNIV.

This soft, conductive polymer mesh can be rolled up and injected into the brains of mice.

The Harvard team solved these problems by using a mesh of conductive polymer threads with either nanoscale electrodes or transistors attached at their intersections. Each strand is as soft as silk and as flexible as brain tissue itself. Free space makes up 95% of the mesh, allowing cells to arrange themselves around it.

In 2012, the team showed² that living cells grown in a dish can be coaxed to grow around these flexible scaffolds and meld with them, but this ‘cyborg’ tissue was created outside a living body. “The problem is, how do you get that into an existing brain?” says Lieber.

The team’s answer was to tightly roll up a 2D mesh a few centimetres wide and then use a needle just 100 micrometres in diameter to

inject it directly into a target region through a hole in the top of the skull. The mesh unrolls to fill any small cavities and mingles with the tissue (see ‘Bugging the brain’). Nanowires that poke out can be connected to a computer to take recordings and stimulate cells.

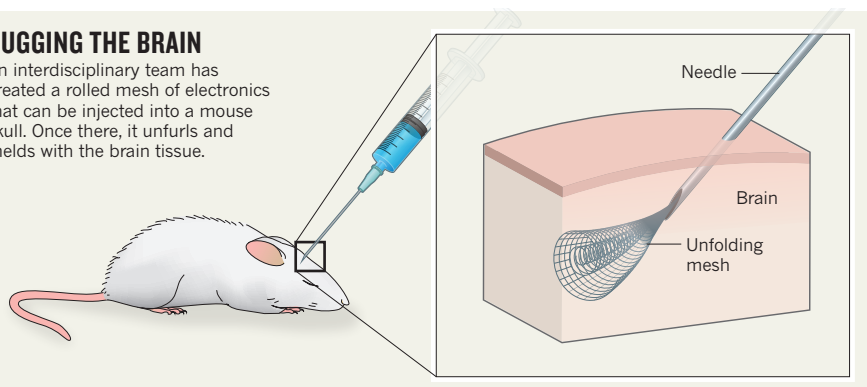
So far, the researchers have implanted meshes consisting of 16 electrical elements into two brain regions of anaesthetized mice, where they were able to both monitor and stimulate individual neurons. The mesh integrates tightly with the neural cells, says Jia Liu, a member of the Harvard team, with no signs of an elevated immune response after five weeks. Neurons “look at this polymer network as friendly, like a scaffold”, he says.

The next steps will be to implant larger meshes containing hundreds of devices, with different kinds of sensors, and to record activity in mice that are awake, either by fixing their heads in place, or by developing wireless technologies that would record from neurons as the animals moved freely. The team would also like to inject the device into the brains of newborn mice, where it would unfold further as the brain grew, and to add hairpin-shaped nanowire probes to the mesh to record electrical activity inside and outside cells.

When Lieber presented the work at a conference in 2014, it “left a few of us with our jaws dropping”, says Yuste. ▶

BUGGING THE BRAIN

An interdisciplinary team has created a rolled mesh of electronics that can be injected into a mouse skull. Once there, it unfurls and melds with the brain tissue.



► There is huge potential for techniques that can study the activity of large numbers of neurons for a long period of time with only minimal damage, says Jens Schouenborg, head of the Neuronano Research Centre at Lund University in Sweden, who has developed a gelatin-based 'needle' for delivering electrodes to the brain³. But he remains sceptical of this technique: "I would like to see more evidence of the implant's long-term compatibility with the body," he says.

Rigorous testing would be needed before such a device could be implanted in people. But, says Lieber, it could potentially treat brain damage caused by a stroke, as well as Parkinson's disease.

Lieber's team is not funded by the US government's US\$4.5-billion Brain Research through Advancing Innovative Neurotechnologies (BRAIN) initiative, launched in 2013, but the work points to the power of that effort's multidisciplinary approach, says Yuste, who

was an early proponent of the BRAIN initiative. Bringing physical scientists into neuroscience, he says, could help to "break through the major experimental and theoretical challenges that we have to conquer in order to understand how the brain works". ■

1. Liu, J. *et al. Nature Nanotechnol.* <http://dx.doi.org/10.1038/nnano.2015.115> (2015).
2. Tian, B. *et al. Nature Mater.* **11**, 986–994 (2012).
3. Lind, G., Linsmeier, C. E., Thelin, J. & Schouenborg, J. J. *Neural Eng.* **7**, 046005 (2010).

BUSINESS

Start-ups fight for a place in Boston's biotech hub

Competition for lab space threatens Kendall Square's innovative spark.

BY HEIDI LEDFORD

A s venture capitalist Kevin Bitterman gets ready to launch his latest start-up, he knows exactly where he wants it to be: Kendall Square, a densely populated neighbourhood in Cambridge and the heart of Boston's booming biotechnology industry. "You can't walk two feet there without seeing someone in biotech," he says. "That kinetic energy of having everybody squished together — it leads to a lot of advantages you can't get outside the city."

But Bitterman, a partner at the firm Polaris Partners in Boston, Massachusetts, finds himself contemplating the unthinkable: exile to the suburbs. Space in Kendall Square has always been tight, but now it is nearly impossible to find — particularly for young start-ups, he says. Two years ago, when he sought a home for another fledgling firm, Bitterman says he could count the options in the area on one hand. "But at least we had one hand of options to look at," he says. "There's literally nothing now."

The Boston-area biotech community is among the largest and densest in the world, with Kendall Square at its epicentre. The neighbourhood squeezes 120 biomedical firms within a 1.5-kilometre radius. The density and diversity of the biotech ecosystem make Kendall unique, says Fiona Murray, associate dean for innovation at the nearby Massachusetts Institute of Technology (MIT) Sloan School of Management. The area is home to biomedical firms large and small, but also to the investors, patent lawyers, contract research organizations and suppliers they need to support them. "There's an extraordinary supply of human talent," says Murray.

But some say that the region may become



Technology and drug firms dominate the Kendall Square neighbourhood of Cambridge, Massachusetts.

a victim of its own success. Since the 1970s, Kendall Square has evolved from an industrial centre dotted with brick factory buildings into a hub of high-tech and biotech firms such as Biogen and Genzyme. Over the past five years, the technology giants Google and Microsoft and the multinational drug firms Novartis and Pfizer have dramatically expanded their offices and laboratories in the neighbourhood, eager to build close relationships with hot start-ups and the academic powerhouses of Harvard University and MIT. The influx threatens to squeeze out the start-up companies that have helped to make Kendall Square what it is. "There are so many benefits of being right here," says Chuck Wilson, who started the cancer-focused firm Unum Therapeutics in Kendall Square last year. The firm is growing so quickly that it will almost certainly need to leave the neighbourhood

within months to get enough space.

At the same time, more-mature homegrown companies such as Alnylam Pharmaceuticals, which develops RNA-based therapies, and cancer-drug developer ARIAD Pharmaceuticals are expanding. "Companies that were only founded a couple of years ago are now gobbling up a lot of space," says Eric Smith, a partner in the Boston office of the commercial-property firm Transwestern.

Young biotechs also compete with high-tech firms so desperate for office space in Cambridge that they are renting buildings designed to accommodate labs. Since the end of 2012, lab rents in the Kendall Square area have risen by 13% to a monthly rate of just over US\$770 per square metre (see 'Up and away'). Over the same period, monthly office rents rose by 26% to just over \$700 per square metre.

Alexandria Real Estate Equities, one of the largest owners of commercial lab space in the region, says that 99% of its Cambridge properties are occupied. In such a competitive market, most landlords will choose established tenants over potentially unstable start-ups. Although Cambridge has added 465,000 square metres of lab space since 2007, most of that has gone to large firms, says Peter Abair, director of economic development and global affairs at the Massachusetts Biotechnology Council in Cambridge.

SHARED SPACES

The local community recognizes that start-ups need to be nurtured for the biotech hub to thrive, says Peter Parker, a co-founder of LabCentral in Kendall Square. One of several local projects created to provide lab space and equipment to help start-ups get off the ground quickly, LabCentral receives state funding as well as corporate sponsorship from large pharmaceutical firms. It plans to double its occupancy in the next two years. MITIMCo, a division of MIT that manages the institution's sizeable property holdings, has also committed to housing start-ups.

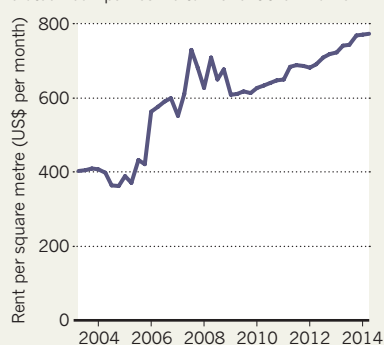
But start-ups may disperse to the suburbs anyway, says José Lobo, who studies urban economies at Arizona State University in Tempe. Kendall Square's story is an anomaly, he says — urban centres around the world have tried to replicate it, mostly without success. And in places where biotech is thriving, such as the San Francisco Bay Area in California and the outskirts of Washington DC, it is more spread out. Having run out of affordable space in Kendall Square, Boston's biotech firms may soon follow that pattern, he says: "I won't be surprised if they leave."

Some already have. Wilson says that Unum Therapeutics is now close to signing a lease on the outskirts of Cambridge. He suspects that more will do the same, forming new start-up clusters in the suburbs. "We'll see how it evolves," he says. "But it'll be a very different feel." ■

SOURCE: TRANSWESTERN REU

UP AND AWAY

The price of lab space in the Kendall Square region of Cambridge, Massachusetts, has risen dramatically over the past decade as drug and biotech companies vie to make it their home.



A medical worker in South Korea handles a sample from a man suspected of having the MERS virus.

SOUTH KOREA

MERS cases spotlight lack of research

Outbreak of Middle East respiratory syndrome in South Korea is controllable, but how it infects humans is a puzzle.

BY DECLAN BUTLER

The world is watching South Korea as the latest outbreak of Middle East respiratory syndrome (MERS) unfolds. But how exactly the virus jumps to humans in the first place is still unknown, and clues to that puzzle lie thousands of kilometres away.

As *Nature* went to press, the cluster of hospital-associated cases in South Korea — the largest MERS outbreak outside the Middle East — had killed 7 people and infected 95, according to the World Health Organization (WHO). Hundreds of schools have been shut. Although the causal coronavirus, MERS-CoV, is considered a potential pandemic threat, specialists told *Nature* that they expect authorities to quickly bring this outbreak under control.

A much bigger challenge than emergency response, they say, is how to stop MERS being transmitted from animals to people in the Middle East, where it is endemic in camels. "The focus on South Korea would be better directed towards Saudi Arabia," says David Heymann, a researcher at the London School of Hygiene and Tropical Medicine and chair of Public Health England, to stop the cases that

continue to spark new outbreaks at the source.

Since it was first detected in Saudi Arabia in 2012, MERS-CoV has infected around 1,200 people worldwide, roughly 450 of whom have died, according to the WHO. The virus is thought to originate in bats and to jump to humans through an intermediate animal, such as camels. It does not easily spread between people, partly because it infects deep areas of the lungs, and is not coughed out. Most of the human infections, however, were the result of human-to-human spread, which can occur in hospitals when certain medical procedures combine with poor infection control to disseminate the virus. The latest clusters began when a South Korean man returned to Seoul from the Middle East, and visited four health-care facilities before he was diagnosed.

There is always a chance that as the virus spreads, it could acquire mutations that allow it to spread more easily between humans. But on 6 June, the South Korean health ministry announced that it had sequenced the virus in the current outbreak and that it was almost identical to past sequences from the Middle East. On the same day, the Chinese Center for Disease Control and Prevention posted a ▶

► separate sequence to the publicly available GenBank database, from a man infected in the South Korean outbreak who then travelled to China, where he felt ill. Christian Drosten, director of the Institute of Virology at the University of Bonn Medical Centre in Germany has analysed this sequence and says that it shows only minor mutations compared with Middle Eastern strains, none in areas of the genome thought to influence infectiousness.

A stream of new cases in South Korea might create the impression that the disease is out of control. But all cases reported so far have clear transmission routes from the initial infection, says Ian Lipkin, an outbreak specialist at Columbia University in New York. The country is now intensively tracing and isolating the contacts of those infected, and implementing strict infection controls in hospitals. Were cases springing up outside of hospitals that would be cause for worry, but that is not happening, says Lipkin.

In the Middle East, however, the virus continues to jump from camels to humans leading to hospital outbreaks. Heymann, who in 2003 led the global effort to contain severe acute respiratory syndrome, or SARS, says that authorities in the Middle East should do more to investigate how people catch the virus from camels.

Such studies would involve investigating the recent activities of infected people, finding out, for instance, whether they had had contact with animal carcasses or bodily fluids, had consumed fluids such as camel milk or urine, or had been near bat colonies. "It's frustrating that all cases from animal infections have not been properly investigated," says Peter Ben Embarek, leader of the WHO's MERS team at the agency's headquarters in Geneva, Switzerland. One obstacle is cultural, in that Saudis tend to be averse to discussing what they consider private matters, he says.

The outbreak in South Korea will probably put pressure on Middle Eastern countries to accelerate research and control of MERS, says Drosten.

Another outstanding mystery is why human cases have not been detected in African countries with large camel populations: Somalia has 7 million camels, and Kenya 3 million, dwarfing Saudi Arabia's population of 260,000. "MERS is circulating in camels in many parts of Africa," says Ben Embarek, "so camel-wise, it's the same picture as in the Middle East." One possibility is that human cases are going undetected because of poor surveillance. Another possibility is that cases in Africa are less likely or less serious, because MERS tends to cause serious illness only in people who have diseases that result from modern lifestyles, such as diabetes, which are more common in Saudi Arabia. ■



NATALIA SHISHLINA

The Yamnaya people are thought to have carried their burial practices and other traditions into Europe.

GENOMICS

DNA deluge reveals Bronze Age secrets

Population-scale studies of ancient genomes hint at roots of technology, languages and diet.

BY EWEN CALLAWAY

Only half a decade after a 4,000-year-old tuft of hair yielded the first ancient-human genome¹, researchers are starting to sequence ancient genomes by the dozen, much as they do with modern genomes.

Such population-scale sequencing is answering long-standing questions about the Eurasian Bronze Age. This tumultuous period between about 3000 BC and 1000 BC saw new technologies and cultural traditions — from the use of finely crafted weaponry and horse-drawn chariots to changes in burial practices — spread across Europe and Asia, starting in the steppe between the Black Sea and the Caspian Sea.

As DNA data flood in, researchers say, the mass-genome approach will paint an increasingly accurate picture of the past and show how ancient events shaped modern humanity — from what we eat to the diseases that ail us. "Christ, what does this mean?" says Greger

Larson, an evolutionary geneticist at the University of Oxford, UK. "In another five years, we'll be talking about tens of thousands of ancient genomes."

The dawn of ancient population genomics is the result of cheap DNA sequencing and the rise of boutique lab techniques that can separate highly degraded ancient DNA from contemporary contaminants.

A team led by palaeogenomicists Morten Allentoft and Eske Willerslev at the Natural History Museum of Denmark in Copenhagen has used these advances to sequence the genomes of 101 people who lived across Eurasia between about 3000 BC and AD 700 (ref. 2). "We could have stopped at 80," says Allentoft. But "we thought, 'Why the hell not? Let's go above 100.'"

The sequences allowed the team to tackle questions that have vexed archaeologists for decades, says Allentoft. For example, researchers have disagreed over whether the cultural changes of the Bronze Age were the result

of migration or simply the spread of ideas. Allentoft and his colleagues found evidence for migration, in the form of a massive shift in the genetic make-up of northern and central Europeans at the start of the Bronze Age. Before 3000 BC, their genomes resembled those of early farmers from the Middle East and even earlier European hunter-gatherers. By 2000 BC, their genomes looked more like those of people from the Yamnaya culture, which arose on the steppe around 2900 BC.

The findings echo those of a team that sequenced 69 ancient Europeans³. Both groups speculate that the Yamnaya migration was at least partly responsible for the spread of the Indo-European languages into Western Europe.

Allentoft's team found genetic traces of the Yamnaya in people who lived near the Altai Mountains in central Russia from 2900 BC to 2500 BC, potentially explaining why Indo-European languages are spoken so far into Asia. "It's pretty clear that these eastern cultures in the Bronze Age are linked to the Yamnaya," says Pontus Skoglund, a population geneticist at Harvard Medical School in Boston, Massachusetts. But he is not yet convinced that the culture's wanderings explain the origins of all Indo-European languages.

Ancient population genomics also offer insights on physical and physiological traits.

Allentoft's team found that the ability to digest milk into adulthood — nearly universal in northern Europeans today — was rare in Bronze Age Europeans, contradicting earlier claims that the trait helped early European farmers to gain calories from milk. Of the 101 sequenced individuals, the Yamnaya were most likely to have the DNA variation responsible for lactose tolerance, hinting that the steppe migrants might have eventually introduced the trait to Europe.

Another team has analysed⁴ DNA from 83 ancient Europeans and discovered that a mutation linked to thick hair and numerous sweat glands, once thought to have emerged in East Asians, was common in Scandinavians as early as 7,700 years ago — potentially revealing a connection between these groups. That analysis, posted on the preprint server bioRxiv in March, also found evidence of evolutionary pressure on height: Iberians seem to have become shorter after farming arrived in what is now Spain and Portugal 8,000 years ago, whereas the Yamnaya who migrated out of the steppe appear to have been taller than their neighbours.

In future, researchers are likely to probe genomes to see how past events shaped modern susceptibility to disease, says Larson. For instance, survivors of the fourteenth century Black Death, which killed around half of Europeans, may have carried gene variants that protect against certain infections.

"It's an interesting time, because the technology is moving faster than our ability to ask questions of it," says Larson, whose lab has also amassed around 4,000 samples from ancient dogs and wolves to chart the origins of domestic dogs. "Let's just sequence everything and ask questions later." ■ [SEE NEWS & VIEWS P.164](#)

1. Rasmussen, M. *et al.* *Nature* **463**, 757–762 (2010).
2. Allentoft, M. E. *et al.* *Nature* **522**, 167–172 (2015).
3. Haak, W. *et al.* *Nature* <http://dx.doi.org/10.1038/nature14317> (2015).
4. Mathieson, I. *et al.* Preprint at bioRxiv <http://dx.doi.org/10.1101/016477> (2015).

CLARIFICATIONS

It could have been clearer in the News story 'Ebola R&D woes spur action' (*Nature* **521**, 405–406; 2015) that the US Food and Drug Administration was not consulted about or involved in the design of the brincidofovir study; the agency advocated generally for randomized clinical trials on drugs against Ebola. In the News Feature 'CRISPR, the disruptor' (*Nature* **522**, 20–24; 2015), the June 2012 entry in the graphic entitled 'The rise of CRISPR' was ambiguous. The researchers had targeted the CRISPR system to specific DNA sequences, highlighting its potential for genome editing.



THE MILITARY-BIOSCIENCE COMPLEX

THE US DEPARTMENT OF DEFENSE IS MAKING A BIG PUSH INTO BIOLOGICAL RESEARCH — BUT SOME SCIENTISTS QUESTION WHETHER ITS HIGH-RISK APPROACH CAN WORK.

BY SARA REARDON

When Geoffrey Ling talks about the future of technology, his ideas go flying around the room like a whirlwind. Ling eagerly describes a world in which people live far beyond their natural lifespans, minds can be downloaded into external ‘hard drives’ for enhancement by artificial intelligence and robots and aircraft are controlled by human thought.

“It’s abso-posi-frickin-lutely going to happen,” he declares. “The next 20 years are going to make our heads spin, because we’ve already crossed over into that realm.”

Ling should know: he is doing as much as anyone to make these

visions real. A neurologist by training, he is also a US Army colonel and director of the first biology funding office to operate within the Defense Advanced Research Projects Agency (DARPA), the Pentagon’s avant-garde research arm. The Biological Technologies Office (BTO), which opened in April 2014, aims to support extremely ambitious — some say fantastical — technologies ranging from powered exoskeletons for soldiers to brain implants that can control mental disorders.

DARPA’s plan for tackling such projects is being carried out in the same frenetic style that has defined the agency’s research in other fields. Ever since it was created in 1958, a year after the Soviet Union beat the United

A prosthetic arm developed at Johns Hopkins University and funded by DARPA can be controlled by the wearer's own nerves.

States into space by launching the world's first artificial satellite, Sputnik, the agency's mission has been to prevent any more such surprises by getting there first. So DARPA's programme managers at the BTO are free to pour tens of millions of dollars into ambitious projects without waiting around for niceties such as peer review. And by working closely with its contractors as they develop their technology, the agency aims to drive discoveries across the often-deadly gap between basic research and commercialization.

That aggressive, high-risk strategy has had spectacular pay-offs — most famously with the agency's development of the Internet in the 1970s. And that has happened often enough to inspire imitators such as ARPA-E, a branch of the US Department of Energy that is devoted to high-risk research into alternative energy sources.

But some wonder whether DARPA's full-speed-ahead model will work as well for biology as it has for the physical sciences and hardware. Living systems are much more complex, they argue, with a multitude of variables that are either unknown or difficult to engineer and control. And because so much of the agency's biological research is directly applicable to humans, the work is fraught with ethical concerns — not to mention the possibility that even the most benign-sounding developments could be co-opted for war. Synthetic organisms designed to produce greener biofuels could also make explosives, for example, and brain-stimulation technology intended to heal wounded soldiers could also enhance combat abilities.

Edward Hammond, a biology-policy consultant in Austin, Texas, wonders whether the agency often has ulterior motives when it contracts researchers. "You don't ever really know what DARPA wants," he says. "But they're pretty good at finding people who are resolving questions they're interested in for other reasons."

Still, many biologists are willing to accept money from the Department of Defense (DOD), on the grounds that innovations such as better prosthetics and improved mental-health treatments are needed no matter who is paying for them. And Ling insists that DARPA understands the concerns: every programme in the BTO has a bioethics advisory board. Besides, he says, if visionary biotechnologies are inevitable, then it is DARPA's duty to race ahead and invent them.

"Some people think it's scary," he says, contemplating that future. "But I think it's rather exhilarating."

TIME TO COMBINE

DARPA's embrace of bioscience began in earnest in 2001, when anthrax spores posted to media offices and members of the US Congress brought concerns about bioterrorism to the fore. Then came the wars in Afghanistan and Iraq, which led the agency to invest in fields such as neuroscience, psychology and brain-computer interfaces — all with the intention of helping injured veterans. By 2013, the number of biology-related programmes had grown such that DARPA decided to consolidate them under one roof. The natural choice to head the new office and its US\$288-million annual budget was Ling, who was deputy director of DARPA's science division at the time.

The office will certainly speed up research, says George Dyson, an independent science historian in Bellingham, Washington, and not least because of the military's culture of completing missions quickly, without lengthy reflection or debate. Looking at what DARPA has already done in fields such as computing, says Dyson, "it's always the military who move quickly enough to fund the interesting things".

A good example is DARPA's reaction to US President Barack Obama's 2013 announcement of the BRAIN initiative: a high-profile, multi-agency effort to understand the circuitry of the brain. The National Institutes of Health (NIH) spent months designing a ten-year strategic plan for the initiative before distributing its share of the money, and the National Science Foundation (NSF) opened a competition for its spending

share to any research project related to brain networks. But DARPA quickly funnelled more than \$50 million into just a few five-year programmes.

These efforts now fall under the remit of the BTO. One, called Restoring Active Memory, is attempting to create a stimulation device that restores soldiers' ability to form memories after brain damage. Another, called SUBNETS (System-Based Neurotechnology for Emerging Therapies), is developing a brain implant that can treat seven mental and neurological disorders. As a first step, both projects are monitoring the brain activity of people with epilepsy who have had temporary electrodes implanted to locate the origin of their seizures. The investigators ask these patients to carry out memory exercises, or to perform tasks that involve neural pathways that might be impaired in addiction or depression, and record the electrical patterns that result.

The pay-offs could still be some way off, however. "There's no question this is a very ambitious goal," says Edward Chang, a neurosurgeon at the University of California, San Francisco, who co-leads one of the SUBNETS teams. "I don't think anyone is naive enough to think they'll be easily solved in the next five years."

As ambitious as DARPA is, however, its funding process can be unsettling for researchers who are accustomed to elaborately peer-reviewed grants from civilian agencies. At DARPA, much of the authority is vested in the programme managers, who rotate in and out from academia, industry and the armed services. They alone design the initiatives, invite researchers to apply for contracts with specific goals and milestones and select the groups they think are most likely to achieve the goals. Then they work closely with the researchers to guide the project as it proceeds.

DARPA calls its grant recipients 'performers' — and if they do not meet their milestones, the axe can fall quickly. In 2007, for example, DARPA started a programme called RealNose: an effort to develop a synthetic dog nose with real olfactory receptors for detecting odorants such as chemical weapons. But the agency killed the programme three years later, after it became clear that the receptor proteins were too unstable at room temperature.

"IT'S ALWAYS THE MILITARY WHO MOVE QUICKLY ENOUGH TO FUND THE INTERESTING THINGS."

Researchers who follow DARPA's choreography are almost always free to publish their results, says BTO deputy director Alicia Jackson: very few of the agency's projects are classified as secret. But DARPA grant recipients do give up a certain amount of freedom: if they come across an interesting scientific question as they work, for example, they cannot use DARPA funding to pursue it. "Initially it was a change in culture," says Emad Eskandar, a neurosurgeon at Massachusetts General Hospital in Boston and director of one of the SUBNETS programmes. But Eskandar and his partner, psychiatrist Darin Dougherty, maintain that DARPA's oversight has made the project better. "It's helped us to focus and move ahead," Dougherty says.

Certainly, Ling is determined to prove that DARPA's model can work as well for biologists as for military contractors. One of his favourite successes is a prosthetic arm that DARPA developed in collaboration with the biotechnology firm DEKA in Manchester, New Hampshire. The device works by picking up the electrical signals that travel from the brain's motor cortex into nerves in the stump, then translating those signals into the appropriate motions of the attached prosthetic hand. This allows wearers to perform difficult tasks such as handling soft fruit and even rock climbing. The device won approval from the US Food and Drug Administration last year — the first nerve-controlled prosthetic to do so — and the company says that it is now working on commercialization. Similar arms are being developed for DARPA at

➔ NATURE.COM
To hear a podcast
on DARPA's biology
push, see:
go.nature.com/cotlqx



An exoskeleton designed through DARPA's Warrior Web programme enhances soldiers' physical abilities.

the Johns Hopkins University in Baltimore, Maryland, and elsewhere; all of them are also being tested in people with paralysis in the hope that brain implants can translate their intentions into electrical signals that drive the hand.

The BTO has also taken over DARPA's health programmes, including one that is seeking to turn bacteria that prey on other bacteria into therapeutic antimicrobial agents. Other programmes have more obvious military applications, such as an exoskeleton that boosts a soldier's strength and speed. A programme called Narrative Networks studies how the brain reacts to different stories and arguments, which could be helpful for planning how to convince a disaster-stricken village to accept US military aid, or to turn terrorists away from their agendas. And several synthetic-biology initiatives are making biological systems that can be programmed to produce any compound a user wants, including some that do not exist in nature. These could include materials for making lightweight body armour, coatings for strengthening equipment, tissues that can be used to repair wounds, and more-efficient biofuels.

Ling and his DARPA colleagues revel in such ideas — the more far out, the better. “We look for ways to say yes, not no,” he says.

For all its breakthrough successes, however, there is little evidence that DARPA's fast-track approach is consistently any better than peer review at choosing winners. “They’ve been successful when they’ve been successful,” says Jonathan Moreno, a bioethicist at the University of Pennsylvania in Philadelphia. A DARPA spokesperson says that the agency cannot determine how often goals are met or contracts are cancelled. One reason is that the goalposts keep moving: if a project starts to seem unfeasible, programme managers often change the criteria for success and salvage what they can rather than cancelling the contract. Another is that unlike civilian agencies such as the NSF and the NIH, DARPA does not make public the grants that it makes. Nor does it conduct internal analyses that could determine whether its programme managers are choosing the best teams and paying for the best science that they possibly could.

“To me, that’s a big problem,” says Pierre Azoulay, an economist at Massachusetts Institute of Technology in Cambridge. “Pointing to great successes is not enough,” he says. The agency’s idea of programme evaluation is “very much in the mode of, ‘Look, the Internet!’”

But Jackson literally laughs at the idea that the BTO should be more introspective. The office’s budget is 1% of the size of the NIH’s, she says, with little margin for overhead costs. And besides, she says, “we go with whoever can get the job done” — never mind factors such as experience or lab size. “I think we have a really good track record in our 50-plus-year history,” she says. Listing DARPA’s successes, she starts with the Internet.

But if DARPA is not slowing down to evaluate its successes, is it evaluating the effect they could have on society? Ling says yes, pointing

to the ethicists who provide ongoing guidance on the implications of the BTO’s work. That is far beyond the level of scrutiny given to most NIH- and NSF-funded projects, notes James Giordano, a neuroethicist at Georgetown University in Washington DC, and an adviser on SUBNETS. Usually, these undergo ethics evaluation only at their beginning or end. Moreno agrees. “The irony is that people think the national-security world is so far behind the civilian world on these things,” he says. “But again and again, DOD has been ahead.”

Nevertheless, some researchers continue to be sceptical. At Oregon Health & Science University in Portland, emeritus neuroscientist Curtis Bell worries that technologies such as brain stimulation could be used to subdue people, in a similar way to the prefrontal lobotomies that were used in the mid-twentieth century to deal with some troublesome prisoners. “You could imagine such things being more sophisticated nowadays,” he says. “You wouldn’t need to damage all the frontal lobes if you could go to a specific nucleus and alter someone’s personality.”

Dyson points out that there is no guarantee that the Pentagon will actually listen to ethicists’ concerns — or to DARPA’s. “Some of these technologies are absolutely fascinating and intriguing and hold all this promise for good, but they’re very close to being weaponized easily,” he says. And, says Moreno, although many people in the military think deeply about the implications of new technologies, the worry is that the political authorities above them may not allow them much freedom to slow down or change direction.

Of particular concern are the BTO’s synthetic-biology programmes. The Pentagon has talked about engineering bacteria to clean up sites contaminated by radiation or chemical weapons, stoking fears that

THE AGENCY’S IDEA OF PROGRAMME EVALUATION IS “VERY MUCH IN THE MODE OF, ‘LOOK, THE INTERNET!’”

these organisms could get out of control when released into the environment. Although there is no reason to think that the United States is creating synthetic biological weapons, some fear even the intimation that microbes are strategically useful. “It’s sending a signal that there’s a role for synthetic-biology products for use in the field,” says Hammond. “I would be concerned about that, and I’m concerned that DARPA doesn’t seem to be.”

But other researchers are more supportive of the BTO. Ultimately, says Giordano, it may not matter who funds the research and who accepts the funding, because anyone can use published research for their own ends. “Individuals who look at DOD funding as Darth Vader science don’t recognize that any science can be channelled through Darth Vader channels.”

That is exactly why Ling feels that DARPA needs to jump into controversial science without hesitation: if the United States does not do it, someone else will. “The only thing we can do is do the work,” he says, “but do it in a way where we’re thinking about the untold consequences and how to mitigate them.”

Ling says that he plans to keep expanding his office over the next year — how far depends on funding — to anticipate surprises coming from any sector. The BTO currently has 11 programme managers specializing in fields from infectious disease to natural ecosystems, and is looking to expand its repertoire to even more-far-flung fields such as palaeontology and astronomy. An expert in exoplanets, Ling says, could develop projects in preparation for the possibility of threats from outer space as well as the more likely scenario that signs of life will be discovered on another planet. “That is without a doubt going to be the most exciting scientific news in the history of mankind,” he says. “And I’d love for it to be funded by DARPA.” ■

Sara Reardon is a reporter for Nature in Washington DC.



Super vegetables

Long overlooked in parts of Africa, indigenous greens are now capturing attention for their nutritional and environmental benefits.

One lunchtime in early March, tables at Nairobi's K'Osewe restaurant are packed. The waiting staff run back and forth from the kitchen, bringing out steaming plates of deep-green African nightshade, vibrant amaranth stew and the sautéed leaves of cow-peas. The restaurant is known as the best place to come for a helping of Kenya's traditional leafy green vegetables, which are increasingly showing up on menus across the city.

Just a few years ago, many of those plates would have been filled with staples such as collard greens or kale — which were introduced to Africa from Europe a little over a century ago. In Nairobi, indigenous vegetables were once sold almost exclusively at hard-to-find specialized markets; and although these plants have been favoured by some rural populations in Africa, they were largely ignored by seed companies and researchers, so they lagged behind commercial crops in terms of

BY RACHEL CERNANSKY

productivity and sometimes quality.

Now, indigenous vegetables are in vogue. They fill shelves at large supermarkets even in Nairobi, and seed companies are breeding more of the traditional varieties every year. Kenyan farmers increased the area planted with such greens by 25% between 2011 and 2013. As people throughout East Africa have recognized the vegetables' benefits, demand for the crops has boomed.

This is welcome news for agricultural researchers and nutritional experts, who argue that indigenous vegetables have a host of desirable traits: many of them are richer in protein, vitamins, iron and other nutrients than popular non-native crops such as kale, and they are better able to endure droughts and pests. This makes the traditional varieties a potent weapon against dietary deficiencies. "In Africa,

malnutrition is such a problem. We want to see indigenous vegetables play a role," says Mary Abukutsa-Onyango, a horticultural researcher at Jomo Kenyatta University of Agriculture and Technology in Juja, Kenya, who is a major proponent of the crops.

Scientists in Africa and elsewhere are now ramping up studies of indigenous vegetables to tap their health benefits and improve them through breeding experiments. The hope is that such efforts can make traditional varieties even more popular with farmers and consumers. But that carries its own risk: as indigenous vegetables become more widespread, researchers seeking faster-growing crops may inadvertently breed out disease resistance or some of the other beneficial traits that made these plants so desirable in the first place.

"It is important

Women sell African nightshade and other green vegetables at a market in Nairobi.

PETE MULLER/PRIME FOR NATURE that when we promote a specific crop, that we try to come up with different varieties,” says Andreas Ebert, gene-bank manager at the World Vegetable Center (AVRDC), an agricultural-research organization based in Shanhua, Taiwan. If the increasing popularity of these vegetables limits choices, he says, “the major benefits we are currently seeing will be lost”.

PROTEIN FROM PLANTS

For Abukutsa, indigenous vegetables bring back memories of her childhood. Cow’s milk, eggs and some fish made her ill, so doctors advised her to avoid all animal protein. Instead, the women in her family made tasty dishes out of the green vegetables that grew like weeds around her house. Her mother often cooked the teardrop-shaped leaves of African nightshade (*Solanum scabrum*), as well as dishes of slimy jute mallow (*Corchorus olitorius*) and the greens of cowpeas, known elsewhere as black-eyed peas (*Vigna unguiculata*). One grandmother always cooked pumpkin leaves (*Cucurbita moschata*) with peanut or sesame paste. Abukutsa relished them all and ate the greens with ugali, a polenta-like dish common in East Africa.

She chose to pursue a career in agriculture because she wanted to “unravel the potential hidden in African indigenous vegetables”, she says. Now, she is considered a leader across Africa, and increasingly around the world, in a robust, rapidly growing field. “She’s almost like the mother of indigenous vegetables in Kenya,” says Jane Ambuko, head of horticulture at the University of Nairobi.

Abukutsa started out in the early 1990s, surveying and collecting Kenya’s indigenous plants to investigate the viability of the seeds that farmers were using. In the decades since, she has come to focus mainly on the vegetables’ nutritional properties.

Today, she is far from alone. The AVRDC has a dedicated research and breeding programme at its office in Arusha, Tanzania, and the Kenya Agricultural and Livestock Research Organization in Nairobi does similar work. Other health and agriculture organizations in both East and West Africa focus on boosting consumer use and improving the viability and yield of these crops. That fits into a global trend emphasizing bioregional foods — using crops that are well adapted for a given climate and environment, rather than foreign plants that tend to be less nutritious and require extra water or fertilizers.

Most of the indigenous vegetables being studied in East Africa are leafy greens, almost all deep green in colour and often fairly bitter. Kenyans especially love African nightshade and amaranth leaves (*Amaranthus* sp.). Spider plant (*Cleome gynandra*), one of Abukutsa’s favourites for its sour taste, grows wild in East Africa as well as South Asia. Jute mallow has a texture that people love or hate. It turns slimy when cooked — much like okra. Ebert says

that moringa (*Moringa oleifera*) is not only one of the most healthful of the indigenous vegetables — both nutritionally and medicinally — but it is also common in many countries around the world.

Research by Abukutsa and others shows that amaranth greens, spider plant and African nightshade pack substantial amounts of protein and iron — in many cases, more than kale and cabbage¹. These vegetables are generally rich in calcium and folate as well as vitamins A, C and E (ref. 2).

Researchers risk eliminating the traits that make indigenous vegetables so desirable in the first place.

In recent years, Abukutsa has been studying how to maximize nutritional benefits using different cooking methods. Compared with raw vegetables, boiled and fried greens contain much more usable iron³ and could help to combat the high rates of anaemia in parts of East Africa. They can also be important sources of protein, she says. “Some people just live on vegetables, and they cannot maybe afford meat.”

Abukutsa is currently studying the antioxidant activity of indigenous vegetables, as well as how resilient they are to the effects of climate change. Most of the traditional varieties are ready for harvest much faster than non-native crops, so they could be promising options if the rainy seasons become more erratic — one of the predicted outcomes of global warming. Slenderleaf (*Crotalaria* sp.) is particularly hardy during drought because it quickly establishes its taproot. “If we have a short rain because of climate change, it can survive,” she says. She is working with other research partners to select vegetables with increased tolerance for variations in rainfall and temperature.

Early on, Abukutsa recognized that she needed to do more to convince people to add indigenous vegetables to their diets. Since around 2000, she has led public education campaigns and worked with restaurants and supermarkets around Kenya to find out what

they would need to start selling these foods. A simple but significant problem was that people did not know how to cook the vegetables.

Unlike larger leafy vegetables such as kale, many of the indigenous varieties have small leaves that must be separated from their stems individually before cooking — a laborious process. Recipes are often vegetable-specific; spider plant can be cooked with sour milk, for example, but cowpea leaves go better with soya bean or peanut paste. Although older generations and some rural populations know what to do with nearly any local vegetable, much of the region’s traditional cooking knowledge has been lost. So Abukutsa got to work on collecting and testing recipes to maximize the amount of iron and other nutrients the dishes contain. K’Osewe was one of the first restaurants to take an active interest, and others soon followed.

For Abukutsa, indigenous vegetables are not just a research subject — they remain a central part of her own diet. “Today at lunchtime, I ate pumpkin leaves and nightshade,” she says.

The vegetables’ new-found popularity is spreading throughout East Africa. At a bustling market in Arusha, a young woman wearing a light-blue headscarf shops for sweet-potato leaves (*Ipomoea batatas*), known locally as matembele, which have a reputation for improving the blood. She buys them from an elderly woman who sells almost exclusively indigenous vegetables under a large red umbrella that protects her stock from the afternoon sun. She says her sales of such plants have climbed substantially over the past five years.

GLOBAL APPEAL

Green vegetables are not the only indigenous crops attracting researchers’ attention. In the 1990s, the US National Research Council (NRC) in Washington DC convened a panel to examine the potential of Africa’s ‘lost crops’, including grains, fruits and vegetables. Chaired by renowned agricultural researcher Norman Borlaug, the panel concluded that native plants held tremendous potential for improving food security and nutritional intake across Africa, and should be a greater focus for researchers⁴. Today, the World Agroforestry Centre in Nairobi is studying a range of Africa’s more than 3,000 indigenous fruit species, and finding that they are generally more nutritious, drought-tolerant and pest- and disease-resistant than their exotic counterparts.

But vegetables have gained the most notice, both in the marketplace and among researchers. Raymond Vodouhe, a plant breeder and geneticist with Bioversity International in Cotonou, Benin, says that his team’s work in West Africa has focused on domesticating wild vegetables. The hardy wild plants help African families to get through periods of drought or crop failure, but are threatened by deforestation and other types of land-clearing. By domesticating them, researchers can give farmers more-reliable access to indigenous vegetables so that they can better endure lean times.

The AVRDC is doing active research on native species in Asia and Oceania, as well

➔ **NATURE.COM**
To see some of Africa’s super greens, visit:
go.nature.com/fh7496



Nightshade and other indigenous vegetables helped to sustain Mary Abukutsa-Onyango when she was a child. She went on to pioneer research in these crops.

as Africa. “A rich diversity of indigenous vegetable species exists throughout these areas,” says Ebert, pointing to okra and African eggplant (*Solanum aethiopicum*) in Mali, bitter melon (*Momordica charantia*) and Malabar spinach (*Basella alba*) in India, and slippery cabbage (*Abelmoschus manihot*) in the Pacific Islands. “The challenge we face is selecting which indigenous vegetable species to study — with more than 2,000 plants that can be considered and consumed as vegetables, and very limited research funds, it’s a tough choice.” Less than 10% of the AVRDC’s roughly US\$20-million annual budget goes to studying indigenous vegetables, he says.

A main focus has been basic problems such as difficulties with germination and a lack of information about how best to store seeds. Indigenous vegetables are not up to modern farming standards for characteristics such as uniformity of seeds and yield, so there is a lot of catching up to do.

But efforts to improve indigenous vegetables could come at a cost, say researchers. If breeders focus only on increasing yields, they could accidentally eliminate nutritional benefits. And if farmers seek to drive up production through monocrop agriculture — planting just one crop — they risk losing some of the qualities that make these vegetables such a draw. Plots with single crops, for example, face higher risks of being completely wiped out by insects or diseases.

At the AVRDC’s office in Arusha in late February, vegetable breeder Fekadu Dinssa walks through a screened enclosure filled with plants used for breeding. He surveys a table

covered with starter trays of little amaranth plants from 57 breeding lines. In one tray, the plants are twice as tall as their neighbours, but their pale colour will not be popular in the market, he says. Dinssa wants to breed the fast-growing trait into other lines to develop a new type of commercially viable amaranth. It is a trial-and-error process that can take years.

STRENGTH IN DIVERSITY

As indigenous vegetables are planted in greater numbers, it will be a challenge to prevent less-common varieties from disappearing, say researchers. That could threaten the crops’ resilience, because different varieties can carry separate genes for resistance to pathogens and pests. Loss of diversity could also limit the vegetables’ appeal. In Kenya, for example, coastal communities tend to like giant African nightshade, whereas western communities prefer a variety with smaller leaves that has a much more bitter taste.

Some narrowing of choices has already happened. Simlaw Seeds in Nairobi, a division of Kenya Seed Company, sells only a couple of varieties each of amaranth and African nightshade, chosen because they are the most popular at the national level. “Of course it’s a concern, because practically speaking, we can’t promote them all,” says Abukutsa. She and other researchers compromise by promoting certain types while trying to preserve the full diversity in gene banks in Kenya and at the AVRDC. The researchers also encourage communities to continue growing the varieties they have traditionally favoured.

Calestous Juma, director of the Science,

Technology, and Globalization Project at Harvard University in Cambridge, Massachusetts, sees these efforts as crucial. And with advances in genomics, he says, researchers should seek ways to improve indigenous crops — by lengthening their shelf life, for example — and to use them in breeding other plants. “They may have traits that may be useful for other crops.”

Juma, who served on the NRC’s lost-crops panel, urges more agricultural research centres in Africa to study these vegetables. The work that Abukutsa and her colleagues are doing, he says, “should be done at every university.”

On a hot Wednesday morning in March, Abukutsa walks around the university campus to survey some of her students’ work. One has spread amaranth leaves in a wooden box in the sunlight to test how drying will alter the plants’ nutritional profile. Abukutsa stops to talk to another student standing amid dozens of rows of recently sprouted African nightshade plants, part of an experiment on their genetic diversity. “We’ve come so far,” Abukutsa says, “but there’s still so much to be done.” ■

Rachel Cernansky is a freelance writer in Denver, Colorado.

1. Abukutsa, M. O. O. *African Indigenous Vegetables in Kenya: Strategic Repositioning in the Horticultural Sector* (JKUAT, 2010).
2. Yang, R.-Y. & Keding, G. B. in *African Indigenous Vegetables in Urban Agriculture* (eds Shackleton, C. M., Pasquini, M. W. & Drescher, A. W.) Ch. 4 (Earthscan, 2009).
3. Habwe, F. O., Walingo, M. K., Abukutsa-Onyango, M. O. & Oluoch, M. O. *Afr. J. Food Sci.* **3**, 393–397 (2009).
4. NRC. *Lost Crops of Africa: Volume II: Vegetables* (National Academies Press, 2006).

COMMENT

REPRODUCIBILITY Biologists urged to use mouse repositories **p.151**



PALAEoANTHROPOLOGY A history of lumpers, splitters, rogues and rivalries **p.154**

CAREERS Use leisure of retirement to mine the literature **p.156**

CONSERVATION Phosphate mining threatens Pacific atoll culture and wildlife **p.156**



Pull together for fusion

ITER director-general **Bernard Bigot** explains how he will strengthen leadership and management to refocus the project's aim of harnessing nuclear fusion.

Ten years ago this month, China, the European Union, Japan, South Korea, Russia and the United States agreed on the location for the world's largest nuclear-fusion experiment: ITER, the International Thermonuclear Experimental Reactor, which they had decided to build jointly. India joined six months later. The project's aim is to fuse two isotopes of hydrogen — tritium and deuterium — to deliver a powerful, clean source of electricity. This requires the containment of plasma at temperatures ten times higher than the Sun's core.

Roughly €4-billion (US\$4.4-billion) worth of construction contracts and €3 billion in manufacturing contracts worldwide are under way. The first large components are

being delivered to the site at St-Paul-lez-Durance in southern France for assembly.

The project has been plagued by delays and difficulties. The seven ITER members are designing and manufacturing key components. When deadlines or standards are not met, the knock-on effects across the whole project can be dire. Late contracts for tools have kept one of the largest buildings — in which ring-shaped magnets up to 24 metres in diameter will be manufactured — inactive since its completion in December 2011. When problems arise, bickering ensues as to who should foot the bill.

I have been a privileged observer from the start, as the high representative for ITER in the host country, France. Because France itself is not a formal member of

ITER — it contributes to the European Union budget for the project and to some basic site infrastructures — I, like many others, could only witness with frustration the slipping of the schedule despite the best efforts of the more than 2,000 dedicated people working on ITER.

Since becoming director-general of the ITER Organization, which manages the project, in March, I have realized that ITER's main problem has been the lack of a clearly defined authority to oversee the entire project. Having someone firmly in the driving seat, with the power to take decisions, is the key to success in any project. I have learned this over the course of my career — through building an innovative higher-education institute from scratch (École Normale ►

ILLUSTRATION BY DAVID PARKINS

► Supérieure de Lyon) and as head of the French Alternative Energies and Atomic Energy Commission for 12 years.

Here, I set out my vision for ITER. The project must overcome its organizational problems so that it can deliver on its promise of taking a firm step towards harnessing an unlimited, continuous, safe and clean source of energy. These lessons apply to any major international collaboration.

A ROCKY TRANSITION

Since construction began on ITER five years ago, it has become increasingly apparent that the project's management structure is poorly adapted to the challenge of building a large, complex research facility.

Take the 8,000-tonne ITER vacuum vessel, the doughnut-shaped central component of the 'tokamak' reactor that houses the fusion reactions. Seven of its nine sectors are to be manufactured in Europe and two in South Korea, with each region or country taking responsibility for how they are sourced. Having two contractors is a risk, because each has its own manufacturing techniques; duplicating the processes that validate the quality and function of components, such as fabricating mock-ups, adds to the cost; and the tolerance margins that each contractor has adopted differ. Yet the ITER Organization is responsible for assembling the final vessel.

Any modification has a cascading impact on other components. This has generated an almost endless to-and-fro between the ITER

Organization, procuring member countries and suppliers. This situation has already cost ITER tens of millions of euros.

People know there is a problem. A 2013 management-assessment report described the decision-making process at the ITER Organization as "ill-defined and poorly implemented". The management structure has proved incapable of solving issues and responding to the project's needs, so accumulating technical difficulties have led to stalemates, misunderstandings and tension between staff around the world. These problems stem from how the organization was set up through an international treaty in 2007 (see 'The Promethean dream').

First, deputy director-generals from each member country or region were given responsibility for one large technical or administrative department of the ITER Organization. These managers also acted as official representatives for their nation or nations.

Second, the procurement of components, systems and buildings is split among the member states so that each could gain experience. The work is assigned according to the industrial capacities of members and a cost-sharing scheme that allocates 45.5% to the European Union (as the host) and just over 9% to each of the others. Each member has a

"Is it possible to realize the Promethean dream of bringing the fire of the Sun down to Earth?"

procurement centre, called a domestic agency, that is legally and administratively independent from the central ITER Organization.

The organization is responsible for validating the design of the facility; compliance with safety regulations; coordination of manufacturing and quality control of the numerous components; their on-site assembly; and later, the operation of the facility.

Paperwork abounds. For each work package, the organization signs a procurement arrangement with the relevant domestic agency that details all technical specifications and management requirements. The domestic agency then launches a call for tender to select a company or consortium to do the work.

Such a system has benefits: procurements are shared widely, industries in member states develop, spin-offs are generated, jobs are created and specialists trained. Intellectual property generated by the project is shared. But it has become ever more obvious — as successive reports have pointed out — that the costs outweigh the benefits.

TEAM BUILDING

I accepted the job of director-general on the condition that the position was newly invested with full authority over the whole project. Authority and a radical redefinition of how the organization interacts with the domestic agencies are at the core of the action plan that I submitted to the ITER Council in January, before my formal appointment.

The domestic agencies will retain their distinct legal identity. But they will be integrated functionally and put on an equal footing with the departments in what we now call the ITER Organization Central Team, based in St-Paul-lez-Durance.

A new executive project board brings together the managers of the central team and the domestic agencies at least once a month, in person or by video conference. Disputes can be settled and decisions taken swiftly.

Technical issues — from construction to radioprotection and cryogenics — are handled by project teams of 20 to 50 people, depending on the scope. They comprise staff from the central team and domestic agencies on the basis of technical need, professional skills and experience. When necessary, representatives of contracting industries participate.

It is too late and costly to reverse decisions that have already been made — such as how the tokamak vacuum vessel is fabricated. Problems must be solved downstream; in April, the executive project board formed a joint ITER Organization and domestic agency project team to anticipate and overcome integration and assembly issues. Had this decision been taken earlier it would have saved time, money and frustration.

NUCLEAR FUSION

The Promethean dream

ITER has been political from the start. At a meeting in Geneva, Switzerland, in November 1985, then US President Ronald Reagan and leader of the Soviet Union Mikhail Gorbachev proposed an international effort to develop fusion energy "as an inexhaustible source of energy for the benefit of mankind". Easing geopolitical tensions at the height of the cold war was one of their motives. ITER engaged political leaders in a common venture for the good of all. It gave scientists and engineers around the world an opportunity to acquire knowledge and expertise to lead fusion from research to the commercial phase.

Fusion energy — produced by the melding of the nuclei of light atoms into heavier ones — powers the Sun and stars. Since discovering this in the 1920s, scientists have hoped to recreate fusion reactions and reap the energy produced to generate electricity. ITER's completion will answer the question that has obsessed

three generations of physicists and engineers: is it technologically possible to realize the Promethean dream of bringing the fire of the Sun down to Earth?

Because of the turbulence that arises in a confined, magnetized plasma, a fusion machine aiming for a significant energy gain must be large. The ring-shaped ITER reactor will be about 29 metres high and 29 metres in diameter, housed in a building that will be comparable in size to the Arc de Triomphe in Paris. It requires huge human and financial investment. No nation has the resources to go it alone.

Twenty years on, ITER has seven partners — China, the European Union, India, Japan, South Korea, Russia and the United States — and is managed by the ITER Organization, which was established on 24 October 2007 by an intergovernmental treaty. The design is settled: ITER will be a 'tokamak' (from the Russian acronym for 'toroidal chamber with magnetic coils'). Construction is under way in France.

The ITER Organization and domestic agencies together employ 2,000 people. Changing how ITER is managed will alter its culture. I aim to foster an atmosphere in which each party or individual feels personally responsible for the whole project, not just their area of competence. One of my first actions after becoming director was to address the staff of each domestic agency. The most striking moment was in a video session with all four Asian agencies. For the first time, colleagues in Japan, India, South Korea and China saw the faces of their counterparts, changing the dynamic towards a shared global ambition.

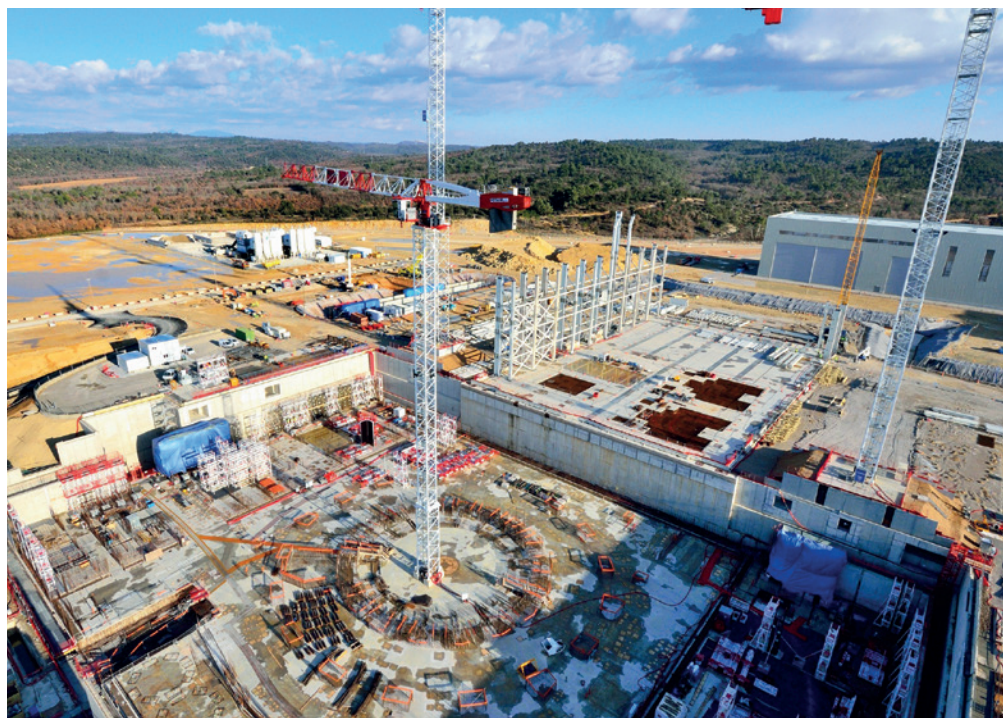
I am also implementing a new type of mobility throughout the project. This will enable appropriate domestic-agency staff to be temporarily seconded to the ITER site, or central-team staff to be assigned to domestic agencies.

The ITER Council has agreed to this new organization. I am grateful for their strong support and the progress already made in solving technical issues and improving communication.

DISCRETIONARY FUND

There is still much more to do. Authority requires the financial means to exercise it. I have asked for the creation of a reserve fund, to be put at my disposal. Each domestic agency will contribute, allowing me to take quick and efficient decisions to address issues as they arise. Terms of reference will be presented to the council in June for approval. The money will be drawn from the contributions of the ITER members in proportion to the amount they pay in.

In my experience of industrial projects, a reserve fund must comprise about 20% of



Construction at St-Paul-lez-Durance, France, site of the ITER nuclear-fusion experiment.

fabrication costs over the duration of construction. In my view, it was naive not to establish such a fund much earlier in ITER's history.

Before the end of this year, I am expected to submit, along with all stakeholders, an updated, robust and reliable schedule to the ITER Council, and a cost and risk analysis. With renewed management and a streamlined organization, we are now ready to prepare for the assembly and commissioning phase, the step before fusion switches on.

Further delays and costs are inevitable.

ITER will meet these challenges if it has the unanimous political support of the seven members, on the basis of the long-term value of fusion technology.

All of us at ITER have a huge, historic responsibility. The project may be the last chance we have this century to demonstrate that fusion is manageable. ■

Bernard Bigot is director-general of the ITER Organization, St-Paul-lez-Durance, France.

e-mail: bernard.bigot@iter.org

Use mouse biobanks or lose them

Now that genetic engineering of mice is so easy, centralized repositories are essential, argue **Kent Lloyd** and colleagues.

Tens of thousands of genetically engineered mice have been bred to probe human biology and disease. Their numbers are poised to mushroom. New genome-editing technologies such as CRISPR/Cas9 mean that making an animal that carries several customized mutations can be done in a matter of months, rather than years. Investigators

who would not previously have considered making mutant mice are now doing so.

But laboratories that can make genetically modified mice are often unable to maintain them. Progeny frequently carry pathogens, lose carefully designed mutations or have other characteristics that confound experiments. So the mice that a researcher might dutifully ship to a colleague can be very

different from those described in a paper. In 2013, the Mutant Mouse Resource and Research Centers (MMRRCs), a consortium of the US National Institutes of Health, found that 32 of around 200 mouse lines deposited with them from individual labs did not match researchers' descriptions. It is no wonder that many preclinical studies performed using mice are not reproducible¹. ►

► As administrators of publicly funded animal repositories charged with preserving and distributing genetically engineered mouse lines, we routinely encounter — and correct — problems introduced by inappropriate breeding, animal husbandry and quality control. We worry that the explosion of new mouse models could create a surge of wasted effort and irreproducible results. Better use of repositories could avoid this problem.

IN THE BANK

For the past 16 years, the MMRRCs have maintained unique mouse models deposited by individual scientists. The collections encompass around 4,600 specific mutations in mice, and tens of thousands of mutations in frozen embryonic stem cells that can be used to generate mice. Last year, the MMRRCs and the Jackson Laboratory (JAX), a US non-profit biomedical-research organization, together distributed more than 200,000 live engineered mice, as well as frozen embryos and sperm representing hundreds of mutant lines. Australia, Europe and Japan also have government-funded repositories.

Mouse lines created by individual labs are often lost because of lack of interest or expertise. Commercial suppliers maintain only those lines that are in high demand. Making mouse lines publicly available from repositories renders these resources more accessible and eliminates costly, redundant efforts. It also relieves scientists of having to house animals and manage their breeding.

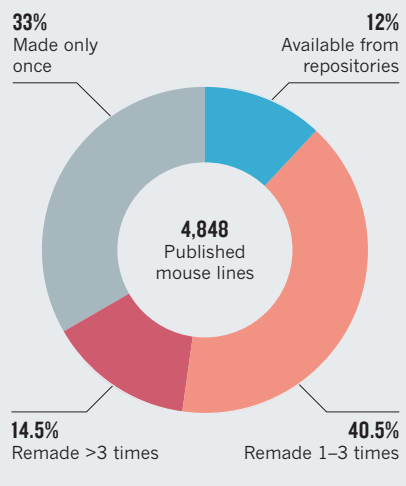
But fewer than half of the roughly 43,000 specific mutations listed in Mouse Genome Informatics, an international database of engineered mice, are listed as available from repositories. This is despite the fact that researchers funded by the US government are strongly encouraged to deposit mice for public distribution. A wide-ranging 2005 survey conducted by the NIH to investigate the extent of the problem found that, of 4,848 published mouse lines, only 12% were readily available from repositories. This forced scientists to rebuild mice; 2,655 had been remade at least once, and 702 had been remade independently more than three times (see 'Remaking mice'). The survey also spurred the Knockout Mouse Project (KOMP), which with international

A mouse bred to be diabetic, obese and hyperglycaemic.



REMAKING MICE

When engineered animals are unavailable, researchers make them again. The most recent comprehensive survey, carried out in 2005, found that researchers had made thousands of mouse lines more than once, wasting animals, time and money.



partners has made around 15,000 knockout alleles in embryonic stem cells, all deposited in repositories, including the KOMP Repository.

Since the survey, journals and funders have become more strict about requiring depositions. Yet we estimate that fewer than 20% of mouse lines are submitted. The rate is likely to fall as more scientists are able to engineer lines.

QUALITY CONTROL

Most researchers who use mice are experts in their fields rather than in mouse genetics, husbandry or pathology. Reagents remain relatively constant; a mouse is a living, breeding creature. Change is the default, and change over generations must be understood, monitored and managed.

Ordering a breeding pair of mice from a repository typically takes 3–5 weeks and costs US\$400–600, more if mice must be created from frozen stocks. (Engineering a mouse from scratch can cost upwards of \$20,000.) Many researchers prefer to get animals straight from a colleague. Although sharing is laudable, mice obtained from research labs rarely go through the rigorous checks that are standard practice in repositories.

Receiving labs are risking the reliability of subsequent experiments — and perhaps even the health of their vivaria.

Repositories ensure the quality and welfare of distributed animals and supply expertise to guide reliable studies.

This means that researchers learn more from the animal experiments they conduct. They address the problem of improperly identified animals in several ways. By the time results from an engineered mouse line are published in a paper, the line has probably bred through several generations and undergone genetic drift. Repositories can accept a mouse line on article submission (and even hold off distribution until publication) and maintain animals closer to the original description.

What is more, repositories routinely analyse animals' genomes before making them available and so catch mistakes. Sometimes researchers overlook mutations that have been engineered into a mouse line, which can alter the animals' traits or corrupt attempts at appropriate breeding. In 2013, genetic tests on 416 mutant mouse lines submitted to JAX and the MMRRCs found that 15% carried mutations for traits other than that specified, or contained genetic markers used to track mouse breeding not intended to be part of the line. The most frequent mix-up is essentially a typo: a common strain annotated as C57BL/6J is instead another called C57BL/6N. Although the pups look identical, the mice are very different. The 6N mice quickly develop bad eyesight, and 6J mice are susceptible to diabetes and obesity. Such traits can cause results to be misinterpreted and experiments to be irreproducible.

Researchers might also treat a line as breeding pure (with no mixing of genetic backgrounds) when it does not. All MMRRCs have received submissions of engineered lines that contained a mixture of mice carrying the mutation and 'wild-type' mice. We have also encountered many instances in which a genetic

marker (such as a fluorescent protein) was decoupled from the mutation it was supposed to identify. No surprise, then, that researchers who receive mice from colleagues can conduct several rounds of experiments, only to find that they have been studying mice that lack the desired mutation.

Another underappreciated source of variability is microbes. Identical mutations in a gene active in T cells made at two institutions revealed similarities on the molecular and cellular levels, but profound differences in the animals. At one institution, mice consistently developed prolapsed rectums and died two months after birth. Careful investigation revealed that this was caused by a stealth outbreak of the bacterium *Helicobacter hepaticus*². Repositories control for pathogens through frequent monitoring — and the ability to revive the strain under germ-free conditions from frozen embryos or gametes.

The microbiome (the collective DNA

SOURCE: NIH/THE JACKSON LABORATORY

JENNIFER L. TORRANCE/THE JACKSON LABORATORY



Littermates are often a mixture of mice carrying a required mutation and 'wild type'.

of microbes residing in the gut), which can vary for mice at different institutions even when they are fed identical diets, also causes surprising differences. Repositories are beginning to use DNA sequencing to define common variables such as diet, housing and other factors that may modulate microbiota³. This could reveal the effects of these variables on a variety of mouse traits, and make animal studies conducted by collaborating investigators more efficient and reproducible.

Finally, repositories can help to pin down unexpected causes of mouse traits, making the mice more useful to researchers. For example, a strong difference between two strains' responses to cocaine and methamphetamine was recently mapped to a site in a single gene that differed between the strains⁴. At the MMRRRC at the University of North Carolina at Chapel Hill, work to sort out crosses between mouse lines generated a variety of traits, including a line of mice that developed severe inflammation in the gut. The line has now been distributed to several organizations as a model for the human disease known as spontaneous colitis⁵.

FOUR STEPS FORWARD

If these benefits are to accrue, researchers must deposit their mice in repositories. Currently they may not for three reasons: they are unaware that repositories exist; they mistakenly think that they must pay for submission; or they want greater control over when and how their lines are distributed. Scientists should be better global citizens, and funders and journals must be more diligent in creating and enforcing requirements for deposition.

Next, scientists must use mice from repositories. The catalogue number and other documentation that repositories supply will ensure clear tracking of the mice, and the quality control that repositories routinely perform will ensure that descriptions match the actual mouse. The ARRIVE (Animals in Research: Reporting *In Vivo* Experiments) guidelines⁶, increasingly followed by publications that report animal research, should be amended to encourage acquisition from repositories. Mice obtained from non-specialists should undergo documented quality control — from genotyping to pathogen monitoring.

Third, repositories must work together to enhance their services. They should organize themselves into an integrated global network to share best practices, harmonize protocols and procedures, and innovate. Goals should include the development of certified quality-control practices and streamlining institutional transfer agreements to take in new mouse strains and to guarantee better distribution, particularly across international borders.

Continued investment is all the more important as researchers are called on to meet government mandates that may require individual studies to include more animals. Recent examples include Research Councils UK's requirement for researchers to statistically validate the numbers of mice used and the NIH's mandate to study both male and female mice⁷. Meanwhile, more mouse lines are being made by individual labs, and the International Mouse Phenotyping Consortium is set to complete more than 20,000 mouse models by 2021, encompassing

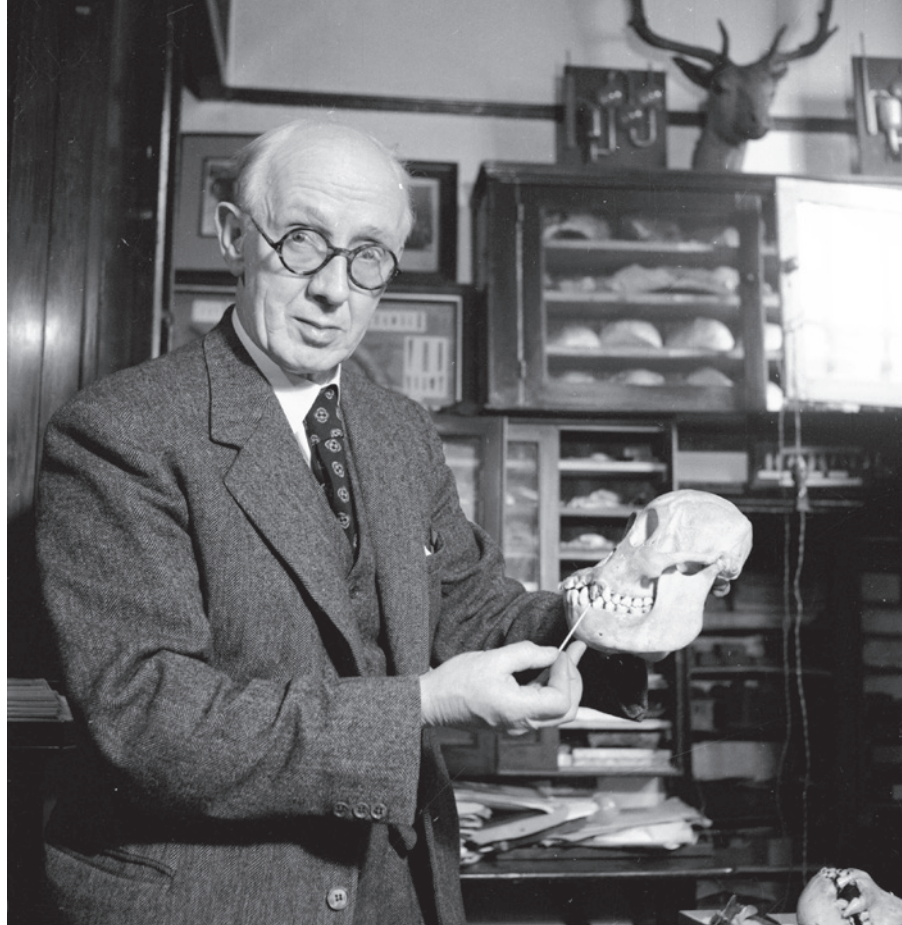
virtually the entire mouse genome.

Without sufficient investment, we fear a vicious cycle in which repositories are unable to cope with increasing demands and become less able to serve the scientific community, keeping fewer live mice ready for distribution. Worse, they will close. (At least one already has.)

Like money in the bank, repositories keep mouse models safe, secure and available for withdrawal. Just as a bank makes returns on investments, repositories add scientific value and utility to deposited mouse lines: they increase reliability through curation, preservation, genetic quality control, protection from pathogens and more. ■

Kent Lloyd is director of the Mutant Mouse Resource and Research Center (MMRRC) at the University of California, Davis, California, USA. **Craig Franklin** is director of the MMRRC at the University of Missouri, Columbia, Missouri, USA. **Cat Lutz** is director of the MMRRC at the Jackson Laboratory in Bar Harbor, Maine, USA. **Terry Magnuson** is director of the MMRRC at the University of North Carolina at Chapel Hill, North Carolina, USA.
e-mail: kclloyd@ucdavis.edu

1. Perrin, S. A. *Nature* **507**, 423–425 (2014).
2. Franklin, C. L. *ILAR J* **47**, 140–154 (2006).
3. Ericsson, A. C. et al. *PLoS ONE* **10**, e0116704 (2015).
4. Kumar, V. et al. *Science* **342**, 1508–1512 (2013).
5. Rogala, A. R. et al. *Mamm. Genome* **25**, 95–108 (2014).
6. Kilkenny, C., Browne, W. J., Cuthill, I. C., Emerson, M. & Altman, D. G. *PLoS Biol.* **8**, e1000412 (2010).
7. Clayton, J. A. & Collins, F. S. *Nature* **509**, 282–283 (2014).



Piltown Man (held by Alvan Marston, who helped to debunk the fraud), misled some palaeontologists.

HUMAN EVOLUTION

How we misread our own story

William Davies ponders a chronicle unwinding the twisted strands of thinking on human evolution.

In *The Strange Case of the Ricketty Cossack*, palaeoanthropologist Ian Tattersall outlines the history of thought on human evolution clearly and insightfully, allowing readers to make up their own minds about the motives and actions of key figures. The field, he reveals, has both benefited and suffered from involving other disciplines. Concepts rejected elsewhere have been applied to palaeoanthropology, and these have reinforced the fallacious idea that human evolution is distinct from that of other life forms. The history of the field reveals a divide between those who prefer linear sequences of speciation, and those that prefer a many-branched tree — the ‘lumpers’ and ‘splitters’.

From the mid-nineteenth century, the study of human origins bristled with self-appointed experts. The book’s title refers to a case in point: in the late 1850s, physiologist

August Franz Mayer identified Neanderthal remains from northern Germany as belonging to a Cossack soldier with rickets who had died in 1814 and somehow become buried in 2 metres of fossiliferous deposits. Other anatomists, including Thomas Henry Huxley, were happy to agree that the individual anatomical features of Neanderthals fell within the range of variation in *Homo sapiens*.

The lack of connection between those who recovered the fossilized and archaeological remains of early hominins, and those who sought to interpret them, is perhaps the most striking feature of the first 60–70 years of palaeoanthropology. It ensured that wider archaeological and ecological contexts were all but ignored in the application of predetermined (and untested) theories. So, for early-twentieth-century anatomist Marcellin Boule, fossils such as the Javan *Homo erectus* and the European

Neanderthals represented extinguished side-branches on a developmental tree that led to *H. sapiens* by other means.

The archaeological situation was not much better. Gabriel de Mortillet’s pronouncements in the 1870s that stone-working must have developed before bone-working led him to ignore stratigraphic evidence from Upper Palaeolithic sites in France that had been correctly sequenced by Édouard Lartet years before. The Piltown Man fraud of 1912 was designed to appeal to prejudices in favour of early development of a large brain (and even included a bone artefact carved to resemble a cricket bat; see C. Stringer *Nature* **492**, 177–179; 2012). Anyone who had focused on how the Piltown remains had been recovered and on their context would have been sceptical of such predeterminism.

Tattersall provides a useful discussion of the chaotic and idiosyncratic nomenclature created in the first half of the twentieth century. Almost every hominin fossil was classified as its own species, so people had little sense of broader patterns. Enter evolutionary biologist Ernst Mayr. A proponent of the evolutionary synthesis of the 1930s and 1940s, which unified Mendelian genetic inheritance with Darwinian natural selection, Mayr demanded that palaeoanthropology be aligned with wider evolutionary research. As a result of his address at the international meeting ‘The Origin and Evolution of Man’ in 1950, the number of hominin species was reduced. The postulated ancestors of *H. sapiens* were lumped into a single lineage of gradually evolving subspecies separated by barriers such as oceans and extending back at least 2 million years.

A change in analytic methods was needed before this single-species hypothesis could be supplanted by branching taxonomies with complex patterns of localized speciation, extinction and population replacement. In the mid-1970s, palaeoanthropologists began to use cladistic analyses (which group organisms on the basis of shared characteristics) to evaluate possible links between species. But using such methods, Tattersall and palaeontologist Niles Eldredge found it difficult to demonstrate that *H. erectus* was an ancestor of *H. sapiens*.

NATURE.COM
For more on human evolution:
go.nature.com/un4sof

Meanwhile, the idea of punctuated equilibria (periods of little evolutionary change



The Strange Case of the Ricketty Cossack: And Other Cautionary Tales from Human Evolution

IAN TATTERSALL
Palgrave Macmillan:
2015.

MAURICE AMBLER/PICTURE POST/GETTY

interspersed with rapid diversification, a concept that Eldredge co-developed) has been applied to hominin fossils and to successions of archaeological 'cultures', solely on the basis of recovered artefacts. But as Tattersall points out, views of transitional fossils and cultures as denoting sudden shifts between stable states are poorly theorized.

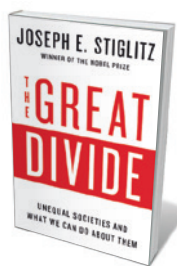
The single-species hypothesis has never quite disappeared. It has been reinvented as multiregional evolution from the 1970s onwards, by Milford Wolpoff and others. They model the transition to *H. sapiens* at the global scale, positing regional populations all effectively occupying the same niche wherever they happen to be, and interbreeding so that the species develops at the same rate everywhere. That would make increases in hominin brain size part of a universal trend. However, Tattersall identifies three separate episodes of relative brain-size increase within *Homo*: in *H. erectus* in Asia, and then, much later, in Neanderthals in Europe and *H. sapiens* in Africa. Regional and multiregional approaches still coexist, but current evidence tends to support the regionalized approach. The niches occupied by our ancestors and their relatives were likely to have been more varied than multi-regionalists would believe. There remains the question of how much the accuracy and precision of dating methods (and the quantity of data available) condition our discussions. If we had more and better dates, would we have a finer-grained view of change and variation?

The Strange Case of the Rickety Cossack is an interesting critical evaluation of how palaeoanthropology has developed. Rivalries between teams are delineated and used to explain how we know what we know. Many new hominin species have been identified in recent years, but it is not yet clear how they are related to us. More work is needed on the classification of skeletal material from Dmanisi in Georgia, which encompasses extraordinary morphological variety, and from Flores in Indonesia, where the 'hobbit' *Homo floresiensis* was found (see C. Stringer *Nature* **514**, 427–429; 2014).

Some of Tattersall's assertions will generate heated debate — particularly the claim that the large-brained Neanderthals were empirical artisans, rather than symbolic artists. Current archaeological evidence indicates that Neanderthals were able to innovate, but that these innovations may have been kept within small-scale social networks. By contrast, the future of palaeoanthropology lies in its ability to make extensive connections. ■

William Davies is director of the Centre for the Archaeology of Human Origins at the University of Southampton, UK.
e-mail: s.w.g.davies@soton.ac.uk

Books in brief



The Great Divide: Unequal Societies and What We Can Do About Them

Joseph E. Stiglitz W. W. NORTON (2015)

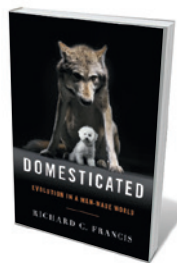
That 1% of the world now owns nearly half of the wealth is weakening the global economy. So argues Nobel-prizewinning economist Joseph Stiglitz in this collection of writing originally published in *Vanity Fair* and elsewhere. He ranges with searing honesty from the deregulation and tax cuts for the rich that spurred the 2008 meltdown to the ebbing of socio-economic mobility. His solutions to the crisis are presented authoritatively as eminently doable — from boosting corporate taxes to investing in science and education.



A Natural History of English Gardening

Mark Laird YALE UNIVERSITY PRESS (2015)

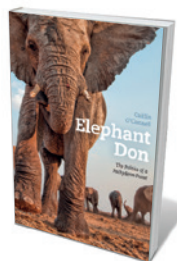
In this vast, stunningly illustrated history of gardening in England, landscape historian Mark Laird focuses on a fertile moment — the mid-seventeenth to early nineteenth centuries. During that time, he argues, natural history (the discovery of order in nature) emerged from the evolution of the garden (nature's ordered microcosm). Laird marshals climatic events such as the Little Ice Age winter of 1683 and the drought a century later to contextualize advances in forestry and garden design by John Evelyn, and in horticultural science by Mary Somerset, Duchess of Beaufort, among other developments.



Domesticated: Evolution in a Man-Made World

Richard C. Francis W. W. NORTON (2015)

We humans evolve side by side with other animals in the process of domestication, and in this intriguing study, science journalist Richard Francis tracks those changes. As he shows, both natural and artificial selection have worked powerfully to create diversity in size and shape in domesticated animals, notably the dog. Yet "evolution is still fundamentally conservative", he notes: the wolf lingers in the chihuahua. Francis presents numerous case studies, from ferrets and camels to reindeer and us. Our self-domestication, he avers, has driven the cultural dynamism that has made us what we are.



Elephant Don: The Politics of a Pachyderm Posse

Caitlin O'Connell UNIVERSITY OF CHICAGO PRESS (2015)

The jaunty title belies the scholarly weight of Caitlin O'Connell's study on social behaviour in a group of African bull elephants in Namibia's Etosha National Park. O'Connell, who also works on the role of vibration in mammal communication, offers a riveting account. We see the pachyderms dipping their trunks into the mouth of dominant bull Greg; battling or welcoming would-be members; and, when Greg disappears, standing tail to tail, facing out as if listening for some seismic clue. Full of vivid detail, such as waking up to the "demonic-sounding giggling" of hyenas.



Plankton: Wonders of the Drifting World

Christian Sardet UNIVERSITY OF CHICAGO PRESS (2015)

They have vital roles in climate and food chains, but their minuscule size means that plankton impinge little on the public consciousness. In this beautiful book, marine scientist Christian Sardet shows that tiny plankton, not enormous blue whales, are the real stars of the ocean. Macro pictures of the huge variety of plankton forms and short details of their lives force a reconsideration of our view of them as part of an amorphous soup. A celebration of the small, and an unalloyed joy. (See the *Nature* video at go.nature.com/gegecq.) **Barbara Kiser**

Correspondence

The joys of research in retirement

After retiring some ten years ago at the age of 65, I still wanted to do some worthwhile research (*Nature* **521**, 20–23; 2015).

I had only a chair and a table for support. These props came courtesy of my former employer, along with online access to the scientific literature. I was originally a researcher in two very different fields — surface science and nanoparticle-related health effects — so I set about re-evaluating publications in both areas. New ideas emerged, sparking successful collaborations with former colleagues who had the necessary equipment to investigate them.

I have written and published 30 mostly single-author papers since retirement. Most notable is a 123-page review that took me almost 2 years to prepare, allowing me to invalidate a theory that was more than 30 years old (K. Wittmaack *Surf. Sci. Rep.* **68**, 108–230; 2013). I reckon that I have learned more per unit time during this phase than I did during my ‘active’ career. And still I keep going.

Colleagues with retirement in sight should give up the idea that science can only be advanced with a sizeable research team. Sit down and take the literature to pieces, then put the puzzle together again in light of your newly gained insight. Gratifying work awaits.

Klaus Wittmaack *Helmholtz-Zentrum München, Institute of Radiation Protection, Germany.*
wittmaack@helmholtz-muenchen.de

Phosphate mining risks atoll culture

Mataiva atoll in the Pacific Ocean has an unusual morphology: its central lagoon is divided into numerous shallow basins by a network of slightly submerged coral shoals. This extremely rare geological feature, known as a reticulated lagoon, is now under threat from the global demand for

phosphate, used in agriculture.

International companies and the government of French Polynesia have attempted to mine Mataiva’s rich phosphate resources since the 1980s, but have so far been thwarted by its inhabitants.

Opposition was on the basis of the potentially disruptive effects of mining on the population’s identity and on its culture of coconut farming and fishing. An 18-month test of the extraction process in 1986 destroyed and polluted fish habitats to the extent that people reportedly could not eat lagoon fish for 10 years. Island people also feared the loss of land rights, because their livelihoods depend on farming and drying coconut flesh (copra).

The government this year announced its decision to resume phosphate extraction. Resistance is now dangerously weakened as the atoll’s elders dwindle and the younger generation moves away, severing the cultural attachment to the atoll’s traditional way of life. The world’s geological patrimony is again at stake.

Alexandre Magnan *Institute for Sustainable Development and International Relations (IDDRI), Sciences Po, Paris, France.*

Virginie Duvat *Littoral, Environment and Societies Research Unit (LIENSs, UMR 7266), University of La Rochelle and*

CNRS, La Rochelle, France.
alexandre.magnan@iddri.org

Share surplus animal tissue

Strict regulations govern the use of laboratory animals in research (see, for example, K. Davies *Nature* **521**, 7; 2015), but scientists are under increasing pressure to justify their experiments and address public concerns (*Nature* **520**, 271–272; 2015). Initiatives such as SEARCHBreast avoid the need to set up further *in vivo* models by using surplus archival tissue from previous animal studies.

SEARCHBreast (for ‘Sharing Experimental Animal Resources: Coordinating Holdings in Breast Cancer’) is a searchable platform of tissues, resources and information derived from animal models of breast cancer (www.searchbreast.org). These materials can be deployed for characterizing tumour biomarkers and genetically engineered animal models, for example, or for investigating treatment effects on archived human-to-mouse xenografts.

The ‘SEARCH’ blueprint translates to other diseases: for example, ShARM (Shared Ageing Research Models; www.sharmuk.org) aims to

accelerate research on ageing. Such resources support official ‘replacement, refinement and reduction’ policies (see www.nc3rs.org.uk/the-3rs) and save time and money.

Valerie Speirs *Leeds Institute of Cancer and Pathology, University of Leeds, UK.*

v.speirs@leeds.ac.uk

**On behalf of 7 correspondents (see go.nature.com/gthlzc for full list).*

Climate advisers must be astute

Oliver Geden suggests that scientific advisers on climate should resist becoming “political entrepreneurs” by making their advice more palatable (*Nature* **521**, 27–28; 2015). In fact, climate advisers need to be astute political entrepreneurs if they are to present the benefits of a policy change without exaggerating claims.

Political pragmatism is not for helping policy-makers to justify the status quo, but rather for presenting persuasive scientific evidence alongside other issues (D. C. Rose *Nature Clim. Change* **4**, 1038; 2014). Entrepreneurial climate scientists can offer fresh solutions to policy-makers, point out the improvements their ideas would provide and explain how they would work in practice. These entrepreneurs take the concerns of other scientists and policy-makers into account, build professional networks, and use every opportunity to maximize political influence (M. Mintrom and P. Norman *Policy Stud. J.* **37**, 649–667; 2009).

Optimizing science presentation does not mean compromising on technical rigour or integrity. Climate scientists can increase their understanding of how policy-makers use the evidence they provide, as Geden recommends, and so deploy it more effectively to argue for policy change.

David C. Rose *University of Cambridge, UK.*
dcr31@hermes.cam.ac.uk



MALARIA

A master lock for deadly parasites

An RNA-interference screen has identified the protein CD55, expressed on the surface of red blood cells, as an essential receptor for infection of the cells by the malaria parasite *Plasmodium falciparum*.

WAI-HONG THAM & ALEXANDER T. KENNEDY

There are trillions of cells in the human body and around 200 distinct cell types, some of which can be hijacked as safe houses by deadly pathogens. Malaria parasites, which infect millions of humans annually, have a preference for residing in liver and blood cells. To enter these cells, the parasites make proteins that recognize other proteins on the target cell's surface. By analogy, the parasite proteins fit in a key-like fashion to their locks, the red blood cell proteins. But only a handful of these lock-and-key combinations has been discovered. Writing in *Science*, Egan *et al.*¹ combine two exciting technologies — RNA interference and *ex vivo* production of red blood cells — to identify other receptor proteins involved in malaria-parasite entry.

In 1975, live imaging of malaria parasites entering red blood cells highlighted a dynamic process with distinct observable steps². The form of the malaria parasite that enters these cells is a merozoite, characterized by an ovoid shape and an apical tip. After initial contact with the red blood cell, the merozoite reorients so that its apical tip is in close proximity to the cell surface. Parasite proteins in the apical prominence recognize red blood cell proteins, triggering irreversible commitment to entry — turning the key in the lock and opening the door. Subsequently, a tight junction forms between parasite and red blood cell membranes, propelling the parasite

into the cell and beginning the blood stage of infection. Intensive efforts to develop a vaccine against this stage have focused on identifying all the lock-and-key combinations involved in parasite invasion and on ways to block parasite entry.

Egan *et al.* have performed the first large knockdown screen of red blood cell proteins that are bound by the most lethal human malaria parasite, *Plasmodium falciparum*. The researchers targeted 42 genes that encode proteins determining blood group, on the basis that all *P. falciparum* receptors known so far belong to this protein group and that these genes are not involved in red blood cell production (Fig. 1). The authors inserted a library of small hairpin RNA molecules (shRNAs) that bind to, and thus inhibit expression of, these genes into isolated haematopoietic progenitor cells (which give rise to all blood cells), and then induced these cells to proliferate and differentiate into red blood cells. Once the cells were mature enough to sustain parasite development, they were infected with *P. falciparum* expressing green fluorescent protein, thus allowing infected cells to be identified.

The authors then sequenced the shRNAs in these cells and compared the levels of each shRNA between infected and non-infected cell populations. Positive targets were identified as genes whose corresponding shRNAs were under-represented in the infected population, following the logic that inhibiting these genes impairs parasite infection. Among the

authors' positive hits were genes encoding the proteins basigin and complement receptor 1 (CR1), which are known to be involved in *P. falciparum* invasion^{3,4}. More excitingly, they identified the cell-surface protein CD55 as the top-ranked candidate for a new entry portal for *P. falciparum*.

A key aspect of this discovery is that CD55 is an essential lock in the invasion process: Egan and colleagues show that diverse *P. falciparum* laboratory strains and field isolates could not infect red blood cells lacking CD55. The parasite uses several lock-and-key combinations to enter red blood cells, to maximize its opportunities for entry⁵, and this redundancy presents a huge hurdle to the development of vaccines to block blood-stage infection. Therefore, interactions that are essential in the invasion process provide attractive vaccine candidates. The effect of loss of CD55 on parasite invasion is similar to the loss of basigin, whose parasite protein partner PfRh5 is a leading blood-stage vaccine candidate⁶. Clearly, an outstanding question stemming from this work is the identification of the *P. falciparum* protein that binds to CD55. If CD55 is a crucial host factor for *P. falciparum* invasion, the hypothesis would be that the parasite ligand is also an essential factor and thus warrants inclusion in the vaccine-development pipeline.

Egan *et al.* also show that loss of CD55 on red blood cells affects the proliferation of diverse *P. falciparum* strains. The authors suggest that CD55 may be involved in the

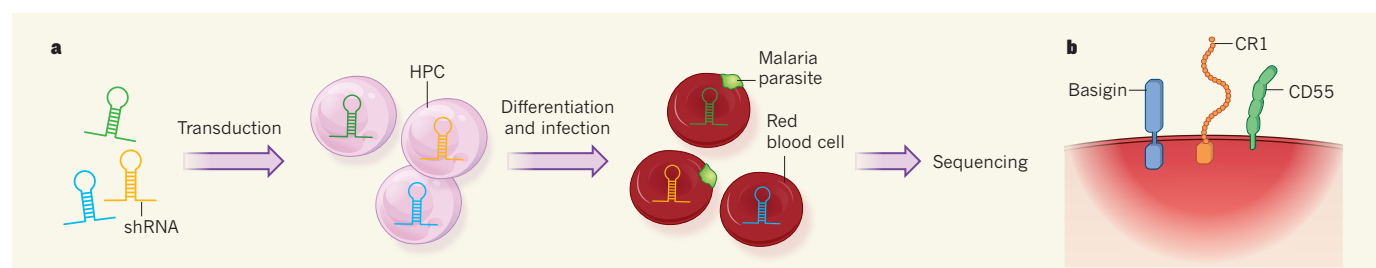


Figure 1 | RNA interference identifies malaria-parasite entry receptors. **a**, To identify proteins on red blood cells to which malaria parasites bind, Egan *et al.*¹ created a library of short hairpin RNA (shRNA) molecules that block the expression of genes encoding blood-group proteins. These shRNAs were transduced into haematopoietic progenitor cells (HPCs), and the HPCs were induced to proliferate and differentiate into red blood cells. The authors then infected the cells with fluorescent malaria parasites and

compared the abundance of shRNA molecules in uninfected and infected cells; those shRNAs that were under-represented in the infected population were determined to correspond to genes encoding receptor proteins for parasite entry, because inhibition of these genes would inhibit the parasite's ability to infect. **b**, Alongside the known parasite receptors CR1 and basigin, the authors identified several new candidates, of which CD55 was the top hit.

CELL BIOLOGY

irreversible-commitment phase of parasite invasion. This hypothesis should be further explored using live and high-resolution imaging of merozoites attempting to infect CD55-deficient red blood cells. It will be interesting to determine whether the loss of CD55 affects the establishment of commitment, deformation of the red blood cell surface or signalling for tight-junction formation during the early stages of parasite invasion.

Could CD55 be a therapeutic target for malaria infections? Although some healthy humans exist without CD55 on their blood cells, important caveats arise for individuals living in malarious regions. Field studies show a correlation between declining CD55 levels on red blood cells and severe malarial anaemia, potentially due to the destruction of red blood cells by the complement system⁷, an arm of the immune system that is regulated by CD55. An alternative avenue could be to explore the potential of soluble CD55 as a competitor to red blood cell CD55 for merozoite binding, and thus an inhibitor of parasite growth.

An emerging theme in *P. falciparum* invasion is that the parasite exploits complement regulators as entry receptors. In humans, CR1 and CD55 protect self-tissues from complement attack. A variable currently missing from experimental work monitoring *P. falciparum* invasion is the addition of active complement-system components during parasite entry. For example, complement activation is known to modulate the behaviour of both CD55 and CR1 on membranes, resulting in changes in red blood cell deformability that may affect merozoite entry^{8,9}. Binding of parasite ligands to these receptors may interfere with their regulatory roles (as is the case with CR1), and the consequences of this for red blood cell survival during infection need to be understood. Current research has led to a remarkable deconstruction of the distinct steps in *P. falciparum* invasion¹⁰, but future challenges will be to understand merozoite entry in the context of complement activation and immune attack. ■

Wai-Hong Tham and Alexander T. Kennedy are at the Walter and Eliza Hall Institute, Parkville, Victoria 3052, Australia, and the Department of Medical Biology, University of Melbourne, Parkville. e-mail: tham@wehi.edu.au

1. Egan, E. S. *et al. Science* **348**, 711–714 (2015).
2. Dvorak, J. A., Miller, L. H., Whitehouse, W. C. & Shiroishi, T. *Science* **187**, 748–750 (1975).
3. Tham, W.-H. *et al. Proc. Natl Acad. Sci. USA* **107**, 17327–17332 (2010).
4. Crosnier, C. *et al. Nature* **480**, 534–537 (2011).
5. Cowman, A. F. & Crabb, B. S. *Cell* **124**, 755–766 (2006).
6. Douglas, A. D. *et al. Cell Host Microbe* **17**, 130–139 (2015).
7. Biryukov, S. & Stoute, J. A. *Trends Mol. Med.* **20**, 293–301 (2014).
8. Glodek, A. M. *et al. Blood* **116**, 6063–6071 (2010).
9. Karnchanaphanurach, P. *et al. J. Clin. Invest.* **119**, 788–801 (2009).
10. Riglar, D. T. *et al. Cell Host Microbe* **9**, 9–20 (2011).

Nuclear dilemma resolved

After cell division, membranes become fused around the nucleus to encapsulate the cell's chromosomes. It emerges that this process is regulated by the ESCRT-III protein complex. SEE LETTERS P.231 & P.236

BRIAN BURKE

The chromosomes of animal, plant and fungal cells are enclosed within a nucleus, which is encapsulated by a membranous structure called the nuclear envelope. This poses a problem when the time comes for cells to divide, because chromosomes segregate into two daughter cells by binding to and moving along a structure called the mitotic spindle, which, at least in multicellular organisms, is located outside the nucleus. In vertebrate cells, the nuclear

envelope is normally partly or completely disassembled before chromosome segregation, and new envelopes are assembled afterwards — a process that requires extensive membrane fusion. However, the mechanisms by which membrane fusion occurs have long puzzled cell biologists. In this issue, Olmos *et al.*¹ (page 236) and Vietri *et al.*² (page 231) reveal that the nuclear envelope co-opts a membrane-sculpting protein complex called ESCRT-III to bring about reassembly.

The nuclear envelope completely encloses an

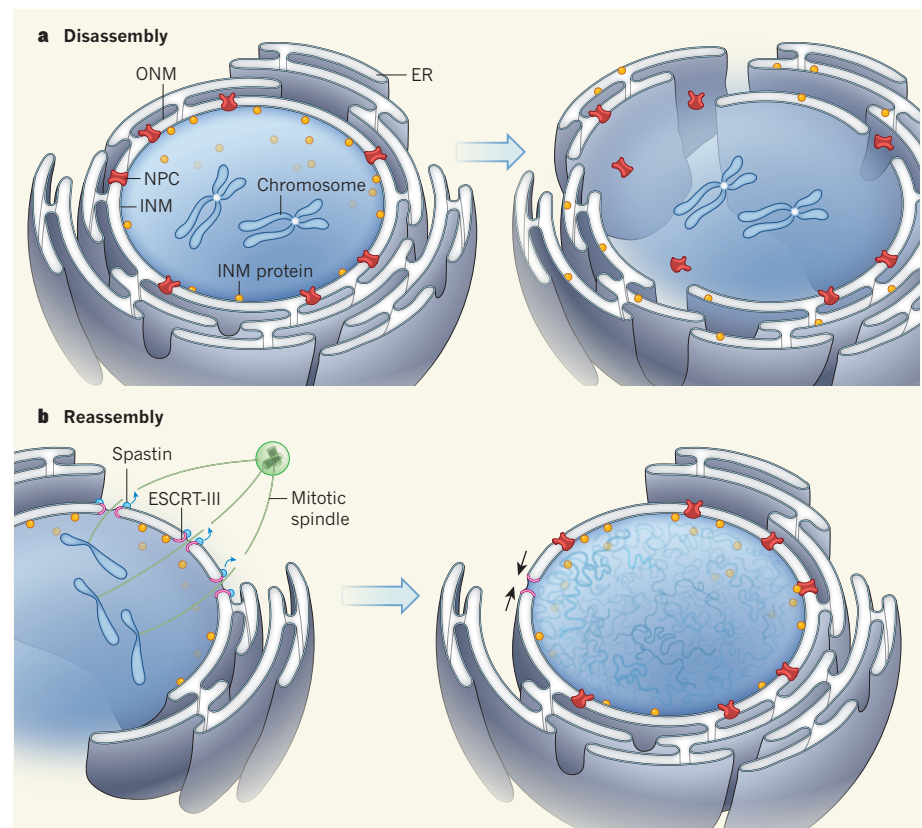


Figure 1 | Resealing the nuclear envelope. **a**, The nuclear envelope is composed of inner and outer nuclear membranes (INM and ONM, respectively). The two are joined at junctions filled by nuclear pore complexes (NPCs), and the ONM is joined to another membranous structure, the endoplasmic reticulum (ER). During cell division, the nuclear envelope disassembles, and INM proteins disperse into the ER. **b**, As the cell divides, chromosomes (which separate and then become decondensed) are pulled to opposite poles of the cell by a structure called the mitotic spindle. Vietri *et al.*² demonstrate that the ESCRT-III protein complex recruits the enzyme spastin to sever the mitotic spindle. Both this group and Olmos *et al.*¹ show that ESCRT-III then promotes resealing of the nuclear envelope (black arrows).

essentially spherical space³ and is composed of inner and outer nuclear membranes. The two membranes are periodically joined at annular junctions, forming channels that connect the inside of the nucleus with the cell's cytoplasm. These channels are occupied by multiprotein nuclear pore complexes (NPCs), which regulate the trafficking of macromolecules across the envelope.

The outer nuclear membrane is also connected to a membrane network called the endoplasmic reticulum, which permeates much of the cytoplasm. As such, the inner and outer nuclear membranes and the endoplasmic reticulum constitute a single continuous membrane system. When the nuclear envelope breaks down during cell division, NPCs disassemble and the nuclear membranes are peeled open. This causes the constituents of the nuclear membrane to disperse into the endoplasmic reticulum, where the proteins of the two structures become intermingled⁴ (Fig. 1a).

The nuclear membranes start to re-form as the chromosomes segregate to opposite poles of the cell. Membranes from the endoplasmic reticulum attach to and spread out over the surfaces of the mass of chromosomes, a process that is mediated by proteins of the inner nuclear membrane (Fig. 1b). But what mechanism is in place to close gaps within the membranes that eventually surround the daughter nuclei? Perhaps these holes are never actually sealed, but are instead plugged by reassembled NPCs. But this cannot be the whole story, because a sealed envelope can form even in the absence of NPCs⁵. Indeed, the enzyme p97 can drive fusion at annular junctions between the inner and outer nuclear membranes⁶ to seal NPC-free holes in the nuclear envelope. However, a full understanding of this fusion process has remained out of reach.

The ESCRT-III complex is known^{7,8} to have roles in the formation of certain intracellular vesicles, in the budding of retroviruses from the membranes of infected cells, and in the abscission process that separates two daughter cells at the end of cell division. What all these seemingly disparate events have in common is that they involve membrane fusion, which generates a membrane-bound compartment that is separate from, but topologically identical to, the cell's cytoplasm. In each case, components of ESCRT-III act as a molecular drawstring that constricts the neck of a membrane bud (or even of an entire cell) to promote annular fusion. This process is strikingly similar to the topological changes that occur when holes in the re-forming nuclear membranes are closed.

The current studies^{1,2} demonstrate that components of ESCRT-III accumulate transiently at the edge of gaps in re-forming nuclear membranes — just as would be expected if the complex mediated the fusion of nuclear membranes. Such a role is borne out by the observation, made by both groups, that depletion of the components of ESCRT-III results

in failure to seal the nuclear envelope. Olmos *et al.* also show that p97 and its cofactor protein, UFD1, are essential for the recruitment of key ESCRT-III subunits to the re-forming envelope.

Vietri *et al.* further reveal that ESCRT-III has a complementary role in disassembling the mitotic spindle. The microtubule structures that make up much of the spindle are attached to separating chromosomes, so they must be eliminated before the nuclear envelope can be sealed. Vietri and colleagues show that this elimination is carried out by spastin, a microtubule-severing protein that is attracted to the spindles by ESCRT-III.

These authors find that interference with spastin results in delayed disassembly of the spindle, and prolonged association of ESCRT-III with the re-forming envelope. Not surprisingly, interference with ESCRT-III also impairs spindle disassembly. So ESCRT-III and spastin coordinate spindle disassembly with closure of the nuclear envelope. This represents a striking parallel with abscission, in which spastin severs the spindle microtubules that pass between the two daughter cells.

Together, the current studies reveal a previously unknown role for ESCRT-III in re-forming the nuclear envelope. The association, albeit transient, between ESCRT-III and nuclear membranes raises the question of whether this complex, or a functional equivalent, might have other roles in envelope maintenance. Indeed, there are several situations in which such activity might be required.

For instance, some macromolecular complexes in fruitflies are exported from the nucleus by budding through the inner nuclear membrane, bypassing NPCs⁹. Capsid

structures containing DNA from herpes simplex viruses exit the nucleus in a similar manner¹⁰. These movements involve the type of membrane remodelling that is a hallmark of ESCRT-III. More dramatically, the Vpr protein, which is produced by HIV, is associated with transient ruptures of the nuclear envelope¹¹, and the membrane is again probably resealed through a similar mechanism. Finally, the elimination of misassembled NPCs in yeast has been shown¹² to depend on ESCRT-III. In the light of these phenomena, it would be no great surprise if ESCRT or ESCRT-like complexes were shown to have other, hitherto unappreciated, roles in nuclear-envelope dynamics. ■

Brian Burke is at the Institute of Medical Biology, 138648 Singapore.

e-mail: brian.burke@imb.a-star.edu.sg

1. Olmos, Y., Hodgson, L., Mantell, J., Verkade, P. & Carlton, J. G. *Nature* **522**, 236–239 (2015).
2. Vietri, M. *et al.* *Nature* **522**, 231–235 (2015).
3. Wilson, K. L. & Dawson, S. C. *J. Cell Biol.* **195**, 171–181 (2011).
4. Wandke, C. & Kutay, U. *Cell* **152**, 1222–1225 (2013).
5. Macaulay, C. & Forbes, D. J. *J. Cell Biol.* **132**, 5–20 (1996).
6. Hetzer, M. *et al.* *Nature Cell Biol.* **3**, 1086–1091 (2001).
7. Henne, W. M., Stenmark, H. & Emr, S. D. *Cold Spring Harb. Perspect. Biol.* **5**, a016766 (2013).
8. Raiborg, C. & Stenmark, H. *Nature* **458**, 445–452 (2009).
9. Speese, S. D. *et al.* *Cell* **149**, 832–846 (2012).
10. Pawliczek, T. & Crump, C. M. *J. Virol.* **83**, 11254–11264 (2009).
11. de Noronha, C. M. C. *et al.* *Science* **294**, 1105–1108 (2001).
12. Webster, B. M., Colombi, P., Jäger, J. & Lusk, C. P. *Cell* **159**, 388–401 (2014).

This article was published online on 3 June 2015.

NANOPHOTONICS

Bright future for hyperbolic chips

The unusual properties of hyperbolic metamaterials, such as their ability to propagate light on the nanoscale without diffraction, have been realized in two-dimensional devices, heralding improved photonic circuits. [SEE LETTER P.192](#)

GUY BARTAL

Devices known as photonic integrated circuits^{1,2} could succeed electronic circuits in future data-storage, computation and communications technologies, because they would allow improved data bandwidths and lower energy consumption. But such devices lag behind their electronic counterparts because they are limited by diffraction effects that restrict their

applications to micrometre scales, whereas electronics have already reached the nanometre scale. This shortcoming is due to the fact that the electromagnetic properties of typical optical media hinder the relay of tiny optical features. If a beam narrower than (or comparable to) the wavelength of light travels through such media, it will either be distorted when it reaches its destination, because of diffraction, or it will not get there at all, because of exponential decay. This is a

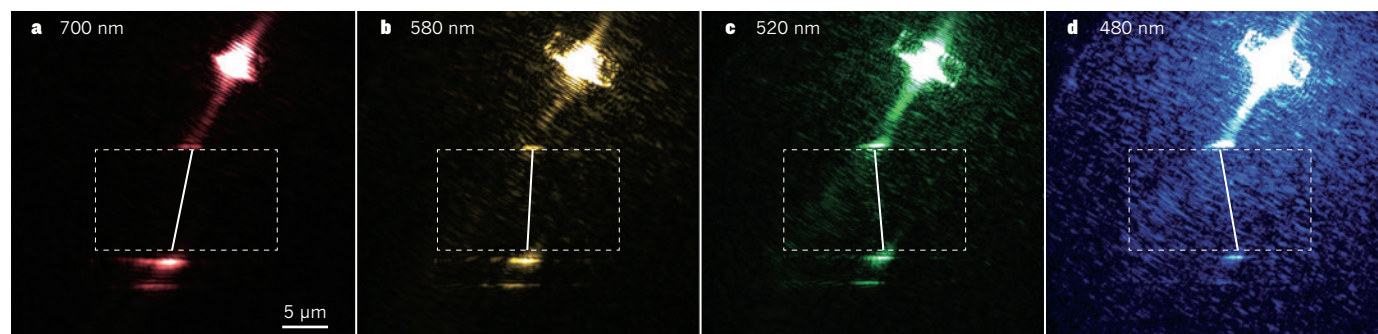


Figure 1 | Normal versus negative refraction in a hyperbolic metasurface (HMS). This set of images illustrates the effect of wavelength on the refraction of optical beams as they impinge on the interface of a silver film with the HMS grating, in a device built by High and colleagues³. The grating consists of nanoscale grooves. In **a** and **b**, a beam is refracted in the normal sense, whereas in **c** and **d** negative refraction occurs

(the respective wavelengths are labelled). In each case, the dotted box indicates the area covered by the HMS and the solid line indicates the angle of refraction. Devices based on nanoscale photonic circuits will be able to exploit this phenomenon to facilitate wavelength-based switching and routing of light and to increase the amount of information transferred.

fundamental limitation of propagating waves.

On page 192 of this issue, High *et al.*³ report the first experimental realization of two-dimensional 'hyperbolic metasurfaces' (HMSs)^{4,5}. The authors' HMSs exhibit a range of unconventional properties, including colour-dependent negative refraction and diffraction-less propagation, coupled with low optical-transmission losses — all packed in a tiny chip.

Hyperbolic metamaterials (HMMs) are artificial structures whose optical properties are highly direction dependent. They are made of ultrathin multilayers⁶ or dense nanowire arrays⁷, and are renowned for their ability to overcome the diffraction limit by enabling the propagation of ultra-small features of electromagnetic waves^{4,8–10}. Moreover, they can support greater photon energy densities than can conventional materials, thereby enhancing the interaction of light with matter^{11,12} — a property that can lead to improved signal modulation and decreased energy consumption. These are key ingredients for bringing HMMs to the front line of integrated circuitry, on a par with electronics. Their unusual properties could also expand their applicability beyond that of run-of-the-mill optical media.

Until recently, HMMs have been fabricated only in three-dimensional configurations, making them unsuitable for integration on flat chips. Furthermore, these composite devices often contain metallic parts that absorb light and cause losses from resistivity, weakening their electromagnetic-power throughput. Also, preventing diffraction requires a certain design that inevitably maximizes the damping of electromagnetic waves¹⁰, reducing the waves' effective propagation distances to less than 1 μm.

High and colleagues overcame these issues by fabricating an HMS consisting of a nanoscale grating on a single-crystal silver film — a design that can prevent diffraction without causing excessive losses from resistivity. Moreover, using sophisticated crystal-growth techniques and cutting-edge patterning methods, the authors were able to further minimize

both resistivity and scattering losses and to achieve operational propagation distances.

What new on-chip functionalities result from this work? The hallmark property of HMMs is negative refraction, the ability to bend a beam that crosses from one medium into the HMM in the 'wrong' direction — essentially, breaking the law of refraction. Negative refraction is not typically observed in naturally occurring materials, but it has been demonstrated in various metamaterials in the past 15 years^{6,13,14}. Not only have High *et al.* produced the first chip to exhibit negative refraction, but they have also shown that the effect can be wavelength dependent (Fig. 1); that is, their device allows certain colours of visible light to be refracted in the 'wrong' sense, whereas others refract normally.

This property could facilitate wavelength-based switching and routing of light in photonic circuits. No less importantly, it could be used to counter the natural tendency of a tightly focused light beam to expand as it travels, because the transition from normal to negative refraction occurs at a certain wavelength that depends on the material's design. At this wavelength, the beam impinging on the HMS does not diffract, but propagates unimpeded without sideways loss of energy, irrespective of the beam's launch angle or width (see Fig. 3a, b of High and colleagues' paper³). The devices built by the authors take advantage of this effect, so that each groove of the grating can channel this particular wavelength, regardless of how closely spaced the grooves are or how small their intrinsic width is compared with the wavelength in question. In fully fledged HMS devices, this would allow a substantial increase in the information capacity transferred across small chips. Diffraction-less 2D imaging could be one of many other potential applications.

High and colleagues further demonstrate that they can selectively route light beams of visible frequency not only by the beams' colour, but also by the photons' spin. Spin is a fundamental signature of photons, and is

associated with the circular polarization of electromagnetic waves (the direction of rotation of the electric field in time and space). In one of the devices demonstrated in the current work, a beam of left-handed polarization is diverted to a direction opposite to that of a right-polarized beam. Although this phenomenon has been previously demonstrated in metasurfaces¹⁵ and HMMs¹⁶, what is unique here is the combination in prototype devices of colour sensitivity, polarization-dependent refraction, enhanced light-matter interaction and significant reduction in optical losses. The ability to encapsulate these desirable properties on a chip could form the backbone of a robust photonic system, suitable not only for high-capacity data transmission, but also for quantum-communications and quantum-memory applications. ■

Guy Bartal is in the Department of Electrical Engineering and the Russell Berrie Nanotechnology Institute, Technion-Israel Institute of Technology, Haifa 32000, Israel. e-mail: guy@ee.technion.ac.il

- Almeida, V. R., Barrios, C. A., Panepucci, R. R. & Lipson, M. *Nature* **431**, 1081–1084 (2004).
- Huang, K. C. Y. *et al. Nature Photon.* **8**, 244–249 (2014).
- High, A. A. *et al. Nature* **522**, 192–196 (2015).
- Poddubny, A., Iorsh, I., Belov, P. & Kivshar, Y. *Nature Photon.* **7**, 948–957 (2013).
- Liu, Y. & Zhang, X. *Appl. Phys. Lett.* **103**, 141101 (2013).
- Liu, Z., Lee, H., Xiong, Y., Sun, C. & Zhang, X. *Science* **315**, 1686 (2007).
- Yao, J. *et al. Science* **321**, 930 (2008).
- Jacob, Z., Alekseyev, L. V. & Narimanov, E. *Opt. Express* **14**, 8247–8256 (2006).
- Salandrino, A. & Engheta, N. *Phys. Rev. B* **74**, 075103 (2006).
- Smolyaninov, I. I., Hung, Y.-J. & Davis, C. C. *Science* **315**, 1699–1701 (2007).
- Yang, X., Yao, J., Rho, J., Yin, X. & Zhang, X. *Nature Photon.* **6**, 450–454 (2012).
- Cortes, C. L., Newman, W., Molesky, S. & Jacob, Z. *J. Opt.* **14**, 063001 (2012).
- Shelby, R. A., Smith, D. R. & Schultz, S. *Science* **292**, 77–79 (2001).
- Valentine, J. *et al. Nature* **455**, 376–379 (2008).
- Bomzon, Z., Biener, G., Kleiner, V. & Hasman, E. *Opt. Lett.* **27**, 1141–1143 (2002).
- Kapitanova, P. V. *et al. Nature Commun.* **5**, 3226 (2014).

The micronucleus gets its big break

Extensive chromosomal rearrangement — chromothripsis — is seen in several cancers. Imaging and sequencing of single cells shows that this phenomenon can occur inside cellular anomalies known as micronuclei. [SEE ARTICLE P.179](#)

KRISTIN A. KNOUSE & ANGELIKA AMON

It has long been assumed that cancer evolves through the gradual accumulation of genetic alterations, but recent analyses of cancer genomes have challenged the universality of this hypothesis. At least 2% of all cancers, and more than 10% of brain cancers, exhibit chromothripsis — the extensive rearrangement of one or a few chromosomes^{1,2}. In these cases, it seems that a chromosome shatters into pieces and is then stitched back together, with some segments being reincorporated, albeit in a random order and orientation, while others are left behind. Modelling suggests that these rearrangements arise from a single catastrophic event, rather than through several independent or consecutive chromosomal rearrangements¹. On page 179 of this issue, Zhang *et al.*³ show that chromothripsis can occur when faulty cell division results in the formation of structures called micronuclei that contain isolated chromosomes.

Perhaps the most peculiar aspect of chromothripsis is that the rearrangements are largely confined to a single chromosome. This suggests that the causative event occurs during cell division (mitosis), when chromosomes are spatially distinct, rather than during the remainder of the cell cycle (interphase), when the chromosomes are closely juxtaposed. Insight into the cause of chromothripsis has come from studies of chromosome mis-segregation. Occasionally, individual chromosomes fail to attach properly to the mitotic spindle, a structure that forms during cell division to segregate chromosomes. Improperly attached chromosomes lag in the spindle midzone when the other chromosomes are pulled to opposite spindle poles, and these lagging chromosomes either segregate to the proper daughter cell or end up in the incorrect daughter cell. Either way, their delayed segregation means that they often fail to incorporate into the main nucleus of the daughter cells, but instead form a smaller satellite nucleus, or micronucleus (Fig. 1).

Micronuclei are not a safe place for chromosomes: their membranes are prone to rupture, which exposes the DNA to the cytoplasm⁴, and they have reduced import of DNA replication and repair factors, which can lead to DNA damage when DNA is replicated during the

S phase of the cell cycle⁵. Thus, micronuclei provide an environment ripe for chromothripsis, but there has been no direct evidence that it actually occurs in this context.

Zhang *et al.*³ demonstrate a direct association between micronuclei and chromothripsis by combining live-cell imaging and whole-genome sequencing (a combined technique referred to as 'LookSeq'). The authors induced micronucleus formation by transiently treating cells with nocodazole, a chemical agent that destabilizes the mitotic spindle and increases the frequency of improper chromosome attachment, lagging chromosomes and micronuclei. Through live imaging, the authors identified micronucleated cells that underwent micronuclear rupture during S phase and that subsequently divided to produce two daughter

cells. The authors then isolated and sequenced each daughter cell (Fig. 1).

But how could the researchers determine whether being in a micronucleus affects chromosomal structure? They show that DNA in micronuclei is poorly replicated and thus assumed that the micronuclear chromosome would not be equally distributed to the two daughter cells after cell division. This process would generate an asymmetry in the number of chromosomes (copy number) and their parental origin (haplotype) between the two daughter cells, enabling identification of the micronuclear chromosome. For example, imagine that nocodazole treatment caused the maternal copy of chromosome 2 to segregate properly but form a micronucleus. This micronucleated cell would then replicate all the chromosomes but under-replicate maternal chromosome 2 in the micronucleus. After cell division, one daughter cell would have two copies of chromosome 2 (the normal paternal haplotype and the micronuclear maternal haplotype), and the other daughter cell would have only one copy of chromosome 2 (the paternal haplotype). A copy-number and haplotype asymmetry would also exist if the lagging chromosome segregated improperly.

Zhang *et al.* found one or two chromosomes showing copy-number asymmetry in all the daughter-cell pairs they sequenced. They then used cells in which only one copy

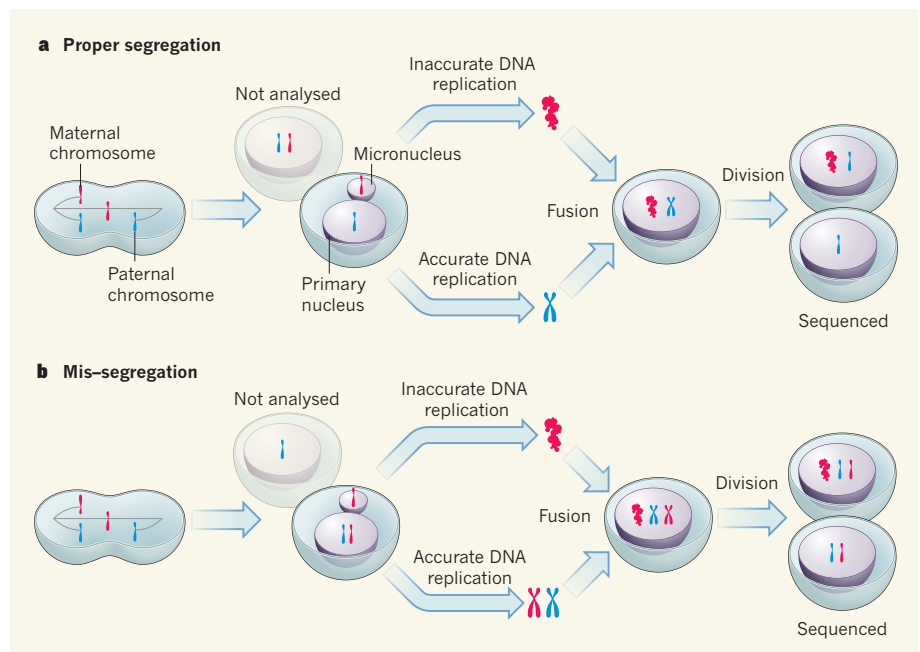


Figure 1 | Following the fate of a micronucleus. Zhang *et al.*³ treated dividing cells with the chemical nocodazole to generate lagging chromosomes that either segregate properly (a) or mis-segregate (b); in both cases, extranuclear, chromosome-containing structures called micronuclei were formed in one of the two daughter cells. The authors imaged these cells through another complete cell cycle and observed the micronuclei undergoing membrane rupture and inaccurate DNA replication. The micronucleus and the primary nucleus then fused and the cells divided; the chromosome that had been within the micronucleus was partitioned to just one of the daughter cells. By sequencing both daughter cells, the authors were able to identify the micronuclear chromosome on the basis of its copy-number asymmetry. These chromosomes contained structural rearrangements that resemble the 'chromosome shattering' known as chromothripsis.

of a chromosome remained to determine the arrangement of sequence variations for each chromosome haplotype. This allowed them to use sequence data to calculate the copy number of each haplotype in each cell and thereby identify the putative micronuclear chromosome.

The authors' sequence data further showed that micronuclear chromosomes had significantly more structural rearrangements than other chromosomes. Most of the rearrangements seemingly arose through a breakage and rejoining mechanism, which could be secondary to faulty DNA replication in the micronucleus. The transient lifespans of micronuclei and their tendency to contain only one or two chromosomes thus elegantly account for the focal nature of chromothripsis. Presumably, once the cell proceeds into the next division and the micronucleus reincorporates into the main nucleus, the damaged chromosomes are

exposed to appropriate levels of replication and repair factors, and the rearrangements could become stabilized over subsequent generations. The discovery of mitotic defects as an origin of chromothripsis provides further evidence that chromosome mis-segregation and DNA rearrangements, both of which are observed in tumour cells, can be mechanistically linked⁶.

Zhang *et al.* identified extensive rearrangements in nearly all micronuclear chromosomes, indicating that ruptured micronuclei lead to extensive mutation. Examining micronucleated cells before DNA replication, and cells in which micronuclei do not rupture, could reveal whether DNA replication is required for chromothripsis, and determine whether chromothripsis is but one of many possible outcomes for micronuclear chromosomes. LookSeq is a powerful method to address these and many other questions, providing

knowledge on both the history of a cell and the architecture of its genome. ■

Kristin A. Knouse and Angelika Amon are at the Koch Institute for Integrative Cancer Research, Department of Biology, Howard Hughes Medical Institute, Massachusetts Institute of Technology, Cambridge, Massachusetts 02139, USA.
e-mail: angelika@mit.edu

1. Stephens, P. J. *et al.* *Cell* **144**, 27–40 (2011).
2. Zack, T. I. *et al.* *Nature Genet.* **45**, 1134–1140 (2013).
3. Zhang, C.-Z. *et al.* *Nature* **522**, 179–184 (2015).
4. Hatch, E. M., Fischer, A. H., Deerinck, T. J. & Hetzer, M. W. *Cell* **154**, 47–60 (2013).
5. Crasta, K. *et al.* *Nature* **482**, 53–58 (2012).
6. Janssen, A., van der Burg, M., Szuhai, K., Kops, G. J. P. L. & Medema, R. H. *Science* **333**, 1895–1898 (2011).

This article was published online on 27 May 2015.

CLIMATE SCIENCE

Timing is everything during deglaciations

Links between various climate records for the North Atlantic Ocean and the Mediterranean Sea have helped to identify a potential mechanism that enhanced sea-level rise during the last interglacial time interval. [SEE LETTER P.197](#)

KATHARINA BILLUPS

As everyone who enjoys a good murder mystery knows, establishing the *modus operandi* of the villain is crucial to solving the crime. Similarly, understanding the forces that drive climate change requires an unambiguous reconstruction of the sequence of events involved. In this vein, Marino *et al.*¹ (page 197) have unravelled a chain of events characterizing the melting of the large polar ice sheets that existed about 140,000 years ago. This deglaciation led to the last interglacial interval — the last time that Earth underwent an interval of peak warmth between glacial periods, and at which the sea level was similar to or perhaps slightly higher than it is today². The findings reveal fundamental differences between the two most recent glacial-to-interglacial transitions.

Numerous publications^{3,4} have provided a comprehensive picture of the timings of events that make up the most recent glacial-to-interglacial transition, which began 20,000 years ago. These events culminated in our current interglacial epoch, the Holocene. But such a detailed picture is more difficult to assemble further back in time, given the inherent difficulties in dating older geological materials.

The problem is that the availability of radiometrically dated materials needed to determine an accurate sequence of events decreases the further back in time one goes. Other means of establishing ages must

therefore be used. But ages derived from, for example, astrochronology (which allows sediments to be dated using timescales calibrated by astronomical events), are more often than not further apart than the events of interest. This plagues all studies trying to resolve rapid climate changes occurring on timescales of about 10,000 years or less, which includes the timescale over which major deglaciations take place.

In their search for the chain of climatic events leading up to the last interglacial interval, Marino and colleagues have provided a solution to the age-model problem. They adjusted individual climate proxy records for the ocean (oxygen-isotope records from the fossilized remains of unicellular marine organisms called foraminifera) to oxygen-isotope records derived from speleothems — inorganic

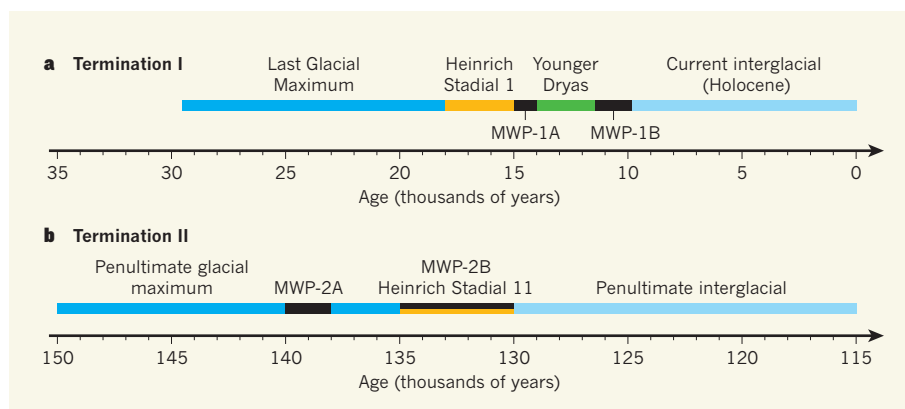


Figure 1 | Glacial-to-interglacial transitions. **a**, Termination I (TI) was the most recent time during which Earth passed from a glacial to an interglacial period. The Last Glacial Maximum represents the period when ice sheets were at their maximum extent. This was followed by a cooling event (Heinrich Stadial 1) and then the main phase of deglaciation, meltwater pulse 1A (MWP-1A). Deglaciation was interrupted by a return to almost full glacial conditions — the Younger Dryas — before the final deglaciation phase, MWP-1B. Ages for individual events in TI are taken from refs 4 and 9. **b**, Marino *et al.*¹ report the sequence of events for Termination II, the penultimate glacial-to-interglacial transition. In contrast to TI, the cooling event (Heinrich Stadial 11) coincided with the main deglaciation phase (MWP-2B). MWP-2A represents a relatively minor meltwater pulse earlier in the transition.

carbonate deposits in caves — which have radiometrically constrained chronologies for this interval of time.

This approach is not new. But the novelty of the current work lies in the fact that all records come from the Mediterranean region, and are thus naturally coupled through the local hydrological cycle and through oxygen-isotope fractionation within it, thereby providing a basis for clear correlations. Once the oxygen-isotope records from different Mediterranean sites are placed in a common temporal framework, the relative timing of associated climate parameters emerges. Temporal relationships can then be established between changes in sea surface temperatures, meltwater pulses and the deposition of ice-rafted debris onto the ocean floor.

The revised chronology of the proxy records examined by Marino and co-workers points to a pivotal difference in climate dynamics between the most recent and the penultimate glacial-to-interglacial transitions, which are also known as Terminations I and II, respectively. Both are associated with times when summer insolation (incoming solar radiation) in the Northern Hemisphere and atmospheric carbon dioxide levels were increasing. One would therefore expect the ensuing ice-sheet melt-back behaviour to have been similar as well. But it was not.

It is known that, during Termination I, there was a period of maximum cooling in the North Atlantic called Heinrich Stadial 1, which coincided with peak iceberg discharge (Fig. 1a). This was followed by the major phase of deglaciation, known as meltwater pulse 1A. Deglaciation was subsequently interrupted by a return to almost full glacial conditions — the Younger Dryas — before the final ice retreat during meltwater pulse 1B.

By contrast, Marino and colleagues' chronology shows that the main phase of deglaciation (meltwater pulse 2B) during Termination II occurred during the period of maximum North Atlantic cooling and iceberg discharge (Heinrich Stadial 11). In short, Heinrich Stadial 1 preceded the major phase of ice-sheet retreat, whereas Heinrich Stadial 11 coincided with it (Fig. 1b). This means that not all terminations are equal, making it much more difficult to find an underlying forcing mechanism.

North Atlantic cooling and enhanced iceberg discharge during Heinrich Stadial 11 might seem to be at odds with background climate warming and deglaciation. But as the authors point out, the new chronology also reveals that Heinrich Stadial 11 coincided with warming in the Southern Hemisphere, as recorded by ice cores⁵. Warming in one hemisphere coinciding with cooling in the other is a well-characterized phenomenon called the bipolar see-saw⁶. The term refers to ocean-surface heat transport from the Southern to the Northern Hemisphere as part of a

large-scale circulation process (the meridional overturning circulation) in the Atlantic Ocean. During Heinrich Stadial 11, relatively slow ocean circulation allowed heat to build up in the Southern Hemisphere. The authors suggest that this warming stimulated melting of the Antarctic ice sheet, contributing to the enhanced sea-level rise associated with the penultimate deglaciation.

Marino and co-workers' study exemplifies how the nature of the temporal ties between climate records can affect the reconstruction and understanding of climate events. The researchers provide a specific solution to the timing of events during Termination II. However, the generality of their approach is limited by the assumptions that need to be made about climatological links between radiometrically dated speleothem and marine proxy records from dissimilar oceanographic regions.

Rapid deglaciations such as Terminations I and II are part of an asymmetric climate pattern that begins with slow ice-sheet build-up followed by rapid ice-sheet melt-back. This sequence repeats on timescales of about 100,000 years and first appears in the geological record of climate change about 900,000 years ago⁷. There are no obvious direct external forcing mechanisms for this pattern, unlike the

shorter climate cycles that occur on timescales of 41,000 to 19,000 years. The evolution of the 100,000-year climate cycle is therefore one of the big unsolved mysteries in palaeoceanographic research⁸. A robust temporal reference frame for the sequence of events defining each deglaciation, such as that assembled by Marino *et al.* for the penultimate one, should help to build a consensus about the *modus operandi* behind this climate pattern. ■

Katharina Billups is at the School of Marine Science and Policy, University of Delaware, Lewes, Delaware 19958, USA.
e-mail: kbillups@udel.edu

1. Marino, G. *et al.* *Nature* **522**, 197–201 (2015).
2. Grant, K. M. *et al.* *Nature Commun.* **5**, 5076; <http://dx.doi.org/10.1038/ncomms6076> (2014).
3. Fairbanks, R. G. *Nature* **342**, 637–642 (1989).
4. Denton, G. H. *et al.* *Science* **328**, 1652–1656 (2010).
5. Masson-Delmotte, V. *et al.* *Quat. Sci. Rev.* **29**, 113–128 (2010).
6. Broecker, W. S. *Paleoceanography* **13**, 119–121 (1998).
7. Pisias, N. G. & Moore, T. C. Jr *Earth Planet. Sci. Lett.* **52**, 450–458 (1981).
8. Ruddiman, W. F. *Earth's Climate: Past and Future* 3rd edn, Ch. 12 (Freeman, 2013).
9. Lambeck, K., Rouby, H., Purcell, A., Sun, Y. & Sambridge, M. *Proc. Natl Acad. Sci. USA* **111**, 15296–15303 (2014).

HUMAN EVOLUTION

Ancient DNA steps into the language debate

Two studies of ancient human DNA reveal expansions of Bronze Age populations that shed light on the long-running debate about the origins and spread of Indo-European languages. SEE ARTICLE P.167 & LETTER P.207

JOHN NOVEMBRE

The archaeological adage that pots are not people expresses the challenge of using cultural artefacts to trace the movement of populations. To surmount this obstacle, archaeologists and population geneticists are joining forces to extract DNA from human remains that are found with archaeological evidence of ancient cultures. In this issue, Haak *et al.*¹ (page 207) and Allentoft *et al.*² (page 167) report two of the largest studies of ancient DNA to date. Combined, the studies analyse 170 samples, and each group brings evidence to bear on a long-standing controversy about the origins of the Indo-European language family.

Indo-European languages have been spoken across Europe and in central and southern Asia since the beginning of recorded history. This is a broad language family, including Italic, Germanic, Slavic, Hindi and Tocharian

languages, among others. When and where the precursor of these languages began to spread has long been a subject of debate³. There are two main theories: the Anatolian and the steppe hypotheses.

The Anatolian hypothesis posits that Proto-Indo-European spread with farming out of Anatolia (a region that lies within modern-day Turkey) during the Neolithic period, approximately 7000 BC. Some archaeological and genetic data support this hypothesis, as does a phylogenetic analysis of linguistic data⁴. By contrast, the steppe hypothesis^{3,5} supposes that Proto-Indo-European spread from the Pontic-Caspian steppe (a region of modern-day Russia, Ukraine and Kazakhstan that lies north of the Black Sea and stretches eastwards to the Caspian Sea; Fig. 1a). Recent versions of the hypothesis argue that the language spread during the late Copper Age and early Bronze Age, between 3700 BC and 2000 BC, carried

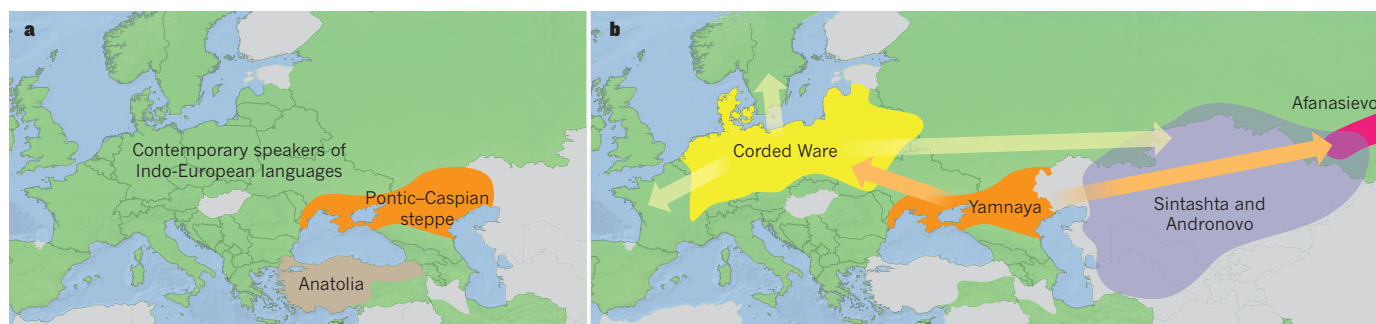


Figure 1 | The spread of Indo-European languages. **a**, Indo-European languages have been spoken across a broad area of Eurasia throughout recorded history (countries in which these languages are spoken today are marked in green). Two geographical origins for these languages have been proposed: Anatolia and the Pontic–Caspian steppe. **b**, Haak *et al.*¹ and Allentoft *et al.*² analysed ancient DNA taken from samples from across Europe and central Asia. Their data point to human migration from a steppe culture, the Yamnaya.

They conclude that the Corded Ware culture of central Europe had ancestry from the Yamnaya. Allentoft *et al.* also show that the Afanasievo culture to the east is related to the Yamnaya, and that the Sintashta and Andronovo cultures had ancestry from the Corded Ware. Arrows indicate migrations — those from the Corded Ware reflect the evidence that people of this archaeological culture (or their relatives) were responsible for the spreading of Indo-European languages. All coloured boundaries are approximate.

by pastoralist horse-riders empowered by the innovation of wheeled wagons — probably the people associated with a culture known to archaeologists as the Yamnaya³.

Previous studies of both modern and ancient DNA^{6,7} have suggested an influx of people into Europe from modern Eurasia after the spread of Neolithic farming. However, the details have been hazy, and any role for steppe populations has been unclear. To resolve this uncertainty, Haak *et al.* and Allentoft *et al.* obtained ancient human DNA samples from a broad swathe of archaeological cultures from Europe and central Asia dating from around 6000 BC to 900 BC. Although each study used different strategies (Allentoft *et al.* sequenced whole genomes, whereas Haak *et al.* targeted select regions), the groups successfully obtained around 101 and 69 samples, respectively — a remarkable achievement. The sequencing data are poor by the standards applied to modern DNA, but they are sufficient to discern broad brushstrokes of human migration.

Both studies found a genetic affinity between samples from a central European culture known as Corded Ware, which existed from around 2500 BC, and samples from the earlier Yamnaya steppe culture. This similarity between distant populations is best explained by a substantial westward expansion of the Yamnaya or their close relatives into central Europe (Fig. 1b). Such an expansion is consistent with the steppe hypothesis, which argues that Corded Ware cultures were a conduit for the dispersal of Indo-European languages into Europe. The results also help to explain a mysterious ancestry found in both Europe and the Americas⁸, and in ancient DNA from a boy who lived 24,000 years ago in eastern Siberia⁹. Both groups of researchers suggest that this ancestry entered Europe through the expansion of Yamnaya-related peoples, who are descended from the north Eurasian populations that contributed to the peopling of the Americas.

The data also suggest that steppe populations expanded eastwards. Allentoft *et al.*

found that the Afanasievo culture from central Asia shows genetic affinity with the Yamnaya. They also found evidence to support theories of a back-migration from Corded Ware-related populations³ that contributed to the origins of the Sintashta culture in the Urals and their descendants, the Andronovo. This is particularly interesting because the steppe hypothesis supposes that an eastward migration of steppe-descendant populations helped to give rise to Tocharian, a branch of Indo-European once spoken in western China.

Together, these studies argue that Bronze Age population movements were important in shaping the genetics of Eurasia. Ancient DNA cannot prove how language spread, of course, and more data will help to refine our understanding, but expansions of Yamnaya-related peoples add weight to the steppe hypothesis. If genes were moving en masse, it is likely that words were too.

It remains to be seen whether ancient DNA samples will also support the hypothesis that the Indo-Iranian branch of Indo-European can be traced to a southward migration from the steppe. Research on modern DNA¹⁰ has posited the existence of an ancient north Indian population — can this be linked directly to the steppe populations? The size of the ancestral steppe populations and the rate at which they expanded also remain to be determined. Finally, the migratory models put forward by the two groups differ in terms of how Near Eastern populations such as Armenians relate to the steppe. Haak and colleagues' model implies that Near Eastern populations contribute ancestry to the Yamnaya, but aspects of Allentoft and co-workers' data do not support such admixture. Future studies should resolve these questions.

Nonetheless, these two studies represent a milestone in a 200-year-old debate. Tragically, this debate figured heavily in the racist politics and science of the nineteenth and early twentieth centuries in Europe³. The current research takes place in a more open and humane

framework, and this should be encouraged and protected. It will be exciting to see what the careful use of ancient DNA will reveal about the history of other language families and their speakers.

The studies also foreshadow how studies of ancient DNA will empower studies of adaptive evolution. For instance, Allentoft *et al.* observed that the spread of a mutation that allows humans to drink milk into adulthood began only in the Bronze Age, later than previously supposed — a finding replicated by Haak and colleagues in another paper¹¹.

One final point is that the genomes of living people vary more or less continuously with geography in most regions of the globe¹². But these two studies suggest that the relatively continuous patterns seen in modern DNA can be teased apart and understood in terms of a complex history of expansions and mixtures of ancient populations. Clearly, intersecting ancient DNA with archaeological and linguistic research promises to yield great progress in the study of prehistory. ■

John Novembre is in the Department of Human Genetics, University of Chicago, Chicago, Illinois 60637, USA.
e-mail: jnovembre@uchicago.edu

1. Haak, W. *et al.* *Nature* **522**, 207–211 (2015).
2. Allentoft, M. E. *et al.* *Nature* **522**, 167–172 (2015).
3. Anthony, D. W. *The Horse, the Wheel, and Language: How Bronze-Age Riders From the Eurasian Steppes Shaped the Modern World* (Princeton Univ. Press, 2007).
4. Bouckaert, R. *et al.* *Science* **337**, 957–960 (2012).
5. Gimbutas, M. *The Prehistory of Eastern Europe Part 1* (Peabody Museum, 1956).
6. Brandt, G., Szécsényi-Nagy, A., Roth, C., Alt, K. W. & Haak, W. *J. Hum. Evol.* **79**, 73–92 (2015).
7. Lazaridis, I. *et al.* *Nature* **513**, 409–413 (2014).
8. Patterson, N. *et al.* *Genetics* **192**, 1065–1093 (2012).
9. Raghavan, M. *et al.* *Nature* **505**, 87–91 (2014).
10. Moorjani, P. *et al.* *Am. J. Hum. Genet.* **93**, 422–438 (2013).
11. Mathieson, I. *et al.* Preprint at *bioRxiv* <http://dx.doi.org/10.1101/016477> (2015).
12. Wang, C., Zöllner, S. & Rosenberg, N. A. *PLoS Genet.* **8**, e1002886 (2012).

Population genomics of Bronze Age Eurasia

Morten E. Allentoft^{1*}, Martin Sikora^{1*}, Karl-Göran Sjögren², Simon Rasmussen³, Morten Rasmussen¹, Jesper Stenderup¹, Peter B. Damgaard¹, Hannes Schroeder^{1,4}, Torbjörn Ahlström⁵, Lasse Vinner¹, Anna-Sapfo Malaspinas¹, Ashot Margaryan¹, Tom Higham⁶, David Chivall⁶, Niels Lynnerup⁷, Lise Harvig⁷, Justyna Baron⁸, Philippe Della Casa⁹, Paweł Dąbrowski¹⁰, Paul R. Duffy¹¹, Alexander V. Ebel¹², Andrey Epimakhov¹³, Karin Frei¹⁴, Mirosław Furmanek⁸, Tomasz Gralak⁸, Andrey Gromov¹⁵, Stanisław Gronkiewicz¹⁶, Gisela Grupe¹⁷, Tamás Hajdu^{18,19}, Radosław Jarysz²⁰, Valeri Khartanovich¹⁵, Alexandr Khokhlov²¹, Viktória Kiss²², Jan Kolář^{23,24}, Aivar Kriiska²⁵, Irena Lasak⁸, Cristina Longhi²⁶, George McGlynn¹⁷, Algimantas Merkevičius²⁷, Inga Merkyte²⁸, Mait Metspalu²⁹, Ruzan Mkrtchyan³⁰, Vyacheslav Moiseyev¹⁵, László Paja^{31,32}, György Pálfi³², Dalia Pokutta², Łukasz Pospieszny³³, T. Douglas Price³⁴, Lehti Saag²⁹, Mikhail Sablin³⁵, Natalia Shishlina³⁶, Václav Smrčka³⁷, Vasili I. Soenov³⁸, Vajk Szeverényi²², Gusztáv Tóth³⁹, Synaru V. Trifanova³⁸, Liivi Varul²⁵, Magdolna Vicze⁴⁰, Levon Yepiskoposyan⁴¹, Vladislav Zhitenov⁴², Ludovic Orlando¹, Thomas Sicheritz-Pontén³, Søren Brunak^{3,43}, Rasmus Nielsen⁴⁴, Kristian Kristiansen² & Eske Willerslev¹

The Bronze Age of Eurasia (around 3000–1000 BC) was a period of major cultural changes. However, there is debate about whether these changes resulted from the circulation of ideas or from human migrations, potentially also facilitating the spread of languages and certain phenotypic traits. We investigated this by using new, improved methods to sequence low-coverage genomes from 101 ancient humans from across Eurasia. We show that the Bronze Age was a highly dynamic period involving large-scale population migrations and replacements, responsible for shaping major parts of present-day demographic structure in both Europe and Asia. Our findings are consistent with the hypothesized spread of Indo-European languages during the Early Bronze Age. We also demonstrate that light skin pigmentation in Europeans was already present at high frequency in the Bronze Age, but not lactose tolerance, indicating a more recent onset of positive selection on lactose tolerance than previously thought.

The processes that created the genetic landscape of contemporary human populations of Europe and Asia remain contentious. Recent studies have revealed that western Eurasians and East Asians diverged outside Africa between 45 and 36.2 thousand years before present (45 and 36.2 kyr BP)^{1,2} and that East Asians, but not Europeans, received subsequent gene flow from remnants of an earlier migration into Asia of Aboriginal Australian ancestors at some point before 20 kyr BP³. There is evidence that the western Eurasian branch constituted a meta-population stretching from Europe to Central Asia^{2,4} and that it contributed genes to both modern-day western Eurasians⁴ and early

indigenous Americans^{4–6}. The early Europeans received gene flow from the Middle East during the Neolithisation (transition from hunting-gathering to farming) around 8–5 kyr BP^{7–12} and possibly also from northern Asia¹⁰. However, what happened hereafter, during the Bronze Age, is much less clear.

The archaeological record testifies to major cultural changes in Europe and Asia after the Neolithic period. By 3000 BC, the Neolithic farming cultures in temperate Eastern Europe appear to be largely replaced by the Early Bronze Age Yamnaya culture, which is associated with a completely new perception of family, property and

¹Centre for GeoGenetics, Natural History Museum, University of Copenhagen, Øster Voldgade 5–7, 1350 Copenhagen K, Denmark. ²Department of Historical Studies, University of Gothenburg, 405 30 Gothenburg, Sweden. ³Center for Biological Sequence Analysis, Department of Systems Biology, Technical University of Denmark, 2800 Kgs Lyngby, Denmark. ⁴Faculty of Archaeology, Leiden University, 2300 Leiden, The Netherlands. ⁵Department of Archaeology and Ancient History, Lund University, 221 00 Lund, Sweden. ⁶Oxford Radiocarbon Accelerator Unit, University of Oxford, Oxford OX1 3QY, UK. ⁷Unit of Forensic Anthropology, Department of Forensic Medicine, University of Copenhagen, 2100 Copenhagen, Denmark. ⁸Institute of Archaeology, University of Wrocław, 50-139 Wrocław, Poland. ⁹Archaeological Institute, University of Zurich, CH-8006, Zurich, Switzerland. ¹⁰Department of Anatomy, Wrocław Medical University, 50-368 Wrocław, Poland. ¹¹Department of Anthropology, University of Toronto, Toronto ONM5S 2S2, Canada. ¹²Department of Archaeology and General History, Gorno-Altai State University, 649000 Gorno-Altai, Russia. ¹³Institute of History and Archaeology RAS (South Ural Department), South Ural State University, 454080 Chelyabinsk, Russia. ¹⁴Environmental Research and Material Science and Centre for Textile Research, The National Museum of Denmark, 1471 Copenhagen K, Denmark. ¹⁵Peter the Great Museum of Anthropology and Ethnography (Kunstkamera) RAS, 199034 St Petersburg, Russia. ¹⁶Department of Anthropology, Polish Academy of Sciences, 50-449 Wrocław, Poland. ¹⁷Biocentre of the Ludwig-Maximilians-University München, 82152 Munich, Germany. ¹⁸Department of Biological Anthropology, Institute of Biology, Eötvös Loránd University, H-1117 Budapest, Hungary. ¹⁹Department of Anthropology, Hungarian Natural History Museum, H-1083 Budapest, Hungary. ²⁰The Archaeological Museum of Wrocław, 50-077 Wrocław, Poland. ²¹Samara State Academy of Social Science and Humanities, 443099 Samara, Russia. ²²Institute of Archaeology of the Hungarian Academy of Sciences, Research Center for the Humanities, H-1250 Budapest, Hungary. ²³Institute of Archaeology and Museology, Faculty of Arts, Masaryk University, CZ-602 00 Brno, Czech Republic. ²⁴Department of Vegetation Ecology, Institute of Botany of the Czech Academy of Sciences, CZ-602 00 Brno, Czech Republic. ²⁵Department of Archaeology, University of Tartu, 51003 Tartu, Estonia. ²⁶Archaeological Superintendence of Lombardy, 20123 Milano, Italy. ²⁷Department of Archaeology, University of Vilnius, LT-01513 Vilnius, Lithuania. ²⁸The SAXO Institute, University of Copenhagen, 2300 Copenhagen S, Denmark. ²⁹Department of Evolutionary Biology, Estonian Biocentre and University of Tartu, 51010 Tartu, Estonia. ³⁰Department of History, Yerevan State University, 0025 Yerevan, Armenia. ³¹Hungarian National Museum, H-1083 Budapest, Hungary. ³²Department of Biological Anthropology, University of Szeged, H-6726 Szeged, Hungary. ³³Institute of Archaeology and Ethnology of the Polish Academy of Sciences, 61-612 Poznań, Poland. ³⁴Laboratory for Archaeological Chemistry, University of Wisconsin-Madison, Madison, Wisconsin 53706, USA. ³⁵Zoological Institute of the Russian Academy of Sciences, 199034 St Petersburg, Russia. ³⁶Department of Archaeology, State Historical Museum, 109012 Moscow, Russia. ³⁷Institute for History of Medicine and Foreign Languages of the First Faculty of Medicine, Charles University, 121 08 Prague, Czech Republic. ³⁸Research Center for the History and Culture of the Turkic Peoples, Gorno-Altai State University, 649000 Gorno-Altai, Russia. ³⁹Department of Pre- and Early History, Institute of Archaeological Sciences, Faculty of Humanities, Eötvös Loránd University, H-1088 Budapest, Hungary. ⁴⁰Matrica Museum, 2440 Százhalombatta, Hungary. ⁴¹Laboratory of Ethnogenomics, Institute of Molecular Biology, National Academy of Sciences, 0014 Yerevan, Armenia. ⁴²Department of Archaeology, Faculty of History, Moscow State University, 119991 Moscow, Russia. ⁴³Novo Nordisk Foundation Center for Protein Research, University of Copenhagen, 2200 Copenhagen, Denmark. ⁴⁴Center for Theoretical Evolutionary Genetics, University of California, Berkeley, California 94720-3140, USA.

*These authors contributed equally to this work.

personhood^{13,14}, rapidly stretching from Hungary to the Urals¹⁵. By 2800 BC a new social and economic formation, variously named Corded Ware, Single Grave or Battle Axe cultures developed in temperate Europe, possibly deriving from the Yamnaya background, and culturally replacing the remaining Neolithic farmers^{16,17} (Fig. 1). In western and Central Asia, hunter-gatherers still dominated in Early Bronze Age, except in the Altai Mountains and Minusinsk Basin where the Afanasievo culture existed with a close cultural affinity to Yamnaya¹⁵ (Fig. 1). From the beginning of 2000 BC, a new class of master artisans known as the Sintashta culture emerged in the Urals, building chariots, breeding and training horses (Fig. 1), and producing sophisticated new weapons¹⁸. These innovations quickly spread across Europe and into Asia where they appeared to give rise to the Andronovo culture^{19,20} (Fig. 1). In the Late Bronze Age around 1500 BC, the Andronovo culture was gradually replaced by the Mezhovskaya, Karasuk, and Koryakova cultures²¹. It remains debated if these major cultural shifts during the Bronze Age in Europe and Asia resulted from the migration of people or through cultural diffusion among settled groups^{15–17}, and if the spread of the Indo-European languages was linked to these events or predates them¹⁵.

Archaeological samples and DNA retrieval

Genomes obtained from ancient biological remains can provide information on past population histories that is not retrievable from contemporary individuals^{4,22}. However, ancient genomic studies have so far been restricted to single or a few individuals because of the degraded nature of ancient DNA making sequencing costly and time consuming²³. To overcome this, we increased the average output of

authentic endogenous DNA fourfold by: (1) targeting the outer cementum layer in teeth rather than the inner dentine layer^{24,25}, (2) adding a ‘pre-digestion’ step to remove surface contaminants^{24,26}, and (3) developing a new binding buffer for ancient DNA extraction (Supplementary Information, section 3). This allowed us to obtain low-coverage genome sequences (0.01–7.4× average depth, overall average equal to 0.7×) of 101 Eurasian individuals spanning the entire Bronze Age, including some Late Neolithic and Iron Age individuals (Fig. 1, Supplementary Information, sections 1 and 2). Our data set includes 19 genomes, between 1.1–7.4× average depth, thereby doubling the number of existing Eurasian ancient genomes above 1× coverage (ref. 27).

Bronze Age Europe

By analysing our genomic data in relation to previously published ancient and modern data (Supplementary Information, section 6), we find evidence for a genetically structured Europe during the Bronze Age (Fig. 2; Extended Data Fig. 1; and Supplementary Figs 5 and 6). Populations in northern and central Europe were composed of a mixture of the earlier hunter-gatherer and Neolithic farmer¹⁰ groups, but received ‘Caucasian’ genetic input at the onset of the Bronze Age (Fig. 2). This coincides with the archaeologically well-defined expansion of the Yamnaya culture from the Pontic-Caspian steppe into Europe (Figs 1 and 2). This admixture event resulted in the formation of peoples of the Corded Ware and related cultures, as supported by negative ‘admixture’ f_3 statistics when using Yamnaya as a source population (Extended Data Table 2, Supplementary Table 12). Although European Late Neolithic and Bronze Age cultures such

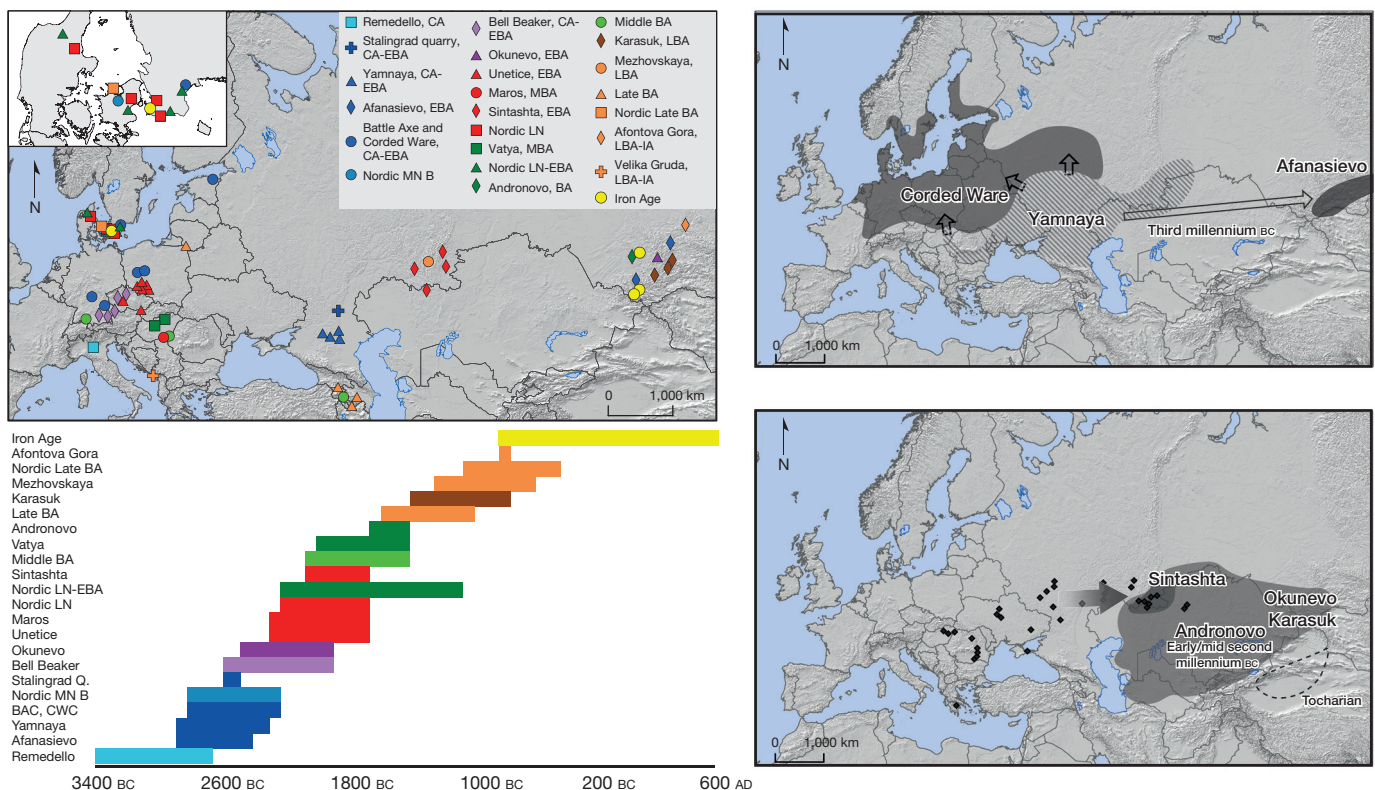


Figure 1 | Distribution maps of ancient samples. Localities, cultural associations, and approximate timeline of 101 sampled ancient individuals from Europe and Central Asia (left). Distribution of Early Bronze Age cultures Yamnaya, Corded Ware, and Afanasievo with arrows showing the Yamnaya expansions (top right). Middle and Late Bronze Age cultures Sintashta, Andronovo, Okunevo, and Karasuk with the eastward migration indicated

(bottom right). Black markers represent chariot burials (2000–1800 BC) with similar horse cheek pieces, as evidence of expanding cultures. Tocharian is the second-oldest branch of Indo-European languages, preserved in Western China. CA, Copper Age; MN, Middle Neolithic; LN, Late Neolithic; EBA, Early Bronze Age; MBA, Middle Bronze Age; LBA, Late Bronze Age; IA, Iron Age; BAC, Battle Axe culture; CWC, Corded Ware culture.

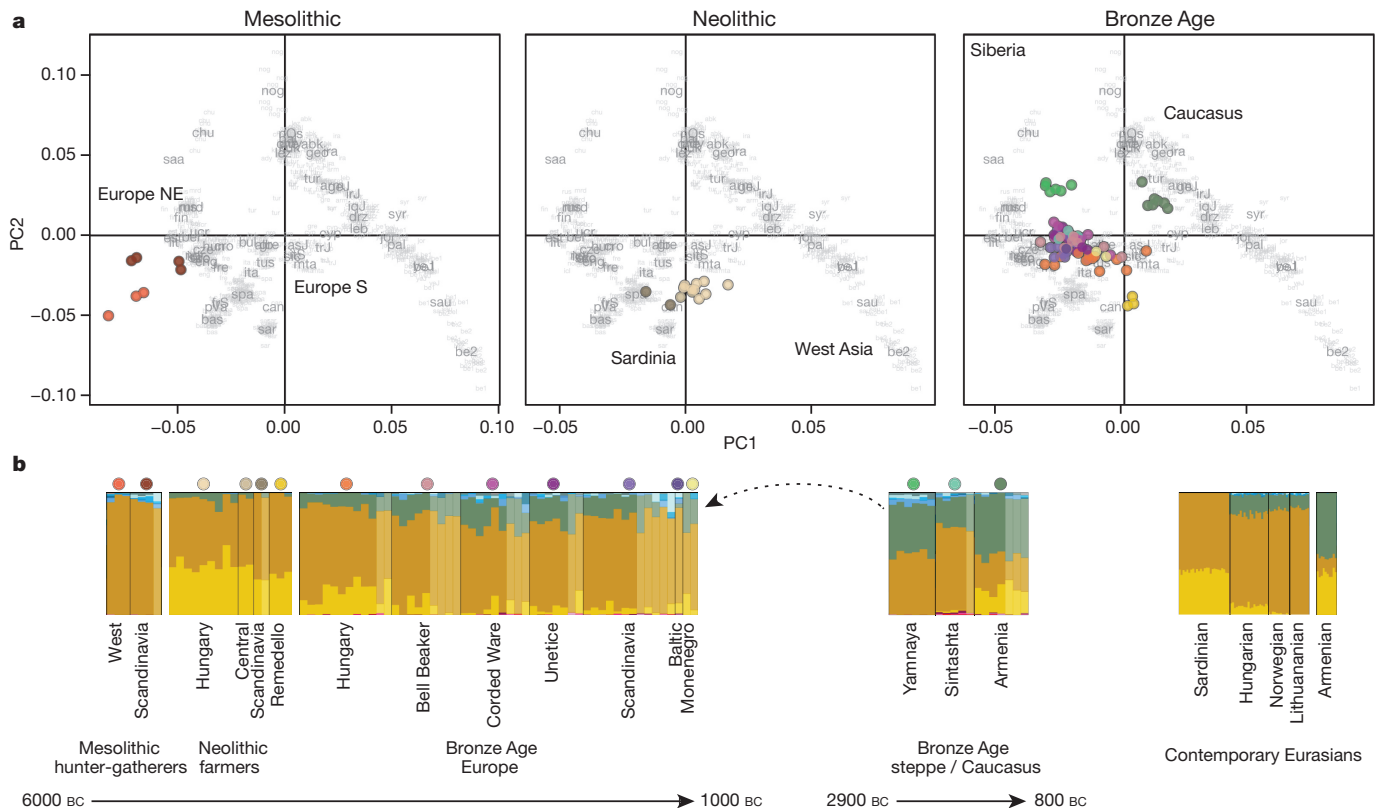


Figure 2 | Genetic structure of ancient Europe and the Pontic-Caspian steppe. **a**, Principal component analysis (PCA) of ancient individuals ($n = 93$) from different periods projected onto contemporary individuals from Europe, West Asia, and Caucasus. Grey labels represent population codes showing coordinates for individuals (small) and population median (large). Coloured circles indicate ancient individuals **b**, ADMIXTURE ancestry components

($K = 16$) for ancient ($n = 93$) and selected contemporary individuals. The width of the bars representing ancient individuals is increased to aid visualization. Individuals with less than 20,000 SNPs have lighter colours. Coloured circles indicate corresponding group in the PCA. Probable Yamnaya-related admixture is indicated by the dashed arrow.

as Corded Ware, Bell Beakers, Unetice, and the Scandinavian cultures are genetically very similar to each other (Fig. 2), they still display a cline of genetic affinity with Yamnaya, with highest levels in Corded Ware, lowest in Hungary, and central European Bell Beakers being intermediate (Fig. 2b and Extended Data Table 1). Using D -statistics, we find that Corded Ware and Yamnaya individuals form a clade to the exclusion of Bronze Age Armenians (Extended Data Table 1) showing that the genetic ‘Caucasus component’ present in Bronze Age Europe has a steppe origin rather than a southern Caucasus origin. Earlier studies have shown that southern Europeans received substantial gene flow from Neolithic farmers during the Neolithic⁹. Despite being slightly later, we find that the Copper Age Remedello culture in Italy does not have the ‘Caucasian’ genetic component and is still clustering genetically with Neolithic farmers (Fig. 2; Extended Data Fig. 1 and Supplementary Fig. 6). Hence this region was either unaffected by the Yamnaya expansion or the Remedello pre-dates such an expansion into southern Europe. The ‘Caucasian’ component is clearly present during Late Bronze Age in Montenegro (Fig. 2b). The close affinity we observe between peoples of Corded Ware and Sintashta cultures (Extended Data Fig. 2a) suggests similar genetic sources of the two, which contrasts with previous hypotheses placing the origin of Sintashta in Asia or the Middle East²⁸. Although we cannot formally test whether the Sintashta derives directly from an eastward migration of Corded Ware peoples or if they share common ancestry with an earlier steppe population, the presence of European Neolithic farmer ancestry in both the Corded Ware and the Sintashta, combined with the absence of Neolithic farmer ancestry in the earlier Yamnaya, would suggest the former being more probable (Fig. 2b and Extended Data Table 1).

Bronze Age Asia

We find that the Bronze Age in Asia is equally dynamic and characterized by large-scale migrations and population replacements. The Early Bronze Age Afanasievo culture in the Altai-Sayan region is genetically indistinguishable from Yamnaya, confirming an eastward expansion across the steppe (Figs 1 and 3b; Extended Data Fig. 2b and Extended Data Table 1), in addition to the westward expansion into Europe. Thus, the Yamnaya migrations resulted in gene flow across vast distances, essentially connecting Altai in Siberia with Scandinavia in the Early Bronze Age (Fig. 1). The Andronovo culture, which arose in Central Asia during the later Bronze Age (Fig. 1), is genetically closely related to the Sintashta peoples (Extended Data Fig. 2c), and clearly distinct from both Yamnaya and Afanasievo (Fig. 3b and Extended Data Table 1). Therefore, Andronovo represents a temporal and geographical extension of the Sintashta gene pool. Towards the end of the Bronze Age in Asia, Andronovo was replaced by the Karasuk, Mezhovskaya, and Iron Age cultures which appear multi-ethnic and show gradual admixture with East Asians (Fig. 3b and Extended Data Table 2), corresponding with anthropological and biological research²⁹. However, Iron Age individuals from Central Asia still show higher levels of West Eurasian ancestry than contemporary populations from the same region (Fig. 3b). Intriguingly, individuals of the Bronze Age Okunevo culture from the Sayano-Altai region (Fig. 1) are related to present-day Native Americans (Extended Data Fig. 2d), which confirms previous craniometric studies³⁰. This finding implies that Okunevo could represent a remnant population related to the Upper Palaeolithic Mal'ta hunter-gatherer population from Lake Baikal that contributed genetic material to Native Americans⁴.

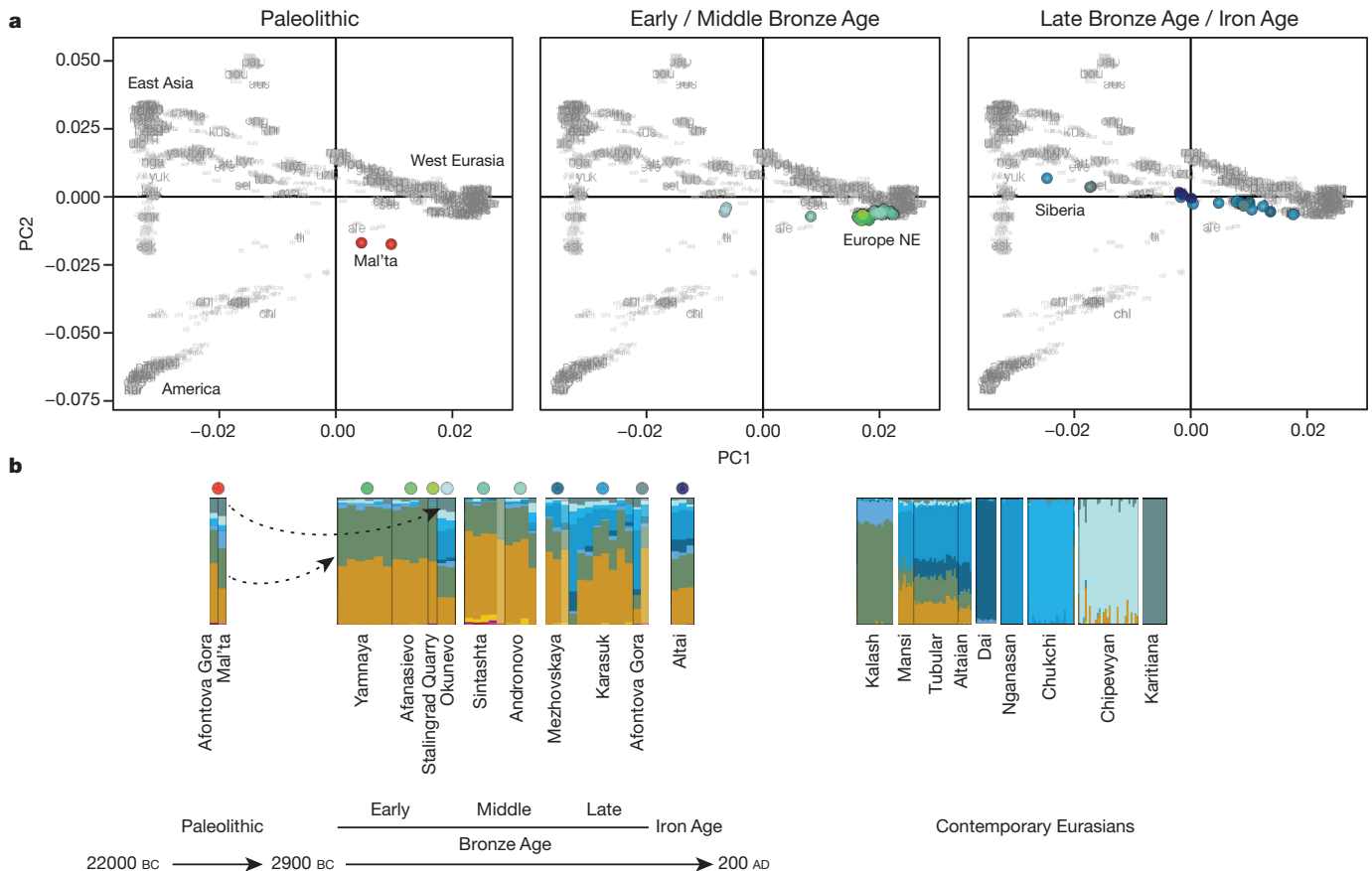


Figure 3 | Genetic structure of Bronze Age Asia. **a**, Principal component analysis (PCA) of ancient individuals ($n = 40$) from different periods projected onto contemporary non-Africans. Grey labels represent population codes showing coordinates for individuals (small) and population median (large). Coloured circles indicate ancient individuals. **b**, ADMIXTURE ancestry components ($K = 16$) for ancient ($n = 40$) and selected contemporary

individuals. The width of the bars representing ancient individuals is increased to aid visualization. Individuals with less than 20,000 SNPs have lighter colours. Coloured circles indicate corresponding group in the PCA. Shared ancestry of Mal'ta with Yamnaya (green component) and Okunevo (grey component) is indicated by dashed arrows.

Spread of the Indo-European languages

Historical linguists have argued that the spread of the Indo-European languages must have required migration combined with social or demographic dominance, and this expansion has been supported by archaeologists pointing to striking similarities in the archaeological record across western Eurasia during the third millennium BC^{15,18,31}. Our genomic evidence for the spread of Yamnaya people from the Pontic-Caspian steppe to both northern Europe and Central Asia during the Early Bronze Age (Fig. 1) corresponds well with the hypothesized expansion of the Indo-European languages. In contrast to recent genetic findings³², however, we only find weak evidence for admixture in Yamnaya, and only when using Bronze Age Armenians and the Upper Palaeolithic Mal'ta as potential source populations ($Z = -2.39$; Supplementary Table 12). This could be due to the absence of eastern hunter-gatherers as potential source population for admixture in our data set. Modern Europeans show some genetic links to Mal'ta⁴ that has been suggested to form a third European ancestral component (Ancestral North Eurasians (ANE))¹⁰. Rather than a hypothetical ancient northern Eurasian group, our results reveal that ANE ancestry in Europe probably derives from the spread of the Yamnaya culture that distantly shares ancestry with Mal'ta (Figs 2b and 3b and Extended Data Fig. 3).

Formation of Eurasian genetic structure

It is clear from our autosomal, mitochondrial DNA and Y chromosome data (Extended Data Fig. 6) that the European and Central

Asian gene pools towards the end of the Bronze Age mirror present-day Eurasian genetic structure to an extent not seen in the previous periods (Figs 2 and 3; Extended Data Fig. 1 and Supplementary Fig. 6). Our results imply that much of the basis of the Eurasian genetic landscape of today was formed during the complex patterns of expansions, admixture and replacements during this period. We find that many contemporary Eurasians show lower genetic differentiation (F_{ST}) with local Bronze Age groups than with earlier Mesolithic and Neolithic groups (Extended Data Figs 4 and 5). Notable exceptions are contemporary populations from southern Europe such as Sardinians and Sicilians, which show the lowest F_{ST} with Neolithic farmers. In general, the levels of differentiation between ancient groups from different temporal and cultural contexts are greater than those between contemporary Europeans. For example, we find pairwise $F_{ST} = 0.08$ between Mesolithic hunter-gatherers and Bronze Age individuals from Corded Ware, which is nearly as high as F_{ST} between contemporary East Asians and Europeans (Extended Data Fig. 5). These results are indicative of significant temporal shifts in the gene pools and also reveal that the ancient groups of Eurasia were genetically more structured than contemporary populations. The diverged ancestral genomic components must then have diffused further after the Bronze Age through population growth, combined with continuing gene flow between populations, to generate the low differentiation observed in contemporary west Eurasians.

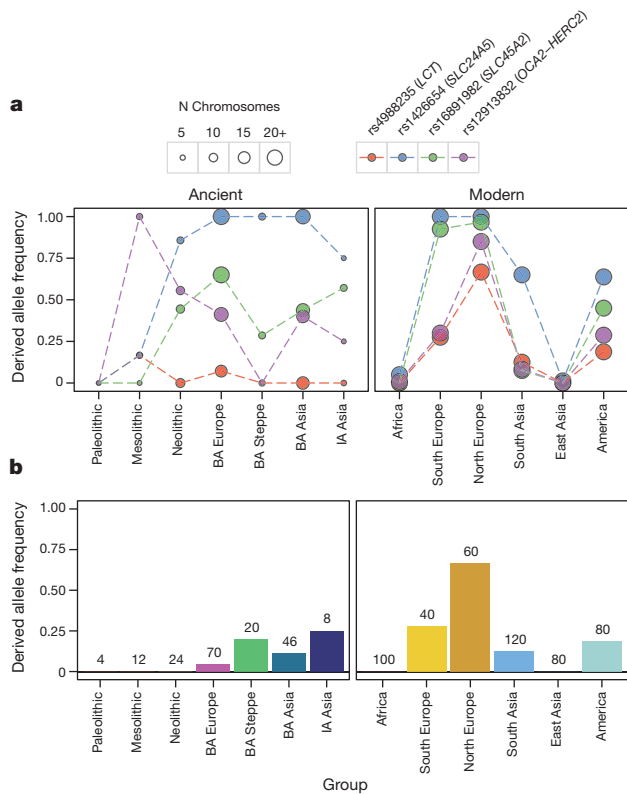


Figure 4 | Allele frequencies for putatively positively selected SNPs.

a, Coloured circles indicate the observed frequency of the respective SNP in ancient and modern groups (1000 Genomes panel). The size of the circle is proportional to the number of samples for each SNP and population. **b**, Allele frequency of rs4988235 in the *LCT* (lactase) gene inferred from imputation of ancient individuals. Numbers indicate the total number of chromosomes for each group. BA, Bronze Age; IA, Iron Age.

Temporal dynamics of selected SNPs

The size of our data set allows us to investigate the temporal dynamics of 104 genetic variants associated with important phenotypic traits or putatively undergoing positive selection³³ (Supplementary Table 13). Focusing on four well-studied polymorphisms, we find that two single nucleotide polymorphisms (SNPs) associated with light skin pigmentation in Europeans exhibit a rapid increase in allele frequency (Fig. 4). For rs1426654, the frequency of the derived allele increases from very low to fixation within a period of approximately 3,000 years between the Mesolithic and Bronze Age in Europe. For rs12913832, a major determinant of blue versus brown eyes in humans, our results indicate the presence of blue eyes already in Mesolithic hunter-gatherers as previously described³³. We find it at intermediate frequency in Bronze Age Europeans, but it is notably absent from the Pontic-Caspian steppe populations, suggesting a high prevalence of brown eyes in these individuals (Fig. 4). The results for rs4988235, which is associated with lactose tolerance, were surprising. Although tolerance is high in present-day northern Europeans, we find it at most at low frequency in the Bronze Age (10% in Bronze Age Europeans; Fig. 4), indicating a more recent onset of positive selection than previously estimated³⁴. To further investigate its distribution, we imputed all SNPs in a 2 megabase (Mb) region around rs4988235 in all ancient individuals using the 1000 Genomes phase 3 data set as a reference panel, as previously described¹². Our results confirm a low frequency of rs4988235 in Europeans, with a derived allele frequency of 5% in the combined Bronze Age Europeans (genotype probability > 0.85) (Fig. 4b). Among Bronze Age Europeans, the highest tolerance frequency was found in Corded Ware and the closely-related Scandinavian Bronze Age cultures (Extended Data Fig. 7).

Interestingly, the Bronze Age steppe cultures showed the highest derived allele frequency among ancient groups, in particular the Yamnaya (Extended Data Fig. 7), indicating a possible steppe origin of lactase tolerance.

Implications

It has been debated for decades if the major cultural changes that occurred during the Bronze Age resulted from the circulation of people or ideas and whether the expansion of Indo-European languages was concomitant with these shifts or occurred with the earlier spread of agriculture^{13,15,35,36}. Our findings show that these transformations involved migrations, but of a different nature than previously suggested: the Yamnaya/Afanasievo movement was directional into Central Asia and the Altai-Sayan region and probably without much local infiltration, whereas the resulting Corded Ware culture in Europe was the result of admixture with the local Neolithic people. The enigmatic Sintashta culture near the Urals bears genetic resemblance to Corded Ware and was therefore likely to be an eastward migration into Asia. As this culture spread towards Altai it evolved into the Andronovo culture (Fig. 1), which was then gradually admixed and replaced by East Asian peoples that appear in the later cultures (Mezhevskaya and Karasuk). Our analyses support that migrations during the Early Bronze Age is a probable scenario for the spread of Indo-European languages, in line with reconstructions based on some archaeological and historical linguistic data^{15,31}. In the light of our results, the existence of the Afanasievo culture near Altai around 3000 BC could also provide an explanation for the mysterious presence of one of the oldest Indo-European languages, Tocharian in the Tarim basin in China³⁷. It seems plausible that Afanasievo, with their genetic western (Yamnaya) origin, spoke an Indo-European language and could have introduced this southward to Xinjiang and Tarim³⁸. Importantly, however, although our results support a correspondence between cultural changes, migrations, and linguistic patterns, we caution that such relationships cannot always be expected but must be demonstrated case by case.

Online Content Methods, along with any additional Extended Data display items and Source Data, are available in the online version of the paper; references unique to these sections appear only in the online paper.

Received 14 February; accepted 1 May 2015.

1. Fu, Q. *et al.* Genome sequence of a 45,000-year-old modern human from western Siberia. *Nature* **514**, 445–449 (2014).
2. Seguin-Orlando, A. *et al.* Genomic structure in Europeans dating back at least 36,200 years. *Science* **346**, 1113–1118 (2014).
3. Rasmussen, M. *et al.* An Aboriginal Australian genome reveals separate human dispersals into Asia. *Science* **334**, 94–98 (2011).
4. Raghavan, M. *et al.* Upper Palaeolithic Siberian genome reveals dual ancestry of Native Americans. *Nature* **505**, 87–91 (2014).
5. Raghavan, M. *et al.* The genetic prehistory of the New World Arctic. *Science* **345**, 1255–1258 (2014).
6. Rasmussen, M. *et al.* The genome of a Late Pleistocene human from a Clovis burial site in western Montana. *Nature* **506**, 225–229 (2014).
7. Bramanti, B. *et al.* Genetic discontinuity between local hunter-gatherers and Central Europe's first farmers. *Science* **326**, 137–140 (2009).
8. Malmström, H. *et al.* Ancient DNA reveals lack of continuity between Neolithic hunter-gatherers and contemporary Scandinavians. *Curr. Biol.* **19**, 1758–1762 (2009).
9. Skoglund, P. *et al.* Origins and genetic legacy of Neolithic farmers and hunter-gatherers in Europe. *Science* **336**, 466–469 (2012).
10. Lazaridis, I. *et al.* Ancient human genomes suggest three ancestral populations for present-day Europeans. *Nature* **513**, 409–413 (2014).
11. Haak, W. *et al.* Ancient DNA from European early Neolithic farmers reveals their Near Eastern affinities. *PLoS Biol.* **8**, e1000536 (2010).
12. Gamba, C. *et al.* Genome flux and stasis in a five millennium transect of European prehistory. *Nature Commun.* **5**, 5257 (2014).
13. Kristiansen, K. in *The World System and the Earth System. Global Socioenvironmental Change and Sustainability Since the Neolithic* (eds Hornborg, B. & Crumley, C.) (Left Coast Press, 2007).
14. Shishlina, N. *Reconstruction of the Bronze Age of the Caspian Steppes. Life Styles and Life Ways of Pastoral Nomads*. Vol. 1876 (Archaeopress, 2008).
15. Anthony, D. *The Horse, The Wheel and Language. How Bronze-Age Riders from the Eurasian Steppes Shaped the Modern World* (Princeton Univ. Press, 2007).

16. Harrison, R. & Heyd, V. The Transformation of Europe in the third millennium BC: the example of 'Le Petit-Chasseur I + III' (Sion, Valais, Switzerland). *Præhistorische Zeitschrift* **82**, 129–214 (2007).
17. Vandkilde, H. *Culture and Change in the Central European Prehistory, 6th to 1st millennium BC* (Aarhus Univ. Press, 2007).
18. Kristiansen, K. & Larsson, T. *The Rise of Bronze Age Society. Travels, Transmissions and Transformations* (Cambridge Univ. Press, 2005).
19. Hanks, B. K., Epimakhov, A. V. & Renfrew, A. C. Towards a refined chronology for the Bronze Age of the southern Urals, Russia. *Antiquity* **81**, 353–367 (2007).
20. Kuznetsov, P. F. The emergence of Bronze Age chariots in Eastern Europe. *Antiquity* **80**, 638–645 (2006).
21. Koryakova, L. & Epimakhov, A. V. *The Urals and Western Siberia in the Bronze and Iron Ages* (Cambridge Univ. Press, 2007).
22. Rasmussen, M. *et al.* Ancient human genome sequence of an extinct Palaeo-Eskimo. *Nature* **463**, 757–762 (2010).
23. Carpenter, M. L. *et al.* Pulling out the 1%: whole-genome capture for the targeted enrichment of ancient DNA sequencing libraries. *Am. J. Hum. Genet.* **93**, 852–864 (2013).
24. Barros Damgaard, P. d. *et al.* Improving access to endogenous DNA in ancient bones and teeth. Preprint at *bioRxiv* <http://dx.doi.org/10.1101/014985> (2015).
25. Adler, C. J., Haak, W., Donlon, D., Cooper, A. & The Genographic Consortium. Survival and recovery of DNA from ancient teeth and bones. *J. Archaeol. Sci.* **38**, 956–964 (2011).
26. Orlando, L. *et al.* True single-molecule DNA sequencing of a Pleistocene horse bone. *Genome Res.* **21**, 1705–1719 (2011).
27. Olalde, I. & Laluzza-Fox, C. Modern humans' paleogenomics and the new evidences on the European prehistory. *Science and Technology of Archaeological Research* **1**, <http://dx.doi.org/10.1179/2054892315Y.0000000002> (2015).
28. Grigoriev, S. *Ancient Indo-Europeans* (Charoid, 2002).
29. Bendezu-Sarmiento, J. *De l'Âge du Bronze et l'Âge du Fer au Kazakhstan, gestes funéraires et paramètres biologiques. Identités culturelles des population Andronovo et Saka* (De Boccard, 2007).
30. Kozintsev, A. G., Gromov, A. V. & Moiseyev, V. G. Collateral relatives of American Indians among the Bronze Age populations of Siberia? *Am. J. Phys. Anthropol.* **108**, 193–204 (1999).
31. Kristiansen, K. in *Becoming European. The transformation of third millennium Northern and Western Europe* (eds Prescott, C. & Glørstad, H.) (Oxbow Books, 2012).
32. Haak, W. *et al.* Massive migration from the steppe was a source for Indo-European languages in Europe. *Nature* <http://dx.doi.org/10.1038/nature14317> (this issue).
33. Olalde, I. *et al.* Derived immune and ancestral pigmentation alleles in a 7,000-year-old Mesolithic European. *Nature* **507**, 225–228 (2014).
34. Itan, Y., Powell, A., Beaumont, M. A., Burger, J. & Thomas, M. G. The origins of lactase persistence in Europe. *PLoS Computational Biol.* **5**, e1000491 (2009).
35. Mallory, J. *In Search of the Indo-Europeans. Language, Archaeology and Myth* (Thames & Hudson, 1987).
36. Renfrew, A. C. *Archaeology and Language. The Puzzle of Indo-European Origins* (Penguin, 1987).
37. Mallory, J. & Mair, V. *The Tarim Mummies. Ancient China and the Mystery of the Earliest People from the West* (Thames & Hudson, 2000).
38. Keyser, C. *et al.* Ancient DNA provides new insights into the history of south Siberian Kurgan people. *Hum. Genet.* **126**, 395–410 (2009).

Supplementary Information is available in the online version of the paper.

Acknowledgements We thank K. Magnussen, L. A. Petersen, C. D. Mortensen and A. Seguin-Orlando at the Danish National Sequencing Centre for help with the sequencing. We thank C. G. Zacho for technical assistance. The project was funded by The European Research Council (FP/2007-2013, grant no. 269442, The Rise), The University of Copenhagen (KU2016 programme), Marie Curie Actions of the European Union (FP7/2007-2013, grant no. 300554), The Villum Foundation (Young Investigator Programme, grant no. 10120), Frederik Paulsen, The Miller Institute, University of California, Berkeley, The Lundbeck Foundation, and The Danish National Research Foundation.

Author Contributions E.W. and K.K. initiated and led the study. M.E.A., J.S., L.V., H.S., P.B.D., A.M., M.R., L.S. performed the DNA laboratory work. M.Si., S.R., M.E.A., A.-S.M., P.B.D., A.M. analysed the genetic data. K.-G.S., T.A., N.L., L.H., J.B., P.D.C., P.D., P.R.D., A.E., A.V.E., K.F., M.F., G.G., T.G., A.G., S.G., T.H., R.J., J.K., V.K., A.K., V.K., A.K., I.L., C.L., A.M., G.M., I.M., M.M., R.M., V.M., D.Po., G.P., L.P., D.Pr., L.P., M.Sa., N.S., V.Sm., V.Sz., V.I.S., G.T., S.V.T., L.V., M.V., L.Y., V.Z. collected the samples and/or provided input to the archaeological interpretations. T.H. and D.C. conducted radiocarbon dating. T.S.-P., L.O., S.B., R.N. provided input to the genetic analyses. E.W., K.K., M.E.A., M.Si., K.-G.S. wrote the paper with input from all co-authors.

Author Information DNA sequence alignments are available from the European Nucleotide Archive (<http://www.ebi.ac.uk/ena>) under accession number PRJEB9021. Reprints and permissions information is available at www.nature.com/reprints. The authors declare no competing financial interests. Readers are welcome to comment on the online version of the paper. Correspondence and requests for materials should be addressed to E.W. (ewillerslev@snm.ku.dk).

METHODS

DNA extraction and library preparation. A total of 603 human Bronze Age samples from across Eurasia were selected for initial molecular ‘screening’ to assess DNA preservation and hence the potential for genome-scale analyses. The samples consisted almost exclusively of teeth, but also a few bone and hair samples were included. All the molecular work (pre-library amplification) was conducted in dedicated ancient DNA clean laboratory facilities at the Centre for GeoGenetics, Natural History Museum, University of Copenhagen.

Preferentially targeting the outer cementum layer in teeth rather than the dentine allowed us to maximize access to endogenous DNA^{24,25} (Supplementary Information, section 3). The amount of starting material varied, but was generally 100–600 mg. We also added a ‘pre-digestion’ step to the extraction protocol, where the drilled bone or tooth powder is incubated in an EDTA-based buffer before complete digestion to facilitate the removal of surface contaminants^{24,26} (Supplementary Information, section 3). Additionally, we developed a new DNA binding buffer for extraction that proved more efficient in recovering short DNA fragments compared to previous protocols (Supplementary Information, section 3). DNA libraries for sequencing were prepared using NEBNext DNA Sample Prep Master Mix Set 2 (E6070) and Illumina-specific adapters³⁹ following established protocols^{39–41}. The libraries were ‘shot-gun’ sequenced in pools using Illumina HiSeq2500 platforms and 100-bp single-read chemistry (Supplementary Information, section 3).

Molecular screening. For the molecular screening phase we generally generated between 5 and 20 million reads per library and these were used to evaluate the state of molecular preservation. Candidate samples were selected for further sequencing if they displayed a >10% C–T misincorporation damage signal in the 5′ ends as an indication of authentic ancient DNA^{42,43}, and a human DNA content >0.5% (Supplementary Information, section 3).

Genomic capture. We selected 24 samples with relatively low human DNA content (0.5–1.1%) for a whole-genome capture experiment²³ to enrich for the low human DNA fraction in these samples. The capture was performed using the MYbait Human Whole Genome Capture Kit (MYcroarray, Ann Arbor, MI), following the manufacturer’s instructions (<http://www.mycroarray.com/pdf/MYbaits-manual.pdf>). After amplification, the libraries were purified using Agencourt AMPure XP beads, quantified using an Agilent 2100 bioanalyzer, pooled in equimolar amounts, and sequenced on Illumina HiSeq 2500, as described above. Methods and results are found in Supplementary Information, section 3.

Bioinformatics. The Illumina data was basecalled using Illumina software CASAVA 1.8.2 and sequences were de-multiplexed with a requirement of full match of the 6 nucleotide index that was used for library preparation. Adaptor sequences and leading/trailing stretches of Ns were trimmed from the reads and additionally bases with quality 2 or less were removed using AdapterRemoval-1.5.4. Trimmed reads of at least 30 bp were mapped to the human reference genome build 37 using bwa-0.6.2 (ref. 44) with the seed disabled to allow for higher sensitivity⁴⁵. Mapped reads were filtered for mapping quality 30 and sorted using Picard (<http://picard.sourceforge.net>) and SAMtools⁴⁶. Data was merged to library level and duplicates removed using Picard MarkDuplicates (<http://picard.sourceforge.net>) and hereafter merged to sample level. Sample level BAMs were re-aligned using GATK-2.2-3 and hereafter had the md-tag updated and extended BAQs calculated using SAMtools calmd⁴⁶. Read depth and coverage were determined using pysam (<http://code.google.com/p/pysam/>) and BEDtools⁴⁷. Statistics of the read data processing are shown in Supplementary Table 6.

DNA authentication. DNA contamination can be problematic in samples from museum collections that may have been handled extensively. To secure authenticity, we used the Bayesian approach implemented in mapDamage 2.0 (ref. 48) and recorded the following three key damage parameters for each sample: (1) the frequency of C→T transitions at the first position at the 5′ end of reads, (2) λ , the fraction of bases positioned in single-stranded overhangs, and (3) δ s, the estimated C→T transition rate in the single-stranded overhangs (Supplementary Information, section 5). For further sequencing and downstream analyses we only considered individuals displaying at least 10% C→T damage transitions at position 1. MapDamage outputs are summarized in Supplementary Table 7.

We also estimated the levels of mitochondrial DNA contamination. We used contamMix 1.0–10 (ref. 49) that generates a moment-based estimate of the error rate and a Bayesian-based estimate of the posterior probability of the contamination fraction. We conservatively removed individuals with indications of contamination >5% (Supplementary Information, section 5). For males with sufficient depth of coverage we also estimated contamination based on the X chromosome³ as implemented in ANGSD⁵⁰ (Supplementary Information, section 5). Results are shown in Supplementary Table 8. After implementing the 0.5% cut-off for human DNA content, combined with these ancient DNA

authentication criteria, our final sample consisted of 101 individuals (Supplementary Information, section 1).

Data sets. We constructed two data sets for population genetic analysis by merging ancient DNA data generated in this as well as previous studies with two reference panels of modern individual genotype data (Supplementary Information, section 6). For both data sets, genotypes for all ancient individuals were obtained at all variant positions in the reference panel, discarding variants where alleles for the ancient individuals did not match either of the alleles observed in the panel. Genotypes for low-coverage samples (including all data generated in this study) were obtained by randomly sampling a single read with both mapping and base quality ≥ 30 . Genotypes for high-coverage samples were called using the ‘call’ command of bcftools (<https://github.com/samtools/bcftools>) and filtering for quality score (QUAL) ≥ 30 . Error rates and inclusion thresholds for low coverage samples were obtained by performing PCA and model-based clustering (described below) on subsampled data sets of higher coverage individuals. For population genetic analyses (D and f statistics, F_{ST}) we obtained sample allele frequencies for the ancient groups (Supplementary Table 9) at each SNP by counting the total number of alleles observed, treating the low coverage individuals as haploid. See Supplementary Information, section 6 for more details.

PCA and model-based clustering. We performed principal component analysis with EIGENSOFT⁵¹, projecting ancient individuals onto the components inferred from sets of modern individuals by using the ‘lsqproject’ option of *smartpca*. The data set was converted to all homozygous genotypes before the analysis, by randomly sampling an allele at each heterozygote genotype of modern and high-coverage ancient individuals. See Supplementary Information, section 6 for more details.

Model-based clustering analysis was carried out using the maximum-likelihood approach implemented in ADMIXTURE⁵². We used an approach where we first infer the ancestral components using modern samples only, and then ‘project’ the ancient samples onto the inferred components using the ancestral allele frequencies inferred by ADMIXTURE (the ‘P’ matrix). We ran ADMIXTURE on an LD-pruned data set of all 2,345 modern individuals in the Human Origins SNP array data set, assuming $K = 2$ to $K = 20$ ancestral components, selecting the best of 50 replicate runs for each value of K . See Supplementary Information, section 6 for more details. Genotypes where the ancient individuals showed the damage allele at C > T and G > A SNPs were excluded for each low coverage ancient individual.

D- and f-statistics and population differentiation. We used the D and f statistic framework⁵³ to investigate patterns of admixture and shared ancestry in our data set. All statistics were calculated from allele frequencies using the estimators described previously⁵³, with standard errors obtained from a block jackknife with 5 Mb block size. We investigated population differentiation by estimating F_{ST} for all pairs of ancient and modern groups from allele frequencies using the sample-size corrected moment estimator of Weir and Hill⁵⁴, restricting the analysis to SNPs where a minimum two alleles were observed in each population of the pair. See Supplementary Information, section 6 for more details.

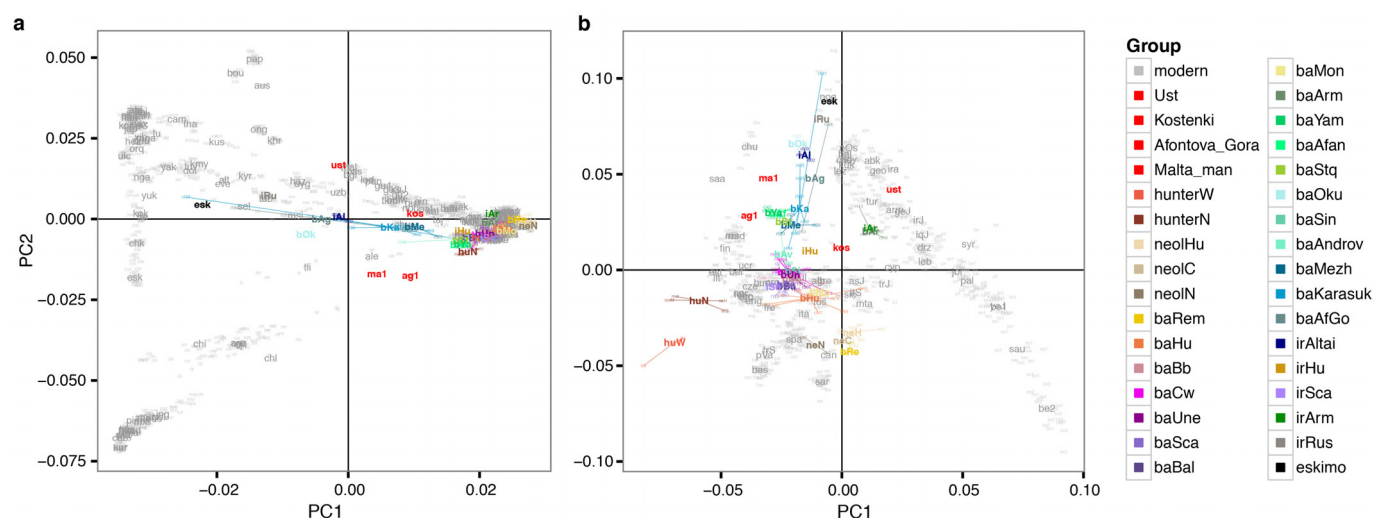
Phenotypes and positive selection. To investigate the temporal dynamics of SNPs associated with phenotypes or putatively under positive selection, we estimated allele frequencies for a catalogue of 104 SNPs³³ in all ancient and modern groups in the 1000 Genomes data set. Genotypes for the *LCT* region were imputed from genotype likelihoods with the 1000 Genomes Phase 3 reference panel⁵⁵ using BEAGLE⁵⁶. See Supplementary Information, section 6 for more details.

Data reporting. No statistical methods were used to predetermine sample size. The experiments were not randomized. The investigators were not blinded to allocation during experiments and outcome assessment.

Code availability. Source code with R functions used in the analysis for this study is available as an R package at GitHub <https://github.com/martinsikora/admixr>.

39. Meyer, M. & Kircher, M. Illumina sequencing library preparation for highly multiplexed target capture and sequencing. *Cold Spring Harb. Protocols* (2010).
40. Orlando, L. et al. Recalibrating *Equus* evolution using the genome sequence of an early Middle Pleistocene horse. *Nature* **499**, 74–78 (2013).
41. Malaspina, A.-S. et al. Two ancient human genomes reveal Polynesian ancestry among the indigenous Botocudos of Brazil. *Curr. Biol.* **24**, R1035–R1037 (2014).
42. Willerslev, E. & Cooper, A. Ancient DNA. *Proc. Royal Soc. B* **272**, 3–16 (2005).
43. Briggs, A. W. et al. Patterns of damage in genomic DNA sequences from a Neandertal. *Proc. Natl Acad. Sci. USA* **104**, 14616–14621 (2007).
44. Li, H. & Durbin, R. Fast and accurate short read alignment with Burrows–Wheeler transform. *Bioinformatics* **25**, 1754–1760 (2009).
45. Schubert, M. et al. Improving ancient DNA read mapping against modern reference genomes. *BMC Genomics* **13**, 178 (2012).
46. Li, H. et al. The Sequence Alignment/Map format and SAMtools. *Bioinformatics* **25**, 2078–2079 (2009).

47. Quinlan, A. R. & Hall, I. M. BEDTools: a flexible suite of utilities for comparing genomic features. *Bioinformatics* **26**, 841–842 (2010).
48. Jónsson, H., Ginolhac, A., Schubert, M., Johnson, P. & Orlando, L. mapDamage2.0: fast approximate Bayesian estimates of ancient DNA damage parameters. *Bioinformatics* (2013).
49. Fu, Q. *et al.* DNA analysis of an early modern human from Tianyuan Cave, China. *Proc. Natl Acad. Sci. USA* **110**, 2223–2227 (2013).
50. Korneliussen, T. S., Albrechtsen, A. & Nielsen, R. ANGSD: analysis of next generation sequencing data. *BMC Bioinformatics* **15**, (2014).
51. Patterson, N., Price, A. L. & Reich, D. Population structure and Eigenanalysis. *PLoS Genet.* **2**, e190 (2006).
52. Alexander, D. H., Novembre, J. & Lange, K. Fast model-based estimation of ancestry in unrelated individuals. *Genome Res.* **19**, 1655–1664 (2009).
53. Patterson, N. *et al.* Ancient admixture in human history. *Genetics* **192**, 1065–1093 (2012).
54. Weir, B. S. & Hill, W. Estimating F-statistics. *Annu. Rev. Genet.* **36**, 721–750 (2002).
55. Nyström, V. *et al.* Microsatellite genotyping reveals end-Pleistocene decline in mammoth autosomal genetic variation. *Mol. Ecol.* **21**, 3391–3402 (2012).
56. Browning, S. R. & Browning, B. L. Rapid and accurate haplotype phasing and missing-data inference for whole-genome association studies by use of localized haplotype clustering. *Am. J. Hum. Genet.* **81**, 1084–1097 (2007).

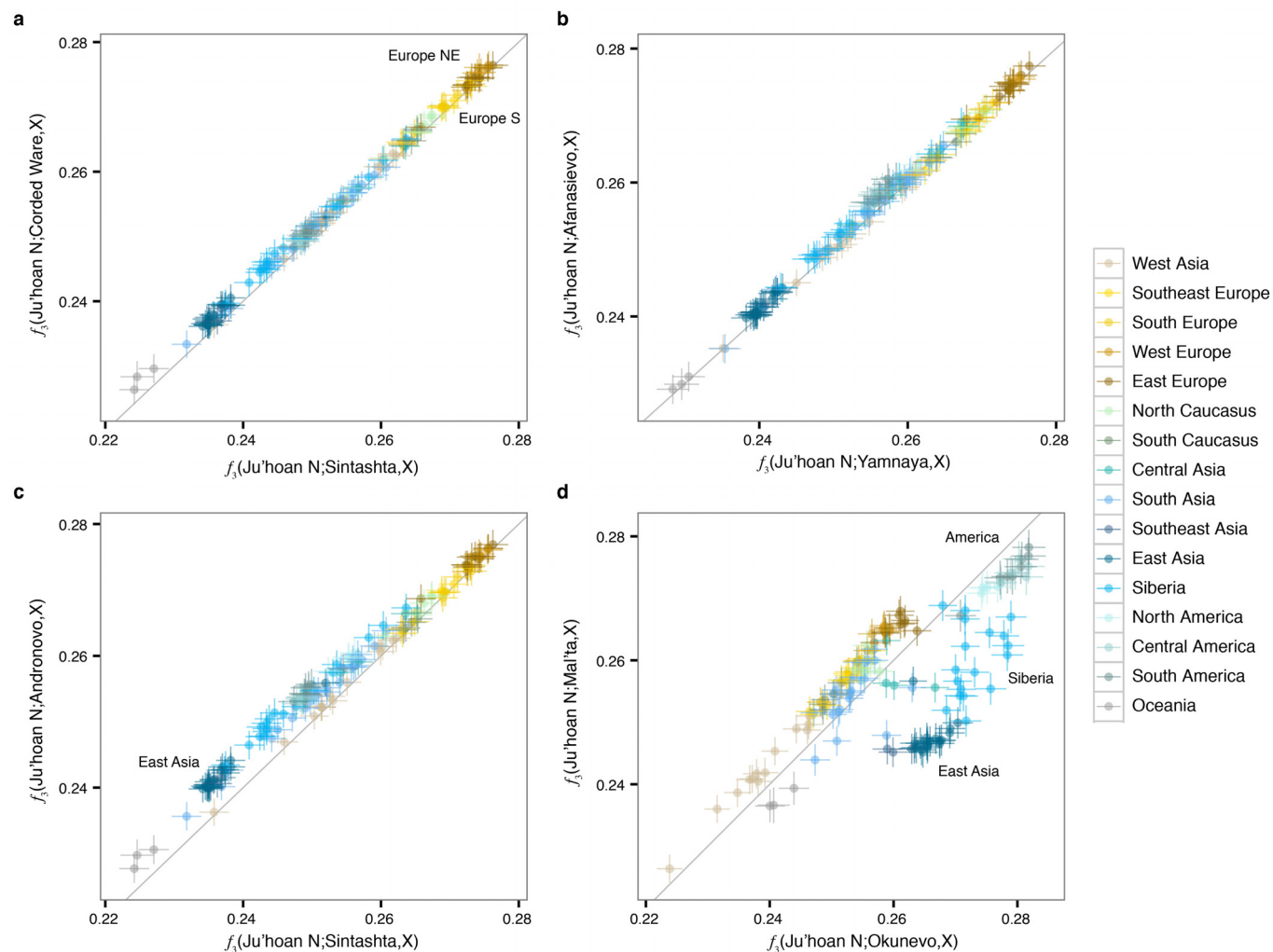


Extended Data Figure 1 | Principal component analysis of ancient genomes.

a, b, Principal component analysis of ancient individuals projected onto contemporary individuals from non-African populations (a), Europe, West Asia and the Caucasus (b). Grey labels represent population codes indicating

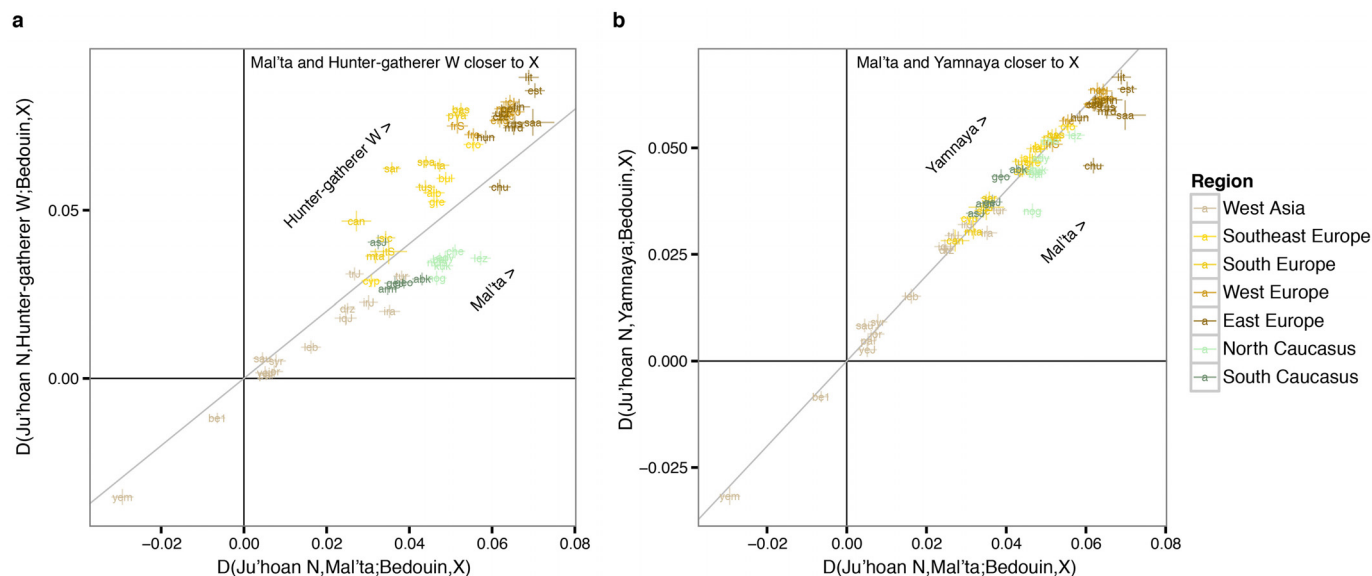
coordinates for individuals (small) and median of the population (large).

Coloured labels indicate positions for ancient individuals (small) and median for ancient groups (large). Ancient individuals within a group are connected to the respective median position by coloured lines.



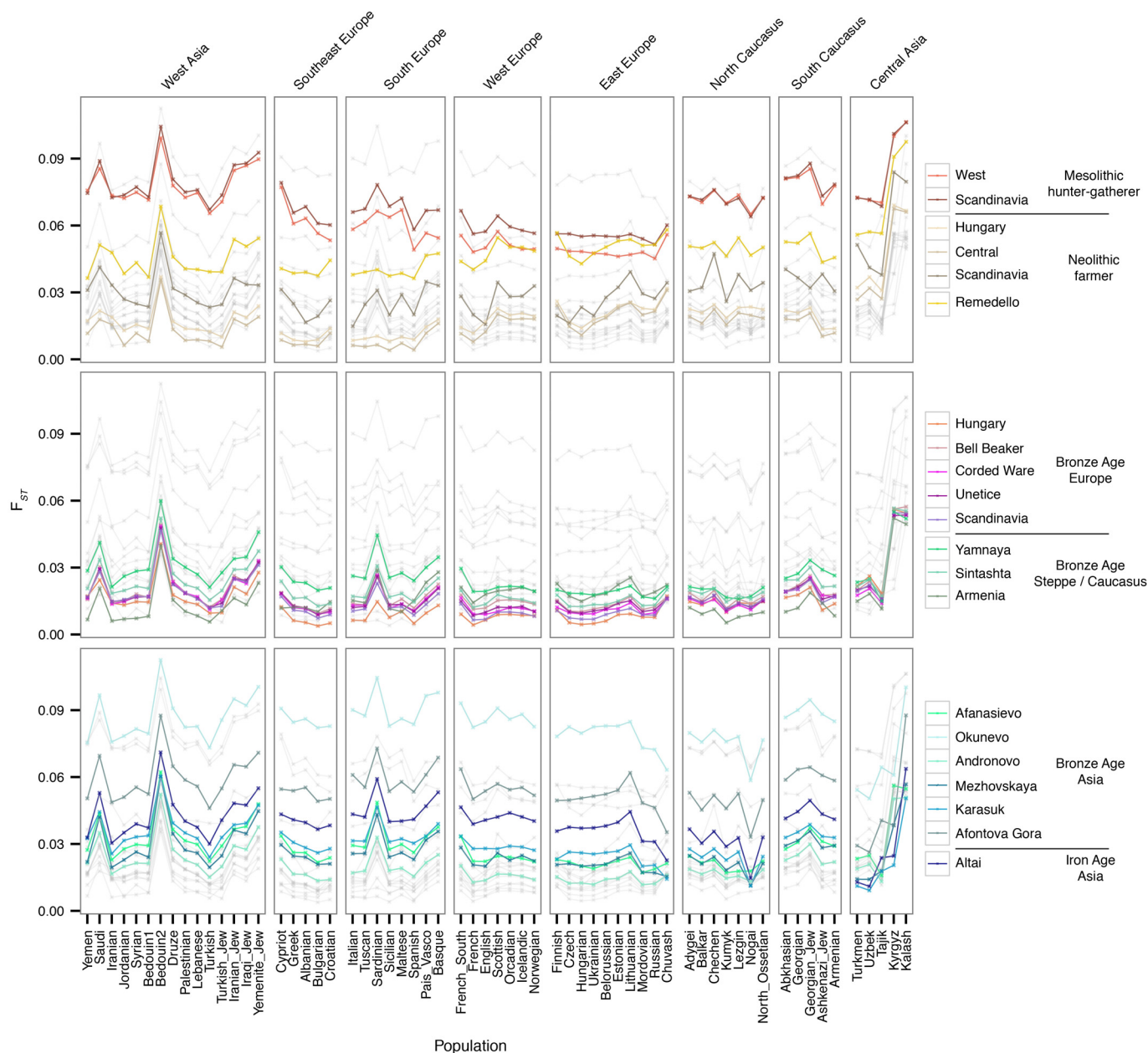
Extended Data Figure 2 | Pairwise outgroup f_3 statistics. Panels depict pairwise plots of outgroup f_3 statistics of the form $f_3(\text{Ju'hoan North}; \text{Population}_1, \text{Population}_2)$, showing the correlation of the amount of shared genetic drift for a pair of ancient groups (Population_1) with all modern populations (Population_2) in the Human Origins data set (panel A). Closely

related ancient groups are expected to show highly correlated statistics.
a, Sintashta/Corded Ware. **b**, Yamnaya/Afanasievo. **c**, Sintashta/Andronovo.
d, Okunevo/Mal'ta. Coloured circles indicate modern populations; error bars indicate ± 1 standard error from the block jackknife.



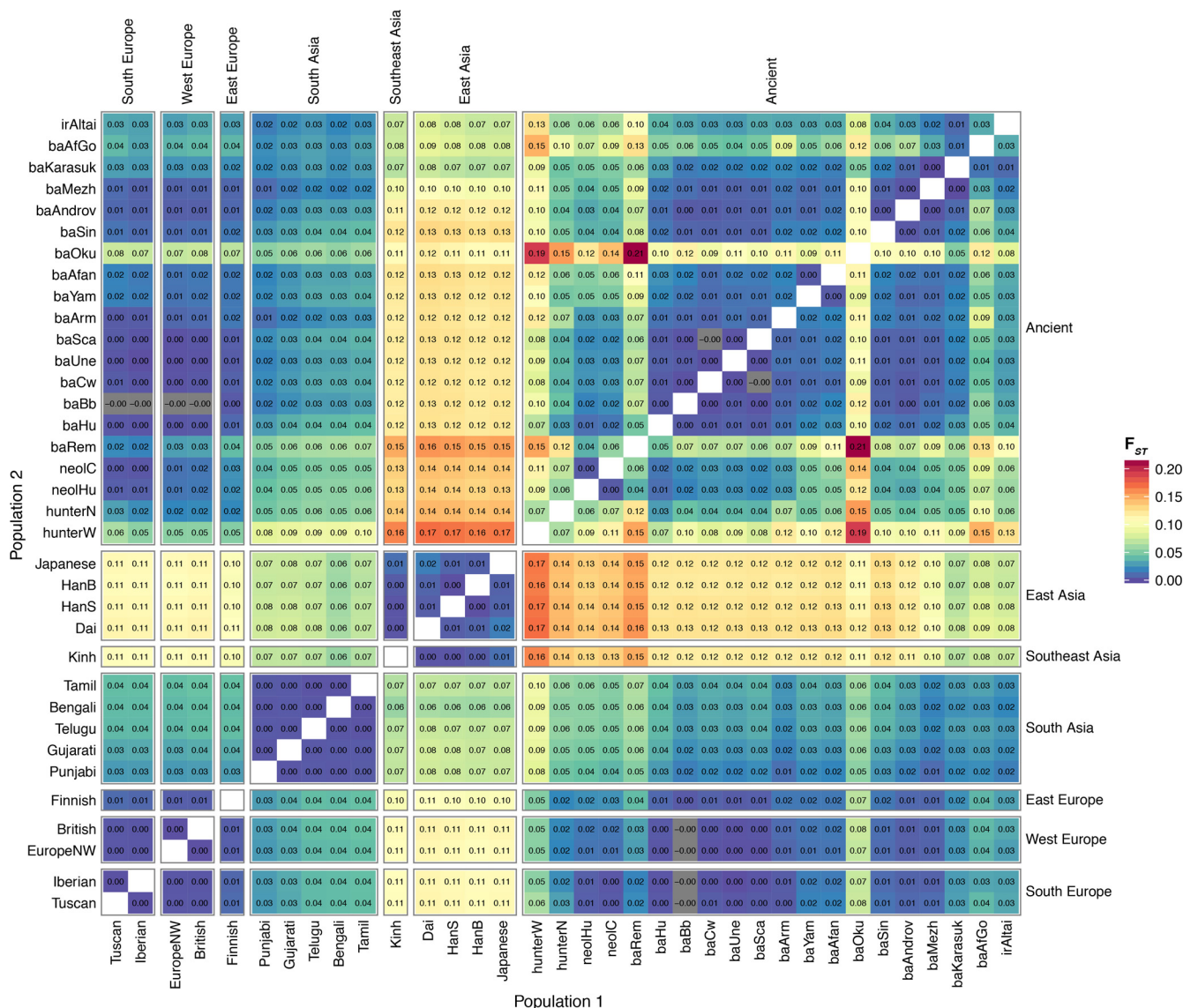
Extended Data Figure 3 | Yamnaya ancestry mirrors Mal'ta ancestry in present-day Europeans and Caucasians. Panels show pairwise plots of D -statistics $D(\text{Outgroup, Ancient})(\text{Bedouin, Modern})$, contrasting Mal'ta (MA1) and Hunter-gatherers (a), and MA1 and Yamnaya (b). Coloured labels

indicate modern populations, with lines corresponding to ± 1 standard error of the respective D -statistic from block jackknife. Text away from the diagonal line indicates an ancient group with relative increase in allele sharing with the respective modern populations.

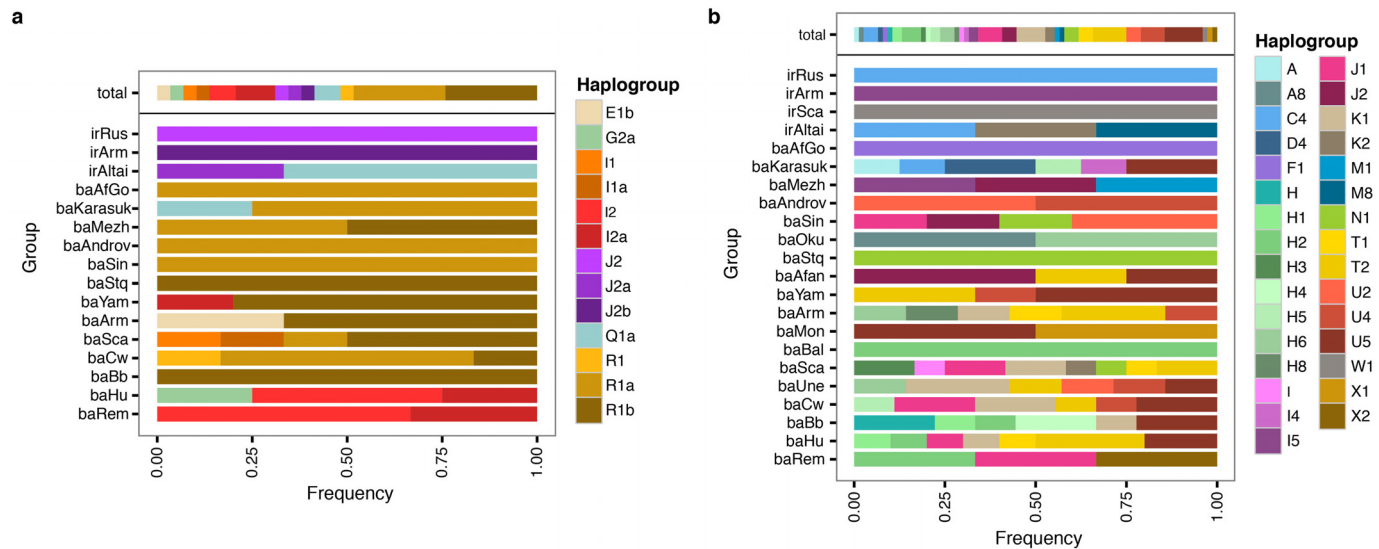


Extended Data Figure 4 | Genetic differentiation between ancient and modern groups in Human Origins data set. Panels show F_{ST} between pairs of modern and ancient groups (coloured lines) for subsets of ancient groups, with

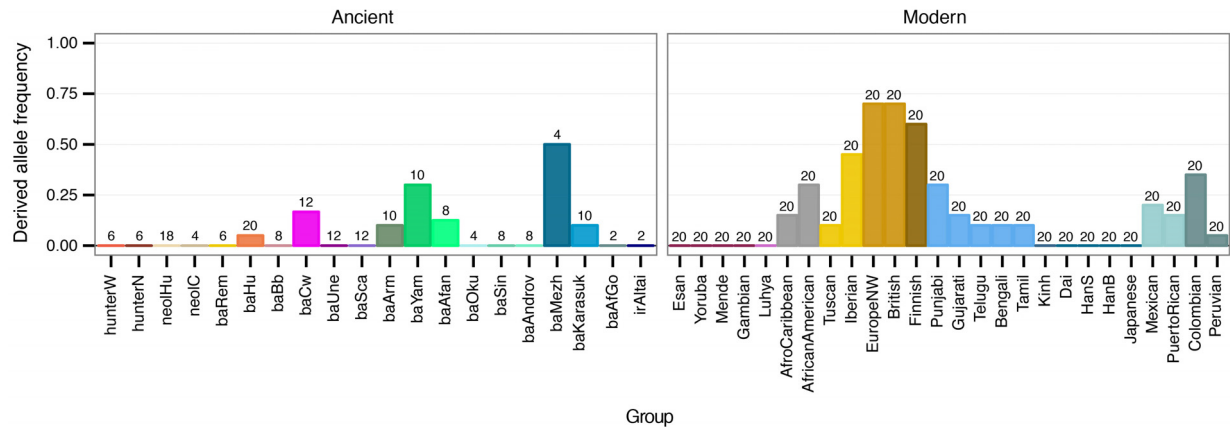
results for the remaining groups in the background (grey). Top, early Europeans. Middle, Bronze Age Europeans and steppe/Caucasus. Bottom, Bronze Age Asians. Results based on Human Origins data set (panel A).



Extended Data Figure 5 | Genetic differentiation between ancient and modern groups in 1000 Genomes data set. Matrix of pairwise F_{ST} values between modern and ancient groups in the 1000 Genomes data set (panel B).



Extended Data Figure 6 | Distribution of uniparental lineages in Bronze Age Eurasians. a, b, Barplots showing the relative frequency of Y chromosome (a) and mitochondrial DNA lineages (b) in different Bronze Age groups. Top row shows overall frequencies for all individuals combined.



Extended Data Figure 7 | Derived allele frequencies for lactase persistence in modern and ancient groups. Derived allele frequency of rs4988235 in the *LCT* gene inferred from imputation of ancient individuals. Numbers indicate the total number of chromosomes for each group.

Extended Data Table 1 | Selected D-test results from 1000 Genomes data set (panel B)

Configuration	D	Z	Interpretation
D(Yoruba,Neolithic Central)(Remedello,Hungary)	-0.022	-6.2	Remedello is closer to Neolithic farmers than BA Hungarians
D(Yoruba,Neolithic Central)(Hungary,Corded Ware)	-0.014	-5.5	BA Hungarians are closer to Neolithic farmers than Corded Ware
D(Yoruba,Neolithic Central)(Bell Beaker,Corded Ware)	-0.009	-3.4	Bell Beaker is closer to Neolithic farmers than Corded Ware
D(Yoruba,Neolithic Central)(Corded Ware,Yamnaya)	-0.018	-7.0	Corded Ware is closer to Neolithic farmers than Yamnaya
D(Yoruba,Neolithic Central)(Sintashta,Yamnaya)	-0.014	-4.9	Sintashta is closer to Neolithic farmers than Yamnaya
D(Yoruba,Yamnaya)(Hungary,Bell Beaker)	0.011	4.5	Bell Beaker is closer to Yamnaya than BA Hungarians
D(Yoruba,Yamnaya)(Hungary,Corded Ware)	0.016	6.7	Corded Ware is closer to Yamnaya than BA Hungarians
D(Yoruba,Yamnaya)(Hungary,Sintashta)	0.011	4.8	Sintashta is closer to Yamnaya than BA Hungarians
D(Yoruba,Armenia)(Yamnaya,Corded Ware)	0.002	0.9	Corded Ware and Yamnaya form a clade to the exclusion of BA Armenians
D(Yoruba,Corded Ware)(Yamnaya,Armenia)	-0.015	-5.8	
D(Yoruba,Yamnaya)(Armenia,Corded Ware)	0.018	6.8	
D(Yoruba,Yamnaya)(Afnasievo,Karasuk)	-0.047	-17.7	Yamnaya and Afnasievo form a clade to the exclusion of other ancient groups*
D(Yoruba,Afnasievo)(Yamnaya,Karasuk)	-0.038	-16.0	
D(Yoruba,Karasuk)(Yamnaya,Afnasievo)	0.008	3.6	

*Results are shown for Karasuk as group X, which is the only ancient group with $Z > 3$ for D(Yoruba, X)(Yamnaya, Afnasievo)

Extended Data Table 2 | f_3 statistic results for ancient groups

Group	f_3 outgroup*			f_3 admixture†		
	Population with highest f_3 outgroup	f_3	SE	Example population pair with $f_3 < 0$	f_3	Z
Ust-Ishim	Surui	0.240	0.003			
Kostenki‡	Hunter-gatherer W	0.266	0.003			
Afontova Gora‡	Mal'ta	0.317	0.005			
Mal'ta‡	Afontova Gora	0.317	0.005			
Hunter-gatherer W	Hunter-gatherer Scandinavia	0.313	0.002			
Hunter-gatherer Scandinavia	Hunter-gatherer W	0.313	0.002	(Hunter-gatherer W,Mal'ta)§	-0.005	-1.78
Neolithic Hungary	Neolithic Central	0.287	0.002	(Hunter-gatherer W,Neolithic Central)§	-0.002	-1.09
Neolithic Central	Neolithic Hungary	0.287	0.002			
Neolithic Scandinavia‡	Neolithic Central	0.285	0.003			
Remedello	Neolithic Scandinavia	0.284	0.003			
BA Hungary	Hunter-gatherer W	0.284	0.002	(Hunter-gatherer W,BA Armenia)	-0.011	-8.69
Bell Beaker	Hunter-gatherer W	0.278	0.002	(Remedello,Yamnaya)	-0.007	-4.31
Corded Ware	Hunter-gatherer W	0.279	0.002	(Neolithic Hungary,Yamnaya)	-0.009	-6.16
Unetice	Hunter-gatherer W	0.278	0.002	(Neolithic Central,Afanasievo)	-0.008	-6.07
BA Scandinavia	Hunter-gatherer W	0.282	0.002	(Hunter-gatherer W,BA Armenia)	-0.013	-9.61
BA Baltic‡	Hunter-gatherer Scandinavia	0.276	0.008			
BA Montenegro	Scottish	0.275	0.005			
BA Armenia	IA Armenia	0.270	0.005	(Neolithic Hungary,Okunevo)	-0.006	-2.66
Yamnaya	Afanasievo	0.284	0.002	(Neolithic Central,Mal'ta)§	-0.004	-2.32
Afanasievo	Yamnaya	0.284	0.002			
Stalingrad quarry‡	BA Afontova Gora	0.287	0.007			
Okunevo	Karitiana	0.282	0.003			
Sintashta	Andronovo	0.278	0.002	(Neolithic Central,Okunevo)§	-0.004	-2.43
Andronovo	Hunter-gatherer Scandinavia	0.280	0.002	(Remedello,Mal'ta)	-0.005	-5.13
Mezhovskaya	Andronovo	0.277	0.002	(Sintashta,HanB)	-0.012	-5.62
Karasuk	BA Afontova Gora	0.276	0.003	(Andronovo,HanB)	-0.022	-27.49
BA Afontova Gora	Nganasan	0.282	0.003	(Remedello,Okunevo)§	-0.002	-0.15
IA Altai	BA Afontova Gora	0.274	0.004	(Afanasievo,HanB)	-0.017	-10.88
IA Hungary‡	Lithuanian	0.273	0.002			
IA Scandinavia‡	Hunter-gatherer Scandinavia	0.278	0.003			
IA Armenia‡	Bell Beaker	0.275	0.004			
IA Russia‡	Nganasan	0.285	0.003			

*Human origins data set (panel A); †1000 Genomes data set (panel B); ‡group with single individual; §pair with lowest f_3 reported for groups with negative f_3 without significant Z-score after correcting for multiple hypothesis tests ($-4.1 < \min(Z) < 0$; 1,260 tests per group); ||too few markers with data from more than one chromosome.

Cloning and variation of ground state intestinal stem cells

Xia Wang^{1*}, Yusuke Yamamoto^{1*}, Lane H. Wilson^{1,2}, Ting Zhang³, Brooke E. Howitt⁴, Melissa A. Farrow⁵, Florian Kern³, Gang Ning¹, Yue Hong¹, Chiea Chuen Khor^{3,6}, Benoit Chevalier¹, Denis Bertrand³, Lingyan Wu³, Niranjan Nagarajan³, Francisco A. Sylvester⁷, Jeffrey S. Hyams⁸, Thomas Devers⁹, Roderick Bronson¹⁰, D. Borden Lacy⁵, Khek Yu Ho¹¹, Christopher P. Crum⁴, Frank McKeon^{1,3,11,12} & Wa Xian^{1,2,4,11,12}

Stem cells of the gastrointestinal tract, pancreas, liver and other columnar epithelia collectively resist cloning in their elemental states. Here we demonstrate the cloning and propagation of highly clonogenic, ‘ground state’ stem cells of the human intestine and colon. We show that derived stem-cell pedigrees sustain limited copy number and sequence variation despite extensive serial passaging and display exquisitely precise, cell-autonomous commitment to epithelial differentiation consistent with their origins along the intestinal tract. This developmentally patterned and epigenetically maintained commitment of stem cells is likely to enforce the functional specificity of the adult intestinal tract. Using clonally derived colonic epithelia, we show that toxins A or B of the enteric pathogen *Clostridium difficile* recapitulate the salient features of pseudomembranous colitis. The stability of the epigenetic commitment programs of these stem cells, coupled with their unlimited replicative expansion and maintained clonogenicity, suggests certain advantages for their use in disease modelling and regenerative medicine.

While dominating prospective strategies for regenerative medicine, embryonic stem cells and induced pluripotent stem cells (iPSCs) face formidable challenges including risk of teratoma, complex guiding protocols for lineage specificity, and limited regenerative capacity of the lineages ultimately produced^{1–8}. The success and promise of iPSCs have largely overshadowed efforts to harness stem cells intrinsic to regenerative tissues. Green and colleagues developed methods for cloning epidermal stem cells⁹ that form a stratified epithelium upon engraftment, and these methods have been successfully applied to corneal, thymic and airway epithelia^{10–12}. However, stem cells of columnar epithelial tissues resist cloning in a manner that maintains their immaturity during proliferative expansion, and instead must be carried forward as regenerative, differentiating ‘organoids’^{13–18}. Despite their obvious potential in regenerative medicine and constant improvement¹⁹, the very low percentage of clonogenic cells in organoids limits the kinetics of their propagation as well as their utility for exploring the elemental stem cell.

The present study reports the cloning and propagation of ‘ground state’ human intestinal stem cells (ISC^{GS}). This technology offers insights into the molecular and functional features of columnar epithelial stem cells and their utility for disease modelling and regenerative medicine.

Cloning human fetal intestinal stem cells

We developed media (herein SCM-6F8) containing novel combinations of growth factors and regulators of TGF- β /BMP (transforming growth factor- β /bone morphogenetic protein), Wnt/ β -catenin, EGF (epidermal growth factor), IGF (insulin-like growth factor) and Notch

pathways^{9,20,21} that supports the maintenance of human intestinal stem cells in a highly clonogenic, ground state form. Thus single-cell suspensions of intestinal epithelia derived from 20- to 21-week-old fetal demise cases yield colonies comprised of highly immature cells in which differentiation markers can be induced by Notch suppression (Fig. 1a). Following induced differentiation via Wnt withdrawal, we were unable to recover ground state stem cells by our methods (Extended Data Fig. 1a–c).

The clonogenicity of cells in the colonies was determined by single-cell transfer to be greater than 50% (Fig. 1b). This high clonogenicity permits the rapid generation of single-cell ‘pedigree’ lines for expansion and characterization of lineage fates upon differentiation¹² (Fig. 1b). Pedigree lines of ISC^{GS} and tracheobronchial stem cells (TBSC^{GS})¹² grown for several months in culture were differentiated in air–liquid interface (ALI) cultures for 10–30 days (Fig. 1c). The ISC^{GS} formed a highly uniform, 3D serpentine pattern, whereas TBSC^{GS} produced a stratified epithelium with apically positioned ciliated and goblet cells. Histological sections of differentiated ISC^{GS} revealed a columnar epithelium of villus-like structures marked by goblet (Muc2⁺), endocrine (chromogranin A⁺), and Paneth cells and polarized villin expression (Fig. 1d; Extended Data Fig. 1d), indicating that the progeny of a single ISC^{GS} can give rise to all epithelial lineages typically found in the small intestine. Importantly, differentiation of these ground state stem cells is accomplished by exposure to an ALI rather than a removal of factors such as Wnt that maintain immaturity.

While principal component analysis (PCA) of differentially expressed genes of ground state stem cells and ALI-differentiated

¹The Jackson Laboratory for Genomic Medicine, Farmington, Connecticut 06032, USA. ²Department of Genetics and Developmental Biology, University of Connecticut Health Center, Farmington, Connecticut 06032, USA. ³Genome Institute of Singapore, Agency for Science, Technology and Research, 138672 Singapore. ⁴Department of Pathology, Brigham and Women’s Hospital, Boston, Massachusetts 02118, USA. ⁵Department of Pathology, Microbiology, and Immunology, Vanderbilt University School of Medicine, Nashville, Tennessee 37232, USA. ⁶Department of Ophthalmology, Yong Loo Lin School of Medicine, National University of Singapore, 119228 Singapore. ⁷Department of Pediatrics, Division of Gastroenterology, The University of North Carolina at Chapel Hill, Chapel Hill, North Carolina 27599, USA. ⁸Division of Digestive Diseases, Hepatology, and Nutrition, Connecticut Children’s Medical Center, Hartford, Connecticut 06106, USA. ⁹Department of Medicine, University of Connecticut Health Center, Farmington, Connecticut 06032, USA. ¹⁰Department of Microbiology and Immunobiology, Harvard Medical School, Boston, Massachusetts 02115, USA. ¹¹Department of Medicine, National University of Singapore, 119228 Singapore. ¹²Multiclonal Therapeutics, Inc., Farmington, Connecticut 06032, USA.

*These authors contributed equally to this work.

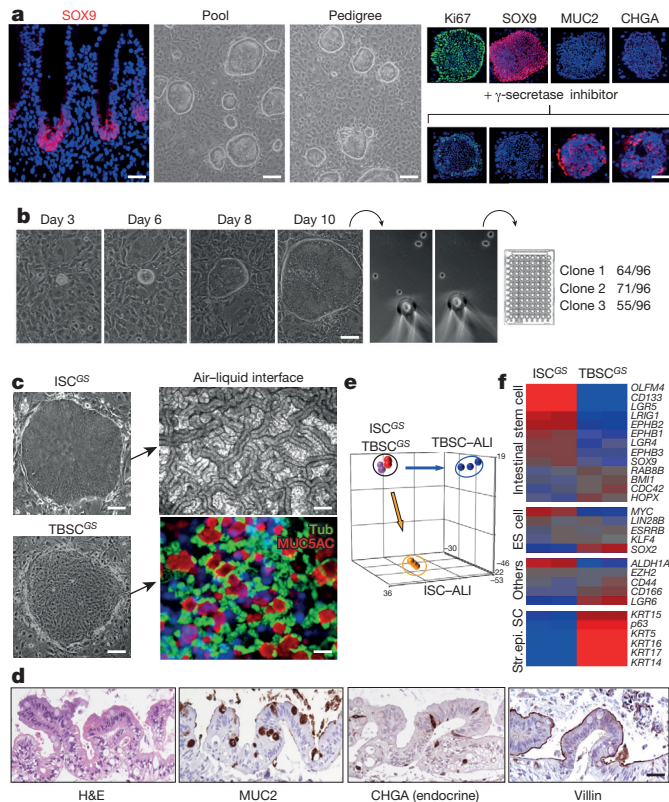


Figure 1 | Cloning stem cells from fetal intestine. **a**, Left, Sox9 expression in fetal intestine, scale bar, 25 μ m; colonies from intestine ($n = 10$ biological replicates; colonies of ISC pedigree ($n = 30$ independent experiments). Scale bar, 75 μ m. Right, ISC colonies stained with indicated antibodies. $n = 4$ technical replicates. Bottom, marker expression following Notch inhibition. $n = 4$ technical replicates. **b**, Left, ISC colony growth. Scale bar, 75 μ m. Right, clonogenicity of colony cells. $n = 3$ biological replicates. **c**, ISC and TBSC pedigrees and ALI differentiation (tubulin, green; Muc5AC, red). Scale bar, 50 μ m left, 25 μ m right top, 25 μ m bottom right; $n = 7$ biological replicates; $n = 3$ technical replicates; 3 independent experiments. **d**, ALI-differentiated ISC. Scale bar, 50 μ m. $n = 7$ biological replicates; $n = 3$ technical replicates; 3 independent experiments. H&E, haematoxylin and eosin staining. **e**, PCA using 2,158 genes (> 2 -fold, $P < 0.05$ by Student's t -test) of ISC and TBSC and corresponding ALI-differentiated epithelia. **f**, Expression heat map of markers in ISC and TBSC. Scale, -2.5 -fold (extreme blue) to $+2.5$ -fold (extreme red). $n = 3$ technical replicates.

tissue showed great divergence as expected for columnar and stratified epithelia, the gene expression profiles of undifferentiated ISC^{GS} and TBSC^{GS} differed by less than 4% (> 2.0 -fold, $P < 0.05$) (Fig. 1e). ISC^{GS} showed high expression of intestinal stem-cell markers such as OLFM4, CD133 (ref. 22), Lgr5 (ref. 23) and Lrig1 (ref. 24), whereas those from the airways had the typical stem cells markers of stratified epithelia (Krt14, Krt5 and Tp63 (ref. 11)) (Fig. 1f).

Intestinal stem cell variation

Approximately one in 2,000 cells from duodenum (I^{du}SC), jejunum (I^{je}SC) and ileum (I^{il}SC) of a 21-week-old fetal intestine form a colony (Fig. 2a). Although these colonies were morphologically indistinguishable in culture, whole-genome expression analysis of multiple pedigrees showed a consistent, region-specific signature of 24–178 genes (> 1.5 -fold, $P < 0.05$; Fig. 2b; Extended Data Fig. 2a).

After 10 days at an ALI, I^{du}SC and I^{je}SC gave rise to a finer pattern of epithelial folds than that produced by I^{il}SC (Fig. 2c). By histology, villi appear progressively more robust along the anterior–posterior axis, with I^{il}SC producing the larger villi and more numerous goblet cells (Fig. 2d, e). Interestingly, the epithelia derived from I^{du}SC expressed markers more typical of gastric epithelium (for example,

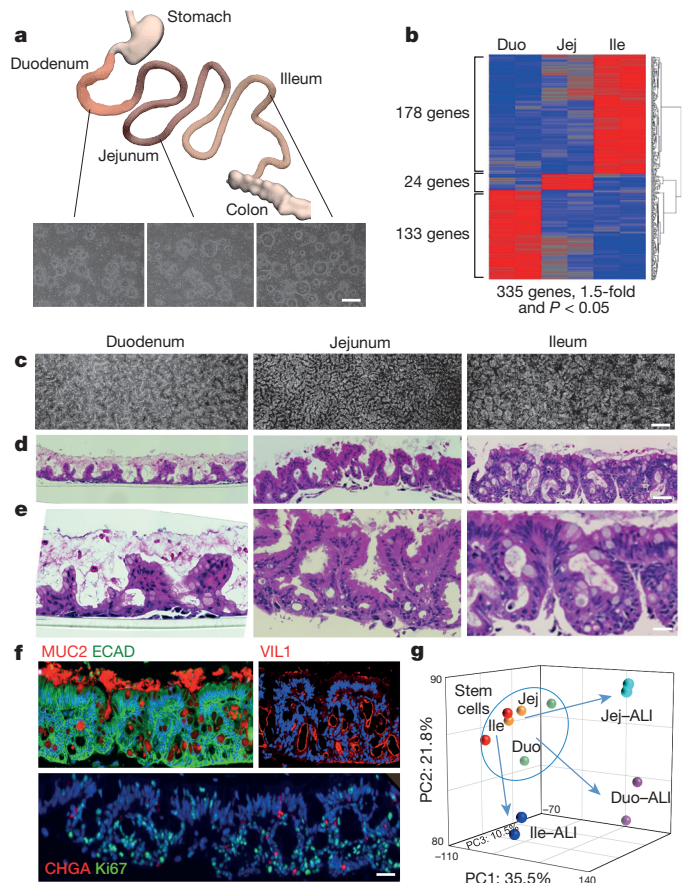


Figure 2 | Stem cells from fetal small intestine. **a**, Depiction of small intestine and clones derived from each. Scale bar, 400 μ m; $n = 3$ biological replicates. **b**, Heat map of pedigrees from duodenum (Duo), jejunum (Jej), and ileum (Ile). **c**, Surface views of ALI cultures. Scale bar, 200 μ m; $n = 30$ technical replicates. **d**, **e**, Histological sections through ALI cultures at low (scale bar, 150 μ m) and high (scale bar, 50 μ m) magnification. **f**, Immunofluorescence on sections of ALI cultures with indicated antibodies. ECAD, E-cadherin. Scale bar, 75 μ m; $n = 3$ technical replicates. **g**, PCA map of stem cell gene expression from the three major regions of the small intestine together with their corresponding ALI-differentiated epithelia.

TFF2 and Muc5AC), consistent with duodenum's location between the stomach and the small intestine (Extended Data Fig. 2b). I^{je}SC-derived epithelium, however, expressed Muc2, consistent with intestinal epithelium (Extended Data Fig. 2c), and I^{il}SC produced an epithelium more akin to colon (Fig. 2f). The pattern of proliferation in the ALI epithelia as measured by Ki67 staining was generally confined to cells proximal to the support membrane (Fig. 2e, f). PCA mapping of gene expression revealed more divergence among ALI-differentiated tissue than among the intestinal stem cells (Fig. 2g).

Colon stem cells

We also generated single-cell pedigree lines from the ascending, transverse, and descending colon from the same 21-week fetal demise case (Fig. 3a). The variation in gene expression between the stem cells of these colonic segments was minimal with signatures of 19–28 genes (> 1.5 -fold, $P < 0.05$; Fig. 3b). As with pedigrees derived from the intestinal epithelium, those from the colon could be propagated for months without loss of clonogenicity (not shown). Differentiation of these colon pedigrees under identical ALI conditions employed for the intestinal stem cells resulted in networks of 3D, large-diameter structures (Fig. 3c). Consistently, the histology of these ALI cultures revealed patterns of broad intestinal glands dominated by goblet cells (Fig. 3d). These ALI-generated tissues showed strong staining for

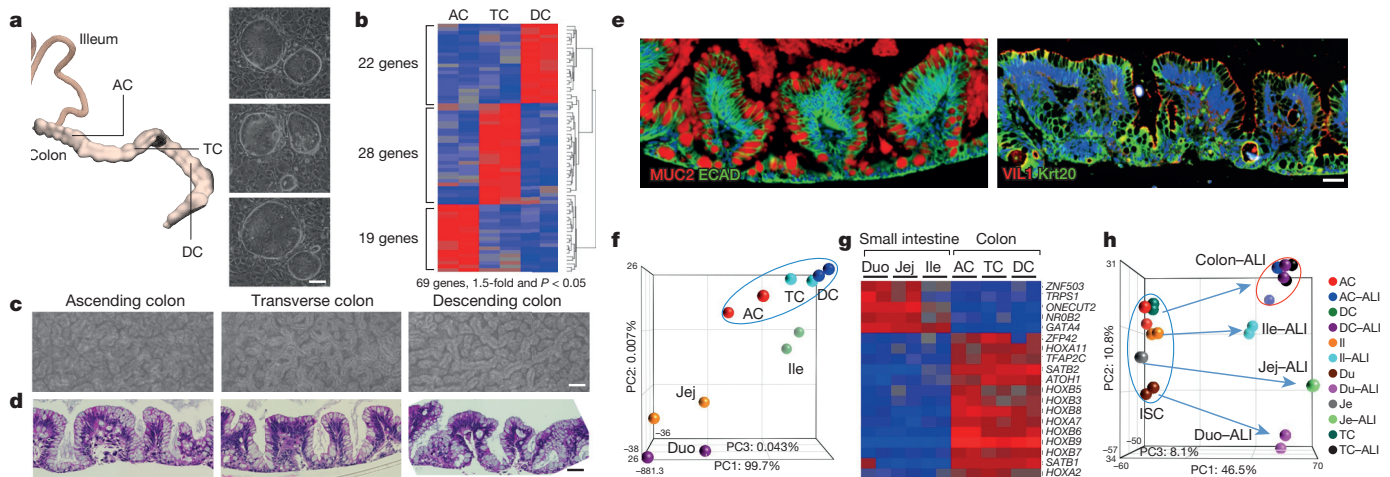


Figure 3 | Stem cells of fetal colon. **a**, Depiction of colon and clones derived from each. Scale bar, 75 μ m; $n = 3$ biological replicates. AC, TC and DC, ascending, transverse and descending colon, respectively. **b**, Expression heat map of pedigrees from the three major divisions of the colon. **c**, Surface images of ALI cultures. Scale bar, 100 μ m; $n = 20$ technical replicates. **d**, Histological sections through ALI cultures of colon stem cells. Scale bar, 75 μ m.

intestinal goblet cell marker *Muc2*, as well as polarized villin and *Krt20*, typical of differentiated colonic epithelium (Fig. 3e). And while the colonic stem cells as a group showed minor differences in gene expression (see Figure 3b), they gave rise to epithelia with more distinct gene expression profiles (Extended Data Fig. 3). PCA mapping of these expression data showed a clustering of the colon stem cells relative to the intestinal stem cells, with increasingly distant spaces occupied by stem cells of the ileum, jejunum and duodenum, respectively (Fig. 3f). This distinction in global gene expression patterns is reflected, for instance, in the differential expression of transcription factors. In particular, *ONECUT2*, *NR0B2*, *TRPS1* and *ZNF503* show relatively high expression in the small intestine stem cells, whereas those of the colon showed a bias for *Hox* genes as well as the global chromatin organizer genes *SATB1* and *SATB2* (Fig. 3g, h).

e, Immunofluorescence on sections through ALI cultures with indicated antibodies. Scale bar, 50 μ m. **f**, PCA map of gene expression of colon and intestine stem cells. **g**, Expression heat map of stem cells of small intestine and colon. **h**, PCA map of gene expression profiles of intestinal stem cells and their corresponding ALI-differentiated epithelia.

Columnar versus stratified epithelia

The expression profiles of stem cells of human intestinal tract enabled a detailed comparison with those of stratified epithelia including human epidermis, corneal epithelium, mammary gland, prostate gland and upper airway. From this analysis it is clear that stratified epithelia, all of which depend on the p53-related stem-cell marker p63 for long-term self-renewal¹¹, occupy a distinct expression space from that of the intestinal stem cells or other columnar epithelial stem cells (Fig. 4a). A survey of genes whose expression is associated with stem cells of one of these two major classes of epithelia revealed a strong bias for *Olfm4*, *CD133* (ref. 22), *Lgr5* (ref. 23), *Nr5a2* (ref. 25), *Id2*, *Lrig1* (ref. 24), *EphB2*, *Ascl2* and *EphB3* in the intestinal stem cells, while the stratified epithelial stem cells expressed *ZNF750*, *TP63* and *KRT5* (Fig. 4b). Many of the markers differentially appearing in the intestinal stem cells, such as *Olfm4*, *Lgr5* and *Ascl2*, are not general

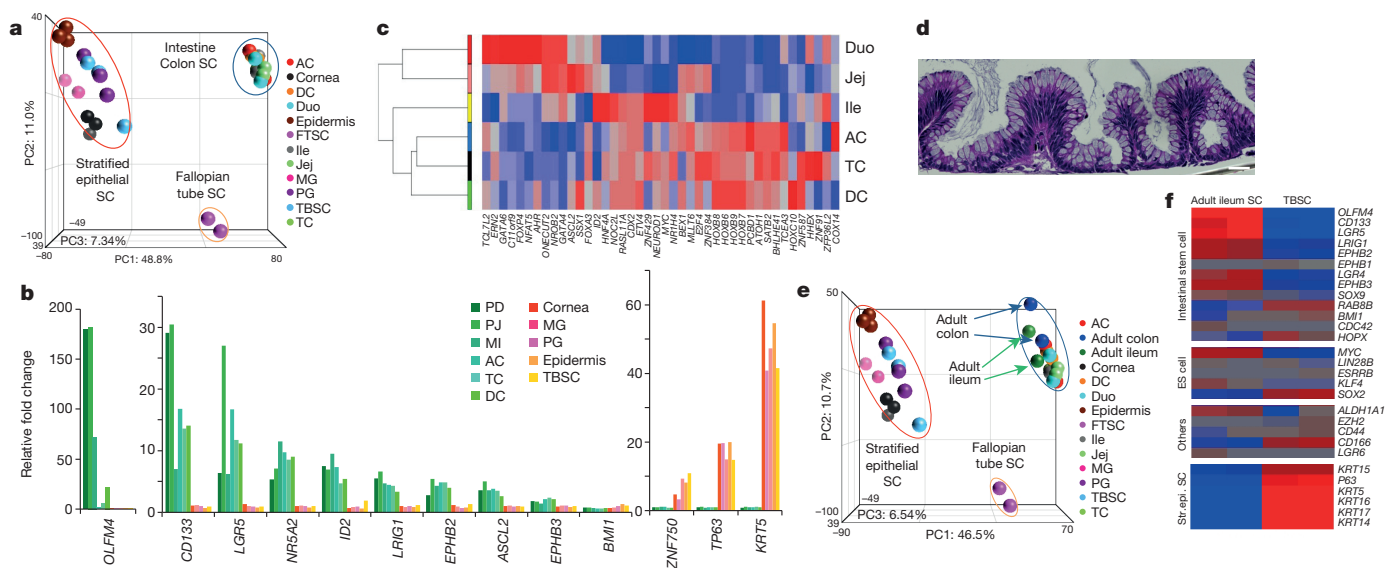


Figure 4 | Differential gene expression in stem cells of stratified and columnar epithelia. **a**, PCA map of stem cells of stratified epithelia (cornea, corneal epithelium; MG, mammary gland; PG, prostate gland; TBSC, tracheo-bronchial epithelial stem cells) and columnar epithelia (FTSC, fallopian tube epithelium). **b**, Gene expression in stem cells (stratified epithelia $n = 3$ technical replicates; columnar epithelia $n = 2$ technical replicates). **c**, Transcription

factors differentially expressed in TBSC and ISC. **d**, ALI-differentiated adult terminal ileum stem cells derived from endoscopic biopsy. Scale bar, 50 μ m; $n = 10$ technical replicates. **e**, PCA map of stem cells of adult terminal ileum, colon, fetal ISCs, and stratified epithelia. **f**, Stem cell markers in adult terminal ileum stem cells and TBSCs.

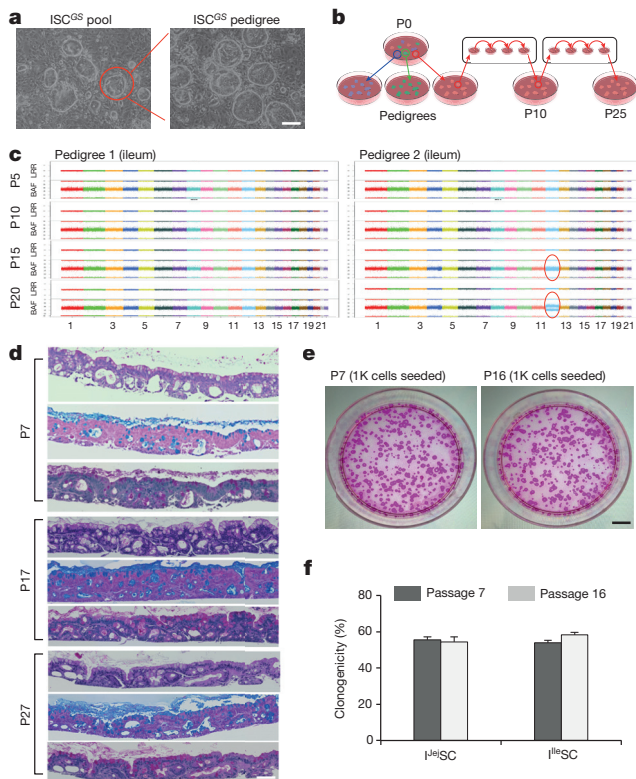


Figure 5 | Genomic stability of ISC in culture. **a**, Clone selection for pedigree generation. Scale bar, 200 μ m. **b**, Serial passaging of pedigrees. **c**, CNV, BAF (B allele frequency) and LRR (log R ratio) profiles of pedigrees at P5 to P20 and trisomy 12 indicated (circle). **d**, ALI-differentiated pedigree 2 at P7, P17, and P27 stained with H&E (top), Alcian blue (middle), and periodic acid Schiff (bottom). Scale bar, 100 μ m; $n = 4$ technical replicates. **e**, Clonogenicity assay revealing Rhodamine red-stained colonies grown 20 days following seeding 1,000 passaged cells. Scale bar, 10mm; $n = 3$ technical replicates. **f**, Quantification of clonogenicity at indicated passage number of ground state stem cells from jejunum ($I^{le}SC$) and ileum ($I^{le}SC$). $n = 3$ biological replicates; error bars, s.d.

columnar epithelial stem cell markers as evidenced by their absence in fallopian tube stem cells, although *Lrig1* is more highly expressed in fallopian tube stem cells than either those of the intestine or the colon (Extended Data Fig. 4a). Notably, *Bmi1*, a member of the Polycomb group (PcG) PRC1-like complex implicated in self-renewal in both haematopoietic²⁶ and as reserve cells for proliferating, *Lgr5*⁺ intestinal stem cells^{27–29}, was not differentially expressed in the cloned intestinal versus stratified epithelial stem cells. And while many of the typical markers of intestinal stem cells such as *Lgr5*, *CD44*, *Lrig1*, *EphB2* and *ASCL2* show a decrease in expression as the intestinal stem cells are differentiated in ALI cultures, *Bmi1* did not (Extended Data Fig. 4b, c). These findings suggest that we are cloning either crypt cells or so-called ‘+4’ cells that have become crypt-like in their expression patterns. We also examined transcription factors differentially expressed in ISC compared to stratified epithelial stem cells in an effort to understand the regiospecificity of commitment programs of stem cells along the intestinal tract (Fig. 4c). In addition to six transcription factors that were uniformly highly expressed in stem cells of the intestinal tract (*CREB3L1*, *Myb*, *NR5A2*, *IRF8*, *HNF4G* and *Mx2*) versus tracheobronchial stem cells, this analysis revealed limited sets of transcription factors differentially expressed in stem cells along the anterior–posterior axis of the intestinal tract that conceivably function in maintaining commitment states. For instance, and consistent with previous observations³⁰, *GATA4* and *GATA6* were expressed most strongly in the anterior portions of the intestinal tract (Fig. 4c). Significantly, the selective deletion of *GATA4*

and *GATA6* in the murine duodenum and jejunum promotes ileal properties and a detrimental phenotype^{30,31}, suggesting a role for these transcription factors in maintaining segmental identity acting at the level of the stem cell. Similarly, the requirement for *Oncut2* in the duodenum³² might be at the level of the duodenal stem cells. It is likely that analyses of cloned stem cells from the various segments of the intestinal tract will help to unravel the roles of such segment-specific transcription factors in the establishment of commitment and differentiation programs. Importantly, the overall properties of ISCs from fetal sources are conserved in those derived from endoscopic biopsies of paediatric and adult cases (Fig. 4d–f).

Genomic and lineage stability

Human embryonic stem cells and iPSC lines acquire with successive passages genomic structural variations, including some that confer a selective advantage^{33,34}. To assess the genomic stability of our ISC^{GS} , we examined copy number (CNV) and single nucleotide variation (SNV) in two independent ISC^{GS} pedigrees derived from the ileum of one fetal demise case after 50 (passage 5; P5), 100 (P10), 150 (P15), and 200 days (P20) of continuous proliferation (Fig. 5a, b). At P5, when single ISC^{GS} pedigrees can be amplified to an estimated 300 million to 75 billion cells, no chromosomal aneuploidies were detected, although one pedigree showed three interstitial deletions affecting two genes (Fig. 5c; Extended Data Fig. 5a; Supplementary Information Table 1). This low level of structural variation was maintained through passage 10, although increased by P15 and at P20 one of the pedigrees showed a frank trisomy of chromosome 12 (Fig. 5c; Extended Data Fig. 5a; Supplementary Information Table 1). A similar upward trend in CNV as a function of passage number was observed in five intestinal pedigrees (pedigrees 3–7) derived from a separate fetal demise case (Extended Data Figs 5, 6; Supplementary Information Tables 1, 2).

By exome sequencing, our original two pedigrees showed few (0–1) non-synonymous mutations through passage 10, and these increased modestly (1–2 new non-synonymous mutations) through P15 and P20 (Extended Data Fig. 5a). None of these non-synonymous mutations have been reported as driver genes in human cancers. A similar trend was observed in the five pedigrees from the second fetal demise case followed through P5 and P25. By P25 the range of non-synonymous SNVs increased to 2–10 per clone, and while not involving obvious cancer driver genes, did include genes such as *ECT2L* and *EP300* that might provide a selective growth advantage (Extended Data Fig. 5c). These data indicate that most pedigrees sustain few genomic changes within the first 100 days of proliferative expansion. By P15 and through P25, however, half the pedigrees showed evidence for aneuploidy as well as an increase in interstitial CNV and SNVs with allele frequencies nearing 0.5, suggesting the rise of an advantaged subclone. We asked how these late-passage genomic changes might affect differentiation by comparing early and late passages of pedigree 2 in ALI differentiation. By all histological criteria, including Alcian blue staining for goblet cells and intestinal marker staining, we could not distinguish the ALI-differentiated epithelia derived from P7, P17 and P27 (Fig. 5d; Extended Data Fig. 7). Similarly, we note that these intestinal stem cell pedigrees do not lose (or gain) clonogenicity when tested at P7 and P16, which remain stably above 50% (Fig. 5e, f). Lastly, we found no evidence of tumorigenicity by these ground state intestinal stem cells, including those at P25 harbouring aneuploidies, following their subcutaneous implantation to immunodeficient (NOD.Cg-Prkdc^{scid} Il2rg^{tm1Wjl}/SzJ) mice³⁵ (Extended Data Fig. 8).

Modelling *Clostridium difficile* infections

C. difficile is a Gram-positive, spore-forming bacterium and the primary cause of nosocomial diarrhoea and pseudomembranous colitis³⁶. The pathogenicity of *C. difficile* is linked to its production of two similar, high molecular weight toxins TcdA and TcdB. While together TcdA and TcdB cause fluid secretion, inflammation, and colonic

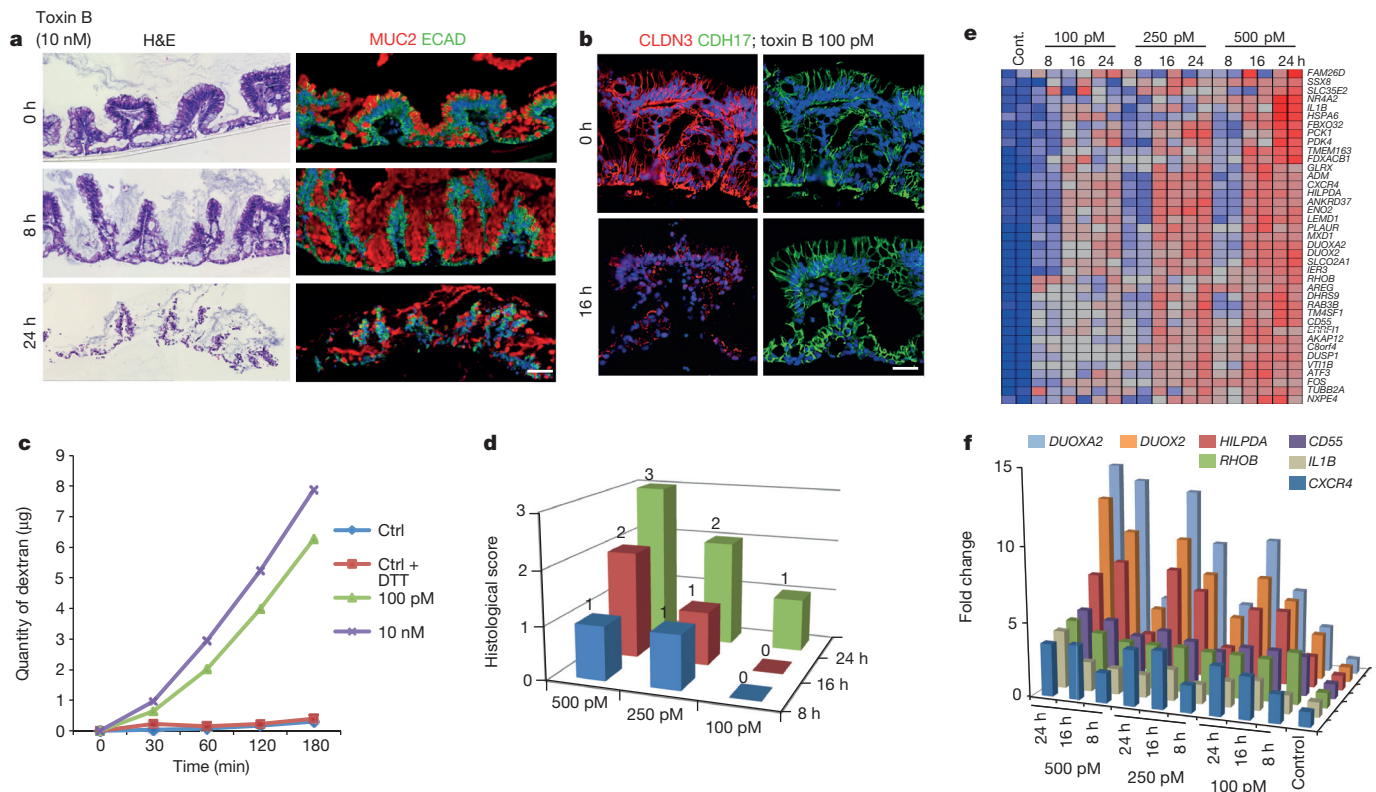


Figure 6 | *C. difficile* toxin B effects on *in vitro*-generated colonic epithelia. **a**, TcdB effects on colonic stem cell-derived epithelia. Scale bar, 100 μ m. $n = 4$ technical replicates. **b**, Tight junction protein claudin 3 (CLDN3; red) and adherens junction marker cadherin-17 (CDH17; green) in ALI colonic epithelium treated with TcdB. Scale bar, 50 μ m; $n = 4$ biological replicates. **c**, Dextran permeability assay on TcdB-treated ALI colonic epithelia. **d**, 3D plot

of histological scoring by gastrointestinal pathologist according to a standard 0–3 rating for colonic epithelial integrity. **e**, Heat map of 39 genes differentially expressed between TcdB (500 pM, 24 h) and controls ($>$ threefold and $P < 0.05$ by Student's *t*-test). **f**, 3D plot of seven selected genes at time points and doses indicated. $n = 2$ technical replicates.

tissue damage, their respective and possible synergistic roles have been difficult to ascertain^{37–39}. We therefore challenged colonic epithelia derived from cloned, ground state colonic stem cells with recombinant TcdB (Fig. 6a, b; Extended Data Fig. 9a, b). At higher concentrations or longer time points there is a loss of goblet cells, disruption of the crypt architecture, cell polarity, and a specific loss of tight versus adherens junction proteins that correlates with increased dextran permeability (Fig. 6c). These dose–response changes in the ALI colonic epithelium mirror those of *C. difficile*-associated pseudomembranous colitis (Fig. 6d, Extended Data Fig. 9a, b). Microarray analysis of ALI-generated colonic epithelia following nine TcdB treatment conditions revealed alterations in gene expression in a time- and dose-dependent manner (Fig. 6e, f; Extended Data Fig. 9c–f). Pathway analysis indicated that TcdB triggers changes in gene expression related to inflammation, RhoB-mediated actin regulation, and junctional dynamics previously implicated in *C. difficile* pathology^{40,41}. In addition, this analysis revealed that *DUOX2* and *DUOX2* were consistently the two highest upregulated genes (Fig. 6e, f). These proteins form an enzyme capable of producing hydrogen peroxide and have been implicated in the inflammation of inflammatory bowel disease (IBD)⁴². Finally, we also tested *C. difficile* TcdA in our model. TcdA is reported to be a specific enterotoxin^{36,37}, and indeed we found that it triggers similar cytopathic and permeability changes in ALI models of human colonic epithelium (Extended Data Fig. 10), albeit at lower doses than those effective for TcdB. Together these findings underscore the potential of this model system to recapitulate and elucidate *C. difficile* pathology.

Discussion

Adult stem cells of the highly regenerative intestinal tract remain largely defined by metabolic, marker profiling, or lineage tracing

experiments *in vivo* or transplantation of cells from intestinal organoids^{23,43,44}. As stem cells comprise only a minor component of organoids—perhaps less than 1%⁴⁵—the molecular features of stem cells of columnar epithelia such as the intestinal tract have remained unclear. Therefore the selective cloning and proliferative expansion of highly clonogenic, ground state intestinal stem cells described here offers a first glimpse into the molecular properties of these cells. Our inability to convert differentiated cells to clonogenic cells supports the notion that we are cloning resident stem cells rather than somehow ‘reprogramming’ differentiated enterocytes. These resident stem cells possess robust epigenetic programs of commitment to regiospecific intestinal differentiation that are stable despite more than six months of continuous propagation. This cell-autonomous regiospecificity of stem cells along the intestinal tract argues against a unitary ‘intestinal stem cell’ or even one each for the histologically recognized segments, but rather a developmentally established spectrum of stem cells that ultimately maintains the histological and functional properties that define these segments. A heuristic deciphering of the commitment code from the regiospecific expression patterns presented here will guide parallel efforts with iPSCs to achieve appropriate lineage fates⁴⁶. Interestingly, many inductive signalling pathways and transcription factors implicated in embryonic gut formation⁴⁷ may act to reinforce commitment codes via continued expression in stem cells of the intestinal tract.

We anticipate that the ability to maintain these stem cells in their elemental state will enable the discovery of epigenetic mechanisms that underlie properties of very long-term self-renewal, exquisitely precise lineage commitment, and the intrinsically directed, self-assembly of differentiated epithelia. Although we demonstrate the potential of clonally-derived colonic epithelia to model the pathogenesis of *C. difficile* toxins, we anticipate the need to restore complexity

in the form of mesenchyme, immune cells, enteric neurons and perhaps components of the microbiome⁴⁸ to fully recapitulate disease dynamics. In particular, enteric maladies such as inflammatory bowel disease represent important medical challenges whose aetiologies most likely reside in interactions between the immune system, intestinal mucosa and intestinal flora^{49,50}. Finally, the ability to clone patient-specific, ground state stem cells from columnar epithelia via endoscopic biopsies, coupled with their orders-of-magnitude expansion kinetics over organoids, favours their use in regenerative medicine, pre-clinical trials and disease modelling.

Online Content Methods, along with any additional Extended Data display items and Source Data, are available in the online version of the paper; references unique to these sections appear only in the online paper.

Received 20 December 2014; accepted 14 April 2015.

Published online 3 June 2015.

- Tabar, V. & Studer, L. Pluripotent stem cells in regenerative medicine: challenges and recent progress. *Nature Rev. Genet.* **15**, 82–92 (2014).
- Okano, H. & Yamanaka, S. iPS cell technologies: significance and applications to CNS regeneration and disease. *Mol. Brain* **7**, 22 (2014).
- Müller, A. M. & Dzierzak, E. A. ES cells have only a limited lymphopoietic potential after adoptive transfer into mouse recipients. *Development* **118**, 1343–1351 (1993).
- Helgason, C. D., Sauvageau, G., Lawrence, H. J., Largman, C. & Humphries, R. K. Overexpression of HOXB4 enhances the hematopoietic potential of embryonic stem cells differentiated *in vitro*. *Blood* **87**, 2740–2749 (1996).
- Bonde, S., Dowden, A. M., Chan, K. M., Tabayoyong, W. B. & Zavazava, N. HOXB4 but not BMP4 confers self-renewal properties to ES-derived hematopoietic progenitor cells. *Transplantation* **86**, 1803–1809 (2008).
- Iuchi, S., Dabelsteen, S., Easley, K., Rheinwald, J. G. & Green, H. Immortalized keratinocyte lines derived from human embryonic stem cells. *Proc. Natl Acad. Sci. USA* **103**, 1792–1797 (2006).
- Amabile, G. *et al.* *In vivo* generation of transplantable human hematopoietic cells from induced pluripotent stem cells. *Blood* **121**, 1255–1264 (2013).
- Suzuki, N. *et al.* Generation of engraftable hematopoietic stem cells from induced pluripotent stem cells by way of teratoma formation. *Mol. Ther.* **21**, 1424–1431 (2013).
- Rheinwald, J. G. & Green, H. Serial cultivation of strains of human epidermal keratinocytes: the formation of keratinizing colonies from single cells. *Cell* **6**, 331–343 (1975).
- Rama, P. *et al.* Limbal stem-cell therapy and long-term corneal regeneration. *N. Engl. J. Med.* **363**, 147–155 (2010).
- Senoo, M., Pinto, F., Crum, C. P. & McKeon, F. p63 is essential for the proliferative potential of stem cells of stratified epithelia. *Cell* **129**, 523–536 (2007).
- Kumar, P. A. *et al.* Distal airway stem cells yield alveoli *in vitro* and during lung regeneration following H1N1 influenza infection. *Cell* **147**, 525–538 (2011).
- Matsuura, R. *et al.* Crucial transcription factors in endoderm and embryonic gut development are expressed in gut-like structures from mouse ES cells. *Stem Cells* **24**, 624–630 (2006).
- Sato, T. *et al.* Single Lgr5 stem cells build crypt-villus structures *in vitro* without a mesenchymal niche. *Nature* **459**, 262–265 (2009).
- Ootani, A. *et al.* Sustained *in vitro* intestinal epithelial culture within a Wnt-dependent stem cell niche. *Nature Med.* **15**, 701–706 (2009).
- Sato, T. *et al.* Paneth cells constitute the niche for Lgr5 stem cells in intestinal crypts. *Nature* **469**, 415–418 (2011).
- Fordham, R. P. *et al.* Transplantation of expanded fetal intestinal progenitors contributes to colon regeneration after injury. *Cell Stem Cell* **13**, 734–744 (2013).
- Middendorp, S. *et al.* Adult stem cells in the small intestine are intrinsically programmed with their location-specific function. *Stem Cells* **32**, 1083–1091 (2014).
- Yin, X. *et al.* Niche-independent high-purity cultures of Lgr5⁺ intestinal stem cells and their progeny. *Nature Methods* **11**, 106–112 (2014).
- Kim, K. A. *et al.* Mitogenic influence of human R-spondin1 on the intestinal epithelium. *Science* **309**, 1256–1259 (2005).
- Dreesen, O. & Brivanlou, A. H. Signaling pathways in cancer and embryonic stem cells. *Stem Cell Rev.* **3**, 7–17 (2007).
- Zhu, L. *et al.* Prominin 1 marks intestinal stem cells that are susceptible to neoplastic transformation. *Nature* **457**, 603–607 (2009).
- Barker, N. *et al.* Identification of stem cells in small intestine and colon by marker gene Lgr5. *Nature* **449**, 1003–1007 (2007).
- Powell, A. E. *et al.* The pan-ErbB negative regulator Lgr1 is an intestinal stem cell marker that functions as a tumor suppressor. *Cell* **149**, 146–158 (2012).
- Botrugno, O. A. *et al.* Synergy between LHR-1 and beta-catenin induces G1 cyclin-mediated cell proliferation. *Mol. Cell* **15**, 499–509 (2004).
- Lessard, J. & Sauvageau, G. Bmi-1 determines the proliferative capacity of normal and leukaemic stem cells. *Nature* **423**, 255–260 (2003).
- Sangiorgi, E. & Capecchi, M. R. Bmi1 is expressed *in vivo* in intestinal stem cells. *Nature Genet.* **40**, 915–920 (2008).
- Tian, H. *et al.* A reserve stem cell population in small intestine renders Lgr5-positive cells dispensable. *Nature* **478**, 255–259 (2011).
- Metcalfe, C., Kijavini, N. M., Ybarra, R. & de Sauvage, F. J. Lgr5⁺ stem cells are indispensable for radiation-induced intestinal regeneration. *Cell Stem Cell* **14**, 149–159 (2014).
- Battle, M. A. *et al.* GATA4 is essential for jejunal function in mice. *Gastroenterology* **135**, 1676–1686 (2008).
- Walker, E. M., Thompson, C. A. & Battle, M. A. GATA4 and GATA6 regulate intestinal epithelial cytodifferentiation during development. *Dev. Biol.* **392**, 283–294 (2014).
- Dusing, M. R., Maier, E. A., Aronow, B. J. & Wiginton, D. A. Onecut-2 knockout mice fail to thrive during early postnatal period and have altered patterns of gene expression in small intestine. *Physiol. Genomics* **42**, 115–125 (2010).
- International Stem Cell Initiative. Screening ethnically diverse human embryonic stem cells identifies a chromosome 20 minimal amplicon conferring growth advantage. *Nature Biotechnol.* **29**, 1132–1144 (2011).
- Avery, S. *et al.* BCL-XL mediates the strong selective advantage of a 20q11.21 amplification commonly found in human embryonic stem cell cultures. *Stem Cell Rep.* **1**, 379–386 (2013).
- Shultz, L. D. *et al.* Human cancer growth and therapy in immunodeficient mouse models. *Cold Spring Harb. Protoc.* <http://dx.doi.org/10.1101/pdb.top073585> (2014).
- Voth, D. E. & Ballard, J. D. *Clostridium difficile* toxins: mechanism of action and role in disease. *Clin. Microbiol. Rev.* **18**, 247–263 (2005).
- Carter, G. P., Rood, J. I. & Lyras, D. The role of toxin A and toxin B in the virulence of *Clostridium difficile*. *Trends Microbiol.* **20**, 21–29 (2012).
- Lyas, D. *et al.* Toxin B is essential for virulence of *Clostridium difficile*. *Nature* **458**, 1176–1179 (2009).
- Farrow, M. A. *et al.* *Clostridium difficile* toxin B-induced necrosis is mediated by the host epithelial cell NADPH oxidase complex. *Proc. Natl Acad. Sci. USA* **110**, 18674–18679 (2013).
- Huelsbeck, J. *et al.* Upregulation of the immediate early gene product RhoB by exoenzyme C3 from *Clostridium limosum* and toxin B from *Clostridium difficile*. *Biochemistry* **46**, 4923–4931 (2007).
- Aktories, K., Schmidt, G. & Just, I. Rho GTPases as targets of bacterial protein toxins. *Biol. Chem.* **381**, 421–426 (2000).
- MacFie, T. S. *et al.* DUOX2 and DUOX2 form the predominant enzyme system capable of producing the reactive oxygen species H₂O₂ in active ulcerative colitis and are modulated by 5-aminosalicylic acid. *Inflamm. Bowel Dis.* **20**, 514–524 (2014).
- Cheng, H. & Leblond, C. P. Origin, differentiation and renewal of the four main epithelial cell types in the mouse small intestine. V. Unitarian theory of the origin of the four epithelial cell types. *Am. J. Anat.* **141**, 537–561 (1974).
- Yui, S. *et al.* Functional engraftment of colon epithelium expanded *in vitro* from a single adult Lgr5⁺ stem cell. *Nature Med.* **18**, 618–623 (2012).
- Wang, F. *et al.* Isolation and characterization of intestinal stem cells based on surface marker combinations and colony-formation assay. *Gastroenterology* **145**, 383–395 (2013).
- Watson, C. L. *et al.* An *in vivo* model of human small intestine using pluripotent stem cells. *Nature Med.* **20**, 1310–1314 (2014).
- Sheaffer, K. L. & Kaestner, K. H. Transcriptional networks in liver and intestinal development. *Cold Spring Harb. Perspect. Biol.* **4**, a008284 (2012).
- Nicholson, J. K. *et al.* Host-gut microbiota metabolic interactions. *Science* **336**, 1262–1267 (2012).
- Brandl, K. & Beutler, B. Creating diseases to understand what prevents them: genetic analysis of inflammation in the gastrointestinal tract. *Curr. Opin. Immunol.* **24**, 678–685 (2012).
- Lees, C. W., Barrett, J. C., Parkes, M. & Satsangi, J. New IBD genetics: common pathways with other diseases. *Gut* **60**, 1739–1753 (2011).

Supplementary Information is available in the online version of the paper.

Acknowledgements This work was supported by grants from Connecticut Innovations (W.X., F.M.), the Joint Council Office of the Agency for Science Technology Research Agency (A*STAR), Singapore (W.X., F.M.), the National Medical Research Council, Singapore (BNB101677A to H.K.Y., F.M., and W.X.; BNB11dec063 to N.N., F.M. and W.X.), the Department of Defense (W81XWH-10-1-0289 to C.P.C.) and the National Institute of Health (AI09575504 to D.B.L.). We thank M. LaLande, B. Lane and B. Seet for support, B. Tennent, B. Knowles and T. McLaughlin for comments on the manuscript, J. Hammer for artwork, L. Lapierre and J. Franklin for histology evaluation. We thank H. Green for advice and support.

Author Contributions Experimental design and conception were done by W.X., F.M., D.B.L., K.Y.H. and C.P.C.; X.W. cloned and differentiated the intestinal stem cells with help from L.H.W., F.K., G.N., B.E.H. and Y.H.; Y.Y., X.W. prepared the genomic and gene expression analyses together with F.K., G.N., C.C.K. and L.W.; T.Z., D.B. and N.N. performed all computational and bioinformatics work. B.H. and C.P.C. obtained fetal tissues and F.A.S., J.S.H. and T.D. provided endoscopic biopsies, and R.B. analysed the xenografts. The *C. difficile* experiments were designed and executed by B.C., L.H.W., M.A.F. and D.B.L.; W.X. and F.M. wrote the manuscript with input from all other authors.

Author Information Data sets generated for this study have been submitted to the National Center for Biotechnology Information Gene Expression Omnibus (GEO) database and the European Nucleotide Archive under accession numbers GSE66749 and SRP056402. Reprints and permissions information is available at www.nature.com/reprints. The authors declare no competing financial interests. Readers are welcome to comment on the online version of the paper. Correspondence and requests for materials should be addressed to W.X. (xianmckeon2014@gmail.com) or F.M. (mckeon.xian@gmail.com).

METHODS

In vitro culture of human small intestinal and colonic epithelial stem cells.

Intestinal tissue from 20- to 21-week-old late fetal demise cases were obtained under parent consent as de-identified material under approved institutional review board protocols at the Brigham and Women's Hospital, Boston, MA, USA (2009P002281). Terminal ileum endoscopic biopsies were obtained under informed consent and institutional review board approval at the Connecticut Children's Medical Center, Hartford, Connecticut USA (15-047-2). Fetal intestinal tissue or 1 mm endoscopic biopsies from terminal ileum were collected into cold F12 media (Gibco, USA) with 5% fetal bovine serum (HyClone, USA) and then minced by sterile scalpel into 0.2–0.5 mm³ sizes to a viscous and homogeneous appearance. The minced tissue was digested in 2 mg ml⁻¹ collagenase type IV (Gibco, USA) at 37 °C for 30–60 min with agitation. Dissociated cells were passed through a 70-µm Nylon mesh (Falcon, USA) to remove aggregates and then were washed four times in cold F12 media, and then seeded onto a feeder layer of lethally irradiated 3T3-J2 cells^{9,12} in c-FAD media⁹ modified to SCM-6F8 media by the addition of 125 ng ml⁻¹ R-spondin1 (R&D systems, USA), 1 µM Jagged-1 (AnaSpec Inc., USA), 100 ng ml⁻¹ human Noggin (Peprotech, USA), 2.5 µM Rock-inhibitor (Calbiochem, USA), 2 µM SB431542 (Cayman chemical, USA), and 10 mM nicotinamide (Sigma-Aldrich, USA). Cells were cultured at 37 °C in a 7.5% CO₂ incubator. The culture media was replaced every two days. Colonies were digested by 0.25% trypsin-EDTA solution (Gibco, USA) for 5–8 min and passaged every 7 to 10 days. To obtain single-cell suspensions colonies were trypsinized by TrypLE Express solution (Gibco, USA) for 8–15 min at 37 °C and cell suspensions were passed through 30-µm filters (Miltenyi Biotec, Germany). Approximately 20,000 epithelial cells were seeded to each well of 6-well plate. Cloning cylinder (Pyrex, USA) and high vacuum grease (Dow Corning, USA) were used to select single colonies for pedigrees. Gene expression analyses were performed on cells derived from passage 4–8 (P4–P8) cultures.

Histology and immunostaining. Histology, haematoxylin and eosin (H&E), Alcian blue, periodic acid-Schiff (PAS), rhodamine B staining, immunohistochemistry, and immunofluorescence were performed using standard techniques. For immunofluorescence and immunohistochemistry, 4% paraformaldehyde-fixed, paraffin-embedded tissue sections were subjected to antigen retrieval in citrate buffer (pH 6.0, Sigma-Aldrich, USA) at 120 °C for 20 min, and a blocking procedure was performed with 5% bovine serum albumin (BSA, Sigma-Aldrich, USA) and 0.05% Triton X-100 (Sigma-Aldrich, USA) in phosphate-buffered saline (PBS; Gibco, USA) at room temperature for 1 h. Primary antibodies used in this study and staining condition were listed in Supplementary Information Table 3. All images were captured by using the Inverted Eclipse Ti-Series (Nikon, Japan) microscope with Lumencor SOLA light engine and Andor Technology Clara Interline CCD camera and NIS-Elements Advanced Research v.4.13 software (Nikon, Japan) or LSM 780 confocal microscope (Carl Zeiss, Germany) with LSM software. Bright field cell culture images were obtained on an Eclipse TS100 microscope (Nikon, Japan) with Digital Sight DSFi1 camera (Nikon, Japan) and NIS-Elements F3.0 software (Nikon, Japan).

Stem cell differentiation. Air-liquid interface (ALI) culture of TBSCs was performed as described^{12,51}. Briefly, for ALI culture of intestinal and colonic epithelial stem cells, Transwell inserts (Corning, USA) were coated with 20% Matrigel (BD Biosciences, USA) and incubated at 37 °C for 30 min to polymerize. 200,000 irradiated 3T3-J2 cells were seeded to each transwell insert and incubated at 37 °C, 7.5% CO₂ incubator overnight. QuadroMACS Starting Kit (LS) (Miltenyi Biotec, Germany) was used to purify the stem cells by removal of feeder cells. 200,000–300,000 stem cells were seeded into each Transwell insert and cultured with SCM-6F8. At confluency (3–7 days), the apical media was removed through careful pipetting and the cultures were continued for an additional 6–12 days before analysis.

Clostridium difficile toxin treatment and epithelial permeability assay. *Clostridium difficile* toxins A and B (TcdA, TcdB) were prepared as described⁵². Intestinal stem cells were differentiated in air-liquid interface cultures as described above and treated with 100, 250, 500 pM and 10 nM TcdA or TcdB for 0, 8, 16, and 24 h). At these time points, membranes with differentiated epithelia were collected for histology and microarray analysis. 4 kDa FITC-dextran (Sigma-Aldrich, USA) was added to the apical chamber of the Transwell chambers for a final concentration of 0.5 mg ml⁻¹. Media was removed from the bottom compartment after different incubation times and fluorescence was read by fluorometer (Infinite M1000 PRO, excitation 490 nm, emission 520 nm, Tecan, USA).

Implantation of intestinal stem cells. Intestinal stem cells (1.5 million cells) from different pedigrees with 50% of Matrigel (BD Bioscience, USA) were subcutaneously implanted into female, six- to eight-week-old immunodeficient (NOD.Cg-Prkdc^{scid} Il2rg^{tm1Wjl}/Sz) mice³⁵ under IACUC approval (100533-

1115) To test spontaneous transformation of the stem cells, mice were monitored every month (up to 4 months).

RNA and genomic DNA sample preparation. For stem cell colonies, RNA was isolated using PicoPure RNA Isolation Kit (Life Technologies, USA). For ALI-differentiated epithelia, RNA was isolated using TRIzol RNA Isolation Kit (Life Technologies, USA). RNA quality (RNA integrity number, RIN) was measured by analysis Agilent 2100 Bioanalyzer and Agilent RNA 6000 Nano Kit (Agilent Technologies, USA). RNAs having a RIN > 8 were used for microarray analysis. Genomic DNA was extracted with DNeasy Blood & Tissue kit (Qiagen, Netherlands) from intestinal and colonic stem cells for CNV analysis and exome capture sequencing. For genomic DNA extraction, human intestinal and colonic stem cells were isolated from mouse 3T3 feeder layer using QuadroMACS Starting Kit (Miltenyi Biotec, Germany). Genomic DNA concentration was measured with Qubit dsDNA BR Assay Kit (Life Technologies, USA).

Expression microarray and bioinformatics. Total RNAs obtained from immature colonies and ALI-differentiated structure were used for microarray preparation with WT Pico RNA Amplification System V2 for amplification of DNA and Encore Biotin Module for fragmentation and biotin labelling (NuGEN Technologies, USA). RNA quality (RNA integrity number, RIN) was measured by analysis using an Agilent 2100 Bioanalyzer and Agilent RNA 6000 Nano Kit (Agilent Technologies, USA). RNAs having a RIN > 8 were used for microarray analysis. All samples were prepared according to manufacturer's instructions and hybridized onto GeneChip Human Exon 1.0 ST Array (Affymetrix, USA). GeneChip operating software was used to process all the Cel files and calculate probe intensity values. To validate sample quality, quality checks were conducted using Affymetrix Expression Console software. The intensity values were log₂-transformed and imported into the Partek Genomics Suite 6.6 (Partek Incorporated, USA). Exons were summarized to genes and a 1-way ANOVA was performed to identify differentially expressed genes. For two-sample statistics, *P* values were calculated by Student's *t*-test for each analysis. Unsupervised clustering and heat map generation were performed with sorted data sets by Euclidean distance based on average linkage clustering, and principal component analysis (PCA) map was conducted using all or selected probe sets by Partek Genomics Suite 6.6. Gene set enrichment analysis (GSEA)⁵³ was performed for *C. difficile* toxin B treatment. For the region-specific gene signature of small intestine and colon comparison (PD, PJ and MI for Fig. 2b and AC, TC and DC for Fig. 3b), differentially-expressed genes were selected with a cut-off value of 1.5-fold and *P* < 0.05 in each comparison (for example, (1) PD vs. PJ and (2) PD vs. MI) and then intersected genes in 2 gene lists of each comparison were taken as region-specific gene sets. In the heat maps (Fig. 2b and 3b), 3 regiospecific gene sets (PD, PJ and MI, or AC, TC and DC) were combined, and the heat maps were made with Euclidean distance based on average linkage clustering. For *C. difficile* toxin B treatment data sets, samples from indicated time points and dosages were compared with control (untreated samples). Differentially-expressed genes (two-fold upregulated and downregulated genes) were counted and plotted in 3D column plots (Extended Data Fig. 8c). In comparison of 500 pM 24 h toxin B treatment with control, 39 genes were significantly upregulated (cut-off value: 3-fold and *P* < 0.05) and a heat map (Fig. 6e) was made with 39 genes using all samples. The whole genome expression data of 500 pM 24 h toxin B treatment vs. control were applied to GSEA program to detect significantly enriched pathway in toxin B treatment. Selected pathways (from KEGG) were shown in Fig. 6d. Data sets generated for this study have been submitted to the National Center for Biotechnology Information Gene Expression Omnibus (GEO) database under accession number GSE66749.

No statistical methods were used to predetermine sample size.

Copy number variation. For copy number variation analysis of stem cell pedigrees and passage 0 pooled sample, genomic DNA samples were genotyped with HumanOmniExpress BeadChip Kit for clone 1 and 2 (passage 5, 10, 15 and 20) (Illumina, USA) and Illumina HumanOmniZhonghua BeadChip Kit for clones 3 to 7 (passage 5 and 25) following the manufacturer's instructions. Analysis of BeadChip was performed using GenomeStudio Software (Illumina, USA). Illumina high-density SNP genotyping data was converted to kilobase-resolution detection of copy number variation. CNV detected in passage 0 pooled samples are considered as germline CNVs and removed in the analysis. The data was generated by PennCNV⁵⁴. Genes within 10 kb of CNV regions are reported. The parameter is set as “-expandleft 10k” and “-expandright 10k”. Other parameters are default. Confidence score > 10 was used as a cutoff. The call rates for CNV were all greater than 99%, and two larger CNV amplification and deletion events were validated by quantitative PCR.

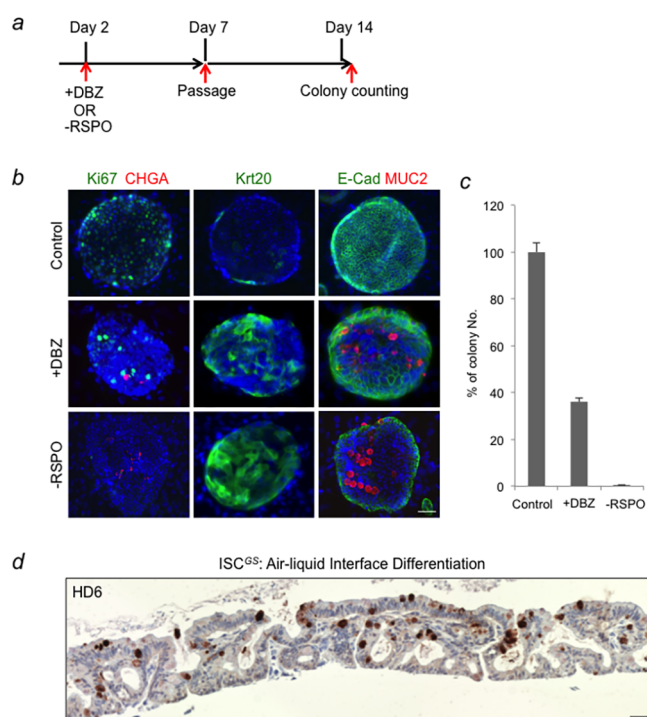
Exome capture sequencing. For exome capture and high-throughput sequencing for intestinal stem cells (pedigree 1 and 2), 50 ng of genomic DNA was used to perform Nextera Expanded Exome Kit (Illumina, USA). For pedigree 3 to 7, 1 µg of genomic DNA was sheared using a Covaris S1 Ultrasonicator (Covaris, USA),

end-repaired, A-tailed, and Adaptor-ligated. Exome capture was performed using a Tru-seq Exome Enrichment Kit (Illumina, USA) following the manufacturer's instructions. Multiplexed libraries were sequenced on an Illumina HiSeq sequencer using 101-bp paired-end reads. Reads were aligned to the reference genome (UCSC hg19) using Burrows Wheeler Aligner (BWA, 0.6.2)⁵⁵. PCR duplicates were removed using PICARD-1.94 (<http://picard.sourceforge.net>). The Genome Analysis Toolkit (GATK framework version 2.6.4)⁵⁶ was used to realign reads near indels and to recalibrate base quality values.

When running GATK, the minimum phred-scaled confidence threshold at which variants were called (-stand_call_conf) was 50, and the minimum phred-scaled confidence threshold at which variants were emitted (-stand_emit_conf) is 30. The criteria of GATK Variant Filtration is as follows: --clusterWindowSize 10--filterExpression "MQ0 > 4 && ((MQ0/(1.0*DP)) > 0.1)"--filterName "HARD_TO_VALIDATE"--filterExpression "DP < 5"--filterName "LowCoverage"--filterExpression "QUAL < 30"--filterName "VeryLowQual"--filterExpression "QUAL > 30 && QUAL < 50"--filterName "LowQual"--filterExpression "QD < 1.5"--filterName "LowQD"--filterExpression "FS > 150"--filterName "StrandBias". Potential mouse genomic DNA contaminant reads were detected by alignment to the mouse genome (UCSC mm10) and those containing less than 3 mismatches were removed from further analysis. SNVs were called in each sample separately using SAMtools v0.1.19⁵⁷ and GATK in the exome capture targeted regions. Variants with at least Q50 confidence, phred-scaled quality score more than 40 and coverage higher than 10 were considered as true SNVs. Variants were annotated with ANNOVAR (version 11 Feb, 2013)⁵⁸. Identical variant calls in intestinal stem cells (passage 5 and higher) when compared to passage 0 pooled samples were used to identify germline SNVs. Sanger sequencing validation was performed using primers designed with Primer3 software

version 4.0 (<http://frodo.wi.mit.edu/>). Extracted genomic DNA was amplified with titanium Taq polymerase (Clontech Laboratories, CA, USA) and purified PCR products were sequenced in the forward directions using ABI PRISM BigDye Terminator Cycle Sequencing Ready Reaction kits and an ABI PRISM 3730 Genetic Analyzer (Applied Biosystems, CA, USA). We validated by PCR and Sanger sequencing 13 of 14 non-synonymous mutations called by our sequencing efforts suggesting a false discovery rate of less than 10%. Other quality control parameters are shown in Supplementary Information Table 4.

51. Schmidt, D., Hübsch, U., Wurzer, H., Heppt, W. & Aufderheide, M. Development of an *in vitro* human nasal epithelial (HNE) cell model. *Toxicol. Lett.* **88**, 75–79 (1996).
52. Chumbler, N. M. *et al.* *Clostridium difficile* toxin B causes epithelial cell necrosis through an autoproduct-independent mechanism. *PLoS Pathog.* **8**, e1003072 (2012).
53. Subramanian, A. *et al.* Gene set enrichment analysis: a knowledge-based approach for interpreting genome-wide expression profiles. *Proc. Natl Acad. Sci. USA* **102**, 15545–15550 (2005).
54. Wang, K. *et al.* PennCNV: an integrated hidden Markov model designed for high-resolution copy number variation detection in whole-genome SNP genotyping data. *Genome Res.* **17**, 1665–1674 (2007).
55. Li, H. & Durbin, R. Fast and accurate short read alignment with Burrows-Wheeler Transform. *Bioinformatics* **25**, 1754–1760 (2009).
56. McKenna, A. *et al.* The Genome Analysis Toolkit: a MapReduce framework for analyzing next-generation DNA sequencing data. *Genome Res.* **20**, 1297–1303 (2010).
57. Li, H. *et al.* The Sequence Alignment/Map format and SAMtools. *Bioinformatics* **25**, 2078–2079 (2009).
58. Wang, K., Li, M. & Hakonarson, H. ANNOVAR: functional annotation of genetic variants from high-throughput sequencing data. *Nucleic Acids Res.* **38**, e164 (2010).



Extended Data Figure 1 | Loss of clonogenicity in differentiated ISC.

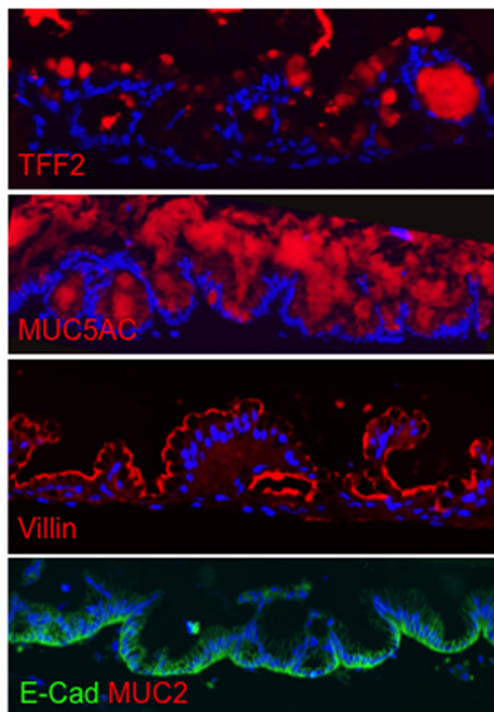
a, Schematic of ISC differentiation using either the γ -secretase inhibitor dibenzazepine (DBZ) or withdrawal of the Wnt regulator R-spondin 1 (Rspo1). ISCs were plated on day 0, DBZ added or Rspo1 removed at day 2, and colonies passaged en masse at day 7. At day 14, after 7 days of continuous growth, colonies were counted. **b**, Micrographs show immunofluorescence at day 7 colonies grown without Rspo1 or in the presence of DBZ for 5 days using antibodies to Ki67, chromogranin A (CHGA), keratin 20 (Krt20), E-cadherin (E-cad), and mucin 2 (Muc2). Scale bar, 50 μ m; $n = 4$ technical replicates. **c**, Histogram shows colony formation in each condition normalized to control ISCs. $n = 4$ biological replicates; error bars, s.d. **d**, Staining of ALI-differentiated intestinal stem cells with monoclonal antibody HD6 directed to Paneth cells. Scale bar, 50 μ m; $n = 4$ technical replicates.

a

Cell types	Gene symbol											
Du-high	ABCB6	ABHD2	ABHD2	ACOX1	ADAM28	AHNAK	AKR1B10	ALDH3A1	ANXA1	ANXA10	ANXA5	ARHGAP24
133 genes	ARL4C	BACE2	BCAS1	BICC1	BTD	C11orf9	C4orf34	CA2	CAPG	CAPN6	CD24	CD59
	CLDN18	CNOT7	CRIP1	CTSD	CXCL17	CYP2C18	CYP3A5	CYSTM1	DNM2	DPCR1	EH2D	EPB41L1
	FAM110B	FAM177B	FAM189A2	FN1	FOSB	FSIP2	FUT9	FXD3	GALNT3	GALNT7	GNAQ	GPR87
	GPRC5B	HIPK2	HMGCS2	HOXB8	HS3ST5	HSPB1	HTR1B	IL18R1	IL2RA	KCNE3	KLF4	LEPREL1
	LGMN	LPAR1	LRP1	LYPD6B	MAOB	MEIS2	METTL7A	MFS1D	MITF	MLPH	MSMB	MUC1
	MXD1	MYEOV	NDUFB1P1	NEK6	NFAT5	NKX6-3	NTRK2	OASL	P4HA1	PART1	PCDH7	PGC
	PLA2G10	PLXNA2	PP7080	PPARGC1A	PSCA	PVRIG	PXDC1	QKI	RAB27B	RBMS1	RERG	RETSAT
	RGNEF	RHBDL2	RHOBTB1	RNF128	RNF183	ROBO1	S100P	SCIN	SFTA2	SGK2	SLC16A3	SLC19A3
	SLC26A9	SLC41A2	SLC44A4	SLC45A3	SLC4A4	SLC9A1	SLC9A2	SLC9A3	SMPDL3A	SPINK1	STEAP1	SULT1C2
	SYT9	TFF1	TFF2	TFF3	TM4SF1	TPBG	TRAK1	TSHZ2	TSPAN1	TSPAN31	UGDH	VSIG1
	VSIG2											
Je-high	BDKRB2	C2CD4A	CCR1	CHRM3	CPVL	CYP2A13	EPHB1	FAM47B	FMOD	GLDC	HSD17B7P2	IFITM3
24 genes	LGR5	ODAM	OR8J1	PHYHIP1	RTP4	SES1	SHPK	SLC26A2	STARD13	TPH1	UNC93A	ZRSR2
Il-high	ABCB1	ABCC2	ABCG2	ACE2	ACOX2	ADH4	ADH6	AKAP7	ALDOB	ANPEP	ANXA2P2	APOB
178 genes	AREG	BTNL3	C17orf72	C1orf201	C1orf21	C3orf26	C3orf52	C4BPB	CACNA1E	CCL25	CCND2	CD52
	CDH17	CDX2	CEACAM1	CEACAM5	CELA3A	CELA3B	CHGA	CIDEA	CLCA1	CLIC5	CLRN3	CPE
	CSF1R	CYBRD1	CYP2A7	DACH1	DENND1A	DHRS11	DKK1	DMBT1	DOK3	DPP4	DSG3	DUSP5
	EFCAB4B	EGR2	EML1	EREG	F2R	FABP2	FABP6	FAM105A	FCGBP	FGF23	FITM2	FOLH1
	FRZB	GALNT8	GBA3	GCET2	GDAP1	GFOD1	GHRL	GIP	GJA1	GLS	GPA33	GSDMB
	GSTA2	GUCY2C	HEPACAM2	HHLA2	HLA-DRB1	HNF4G	HTR1D	IL18	IL2RG	IL32	INE1	IRF8
	ITLN1	JAG1	KIAA0226L	KIRREL	KLF7	KRT20	KRT33B	KRT80	L1TD1	LCT	LEAP2	LGALS2
	LGALS3	LINC00483	LOC100132099	MANBAL	MAOA	MARCH3	MARCH8	MB21D2	MEP1A	MEP1B	MICAL2	MIR17HG
	MLN	MOGAT3	MRPS18A	MUC13	MUC17	MYO1A	MYO1E	MYO7B	NABP1	NELL2	NIPAL1	NME5
	NODAL	NOX1	NPY6R	NR1H4	O3FAR1	OSR2	OSTBETA	OSTalpha	OTC	PADI2	PAPSS2	PDE10A
	PDE3A	PDP1	PI3	PLA2G12B	PLK1S1	PMP22	PRAP1	RASGRF2	RBP2	RGS2	RHOB	RNF182
	RNF217	SARM1	SATB2	SEMA3D	SEMA6D	SERTAD1	SI	SIDT1	SLC17A4	SLC2A5	SLC30A2	SLC46A3
	SLC6A20	SLC7A6	SNX10	TCEANC	TGFB1	THEM4	TM4SF20	TM6SF2	TMEM45B	TRIM36	TUBAL3	TUFT1
	UGT2B15	VTN	XDH	YAE1D1	ZG16	ZNF208	ZNF347	ZNF502	ZNF705G	ZYX		

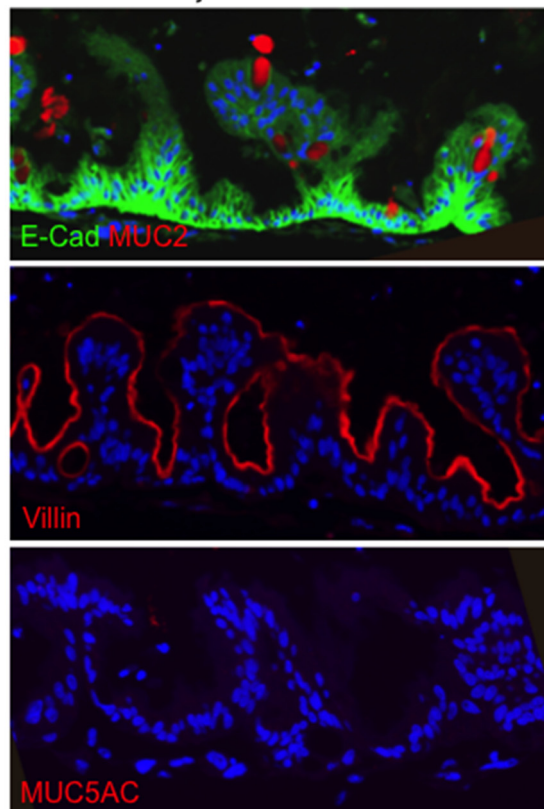
b

Duodenum SC ALI



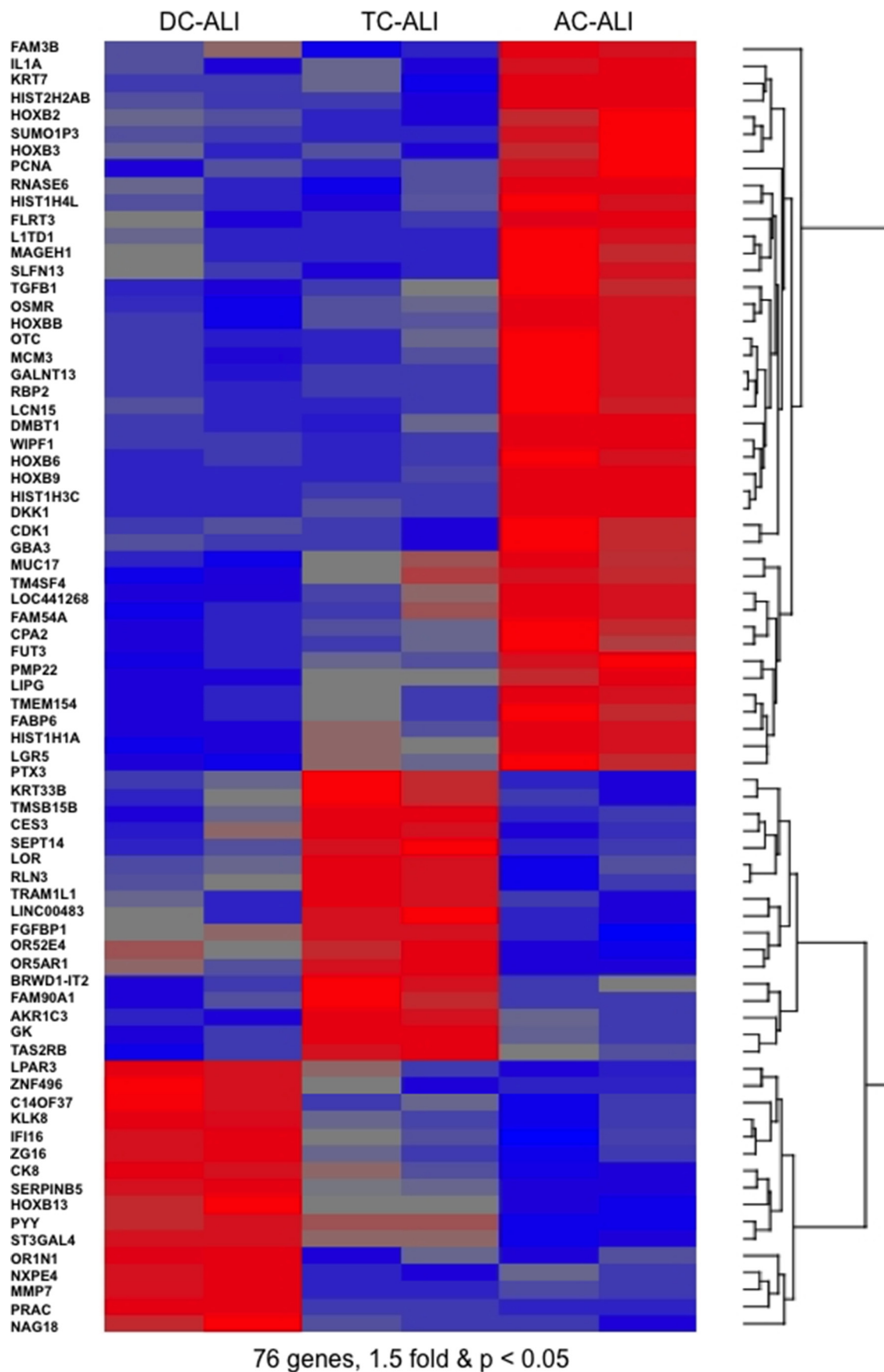
c

Jejunum SC ALI

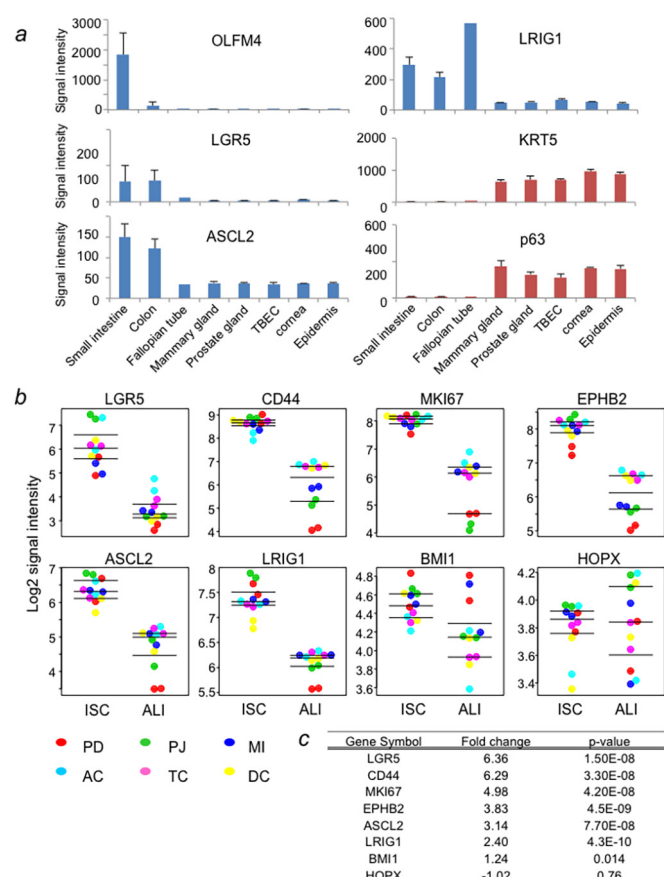


Extended Data Figure 2 | Intestinal stem cell expression profiles. **a**, List of genes differentially expressed in ISC derived from duodenum, jejunum and ileum. These data correspond to heat map of Fig. 2b. **b**, Immunofluorescence labelling of ALI-differentiated ISCs from duodenum with antibodies against

Tff2, mucin 5AC, villin, E-cadherin, and mucin 2. **c**, Immunofluorescence labelling of ALI-differentiated epithelia from jejunum stem cells with antibodies to E-cadherin, mucin 2, villin, and mucin 5AC. Scale bar, 50 μ m; $n = 10$ technical replicates.



Extended Data Figure 3 | Differential gene expression in epithelia derived from colonic stem cells. Heat map of differentially expressed (>1.5 -fold, $P < 0.05$) genes in ALI cultures derived from stem cell pedigrees of ascending, transverse, and descending colon.



Extended Data Figure 4 | Differential gene expression across columnar and stratified epithelial stem cells. **a**, Histograms of expression microarray signal intensity of selected genes across averaged intestine and colon ISCs, stratified epithelial stem cells, and stem cells of the fallopian tube (FT). Biological replicates $n = 2-6$ (FT = 2, stratified epithelia = 3, colon, intestine = 6); error bars, s.d. **b**, Dot plot showing expression microarray data of indicated genes for stem cell pedigrees (ISC; Duo, duodenum; Jej, jejunum; Ile, ileum; AC, ascending colon; TC, transverse colon; DC, descending colon) derived from various regions of the intestinal tract before and after air-liquid interface (ALI) differentiation. Biological replicates $n = 2$ (total 12 data sets) for stem cells, technical replicates $n = 2$ for ALI. **c**, Chart of aggregate P values by Student's t -test for gene expression changes between ground state stem cells and their ALI-differentiated counterparts.

a CNVs and SNVs in 2 clones of Fetus-1

CNV	Pedigree 1				Pedigree 2			
	P5	P10	P15	P20	P5	P10	P15	P20
amp	0 (0)	0 (0)	0 (0)	0 (0)	0 (0)	0 (0)	9 (4)	1 (1) + Chr12 ²ⁿ
del	3 (2)	0 (0)	2 (13)	4 (13)	0 (0)	1 (1)	1 (1)	1 (1)
SNV	Not detected	Not detected	SPEF2 (ns)	SPEF2 (ns)	IL1RAP (ns)	IL1RAP (ns)	IL1RAP (ns), CMYA5 (ns)	IL1RAP (ns), CMYA5 (ns)

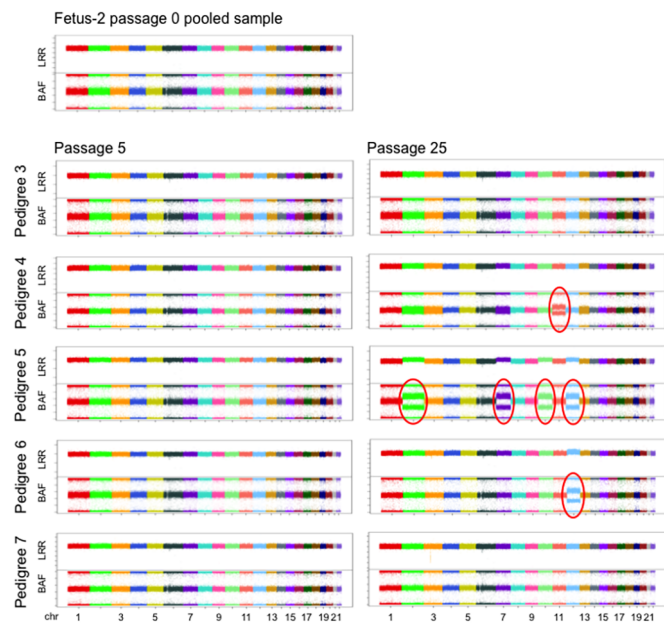
b Gene list for CNVs in 5 clones of Fetus-2

Genes affected by amplified region		Gene symbol	
Pedigree 3	P5	No genes	
P25		C19orf61	
Pedigree 4	P5	ACAP2	
P25		Chr 11 trisomy	
Pedigree 5	P5	SEPSECS	
P25		Chr 2, 7, 10 and 12 trisomies	
Pedigree 6	P5	No genes	
P25		SATB1	
Pedigree 7	P5	No genes	
P25		LOC152225	
Genes affected by deleted region		Gene symbol	
Pedigree 3	P5	GPCRLTM7 NCK1 RIMS2	
P25		ACAP2 APBB1P ASXL2 BMPR2 BNIP2 CFL2 FAM193A FANCA FARS2 FHIT	
		HERC1 HERC4 IL2RA IL2RA LUC7L2 MAPK6 MARVELD2 MIR1288 MYPN NBEAL1	
		NCK1 NFAT5 PHC3 PIGL RNF150 RNF216 RNF4 RPGRIP1 SIRT1 SKIL	
		SLC35F2 SNORA70B SPPL2A TMC07 TMEM116 TMEM22 TRPM7 WWOX ZFR	
Pedigree 4	P5	No genes	
P25		FHIT	
Pedigree 5	P5	AGBL2 ARCN1 C16orf73 CLDN3 CLPTM1 GABPB2 HERC4 ITFG3 LOC401109 MLLT11	
		NCRNA00254 PIGL PKD1L2 PTPRJ SIRT1 WWP2 ZNF804A	
	P25	BNIP2 C1orf129 C4orf34 CENPV CFL2 CRYM FANCA GPR160 GTF2A2 IL4	
		KIF3A LOC644656 MIR1288 NCK1 NCRNA00169 NFAT5 PHC3 PIGL SNORA23 TMEM22	
		TRPM7 WEE1 ZNF143	
Pedigree 6	P5	AOR ASH1L C11orf65 OSBPL1A PNPT1 POU5F1P4 RAB39 RNF111 SAP30 SCRG1	
		SPPL2A ZNF43	
P25		FHIT	
Pedigree 7	P5	No genes	
P25		FHIT	

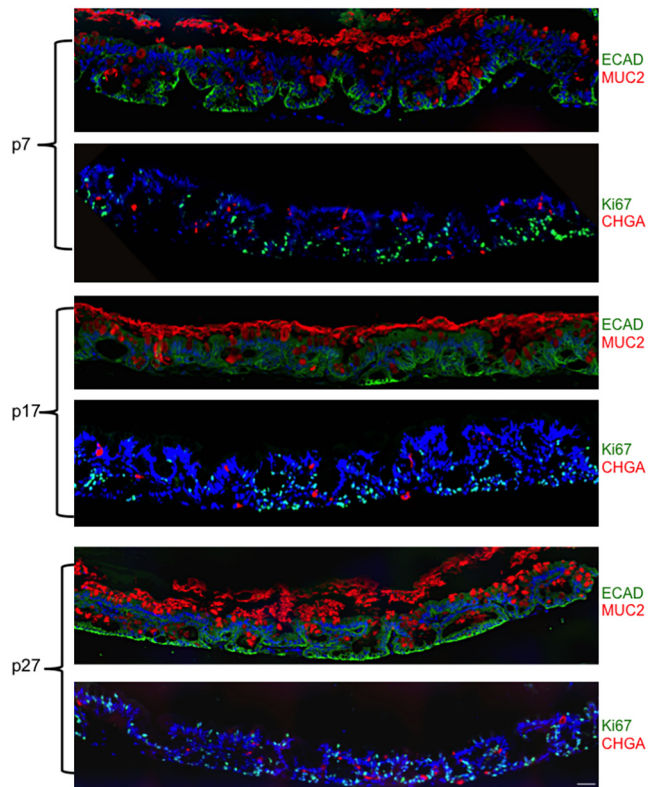
c Gene list for SNVs in 5 clones of Fetus-2

Clone No.	Passage	Gene symbol of nonsynonymous SNV	
Pedigree 3	Passage 5	BSN	
	Passage 25	KIAA0226 ATP7A	
Pedigree 4	Passage 5	RBMXL1	
	Passage 25	DOCK10 CXCR7 FAM135A CYP11B2 PTDS2 CDH8 KRTAP4-5 PSMC5 BPIFC ANKRD55	
Pedigree 5	Passage 5	No SNVs	
	Passage 25	BAI1 CACNA1B ASUN LRRC37A3	
Pedigree 6	Passage 5	FAM157A KCNMA1	
	Passage 25	TMEM48 CCT3 ECEL1 ECT2L CAMK2B VIPR2 KCNMA1 DTX4 PVRL2	
Pedigree 7	Passage 5	No SNVs	
	Passage 25	ANKRD17 ADAMTS12 KCNH2 KIF19 KRTAP23-1 EP300	

Extended Data Figure 5 | Genes affected by CNV and SNV events in intestinal stem cell pedigrees during passaging. **a**, Summary of CNV (events (genes affected)) and non-synonymous SNV in pedigrees 1 and 2 at P5 to P20. **b**, Summary of genes altered by interstitial CNV amplifications (top) or deletions (bottom) in ISC pedigrees 3 to 7 at P5 and P25. **c**, Summary of genes sustaining non-synonymous SNV in five ISC pedigrees at P5 and P25.



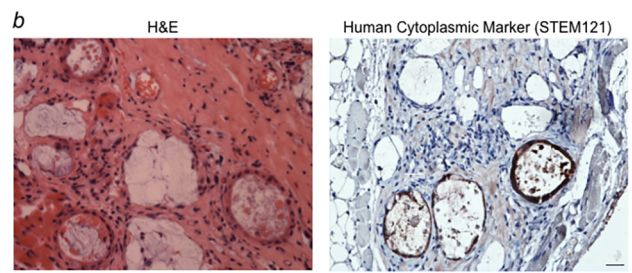
Extended Data Figure 6 | Whole-genome CNV profiles for intestinal stem cell pedigrees 3–7 at P5 and P25. Regions marked by ovals represent aneuploidy.



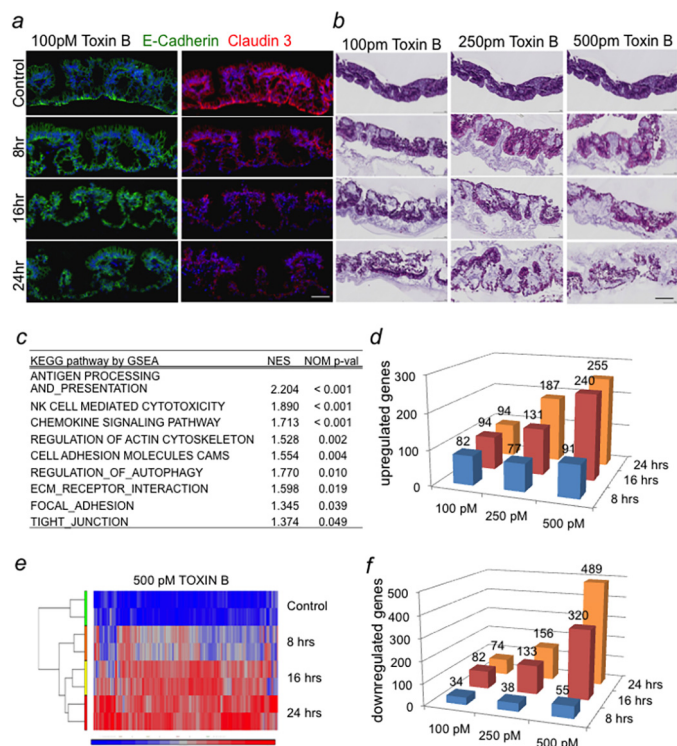
Extended Data Figure 7 | Impact of ISC^{GS} passaging on ALI differentiation. ALI differentiation of intestinal pedigree 2 initiated from cells at the indicated passage number. As indicated, histological sections of differentiated epithelia were stained with antibodies to either E-cadherin (ECAD, green) and mucin 2 (Muc2, red), or Ki67 (green) and chromogranin A (CHGA, red). Scale bar, 75 μ m; n = 4 technical replicates.

a

Time	4	8	12	16
Name	wks	wks	wks	wks
Pedigree 3 P6	0/2	0/2	0/2	0/2
Pedigree 3 P25	0/2	0/2	0/2	0/2
Pedigree 5 P6	0/2	0/2	0/2	0/2
Pedigree 5 P25	0/2	0/2	0/2	0/2
Pedigree 7 P6	0/2	0/2	0/2	0/2
Pool	0/2	0/2	0/2	0/2
Cancer Cells	0/8	2/8	5/8	8/8

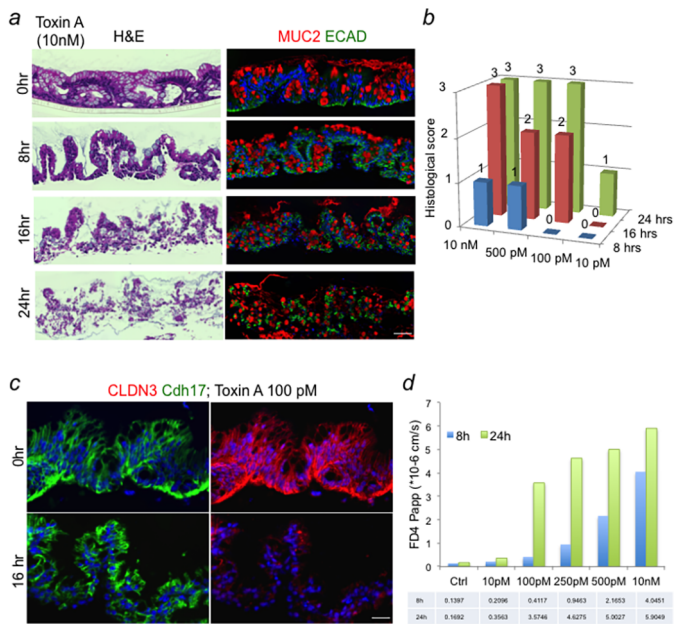


Extended Data Figure 8 | ISC^{GS} tumorigenicity assays in immunodeficient mice. **a**, Quantification of tumour formation assessments at 4–16 weeks following subcutaneous inoculation of two million cells of the indicated ISC pedigrees at passage 6 or passage 25 at 4–16 weeks. ‘Pool’ indicates total set of clones derived from P0 ileum culture before pedigree generation. ‘Cancer cells’ refers to propagating cells from case of high-grade serous ovarian cancer. **b**, Left, histological section through site of injection of 1 million cells from pedigree 3. Right, section of injection site stained with antibody (STEM121) to human epithelial cells (brown) revealing benign cysts. Scale bar, 15 μ m.



Extended Data Figure 9 | Dose- and time-dependency of TcdB pathology in

ALI-generated colonic epithelia. **a**, Immunofluorescence localization of adherens junction marker E-cadherin and tight junction marker claudin 3 in ALI-differentiated epithelia derived from transverse colon stem cells following exposure to 100 pM TcdB for the indicated durations. $n = 4$ technical replicates. Scale bar, 100 μm . **b**, Representative H&E images of ALI cultures at indicated times and concentration of TcdB exposure. Scale bar, 250 μm ; $n = 4$ technical replicates. **c**, Gene set enrichment analysis of whole-genome expression data from colonic epithelia treated with 500pM TcdB for 24 h and control samples showing enriched KEGG pathway sets. NES, normalized enrichment score; NOM P value, nominal P value. **d**, 3D plot of upregulated genes at the indicated time points and dosages $> \text{twofold}$, $P < 0.05$. $n = 2$ technical replicates. **e**, Heat map of upregulated genes in 500 pM TcdB samples. The genes (237 genes) were chosen by cutoff values ($> \text{twofold}$, $P < 0.05$). Three time points (8, 16 and 24 h) are shown. **f**, 3D plot of downregulated genes at the indicated time points and dosages $> \text{twofold}$, $P < 0.05$. $n = 2$ technical replicates.



Extended Data Figure 10 | Dose- and time-dependency of TcdA pathology in ALI-generated colonic epithelia. **a**, Left, representative H&E images of ALI cultures at indicated times and concentration of TcdA exposure; right, immunofluorescence localization of adherens junction marker E-cadherin (ECAD; green) and mucin 2 (MUC2; red) in ALI-differentiated epithelia derived from transverse colon stem cells following incubation with 10 nM TcdA for the indicated durations. Scale bar, 100 μ m; n = 4 technical replicates. **b**, 3D plot of histological scoring of representative H&E time points and concentrations performed by a gastrointestinal pathologist according to a standard 0–3 rating for colonic epithelial integrity. **c**, Distribution of tight junction marker claudin 3 (Cldn3) and adherens junction marker (Cdh17) following treatment of ALI colonic epithelium with TcdA for the indicated times and doses. Scale bar, 50 μ m; n = 4 technical replicates. **d**, Histogram of permeability of ALI colonic epithelium (Papp) to small molecules (FD4, molecular mass 4,400 Da) following exposure to the indicated doses of TcdA for the indicated times.

Chromothripsis from DNA damage in micronuclei

Cheng-Zhong Zhang^{1,2,3,4*}, Alexander Spektor^{2,4,5*}, Hauke Cornils^{2,4*}, Joshua M. Francis^{1,3*}, Emily K. Jackson^{2,4,6}, Shiwei Liu^{2,4}, Matthew Meyerson^{1,3,7,8} & David Pellman^{2,3,4,6}

Genome sequencing has uncovered a new mutational phenomenon in cancer and congenital disorders called chromothripsis. Chromothripsis is characterized by extensive genomic rearrangements and an oscillating pattern of DNA copy number levels, all curiously restricted to one or a few chromosomes. The mechanism for chromothripsis is unknown, but we previously proposed that it could occur through the physical isolation of chromosomes in aberrant nuclear structures called micronuclei. Here, using a combination of live cell imaging and single-cell genome sequencing, we demonstrate that micronucleus formation can indeed generate a spectrum of genomic rearrangements, some of which recapitulate all known features of chromothripsis. These events are restricted to the mis-segregated chromosome and occur within one cell division. We demonstrate that the mechanism for chromothripsis can involve the fragmentation and subsequent reassembly of a single chromatid from a micronucleus. Collectively, these experiments establish a new mutational process of which chromothripsis is one extreme outcome.

Most cancer genomes are extensively altered by point mutations and chromosome rearrangements. Although mutations are generally thought to accumulate gradually, over many cell division cycles^{1,2}, recent cancer genome sequencing provides evidence for mutational processes that generate multiple mutations “all-at-once” during a single cell cycle³. The most striking example of such an event is “chromothripsis”, where a unique pattern of clustered rearrangements occurs, typically involving only a single chromosome or a few chromosomes^{4–7}.

Several models have been proposed to explain the rearrangements in chromothripsis. One proposal is that the affected chromosome is somehow fragmented, with random joining of some segments and loss of others⁴. This model explains the characteristic pattern of DNA copy number in chromothripsis—oscillation between two copy number states, with islands of DNA retention and heterozygosity interspersed with regions of DNA loss. An alternative hypothesis is that chromothripsis is generated by DNA replication errors: collapsed replication forks trigger cycles of microhomology-mediated break-induced replication (MMBIR), where distal sequences are copied to the sites of replication fork collapse by template-switching⁸. Evidence for the latter model comes from templated insertions detected at translocation junctions and sequence triplications^{8,9}. Both models have only indirect support from genomic sequencing and have not been tested experimentally¹⁰.

We recently proposed that the physical isolation of chromosomes in aberrant nuclear structures called micronuclei might explain the localization of DNA lesions in chromothripsis¹¹. Micronuclei are a common outcome of many cell division defects, including mitotic errors that mis-segregate intact chromosomes, and errors in DNA replication or repair that generate acentric chromosome fragments^{12,13}. We previously found that the partitioning of intact chromosomes into newly formed micronuclei leads to cytological evidence of DNA damage, specifically on the mis-segregated chromosome¹¹. After mitosis, chromosomes from micronuclei can be reincorporated

into daughter nuclei¹¹, potentially integrating mutations from the micronucleus into the genome.

Here, using an approach combining live cell imaging with single-cell genomic analysis that we call ‘Look-Seq’, we demonstrate that micronucleus formation can generate a spectrum of complex chromosomal rearrangements, providing the first direct experimental evidence for a mechanism leading to chromothripsis.

Damage to micronuclei after S phase entry

To determine if micronucleus formation leads to chromosome rearrangements, we first sought to clarify the cell population where rearrangements would most likely occur. Previously, we found that newly formed micronuclei do not have marked levels of DNA damage in G1, but damaged micronuclei accumulate as cells progress into the S and G2 phases of the cell cycle¹¹, suggesting a link between DNA damage and DNA replication. Additionally or alternatively, the nuclear envelopes of micronuclei are prone to irreversible “rupture” as defined by the abrupt loss of soluble nuclear proteins¹⁴. Nuclear envelope rupture in micronuclei is strongly associated with DNA damage, but occurs at random, not specifically during S phase¹⁴.

To re-examine the timing of DNA damage, micronuclei were generated in synchronized cells by a nocodazole release procedure¹¹. As expected^{11,14}, no significant DNA damage was detected in ruptured micronuclei during G1, but damage was common during S and G2 phases as indicated by fluorescence labelling for γ -H2AX or Gam, a bacteriophage protein that marks double strand breaks¹⁵ (Extended Data Fig. 1a, b). Moreover, micronuclei from serum-starved G0 cells showed little detectable DNA damage, despite rupture of the micronuclear envelope during G0¹⁴ (Extended Data Fig. 1c). Therefore, DNA damage is not triggered by nuclear envelope rupture alone, but also requires entry into S phase.

Consistent with this conclusion, cell labelling with 5-ethynyl-2'-deoxyuridine (EdU) demonstrated that most damaged micronuclei

¹Department of Medical Oncology, Dana-Farber Cancer Institute, Boston, Massachusetts 02215, USA. ²Department of Pediatric Oncology, Dana-Farber Cancer Institute, Boston, Massachusetts 02215, USA. ³Broad Institute of Harvard and MIT, Cambridge, Massachusetts 02142, USA. ⁴Department of Cell Biology, Harvard Medical School, Boston, Massachusetts 02115, USA. ⁵Department of Radiation Oncology, Dana-Farber Cancer Institute, Boston, Massachusetts 02215, USA. ⁶Howard Hughes Medical Institute, Chevy Chase, Maryland 20815, USA. ⁷Department of Pathology, Harvard Medical School, Boston, Massachusetts 02115, USA. ⁸Center for Cancer Genome Discovery, Dana-Farber Cancer Institute, Boston, Massachusetts 02215, USA.

*These authors contributed equally to this work.

had initiated DNA replication (Extended Data Fig. 1d). However, overall EdU incorporation was markedly lower in micronuclei compared to the cell's primary nucleus, irrespective of whether the micronuclei were ruptured or intact^{11,14} (Fig. 1a). Thus, chromosomes in micronuclei are under-replicated in general, even though the majority of the damaged micronuclei have initiated DNA replication. These results focused the experiments below on micronuclei that rupture after S phase entry.

Look-Seq strategy

We designed a procedure to determine the genomic consequences of DNA damage in ruptured micronuclei (Fig. 1b). Non-transformed human RPE-1 cells were synchronized by nocodazole release, sorted into 384 well plates, and wells containing a single micronucleated cell were identified. By live cell imaging, we identified cells where the micronuclear envelope ruptured after the beginning of S phase (Methods). These experiments were performed after small interfering RNA (siRNA)-mediated knockdown of p53 because chromosome mis-segregation after nocodazole release induces a p53-dependent G1 cell cycle arrest^{16,17}. After one division of the micronucleated cell, we selected daughters with no detectable micronuclei, indicating the micronuclear chromosome was reincorporated into daughters' primary nuclei. Cells with reincorporation were selected because nuclear envelope rupture inactivates nuclear processes such as DNA replication and transcription¹⁴, and we presume that the damaged chromosome from the micronucleus may require exposure to a normal nucleoplasm, with functional DNA repair pathways, to generate rearrangements. Daughter cells were then separated, amplified (multi-strand displacement amplification, MDA), sequenced, and analysed independently¹⁸ (see Methods, Supplementary Table 1).

Identifying the micronuclear chromosome

Micronucleated cells will be of two kinds: disomic for the chromosome in the micronucleus (Fig. 2a, left schematic), if the lagging chromosome was segregated into the correct daughter cell (albeit partitioned into a micronucleus); or trisomic for the affected chromosome (Fig. 2a, right schematic), if the lagging chromosome was mis-segregated. The division of a disomic micronucleated cell will produce one near-disomic daughter with the under-replicated chromosome from the micronucleus, and one monosomic daughter, hereafter referred to as a 2:1 asymmetric copy number pattern. Similarly, the division of a trisomic micronucleated cell will produce one near-trisomic daughter with the micronuclear chromosome, and one disomic daughter, or a 3:2 pattern. In either pattern, we refer to the daughter cell with the higher DNA copy number as the 'plus' cell and the other daughter as the 'minus' cell. Thus, reduced DNA

replication in the ruptured micronucleus creates an odd chromosome number and a copy number asymmetry between the daughters. This asymmetry identifies the mis-segregated chromosome and demonstrates that mis-segregation is a *de novo* event that occurred during the last cell division (Fig. 2a). Because the plus daughter has the chromosome from the micronucleus, rearrangements, if observed, should be concentrated in the plus daughter and associated with the 'extra' chromatid from the micronucleus; we refer to the haplotype of this chromatid as the 'gained' or 'mis-segregated' haplotype.

We sequenced 10 control daughter cell pairs from non-micronucleated mother cells and 9 experimental pairs derived from micronucleated cells (Supplementary Videos 1–9). All controls underwent siRNA-mediated knockdown of p53 (C1–C4 and N1–N6), and six of these also were carried through the nocodazole release protocol (N1–N6). DNA copy-number analysis (Methods, Supplementary Table 2) identified the known clonal gains of chromosome (Chr.) 10q and subclonal gains of Chr. 12 in the RPE-1 line (ref. 11 and Fig. 2b), validating our arm-level copy number measurements. As expected, sporadic chromosome gains or losses—shared between the daughters—were also detected. These shared aneuploidies were presumably present in the mother-cell primary nucleus and underwent normal replication and segregation.

In contrast to the non-micronucleated controls (Fig. 2b, top and middle panels), the 9 daughter pairs derived from cells with ruptured micronuclei (MN) all contained at least one chromosome with copy number asymmetry, with either a 2:1 (MN1–MN6) or 3:2 (MN7–MN9) segregation pattern (Fig. 2b, bottom panel). In the pair of MN8 daughter cells, the 3:2 ratio for both Chr. 4 and Chr. 11 (Fig. 2b) suggests that these chromosomes were both in the micronucleus observed by imaging. In the MN7 daughters, we observed a 3:2 ratio only for the q arm of Chr. 1 (Fig. 2b; also see Extended Data Fig. 3). Most likely, an acentric Chr. 1q fragment was generated by the cleavage of a chromosome bridge from the previous mitosis¹⁹, and partitioned into the micronucleus in the MN7 mother.

We developed a method to determine loss-of-heterozygosity (LOH) in single-cell genomes (Methods) that is insensitive to the amplification bias inherent to MDA²⁰. This analysis confirmed genuine monosomy of chromosomes in the minus daughters of 2:1 mis-segregations (Extended Data Fig. 2a–c). From the sequencing of these hemizygous chromosomes we determined the haplotype phase (genotypes at polymorphic sites for each homologue) and devised a method to measure the copy number for each homologue (Extended Data Fig. 3a, Methods). This haplotype copy number information enabled us to identify amplification bias affecting both homologues equally (Extended Data Fig. 3b) and distinguish it from true copy number alterations affecting one homologue (Extended Data Fig. 3c); this

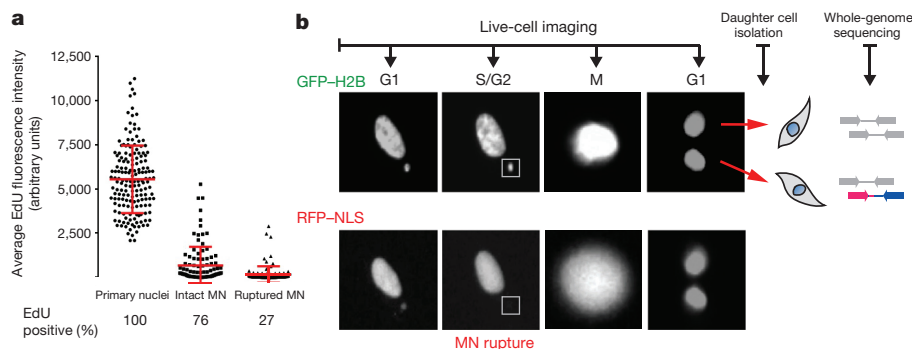


Figure 1 | Look-Seq procedure to analyse DNA damage from the under-replicated chromosomes in micronuclei. **a**, Reduced DNA replication in both intact and ruptured micronuclei. Left, fluorescence intensity measurements after continuous EdU labelling following release from a nocodazole block. EdU intensity is normalized to nuclear area ($N > 100$ from two experiments for each category, see Methods). Red bars, mean and standard deviation. **b**, Look-Seq

strategy. Nuclei are labelled with green fluorescent protein-conjugated histone H2B (GFP-H2B). Disruption of the micronuclear envelope is visualized by the loss of a nuclear localized red fluorescent protein (RFP-NLS); reincorporation of the micronucleus is inferred from the absence of micronuclei in either G1 daughter.

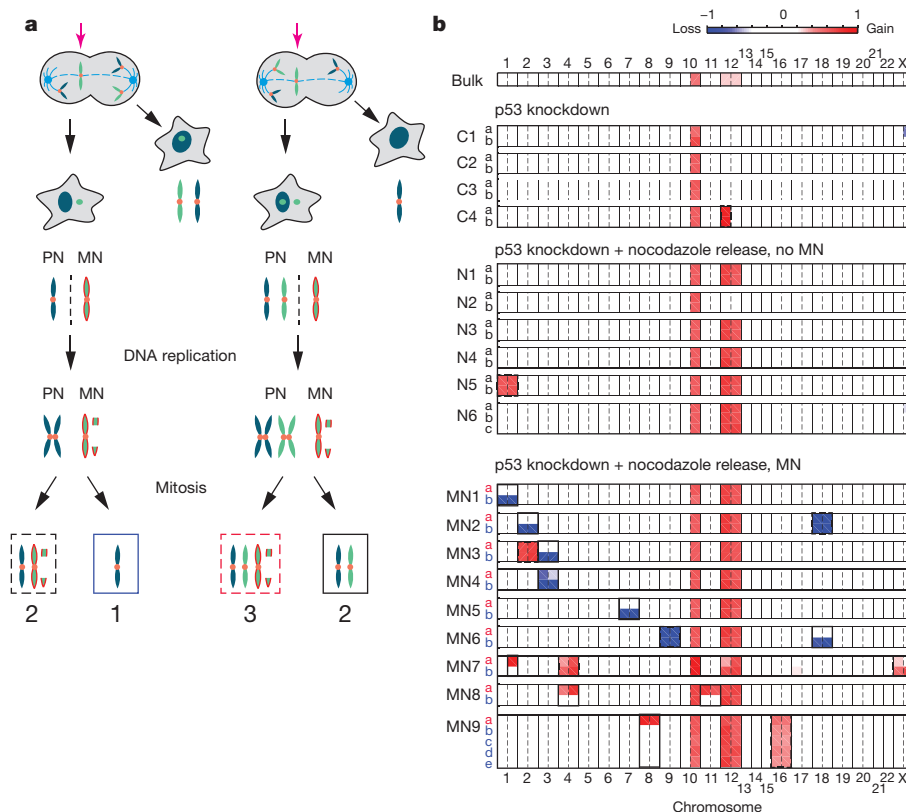


Figure 2 | Identification of the mis-segregated chromosome by DNA copy number analysis. **a**, Predicted DNA copy number outcomes for daughter cells derived from a micronucleated mother cell. Left, lagging chromosome (magenta arrow) is correctly segregated, but partitioned into a micronucleus (MN); right, lagging chromosome is mis-segregated into a micronucleus. The chromosome in the micronucleus is under-replicated and asymmetrically segregated, resulting in either a 2:1 (left) or 3:2 (right) copy number ratio in daughter cells. Homologue in the micronucleus, light green; homologue in the primary nucleus (PN), blue; red outline indicates the under-replicated chromosome from the micronucleus. Hatched box, 'plus' daughter; solid box, 'minus' daughter. **b**, Heat map of arm-level DNA copy number (\log_2 ratio) in daughter cells derived from micronucleated mothers (MN1–MN9) or

analysis further confirmed the predicted 3:2 mis-segregation pattern (Fig. 2a, right schematic).

Localized chromosome rearrangements

We next tested the prediction that there would be a concentration of rearrangements on the mis-segregated chromosome. *De novo* rearrangements were detected by clustering of discordant read pairs¹⁸ (Methods, Supplementary Table 3). Rearrangements on the normally segregated control chromosomes were uniformly distributed (Extended Data Fig. 4a), as would be expected for background errors from MDA-based whole-genome amplification. By contrast, there was a significant enrichment of rearrangements (median: 12.5-fold) on the mis-segregated chromosomes identified by copy number asymmetry relative to the normally segregated control chromosomes (Extended Data Fig. 4b, top panel). Remarkably, the concentration of rearrangements on the mis-segregated chromosomes was observed in 8 of 9 post-micronuclear cell pairs ($P < 10^{-4}$, Bonferroni corrected one-sided Poisson test).

As short-range inversions are amplification errors reported to occur frequently during MDA, we analysed inverted-type and non-inverted type rearrangements separately (Extended Data Fig. 5a–c, Methods). Power-law scaling analysis revealed that inversions were enriched at breakpoint distances < 150 kilobase (kb) (Extended Data Fig. 5a, b) and were randomly distributed (Extended Data Fig. 4b), as expected for MDA errors (Methods). Long-range rearrangements (> 150 kb or interchromosomal) on the normally segregated

non-micronucleated controls (C1–C4, N1–N6, see Supplementary Table 2). Mother cells are listed on the left with daughters, 'a' and 'b'. For micronucleated mothers, 'a' (in red) represents the plus daughter and 'b' (in blue) represents the minus daughter. Chromosomes are shown on the x axis; dotted lines separate p and q arms. Pre-existing aneuploidies in mother cell, dashed boxes; *de novo* mis-segregations with copy number asymmetry, solid boxes. Top panel, bulk RPE-1 line; top middle panel, daughters from non-micronucleated mothers; middle panel, non-micronucleated controls after nocodazole release; bottom panel, daughter cells from micronucleated mothers. For N6, one daughter cell divided once, producing three cells. For MN9, extra time was provided for additional cell divisions: the plus daughter did not divide whereas the minus daughter divided twice, generating five cells in total.

chromosome were also randomly distributed (Supplementary Tables 4 and 5). By contrast, the enrichment of long-range rearrangements specifically on the mis-segregated chromosomes was even more significant after elimination of short-range rearrangements (Fig. 3a, Extended Data Fig. 4b).

As predicted, the rearrangements in the mis-segregated chromosome occurred predominantly in the plus daughter cell (Fig. 3b, Extended Data Fig. 4c), with a few informative exceptions to be discussed below. PCR amplification across rearrangement junctions from whole-genome-amplified DNA (Extended Data Fig. 6a) confirmed the rearrangements, but could not exclude amplification errors. However, by sequencing rearrangement junctions with nearby heterozygous sites (Extended Data Fig. 6b–d, Methods), we found that every rearrangement tested was associated with the gained haplotype (Extended Data Table 1, Supplementary Table 5), indicating that the rearrangements occurred on the mis-segregated chromatid. Interestingly, we sometimes detected an unaltered product in addition to the rearranged product with the mis-segregated haplotype. We hypothesize that these two products may be generated by breakage of a partially replicated sequence near a replication fork with only one side of the break participating in the rearrangement (Extended Data Fig. 6e). Thus, there is a marked concentration of long-range rearrangements associated with the gained haplotype in the plus daughter cell, indicating that these rearrangements originate from the breakage of the chromatid in the ruptured micronucleus.

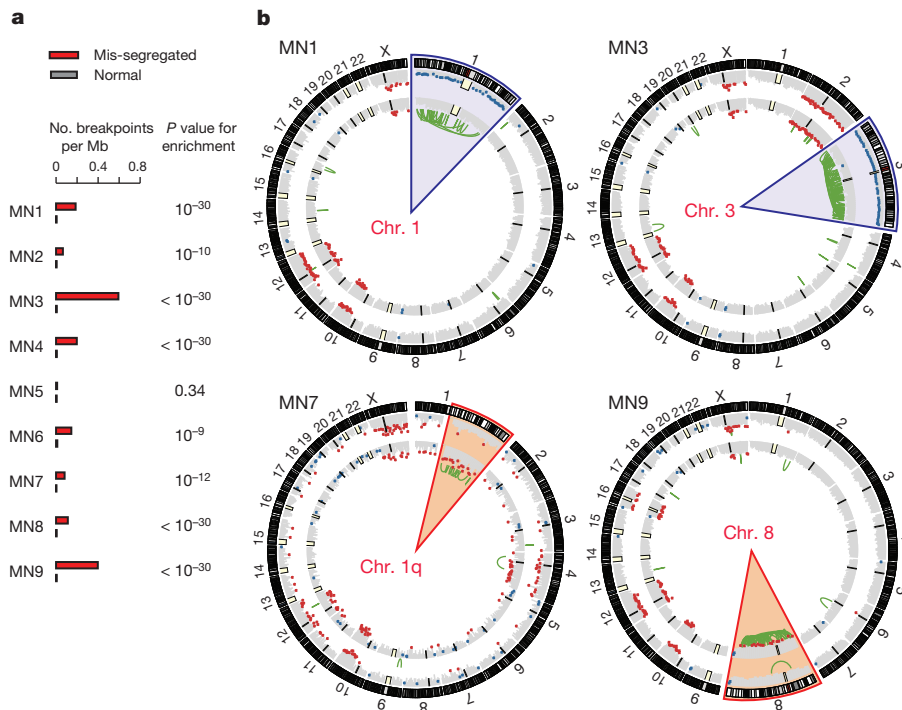


Figure 3 | Enrichment of long-range rearrangements on the mis-segregated chromosome in the predicted daughter cell.

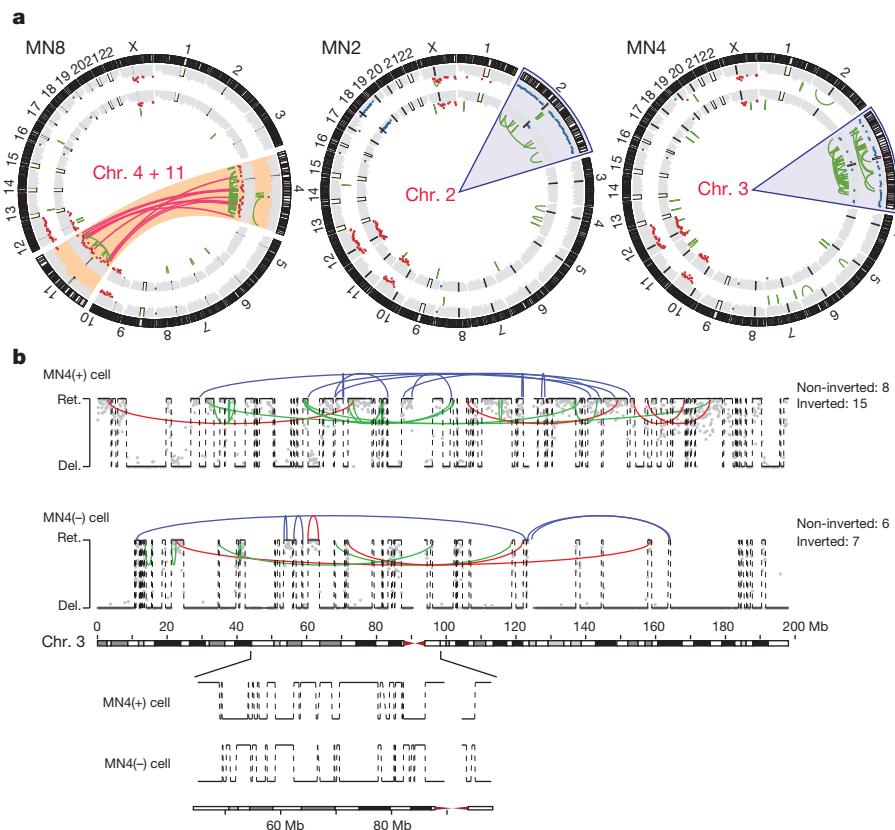
a, Left, frequency of long-range rearrangements detected in the mis-segregated chromosomes (both plus and minus cell, red bars) compared with the remaining chromosomes (grey bars): number of breakpoints per Mb is normalized for DNA copy number and the detection sensitivity. Right, P values for enrichment derived from a one-sided Poisson test (Methods). **b**, CIRCOS plots showing DNA copy number (grey histograms) and long-range intrachromosomal rearrangements (green links) for four daughter pairs from micronucleated mothers. Outside ring, chromosome banding pattern. Grey histograms, DNA copy number (5 Mb bins) for the minus cell (outer ring) and the plus cell (inner). (For MN9, one 'grandchild' of the minus daughter is shown, see Fig. 2). Red dots, bins with significant gains ($>1.35 \times$ mean); blue dots, bins with significant loss ($<0.6 \times$ mean). Loss of 19p and gain of Xq are seen in all single cell samples but not in the bulk and are attributed to systematic amplification bias (Extended Data Fig. 3b). Light blue cones, chromosomes with 2:1 mis-segregations; orange cones, 3:2 mis-segregations.

The translocation junctions for long-range rearrangements had several notable features. Unlike control chromosomes, microhomology was observed at $>50\%$ of the junctions from the mis-segregated chromosomes, a higher frequency than expected by chance²¹ (Extended Data Fig. 7a). Microhomology could originate from alternative non-homologous end joining or MMBIR⁸. In the MN6 plus daughter, 14 out of 16 breakpoints formed an uninterrupted chain (Extended Data Fig. 7b). These chained translocations resemble

examples of germline chromothripsis²² that are presumed to preserve chromosome copy number because of the selection for viability³. At some translocation junctions, we also identified short insertions (50–500 base pairs, bp) originating from other widely dispersed sites on the mis-segregated chromosome (Extended Data Fig. 7c). In one example (MN9), 8 short segments from all over Chr. 8 were inserted into a single junction, also on Chr. 8. Such short 'templated' insertions are a well-described characteristic of MMBIR⁹.

Figure 4 | Two-state oscillating copy-number patterns characteristic of chromothripsis.

a, CIRCOS plots for three daughter cell pairs where both daughters received fragments of the mis-segregated chromatid. The MN8 minus daughter contains two Chr. 4 fragments missing from the plus daughter; the MN2 minus daughter contains one segment of Chr. 2q missing from the plus daughter; for the MN4 pair, dozens of Chr. 3 fragments are reciprocally distributed between the daughters. **b**, Reciprocal distribution of fragments of the mis-segregated chromatid results in two-state copy number oscillations (retention (Ret.) or deletion (Del.)) of the mis-segregated haplotype in both daughters. Grey dots, average copy number of the mis-segregated haplotype (100 kb bins). The other haplotype is intact in both daughters (shown in Extended Data Fig. 8b). Blue links indicate non-inverted type rearrangements; green links indicate inverted type rearrangements. Red links indicate rearrangements directly associated with the mis-segregated haplotype by nearby SNPs (Supplementary Table 5). Reciprocal distribution of Chr. 3 fragments is evident from the complementarity of DNA copy-number in both daughters shown for the 50–100 Mb region (inset, bottom).



In the MN8 daughters, both Chrs. 4 and 11 were mis-segregated with a 3:2 ratio (Fig. 2b). Interestingly, in the plus cell, we not only detected intrachromosomal rearrangements in Chrs. 4 and 11, but also 8 translocations between these chromosomes (Fig. 4a, left panel). Thus, the MN8 mother probably had copies of Chrs. 4 and 11 within the single micronucleus detected by imaging, generating translocations both within and between chromosomes.

Evidence for chromosome fragmentation

One distinguishing feature of chromothripsis is the oscillation of DNA copy number between only two states⁷. This feature of chromothripsis was identified on the mis-segregated chromosome in three cell pairs, MN2, MN4 and MN8 (Fig. 4a, Extended Data Fig. 8a–c), most strikingly in the MN4 daughters. For this pair, one intact Chr. 3 haplotype was distributed evenly to both daughters (Extended Data Fig. 8b), whereas the other haplotype displayed a pattern of alternating retention and loss (Fig. 4b). Combining the copy number for both haplotypes yields an oscillating pattern: hemizygous regions with one copy alternate with heterozygous regions with two copies. Remarkably, segments of the fragmented haplotype that were gained in one daughter were almost always lost from the other and vice versa. Of all fragments of the mis-segregated Chr. 3 haplotype detected in either daughter, 97% were mutually exclusively distributed between the two daughters, with only 3% shared by both. Moreover, long-range rearrangements in both daughter cells were almost completely (>90%) restricted to regions where the fragmented haplotype was retained ($P \approx 10^{-4}$ for the plus daughter and 10^{-12} for the minus daughter, binomial test) and directly associated with the gained haplotype when adjacent polymorphisms were present (Fig. 4b). Therefore, the division of the MN4 mother cell generated the canonical features of chromothripsis in both daughters. A single chromatid from a micronucleus was fragmented and randomly distributed between daughter cells, followed by the joining of fragments in random order and orientation. Thus, the majority of DNA segments that are ‘lost’ in one cell are, in fact, distributed to the other.

Potential nascent double minutes

One way that chromothripsis may promote tumour development is by generating double minute chromosomes^{3,5}, small circular acentric chromosomes that can be present at very high copy number and carry oncogenes²³. Intriguingly, in the MN4 daughters, we detected four 1–3 megabase (Mb) circular chromosomes, which may represent examples of the initial step in generating double minutes²⁴ (Fig. 5). Evidence that these are true circular chromosome fragments not only comes from sequencing reads spanning the junctions, but also because the junctions fall at boundaries where the mis-segregated haplotype is deleted. These deletions confirm that the junctions occur at genuine break sites and also exclude the possibility that the junctions result from tandem duplications.

Discussion

The experiments described here define a new mutational process that provides one mechanistic explanation for chromothripsis, a unique pattern of localized chromosome rearrangements observed in cancer and congenital diseases. By recapitulating chromothripsis in the laboratory, we establish that it can occur after an intact chromosome is partitioned into a micronucleus. These findings highlight the critical importance of nuclear architecture and nuclear envelope integrity for the maintenance of genome stability in eukaryotic cells²⁵.

After the division of micronucleated cells, we observed extensive localized chromosome rearrangements, some of which bear all the hallmarks of chromothripsis. The following evidence indicates that these rearrangements occurred on the chromosome from the micronucleus. First, chromosomes in micronuclei are under-replicated and accumulate marked evidence of DNA damage^{11,14}. Under-replication of the chromosome in the micronucleus creates a copy number asymmetry

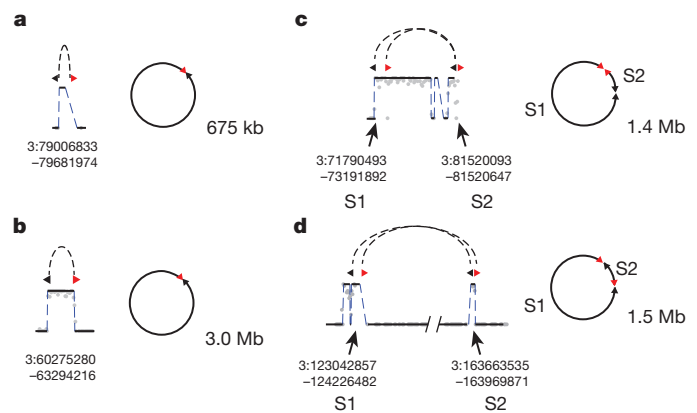


Figure 5 | Circular chromosomal structures resulting from chromothripsis. a–d, Shown are four circular structures formed by single segments (a and b) or by multiple separate segments (c and d); a and c are from the MN4 plus daughter; b and d are from the MN4 minus daughter. In each panel, circularized fragments are shown with the reference coordinates on the left (S1 and S2 denote separate segments), with 5' breaks (black triangles) and 3' breaks (red triangles) linked by rearrangements indicated by dashed lines; resulting circular structures are illustrated on the right (not to scale).

between the daughters, identifying the mis-segregated chromosome and establishing mis-segregation as a *de novo* event. Second, there is a highly significant enrichment of chromosome rearrangements only on the mis-segregated chromosome after the division of micronucleated cells; it is never observed on normally segregated chromosomes after division of either micronucleated or control cells. Third, the rearrangements are associated with the chromatid in the micronucleus identified from the gained haplotype. Thus, the partitioning of chromosomes into micronuclei is an ‘all-at-once’ catastrophe that can trigger extensive mutagenesis at a surprisingly high frequency.

Our results show that partitioning chromosomes into micronuclei can have diverse consequences for genome structure. In addition to intrachromosomal rearrangements, we find that the partitioning of more than one chromosome into one micronucleus can generate translocations between chromosomes. We speculate that the reassembly of fragments from one or more chromosomes in a micronucleus could generate ring chromosomes, which are observed in a number of human cancers, and whose formation has recently been suggested to involve chromothripsis²⁶. We also observed circularized fragments originating from the mis-segregated chromosome. Circularization of shattered chromosome fragments provides an appealingly simple mechanism for the first step in generating double minute chromosomes²⁴, which are frequent conduits for oncogene amplification in tumours^{4,5,23} and were previously linked to chromothripsis³.

Our experiments provide insight into the mechanism of chromothripsis. Elegant statistical analysis led to the proposal that chromothripsis could involve the ‘shattering’ and reassembly of a chromosome, with ‘loss’ of some segments⁴. However, the molecular mechanism or even the feasibility of such an event was not clear. Our analysis directly establishes that a chromatid can indeed be fragmented, with fragments distributed between daughter cells. In addition to validating the shattering and reassembly mechanism, our findings also explain the segmental DNA loss that characterizes many examples of chromothripsis: loss may simply occur by partitioning of chromosome segments into a daughter cell that does not expand and does not contribute to the final population. Chromothripsis has also been suggested to originate from DNA replication errors that generate MMBIR⁹. MMBIR could be an independent mechanism causing chromothripsis, or an additional contributing factor. In agreement with this latter possibility, we detect short, potentially ‘templated’ insertions at a minority of translocation junctions that are consistent with co-occurring MMBIR²⁷.

The data here establish that the rupture of micronuclei during S phase is one important source of mutagenesis. However, as we previously proposed¹¹, there may be more than one defect in micronuclei that generates DNA damage. Intact micronuclei exhibit reduced or delayed DNA replication and also fail to normally accumulate several DNA replication and repair proteins (ref. 11 and A. Spektor, E. Jackson & D. Pellman, unpublished data). If the short insertions we observe at translocation junctions result from replication defects and MMBIR⁸, given that nuclear envelope rupture seems to terminate most nuclear activity¹⁴, MMBIR probably occurred in the intact micronucleus before rupture, or after reincorporation of the micronucleus into a daughter cell nucleus. Because micronuclei replicate asynchronously with the primary nucleus, many cells enter mitosis with micronuclei that are still undergoing DNA replication^{11,28}. This results in premature chromosome compaction, which is proposed to cause DNA breakage, best documented at chromosome fragile sites²⁹.

Our findings define a new mutagenesis pathway that generates a spectrum of localized chromosomal rearrangements, some of which have all the features of chromothripsis. Consistent with other recent work^{16,30,31}, the results here show that mitotic chromosome segregation errors can be heavily mutagenic, which has important implications for how mitotic errors and the accompanying aneuploidy might contribute to cancer or other human diseases. Mitotic chromosome segregation errors occur frequently, resulting in 1–5% aneuploidy in normal tissues in mice³². Chromothripsis is reported in a few percent of human cancers^{33,34} and in rare human congenital disorders⁶. However, the actual rate of chromothripsis is likely to be much higher because most events are expected to compromise cellular fitness, and these events would only be detected by single-cell analysis³². Furthermore, we find that DNA damage from micronuclei can lead to a moderate degree of rearrangement that might not, *ex post facto*, be recognized as related to chromothripsis. Micronuclei may therefore be an important, but previously unappreciated, source of genetic variation.

Online Content Methods, along with any additional Extended Data display items and Source Data, are available in the online version of the paper; references unique to these sections appear only in the online paper.

Received 22 November 2014; accepted 20 April 2015.

Published online 27 May 2015.

1. Yates, L. R. & Campbell, P. J. Evolution of the cancer genome. *Nature Rev. Genet.* **13**, 795–806 (2012).
2. Hellday, T., Eshtad, S. & Nik-Zainal, S. Mechanisms underlying mutational signatures in human cancers. *Nature Rev. Genet.* **15**, 585–598 (2014).
3. Zhang, C. Z., Leibowitz, M. L. & Pellman, D. Chromothripsis and beyond: rapid genome evolution from complex chromosomal rearrangements. *Genes Dev.* **27**, 2513–2530 (2013).
4. Stephens, P. J. *et al.* Massive genomic rearrangement acquired in a single catastrophic event during cancer development. *Cell* **144**, 27–40 (2011).
5. Rausch, T. *et al.* Genome sequencing of pediatric medulloblastoma links catastrophic DNA rearrangements with TP53 mutations. *Cell* **148**, 59–71 (2012).
6. Kloosterman, W. P. *et al.* Constitutional chromothripsis rearrangements involve clustered double-stranded DNA breaks and nonhomologous repair mechanisms. *Cell Rep.* **1**, 648–655 (2012).
7. Korbel, J. O. & Campbell, P. J. Criteria for inference of chromothripsis in cancer genomes. *Cell* **152**, 1226–1236 (2013).
8. Liu, P., Carvalho, C. M., Hastings, P. J. & Lupski, J. R. Mechanisms for recurrent and complex human genomic rearrangements. *Curr. Opin. Genet. Dev.* **22**, 211–220 (2012).
9. Liu, P. *et al.* Chromosome catastrophes involve replication mechanisms generating complex genomic rearrangements. *Cell* **146**, 889–903 (2011).
10. Kinsella, M., Patel, A. & Bafna, V. The elusive evidence for chromothripsis. *Nucleic Acids Res.* **42**, 8231–8242 (2014).
11. Crasta, K. *et al.* DNA breaks and chromosome pulverization from errors in mitosis. *Nature* **482**, 53–58 (2012).
12. Terradas, M., Martin, M., Tusell, L. & Genesca, A. Genetic activities in micronuclei: is the DNA entrapped in micronuclei lost for the cell? *Mutat. Res.* **705**, 60–67 (2010).

13. Hoffelder, D. R. *et al.* Resolution of anaphase bridges in cancer cells. *Chromosoma* **112**, 389–397 (2004).
14. Hatch, E. M., Fischer, A. H., Deerinck, T. J. & Hetzer, M. W. Catastrophic nuclear envelope collapse in cancer cell micronuclei. *Cell* **154**, 47–60 (2013).
15. Shee, C. *et al.* Engineered proteins detect spontaneous DNA breakage in human and bacterial cells. *Elife* **2**, e01222 (2013).
16. Ganem, N. J. & Pellman, D. Linking abnormal mitosis to the acquisition of DNA damage. *J. Cell Biol.* **199**, 871–881 (2012).
17. Uetake, Y. & Sluder, G. Prolonged prometaphase blocks daughter cell proliferation despite normal completion of mitosis. *Curr. Biol.* **20**, 1666–1671 (2010).
18. Francis, J. M. *et al.* EGFR variant heterogeneity in glioblastoma resolved through single-nucleus sequencing. *Cancer Discov.* **4**, 956–971 (2014).
19. Hayashi, M. T., Cesare, A. J., Fitzpatrick, J. A., Lazzerini-Denchi, E. & Karlseder, J. A telomere-dependent DNA damage checkpoint induced by prolonged mitotic arrest. *Nature Struct. Mol. Biol.* **19**, 387–394 (2012).
20. Zhang, C.-Z. A. *et al.* Calibrating genomic and allelic coverage bias in single-cell sequencing. *Nature Commun.* **6**, 6822 (2015).
21. Simsek, D. *et al.* DNA ligase III promotes alternative nonhomologous end-joining during chromosomal translocation formation. *PLoS Genet.* **7**, e1002080 (2011).
22. Chiang, C. *et al.* Complex reorganization and predominant non-homologous repair following chromosomal breakage in karyotypically balanced germline rearrangements and transgenic integration. *Nature Genet.* **44**, 390–397 (2012).
23. Storlazzi, C. T. *et al.* Gene amplification as double minutes or homogeneously staining regions in solid tumors: origin and structure. *Genome Res.* **20**, 1198–1206 (2010).
24. Carroll, S. M. *et al.* Double minute chromosomes can be produced from precursors derived from a chromosomal deletion. *Mol. Cell Biol.* **8**, 1525–1533 (1988).
25. Misteli, T. & Soutoglou, E. The emerging role of nuclear architecture in DNA repair and genome maintenance. *Nature Rev. Mol. Cell Biol.* **10**, 243–254 (2009).
26. Garsed, D. W. *et al.* The architecture and evolution of cancer neochromosomes. *Cancer Cell* **26**, 653–667 (2014).
27. Haber, J. E. *Genome stability: DNA repair and recombination* (Garland Science, 2014).
28. Sen, S., Hittelman, W. N., Teeter, L. D. & Kuo, M. T. Model for the formation of double minutes from prematurely condensed chromosomes of replicating micronuclei in drug-treated Chinese hamster ovary cells undergoing DNA amplification. *Cancer Res.* **49**, 6731–6737 (1989).
29. El Achkar, E., Gerbault-Seureau, M., Muleris, M., Dutrillaux, B. & Debatisse, M. Premature condensation induces breaks at the interface of early and late replicating chromosome bands bearing common fragile sites. *Proc. Natl Acad. Sci. USA* **102**, 18069–18074 (2005).
30. Sheltzer, J. M. *et al.* Aneuploidy drives genomic instability in yeast. *Science* **333**, 1026–1030 (2011).
31. Janssen, A., van der Burg, M., Szuhai, K., Kops, G. J. & Medema, R. H. Chromosome segregation errors as a cause of DNA damage and structural chromosome aberrations. *Science* **333**, 1895–1898 (2011).
32. Knouse, K. A., Wu, J., Whittaker, C. A. & Amon, A. Single cell sequencing reveals low levels of aneuploidy across mammalian tissues. *Proc. Natl Acad. Sci. USA* **111**, 13409–13414 (2014).
33. Zack, T. I. *et al.* Pan-cancer patterns of somatic copy number alteration. *Nature Genet.* **45**, 1134–1140 (2013).
34. Malhotra, A. *et al.* Breakpoint profiling of 64 cancer genomes reveals numerous complex rearrangements spawned by homology-independent mechanisms. *Genome Res.* **23**, 762–776 (2013).

Supplementary Information is available in the online version of the paper.

Acknowledgements We thank R. Beroukhim, J. Walter and N. Ganem for comments on the manuscript, V. A. Adalsteinsson and J. C. Love for help with preliminary experiments, and A. Salic and S. Rosenberg for reagents. A.S. was a resident in the American Board of Radiology Holman Research Pathway; H.C. was a fellow of the Leukemia and Lymphoma Society; C.-Z.Z., J.M.F. and M.M. were supported by the Bridge Project of the Dana-Farber Cancer Institute and the Koch Institute of MIT; M.M. and D.P. were supported by the Claudia Adams Barr Program in Innovative Cancer Research; D.P. is a HHMI investigator and is supported by NIH grant GM083299-18.

Author Contributions D.P. and M.M. initiated the project. D.P. conceived the idea and supervised all aspects of the work. H.C., J.M.F., D.P., A.S. and C.-Z.Z. designed the experiments. D.P., A.S., C.-Z.Z. and M.M. wrote the manuscript, with edits from all authors. C.-Z.Z. developed and performed the computational analysis; H.C. and A.S. developed and performed the Look-Seq protocol; E.K.J., S.L. and A.S. performed the cell biological analysis experiments in Fig. 1 and Extended Data Fig. 1. J.M.F. and H.C. generated sequencing libraries; J.M.F. and C.-Z.Z. designed and performed the PCR validation of rearrangements.

Author Information The sequencing data in this study have been deposited into the Sequence Read Archive (SRP052954). Reprints and permissions information is available at www.nature.com/reprints. The authors declare competing financial interests: details are available in the online version of the paper. Readers are welcome to comment on the online version of the paper. Correspondence and requests for materials should be addressed to D.P. (david_pellman@dfci.harvard.edu).

METHODS

No statistical methods were used to predetermine sample size.

Cell culture and treatment. U2OS, telomerase-immortalized RPE-1 cells (ATCC), and all derivative cell lines generated for this study were tested for Mycoplasma, and were grown in phenol red-free DMEM:F12 media containing 10% FBS, 100 IU ml⁻¹ penicillin, and 100 µg ml⁻¹ streptomycin. All cells were maintained at 37°C with 5% CO₂ atmosphere. For cell cycle synchronization and induction of MN, cells were treated with 100 ng ml⁻¹ nocodazole (Sigma) for 6 h. Mitotic cells were collected and washed three times with fresh medium containing 10% FBS before plating. To arrest cells in G₀, nocodazole-treated cells were washed 3 times with media containing 0.01% FBS following mitotic shake-off and then re-plated in media containing 0.01% FBS. After 3 h, cells were placed in a serum-free DMEM:F12 media. For EdU incorporation experiments, cells were incubated in the presence of 10 mM EdU from the time of mitotic shake-off.

Generation of cell lines. Lentivirus or retrovirus carrying genes of interest were generated by transfection of 293FT cells with the appropriate packaging plasmids (Lentivirus, pMD2.G and psPAX2; Retrovirus, pUMVC and pVSV-G) using Lipofectamine 2000 (Life Technologies), according to the manufacturer's instructions. RPE-1 cells were infected for 16–24 h with virus in the presence of 10 µg ml⁻¹ polybrene, washed, and allowed to recover for 24 h before selection with an antibiotic or by fluorescence cell sorting.

RNA interference. Sequence information of the small interfering RNA (siRNA) pools used from Dharmacon are as follows, Human TP53 ON-TARGETplus SMARTpool siRNA L-003329-00-0005, (J-003329-14) GAAUUUGCGUG UGGAGUA, (J-003329-15) GUGCAGCUGUGGUUGAAU, (J-003329-16) GCAGUCAGAUCCUAGCGUC, (J-003329-17) GGAGAAUUAUUCACCC UUC. Cells were transfected with 40 nM siRNA using Lipofectamine 3000 transfection reagent (Life Technologies) per manufacturer's instructions.

DNA constructs. Plasmid encoding cDNA for H2B-GFP was obtained from Addgene (Plasmid 11680). Constructs encoding TDRFP-NLS and NLS-eGFP were a gift from A. Salic. Emerald GFP-Gam was a gift of S. Rosenberg.

Reagents and antibodies. DNA damage was detected using phospho-histone H2A.X (Ser139) antibody for γ-H2AX (1:300–500, Cell Signaling Catalog Number 2577S). Nocodazole was purchased from Sigma-Aldrich. Secondary antibodies used were Alexa Fluor 488 (green), 594 (red) and 647 (far red) (1:1,000, Life Technologies).

Detection of EdU incorporation. Detection of EdU incorporation was performed using Click-iT Plus EdU Alexa Fluor imaging kits 594 and 647 (Life Technologies) per manufacturer's instructions.

Live cell imaging, single-cell isolation and daughter cell separation. RPE-1 cells expressing H2B-GFP and GFP-NLS were treated as described above to induce micronuclei after depletion of p53 by siRNA. After mitotic shake-off, cells were re-plated and allowed to progress into G₁ phase for 4 h. Afterwards cells were trypsinized and single-cell sorted into 384-well µClear plates (Greiner) using FACS. Following single cell sorting, cells were incubated for 2 h to allow for cell attachment and spreading. Plates were mounted on a Nikon TE2000-E2 inverted microscope equipped with the Nikon Perfect Focus system. The microscope was enclosed within a temperature- and CO₂-controlled environment that maintained an atmosphere of 37°C and 3–5% humidified CO₂. Wells containing single cells of interest were identified manually and fluorescence and differential interference contrast images were captured every 30 min with a 20× NA 0.5 Plan Fluor objective for up to 48 h or until the majority of cells had progressed through mitosis. All captured images were analysed using NIS-Elements software.

Wells containing cells of interest, having completed mitosis, were washed with PBS and cells were subsequently trypsinized. After addition of an excess of fresh medium, daughter cells were separated by limited dilution into new wells in a fresh 384-well µClear plate. Successful separation and transfer into new wells was monitored using a fluorescence microscope. In cases where both daughters ended up in the same well, separation by limited dilution was repeated. After separation, the cells were left to attach for up to 4 h before cell lysis.

Indirect immunofluorescence. Cells were washed in PBS and fixed in 4% paraformaldehyde for 20 min; cells were then extracted in PBS-0.5% Triton X-100 for 5 min, washed 3 times with PBS, blocked for 30 min in PBS containing 3% BSA (PBS-BSA) and incubated with primary antibodies diluted in PBS-BSA for 60 min. Samples were washed 3 times for 5 min with PBS-0.05% Triton X-100 and primary antibodies were detected using species-specific fluorescent secondary antibodies (Life Technologies). Samples were washed 3 more times for 5 min with PBS-0.05% Triton X-100 before DNA detection (2.5 µg ml⁻¹ Hoechst). For pre-extraction, cells were washed once with PBS, and then incubated in CSK buffer (100 mM NaCl, 300 mM sucrose, 3 mM MgCl₂ and 10 mM PIPES pH 6.8) containing 0.5% Triton X-100 for 5 min on ice. Cells were then washed 3 times with PBS, fixed and processed as above.

Image acquisition and analysis. Immunofluorescence images were collected with a Yokogawa CSU-22 spinning disk confocal system with Borealis modification, which was attached to a Nikon Ti-E inverted microscope (Nikon Instruments, Melville, NY). Laser excitation of the fluorophores was performed sequentially using the 405 nm, 488 nm, and 561 nm and 642 nm lasers. Images were acquired using a 60× Plan Apo NA 1.4 oil objective with a CoolSnapHQ2 CCD camera (Photometrics). Acquisition parameters, shutters, filter positions and focus were controlled by Metamorph software (Molecular Devices), which was also used for image analysis. Regions of interest were defined for micronuclei and corresponding primary nuclei, and average fluorescence intensities were determined. Background values were subtracted from a region the same size and shape as the micronucleus, set equidistant from the primary nucleus.

Thresholds were set to exclude cells that were not synchronized after mitotic shake-off. In G₁ phase samples, cells were excluded if the primary nucleus contained visible EdU. In S or G₂ phase samples, cells were excluded if there were low levels of replication in the primary nucleus, operationally defined by an average fluorescence intensity threshold. Additional average fluorescence intensity thresholds for γ-H2AX were used to exclude rare cells from all samples (<5%) where the primary nucleus had significant DNA damage, and to define γ-H2AX positive micronuclei. For EdU detection, micronuclei were scored as EdU positive if their EdU signal was >3 standard deviations above the mean background.

Each immunofluorescence experiment included two biological replicates. Number of cells counted (N) for each experiment were as follows (biological replicate 1, biological replicate 2, total): Fig. 1a: primary nuclei (83, 83, 166), intact micronuclei (53, 50, 103); ruptured micronuclei (51, 51, 102); Extended Data Fig. 1a: G₁ (63, 69, 132), S (55, 50, 105), G₂ (62, 63, 125); Extended Data Fig. 1b: γ-H2AX (–) micronuclei (87, 63, 150), γ-H2AX (+) micronuclei (109, 73, 182); Extended Data Fig. 1c: G₀ (63, 63, 126), S (53, 50, 103); Extended Data Fig. 1d: γ-H2AX (+) micronuclei (62, 49, 111).

Multi-strand displacement amplification and library construction of single-cell genomic DNA. We chose to amplify single-cell genomes by multi-strand displacement amplification (MDA) with the Phi-29 polymerase³⁵ for four main reasons: first, MDA gives better overall genome coverage than PCR-based methods³⁶ and also gives comparable uniformity^{37–39} to other methods such as MALBAC⁴⁰; this is required for the detection of chromosomal rearrangements. Second, Phi-29 polymerase has the highest processivity and the lowest error rate among existing polymerases^{36,41}. Third, amplification bias due to MDA has been characterized as largely random, even between the two homologues of the same chromosome²⁰; this enables us to estimate the coverage for each homologue, the detection sensitivity for *de novo* variants, and to accurately calculate the copy number for each homologue from the coverage at heterozygous sites. Finally, the high processivity of Phi-29 polymerase consistently generates large amplicons above 10 kb^{42,43}; this enables us to perform Sanger sequencing on the MDA product after PCR to generate phasing information of rearrangements and validate their association with the mis-segregated chromosome, which is crucial in establishing the relationship between chromosomal rearrangements and DNA damage in the micronuclei.

DNA from isolated cells was subject to MDA following lysis using the REPLI-g Single Cell Kit (Qiagen) with minor modification. (Note that we achieved the best overall coverage uniformity with this latest version of REPLI-g from Qiagen as compared to earlier versions of REPLI-g or the RepliPhi enzyme from Epicentre. Comparison of the coverage and uniformity of the single-cell libraries in the current study with previous studies^{40,43} is summarized in Supplementary Table 1 and in ref. 20.) Samples were washed once with PBS and cells were lysed using 10 µl of a 1:1 mixture of the provided lysis buffer and PBS by a brief vortex and spin down, followed by a 10 min incubation at 50°C and then an additional 10 min at room temperature. Lysis was stopped by adding 5 µl of stop solution with vortex and spin down, followed by incubating at room temperature for another 10 min. Whole-genome amplification by MDA was carried out in a total of 50 µl for 80 min at 30°C. Purified genomic DNA (for bulk RPE-1) or amplified DNA (from single cells) was sheared to 300–500 base pair size and used for multiplex genome sequencing libraries as previously described¹⁸.

Library quality was assessed by low-pass sequencing ~0.1× on a MiSeq instrument (Illumina). DNA libraries that passed MiSeq quality control¹⁸ were then sequenced to ~5× per cell on the HiSeq platform (Illumina). Two samples, one from the control group (N3) and one from the MN group (MN4), were subject to additional sequencing to a total depth of ~9× per cell for validation of the enrichment of chromosomal rearrangements on the mis-segregated chromosomes. For the MN9 daughters the plus cell did not divide but the minus cell divided twice. The four progeny cells from the MN9 minus daughter were sequenced to ~6× combined coverage and the plus cell that did not divide

was sequenced to $\sim 4\times$ depth. (The main goal of this experiment had been to obtain biological replicates of cells with potentially chromothriptic damage; however, in this example the plus daughter with rearranged Chr. 8 did not divide). For the three N6 progeny, one cell divided and the other did not before library preparation, all three progeny were sequenced to $\sim 4\times$ depth.

Processing of single-cell sequencing data. Sequencing reads were aligned to the human genome reference (hg19/GRCh37) using bwa (<http://bio-bwa.sourceforge.net/>) in the paired-end mode by “bwa mem”. For both primary and supplementary alignments, duplicated sequencing fragments were removed by MarkDuplicates from the PICARD software suite (<http://picard.sourceforge.net/>). We also generated genotype information by running the UnifiedGenotyper module from GATK (<https://www.broadinstitute.org/gatk/>) at HapMap SNP sites (ftp://gsapubftp-anonymous@ftp.broadinstitute.org/bundle/current/b37/hapmap_3.3.b37.vcf) across all sequenced samples (bulk, controls, MN samples). We identified 884,944 heterozygous sites in the bulk sample sequencing with quality scores ≥ 100 . Genotypes at these heterozygous sites were later used to calculate haplotype coverage and copy number.

DNA copy number analysis from sequencing read depth. The average read depth was calculated by dividing the number of properly aligned read pairs (insert size < 1 kb and having the ‘forward-reverse’ pair orientation) by the total ungapped length of each bin (for binned coverage) or by the ungapped length of the relevant chromosomal arm (for arm-level coverage). The read depth was then normalized by the median value of all bins (or arms) for each sample to calculate the average DNA copy number of each bin.

We corrected for GC-content amplification bias in each library by modifying the strategy described in ref. 44. The overall strategy was to statistically infer read depth variation due to GC content and normalize regional coverage by a GC-content-dependent correction factor. Importantly, we expected the dominant GC-dependent variation to have been generated during MDA before the library preparation; therefore, the average GC-content was calculated for 25 kb bins because the average amplicon size of MDA was previously estimated to be in the range of 10–50 kb^{20,43}.

To generate a reference for the relationship between read depth and GC content, we analysed the sequence coverage of a chromosome (Chr. 6) that was present in all samples at two copies for each library. For each sequencing fragment (read pair) we calculated the average GC-content in the 25 kb bin centred at the leftmost alignment position of the read pair. We then grouped all read pairs into GC strata that differed by 1% GC content and calculated the average read depth for each stratum. A normalizing weight was then derived for each GC stratum to bring the median coverage within each GC stratum to the same value. Each sequencing fragment was then assigned a weight based on the GC composition in its 25 kb neighbourhood. The GC corrected sequencing coverage was generated by random sampling based on the ‘GC-correcting’ weight for each read.

Although GC correction at the amplicon level does reduce the amplification noise at the sub-megabase scale, significant variation at longer scales (> 1 Mb) is still evident after GC correction. To additionally correct for long-range systematic amplification biases, especially in the small chromosomes (most evident in the 19p arm, Fig. 3b and Supplementary Table 2), we normalize the average copy-number CN_a^i for arm a in sample i as

$$x = (\log_2 CN_a^i - \log_2 \overline{CN}_a) \times \frac{\text{median}[\text{std}(\log_2 CN_a)]}{\text{std}(\log_2 \overline{CN}_a)}$$

The first term on the right side of the equation is the standard \log_2 copy number; \overline{CN}_a is the average \log_2 arm-level copy number across all samples (but excluding samples with significant gains or losses defined as 10% difference from the median). Subtracting the average eliminates systematic (recurrent) amplification bias at the arm level (most noticeably on Chr. 19). The second term corrects for variation in amplification bias across different chromosomes: the denominator, $\text{std}(\bullet)$, is the standard deviation that reflects variability in amplification for a given chromosome arm occurring between the different, independently generated, samples; the numerator is the median of the standard deviation across all chromosomes. The standard deviation is small for large chromosomes but becomes bigger for small chromosomes. The normalized \log_2 -scale copy number was plotted in Fig. 2.

The genome-wide coverage of each single-cell library is presented in 5 Mb bins in the CIRCOS plots in Fig. 3b and Fig. 4a. The standard deviation of the normalized bin-level coverage was estimated to be ~ 0.1 from the disomic Chr. 6 for all daughters, except for sample MN7 (s.d. ~ 0.3). The thresholds for significant gains (mean coverage ratio > 1.35) and losses (mean coverage < 0.6) were chosen because they are $\sim 3.5\times$ standard deviations from the mean value (0.95) for MN1–MN6, MN8, MN9, and for coverage > 1.4 and coverage < 0.5 for MN7, corrected for the additional variance. Where there were arm-level copy number

alterations present in single cell samples, but absent from the bulk sequencing, haplotype copy-number analysis (below) was used to discriminate systematic amplification bias (affecting both haplotypes) from true copy number gains or losses (Extended Data Fig. 3).

Detection of loss-of-heterozygosity. The model that the chromosome in a ruptured micronucleus undergoes *de novo* damage (that is, alterations that are not shared between daughters) has the clear prediction that the damage should occur on one of the homologous chromosomes but not the other. Our sequence-read-depth based copy number analysis indicated that some mis-segregated chromosomes are distributed between the daughters in $\sim 2:1$ ratio (Fig. 2a, left panel). This implies that the cell with two copies of the affected chromosome contains the potentially damaged chromosome from the micronucleus and that the other cell should only contain the intact homologue of the mis-segregated chromosome (that is, monosomic). A further prediction, which would independently validate these copy number results, is that the daughter with two copies of the chromosome should be heterozygous at polymorphic sites whereas the other daughter should be hemizygous. To test this prediction, we developed a method to determine the presence or absence of loss-of-heterozygosity (LOH) from the genotypes observed at heterozygous sites.

Because the genotype data are derived from single-cell libraries that are subject to variable amplification, it is non-trivial to distinguish true LOH from incomplete coverage due to uneven amplification by the MDA procedure. To address this problem, we derived an expected relationship between the observed number of sites showing heterozygosity and the observed number of sites showing the reference base (or equivalently, the number of sites showing the alternate base), given the sequence coverage. This relationship was derived with the assumption that the cell has one copy of each homologous chromosome (that is, ‘1:1 heterozygosity’). Knowing the expected heterozygosity at the desired level of coverage, we can then infer LOH, if the sequencing data deviate significantly from what is predicted for 1:1 heterozygosity. Because reference or alternate bases are counted as ‘present’ or ‘absent’, and the number of reads when present is ignored, this relationship is relatively insensitive to variable amplification and holds as long as the two homologues are amplified independently²⁰.

For a cell with a single copy of each homologous chromosome, assume that there are a total of M heterozygous sites and the fractional coverage of each homologous chromosome above a certain sequencing depth is p . (For example, when we required ≥ 3 reads to call a structural variant, p would correspond to the fraction of each homologue covered with ≥ 3 reads, which defined the detection sensitivity discussed later under Estimation of SV detection sensitivity section.) If the two homologues have identical copy number and their amplification bias is independent, then the expected percentage of sites where we should observe both the reference and the alternate bases (that is, both homologues are covered at or above the specified depth) is given by p^2 . If the observed percentage of sites showing heterozygous coverage deviates from this prediction, then it implies that the two homologues have different copy numbers. In particular, it is straightforward to see that when there is complete LOH for a given chromosome, the expected percentage of sites where we should observe both the reference and the alternate bases should be zero, if there are no genotyping, sequencing or systematic amplification errors. However, to determine if there are partial deletions in either homologue, we need to estimate the value of p .

Estimating the fraction of a homologue that should be covered at any given depth by the sequencing data, p , is straightforward if the haplotype phases (that is, the order of reference and alternate bases at heterozygous sites in a single haplotype) of both homologues are known. However, this can be achieved even without knowledge of the haplotype phase as long as each homologue has a complete copy and their average coverage is equivalent, which is true for MDA when the coverage is evaluated over regions that are significantly larger than the amplicon size²⁰. We can account for p as follows. For a total of M heterozygous sites, assume there are fM reference and $(1 - f)M$ alternate bases in haplotype 1. (It will become obvious below that the haplotype composition f will not affect the estimate for p as long as the amplification of different homologues is independent.) For this haplotype we expect to observe the reference base at $p \times fM$ heterozygous sites that are covered by more than the threshold number of sequence reads. For the other haplotype, there are $(1 - f)M$ reference and fM alternate bases, which by the same reasoning predicts that we should observe the reference base at $p \times (1 - f)M$ heterozygous sites above the threshold of coverage. Thus, without separating the two haplotypes, we expect to observe pfM reference bases from the coverage of haplotype 1 and $p(1 - f)M$ from the coverage of haplotype 2, which gives a total number of pM reference bases at all heterozygous sites. The same number is expected for the total number of alternate bases being covered by more than the threshold number of sequence reads. Note that this estimation for p comes directly from the coverage of the reference or alternate

bases at the heterozygous sites but does not rely on knowledge of the haplotype phase or its composition f .

In summary, for a chromosome that consists of two single-copy homologues ('1:1' heterozygosity) and having a total number of M heterozygous sites where the two homologues differ, we expect the following coverage at heterozygous sites:

The number of sites showing reference base coverage: pM

The number of sites showing alternate base coverage: pM

The number of sites showing heterozygous coverage: p^2M

With these expected values we can derive an expected relationship between the fraction of heterozygous coverage relative to the average fractional coverage for the reference and for the alternate bases:

$$\frac{\left[\frac{\text{fraction of sites with heterozygous coverage}}{\left(\left[\frac{\text{fraction of sites with reference coverage}}{2} + \left[\frac{\text{fraction of sites with alternate coverage}}{2} \right]^2 \right)^2} \right]}{p^2} = 1$$

which holds for the '1:1 heterozygosity' scenario. Deviation from this ratio in the observation reflects changes in the copy number of either or both homologues. We therefore define the ratio on the left hand side of the above equation evaluated from the experimental data as a 'heterozygosity coefficient' to gauge the deviation of the homologue copy number from 1:1 heterozygosity.

Importantly, we do not require direct knowledge of the absolute fractional coverage (p) to test whether the ratio on the left side of the equation gives the expected value close to 1. (We will however use this relationship below (section on detection sensitivity) to estimate p as a measure of the detection sensitivity.) It is based only on the relative value for the fraction of heterozygosity divided by the fraction of sites with reference (or of alternate) coverage. This relationship is therefore more robust than a direct test of the observed coverage on a given chromosome against p estimated from a different disomic chromosome, because the coverage p may vary slightly between different chromosomes due to sequence-specific amplification bias.

Results shown in Extended Data Fig. 2 confirmed that for heterozygous chromosomes the heterozygosity coefficient is overall slightly above but close to unity, reflecting only a small degree of correlation for the amplification of the homologues²⁰. For chromosomes that are completely or partially hemizygous (that is, one homologue has complete or partial loss) the heterozygosity coefficients are significantly smaller. Of note, the heterozygosity coefficient is a sensitive method for detecting even a relatively small segment of heterozygosity in a chromosome that is otherwise near completely hemizygous. This is illustrated by the analysis of the MN2 minus daughter, where we could detect a 15 Mb segment of heterozygosity from Chr. 2q (~7% of Chr. 2) that is lost from the plus daughter (Extended Data Fig. 8a).

The method is not, however, sensitive for detecting gains above 1:1 heterozygosity, as occurs when cells undergo 3:2 segregation patterns for the mis-segregated chromosome. For this circumstance, we directly calculated the haplotype copy number based on the haplotype phase information (see below). Note that the determination of the haplotype phase required the LOH analysis: The haplotype phase was obtained from the sequencing data of chromosomes that are inferred to be completely hemizygous by their heterozygosity coefficients, an inference that is independent from and more robust than the read depth-based arm-level copy number data shown in Fig. 2b and Supplementary Table 2.

Haplotype copy number analysis. If the haplotype phase is known, then the copy number ratio of the two homologues, based on their haplotypes, can be directly determined in a given cell. Because the LOH analysis provided confidence of genuine hemizygosity (Extended Data Fig. 2), we were able to use the sequencing data to directly extract the haplotype phase for one homologue and then infer the phase of the other, and deconvolute the sequence coverage for each homologue (Extended Data Fig. 3a).

This analysis was first applied to Chr. X where we observed recurrent gains in the sequence coverage of Xq that is nonetheless absent in the bulk sequencing data (Supplementary Table 2). As can be seen from the example of the haplotype copy number for Chr. X in the MN3 daughters (Extended Data Fig. 3b, top panel), the haplotypes were present in equal copy number in both daughters, enabling us to attribute the read depth variation (between the Xp and the Xq arms) to systematic amplification bias. Variable penetrance of this amplification bias presumably caused the apparent copy-number asymmetry in the C1 and MN7 daughters (Fig. 2b), which were the samples with the most read depth noise. Indeed, haplotype copy-number analysis confirmed that there was no difference in the relative copy number of the two Chr. X homologues in both C1 daughters (Extended Data Fig. 3b, middle panel). It also demonstrated a true gain of one Chr. X haplotype was shared in both MN7 daughters (Extended Data Fig. 3b, bottom panel).

By contrast with the amplification bias, haplotype copy-number analysis verified that there was a gain of a single homologue of the mis-segregated

chromosome in the plus daughters from the 3:2 segregations (MN7 and MN8, Extended Data Fig. 3c), excluding the possibility that the gain is due to mixed segments from both homologues or uniparental trisomy. Moreover, this analysis confirmed that the minus daughters from these cells had a 1:1 ratio of the two homologues. Therefore, the haplotype copy number established the segregation model depicted in Fig. 2a (right panel) for the 3:2 segregation samples.

Knowledge of the haplotype phase was also critical for obtaining the fine structure of copy number alterations. For the daughters with a 2:1 distribution of the mis-segregated chromosome, knowing the haplotype phase enabled a digital readout for whether a segment of that haplotype was deleted or retained (Fig. 4b, Extended Data Fig. 8b). Like the LOH analysis, this readout is minimally affected by amplification noise: heterozygosity is scored as present or absent and differences in the numbers of reads at different heterozygous sites are ignored. (To capture copy number gains, for example, in the 3:2 segregations, the read depth signal is needed and amplification bias will have some effect on the detection of focal gains. We are currently working on methods to address this problem.)

We used the haplotype phase information for Chr. 3 (inferred from the MN3 minus daughter) to generate segmented copy number profiles for the mis-segregated haplotype in both MN4 daughters that contained interspersed deletions (Fig. 4b). Each phaseable SNP served as a probe for the altered haplotype; the boundaries of deletions were identified by a transition from 'covered' (that is, present) probes to 'uncovered' probes or vice versa. For each SNP, we provisionally designated it as being 'covered' if there were reads supporting the haplotype, and 'uncovered' if there were zero supporting reads. This raw signal at each SNP was then smoothed using the coverage of other SNPs within the local bin to eliminate false negative assignments of SNPs not being covered because of amplification bias. We set this bin size to 100 kb because it is much larger than the typical MDA amplicon and therefore unlikely to have been completely lost because of variation in amplification²⁰. In the rare regions with sparsely distributed SNPs, we extended the bin to contain at least 8 flanking phaseable SNPs, which was chosen because with 8 phaseable SNPs, the probability that half of them (4 out of 8) were absent due to variable coverage (false LOH) was less than 0.1% based on the current level of variant detection sensitivity and heterozygous coverage (Supplementary Table 1). (The probability of having sequencing or amplification errors generating false heterozygosity in 4 out of 8 sites is even smaller.) For each SNP, if more than 50% of the nearby SNPs were covered, the SNP of interest was designated as covered; if that value was less than 50%, that SNP was designated as being not covered; if the local coverage was 50%, the SNP was designated as being at the boundary of a deletion. This process was iterated until convergence; the final designation for each SNP can only be 'covered (1)', 'uncovered (0)', or 'boundary (0.5)'. We then connected all SNPs with the same copy number states and identified copy-number changes directly. This procedure was used to generate the segmented copy-number profiles for MN4 daughters in Fig. 4b, with the average coverage for each bin shown as grey dots.

Detection of chromosomal rearrangements. Chromosomal rearrangements were detected from clusters of discordant read pairs. Read pairs were designated to be discordant if both mates mapped to the reference genome and the inferred insert size exceeded 20 kb, irrespective of the orientation of the mapped pair mates. The 20 kb threshold is significantly longer than the average length of the sequencing fragment (~500 bp) but is comparable to the typical size of the amplicon of multi-strand displacement amplification. The choice of a 20 kb threshold thus excludes a large number of short-range artificial chimaeras (mostly of inverted orientation) that result from amplicon annealing or phi-29 polymerase template switches^{39,45}. As explained below, intrachromosomal rearrangements within the 20–100 kb range were also populated by artefacts and we used the frequency of these events on control chromosomes to estimate the background frequency of MDA-generated chimaeras. The control chromosomes included all the chromosomes from the daughters derived from non-micronucleated mothers (C1–C4 and N1–N6) as well as all chromosomes from both daughters from the micronucleated mothers, with the exception of the mis-segregated chromosomes.

We initially applied a low threshold of two discordant read pairs to search for candidate rearrangements. Discordant pairs include both primary discordant pairs, where the two pair mates are aligned to discordant loci, and split reads, where a single read is split into two parts and aligned to non-contiguous segments. A primary discordant pair can contain one mate that itself constitutes a split read; in this scenario, the discordant pair and the split read were counted as a single discordant fragment. Although split read alignment potentially provides base-level breakpoint resolution, the smaller size of each split alignment means that they are more likely to be misaligned to the reference genome due to short interspersed repeats. We therefore required each discordant cluster to consist of at least one primary discordant pair with each mate aligned to discordant loci with

a mapping quality of 30 or greater (from bwa mem, $\sim 0.1\%$ alignment uncertainty). From this first-pass analysis there were a total of 8,179 clusters of discordant pairs in all samples.

Next, we excluded all discordant clusters that consisted of reads from daughters with different mothers, or reads from the bulk RPE-1 line. Such clusters could reflect recurrent artefacts due to inaccuracy in the alignment or in the reference assembly. Although expected to be infrequent, we also cannot exclude the possibility that some of these clusters reflect clonal or subclonal chromosomal rearrangements that accumulated during cell culture. The remaining 2,665 non-recurrent clusters are expected to include both putative *de novo* chromosomal rearrangements and random artefacts due to MDA. There were 2,403 intrachromosomal and 262 interchromosomal clusters that consisted of two or more discordant read pairs. There were 1,088 intrachromosomal and 76 interchromosomal clusters with three or more discordant read pairs. Discordant clusters supported by only two discordant read pairs occurred at a higher frequency than predicted by the haplotype coverage and were especially enriched in short-range events (data not shown). Because of the expectation that amplification artefacts (excepting those that occur very early in the reaction) would be supported by fewer discordant read pairs, we expected more frequent artefacts among the structural variants (SV) supported by only two discordant read pairs and required putative rearrangements be supported by at least three discordant pairs and also by at least one split read. We relaxed these criteria only in a few exceptions where there was additional supporting evidence, such as for the chained rearrangements depicted in Extended Data Fig. 7b, but subsequently performed PCR validation of all the detected events.

Enrichment analysis of chromosomal rearrangements in the mis-segregated chromosome. Random MDA-derived artificial chimaeras and true *de novo* chromosomal rearrangements cannot be distinguished by the variant allele frequency or by the number of discordant pairs. We therefore developed statistical criteria to determine if clusters of rearrangements on the mis-segregated chromosome in the plus daughter cells were significantly enriched relative to the background observed for other chromosomes.

Template switch events in multi-strand displacement amplification can result in frequent short-range chimaeras of the inverted orientation⁴⁵; by contrast, long-range artificial chimaeras or *de novo* chromosomal translocations are not expected to have a preferred orientation. The observed SV events in the single-cell DNA libraries indeed confirmed this prediction (Extended Data Fig. 5a). A substantial enrichment of short-range SVs (20–50 kb) of the inverted type relative to the non-inverted type was observed in all control chromosomes: both daughters from the non-micronucleated mothers (C1–C4, N1–N6) and all chromosomes, excluding the mis-segregated chromosomes, in the daughters from the micronucleated mothers. We therefore excluded short-range SVs from the list of candidate *de novo* rearrangements, even though this likely underestimates the numbers of true *de novo* events.

To rigorously establish a threshold to distinguish short-range from long-range SVs, we looked at the cumulative distribution of inverted and non-inverted type SVs relative to the breakpoint distance (Extended Data Fig. 5b). By simple visual inspection it is clear that at short breakpoint distances, inverted-type SVs are more frequent than non-inverted type SVs. However, the frequencies of inverted and non-inverted type SVs become equivalent at longer breakpoint distances. Power law fitting revealed that events of the intermediate length range (85 non-inverted type SVs in the range of 200 kb \sim 5 Mb) followed a power law scaling, $P(\text{no. SVs} \geq l) \approx l^{-0.32}$. By contrast, short-range inverted-type SVs (632 inverted type SVs < 100 kb) decayed as $\approx l^{-1.18}$, reflecting a much higher frequency of inverted-type SVs at shorter breakpoint separations. The intersection of these two decay curves indicated that at or above 150 kb breakpoint distances, inverted and non-inverted type SVs approximately followed the same distribution. This analysis led us to adopt 150 kb as an operational cut-off for 'long-range' rearrangements that excludes most systematic MDA artefacts. We note that this cut-off does not attenuate signal from the mis-segregated chromosomes, because these chromosomes had a highly significant enrichment of rearrangements separated by > 500 kb breakpoint distances (Extended Data Fig. 5c).

We then estimated the frequency of short- and long-range (including interchromosomal) rearrangements on all control chromosomes to establish the background rates of these events (Extended Data Fig. 4a). The frequency of breakpoints within each chromosome arm was calculated as the ratio of the total number of observed breakpoints divided by the length of the relevant arm, corrected for the copy number of that arm and for the detection sensitivity for each sample (that is, the percentage of each homologue that is covered at or above the threshold depth for variant detection). The arm-level copy number was determined as described above and shown in Supplementary Table 2. The detection sensitivity estimated from sequence coverage (to be discussed further below) is shown in Supplementary Table 1. Short-range rearrangements occurred at an

average frequency of 1.5 events per 100 Mb; long-range rearrangements occurred at an average frequency of 0.5 events per 100 Mb. By a χ^2 test, the distribution of either short-range or long-range events on the control chromosomes was indistinguishable from that expected for a uniform frequency with normally distributed error (minimum $P = 0.18$ for short non-inverted type rearrangements, 3 degrees of freedom).

To determine if the observed structural variants follow a uniform distribution, we performed one-sided Poisson tests of the number of SVs observed in the test chromosome against the background frequency estimated from all chromosomes including the test chromosome on a per-sample basis. In 8 out of 9 daughter cell pairs from micronucleated mothers, there was a significant enrichment of SVs (combining short- and long-range events) on the mis-segregated chromosome (Extended Data Fig. 4a). By contrast, there was no enrichment for short-range rearrangements (Bonferroni corrected $P > 0.3$) on the mis-segregated chromosomes (Extended Data Fig. 4b, middle panel). Moreover, the enrichment of long-range SVs on the mis-segregated chromosome was even more marked, the most extreme case being the MN3 pair, with an estimated P value $< 10^{-100}$. Meanwhile, the only exception, MN5, served as a negative control for the statistical test.

We also performed a Fisher's exact test of the observed number of long-range and short-range events on the mis-segregated as compared with the remaining chromosomes, assuming the short-range events represent an empirical sampling of background events (summarized in Extended Data Table 1). The Fisher's exact test also confirmed the enrichment of long-range events in the mis-segregated chromosome relative to the rest of the genome with the background given by short-range events. MN5 was the only example where the partitioning of a chromosome (Chr. 7) into a micronucleus appeared not to have led to detectable rearrangements.

Finally, we also tested the enrichment of long-range rearrangement breakpoints in each of the normally segregated chromosomes in every sample. The background frequency was estimated by the average among all control chromosomes in each sample, that is, for all chromosomes in each control daughter pair, and for all but the mis-segregated chromosome(s) in each micronucleated daughter pair. No normally segregated chromosome or chromosomal arm reached the significance level of $P = 0.05$ after Bonferroni correction (results for the statistical tests are not shown but raw data are in the Supplementary Tables).

Estimation of SV detection sensitivity. Whole-genome amplification bias results in varied coverage across each chromosome. Even at the same locus, this coverage can be different between the homologous chromosomes. With a requirement of ≥ 3 reads to support a structural variant, we will only detect SV events when the sequence coverage at the sites of rearrangements exceeds this threshold. Importantly, this threshold is required for reads from a single homologue. (For example, even at loci that are covered by more than three reads, it is possible that by random chance all the reads were derived from amplification of the intact homologue, and the variant homologue is missing from the sequencing data.) Therefore, the SV detection sensitivity is equivalent to the expected fraction, p , of each chromosome homologue that is covered, in this case by three or more reads, which can be estimated from coverage at heterozygous sites as discussed above in the section on LOH detection.

For chromosomes that have a single copy of each homologue, the fraction of one homologue that is covered by three or more reads is equal to the fraction of heterozygous sites at which we observe the reference base (or equivalently, the alternate base) by three or more reads. Because there can be subtle variation in the amplification of different chromosomes, we generated a per-cell reference for detection sensitivity, using the coverage at heterozygous sites in Chrs. 5 and 6 consistently. These chromosomes were chosen because the LOH analysis (Extended Data Fig. 2b) and the read-depth analysis (Fig. 2b) indicated that both homologues were present at a 1:1 ratio in every cell that we analysed (1:1 heterozygosity).

Three metrics of haplotype coverage are reported in Supplementary Table 1: the fraction of genome coverage (% of heterozygous sites covered with ≥ 1 read), the fraction of heterozygous coverage (% of heterozygous sites covered with ≥ 1 read corresponding to each genotype), and the detection sensitivity for variants [(% of sites covered by ≥ 3 reads of the reference base + % of sites covered by ≥ 3 reads of the alternate base)/2].

Based on the latter metric, we estimate that at the current sequencing depth ($\sim 5\times$), we should detect 30–40% of all *de novo* structural rearrangements that occur on a single homologue. For two samples, N3 and MN4, we doubled the sequencing depth to $\sim 9\times$ per cell and the estimated detection sensitivity correspondingly reached 60–70%. For example, in the N3 pair, the total number of rearrangements detected from the entire data set was 17, whereas at half the depth, 10 events were detected. Similarly, in the MN4 pair, the total number of rearrangements detected from the entire data set was 38 for the mis-segregated chromosome and 26 for the remainder of the genome; at half the depth, we

observed 21 events in the mis-segregated chromosome and 15 events in the rest of the genome. These observations support the validity of our estimation of the detection sensitivity. Importantly, at higher sequencing depths, the statistical significance associated with the enrichment of rearrangement events in the mis-segregated chromosome only became more pronounced. Thus, although we are almost certainly underestimating the absolute numbers of rearrangements at the current level of sequencing coverage, we can nevertheless support with confidence the conclusion that there is enrichment of rearrangements on the mis-segregated chromosome.

Knowing the detection sensitivity is also important for the statistical inference that the observed unique SVs in each daughter cell are genuine, *de novo* events rather than a random sampling of shared events that are incompletely detected. If we assume that there are a total of N SVs that are shared between the two cells and the detection sensitivity is p_A in the plus daughter, and p_B in the minus daughter, then the number of SV events that are expected to be detected in both cells is Np_Ap_B . Moreover, the number of SVs that are unique to cell A is $Np_A(1 - p_B)$, and the number of SVs that are unique to cell B is $Np_B(1 - p_A)$. Even if we do not know the total number of events, N , the relative fraction of shared versus unique events can be derived from the detection sensitivity. We therefore performed a multinomial test of the number of events observed in each of these categories (shared, unique to cell A, unique to cell B) against these ratios. Based on the results of the multinomial test, the hypothesis that the observations are due to incomplete detection can be rejected except in MN2 (Extended Data Fig. 4c, MN5 does not show enrichment of rearrangements in the mis-segregated chromosome).

Rearrangement validation by PCR. The junction sequence for each rearrangement was constructed from the reference sequence and the breakpoint coordinates of the partner loci. For each rearrangement two primer pairs were designed spanning the rearrangement junction: one pair for the rearranged sequence, the other for the reference sequence (Extended Data Fig. 6, primer data available upon request). When adjacent SNPs were present, PCR primers were designed to incorporate these sites to generate genotype information on the rearranged and the wild-type products. PCR was performed in both daughters: 10 ng of whole-genome amplified DNA was used per reaction and subject to 35 cycles of PCR. The product was gel purified and Sanger sequenced in both directions to validate the rearrangement and to infer the haplotype associated with each product.

Association of rearrangements with the gained haplotype. If rearrangements result from alteration of a single chromatid, then they should all be associated to the same haplotype. Furthermore, a strong prediction of the model that rearrangements occur from damage in micronuclei is that all rearrangements detected in the mis-segregated chromosome should be associated with the gained haplotype.

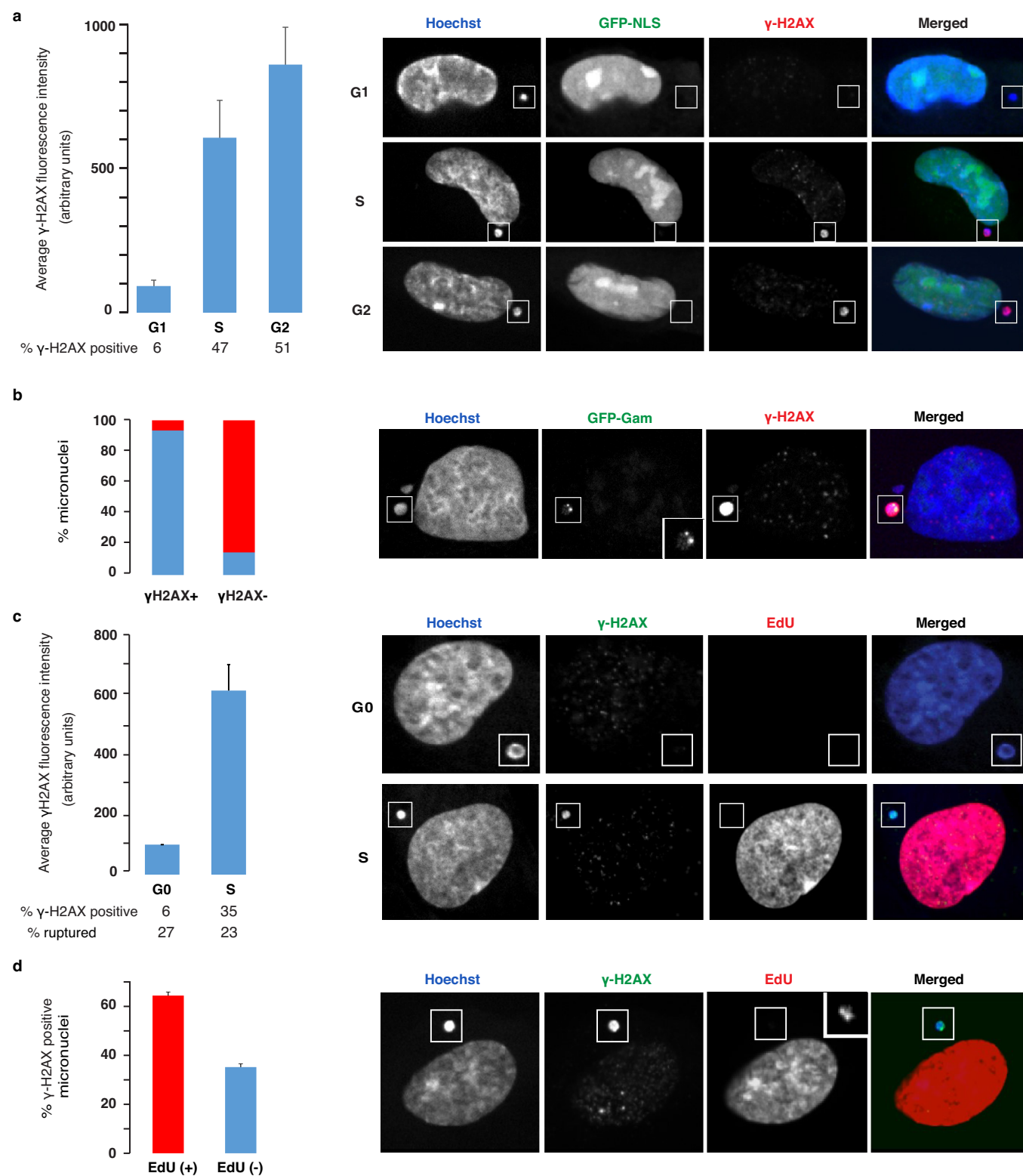
Haplotype phasing (associating rearrangements with a specific haplotype by the genotypes at polymorphic sites) was done in two ways. If a polymorphic site was close enough to a rearrangement junction (that is, within the size range of an average DNA sequencing fragment), we looked for sequencing reads that both covered the polymorphic site and supported the rearrangement (either the read pair was a discordant pair or one pair mate was a split read supporting the rearrangement). We also performed long-range PCR (~1 kb) on the MDA amplified DNA to generate a product that would include the rearrangement junction and incorporate one or more polymorphic sites that were further away and could

not be phased by sequencing reads directly. Sanger sequencing of this product was then used to test for association of the rearrangement with either haplotype. Importantly, Sanger sequencing can demonstrate that the rearranged product was derived only from the gained haplotype. PCR of the reference sequence was also performed on DNA from both daughters to determine the haplotype associated with the wild-type product.

The PCR validation strategy and representative examples are illustrated in Extended Data Fig. 6 and results of the PCR validation and haplotype association are summarized in Extended Data Table 1 and Supplementary Table 5. In each case where we PCR-validated a rearrangement with an informative nearby polymorphism, the rearranged product showed that the rearrangement was linked to the gained haplotype at one or more polymorphic sites. In addition, in all cases, the PCR validation of the wild-type products in the minus daughters always showed the genotype from the intact haplotype. For 2:1 segregations, this polymorphic site was hemizygous, consistent with the segregation model.

Interestingly, the reference sequence PCR product in the plus daughters was hemizygous in some events and heterozygous in others (Supplementary Table 5, Extended Data Fig. 6d). In each case where this product was hemizygous, the genotype corresponded, as expected, to the intact haplotype, that is, the normally segregated chromosome. In other cases where the reference sequence product was heterozygous, the presence of both rearranged and reference sequence products with the gained haplotype is most easily explained by a DNA break at one side of a DNA replication fork (Extended Data Fig. 6e). This result is consistent with the cytological evidence suggesting partial DNA replication (Fig. 1).

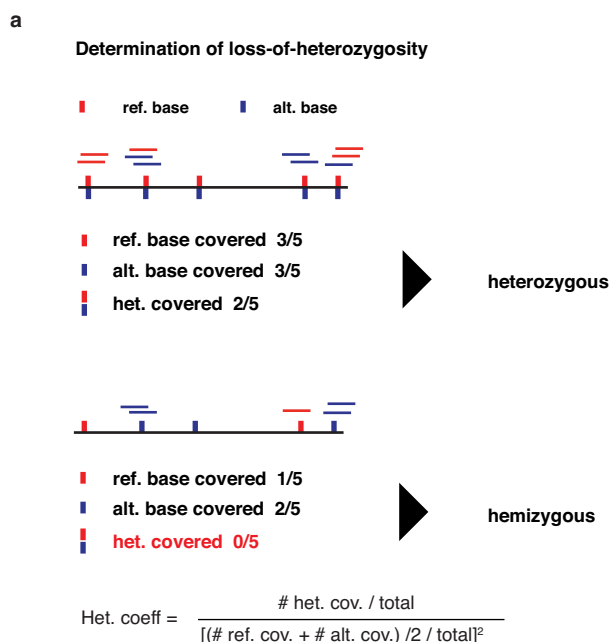
35. Dean, F. B. *et al.* Comprehensive human genome amplification using multiple displacement amplification. *Proc. Natl Acad. Sci. USA* **99**, 5261–5266 (2002).
36. Voet, T. *et al.* Single-cell paired-end genome sequencing reveals structural variation per cell cycle. *Nucleic Acids Res.* **41**, 6119–6138 (2013).
37. De Bourcy, C. F. A. *et al.* A quantitative comparison of single-cell whole-genome amplification methods. *PLoS ONE* **9**, e105585 (2014).
38. Wang, Y. *et al.* Clonal evolution in breast cancer revealed by single nucleus genome sequencing. *Nature* **512**, 155–160 (2014).
39. Evrony, G. D. *et al.* Cell lineage analysis in human brain using endogenous retroelements. *Neuron* **85**, 49–59 (2015).
40. Zong, C. *et al.* Genome-wide detection of single-nucleotide and copy-number variations of a single human cell. *Science* **338**, 1622–1626 (2012).
41. Pinard, R. *et al.* Assessment of whole genome amplification-induced bias through high-throughput, massively parallel whole genome sequencing. *BMC Genomics* **7**, 216 (2006).
42. Lage, J. M. *et al.* Whole genome analysis of genetic alterations in small DNA samples using hyperbranched strand displacement amplification and array-CGH. *Genome Res.* **13**, 294–307 (2003).
43. Evrony, G. D. *et al.* Single-neuron sequencing analysis of L1 retrotransposition and somatic mutation in the human brain. *Cell* **151**, 483–496 (2012).
44. Benjamini, Y. & Speed, T. P. Summarizing and correcting the GC content bias in high-throughput sequencing. *Nucleic Acids Res.* **40**, e72 (2012).
45. Lasken, R. S. & Stockwell, T. B. Mechanism of chimera formation during the Multiple Displacement Amplification reaction. *BMC Biotechnol.* **7**, 19 (2007).
46. Beroukhi, R. *et al.* The landscape of somatic copy-number alteration across human cancers. *Nature* **463**, 899–905 (2010).
47. Lieberman-Aiden, E. *et al.* Comprehensive mapping of long-range interactions reveals folding principles of the human genome. *Science* **326**, 289–293 (2009).



Extended Data Figure 1 | DNA damage and double-strand breaks occur in micronuclei when replication is coincident with nuclear envelope rupture.

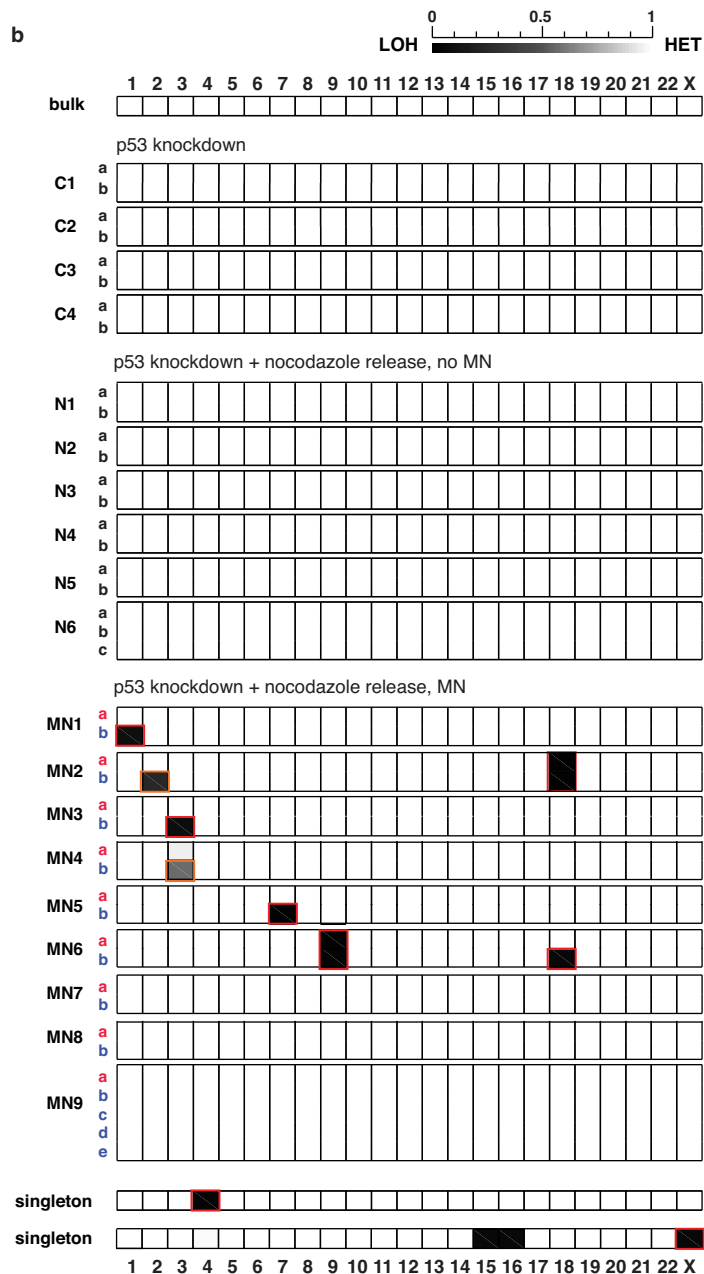
a, Nuclear envelope rupture in G1 is not sufficient to induce DNA damage in micronuclei. Left, graph shows the percentage of ruptured micronuclei, determined by the loss of GFP-NLS, that were positive for γ -H2AX (>3 standard deviations above the mean of S-phase primary nuclei), and the fluorescence intensities for γ -H2AX labelling in the indicated samples. $N > 100$ from two experiments for each time point (see Methods). Error bars, standard error of the mean. Right, images of representative cells with micronuclei highlighted in boxes. **b**, Ruptured micronuclei have double-strand breaks detected by GFP-Gam. Left, graph shows the percentage of micronuclei with one or more GFP-Gam positive foci in γ -H2AX-positive and negative micronuclei in S phase. $N > 100$ from two experiments for each category (see Methods). Right, images of a representative cell with a damaged micronucleus (highlighted in boxes) and an intact micronucleus. Inset, magnification of GFP-Gam signal. **c**, Nuclear envelope rupture of micronuclei in G0 phase cells does not result in significant DNA damage. Micronucleation

was induced in RPE-1 cells by a nocodazole block-and-release protocol, and cells were released into serum-depleted (G0) or serum replete medium (S) for 17 h. Left, graph shows the percentage of micronuclei that were positive for γ -H2AX (>3 standard deviation above the average level in S-phase primary nuclei) as well as the distribution of the fluorescence intensities for γ -H2AX labelling in the indicated samples. Percentage of ruptured micronuclei was from a parallel sample with a GFP-NLS-expressing RPE-1 line. $N > 100$ from two experiments for each time point (see Methods). Right, images of representative cells. Error bars show standard error of the mean. **d**, The majority of damaged micronuclei have initiated DNA replication. Replication was detected by continuous EdU labelling following nocodazole release and integrated EdU signal normalized over nuclear or micronuclear area. Left, percentage of γ -H2AX positive micronuclei that were positive (>3 standard deviation above the background) or negative for EdU. $N > 100$ from two experiments (see Methods). Error bars show standard error of the mean. Right, images of a representative cell. Inset, over-exposure to visualize low-level EdU labelling of the micronucleus.



c

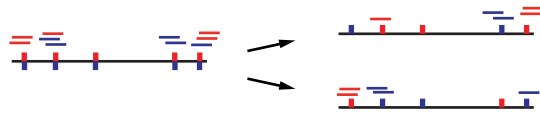
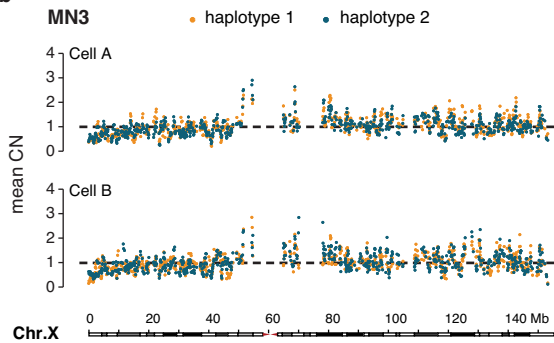
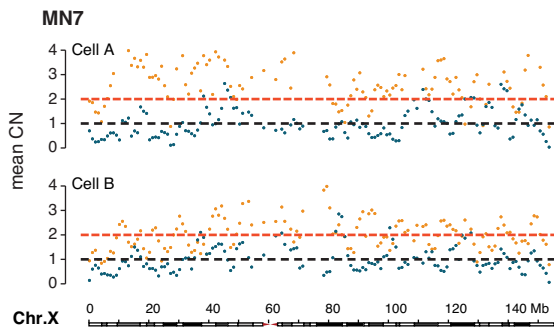
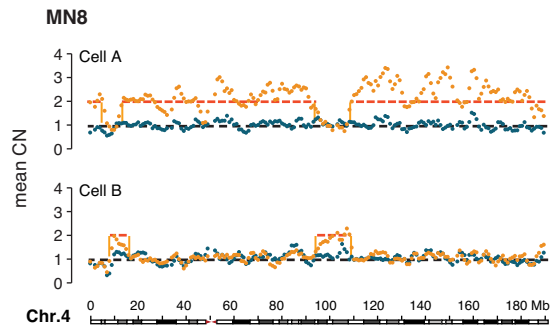
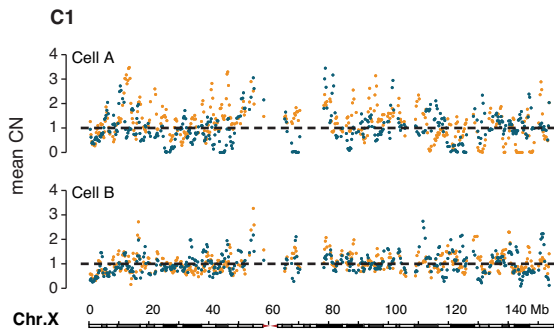
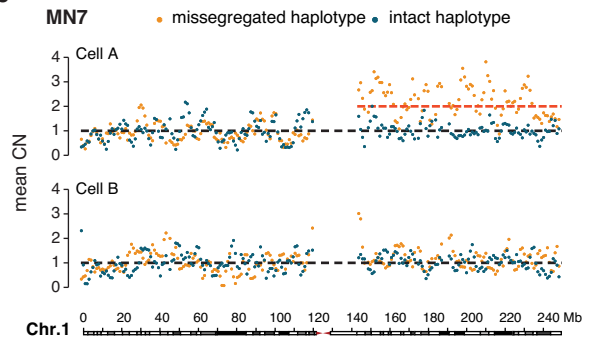
cell id	Chr.	heterozygous sites in bulk	genotype supported by ≥ 1 read			heterozygous coefficient
			Ref.	Alt.	both (Het.)	
MN1(b)	1	64,528	23,555	23,641	919	0.10
MN3(b)	3	60,531	23,438	22,969	777	0.09
MN5(b)	7	49,915	19,677	18,888	216	0.03
MN6(b)	18	24,523	9,792	9,785	225	0.06
MN6(a/b)	9	42,251	16,034	15,880	191	0.03
MN2(a/b)	18	24,523	9,811	9,702	87	0.02
singleton	4	54,813	19,654	17,768	229	0.04
singleton	X	21,843	9,536	9,773	216	0.05
MN2(b)	2	74,605	28,794	28,250	2,656	0.24
MN4(a)	3	60,531	43,562	42,430	28,685	0.94
MN4(b)	3	60,531	32,730	33,401	10,354	0.57
other						1.08 \pm 0.06



Extended Data Figure 2 | Determination of loss-of-heterozygosity.

a, Cartoon comparing the expected single-cell sequencing coverage of heterozygous and hemizygous chromosomes at polymorphic sites. Loss-of-heterozygosity (LOH) can be inferred from the scarcity of heterozygous genotypes without knowing the haplotype phase (that is, the genotypes at polymorphic sites for each homologue). The presence or absence of the reference or the alternate base provides a digital read-out of heterozygosity or LOH that is insensitive to read-depth noise common in single-cell sequencing data. This can be quantified as a heterozygosity coefficient, the ratio of the observed fraction of heterozygosity relative to the expectation for a heterozygous chromosome consisting of a single copy of each homologue ('1:1 heterozygosity'). For a diploid cell with 1:1 heterozygosity, if the fraction of sites that are covered (≥ 1 read per site) for each homologue is denoted as p , then the expected fraction of sites with heterozygous coverage is approximately p^2 . If the chromosomes are equally amplified then $p \approx 1/2(\text{observed reference base} + \text{observed alternate base})/\text{total sites}$ (Methods). **b**, Heat map of the heterozygosity coefficients for all chromosomes from all single cell samples included in Fig. 2b plus two additional single cells ('singletons') with monosomies that were sequenced to identify the haplotype phase of the monosomic chromosomes. Near complete LOH in the MN1, MN3, MN5, and MN6 minus daughter cells independently confirmed the monosomy of the mis-segregated chromosome, as determined from DNA copy number analysis (Fig. 2b). Note that the MN2 and MN6 daughters had monosomies (Chr. 18 in MN2 and Chr. 9 in MN6) shared in both daughters, indicating that the monosomy was pre-existing in the mother cell. Two 'singletons' were identified as having monosomy in Chr. 4 and in Chr. X based on low-pass MiSeq

sequencing. They were each sequenced to $\sim 4.5\times$ to generate the haplotype phase of Chr. 4 and Chr. X. Note that the second singleton also had monosomies in Chrs. 15 and 16; the haplotype phases for these two chromosomes were not used in the current study, so they were omitted from the table in c, but the data are available upon request. **c**, Table summarizing results from the loss-of-heterozygosity analysis. Heterozygosity coefficients are shown for the boxed chromosomes in b, red heterozygosity coefficients indicate complete LOH; orange are partial LOH. For the cell ID, we indicate the individual daughters as 'MN#(a)' or 'MN#(b)'. The cases denoted as 'MN#(a/b)' are monosomies shared in both daughters. The third column lists the number of heterozygous sites detected for the indicated chromosome from the bulk sequencing data (Methods). Columns 4–6 summarize the number of sites at which sequencing coverage from each cell supports the presence of reference bases ('Ref.'), alternate bases ('Alt.'), or both ('Het.'). The last column lists the heterozygosity coefficients calculated for the indicated chromosome in the specified cell or cells. The average heterozygosity coefficient is 1.08 for all chromosomes that did not show LOH from all samples (last row). For chromosomes with near complete LOH (rows 1–8) the small number of heterozygous sites is likely due to genotyping errors (for example, duplicated/homeologous sequences on the same chromosome) or amplification and sequencing errors. The incomplete LOH in the MN2 and MN4 daughters results from the reciprocal distribution of a fragmented chromosome between the two daughters (Extended Data Fig. 8). Note that our calculated heterozygosity coefficient can sensitively detect even a small region of heterozygosity in the MN2 minus cell (Extended Data Fig. 8a).

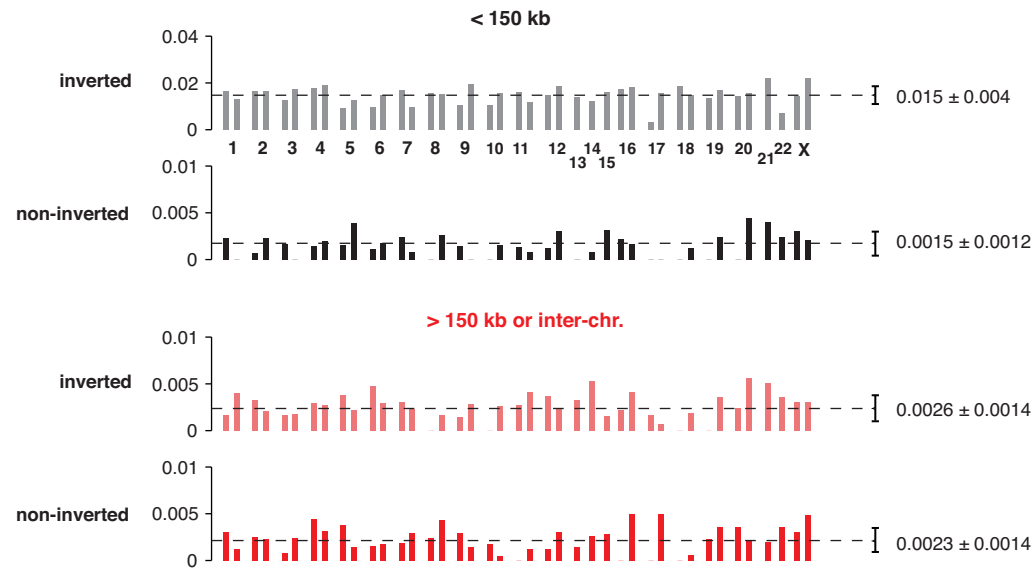
a Evaluation of allelic DNA copy number**b****c**

Extended Data Figure 3 | Calculation of haplotype copy number from phased haplotypes.

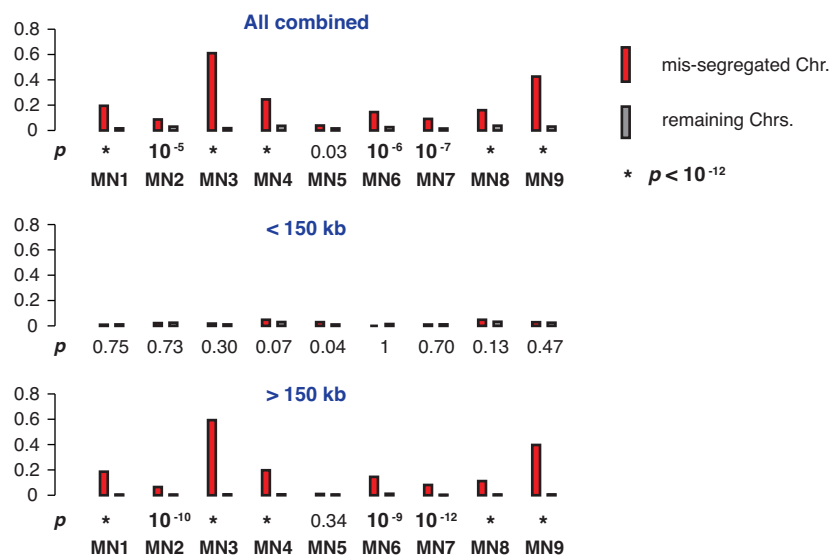
By sequencing monosomic cells we were able to determine the haplotype phases for chromosomes 1, 3, 4, 18, and X (Extended Data Fig. 2). **a**, Cartoon illustrating the strategy to calculate the copy number for each haplotype (homologue) from the coverage at individual polymorphic sites. The example is shown for a cell having one copy of each homologue. The left shows the aggregate sequence data; the right shows the deconvolution of the sequence based on the determined haplotype phase. The haplotype coverage is calculated by dividing the number of sequencing reads from the indicated haplotype by the total number of heterozygous sites. Copy-number alterations affecting only one homologue can be directly identified by calculating the ratio between the two homologues. Note that this approach is robust to any recurrent amplification bias that equally affects both homologues. **b**, Validation of copy-number alterations in Chr. X. The haplotype phase was inferred from the sequence of a singleton cell with monosomic Chr. X. The DNA copy number analysis alone suggested frequent Chr. Xq gains shared in many daughter pairs (including all controls, Supplementary Table 2). We considered it unlikely that these inferred copy number alterations were genuine because they were not present in the bulk sample (Supplementary Table 2). We calculated the haplotype copy number to distinguish true copy-number alterations from a potential systematic amplification bias for Chr. X. Each dot represents the haplotype copy number calculated as the average coverage at all sites within each bin for which phase information could be obtained (that is, where there was coverage in the reference cell that we sequenced with Chr. X monosomy). Haplotype copy number of Chr. X in 0.1 Mb bins in MN3 confirmed that the

small yet significant gain in Xq relative to Xp affects both haplotypes equally, thus excluding the Xq gain as a genuine copy number alteration. Initial read-depth-based copy number analysis (Supplementary Table 2, Methods) also implied that there could be a copy number asymmetry for Chr. Xq for the two daughters from sample C1 as well as for Chr. X between the MN7 daughters (Fig. 2b). Calculation of the copy number of Chr. X for 0.25 Mb bins in C1 confirmed that there is no difference between the two haplotypes in Xq; thus, any variation in the combined sequence coverage likely also reflects amplification bias. By contrast, the copy number of Chr. X in MN7 (1 Mb bins) indicated that there is a true gain of a single haplotype that generates trisomy for Chr. X that is shared (pre-existing) in both daughters. **c**, Use of haplotype copy number to validate the 3:2 segregation patterns in the MN7 and MN8 daughters inferred from DNA copy number. The haplotype phase for Chr. 1 was determined from the sequence of the MN1 minus cell. Coverage of the intact haplotype (blue dots) is evenly distributed between the daughters and throughout the chromosome; the mean coverage of this intact haplotype was used to calculate the normalized copy number of the mis-segregated/gained haplotype. For the MN7 daughters, there is a single copy gain of Chr. 1q in the plus daughter. By contrast, there is no gain of Chr. 1p in either cell, providing an internal control. In MN8, nearly an entire copy of Chr. 4 was gained in the plus daughter, with the exception of two segments partitioned into the minus daughter. The gains and losses both occurred only to the mis-segregated haplotype (orange). The reciprocal gain and loss of these segments in the two daughter cells illustrates the sensitivity of the method.

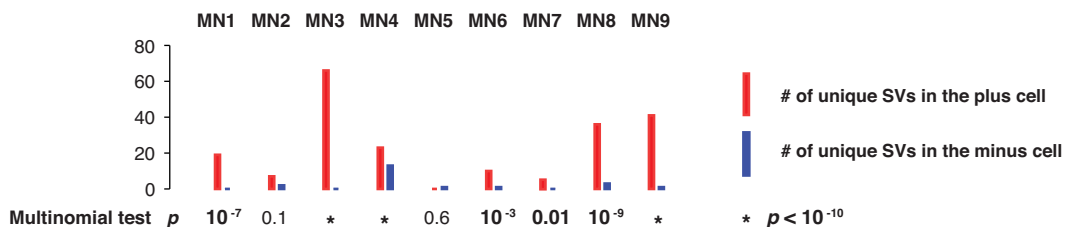
a # of breakpoints per Mb in control chromosomes



b # of breakpoints per Mb in mis-segregated chromosomes vs. control chromosomes



c Distribution of SV events in the mis-segregated chromosome between daughter cells

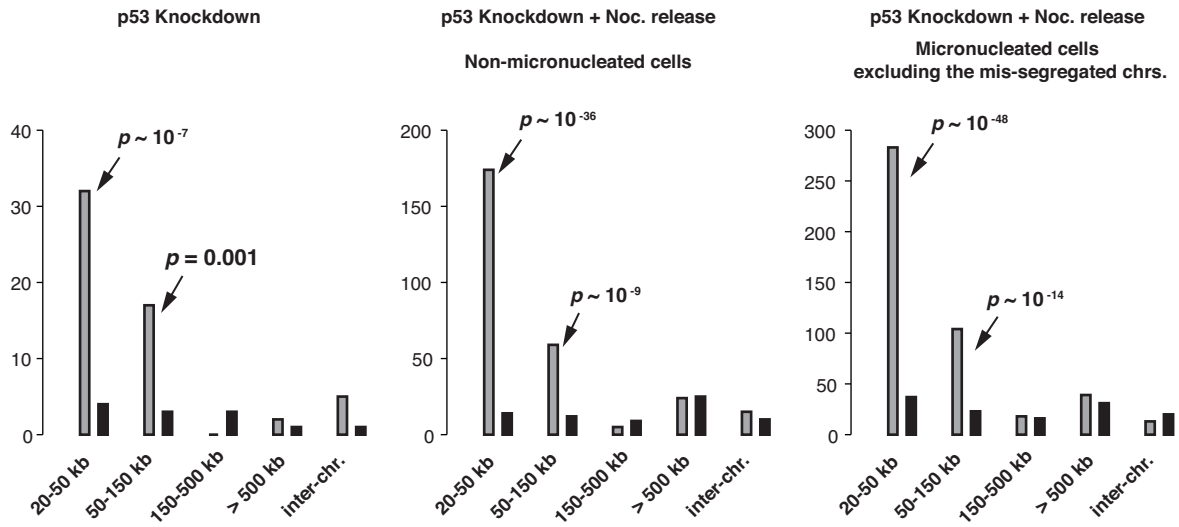


Extended Data Figure 4 | Statistical analysis of the enrichment of structural variants on mis-segregated chromosomes. **a**, No enrichment of structural variants was observed in control chromosomes, including all chromosomes after the division of non-micronucleated mothers plus all normally segregated chromosomes after the division of micronucleated mothers. Shown are the frequencies of short- and long-range chromosomal rearrangements, at inverted ('head-to-head/tail-to-tail') or non-inverted ('head-to-tail/tail-to-head') orientations, detected in all control chromosomes, plotted for each chromosome arm. The frequencies were calculated by dividing the total number of rearrangement breakpoints of each type for each chromosome by the total length of the chromosome and after correcting for copy-number alterations for each chromosome and the detection sensitivity in each sample. Fluctuation around the mean value across the genome is insignificant for all groups ($P > 0.05$, χ^2 test for a normal distribution based on the observation). **b**, Enrichment of structural variants specifically on the mis-segregated chromosomes identified by asymmetric copy number. Top, frequency of all structural variants (breakpoints per Mb, normalized for DNA copy number and detection sensitivity) detected in the mis-segregated chromosomes (both plus and minus cell combined) as compared with all the remaining, normally

segregated chromosomes; middle, frequency of intrachromosomal SVs with breakpoint distance <150 kb, showing no enrichment; bottom, frequency of long-range SVs (intrachromosomal SVs with breakpoint distance >150 kb or joining different chromosomes). P values are derived from a one-sided Poisson test (Methods). **c**, Mutually exclusive distribution of SV breakpoints between the two daughters. There are three categories of events, those unique to cell 'a', those unique to cell 'b', and those shared between both cells. The frequencies in each category can be estimated given the detection sensitivity in each library, which can be inferred from the sequence coverage at heterozygous SNPs (Methods). By a multinomial test, the large number of SVs detected in the mis-segregated chromosome that are unique to each daughter cell cannot be explained by incomplete detection of pre-existing SVs shared between the cells. This contrasts with the few shared events (one each in MN1 and in MN3; none in the others). This conclusion holds for all daughter cell pairs except those from the MN2 and MN5 mothers. For the MN2 daughters the small number of evaluable events does not reach statistical significance. The MN5 daughters are the one negative example where there do not appear to be chromosomes that underwent any significant rearrangement.

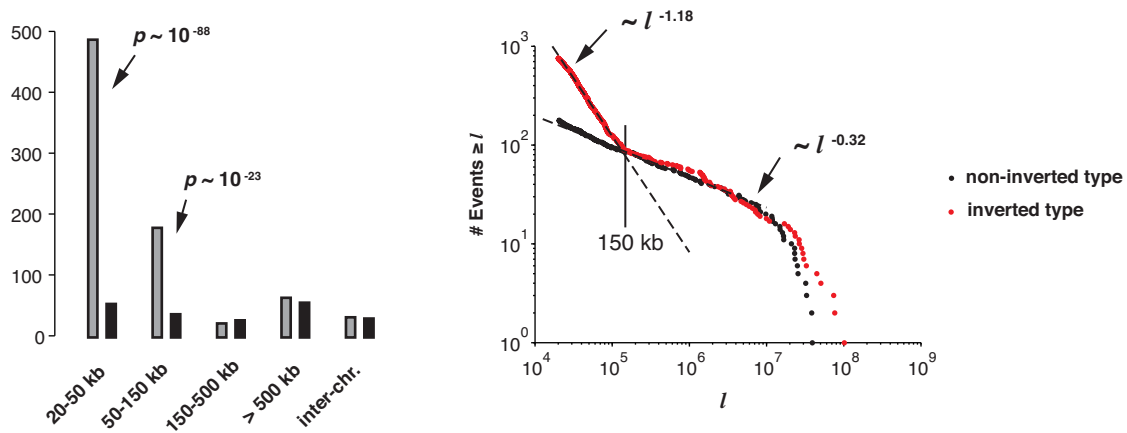
a

inverted type (head-head/tail-tail) non-inverted type (head-tail/tail-head)



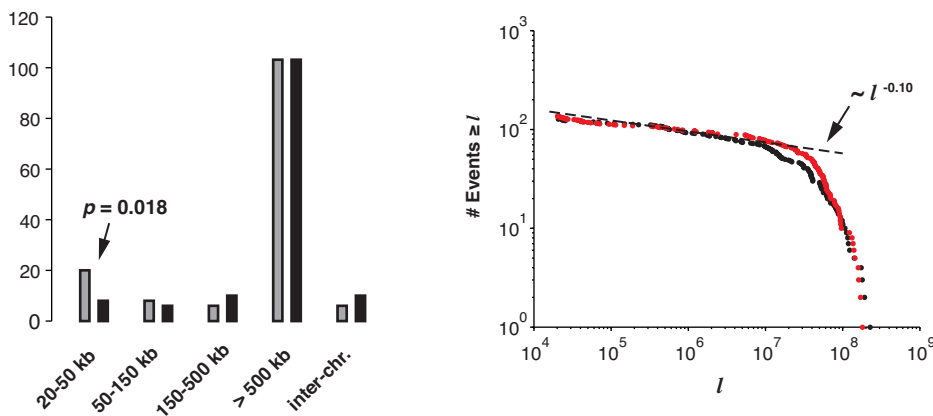
b

All control chromosomes



c

All mis-segregated chromosomes

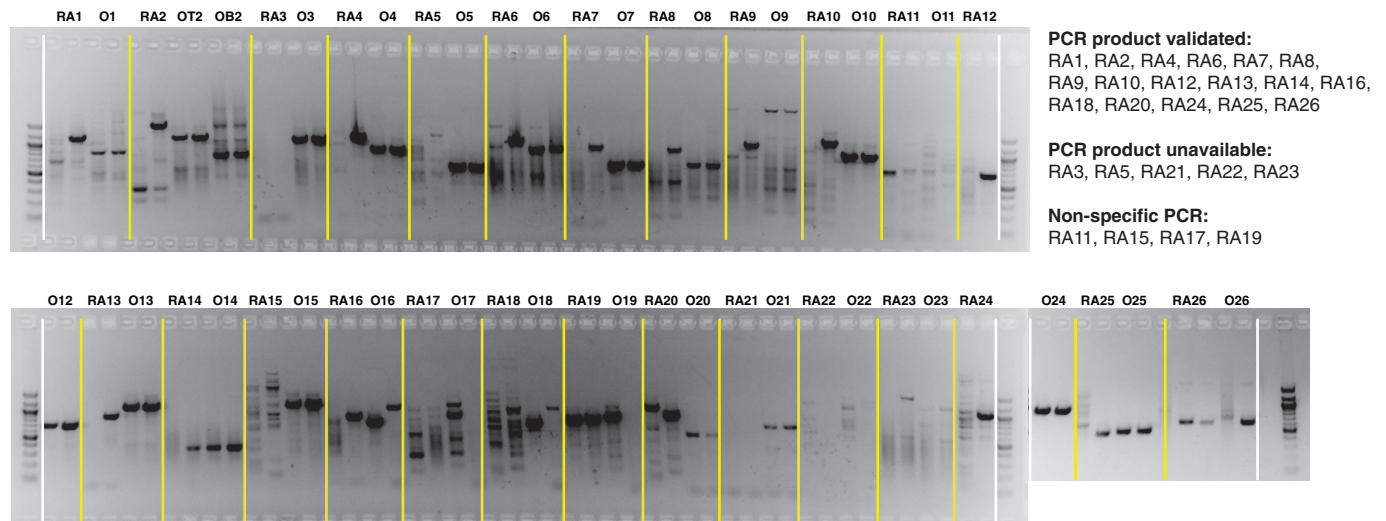


Extended Data Figure 5 | Length distribution of structural variants detected in single cells.

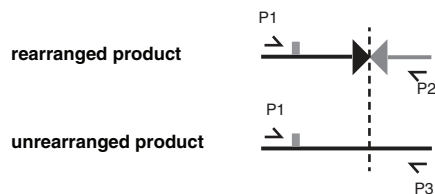
a, Short-range rearrangements in control samples are enriched for the inverted orientation. The number of structural variants (SV) detected in three groups of controls broken down by the distance between the rearranged sequences. Left, p53 knockdown cells (C1-C4); Middle, p53 knockdown + nocodazole release (N1-N6); Right, micronucleated cells (MN1-MN9), but excluding the mis-segregated chromosome. Note a significant enrichment of events in the inverted orientation is observed in the 20–150 kb range in all three groups (binomial test, $P < 0.05$), but there is no such enrichment for SV events with breakpoint distances exceeding 150 kb or joining different chromosomes. The enrichment of short-range inverted type rearrangements can be explained by the fact that Phi-29-based multi-strand displacement (MDA) reaction used to amplify DNA generates frequent short-range inverted chimaeras⁴⁵. **b**, Scaling relationship between the frequency of SVs and the distance between breakpoints in control chromosomes. Left, combined frequency of SVs from all control chromosomes from **a** above. Right, the cumulative distribution of inverted (red dots) or non-inverted (black dots) SV events as a function of breakpoint distance. Note, the graph shows the accumulation from infrequent long-range rearrangements (starting on the right) to more frequent short-range rearrangements (finishing on the left). We expect that genuine rearrangements should equally favour inverted or non-inverted orientations and attribute the bias towards the inverted-type to MDA artefacts. Thus, as a filter for potential MDA artefacts, we used power-law scaling to identify the breakpoint distance above which inverted and non-inverted type rearrangements occur with approximately equal frequency. In the 20–100 kb range, the data for inverted-type rearrangements (632 events total) were best fit by a power law decay of $-1.176 (\pm 0.006, 95\% \text{ confidence interval})$ and for the non-inverted type rearrangements (85 events total) by a power law decay of $-0.395 (\pm 0.005)$. This difference is lost in the range of 200 kb–5 Mb, where the data for inverted-type rearrangements (53 events total) were best fit by a power law decay of $-0.337 (\pm 0.02)$ and for the non-inverted type events by a power law decay of $-0.31 (\pm 0.005)$. The power law fitting for the inverted-type events in the 20–100 kb range and the power law fitting for events in both groups in the 200 kb–5 Mb range (-0.322 ± 0.007) intersected at ~ 150 kb. This established an operational cut-off of 150 kb to define 'long-range' rearrangements, above which there should be no enrichment of inverted-type MDA-generated

artificial chimaeras. **c**, Scaling relationship between the frequency of SVs and the distance between breakpoints in mis-segregated chromosomes. Left, frequency of SVs from all mis-segregated chromosomes. By contrast with the controls in **b**, there is a marked enrichment of long-range SVs in this group with breakpoints > 500 kb apart. Indeed, the frequency of long-range rearrangements in these samples is substantially higher than the frequency of short-range rearrangements. The fact that these SVs are concentrated on the mis-segregated chromosome in the plus daughter cell (Fig. 3b, Extended Data Table 1) suggests that these are genuine rearrangements of the under-replicated chromosome from the micronucleus. Considering only the mis-segregated chromosome, we find a less pronounced difference in the ratio between inverted and non-inverted type rearrangements, even for short-range events. We speculate that this occurs because the mis-segregated chromosome also has a high frequency of genuine short-range rearrangements that are not biased to be in an inverted orientation. These numbers could also reflect a smaller sample size of rearrangements or possibly be due to rearrangement of the damaged chromosome before amplification, altering the relationship of the starting sequence relative to the reference genome. By establishing the 150 kb cutoff to filter for artefacts, we thus likely exclude some genuine short-range events. Finally, we note that our power law scaling analysis for SVs detected in the mis-segregated chromosomes is consistent with other independent estimates for the likelihood of intrachromosomal contacts. The power law dependence of $\sim l^{-0.10}$ (power decay -0.105 ± 0.003 from all events in the range of 150 kb ~ 5 Mb) is equivalent to a density distribution of $p(l) \approx l^{-1.10}$. This dependence is close to the length distribution of somatic copy number alterations ($\sim l^{-1}$) observed in cancers⁴⁶, and also to the distribution of breakpoint distances for somatic chromosomal rearrangements (J. Wala & R. Beroukhir, personal communication). Moreover, it is consistent with the probability of intrachromosomal contacts ($\sim l^{-1.03}$) inferred from Hi-C experiments⁴⁷. The distribution of the long-range breakpoint distances from the mis-segregated chromosomes shown here (150 kb ~ 10 Mb) is significantly different from the distribution of rearrangements from all control chromosomes, shown above in **b** ($P = 0.0043$, Kolmogorov–Smirnov test). By contrast, pairwise comparisons of the distribution of the control samples (**a**, above) showed no significant differences ($P = 0.6$ for all events, $P = 0.9$ for long range events, K-S test).

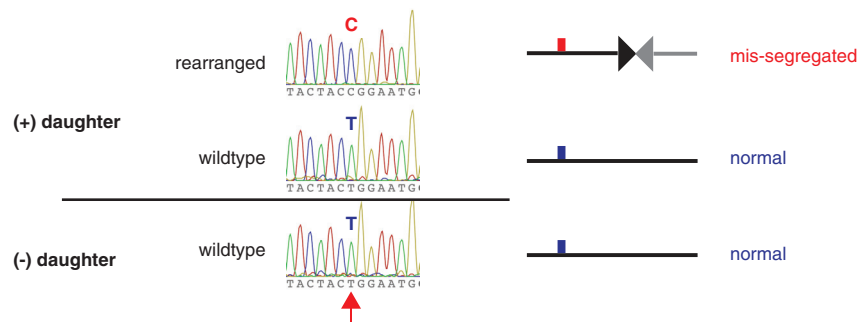
a PCR validation of 26 rearrangements detected in MN3



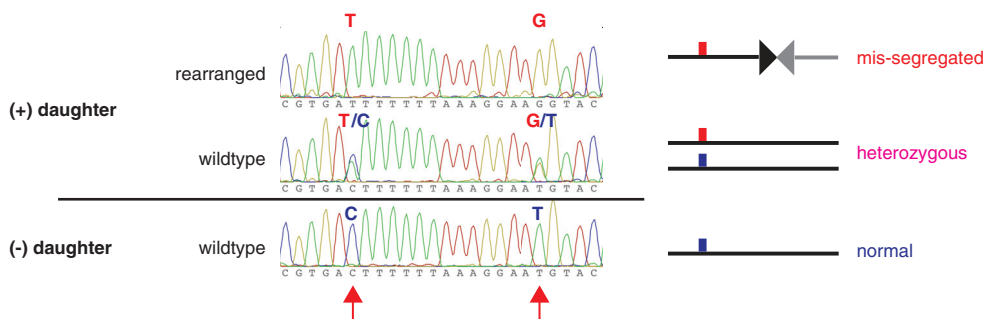
b Phasing of de novo variants



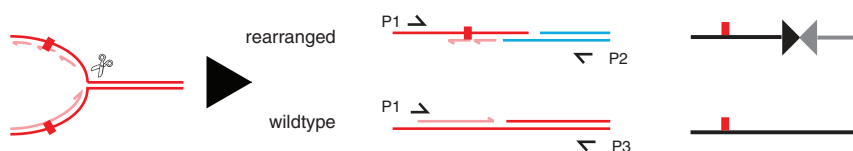
c MN3 (RA6): chr.3:36,860,129(+)--178,169,444(-)



d MN4 (RA8): chr.3:175,282,177(+)--157,520,782(+)



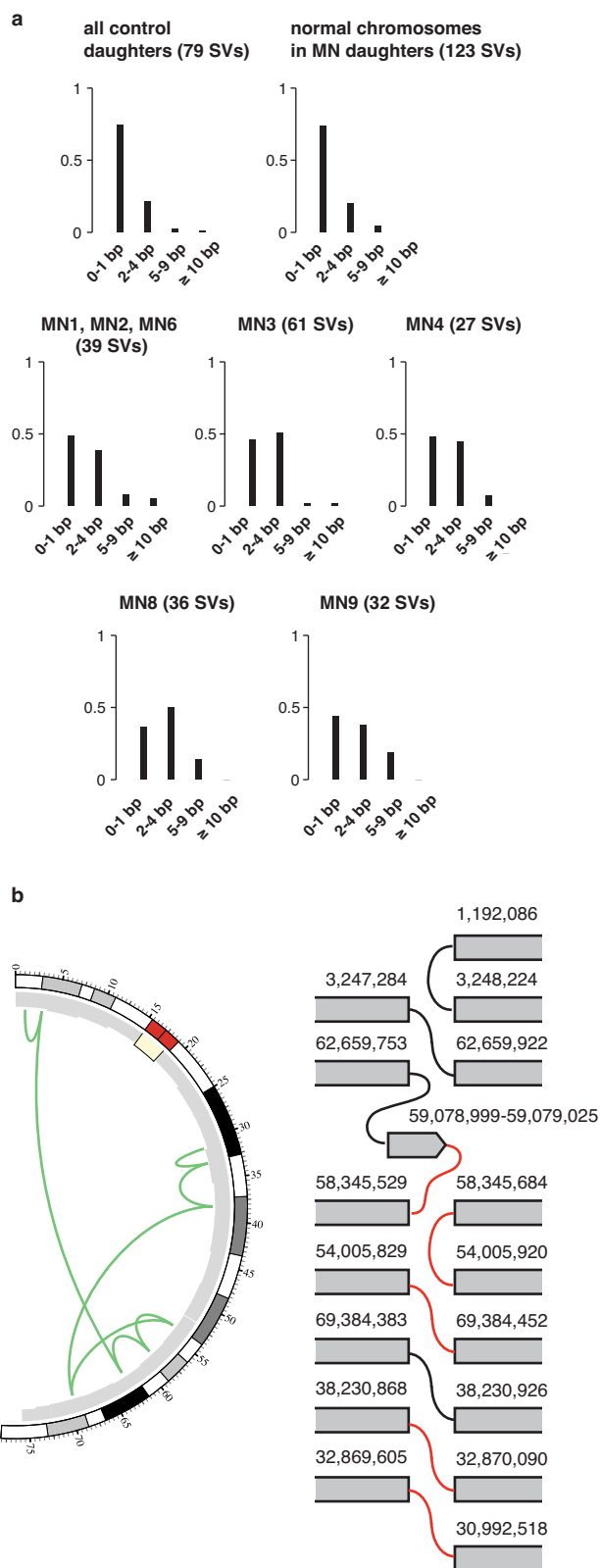
e



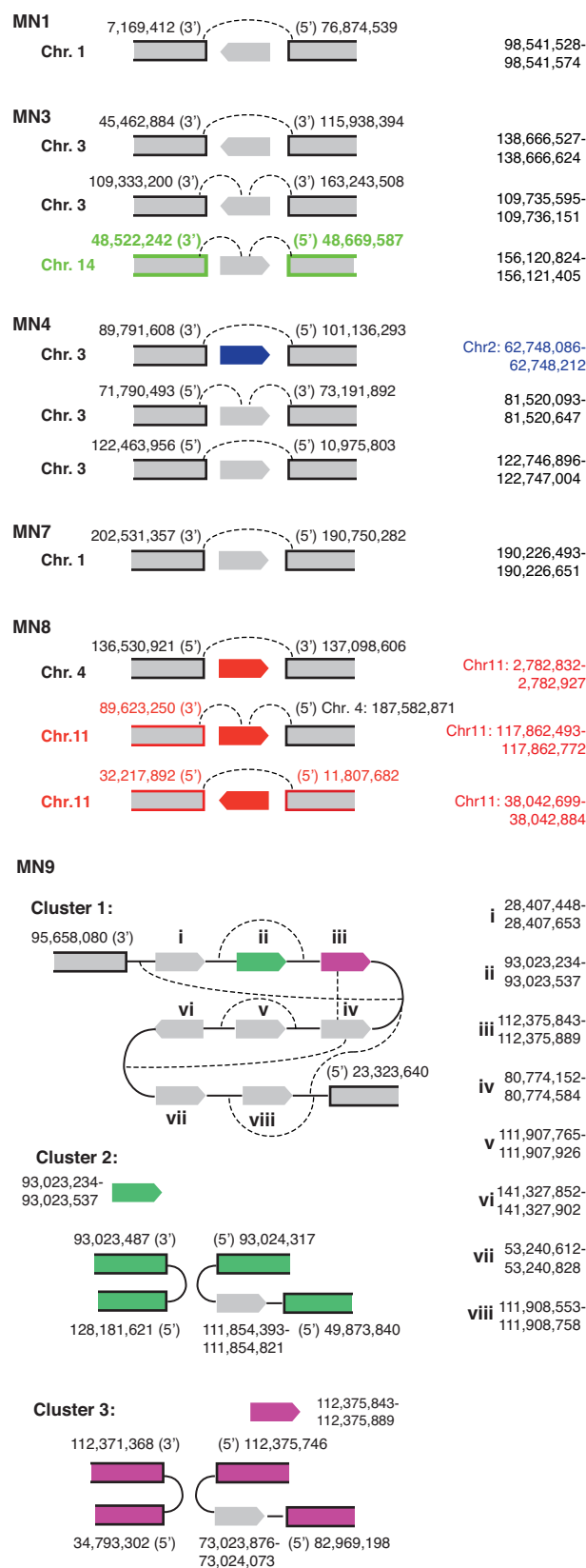
Extended Data Figure 6 | Validation of rearrangements by PCR and haplotype phasing.

a, PCR validation of 26 (out of 66) intrachromosomal rearrangements detected in Chr. 3 of the MN3 plus daughter. The complete results for all samples are summarized in Supplementary Table 5 with examples of the Sanger sequencing results shown below (**c**, **d**). For each rearrangement, two PCR reactions ('RA' across the putative rearrangement junction, 'O' for the reference sequence) were performed on the MDA amplified DNA from both daughter cells. For each sample indicated above the gel, the leftmost lane is the PCR product for the rearrangement-specific primers in the minus daughter; the left middle lane the rearrangement-specific primers in the plus daughter; the right middle lane, the reference-specific primers in the minus daughter; and the right lane, the reference-specific primers in the plus daughter. In 'RA2' where there are heterozygous SNPs on both ends of the rearrangement junction, PCR was performed to generate (and have validated) the genotypes at both sites ('OT2' and 'OB2'). 17 out of 26 PCR products confirmed the rearrangement junction after Sanger sequencing. The remaining 9 PCR reactions generated no product or products that did not correspond to the rearrangement sequence; several of these were due to low sequence complexity near the rearrangement junction that resulted in non-specific primer pairs. **b**, Cartoon showing the strategy for validating rearrangements and associating these rearrangements with the mis-segregated haplotype. Forward PCR primers were chosen 5' from an informative heterozygous site and reverse primers were chosen 3' of the rearrangement breakpoint junction, either in the rearranged DNA sequence or in the reference DNA sequence. PCR was performed to amplify both the rearranged product and the control reference genome product, followed by Sanger sequencing. Here the undetermined base at the polymorphic site is colored grey. **c**, Example of haplotype validation for a rearrangement in MN3 based on an adjacent 'C/T' SNP. From the minus daughter, we were only able to amplify the reference product, which showed a 'T' at the polymorphic site. Because MN3 underwent a 2:1 segregation, the mis-segregated haplotype was inferred to have a 'C' at this polymorphic site. From the plus daughter, we amplified both the rearranged and reference products. As expected, the rearranged showed a 'C' at the polymorphic site, indicating that the rearrangement occurred on the mis-segregated chromosome. Also as expected, there was a 'T' at the polymorphic site on the reference product. The base associated with the mis-segregated haplotype is in red; the base for the normal haplotype is in blue. **d**, Example of haplotype validation for a rearrangement in MN4 yielding three products. In this case, there are two informative polymorphic sites near the rearrangement: the 'T+G' pair is associated with the mis-segregated haplotype and the 'C+T' pair is associated with the intact

reference haplotype. As expected, the minus daughter had the reference product showing the 'C+T' haplotype. Also as expected, the plus daughter had the rearranged product showing the 'T+G' haplotype as well as the reference product showing the 'C+T' haplotype. Somewhat unexpectedly, the plus daughter also had a third product, a reference product associated with the 'T+G' mis-segregated haplotype. We speculate that the presence of both rearranged and reference products with the mis-segregated haplotype results from partial replication of this region of the mis-segregated chromosome. **e**, Proposed partial replication/replication fork breakage model to explain the presence of three products detected in **d** above. Shown on the left is a replication fork on the mis-segregated chromosome, in the middle are the products of replication or recombination, and on the right are the products with the red bar indicating that the products are associated with the mis-segregated haplotype. The original DNA strands are in dark red; the newly synthesized ones are in light red; DNA from a distal rearrangement partner locus is in blue. We hypothesize that breakage of the replication fork (scissors) generates a single-end break that recombines with the distal locus shown in blue. The other end of the replication fork generates a reference product. Importantly, both products should contain the base(s) associated with the mis-segregated haplotype. The presence of both rearranged and reference products containing the mis-segregated haplotype could also occur if the rearrangement is an artificial chimera that arose during MDA amplification. However, such artefacts should not be restricted to a single homologous chromosome: the highly significant enrichment of rearrangements on the mis-segregated chromosome and their association with the mis-segregated/gained haplotype establish that most of these rearrangements are genuine. Notes: 1. Rearrangements were not only associated with the mis-segregated haplotype by PCR, but in some cases this association could be made directly by sequencing read-based phasing using either discordant read pairs or split reads that covered heterozygous SNP sites close to either side of the breakpoint. This analysis enabled us to determine the haplotype association for 10 events in MN3 (3 in addition to Sanger sequencing), 5 events in MN4 (3 in addition to Sanger sequencing), and 6 events in MN8 (5 in addition to Sanger sequencing), all confirmed to be associated with the gained haplotype. 2. For the daughters with a 3:2 segregation pattern, even if the plus cell contained an intact copy of the mis-segregated chromosome, we expect a replicate of this homologue to be present in the minus cell because that copy of the homologue was normally segregated. Because we did not detect any rearrangements in the minus cell, the rearrangements detected in the plus daughter can only come from the mis-segregated copy of the homologue in that daughter.



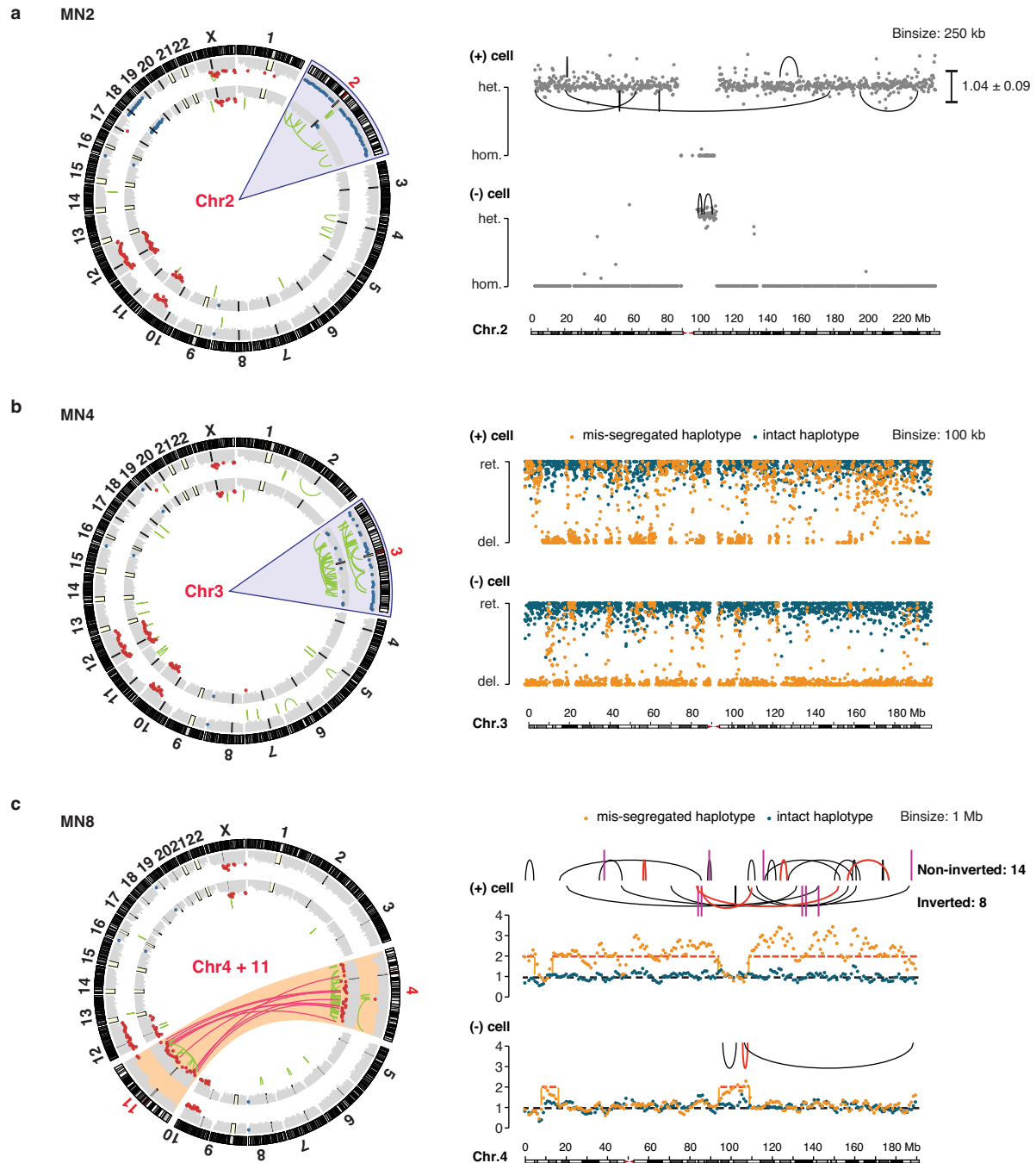
c Short insertions at rearrangement junctions



Extended Data Figure 7 | Sequence features at the rearrangement junctions.

a, Length distribution of microhomology at the junctions of rearrangements in control chromosomes (top), in the mis-segregated chromosomes of daughters with 2:1 segregations (middle), and in the mis-segregated chromosomes from daughters with 3:2 segregations (bottom). The distribution of microhomology at rearrangement junctions detected in all control daughters is indistinguishable to that detected in the control chromosomes in the micronucleated daughters, with ~75% of events showing 0–1 bp homology. By contrast, rearrangements in the mis-segregated chromosomes contain a higher percentage of microhomology: more than 50% of all events exhibited >1 bp homology in every sample. **b**, Chained translocations between breakpoints on Chr. 18 in the MN6 plus daughter. Left, CIRCOS plot for the translocation chain in Chr. 18; Right, translocation links between 16 breakpoints, 14 of which had paired break ends forming a chain. All events were validated by PCR, and red links reflect rearrangements that were associated to the gained haplotype through nearby SNPs (Supplementary Table 5). **c**, Examples of short (50–500 bp) insertions at breakpoint junctions. Insertions are represented as arrows pointing along the 5'→3' orientation of the reference sequence with coordinates shown on the right. Dashed links represent read pairs supporting the given junction. In addition to insertions derived from the mis-segregated chromosome and inserted into rearrangements in the mis-segregated chromosome, we identified additional examples as follows: For the MN3 sample we identified one example of Chr. 3 insertion into a rearrangement between two loci in (normally segregated) Chr. 14. For the MN4 sample we also identified one example where a short segment from (normally segregated) Chr. 2 was inserted into a rearrangement between loci in the mis-segregated Chr. 3. For the MN8 sample, where both Chr. 4 and Chr. 11 were inferred to have been fragmented in the same micronucleus, we identified one example where a rearrangement between loci on Chr. 4 contained a 95 bp insertion from Chr. 11

in the rearrangement junction and another example of a 279 bp segment originated from Chr. 11 inserted into a Chr. 4–Chr. 11 rearrangement junction. In MN9, we have identified >20 insertions at sites of long-range rearrangements on Chr. 8 via local sequence assembly (Supplementary Table 6). Here we show one translocation junction containing 8 short segments from all over Chr. 8. The segments at the boundaries of the rearrangement are in bold outline. Between the boundaries are 8 short insertions (47–433 bps, grey, green or purple bars) from different parts of Chr. 8 (cluster 1). Green and purple bars indicate insertions originating at or near breakpoints of other rearrangements (clusters 2 and 3, correspondingly green or purple). As the average detection sensitivity was ~35% for each library (Supplementary Table 1), it is likely that some insertions could have been missed. Importantly, the insertions only come from distal sites on the mis-segregated chromosome(s) and such insertions are not detected in any control samples. Notes: 1. We can only determine the presence of insertion sequences <500 bp as most sequencing fragments are shorter than 600 bp (99% of fragments are shorter than 600 bp in the DNA library of the MN9 plus daughter, <513 bp for the MN1 plus daughter, <380 bp for the MN3 plus daughter, MN4 daughters, MN8 plus daughter, and <350 bp for the MN7 plus daughter). 2. The MN9 sample has many more insertions than the other samples with the inserted segments frequently derived from sequences near other rearrangement breakpoints. The explanation for this is not clear and future work will require experiments of a larger sample size. However, unlike the MN1–MN8 daughters, which were isolated shortly after division of the micronucleated mother, the MN9 plus cell remained arrested for a ~2 day period of time while the minus daughter divided twice. We speculate that the mis-segregated chromosome in the plus daughter from the MN9 daughter pair have undergone MMBIR as part of the mechanism that combined these Chr. 8 fragments. It is also possible that breakpoint ends in the MN9 plus cell could have been fragmented into small segments.



Extended Data Figure 8 | Evidence of chromosomal fragmentation detected from haplotype copy-number analyses in three examples, MN2, MN4, and MN8. **a**, Inference of chromothripsis of Chr. 2 in the MN2 daughters without knowledge of the Chr. 2 haplotype phase. Left, CIRCOS plot. Right, Plot of the heterozygosity coefficients in 250 kb bins, with rearrangement links indicated (above, non-inverted type; below, inverted type). Note that the MN2 daughters underwent a 2:1 distribution of the mis-segregated chromosome, implying that any chromosomal loss generates loss-of-heterozygosity. The heterozygosity plot demonstrates that a pericentric fragment of 2q is partitioned into the minus cell, whereas the remainder of Chr. 2 is in the plus daughter. Chromosomal rearrangements are only observed in heterozygous regions, consistent with heterozygosity originating from the damaged/under-replicated homologue from the micronucleus. Each dot represents the heterozygosity coefficient in a 250 kb bin (~ 50 heterozygous sites per bin). Bins with fewer than 25 phaseable heterozygous sites or showing only 1–2 observed heterozygous sites are not shown. **b**, Haplotype copy number of Chr. 3 in the MN4 daughters (100 kb resolution). Left, CIRCOS plot. Right, Chr. 3 haplotype

copy number in MN4 daughters calculated from the chromosomal haplotype phase derived from the sequence of the MN3 minus daughter. Each dot represents average haplotype copy number in a 100 kb bin: the normally segregated haplotype (blue dots) is equivalently detected in both daughters whereas the fragmented haplotype (orange dots) shows oscillating and reciprocal retention and loss between the two daughters. **c**, Haplotype copy number of Chr. 4 in the MN8 daughters with rearrangement links. The haplotype phase for Chr. 4 was inferred from the sequence of a single cell with Chr. 4 monosomy (Extended Data Fig. 2c). Gains of the mis-segregated haplotype (orange dots) are reciprocal in both daughters; except for one rearrangement in the plus daughter, all detected breakpoints, including both intrachromosomal events (links) and interchromosomal events with Chr. 11 (vertical magenta lines), are restricted to regions of gains in the mis-segregated haplotype. Red links indicate translocations that are associated with the mis-segregated haplotype by informative SNPs near the breakpoints; black links indicate rearrangements for which phasing validation was not performed (a subset of which have no adjacent SNPs).

Extended Data Table 1 | Summary table of the rearrangements detected in the daughters of micronucleated mothers and their enrichment on the mis-segregated chromosome

Sample	MS Chr.	cell	mean CN of MS Chr.	# of de novo SVs		# of short-range SVs		Poisson test	Fisher's test	PCR validation	haplotype validation
				MS. Chr.	other Chr.	MS. Chr.	other Chr.				
MN1	Chr. 1	(+) cell	2	19	4	3	10	<10 ⁻¹⁰	10 ⁻¹²	7/10	3/3
		(-) cell	1	none	5	none	14				
MN2	Chr. 2	(+) cell	1.7	7	8	0	32	10 ⁻¹⁰	10 ⁻⁸	3/5	2/2
		(-) cell	1.1	2	3	3	40				
MN3	Chr. 3	(+) cell	2	67	12	4	20	<10 ⁻¹⁰	10 ⁻²⁴	17/26	15/15 + 3 [†]
		(-) cell	1	none	1	none	9				
MN4	Chr. 3	(+) cell	1.5	25	12	3	77	<10 ⁻¹⁰	10 ⁻²⁸	10/14	5/5 + 3
		(-) cell	1.2	13	13	5	62				
MN5	Chr. 7	(+) cell	2	1	8	3	17	0.34	0.28		
		(-) cell	1	none	6	none	11				
MN6	Chr. 18	(+) cell	2	5	4	0	21	10 ⁻⁹	10 ⁻⁴	8/8*	5/5
		(-) cell	1	1	20	0	13				
MN7	Chr. 1q	(+) cell	2.9	8	1	1	9	<10 ⁻¹⁰	10 ⁻⁷	3/6	1/1
		(-) cell	2.1	none	5	none	17				
MN8	Chrs. 4 and 11	(+) cell	2.9	36	8	15	51	<10 ⁻¹⁰	10 ⁻²²	7/8	1/1 + 5
		(-) cell	2	3	6	4	23				
MN9	Chr. 8	(+) cell	2.8	41	7	3	29	<10 ⁻¹⁰	10 ⁻²⁸		
		(-) cell	2	1	2	1	20				

MS. Chr., mis-segregated chromosome; CN, copy number. *P* value for enrichment was derived from a one-sided Poisson test of the observed number of rearrangements in the mis-segregated chromosome against the average frequency of rearrangements in the whole genome for each daughter pair. Fisher's test compared the observed numbers of short and long-range rearrangements on the mis-segregated chromosome (both daughters) with the corresponding numbers from the remaining chromosomes in the same daughter cell pair. The enrichment for long-range rearrangements on the mis-segregated chromosomes was highly significant as compared to short-range events, which had no enrichment. PCR validation confirmed the presence of a PCR amplified product and the mapping of the sequence to the two partner loci of the rearrangement (but does not exclude artificial chimaeras); haplotype validation further associated the rearrangement to the gained (mis-segregated) haplotype inferred from haplotype copy number analysis (Extended Data Fig. 3; Methods). Validation results are presented as the number of validated cases divided by the number of total attempts; in haplotype validation, the number of attempts only includes cases where the informative SNP base can be confidently determined by Sanger sequencing that span the rearranged junctions (Supplementary Table 5).

* In the MN6 plus daughter, the standard rearrangement analysis detected five SV events in Chr. 18, three of which were inferred to be in a chain of eight translocations between multiple double-strand breaks. All these eight events were validated by PCR and sequencing, with five out of eight associated to the mis-segregated haplotype. In all statistical analysis of this chromosome (Extended Data Fig. 4b, c) we only counted the five events to ensure consistency with the estimated detection sensitivity.

† We included additional events in the haplotype validation ('+') when the Sanger sequencing was unable to generate the haplotype information, but direct phasing of the rearrangement was possible through supporting short-reads with an adjacent SNP. In both MN3 and MN4 plus daughters, there was one translocation between the mis-segregated chromosome and a different chromosome (see Extended Data Fig. 7c): these events were counted as 'de novo events in the mis-segregated chromosome' although excluding them does not change the statistical analysis.

Small particles dominate Saturn's Phoebe ring to surprisingly large distances

Douglas P. Hamilton¹, Michael F. Skrutskie², Anne J. Verbiscer² & Frank J. Masci³

Saturn's faint outermost ring, discovered in 2009 (ref. 1), is probably formed by particles ejected from the distant moon Phoebe^{2,3}. The ring was detected¹ between distances of 128 and 207 Saturn radii ($R_S = 60,330$ kilometres) from the planet, with a full vertical extent of $40R_S$, making it well over ten times larger than Saturn's hitherto largest known ring, the E ring. The total radial extent of the Phoebe ring could not, however, be determined at that time, nor could particle sizes be significantly constrained. Here we report infrared imaging of the entire ring, which extends from $100R_S$ out to a surprisingly distant $270R_S$. We model the orbital dynamics of ring particles launched from Phoebe, and construct theoretical power-law profiles of the particle size distribution. We find that very steep profiles fit the data best, and that elevated grain temperatures, arising because of the radiative inefficiency of the smallest grains, probably contribute to the steepness. By converting our constraint on particle sizes into a form that is independent of the uncertain size distribution, we determine that particles with radii greater than ten centimetres, whose orbits do not decay appreciably inward over 4.5 billion years, contribute at most about ten per cent to the cross-sectional area of the ring's dusty component.

In the course of mapping the entire sky, NASA's WISE spacecraft⁴ observed Saturn's outer Phoebe ring at a wavelength of $22\text{ }\mu\text{m}$ in June 2010 (Fig. 1). The ring appears in its entirety, spanning an area of sky nearly 7,000 times larger than Saturn itself. Discovered by the Spitzer Space Telescope¹ at wavelengths of $24\text{ }\mu\text{m}$ and $70\text{ }\mu\text{m}$, the Phoebe ring was recently detected at optical wavelengths by Cassini⁵. To highlight the faintest outer material, we suppress the vertical dimension and construct radial traces of the ring in Fig. 2 (Methods). Our measurements show that the ring extends to at least $270R_S$, well beyond the moon Phoebe, which traverses the region $180\text{--}250R_S$. The ring is also clearly seen inward to at least $100R_S$ (Fig. 1a) and to perhaps $50R_S$ (Fig. 1b) before being lost in the glare from Saturn.

To model the ring's structure, we follow the orbital motions of dust grains of multiple sizes launched from Phoebe at different points along its orbit. The most important forces affecting dust in the Phoebe ring are solar radiation pressure and the much weaker Poynting–Robertson drag^{1–3}. Both of these forces arise from interactions with sunlight: the first due to the absorption of solar photons and the second due primarily to the slightly asymmetric re-emission of the absorbed energy⁶. Radiation pressure causes dust grain eccentricities to oscillate with a period of approximately 30 years and is important for grains with radii $s < 100\text{ }\mu\text{m}$. These grains form a distribution that is offset towards the Sun, but still left–right symmetric. Poynting–Robertson drag, although extremely weak, imparts an important systematic inward decay towards Saturn with a characteristic timescale of $1.5 \times 10^5(s)$ years, where s is in units of μm ; hence a 3-cm particle will evolve from Phoebe (with semimajor axis $a = 215R_S$) inward to the moon Iapetus ($a = 60R_S$) over the age of the Solar System¹.

We use the numerical code dI (dust Integrator^{7–11}) to predict the orbits of particles with radii ranging from $4\text{ }\mu\text{m}$ to 10 m released from Phoebe. We launch dust grains with radii of 4, 6, 10, 15, 25, 40, 60 and

$100\text{ }\mu\text{m}$ and with eight different angular positions of Phoebe's pericentre relative to the Sun, an important parameter when radiation pressure is strong. For larger grains, we continue to use five logarithmically spaced sizes per decade in radius, but follow only a single launch condition, as the dynamics of large grains are only weakly affected by radiation pressure. To speed up the integrations, we artificially enhance the rate of Poynting–Robertson drag by a factor ranging from 10 to 450. This results in rapid but otherwise identical orbital evolution as long as the inward drag timescale remains much longer than all other important timescales. We verified that this approximation is valid for our integrations.

We stop the integrations when the dust grains cross the orbit of Titan at $20R_S$ because collisions with that massive satellite occur within $\sim 10,000$ years, far shorter than the timescale for inward migration by Poynting–Robertson drag, even for the smallest particles. Grains with $s > 150\text{ }\mu\text{m}$ remain on fairly low-eccentricity orbits, and so we stop those integrations when they reach Iapetus' orbit—this is an excellent approximation since the inward drag timescale exceeds the Iapetus collision timescale of a few million years. But since the WISE images

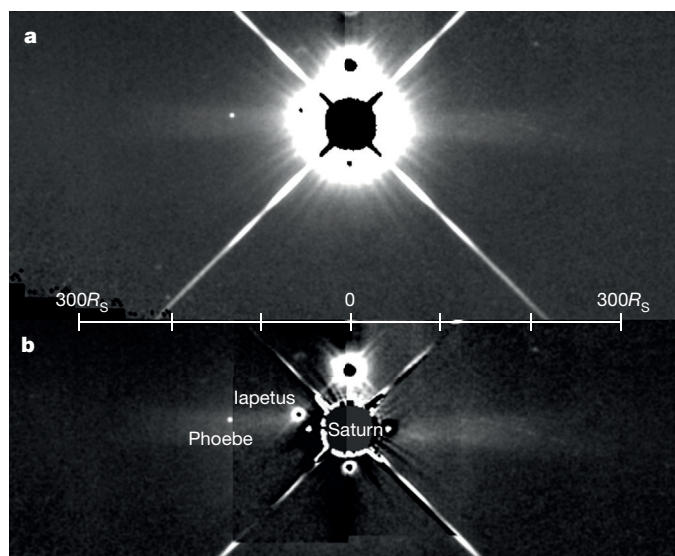


Figure 1 | WISE Band 4 mosaic of the Phoebe ring. **a**, Individual WISE frames manually combined: scattered light from Saturn forms the large white overexposed blob with a black centre while four diagonal diffraction spikes radiate outward. Bright reflections of Saturn are visible as smaller white lumps with black centres at the six and twelve o'clock positions. Iapetus (black dot) and the more distant Phoebe (white dot) are visible at nine o'clock. The Phoebe ring is the white, horizontally oriented $550R_S \times 40R_S$ rectangle. **b**, We subtract $\pm 90^\circ$ rotations of the top frame from itself, yielding clean and cluttered ring ansae (the apparent ends of edge-on rings); here we stitch the two clean ansae together to significantly reduce scattered light and reveal the ring's inner regions. Distance scale applies to **a** and **b**.

¹Department of Astronomy, University of Maryland, College Park, Maryland 20742-2421, USA. ²Department of Astronomy, University of Virginia, Charlottesville, Virginia 22904-4325, USA. ³Infrared Processing and Analysis Center, Caltech, Pasadena, California 91125, USA.

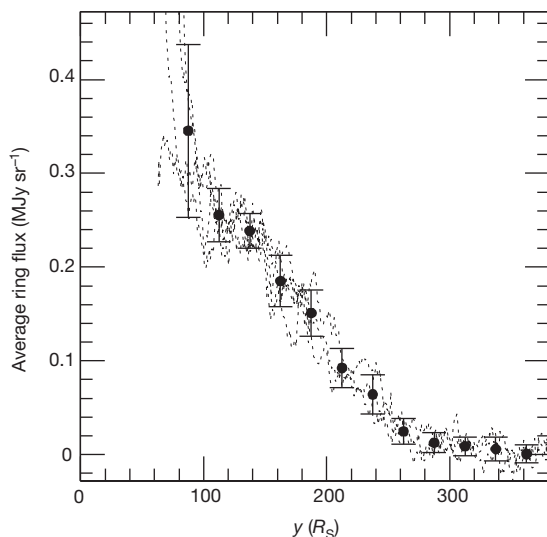


Figure 2 | Measured radial profiles. We sum over 30×40 pixel regions in Fig. 1 and subtract a sky signal as described in Methods to obtain one-dimensional radial profiles from each side of Fig. 1a and b. A fifth curve is derived directly from the WISE Image Atlas. All curves agree to within their intrinsic scatter which provides an important consistency check. Accordingly, the solid black data points with error bars represent the average and the scatter from our five measurements. Ring flux is clearly detectable to at least $270R_S$, well beyond Phoebe's apocentre distance of $250R_S$. All ring profiles agree well inward to about $100R_S$, at which point scattered light from Saturn becomes problematic.

only provide trustworthy fluxes outside about $100R_S$ (Figs 1 and 2), the comparison of data to theory is rather insensitive to the exact details of how the collisional sweeping of Iapetus at $60R_S$ is modelled.

Next, for each simulation we match the WISE viewing geometry by transforming the numerical data (a list of positions versus time for the lifetime of the integration) into a Saturn-centred reference frame that rotates so that the Sun always stays along the x axis. We view this distribution of dust from the direction of the Sun to produce an artificial y - z image on the sky that closely matches the geometry of Fig. 1. We sort the evenly-spaced output from our numerical simulations into line-of-sight bins, sum over the vertical dimension z , and produce predicted profiles of flux versus the y coordinate for each individual grain size whose dynamics we model. For the smallest dust grains, we average the distributions from the eight different Phoebe launch azimuths to get realistic profiles. Finally, we sum together distributions for individual grain sizes with different weighting functions. For simplicity, we assume that particles are continuously created at Phoebe according to a power-law size distribution of the form $N(s)ds \propto s^{-q}ds$, where $N(s)$ is the number of particles of radius s in the range $[s, s + ds]$ and q is the power-law index. This procedure correctly weights the contribution of all particle sizes to the ring flux by explicitly convolving the production function with orbital dynamics including particle lifetimes. The results are theoretical predictions that we normalize to the observed profiles of Fig. 2.

In Fig. 3, we limit particle sizes to the range from $4 \mu\text{m}$, the smallest grains whose orbits are not all immediately forced by radiation pressure onto Titan-crossing orbits, to $100 \mu\text{m}$, roughly the largest size where radiation pressure still matters. All distributions have some difficulty matching the two data points with $y < 120R_S$. These points are the most strongly affected by scattered light from Saturn and by our imperfect subtraction of this scattered light (Fig. 1). Focusing our attention on the more distant points, we note that the steepest power-law distributions ($q = 4$ – 6) fit the data best, highlighting the relative importance of small particles. Such steep particle size distributions are unusual in the Solar System. Nevertheless, steep size distributions of particles launched from Phoebe provide a satisfactory fit to the data.

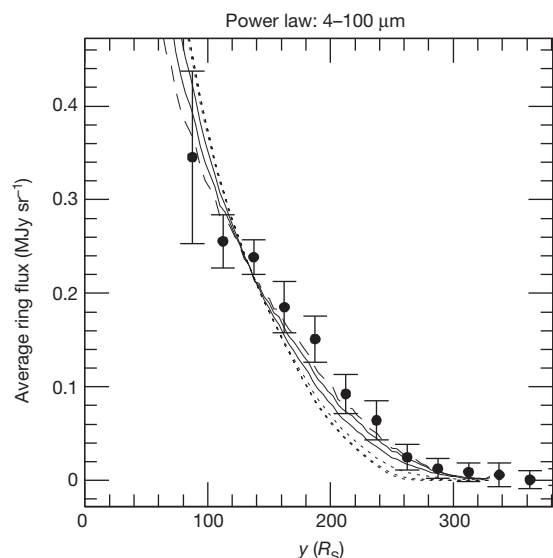


Figure 3 | Theoretical radial profiles for 4– $100 \mu\text{m}$ size distributions. We plot differential power-law particle size distributions with indices $q = 1, 2$ and 3 (dotted lines), 4 and 5 (solid line), and $q = 6$ (dashed line). A $q = 3$ power-law index puts an equal mass of ring particles in each logarithmic size interval; $q = 2$ does the same for surface area. We compute radial profiles for individual particle sizes from our numerical modelling and then combine them with different assumed power-law production rates, normalizing all curves to pass near the data point at $140R_S$. The shallow power-law size distributions (dotted lines) dominated by large particles are a poor match to the data, while steep size distributions more closely match.

As steep power-law distributions are somewhat surprising, we test the effect of the upper cutoff size by raising it above 3 cm , to include ring particles that do not decay inward to Iapetus over the age of the Solar System. For example, 30-cm debris from Phoebe should be confined between $160R_S$ and $250R_S$, perhaps in sufficient quantities to improve the fit of the shallower power-law distributions in that region. In Fig. 4, we extend the size distribution up to 30 cm and find that the shallow power-law distributions, which highlight the contribution of 3 – 30 cm grains, are dramatically affected. Centimetre-sized material produces a ring with a largely empty interior region which, when viewed edge-on, leads to diminished flux close to the planet.

The shallow power-law distributions, however, predict rings that end abruptly at $250R_S$, Phoebe's apocentre, in contrast to the data. Instead of immediately ruling these distributions out, we instead consider relaxing another of our model assumptions. A promising improvement would be to include Phoebe family members (small satellites with Phoebe-like orbital inclinations^{12,13}) as additional sources of ring material. Interestingly, these satellites are all more distant than Phoebe itself. While the known satellites comprise $<1\%$ of Phoebe's cross-sectional area, undiscovered 100-m sized and even kilometre-sized objects could raise this percentage significantly, making this population a correspondingly more important source of ring material. The most relevant effect of these additional sources on the theoretical ring profiles of Fig. 4 would be to raise the predicted ring flux outside $250R_S$ to more closely match the observations.

Two further assumptions might be relaxed. First, the size distribution of particles produced in the ring need not follow a power law, and second, the distribution of particle sizes may be modified by mutual collisions as the material drifts inward towards Iapetus. Collisions are most important for large particles that would otherwise remain in orbit for hundreds of millions to billions of years. Accordingly, shallow power laws with indices of $q = 1$ – 2 , or indeed any other distribution dominated by large particles, would probably evolve towards a more typical collisional distribution with index $q = 3$ – 4 . For these reasons, we continue to favour the steeper size distributions.

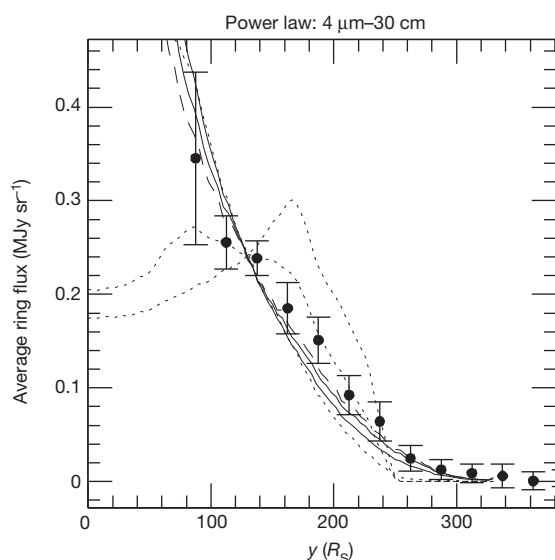


Figure 4 | Theoretical radial profiles for 4 μm –30 cm size distributions. The curves are predictions for assumed differential power-law particle size distributions, as in Fig. 3. Shallow size distributions (dotted lines) predict a ring dominated by large particles, with diminished flux from the ring's interior due to the reduced grain mobility. A distribution with power index $q = 1$, with large particles producing 90% of the observed ring flux, predicts a peak at $170R_S$ that is clearly inconsistent with the data. By contrast, index $q = 2$, with 20% of the flux from 3–30 cm particles, perhaps adequately matches the data, at least interior to Phoebe's apocentre at $250R_S$. Distributions with steeper power-law indices still match the data best.

True particle sizes in the ring, however, are skewed by the enhanced infrared emission of the smallest particles. Because the peak wavelength of a blackbody thermal emission spectrum ($\sim 35 \mu\text{m}$ for $\sim 80 \text{ K}$) is significantly larger than the smallest grains in the ring, these particles emit long-wavelength radiation inefficiently. Thus, the temperatures of small particles rise, more energy is emitted at shorter wavelengths, the emission peak rises and moves closer to the WISE 22 μm band, and the measured flux increases significantly. This drives our best fits towards steeper power-law indices, as the fits actually represent convolutions of the true particle size distribution residing in the ring with the enhanced emission expected from small and relatively hot dust grains.

All of these considerations are suggestive of more complicated size distributions. A broken power law¹⁴ with temperature effects included for the smallest particles would be a logical next step. However, its application is complicated by the fact that the position of the break and the change in the power-law index both depend sensitively on assumptions about the radiating efficiency of the probably irregularly-shaped ring particles. Furthermore, collisions amongst ring particles and with interplanetary debris, sputtering by the solar wind, sand-blasting by

tiny interstellar dust grains, and other unmodelled loss mechanisms are also likely to affect the ring's current particle size distribution. Accordingly, it makes sense to convert the constraints of Fig. 4 into a form independent of any assumed size distribution: we find that soccer-ball-sized and larger rocks ($2s > 20 \text{ cm}$) do not evolve significantly inward over the age of the Solar System and, accordingly, cannot account for more than $\sim 10\%$ of the observed ring flux.

Online Content Methods, along with any additional Extended Data display items and Source Data, are available in the online version of the paper; references unique to these sections appear only in the online paper.

Received 31 October 2014; accepted 2 April 2015.

1. Verbiscer, A. J., Skrutskie, M. F. & Hamilton, D. P. Saturn's largest ring. *Nature* **461**, 1098–1100 (2009).
2. Burns, J. A., Hamilton, D. P., Mignard, F. & Soter, S. in *Physics, Chemistry and Dynamics of Interplanetary Dust* (eds Gustafson, B. A. & Hanner, M. S.) 179–182 (ASP Conference Series, Kluwer, 1996).
3. Tamayo, D., Burns, J. A., Hamilton, D. P. & Hedman, M. M. Finding the trigger to Iapetus' odd global albedo pattern: dynamics of dust from Saturn's irregular satellites. *Icarus* **215**, 260–278 (2011).
4. Wright, E. L. *et al.* The Wide-field Infrared Survey Explorer (WISE): mission description and initial on-orbit performance. *Astrophys. J.* **140**, 1868–1881 (2010).
5. Tamayo, D., Hedman, M. M. & Burns, J. A. First observations of the Phoebe ring in optical light. *Icarus* **233**, 1–8 (2014).
6. Burns, J. A., Lamy, P. L. & Soter, S. Radiation forces on small particles in the solar system. *Icarus* **40**, 1–48 (1979).
7. Hamilton, D. P. Motion of dust in a planetary magnetosphere: orbit-averaged equations for oblateness, electromagnetic, and radiation forces with application to Saturn's E ring. *Icarus* **101**, 244–264 (1993).
8. Hamilton, D. P. Erratum: Motion of dust in a planetary magnetosphere: orbit-averaged equations for oblateness, electromagnetic, and radiation forces with application to Saturn's E-ring. *Icarus* **103**, 161 (1993).
9. Hamilton, D. P. & Kruger, H. The sculpting of Jupiter's gossamer rings by its shadow. *Nature* **453**, 72–75 (2008).
10. Jontof-Hutter, D. & Hamilton, D. P. The fate of sub-micron circumplanetary dust grains I: Aligned dipolar magnetic fields. *Icarus* **218**, 420–432 (2012).
11. Jontof-Hutter, D. & Hamilton, D. P. The fate of sub-micron circumplanetary dust grains II: Multipolar fields. *Icarus* **220**, 487–502 (2012).
12. Gladman, B. *et al.* Discovery of 12 satellites of Saturn exhibiting orbital clustering. *Nature* **412**, 163–166 (2001).
13. Hamilton, D. P. Planetary science: Saturn saturated with satellites. *Nature* **412**, 132–133 (2001).
14. Brooks, S. M., Esposito, L. W., Showalter, M. R. & Throop, H. B. The size distribution of Jupiter's main ring from Galileo imaging and spectroscopy. *Icarus* **170**, 35–57 (2004).

Acknowledgements This publication makes use of data products from the Wide-field Infrared Survey Explorer, which is a joint project of the University of California, Los Angeles, and the Jet Propulsion Laboratory/California Institute of Technology, funded by the National Aeronautics and Space Administration. This research was supported by grants from NASA Outer Planets and Origins (D.P.H.).

Author Contributions F.J.M. led the development of the WISE Image Atlas products and provided optimally background-matched custom mosaics to support this analysis. M.F.S. and A.J.V. did the image processing and data analysis associated with Figs 1 and 2. D.P.H. performed the analytic calculations, ran the numerical models, and produced the theoretical curves of Figs 3 and 4.

Author Information Reprints and permissions information is available at www.nature.com/reprints. The authors declare no competing financial interests. Readers are welcome to comment on the online version of the paper. Correspondence and requests for materials should be addressed to D.P.H. (dphamil@umd.edu).

METHODS

In the course of its all-sky mid-infrared survey, the NASA Wide-field Infrared Survey Explorer (WISE¹) scanned over the position of Saturn 12 times between UT 2010-06-12.85 and UT 2010-06-13.98. Extended Data Fig. 1 shows a subset of the WISE Band 4 (22 μm) 'Level 1B' individual frames that captured ring flux and did not have significant artefacts from Saturn's scattered light. Note that the wavelength of Band 4 has been revised upward from 22.1 μm to 22.8 μm (ref. 15). WISE scanned the sky systematically driven in ecliptic longitude by the steady precession of its orbit of about 1° per day, so from orbit to orbit the position of Saturn shifts several arcminutes across the 47-arcmin-wide frame. Saturn's orbital motion of 1.6 arcmin during the observing period is minor compared with this rate of spacecraft precession. Saturn itself spans only a couple of WISE pixels, so scattered light dominates the 'image' of Saturn on the scale of several arcminutes. In the upper two rows of Extended Data Fig. 1, the bright object embedded in the ring east (left) of Saturn is Phoebe. The ring flux is faint in the individual exposures (~ 3 DN per pixel at 160 Saturnian radii (R_S) compared with pixel-to-pixel RMS noise from the background of 10 DN; DN indicates Digital Number). The ring emission spans ~ 50 pixels in vertical extent and is hundreds of pixels wide, so averaging over the spatial dimension as well as stacking individual frames substantially improves the accuracy of the flux estimate. The pixel scale of the WISE Band 4 Level 1B images is 5.5 arcsec per pixel.

Atlas Images. WISE data products include an Image Atlas that optimally combines Level 1B individual frames into a final calibrated image registered to the celestial reference frame. Given the large spatial extent of the Phoebe ring ($\sim 300R_S$ radius or ~ 40 arcmin), image smearing of the Phoebe ring in the Atlas Images due to Saturn's 1.6 arcmin motion relative to the stellar background is minor compared with extent of the ring flux and small compared with the bins used for fitting of the ring flux in the main text. Two WISE All-Sky Atlas Image fields contain ring flux. In one (1800p030, Extended Data Fig. 2), Saturn lies off the edge of the image and the ring flux is largely uninfluenced by the proximity of Saturn. The adjacent Atlas Image (1784p030) contains Saturn itself, and the excessive flux from the planet caused significant corruption of the faint ring flux and underlying background flux, rendering this automatically generated Image Atlas frame largely useless for determining ring properties.

Custom co-additions. Given the availability of the individual Level 1B exposures contributing to the atlas images, a selection of Level 1B exposures not significantly corrupted by the flux from Saturn itself were offset to compensate for Saturn's motion on the sky and combined with a σ -rejected average to produce another representation of the WISE ring image (Extended Data Fig. 3). In this case, ring flux was reconstructed with fidelity both east and west of Saturn.

Ring flux estimation. Extended Data Fig. 3 shows the region of the ring, as well as background regions above and below the ring, isolated in strips 50 pixels in extent in the latitude direction (perpendicular to the ring). The flux in the ring region was estimated in a series of 8-pixel-wide bins in the longitude direction by calculating the median of the pixel values in each 8×50 pixel region while subtracting the average of the background medians from similar regions above and below the ring. Overall, three ring profiles resulted from extraction from the 1800p030 Atlas Images (ring east side) and the east and west sides of the full image in Extended Data Fig. 3. These profiles are largely independent, as the most significant noise source is the systematic level background offsets resulting from imperfect matching of the offset level in the individual Level 1B frames. These profiles show no evidence of east-west ring asymmetry.

Subtraction of scattered light from Saturn at small radii. The ring profile extractions outlined above suffer from contamination from excess scattered light from Saturn at small separations from the planet. Under the assumption that the scattered light is symmetric about the origin, additional profiles were constructed by rotating the image assembled from the individual Level 1B frames by 90° and subtracting it from itself (bottom half of Fig. 1). Doing so reveals structure (including a clear view of Iapetus) hidden previously by scattered light. The fidelity of this subtraction is only as good as the assumption that the scattered flux is symmetric, since the residual ring profile close to Saturn is a small fraction of the scattered flux being subtracted. Extended Data Fig. 4 shows the result of applying this technique to the bright point source Alpha Tau from the Band 4 WISE Image Atlas. The subtraction is free of significant artefacts that would bias ring flux extraction, and reveals subtle background matching offsets at the 0.2 DN level. Figure 2 contains an east-side and a west-side ring flux extraction from the rotated self-subtracted imagery that partially overlaps the extractions from the wider-field mosaics described above.

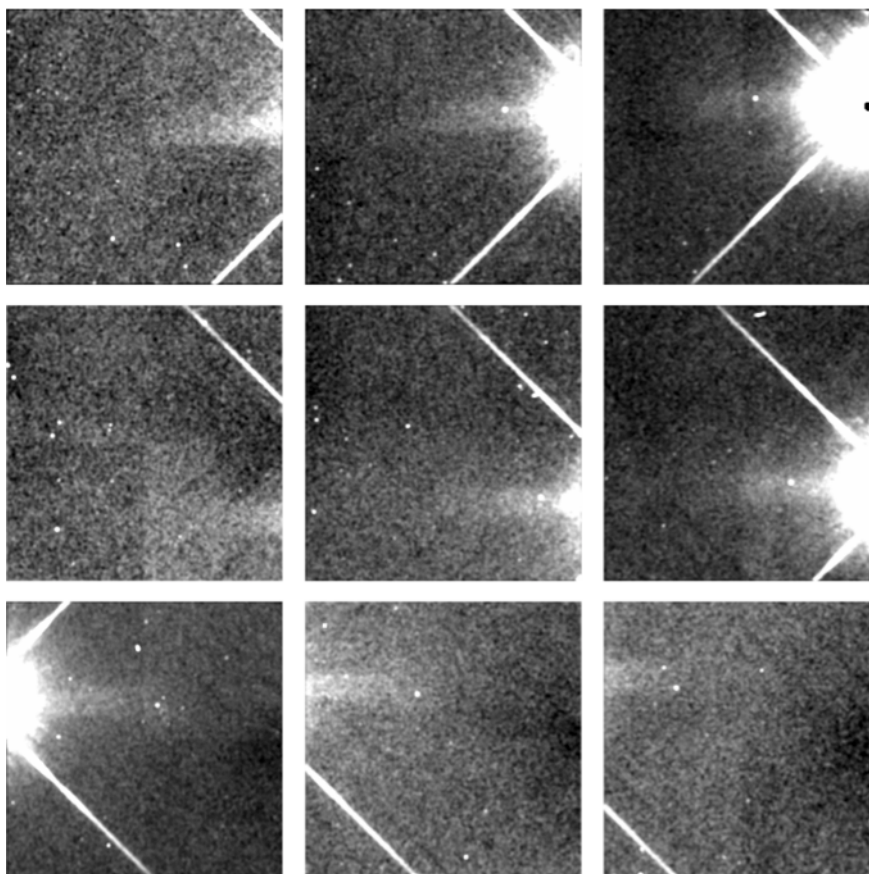
Non-uniform backgrounds. Structure in the background arising from zodiacal dust emission and galactic backgrounds could bias the ring flux measurements described above. Extended Data Figs 5–7 illustrate that the Band 4 background is smooth on the scales addressed here, and that the smooth gradient in background in the ecliptic latitude direction is small compared with the ring flux on the scales that impact the extracted flux. Given that there is a gradient in zodiacal emission increasing from north to south, it is possible that the 90° rotation will shift zodiacal background inappropriately from one ecliptic latitude to another. Fortunately, over the spatial scale of interest the zodiacal emission is nearly constant (becoming largely uniform in the lower portion of the image corresponding to high line number in Extended Data Fig. 6).

Assumptions underlying the model fit. As the ring is optically thin, each point in the radial profile measured in Fig. 2 contains contributions from ring material orbiting at a range of distances from Saturn. We could, in principle, continue to process the data by mathematically removing successive outer layers of ring material to determine the material's intrinsic radial distribution^{16,17}. This approach, however, has two serious disadvantages. First, errors in removing outer layers build up to strongly affect results for the inner layers, especially if the data are relatively noisy as in these WISE images. But even more importantly, the orbits of particles in the Phoebe ring are strongly influenced by radiation pressure and hence expected to be highly elliptical. Thus the distribution of debris in the Phoebe ring deviates from the cylindrical symmetry required by standard data reduction techniques. Accordingly, we choose to proceed by building up entirely theoretical radial profiles of the Phoebe ring to compare directly to the data.

Sample size. No statistical methods were used to predetermine sample size.

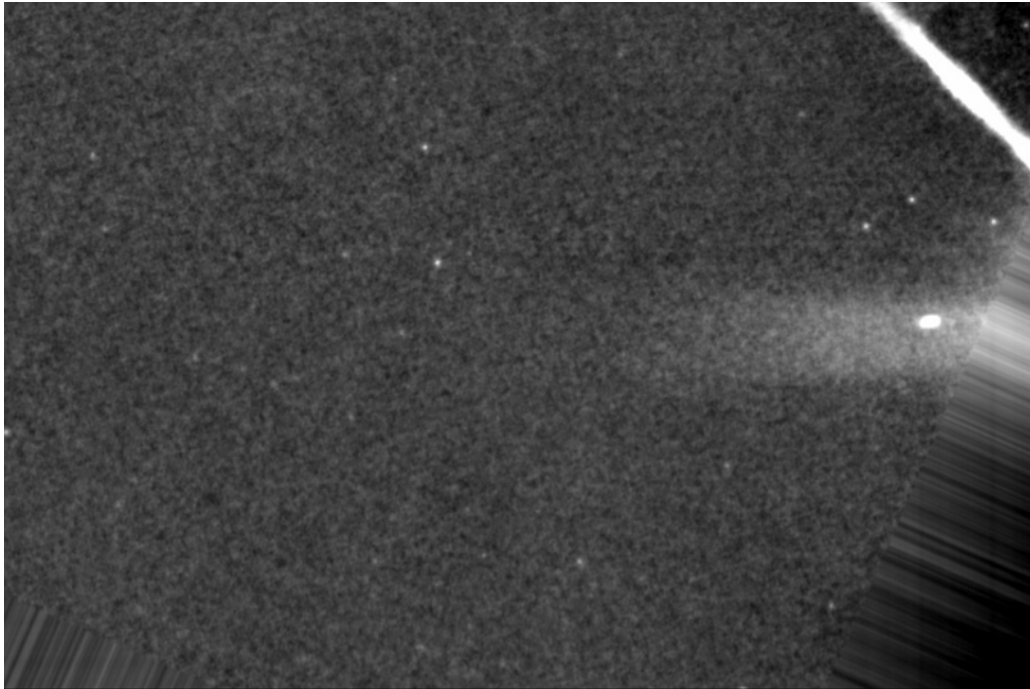
Code availability. We have opted not to make available the numerical codes used to produce Figs 3 and 4, both because the codes were not designed to be easily portable and because we anticipate numerous significant upgrades in the next year.

15. Brown, M. J. I., Jarrett, T. H. & Cluver, M. E. Recalibrating the Wide-field Infrared Survey Explorer (WISE) W4 filter. *Publ. Astron. Soc. Austral.* 31, e049 (2014).
16. Showalter, M. R., de Pater, I., Verbanac, G., Hamilton, D. P. & Burns, J. A. Properties and dynamics of Jupiter's gossamer rings from Galileo, Voyager, Hubble and Keck images. *Icarus* 195, 361–377 (2008).
17. Hedman, M. M., Burns, J. A., Hamilton, D. P. & Showalter, M. R. The three-dimensional structure of Saturn's E ring. *Icarus* 217, 322–338 (2012).



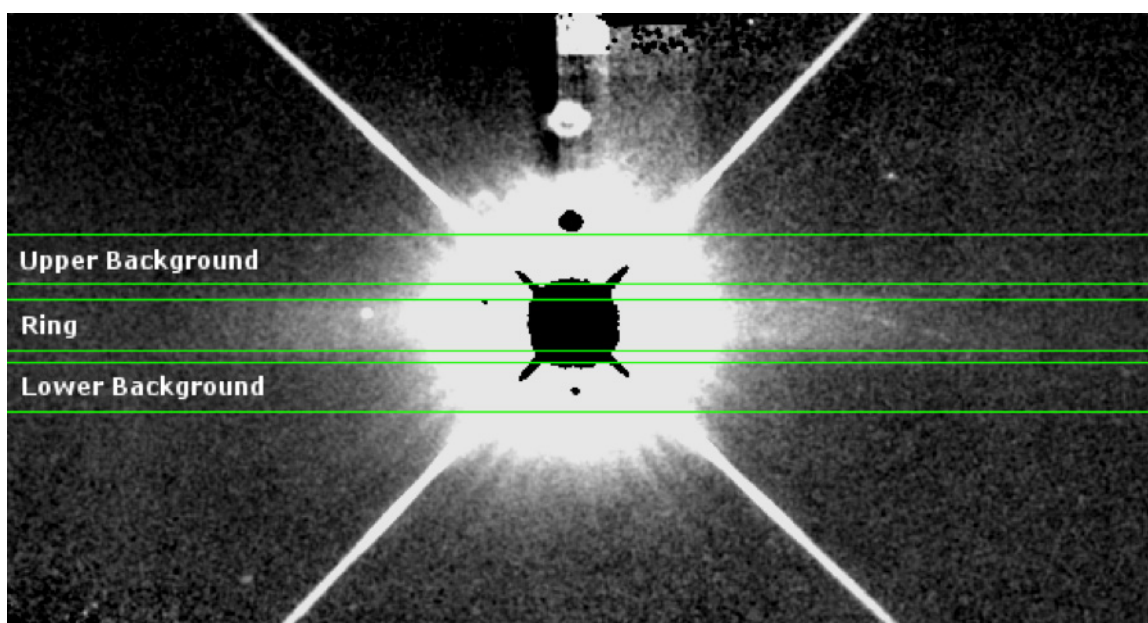
Extended Data Figure 1 | Ring flux in a subset of single (Level 1B) WISE Band 4 ($22\ \mu\text{m}$) exposures. We organize these nine independent images so that each row contains three images centred at approximately the same ecliptic latitude (vertical direction). For each row, spacecraft orbital precession

shifts Saturn in the ecliptic longitude direction so that the planet moves from left to right. The vertical ring extent is about 50 pixels and the horizontal extent exceeds 200 pixels, so even the single exposures can be binned to yield modest signal to noise ratio on the ring.



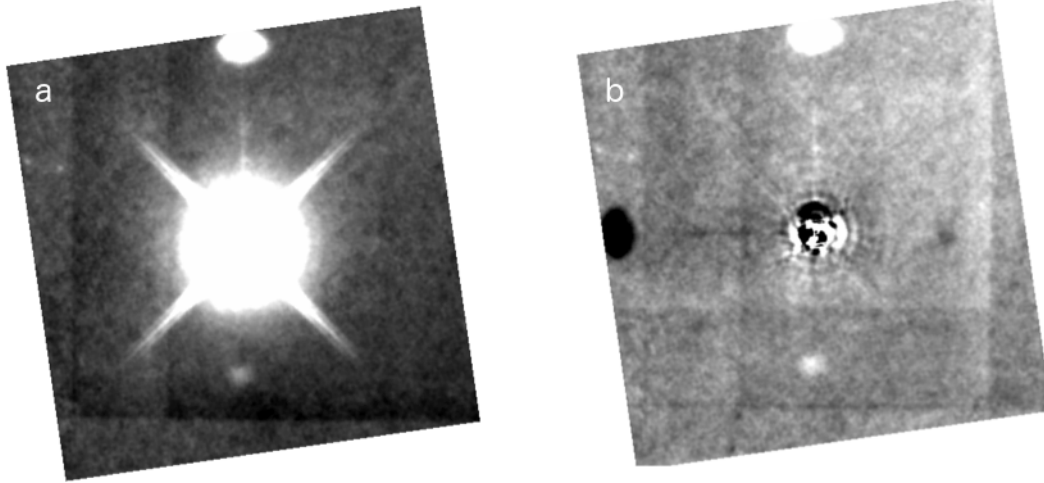
Extended Data Figure 2 | A portion of the WISE Image Atlas frame containing ring emission. The image is rotated so that ecliptic north is up and east is to the left. In this Atlas Image, the bright emission from Saturn is outside the WISE field of view, but one of its diffraction spikes is visible at top

right; processing artefacts to the bottom left and right should be ignored. The ring flux (horizontal stripe) is uncontaminated by Saturn's scattered light, although the orbital motion of Saturn smears the embedded image of Phoebe into a bright oval. The faint point sources are distant stars and galaxies.



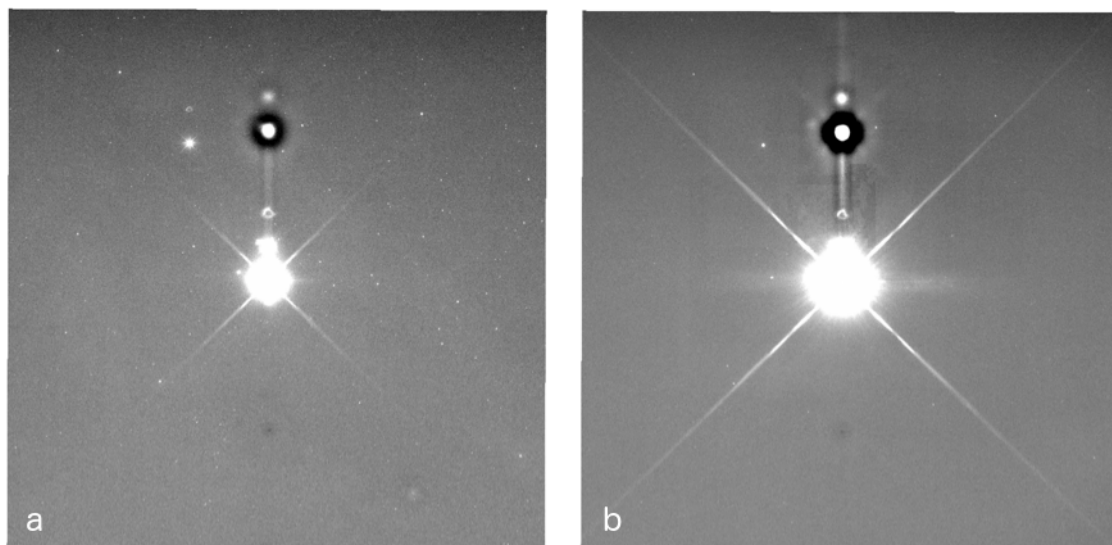
Extended Data Figure 3 | A custom WISE Band 4 mosaic produced from selected Level 1B frames. Each selected Level 1B image was free from significant artefacts from Saturn's scattered light. The frames have been shifted, offset to a common background level and stacked with trimmed average pixel

filtering in Saturn's frame of reference (so that Phoebe, the point source on the east/left side of the ring, appears unsmeared). Ecliptic north is up and east is to the left. Green lines highlight the regions used for flux extraction.



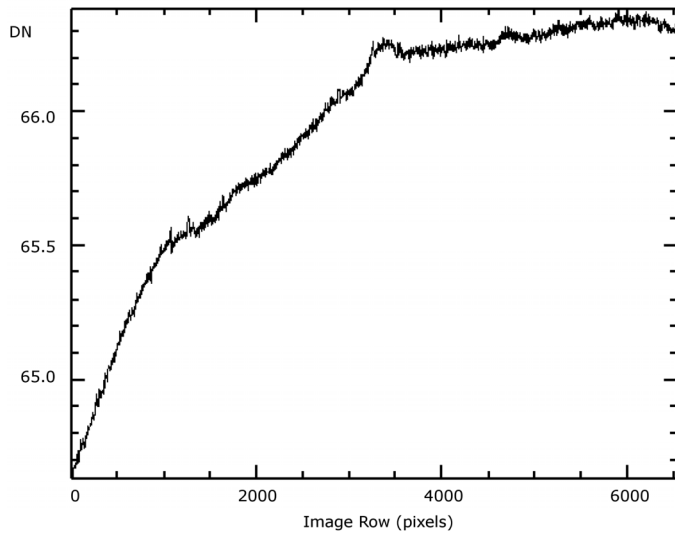
Extended Data Figure 4 | WISE Band 4 images of the star Alpha Tau. **a**, Direct image of the star. **b**, The same image rotated by 90° and subtracted from itself mitigating scattered light. The large blob-shaped artefacts up, down, left and right from the central star are due to the reflection of starlight from the telescope's internal structure. Significant artefacts from azimuthally

asymmetric scattered flux near the star, by contrast, are not evident in the subtracted image **b**. Residuals after subtraction arise largely from frame offset mismatch and are typically of order 0.2 DN in the image in **b** (compared with 3 DN for the ring flux at $160R_S$).



Extended Data Figure 5 | Examination of background structure. **a**, A WISE Band 3 ($12\ \mu\text{m}$) optimally frame-matched mosaic oriented in ecliptic coordinates with north up and east to the left. **b**, Band 4 ($22\ \mu\text{m}$) optimally frame-matched mosaic. The ring is evident in the middle of the Band 4 image,

extending left and right horizontally from the central white over-exposed image of Saturn. The backgrounds are largely uniform, especially in Band 4, with the exception of a north–south gradient characteristic of zodiacal dust emission. Ring flux is not obviously evident in the $12\ \mu\text{m}$ Band 3 exposure.



Extended Data Figure 6 | Quantitative analysis of Band 4 background gradient in units of DN. This figure plots the average background level in DN (vertical axis) row-by-row (horizontal axis) in the Band 4 image shown in Extended Data Fig. 5. The analysis region slightly overlaps the ring flux, which appears as the small bump around line 3300 and establishes the ring plane. The sense of the rotation used in the 90° subtraction carries flux from line numbers 3500–4000 into the ring midplane. Because the DN values are so similar, the bias introduced by the rotation is no greater than 0.1 DN while the inner ring flux is of order 6 DN.



Extended Data Figure 7 | Colour composite of the Phoebe ring. Mosaics of images in WISE Bands 2, 3 and 4 (4.6, 12 and 22 μm) comprise the composite image in ecliptic coordinates. North is up and east is to the left. Scattered light

from Saturn forms the bright white circle at the centre of the image and the ring is the faint horizontal bar that cuts across Saturn.

Small-scale dynamo magnetism as the driver for heating the solar atmosphere

Tahar Amari¹, Jean-François Luciani¹ & Jean-Jacques Aly²

The long-standing problem of how the solar atmosphere is heated has been addressed by many theoretical studies, which have stressed the relevance of two specific mechanisms, involving magnetic reconnection and waves, as well as the necessity of treating the chromosphere and corona together^{1–7}. But a fully consistent model has not yet been constructed and debate continues, in particular about the possibility of coronal plasma being heated by energetic phenomena observed in the chromosphere^{2,3,8–11}. Here we report modelling of the heating of the quiet Sun, in which magnetic fields are generated by a subphotospheric fluid dynamo intrinsically connected to granulation. We find that the fields expand into the chromosphere, where plasma is heated at the rate required to match observations (4,500 watts per square metre) by small-scale eruptions that release magnetic energy and drive sonic motions. Some energetic eruptions can even reach heights of 10 million metres above the surface of the Sun, thereby affecting the very low corona. Extending the model by also taking into account the vertical weak network magnetic field allows for the existence of a mechanism able to heat the corona above, while leaving unchanged the physics of chromospheric eruptions. Such a mechanism rests on the eventual dissipation of Alfvén waves generated inside the chromosphere and that carry upwards the required energy flux of 300 watts per square metre. The model shows a topologically complex magnetic field of 160 gauss on the Sun's surface, agreeing with inferences obtained from spectropolarimetric observations^{12–14}, chromospheric features (contributing only weakly to the coronal heating) that can be identified with observed spicules⁹ and blinkers^{10,11}, and vortices that may be possibly associated with observed solar tornadoes⁸.

Much work has been devoted to the magnetic properties of the Sun's atmosphere, including the interpretation of the polarization observed in some spectral lines^{12–14} and advanced magnetohydrodynamic (MHD) simulations^{15–18}. Of particular interest is the conclusion¹², obtained through a plasma diagnostic technique based on the Hanle effect in atomic and molecular lines and supported by studies based on the Zeeman effect^{13,14}, that the quiet solar photosphere is teeming with a topologically complex, small-scale magnetic field which carries a substantial amount of magnetic energy density, more than sufficient to dominate the overall energy balance of the Sun's atmosphere. As for the MHD studies, some of them^{17,18} describe atmospheric dynamical and heating effects resulting from the interaction of imposed photospheric motions with magnetic fields computed from longitudinal magnetograms of active regions. Other calculations try to include the upper part of the convection zone, but they generally find a dynamo that is too weak¹⁶, perhaps due to the numerical difficulty of modelling a compressible dynamo in a domain open to an atmosphere.

We use an MHD model designed to address the problem of the heating of the quiet-Sun atmosphere, assuming that the source of energy is the above-mentioned small-scale magnetic field. More precisely, we deal with the issue of identifying a mechanism for converting that source of energy into heat², but we do not consider here the

thermodynamic and radiative response of the plasma. In our model, the magnetic field is assumed to be created by a subsurface small-scale dynamo¹⁹ operating in the upper 1.5 Mm of the convection zone. This thin layer, in which the plasma is taken to obey incompressible Boussinesq MHD equations¹⁹, is coupled with an atmospheric region (described by a different set of MHD equations²⁰) that comprises a photosphere and a chromosphere of respective thickness 500 and 1,500 km, as in the actual Sun, and a corona extending up to 15 Mm. The coupling between both regions is performed through an interface at which the lower solution provides boundary conditions for the upper one²⁰. The atmosphere is taken to be initially at equilibrium (Extended Data Fig. 1) and its temperature is kept constant in time—a reasonable assumption given our specific aim. Technical details are given in the Methods section.

We follow the evolution of the coupled system for a time long enough (140 min) to cover many cycles of life and death of the granulation cells (about 8 min for a cell) that develop in the lower layer and induce the dynamo process. When amplification saturates, the self-consistent magnetic field we obtain on the solar surface has a very significant horizontal component (Fig. 1a), in contrast with earlier current-free results²¹. We obtain mean values of 160 and 28 G, respectively, for its strength and vertical component, which is in agreement with both observational values inferred from the polarization in some spectral lines^{12–14} and theoretical values found in the most recent compressible dynamo simulations^{22,23} (see Methods). The field appears to be organized at the granulation scale (that of fluid motions). But it also exhibits more persistent (with a lifetime of 30 min) mesoscale magnetic flux concentrations (Supplementary Video 1) that play an important role in the system evolution and appear to be associated with the bright points observed in H α (ref. 24). We call them 'mesospots', by analogy with active region sunspots. A key quantity for our purpose is the time averaged Poynting flux, whose divergence controls the transfer of energy from the magnetic field to the plasma. This flux, which can be used as a heating input in mean atmospheric models, is found to be consistent (Fig. 1b) with the flux required¹⁰ at the base of the chromosphere (4,500 W m⁻²) and at the transition region (300 W m⁻²).

Besides these mean values, one needs to explain the observed magnetic complexity of the chromosphere and transition region^{4,10,25}. In our model this complexity is driven by the resistive emergence of structures from the subsurface dynamo. The magnetic field that emerges consists of interwoven flux tubes anchored to the photosphere, with many bifurcations (Fig. 1c) and with typical sizes increasing with height (Fig. 1d–g). Its topology is therefore complex, with the chromosphere being split into many magnetic cells delimited by singular surfaces, the so-called separatrices⁶. The magnetic structures emerge with strong twist and shear, and later on suffer additional deformations driven by the surface velocity field. Intense electric currents flow across the magnetic lines and along them, with the parameter α (measuring the ratio of the parallel electric current to the magnetic field strength) being maximal in the chromosphere (Extended Data Fig. 2). In particular, as clearly seen in the lowest parts

¹Centre de Physique Théorique, Ecole Polytechnique, CNRS, F-91128 Palaiseau Cedex, France. ²AIM – Unité Mixte de Recherche CEA – CNRS – Université Paris VII, UMR no. 7158, Centre d'Etudes de Saclay, F-91191 Gif sur Yvette Cedex, France.

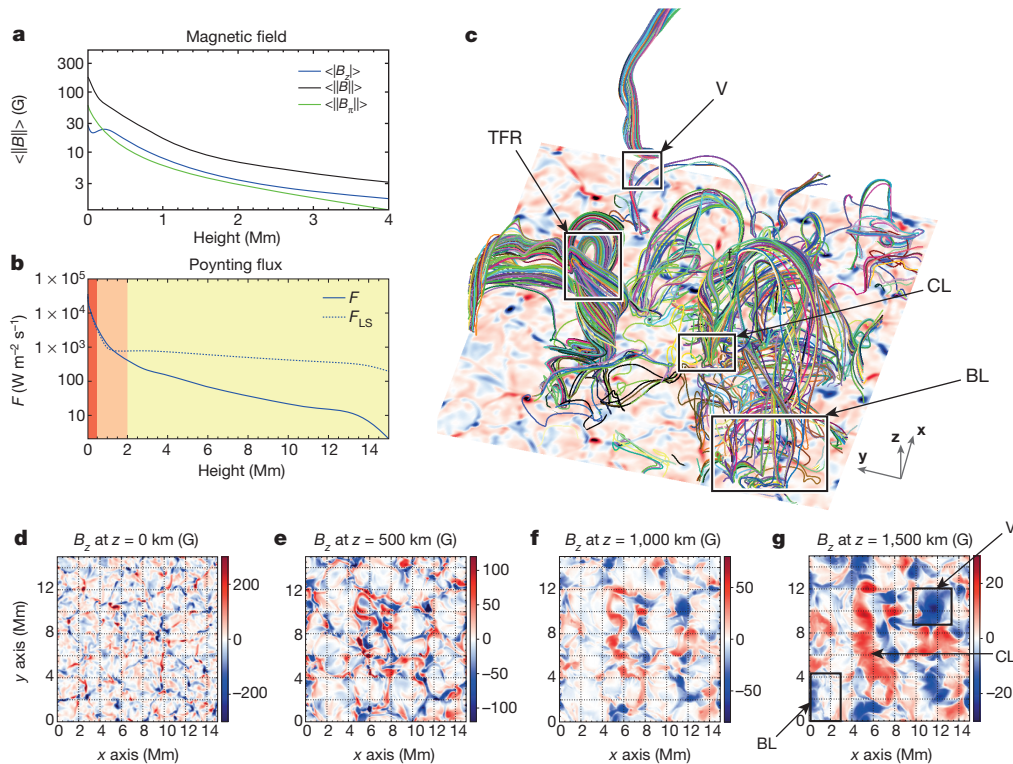


Figure 1 | Magnetic field and Poynting flux. **a**, Intensity of the total (black line), vertical component (blue) and current-free (green) magnetic field. **b**, Time averaged Poynting flux in the photosphere (red shading), chromosphere (orange) and corona (yellow) computed without (blue) and with (dashed blue) the presence of the large-scale vertical magnetic field (mimicking the supergranulation network). **c**, Selected field lines of the global magnetic configuration at time $t = 52.17$ min and characteristic features of its complex topology: a vertical twisted flux tube associated with a core of vortices/torsional motions (boxed area V), a twisted flux rope (TFR), and features that characterize the connection of the magnetic flux tubes to the photosphere, namely concentrated legs (CL) and bifurcating legs (BL). **d–g**, Horizontal cuts of the vertical component of the magnetic field in the low photosphere (**d**, also background image in **c**), at the bottom of the chromosphere (**e**), and in the middle (**f**) and high (**g**) chromosphere.

of Fig. 2a–c and Supplementary Videos 2 and 3, electric currents strongly concentrate near the separatrices, which appear as current sheets. Because of the presence of all these currents, the magnetic energy is far above the energy of the associated current-free magnetic configuration (see Fig. 1a and Extended Data Fig. 3), which has the smallest magnetic energy compatible with the flux distribution on the photospheric boundary.

Chromospheric heating results in our model from the occurrence of many small eruptions triggered by reconnection. A part of the available magnetic free energy is converted by these events into kinetic energy of the plasma, which is viscously dissipated into heat (resistive dissipation adds only a weak contribution), and a quasi-stationary regime sets in where the local (time averaged) rate of magnetic energy dissipation is equal to that of energy injection from regions underneath. The

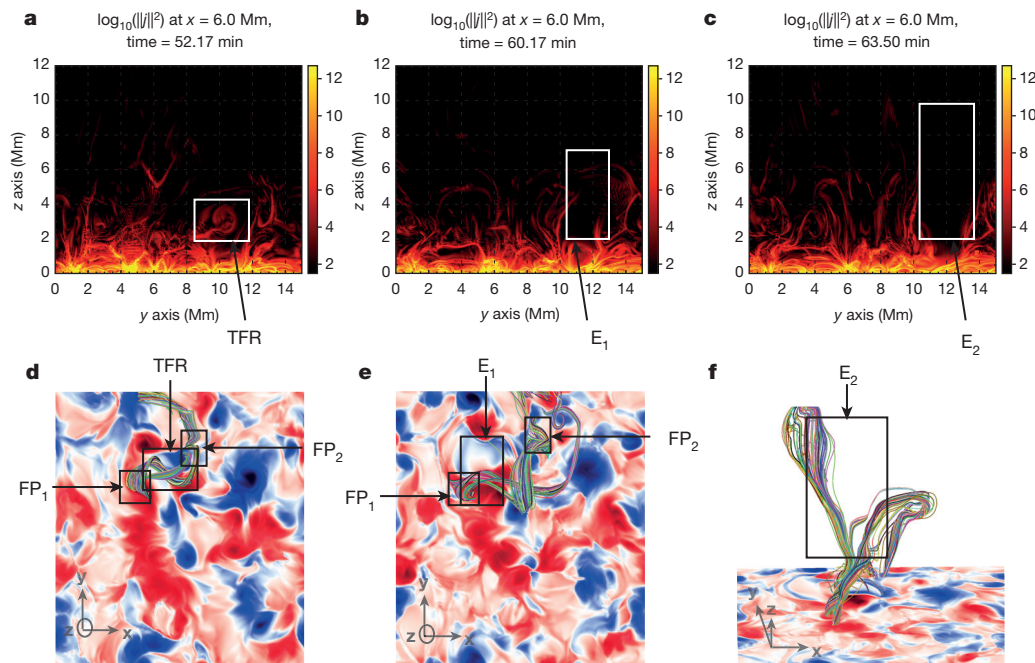


Figure 2 | Twisted flux rope eruption. **a–c**, Vertical cuts at constant x of the logarithm of the square of the modulus of the electric current density (expressed in non-dimensional code units). **a**, The TFR section (boxed) clearly shows that its eruption is associated with opening of the configuration, with current layers structuring the atmosphere at those heights and above (see Supplementary Video 3). **d–f**, Selected field lines showing the evolution of the TFR seen in Fig. 1c, starting from the same time (52.17 min). The background image represents the vertical component of the magnetic field at $z = 1,500$ km, which appears to be organized in stronger ‘spots’ and can reach locally 30 G. **d, e**, The chromospheric trace of the TFR is associated with footpoints FP_1 and FP_2 . Flux changes occur at its chromospheric ‘feet’ FP_2 as seen from **d** to **e**. They imply topological constraints leading to the eruption of the TFR shown at two particular times in boxes E_1 and E_2 drawn in **e** and **f**, respectively.

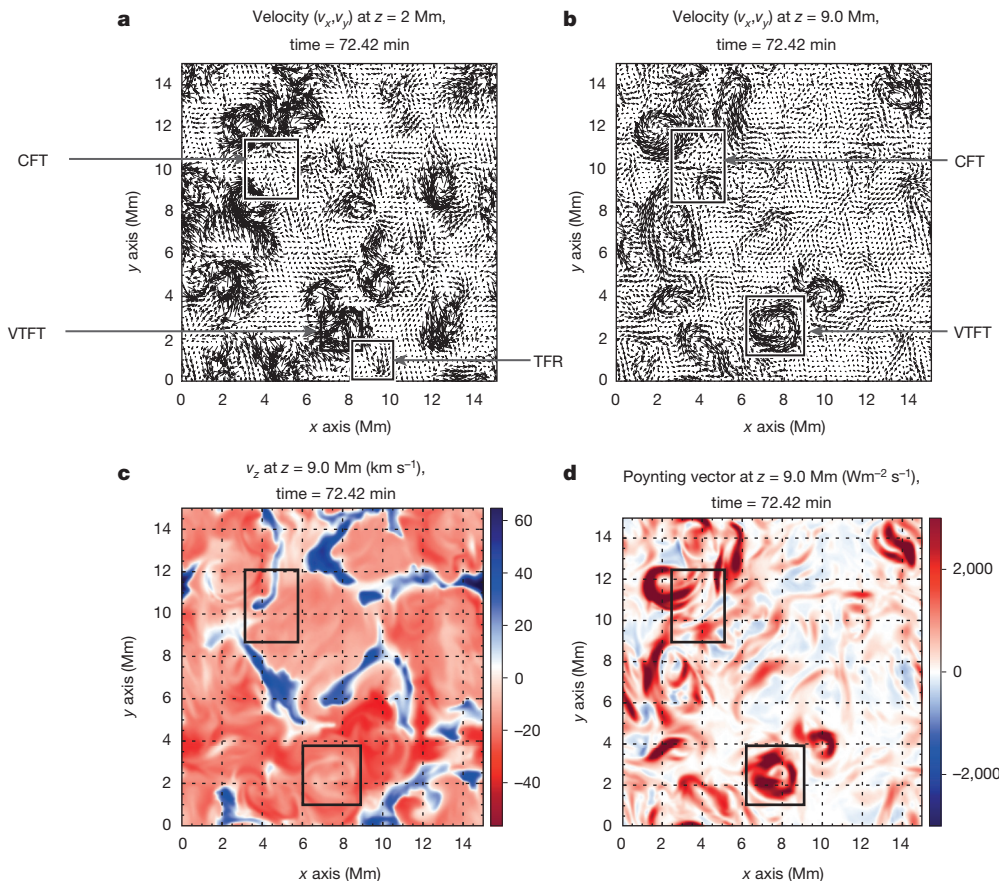


Figure 3 | Torsional motions and Poynting vertical flux. **a, b,** Horizontal slice of the horizontal component of the velocity field at two heights showing persistence of vortex/torsional motions with altitude when the vertical background field of 5 G is added. **c,** Horizontal slice at the same heights as in **b** of the vertical component of the velocity field associated with jet-like features forming in the regions free of vortices near the separatrices. **d,** z -component of the Poynting vector computed at the same heights as in **b**. There is clearly a

correlation between the regions where it takes its largest values and the vortex/torsional motions shown in **a** and **b**. A large amount of energy is transported towards the upper corona through Alfvén waves. The labelled boxes show characteristic magnetic features: twisted flux rope (TFR), cusped flux tube (CFT) with coronal streamer-like shape, and vertical twisted flux tube (VTFT) guiding Alfvén waves.

characteristic timescale for the disruption of magnetic structures is the same as the one associated with their creation—namely, the turbulent cell turnover time, of the order of 8 min. Eruptions are driven in particular by flux annihilation (see Supplementary Video 1), clearly acting on the 8 min timescale, which produces a rapid change in the magnetic topology and a decrease in the confinement of the tubes. As the plasma pressure is larger on average than the magnetic pressure in the chromosphere (while being smaller inside the tubes), magnetically driven fluid motions remain confined, and magnetic energy relaxation acts as a local source, as does the ‘mechanical flux’ used in standard atmospheric models. Moreover, the released energy should also be radiated quite locally owing to the weak thermal conductivity.

Our model also predicts the heating of a thin coronal layer located above the region where plasma and magnetic average pressures become comparable and the complexity of the magnetic field decreases. Coherent structures that are no longer confined generate emerging motions by expanding into the region above. In fact these structures are already present at 1.5 Mm above the surface, where they appear as coherent magnetic flux tubes with a width of about 1–2 Mm and a mean intensity of about 20 G (Fig. 1g). The physics is dominated by the relatively stable mesospots, at the periphery of which dynamical current sheets structuring the plasma are persistently created (as clearly seen in Fig. 2a–c and Supplementary Video 3). Eruptions in the neighbourhood of the mesospots are triggered by mechanisms (for example, flux cancellation) similar to those at work in large-scale eruptive events²⁶ (see Fig. 2d–f), and they lead to plasma ejection at

Alfvénic speed inside structures that can be associated with the ones generically called ‘blinkers’ by observers^{10,11} (see Methods). Backward motions occur through vortices centred on the mesospots that spiral downwards to the surface (areas V in Extended Data Figs 4 and 5), with associated horizontal and vertical velocities that can be as large as 40 km s^{-1} and are then consistent with those observed on the real Sun^{8,27}. The energy so released leads eventually to plasma heating up to a few Mm above the chromosphere in a way that must be strongly dependent on the details of the transport, radiation and dissipation mechanisms, unlike in the chromosphere.

We have thus demonstrated numerically that the heating of the chromosphere and of a thin coronal layer can be consistently explained by our surface dynamo driven model. But in our model the bulk of the corona cannot be heated by eruptions of chromospheric origin, which is in agreement with recently discussed ideas². To also provide an explanation for this heating, the model is now extended by introducing a new ingredient: the existence in the quiet-Sun atmosphere of magnetic loops reaching much higher altitudes than the surface dynamo generated field⁴. These loops are created by a deeper dynamo and their photospheric footpoints are anchored in the supergranulation network. Here we take the existence of this additional field into account by superposing on our model a weak (5 G) magnetic field that is initially vertical and uniform. Owing to the chosen low value, neither the small-scale dynamo^{19,28} nor the chromospheric processes described above are significantly perturbed (see Methods). The magnetic structure resembles that of the well known Mangrove ecosystem on Earth,

with many ‘roots’ diving into the spaces between the granules, and ‘tree trunks’ going towards the corona (Extended Data Fig. 6). But a notable change appears in the corona. In the vertical magnetic flux tubes above each mesospot, Alfvén waves with relatively large lifetime (30–50 min) are generated and propagate upwards (see Fig. 3). They carry a positive Poynting flux (about 300 W m^{-2} at 10 Mm) that is well correlated with the vortices (Fig. 3), and they eventually leave the computational box. This flux is larger than the one obtained without background field (Fig. 1b), which is a clear consequence of the inhibition of turbulent motion dissipation by the presence of coherent flux tubes. The waves are associated with perpendicular and parallel motions analogous to those recently observed²⁴. Perpendicular motions are inhomogeneous, which favours their dissipation through the creation of small length scales. Energy transported by the waves has to be eventually absorbed by the coronal plasma through some specific mechanism, which of course cannot be described by our MHD model¹.

New interesting dynamic features appear, but they do not contribute to coronal heating except very near the bottom of the corona. We find in particular that short lived thin jets (with thickness 200 km and velocity up to 60 km s^{-1} ; see Fig. 3) are launched in the current sheets surrounding the flux tubes associated with mesospots (see Extended Data Fig. 6 and Supplementary Videos 4 and 5 for our calculations, and Supplementary Video 6 for observations). They result from eruptions triggered between the tubes by mechanisms identical to those described above (see Methods). We conjecture that they are associated with type II spicules^{9,29}, a statement that gains support from the fact that the values of the total magnetic field found in our model around 1.5 Mm ($\sim 30 \text{ G}$) are of the order of the averaged observed values, which can reach a maximum of 45 G (ref. 30). The global picture that emerges from our model, where we have localized Alfvén waves transported by magnetic structures reaching higher and higher altitudes and surrounded by jets, is fully consistent with recent observations²⁹.

Online Content Methods, along with any additional Extended Data display items and Source Data, are available in the online version of the paper; references unique to these sections appear only in the online paper.

Received 20 December 2014; accepted 15 April 2015.

- Klimchuk, J. A. On solving the coronal heating problem. *Sol. Phys.* **234**, 41–77 (2006).
- Klimchuk, J. A. Key aspects of coronal heating. *Phil. Trans. R. Soc. A* **373**, 20140256 (2015).
- De Pontieu, B. *et al.* The origins of hot plasma in the solar corona. *Science* **331**, 55–58 (2011).
- Wedemeyer-Böhm, S., Lagg, A. & Nordlund, A. Coupling from the photosphere to the chromosphere and the corona. *Space Sci. Rev.* **144**, 317–350 (2009).
- Priest, E. R., Heyvaerts, J. F. & Title, A. M. A flux-tube tectonics model for solar coronal heating driven by the magnetic carpet. *Astrophys. J.* **576**, 533–551 (2002).
- Parker, E. N. Magnetic neutral sheets in evolving fields. I. General theory. *Astrophys. J.* **264**, 635–641 (1983).
- McIntosh, S. W. *et al.* Alfvénic waves with sufficient energy to power the quiet solar corona and fast solar wind. *Nature* **475**, 477–480 (2011).
- Wedemeyer-Böhm, S. *et al.* Magnetic tornadoes as energy channels into the solar corona. *Nature* **486**, 505–508 (2012).
- Pereira, T. M. D., De Pontieu, B. & Carlsson, M. Quantifying spicules. *Astrophys. J.* **759**, 18–34 (2012).
- Aschwanden, M. J. *et al.* The coronal heating paradox. *Astrophys. J.* **659**, 1673–1681 (2007).
- Subramanian, S. *et al.* What is the true nature of blinkers? *Astron. Astrophys.* **538**, A50 (2012).
- Trujillo Bueno, J., Shchukina, N. & Asensio Ramos, A. A substantial amount of hidden magnetic energy in the quiet Sun. *Nature* **430**, 326–329 (2004).
- Lites, B. *et al.* The horizontal magnetic flux of the quiet-Sun internetwork as observed with the Hinode spectro-polarimeter. *Astrophys. J.* **672**, 1237–1253 (2008).
- Danilovic, S., Schüssler, M. & Solanki, S. K. Probing quiet Sun magnetism using MURaM simulations and Hinode/SP results: support for a local dynamo. *Astron. Astrophys.* **513**, A1 (2010).
- Martinez-Sykora, J. *et al.* Spicule-like structures observed in three-dimensional realistic magnetohydrodynamics simulations. *Astrophys. J.* **701**, 1569–1581 (2009).
- Abbett, W. P. The magnetic connection between the convection zone and corona in the quiet Sun. *Astrophys. J.* **665**, 1469–1488 (2007).
- Bingert, S. S. & Peter, H. Intermittent heating in the solar corona employing a 3D MHD model. *Astron. Astrophys.* **530**, A112 (2011).
- Gudiksen, B. & Nordlund, W. An ab initio approach to the solar coronal heating problem. *Astrophys. J.* **618**, 1020–1030 (2005).
- Cattaneo, F. On the origin of magnetic fields in the quiet photosphere. *Astrophys. J.* **515**, L39–L42 (1999).
- Amari, T., Luciani, J. F. & Aly, J. J. Coronal closure of subphotospheric MHD convection for the quiet Sun. *Astrophys. J.* **681**, L45–L48 (2008).
- Schrijver, C. J. & Title, A. The magnetic connection between the solar photosphere and the corona. *Astrophys. J.* **597**, L165–L168 (2003).
- Vögler, A. & Schüssler, M. A solar surface dynamo. *Astron. Astrophys.* **465**, L43–L46 (2007).
- Rempel, M. Numerical simulations of quiet Sun magnetism: on the contribution from a small-scale dynamo. *Astrophys. J.* **789**, 132 (2014).
- Jess, D. B. *et al.* Alfvén waves in the lower solar atmosphere. *Science* **323**, 1582–1585 (2009).
- De Pontieu, B., Tarbell, B. & Erdelyi, R. Correlation on arcsecond scales between chromospheric and transition region emission in active regions. *Astrophys. J.* **590**, 502–518 (2003).
- Amari, T., Luciani, J. F., Mikic, Z. & Linker, J. A twisted flux rope model for coronal mass ejection and two ribbon flares. *Astrophys. J.* **529**, L49–L52 (2000).
- Hansteen, V. H., Hara, H., De Pontieu, B. & Carlson, M. On redshifts and blueshifts in the transition region and corona. *Astrophys. J.* **718**, 1070–1078 (2010).
- Cattaneo, F., Emonet, T. & Weiss, N. On the interaction between convection and magnetic fields. *Astrophys. J.* **588**, 1183–1198 (2003).
- De Pontieu, B. *et al.* Ubiquitous torsional motions in type II spicules. *Astrophys. J.* **752**, L12 (2012).
- Centeno, R., Trujillo Bueno, J. & Asensio Ramos, A. On the magnetic field of off-limb spicules. *Astrophys. J.* **708**, 1579–1584 (2010).

Supplementary Information is available in the online version of the paper.

Acknowledgements We thank A. L. Ariste for information about measurement heights and values of magnetic fields in the Sun’s photosphere, B. Lites for providing the heights at which the magnetic fields were measured in ref. 13, M. Aschwanden for information about observational properties of loops in the solar atmosphere, and A. Canou for help in dealing with IRIS data. Many thanks go to M. Cheung and Y. Fan for discussion, as well as to A. van Ballegoijen. The numerical simulations performed in this paper were done on the set of computers of the Centre de Physique Théorique (CNRS/Ecole Polytechnique) and of the institute IDRIS of the Centre National de la Recherche Scientifique. We thank the Centre National d’Etudes Spatiales (CNES) for financial support. IRIS is a NASA small explorer mission developed and operated by LMSAL with mission operations executed at NASA Ames Research Center and major contributions to downlink communications funded by the Norwegian Space Center (NSC, Norway) through an ESA PRODEX contract.

Author Contributions T.A. and J.-F.L. planned the various calculations, and discussed the results with J.-J.A. The manuscript was written by T.A., J.-F.L. and J.-J.A.

Author Information Reprints and permissions information is available at www.nature.com/reprints. The authors declare no competing financial interests. Readers are welcome to comment on the online version of the paper. Correspondence and requests for materials should be addressed to T.A. (tahar.amari@polytechnique.edu).

METHODS

Model. Our approach to the global system composed of the upper part of the convection zone (CZ) and the solar atmosphere (SA) rests on the Resistive Layer Model³¹ (RLM). CZ and SA are represented by the two adjacent subregions Ω^{CZ} and Ω^{SA} , respectively, and the magnetized plasma contained in each of them is described by a specific physical model that is detailed below. The two regions are coupled together through a third subregion overlapping them, Ω^{RBL} , where RBL stands for Resistive Boundary Layer. We work here in the plane approximation (the curvature of Sun's surface is neglected), with Ω^{CZ} and Ω^{SA} being taken to be parallelepiped boxes in contact along the plane $\{z = 0\}$ (using Cartesian coordinates (x, y, z)).

It should be noted that similar calculations could also be done, in principle, by replacing either of the two plasma models used here by an alternative (for example, we could describe CZ by a compressible model^{22,23,32} and SA by a model such as Bifrost³³, MURaM³⁴, CO5BOLD³⁵, PENCIL³⁶ or Stagger³⁷).

Upper convection zone model. A subsurface solar dynamo in a closed box has been demonstrated to occur in Boussinesq approximation¹⁹ and more recently confirmed also to occur in compressible MHD^{22,23,32} using a different numerical method as well as different boundary conditions. For simplicity we decided to use the more robust magnetized Boussinesq model for describing the physics in the upper part Ω^{CZ} of the CZ. The incompressible MHD equations are those introduced in a previous paper²⁰. They are as follows:

$$\partial_t \mathbf{v} + \nabla \cdot (\mathbf{v} \otimes \mathbf{v}) = -\nabla \cdot \left[\left(p + \frac{B^2}{2} \right) \mathbf{I} - \mathbf{B} \otimes \mathbf{B} \right] + \nabla \cdot (\sigma \nabla \mathbf{v}) + \sigma R_a \theta \hat{\mathbf{z}} \quad (1)$$

$$\partial_t \mathbf{B} = \nabla \times (\mathbf{v} \times \mathbf{B}) - \nabla \times \left[\left(\frac{\sigma}{\sigma_m} \right) \nabla \times \mathbf{B} \right] \quad (2)$$

$$\partial_t \theta + \nabla \cdot (\theta \mathbf{v}) = \mathbf{v} \cdot \hat{\mathbf{z}} + \Delta \theta \quad (3)$$

$$\nabla \cdot \mathbf{B} = 0, \quad \nabla \cdot \mathbf{v} = 0 \quad (4)$$

with equation (1) implying the equation and boundary condition for p :

$$\Delta p = -\nabla \cdot [\nabla \cdot (\mathbf{v} \otimes \mathbf{v})] + \nabla \cdot \left[-\nabla \cdot \left(\frac{B^2}{2} \mathbf{I} - \mathbf{B} \otimes \mathbf{B} \right) + \sigma R_a \theta \hat{\mathbf{z}} \right] \quad (5)$$

$$\partial_n p = -\sigma \hat{\mathbf{n}} \cdot \nabla \times \nabla \times \mathbf{v} + \hat{\mathbf{n}} \cdot \left[-\nabla \cdot \left(\frac{B^2}{2} \mathbf{I} - \mathbf{B} \otimes \mathbf{B} \right) + \sigma R_a \theta \hat{\mathbf{z}} \right] \text{ on } \partial \Omega^{\text{CZ}} \quad (6)$$

These equations are written with appropriate non-dimensionalization and they are set in the numerical box Ω^{CZ} that extends from $\{z = -1\}$ to $\{z = 0\}$ and has horizontal dimensions 10×10 . The notations are as follows: \mathbf{B} is the magnetic field, \mathbf{v} the plasma velocity, p the plasma pressure, θ the temperature deviation with respect to the linear convective profile $T(z) = T_0 + z\Delta T$ (where $T_0 = T(z = -1)$ and $\Delta T = T_0 - T(z = 0)$), σ the Prandtl number, σ_m the magnetic Prandtl number, and R_a the Rayleigh number.

We use third order Adams-Bashford time integration that is implicit for the dissipation terms present in the momentum (1), magnetic (2), and temperature (3) equations. Equations (5) and (6) for the pressure ensure incompressibility of the flow, and they are solved at each time step by an efficient incomplete LU factorization by level preconditioner³⁸. The convective terms are treated by a third order non-oscillatory upwind scheme. The numerical resolution is $287 \times 287 \times 25$ and the spatial discretization uses a staggered mesh in which \mathbf{v} and \mathbf{B} are evaluated on the faces of the cubic cells, while p and θ are evaluated at the cell centres.

For the boundary conditions, which are taken to be periodic in the two horizontal directions, we impose a horizontal seed magnetic field $B_b = 1$ at the boundary $\{z = -1\}$, we set $v_z(z = -1) = v_z(z = 0) = 0$ and we require $v_{x,y}$ to have vanishing vertical derivatives at $\{z = -1, 0\}$. Note that some authors²² impose a vanishing parallel component of the magnetic field on the upper part of the boundary instead of the condition $v_z(z = 0) = 0$. This last is preferred here as it appears to lead to results in better agreement with the observations.

Initially, we choose the magnetic field to be horizontal, with a strength decreasing linearly from B_b at $z = -1$ to zero at $z = 0$, the velocity to vanish, and give to θ a small fluctuating value in order to trigger the convective instability. We use the same regime parameters as previously¹⁹, with $\sigma = 1$, $R_a = 500,000$ and $\sigma_m = 5$. As discussed below, these values enable us to reach a simple regime of low diffusivity where the dynamo is saturated.

Setting of the physical values in the Boussinesq model. This is a key step for obtaining quantitative results. The Boussinesq model¹⁹ is expressed in dimensionless units. As the surface density, the surface temperature, and the gravity are known, we need to fix two physical units (length and magnetic intensity). We found that this can be done accurately by matching the granulation cell size with

typical data, and the r.m.s. horizontal surface velocity with that furnished by three state-of-the-art models³⁹. With a choice of parameters previously used¹⁹, this gives a length unit of 1.5 Mm—therefore the box Ω^{CZ} has physical dimensions $15 \times 15 \times 1.5$ in Mm—and a velocity unit of 30 m s^{-1} , which sets the magnetic field intensity unit to 5.6 G—then the field imposed at the lower boundary has a strength $B_b = 5.6 \text{ G}$. There is no need for any additional arbitrary input. When the dynamo saturates¹⁹, a quasi-stationary magnetic field is reached.

Atmosphere model. To describe the evolution of the plasma in the SA domain Ω^{SA} , we use our code METEOSOL³⁸, which has been exploited extensively for computing coronal magnetic configurations, in particular in the context of large-scale eruptive phenomena such as Coronal Mass Ejections^{26,40–42}. This code solves the resistive compressible MHD equations, written in non-dimensional form,

$$\rho \partial_t \mathbf{v} = -\rho(\mathbf{v} \cdot \nabla \mathbf{v}) + (\nabla \times \mathbf{B}) \times \mathbf{B} - \nabla p + \nabla \cdot (\nu \rho \nabla \mathbf{v}) + \rho \mathbf{g} \quad (7)$$

$$\partial_t \mathbf{B} = \nabla \times (\mathbf{v} \times \mathbf{B}) - \nabla \times (\eta \nabla \times \mathbf{B}) \quad (8)$$

$$\partial_t \rho + \nabla \cdot (\rho \mathbf{v}) = 0 \quad (9)$$

$$\partial_t p + \nabla \cdot (p \mathbf{v}) = -(\Gamma - 1)p \nabla \cdot \mathbf{v} + H \quad (10)$$

$$p = \rho T \quad (11)$$

$$\nabla \cdot \mathbf{B} = 0 \quad (12)$$

Here ρ denotes the mass density, T the temperature, ν the kinematic viscosity, η the resistivity, \mathbf{g} the gravitational field, and H the heating/cooling term. In the computations reported in this Letter, however, we introduce a major change with respect to the initial version of METEOSOL, which was developed for the numerical simulation of low beta plasmas. We discard the energy equation (10), and close the system by requiring the temperature T in equation (11) to keep a time independent profile $T_0(z)$ (Extended Data Fig. 1). This may appear as an oversimplification if one compares with more advanced models^{33–37}, but those too need to make some restrictive assumptions.

The MHD equations are set in the domain Ω^{SA} that has the same horizontal size as Ω^{CZ} and extends vertically from $\{z = 0\}$ to $\{z = 10\}$, thus representing the part of the corona below 15 Mm. The boundary conditions are periodic in the two horizontal directions and absorbing in the vertical one. The boundary conditions at $\{z = 0\}$ are specified below in the subsection 'Optimizing the RLM parameters'. The code uses a staggered Cartesian non-uniform mesh. The spatial discretization of the operators is defined in such a way that magnetic helicity and topology be well conserved in the weakly resistive limit and the constraint $\nabla \cdot \mathbf{B} = 0$ be satisfied to round-off errors. This latter property is crucial to follow an evolution in which the topology evolves rapidly as a consequence of flux changes, as with those arising at the photospheric level in the quiet Sun.

We use the same kind of velocity limiter as previously⁴³. This results in the saturation of large velocities of the order of 100 km s^{-1} . In phenomena such as jets, the velocities may therefore be underestimated by our computations. The resistive equation is solved implicitly. Convective terms are solved using a high order upwind scheme.

In the present study, the model is initialized with a density profile $\rho_0(z)$ solution of the hydrostatic equation. This profile differs slightly from VAL data⁴⁴. The temperature (density) is slightly smaller (larger), and the temperature step near the transition region is smoothed, as in an oscillatory averaged transition region. This leads to a definition of the various layers: photosphere (width 500 km), chromosphere (width 1,500 km), transition region (at 2,000 km above the surface), and corona (Extended Data Fig. 1). It is worth noting that the temperature profile could have been extended above 1 MK. It is saturated here only to simplify the numerical computations.

Finally, we take $\nu = 0.1$ for the viscosity and $\eta = 0.1$ for the resistivity (in our units). The numerical resolution is $287 \times 287 \times 197$.

Coupling the models of the Sun's interior and exterior. The coupling between the domains Ω^{CZ} and Ω^{SA} is done by introducing at their interface a layer Ω^{RBL} with small thickness δz^{RBL} and enhanced resistivity. This is the key idea at the basis of the RLM³¹, which was introduced to address the following issue: how to close a subphotospheric MHD model at the top of the convection zone domain Ω^{CZ} in order to naturally allow the transfer of magnetic energy and helicity into the SA through a non-current-free magnetic field. As shown in our previous studies^{26,40,41}, the key quantity controlling the transfer of magnetic energy and helicity between two regions is the parallel component E_z of the electric field. In the RLM, this quantity is continuous during the crossing of the layer. Its expression, however, changes from an ideal (or weakly resistive) one near the top of the CZ to a very resistive one inside the layer, and again to an ideal (or weakly resistive) one at the basis of the SA, where it acts as the driver of an evolution in which

non-current-free magnetic fields are naturally produced. This model has been shown to lead to resistive emergence of large-scale twisted flux ropes³¹ producing coronal mass ejections.

Optimizing the RLM parameters. The thickness of the resistive layer needs to be comparable to that of the return layer Δ^{RL} where the convection flow changes its direction from purely vertical to horizontal (the velocity has to match the condition $v_z = 0$, at $z = 0$). Δ^{RL} is much smaller than the length scale L_C of a convection cell. We first choose $\delta z^{\text{RBL}} \approx \Delta^{\text{RL}}$. The other important parameter is the resistivity. It is imposed to exhibit an enhancement inside the boundary layer and to match the resistivity $\eta_{\text{bg}}^{\text{CZ}}$ of Ω^{CZ} and $\eta_{\text{bg}}^{\text{SA}}$ of Ω^{SA} on the lower and upper boundaries of the layer, respectively. We chose a resistivity profile of the Gaussian form $\eta(x, y, z) = \eta_0 \exp\left[-\frac{(z-z_c)^2}{\sigma_z^2}\right] + \eta_{\text{bg}}^{\text{CZ}} \otimes 1_{\text{CZ}} + \eta_{\text{bg}}^{\text{SA}} \otimes 1_{\text{SA}}$, where we have introduced the characteristic functions for Ω^{CZ} (1_{CZ}) and Ω^{SA} (1_{SA}) (the characteristic function 1_D of a domain D takes the value 1 inside D and 0 elsewhere).

Selection of the parameters is guided by the following general considerations. We note that choosing η_0 too large would result in killing the magnetic field emerging into Ω^{SA} while imposing a too small value would prevent field transfer through the boundary $\{z = 0\}$. This determines a range of possible values for η_0 that we further restrict by requiring that a magnetic structure convected in Ω^{CZ} (on timescale τ_C) should not diffuse (on timescale τ_D) before being transferred upwards. This demands $\tau_D \gg \tau_C$ and constrains η_0 to lie near its smallest allowed value. Eventually, we end up with the following choices: $\eta_0 = 1$, $\eta_{\text{bg}}^{\text{CZ}} = 0.1$, $\eta_{\text{bg}}^{\text{SA}} = 0.1$, $z_c = 0$, and $\sigma_z = 0.1$. We have checked that going from these values for the resistivity to smaller ones results in no magnetic field being transferred into Ω^{SA} . This limiting case corresponds exactly to the situation that is considered in various dynamo studies in a closed box^{19,32}.

The boundary conditions at the interface follow. The boundary conditions for Ω^{CZ} are those defined above. For the MHD model in Ω^{SA} , we obtain on $\{z = 0\}$: the horizontal component of the electric field, $E_c(z = 0^+) = E_c(z = 0^-)$, the tangential component of the velocity field, $v_{xy}(z = 0^+) = v_{xy}(z = 0^-)$, and the mass density, $\rho(z = 0^+) = \rho(z = 0^-)$. The magnetic field evolves consistently by the induction equation and does not need to be prescribed.

Global evolution of the system in Ω and initialization of the simulation.

For each time step Δt , the RLM evolution of the system in the global domain $\Omega = \Omega^{\text{CZ}} \cup \Omega^{\text{SA}}$ is performed in three substeps: (i) an ideal MHD substep in Ω^{CZ} , (ii) an ideal MHD substep in Ω^{SA} , and (iii) a purely resistive MHD substep in the whole Ω where we switch on the η -profile defined above.

We first run the simulation until a nonlinearly saturated regime has been reached by the dynamo. When this happens, we replace the field which has been obtained in the atmosphere by the unique current-free magnetic field that has the same vertical component on $\{z = 0\}$, with the plasma being taken to be in hydrostatic equilibrium. Actually, this particular choice could be replaced by any other convenient one, as the system rapidly loses the memory of that condition. After about 10 min, the hydrostatic profile settles down to a quasi-stationary state, with a new average pressure equilibrium and a magnetic field that is no longer current-free, in contrast to the field used in simple models^{21,45}. Our choice for initializing the simulation therefore allows us to prove the strong difference between the magnetic configuration in our model (Fig. 1c) and the associated current-free magnetic configuration (see Extended Data Fig. 3, where field lines are launched from the same footpoints as in Fig. 1c). In particular one can observe in the actual field sheared and twisted structures (carrying electric currents and magnetic helicity, as well as free magnetic energy) that are absent in the current-free configuration.

Properties of the dynamo and of the surface magnetic field. In the nonlinearly saturated dynamo regime, the average magnetic energy is about 20% of the average kinetic energy and then equipartition does not hold globally. Near the surface, however, it holds locally inside the intergranular vortices, where the magnetic and kinetic energy densities are found to be similar, up to fluctuations. These properties are in agreement with those inferred from observations of the scattering polarization in atomic and molecular lines³².

At the surface, the mean magnetic field is found to have a vertical component B_z of intensity 28 G and a total strength of 160 G, in agreement with observed values^{12–14}. This field appears to be structured at the granular scale and also at a mesoscale, with concentrations that have typical values of 500–1,000 G and suffer rapid flux coalescence and cancellation (see Supplementary Video 1). Note that the existence of the mesoscale structuration is an observed property of the surface magnetic field that has been well established by statistical studies and has a direct impact on the eruptive coronal structures.

Two points are worth noting here. (i) More realistic compressible simulations also show the local equipartition of the energy^{23,32} and the mesoscale organization³² mentioned above, and find similar values (for example, 25 G²² and 30 G²³) for the vertical component of the magnetic field at the surface. This gives us

confidence in the adequacy of our MHD Boussinesq model for describing the local surface dynamo, for which it provides the correct values of the lengths, velocities, vertical fields and observed spatial structures. Of course, this model would be quite questionable if it were applied in the deeper interior of the convection zone. (ii) When building up a dynamo model, a delicate issue is the choice of appropriate boundary conditions. This choice, which is never devoid of some arbitrariness, has in general a strong effect on the results. For instance, the vertical component B_z of the surface field computed in a compressible model²³ is found to change from a ‘lower limit’ of 30 G to a ‘upper limit’ of 84 G when closed boundary conditions are replaced by open (for instance, reflecting) conditions on the lower part of the boundary. Moreover, a larger value is obtained in the former case for the ratio of the tangential component of the field to its vertical component. In our incompressible calculations, we use boundary conditions which are close to the closed ones and we are at the lower limit: the behaviour of the field in the surface layer is not influenced by the processes occurring in the deeper layers of the convection zone, which control the solar cycle. Our dynamo thus stays independent of that cycle, in agreement with the observations recalled at the beginning of the main text that suggest that the small-scale surface fields of the quiet Sun are not modulated by the 11-year activity cycle. In the opposite upper limit, on the contrary, the deeper convection zone would get saturated by fields in equipartition filling it by reflection, and would exert a strong influence on the surface field.

Eruption of twisted flux ropes and coronal velocities. During the evolution in the low corona, coherent magnetic flux elements can build up (see the vertical component of the magnetic field shown on Fig. 1d–g) and become the root of twisted flux ropes (TFRs) that are structurally quite similar to the large-scale ones extending in the corona and anchored in active regions’s sunspots. An example of such a TFR is clearly seen inside the box ‘TFR’ of Fig. 1c and its magnification is shown in Fig. 2d. These TFRs evolve in response to magnetic flux changes at their ‘chromospheric’ feet, which leads eventually to their eruptions at upper altitude, as in some models of coronal mass ejections^{26,41}. For the TFR of Fig. 2d, for instance, one can see in Fig. 2e that its ‘upper’ (right) feet FP2 have been subjected to a strong topological change. They have moved from a ‘blue’ polarity to another one that has approached the flux rope, and this results in the eruption seen in E1 and E2 of Fig. 2e, f.

The velocity field. The overall velocity pattern shows striking features that reproduce recent observations^{46,47}: at the end of an eruption, a large volume of plasma shoots upwards (E2 in Fig. 2a–c). These eruptions occur ubiquitously with different strengths, and reach the base of the corona. The matter then falls downwards, with the return flow being organized in vortices concentrated in the quiet flux tubes that are always present and reach the low photosphere (see V and CL in Fig. 1, and Extended Data Figs 4, 5). These vortices correspond to motions spiralling nearly down to the surface (see CL in Extended Data Fig. 4c). We interpret them as the photospheric counterparts to the vortices present in the convection zone. These transport cold matter into the intergranular network, and are the locations of the strong magnetic field amplification at the source of the quiet-Sun magnetic flux tubes. Then both structures actually behave as parts of a unique vortex, artificially cut at the surface by our choice of boundary conditions. In Supplementary Video 2, the horizontal velocity pattern and the current intensity are represented in a horizontal cut at an altitude of 2 Mm. One can see that the vortices are separated by current sheets and disappear when an eruption of their guiding magnetic flux ropes occurs. They move afterwards on the plane with a long lifetime (tens of minutes) that is certainly related to the recycling time at mesoscale.

Magnetic configuration in the vicinity of supergranulation. To take into account the large-scale magnetic field associated with supergranulation²¹, we next add a background vertical field $B_{\text{bg}} = B_0 \hat{z}$ ($B_0 = 5$ G) occupying the whole domain Ω (then the total field stays continuous). In the CZ domain, B_0 is close to the value of the seed field previously used²⁸ and its pressure is only $\sim 10^{-4}$ of the density of kinetic energy of the plasma. Then the added field is too weak to have an effect on the dynamo and to change the average value of the normal component of the surface magnetic field. Of course this result is independent of the particular condition imposed on the lower boundary. In the atmospheric domain and up to chromospheric heights, the resulting magnetic configuration stays about the same as the one previously computed, which completely dominates the background field. Therefore it exhibits the same multipolar character and topological complexity, in agreement with the observations of the supergranulation mixed polarity regions, and its evolution is still driven by photospheric magnetic cancellation/resistive emergence. Higher up, however, the added background field progressively starts to organize vertically most of the coronal magnetic configuration. This is due to the fact that the field passes through a maximum value of 30 G around $z = 1,500$ km and then decreases. Several features characterize the new magnetic topology (Extended Data Fig. 6). (i) Large-scale vertical twisted flux tubes (VTFT) are anchored on the surface magnetic concentrations. They have

their ‘chromospheric feet’ located above the mesospots, inside the bright points observed in $H\alpha$ ²⁴, and extend up to the top of the computational box. (ii) TFRs are still present. They form in the region between the vertical tubes (Fig. 3a), to which they often connect in a continuous way. They reach lower heights than in the case where $B_0 = 0$. They eventually merge with the background field in a way reminiscent of coronal helmet streamers above lower closed structures. This is clearly visible at some times (for example, $t = 72.42$ min) in Supplementary Video 5, whose contents have to be compared with those of Supplementary Video 6 obtained by processing observational data furnished by IRIS. (iii) ‘Open’ cusped flux tube structures (CFT) develop outside twisting motions. (iv) Finally, magnetic arcades (MA) are also present, with some of them located under CFT and exhibiting a multi-polar structure.

Alfvén waves and jets in the vicinity of supergranulation. Not surprisingly, most TFRs and MAs still suffer eruptions. Owing to the connection of these structures to the nearby vertical tubes, however, the eruptions that are triggered differ from those occurring in the absence of the background field by two basic effects. First, the perturbations resulting from the reconnection events happening near the top of the chromosphere generate Alfvén waves that can propagate along the vertical tubes and leave the box. It is worth emphasizing that these waves, whose progressive dissipation should heat the corona, are produced well above the Sun’s surface in our model. This makes a strong difference from most wave coronal heating models in which the waves originate from below that surface and have first to cross the photosphere and the chromosphere without too much attenuation¹. Second, thin jets are launched in the sheets forming the interface between TFR and vertical tubes.

The physics of the eruptions is illustrated in Supplementary Video 4, which shows the evolution of a vertical cut of the z -component of the velocity field. One may observe three dominant features organized around the mesospots and the waves that are generated above them in the VTFT and reach the top of the box (bulk of the corona): (1) the eruptive regions near the transition region launched between VTFT, (2) the jets in the sheets at the boundary with the VTFT, and (3) the downflows ending very near the surface and again correlated with vortex motions. The jets’ lifetimes are short, 1–3 min, but the other structures move in the box with a much longer lifetime, as in the model with no background field. This could match the fact that recurrent jets are often observed at the same location, which in our calculation is related to the long lived mesospots. When superposing the frames of Supplementary Videos 4 and 5 at the same time (for example 72.42 min), one can clearly see in the areas of ‘red’ downward velocities current sheets that are compatible with torsional Alfvén waves, and sheets within the jets and above cusps, as at $y = 11$ Mm. We guess that the jets can be associated with observed spicules of type II^{9,48,49}.

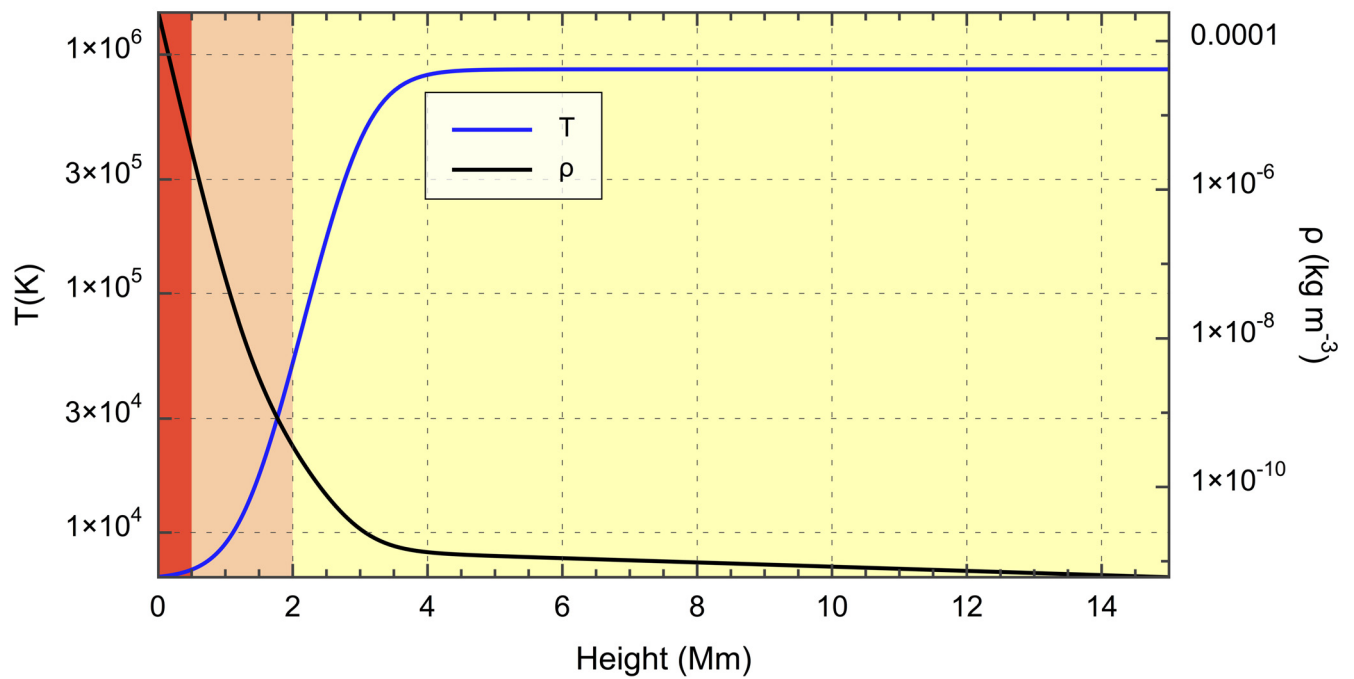
Code availability. We have decided to not make our code available. Some parts of it, which are embedded in a complicated way, are the private property of

institutions. The reader, however, should be able to reproduce our results by using all the information provided in the Methods section.

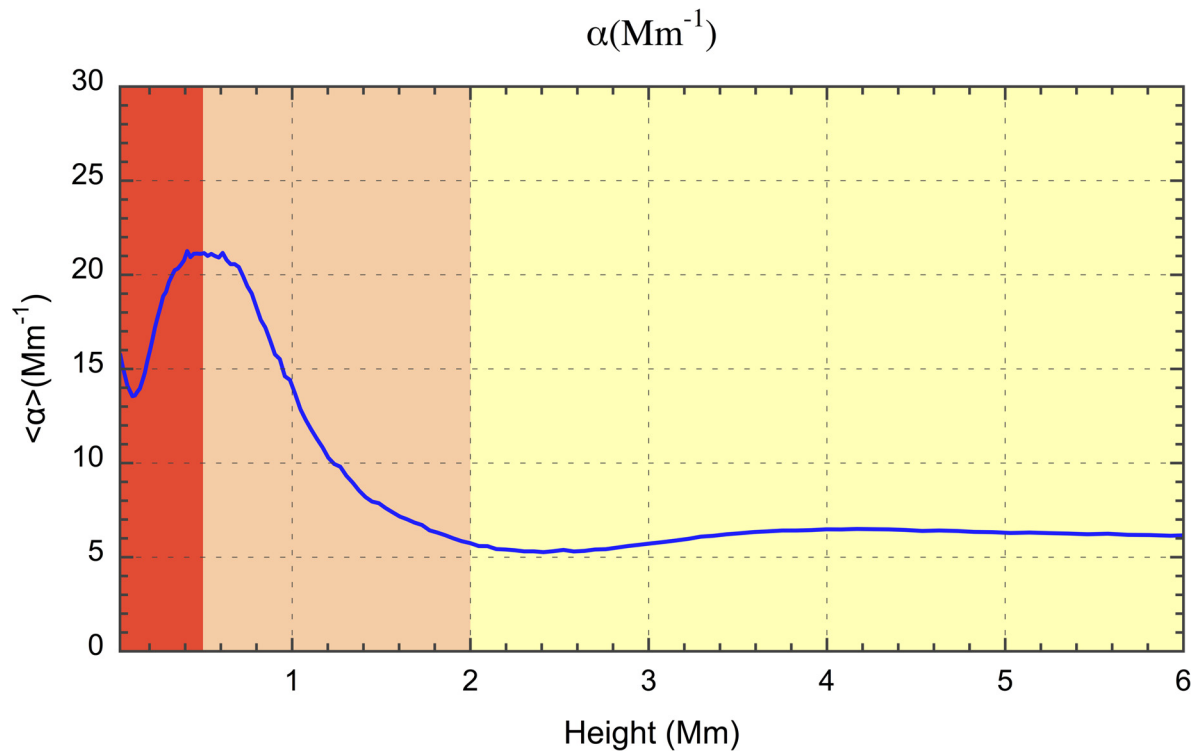
Sample size. No statistical methods were used to predetermine sample size.

31. Amari, T., Luciani, J.-F. & Aly, J.-J. Non-current-free coronal closure of subphotospheric MHD models. *Astrophys. J.* **629**, L37–L40 (2005).
32. Bushby, P. J. & Favier, B. Mesogranulation and small scale dynamo action in the quiet Sun. *Astron. Astrophys.* **562**, A72 (2014).
33. Gudiksen, B. *et al.* The stellar atmosphere simulation code Bifrost. Code description and validation. *Astron. Astrophys.* **531**, A154 (2011).
34. Vögler, A. *et al.* Simulation of magneto-convection in the solar photosphere. Equations, methods, and results of the MURaM code. *Astron. Astrophys.* **429**, 335–351 (2005).
35. Freytag, B. *et al.* Simulations of stellar convection with COBOLD. *J. Comput. Phys.* **231**, 919–959 (2012).
36. Brandenburg, A. & Dobler, W. Hydromagnetic turbulence in computer simulations. *Comput. Phys. Commun.* **147**, 471–475 (2002).
37. Galsgaard, K. & Nordlund, A. Heating and activity of the solar corona 1. Boundary shearing of an initially homogeneous magnetic field. *J. Geophys. Res.* **101**, 13445–13460 (1996).
38. Amari, T., Luciani, J.-F. & Joly, P. A preconditioned semi-implicit scheme for magnetohydrodynamics equations. *SIAM J. Sci. Comput.* **21**, 970–986 (1999).
39. Beeck, B. *et al.* Simulations of the solar near-surface layers with the CO⁵BOLD, MURaM, and Stagger codes. *Astron. Astrophys.* **539**, A121 (2012).
40. Amari, T., Luciani, J.-F., Aly, J.-J., Mikic, Z. & Linker, J. Coronal mass ejection: initiation, magnetic helicity and flux ropes. II. Turbulent diffusion-driven evolution. *Astrophys. J.* **595**, 1231–1250 (2003).
41. Amari, T., Aly, J.-J., Luciani, J.-F., Mikic, Z. & Linker, J. Coronal mass ejection initiation by converging photospheric flows: toward a realistic model. *Astrophys. J.* **742**, L27–L32 (2011).
42. Amari, T., Canou, A. & Aly, J. J. Characterizing and predicting the magnetic environment leading to solar eruptions. *Nature* **514**, 465–469 (2014).
43. Rempel, M., Schüssler, M. & Knölker, M. Radiative magnetohydrodynamic simulation of sunspot structure. *Astrophys. J.* **691**, 640–649 (2009).
44. Vernazza, J. E., Avrett, E. H. & Loeser, R. Structure of the solar chromosphere. III. Models of the EUV brightness component of the quiet Sun. *Astrophys. J. Suppl. Ser.* **45**, 635–725 (1981).
45. Schrijver, C. J. & Title, A. The topology of a mixed-polarity potential field, and inferences for the heating of the quiet solar corona. *Sol. Phys.* **207**, 223–240 (2002).
46. Balmaceda, L. *et al.* Evidence of small-scale magnetic concentrations dragged by vortex motion of solar photospheric plasma. *Astron. Astrophys.* **513**, L6–L9 (2010).
47. Wedemeyer, S. & Steiner, O. On the plasma flow inside magnetic tornadoes on the Sun. *Publ. Astron. Soc. Jpn* **66** (SP1), S10 (2014).
48. Judge, P. G., Tritschler, A. & Low, B. C. Thermal fine structure and magnetic fields in the solar atmosphere: spicules and fibrils. *Astrophys. J.* **730**, L4 (2011).
49. De Pontieu, B., Hansteen, V., Roop van der Voort, L., van Noort, M. & Carlsson, M. High resolution observation and modeling of dynamic fibrils. *Astrophys. J.* **655**, 624–641 (2007).

Temperature and density

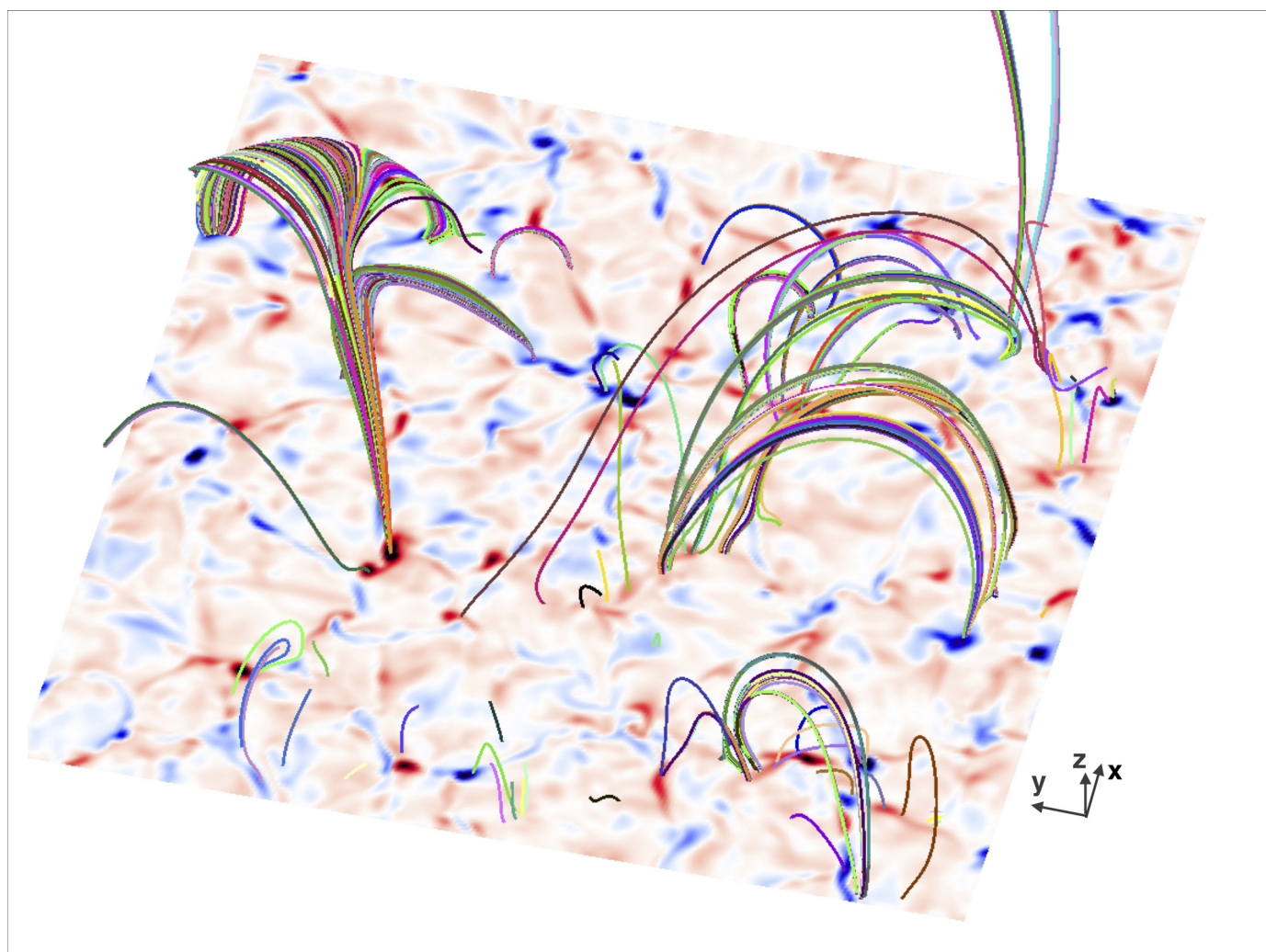


Extended Data Figure 1 | Temperature and density profiles. Shown are profiles of the temperature (blue), which is kept fixed during the simulation, and of the initial density profile (black), using the same colour code as in Fig. 1a for the various layers of the atmosphere.



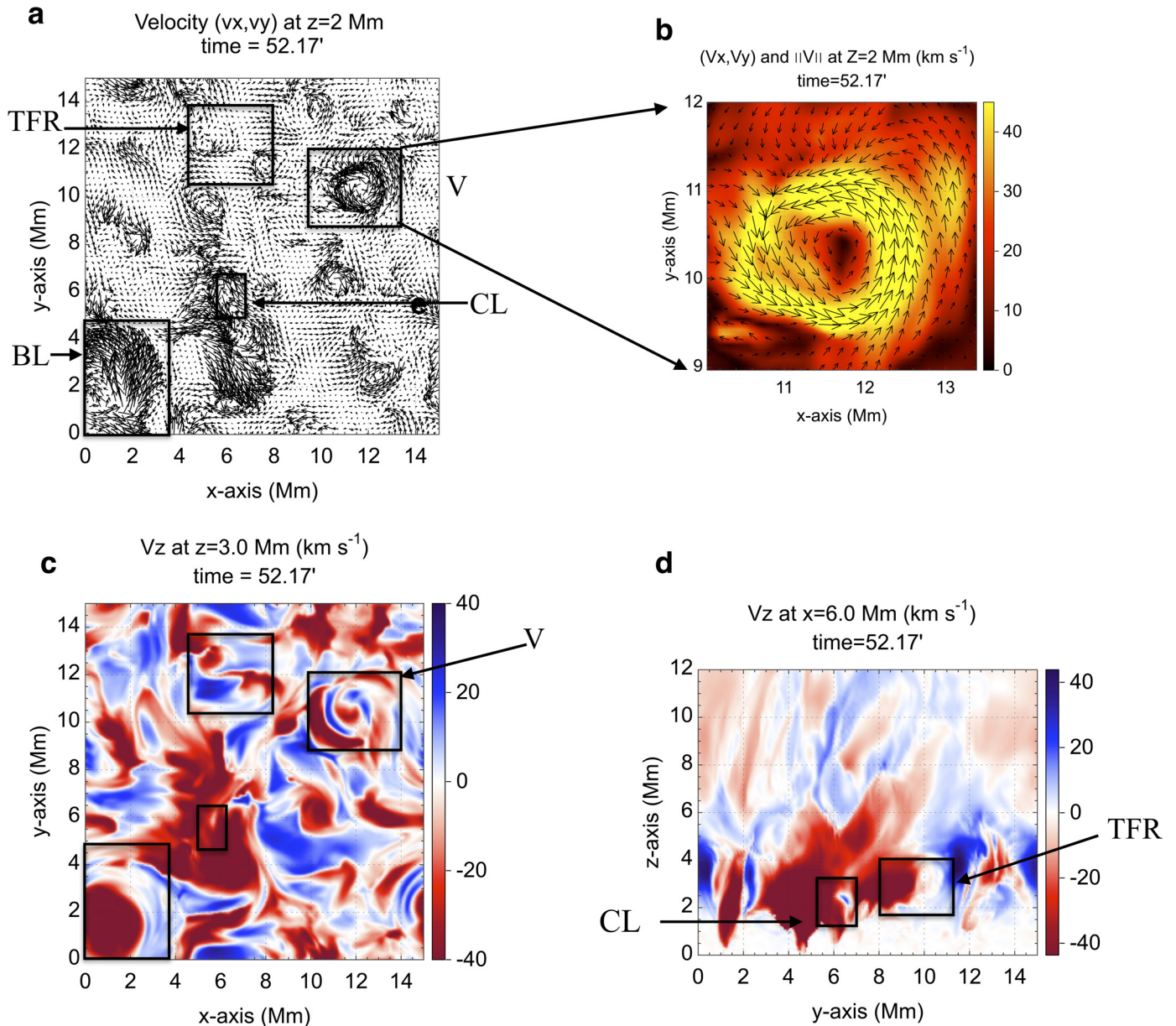
Extended Data Figure 2 | Parallel currents profile. Shown is the profile of the average value of the parameter α associated with the electric currents running along field lines. This quantity appears to take high values in the

confined lower and middle parts of the chromosphere. We use the same colour code as in Fig. 1b for the various layers of the atmosphere.



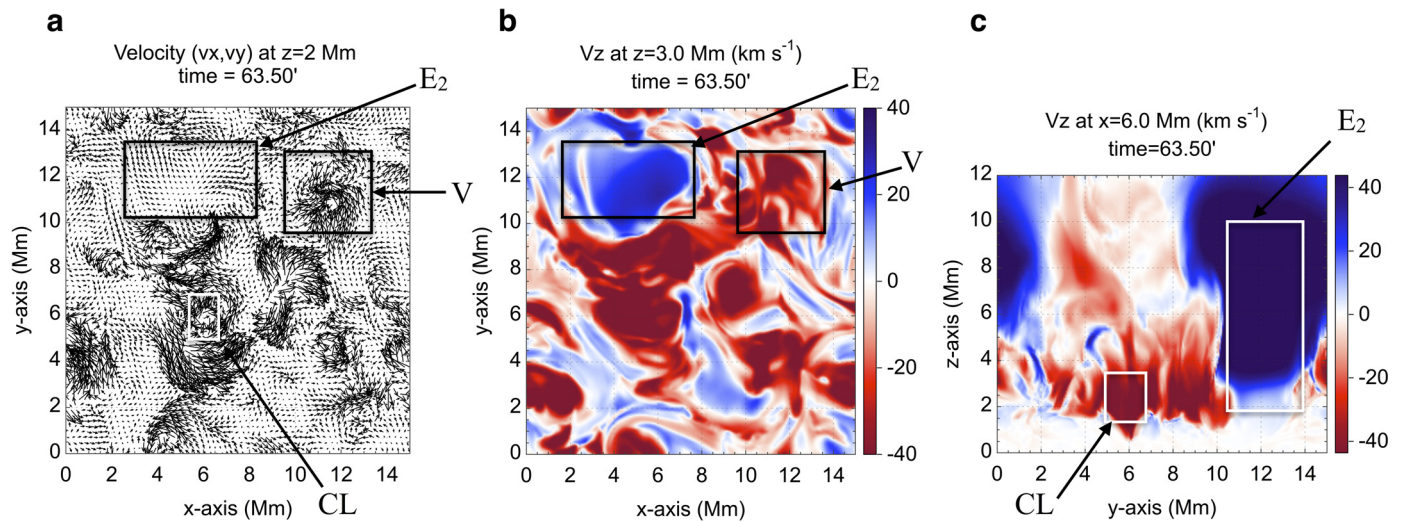
Extended Data Figure 3 | Current-free magnetic configuration. Figure shows selected field lines of an idealized magnetic configuration which is current-free and has the same distribution of vertical component in the photosphere $\{z = 0\}$ as the field shown in Fig. 1c (at time $t = 52.17$ min). The footpoints used to launch the field lines (from various planes) are the same as

those used in Fig. 1c. Although often used in simple models of the quiet Sun, this kind of current-free configuration is very different from the one produced by our model. In particular, it does not exhibit, either in the chromosphere or above, many of the characteristic features (such as shear and twist) of large magnetic energy and electric current density.



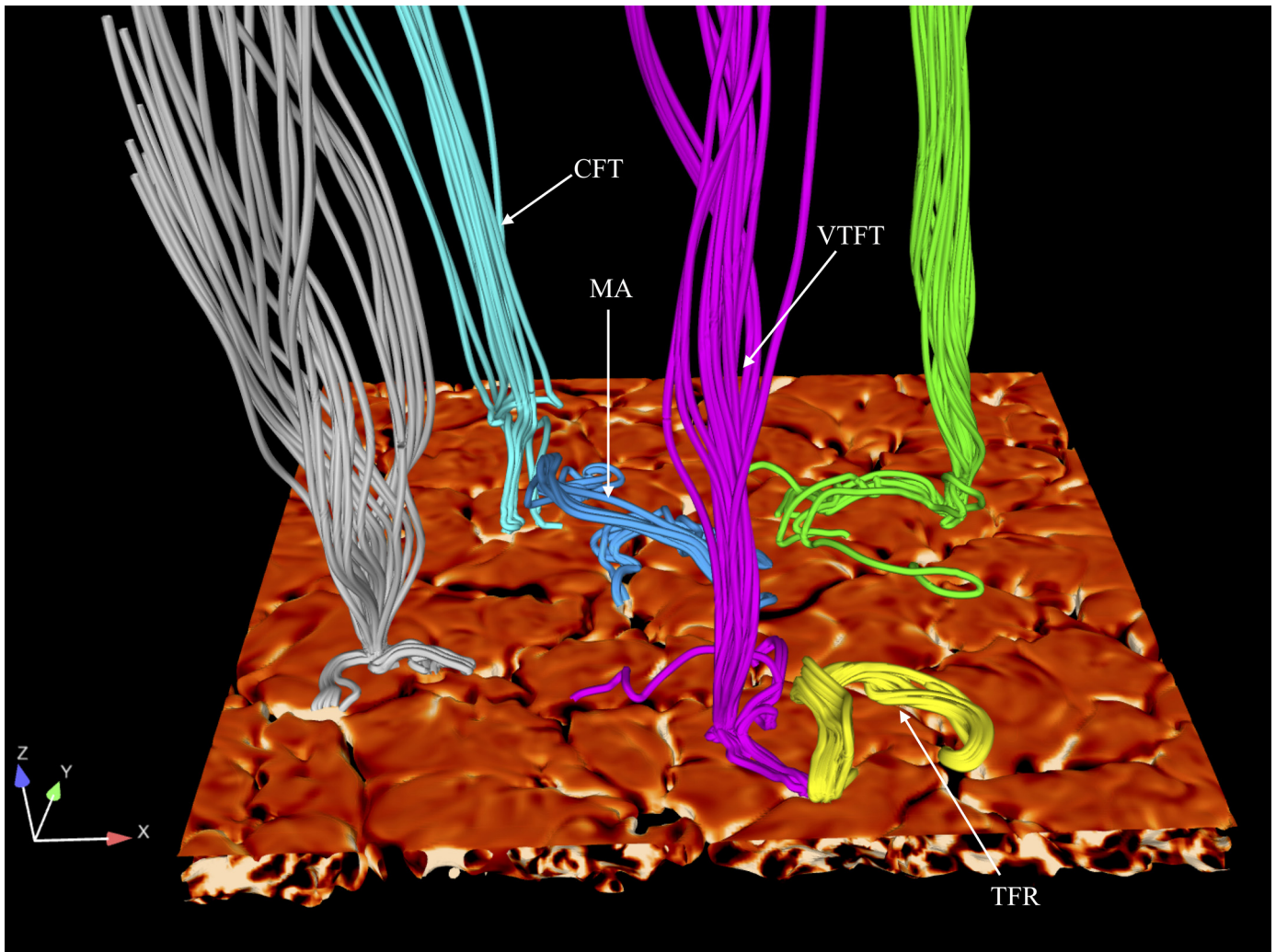
Extended Data Figure 4 | Pre-eruptive flow structure. **a**, Horizontal velocity (v_x, v_y) computed at the top of the chromosphere ($z = 2$ Mm) at the same time ($t = 52.17$ min) as the configuration of Figs 1c and 2d. The flow pattern is clearly organized in regions containing vortex/torsional motions and other ones that are more 'calm'. The feet of the TFR of Fig. 2d are located at the periphery of those flows. **b**, Zoom on one vortex/torsional flow structure V, just above the one shown on Fig. 1c, g, with the norm of (v_x, v_y) as

background. **c**, Horizontal slice of the vertical component v_z of the velocity at $z = 3$ Mm, where v_z starts to show red and blue shifts in the vortex/torsional feature V, while v_z is mostly negative below this height. Other boxed features, located at the same places as in **a**, are shown for information. **d**, Vertical slice of v_z in the plane $x = 6$ Mm. Downward motions associated with CL almost reach the photosphere.



Extended Data Figure 5 | Eruptive flow structure. **a**, Horizontal velocity computed at the top of the chromosphere ($z = 2$ Mm) at the same time ($t = 63.50$ min, that is, during the eruption phase) as the magnetic configuration of Fig. 2f. The eruptive area (E_2) becomes free of vortex/torsional

motions, which are still present elsewhere, as in the vortex/torsional feature (V) and concentrated legs (CL). Large vertical flows associated with the eruption of the TFR are correlated with a positive vertical component v_z shown as a horizontal slice in **b** and as a vertical slice in **c**.



Extended Data Figure 6 | Magnetic configuration with the addition of the background magnetic field. Shown are selected field lines of the magnetic configuration at time $t = 72.42$ min (as in Fig. 3) corresponding to the case where a background vertical magnetic field of 5 G is added to mimic the effects of the supergranulation network. Several characteristic features are represented above an isosurface of the temperature fluctuations coloured with

the vertical component of the magnetic field. They confirm and extend those of Fig. 1c: twisted flux rope (TFR), cusped flux tube (CFT) with coronal streamer-like shape, vertical twisted flux tube (VTFT) guiding Alfvén waves, and magnetic arcades (MA). The structures coloured in grey and green, respectively, are VTFT.

Visible-frequency hyperbolic metasurface

Alexander A. High^{1,2*}, Robert C. Devlin^{3*}, Alan Dibos³, Mark Polking¹, Dominik S. Wild², Janos Perczel^{2,4}, Nathalie P. de Leon^{1,2}, Mikhail D. Lukin² & Hongkun Park^{1,2}

Metamaterials are artificial optical media composed of sub-wavelength metallic and dielectric building blocks that feature optical phenomena not present in naturally occurring materials^{1–7}. Although they can serve as the basis for unique optical devices that mould the flow of light in unconventional ways, three-dimensional metamaterials suffer from extreme propagation losses^{8,9}. Two-dimensional metamaterials (metasurfaces) such as hyperbolic metasurfaces for propagating surface plasmon polaritons^{10,11} have the potential to alleviate this problem. Because the surface plasmon polaritons are guided at a metal–dielectric interface (rather than passing through metallic components), these hyperbolic metasurfaces have been predicted to suffer much lower propagation loss while still exhibiting optical phenomena akin to those in three-dimensional metamaterials. Moreover, because of their planar nature, these devices enable the construction of integrated metamaterial circuits as well as easy coupling with other optoelectronic elements. Here we report the experimental realization of a visible-frequency hyperbolic metasurface using single-crystal silver nanostructures defined by lithographic and etching techniques. The resulting devices display the characteristic properties of metamaterials, such as negative refraction^{1–5} and diffraction-free propagation^{6,7}, with device performance greatly exceeding those of previous demonstrations. Moreover, hyperbolic metasurfaces exhibit strong, dispersion-dependent spin–orbit coupling, enabling polarization- and wavelength-dependent routing of surface plasmon polaritons and two-dimensional chiral optical components^{12–15}. These results open the door to realizing integrated optical meta-circuits, with wide-ranging applications in areas from imaging and sensing to quantum optics and quantum information science.

Our approach for realizing a visible-frequency hyperbolic metasurface (HMS) involves the definition of a nanometre-scale silver/air grating on a sputter-deposited, single-crystalline silver film by electron-beam lithography and plasma etching. Unlike focused-ion-beam milling methods^{5,12}, which produce rough, defect-ridden structures, this new method produces smooth, high-quality silver nanostructures with high aspect ratios, critical for the realization of a surface plasmon polariton (SPP)–HMS. Figure 1 illustrates the materials and structures that form the basis for HMSs. As a starting material, we sputter-deposited a micrometre-thick silver film on a (111)-silicon substrate at 300°C and at high deposition rate ($>1.5 \text{ nm s}^{-1}$)^{16,17}. High-resolution transmission electron microscopy (Fig. 1a), X-ray diffraction, atomic force microscopy, and electron backscatter diffraction measurements (see Supplementary Figs 1, 2 and 3, respectively) reveal that these films are single-crystalline and have root-mean-square roughnesses as low as 300 pm. The ellipsometric characterization (Supplementary Fig. 4) shows that, over a large portion of the visible spectrum, the optical loss in our film is much lower than those reported previously^{18,19} and is comparable to recently reported silver films prepared by molecular beam epitaxy²⁰. Unlike the molecular beam epitaxy process²⁰, however, the sputtering process can rapidly grow single-crystalline films of large thicknesses,

which is crucial for the realization of an HMS because it prevents SPP absorption by the silicon substrate. From the experimentally measured dielectric constants, we determine that the SPP propagation length L_p (defined as the length over which the SPP intensity decays by $1/e$) in a silver film exceeds 100 μm for far-field wavelengths λ greater than 650 nm (Fig. 1b).

Beyond exceptional optical performance, single-crystalline silver films offer mechanical and thermodynamic stability, which is crucial for defining nanoscale features using lithography and etching. We fabricated the silver/air gratings and light in- and out-coupling structures (used to convert far-field light into SPPs and vice versa) by first defining an Al_2O_3 hard mask with electron-beam lithography and then dry-etching silver with argon plasma (see Supplementary Fig. 6 for details). After etching, the residual Al_2O_3 mask was removed with hydrofluoric acid, leaving clean, high-aspect-ratio silver features. Figure 1d and e show scanning electron microscope (SEM) images of representative devices (schematically shown in Fig. 1c with silver ridge height $h = 80 \text{ nm}$, width $w = 90 \text{ nm}$, and pitch $a = 150 \text{ nm}$). The smooth surface of our devices, coupled with the single-crystalline nature of silver, minimizes extrinsic optical losses originating from grain boundaries and surface roughness.

A recent theoretical work¹¹ has predicted that a silver/air grating with appropriate sub-wavelength feature sizes, such as that shown in Fig. 1d and e, should exhibit hyperbolic dispersion for propagating SPPs below a critical wavelength, $\lambda = \lambda_T$ (and elliptical dispersion above it). A simple physical picture provides insight into the transition from hyperbolic to elliptical dispersion in this structure. At short wavelengths, the plasmonic modes are tightly confined to the ridges of the grating, qualitatively similar to the situation in an array of parallel nanowires that exhibits hyperbolic dispersion²¹. In the long wavelength limit, on the other hand, the modes are only weakly confined, and the grating can be considered a perturbation to a flat surface, resulting in elliptical dispersion (for discussion, see Supplementary Figs 7 and 8).

To experimentally verify these predictions, we fabricated a series of devices and tested their optical properties. Figure 2 presents a device, D1, designed to demonstrate negative refraction of SPPs, a known property of hyperbolic metamaterials²². This device consists of a silver/air grating as well as a groove that launches SPPs on flat silver upon far-field excitation (Fig. 2a). The angle of refraction at the flat silver/grating interface was determined by collecting scattered light at the in-coupling structure, the silver-film/grating interface, and the corresponding out-coupling structure. As is clearly shown in Fig. 2b and d (see also Supplementary Figs 9 and 10), the behaviour of D1 changes from normal refraction at $\lambda > 540 \text{ nm}$ to negative refraction at $\lambda < 540 \text{ nm}$. We note that λ_T , at which the device behaviour changes from normal to negative refraction (that is, elliptical to hyperbolic dispersion), can be tuned by varying the device geometry (Supplementary Fig. 11a) or by changing the dielectric environment of silver (for example, by depositing a thin layer of Al_2O_3 on the device; see Supplementary Fig. 11b).

¹Department of Chemistry and Chemical Biology, Harvard University, 12 Oxford Street, Cambridge, Massachusetts 02138, USA. ²Department of Physics, Harvard University, 12 Oxford Street, Cambridge, Massachusetts 02138, USA. ³School of Engineering and Applied Sciences, Harvard University, 12 Oxford Street, Cambridge, Massachusetts 02138, USA. ⁴Department of Physics, Massachusetts Institute of Technology, 77 Massachusetts Avenue, Cambridge, Massachusetts 02139, USA.

*These authors contributed equally to this work.

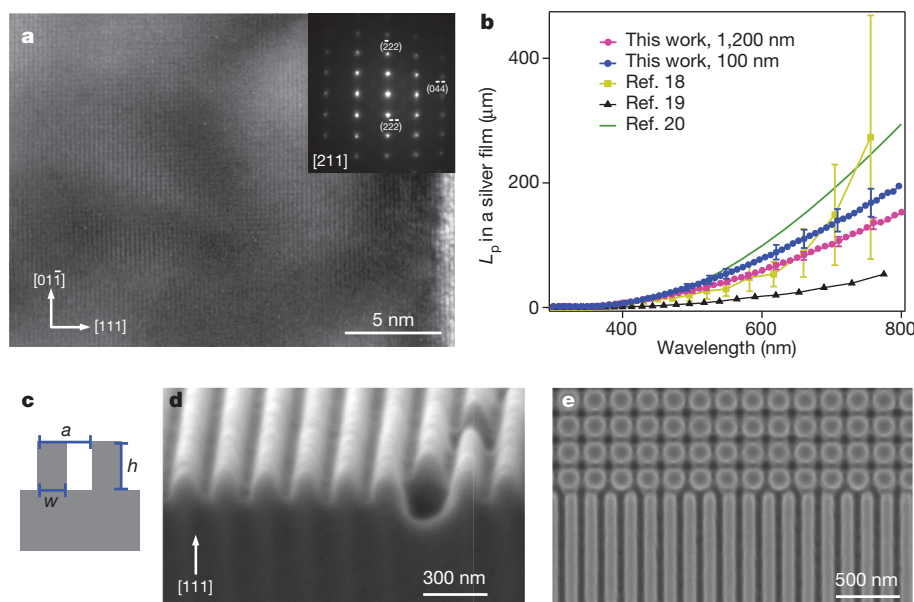


Figure 1 | Single-crystalline silver film and fabricated devices. **a**, High-resolution transmission electron microscopy image taken down the [211] axis that demonstrates the single-crystalline nature of the sputter-deposited silver. The growth direction is from left to right along the [111] direction with the surface of the silver film shown at the far right of the image. The inset shows the electron diffraction pattern. **b**, SPP propagation length L_p on a silver film derived from measured real and imaginary parts of the dielectric constants for

100-nm-thick (blue circles) and 1,200-nm-thick (pink circles) sputtered films. For comparison, propagation lengths calculated using the dielectric constants reported in refs 18–20 (green line) are also shown (error bars are one standard deviation from the average value). **c**, Schematic of HMS, with pitch a , width w and height h . **d**, A cross-sectional SEM image of a fabricated device. **e**, Top-down SEM image of a silver/air grating and out-coupling structures (top).

Figure 3 illustrates a second device, D2, with $\lambda_T = 560$ nm, which exhibits another remarkable phenomenon: diffraction-free propagation. At λ_T , the flat dispersion curve implies that all SPPs propagate parallel to the silver ridges¹¹ (Fig. 4b, Supplementary Fig. 12 and discussions below) and thus SPPs excited on a single silver ridge remain primarily confined to the same ridge despite its sub-wavelength width ($\sim \lambda/6$). In device D2, slots defined directly on individual silver ridges serve as in-coupling structures that convert far-field light to SPPs (or out-coupling structures that convert SPPs to far-field light); see Fig. 3a–c. As shown in Fig. 3d, at $\lambda = 585$ nm, despite being excited by only one in-coupling structure, SPPs scatter off multiple out-coupling structures owing to normal, diffractive propagation. However, at $\lambda_T = 560$ nm SPPs primarily scatter off the out-coupling

structure located on the same ridge as the in-coupling structure (Fig. 3e), signifying diffraction-free propagation. This diffraction-free propagation, coupled with suitably designed ‘magnifying’ out-coupling structures, enables sub-diffraction-resolution imaging and photon routing^{6,7}. Figure 3g presents one such demonstration: at $\lambda_T = 560$ nm, despite SPPs being launched at two in-coupling structures separated by a sub-wavelength spacing of 150 nm, SPPs primarily scatter off the two corresponding out-coupling structures staggered along the propagation axis.

We next demonstrate a new optical phenomenon supported by the silver/air grating: the dispersion-dependent plasmonic spin-Hall effect (PSHE)^{12,13,23,24}, a plasmonic analogue of the electronic Rashba²⁵ and photonic spin-Hall effects^{15,26}. In electronic systems, spin-orbit

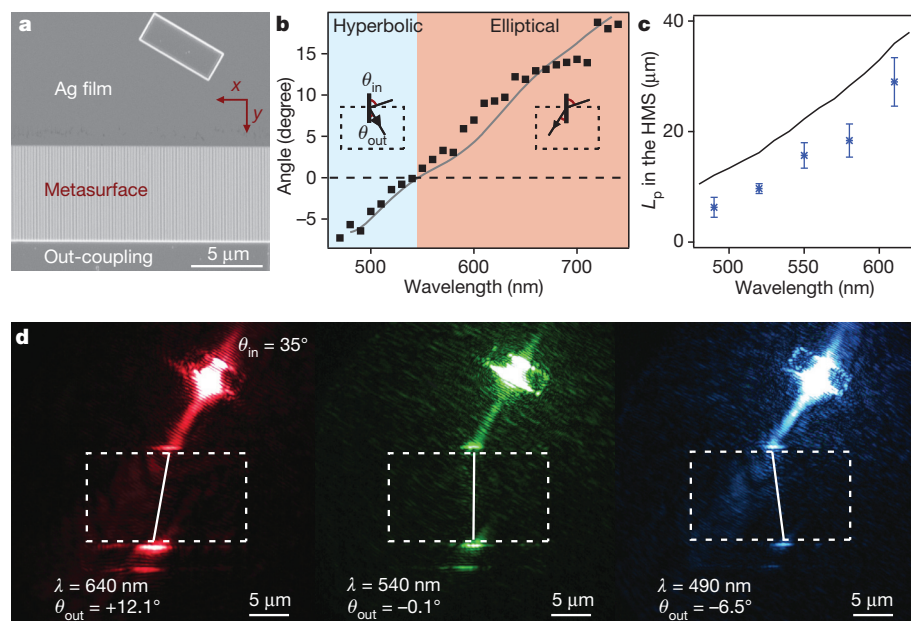


Figure 2 | Measurement of SPP refraction at a flat silver/HMS interface. **a**, An SEM image of a device, D1. Far-field light is converted to SPPs in the silver film via the angled rectangular in-coupling structure at the top of the image. The excitation laser is unpolarized. The SPPs propagate along the silver film, are refracted at the film–metasurface interface, and are then scattered into the far field at the out-coupling structure at the bottom of the image. In this device, the height of the silver ridge is 80 nm, the width is 90 nm, and the pitch is 150 nm. **b**, The angle of refraction θ_{out} as a function of wavelength, with elliptical (red-shaded) and hyperbolic (blue-shaded) dispersion regimes indicated. The solid line is the simulated angle of refraction from FDTD simulations. The input and output angles, θ_{in} and θ_{out} , are defined in the inset, with the dotted box indicating the region of the HMS. **c**, The experimentally measured (blue data points) and simulated (black line) propagation length L_p of SPPs in the HMS (error bars are one standard deviation from the average value). **d**, Images of SPP refraction at the flat silver/HMS interface. The dashed boxes indicate the region of the HMS.

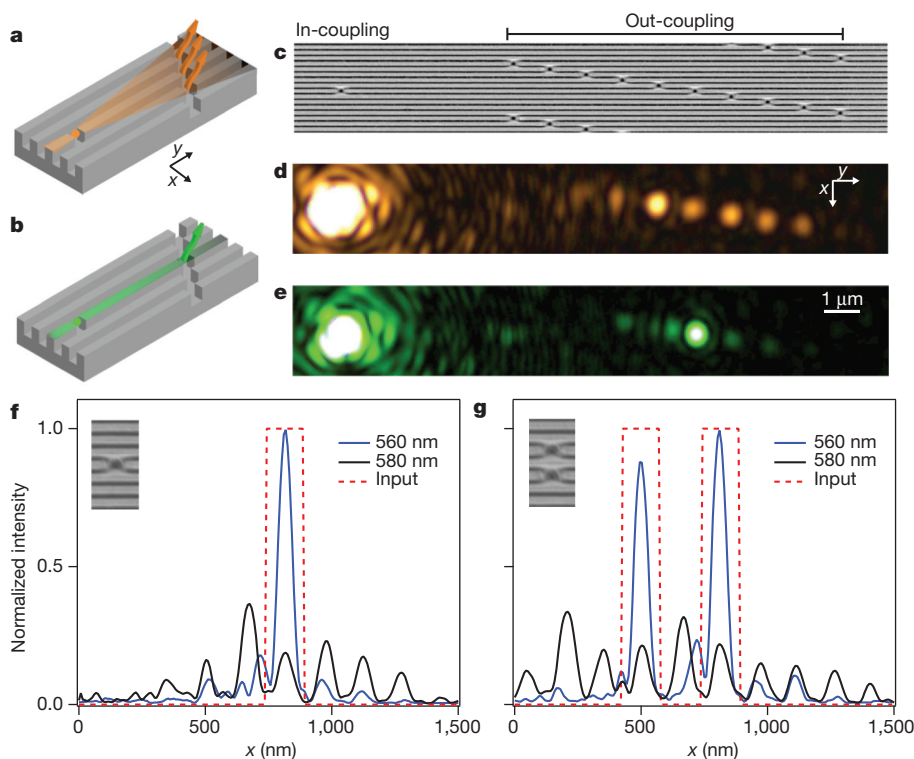


Figure 3 | Observation of diffraction-free SPP propagation. **a**, A schematic for SPP diffraction in a silver/air grating. **b**, A schematic for diffraction-free SPP propagation in a silver/air grating. In **a** and **b** an in-coupling structure defined on a single ridge (left-hand side) acts as a point source of SPPs. SPPs scatter off at the out-coupling structures on the other side that are staggered along the y axis for magnification. **c**, An SEM image of a device, D2. The height of the silver ridge is 80 nm, the width is 90 nm, and the pitch is 150 nm. The y -axis distance between out-coupling structures is 1 μm , thus providing the magnification of 6.7. **d**, **e**, Optical images of SPPs scattering at the out-coupling slots (right-hand side) with SPPs excited with unpolarized light by a single in-coupling structure (inset to Fig. 3f) for $\lambda = 585$ nm (**d**) and $\lambda = \lambda_T = 560$ nm (**e**). **f**, Diagonal cross-sections of optical image across out-coupling slots at $\lambda = 560$ nm (blue) and $\lambda = 585$ nm (black), with the input position marked in red. The x -axis coordinate of the cross-section is indicated on the bottom axis. **g**, Similar cross-sections obtained when two in-coupling notches (inset) are used. In **f** and **g**, the out-coupling intensities are normalized such that the total integrated intensities are equal.

coupling arises due to the lack of inversion symmetry (for example, in the presence of an external electric field) and couples the spin of a charge carrier to its propagation direction. Similarly, in an optical system with tightly confined optical modes, the light propagation direction couples to the electric field rotation, leading to the photonic spin-Hall effect^{15,26}. In the HMS, a PSHE arises from three structural features of the silver/air grating. First, this structure lacks inversion symmetry and exhibits high optical anisotropy for SPPs propagating

parallel and perpendicular to the silver ridges (y - and x -axes, respectively, in Fig. 4a). Second, due to its nanoscale ridged structure, the HMS can support electric field components perpendicular to the SPP propagation direction (for example, E_z and E_x for propagation along y), and thus SPPs can exhibit circular polarization. Third, the dispersion of the system is strongly frequency dependent, such that the direction of the SPP group velocity changes when moving from hyperbolic to elliptical polarization. Combined together, these three features enable

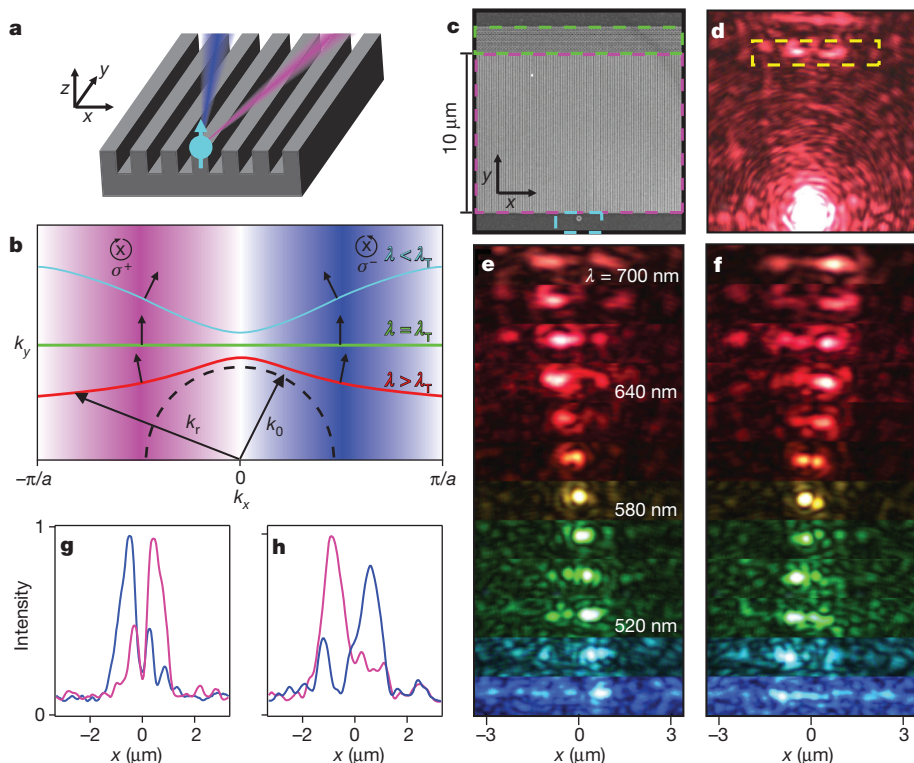


Figure 4 | The dispersion-dependent plasmonic spin-Hall effect (PSHE). **a**, A schematic of the PSHE. In a silver/air grating, SPPs with different helicities propagate into distinct spatial directions. **b**, Illustration of the origin of the PSHE. Positive k_x corresponds to σ^- (blue shading) and negative k_x to σ^+ (magenta shading). The direction of the group velocity (black arrows) is perpendicular to the isofrequency contours at a given dispersion regime: elliptic (red), diffractionless (green), and hyperbolic (cyan). The allowed k_x values extend from $-\pi/a$ to $+\pi/a$, where a is the pitch of the silver/air grating. The dotted black line indicates the free-space isofrequency contour at the same frequency as the red curve. **c**, An SEM image of a device, D3, used to examine PSHE with an in-coupling structure (cyan rectangle), and out-coupling cylinders (green rectangle). **d**, Image of D3 under unpolarized laser excitation of the in-coupling structure. The out-coupling region is marked by the yellow box. **e**, **f**, Image from the out-coupling structures as a function of wavelength collecting only σ^+ (**e**) and σ^- (**f**) polarized light. From bottom to top, the wavelength increases from 480 nm to 700 nm in increments of 20 nm. **g**, **h**, Light intensities measured at the out-coupling structures for σ^+ (magenta) and σ^- (blue) polarized light at $\lambda = 530$ nm (**g**) and $\lambda = 640$ nm (**h**).

the dispersion-dependent PSHE in which the SPP propagation direction and helicity are linked to each other in a frequency-dependent manner (Fig. 4). While the PSHE has been experimentally observed in bulk hyperbolic metamaterials at radio frequencies¹⁴, it has not previously been realized experimentally in the visible frequency regime.

Figure 4c shows a device, D3, which demonstrates the PSHE. In this device, a single circular in-coupling structure near the silver/air grating scatters unpolarized far-field light to propagating SPP modes, and an array of vertical silver cylinders on the other side (diameter 140 nm, height 90 nm) comprises an out-coupling structure that scatters SPPs back to the far field. These out-coupling structures convert the SPP polarization into far-field polarization with minimal distortion (see discussions in Supplementary Fig. 13). As shown in Fig. 4d, when SPPs are excited by the in-coupling structure, they split into two separate (left- and rightward) beams. Polarization-resolved imaging reveals that these split SPP beams exhibit opposite circular polarizations (one predominantly ($\sim 80\%$) σ^+ and the other is σ^- with $\sigma^\pm = E_x \pm iE_y$; Fig. 4g and h). Moreover, this helicity-dependent splitting is strongly wavelength-dependent (Fig. 4e and f). When the silver/air grating exhibits an elliptical dispersion ($\lambda > 580$ nm), the σ^+ (σ^-)-polarized SPPs deflect to the left (right), with the deflection angle decreasing with decreasing λ . When the silver/air grating enters the hyperbolic regime ($\lambda < 580$ nm), this behaviour reverses (similar to the magnetic field switching sign in the electronic Rashba effect), and the σ^+ (σ^-)-polarized SPPs deflect to the right (left). At the diffraction-free propagation point ($\lambda_T = 580$ nm), the splitting between σ^+ and σ^- helicities vanishes.

The physical origin of this dispersion-dependent PSHE can be understood using the isofrequency contour schematically illustrated in Fig. 4b. In the silver/air grating, the SPP helicities are determined by the wave vector that characterizes the electric field. The electric field of an SPP mode is given by $\mathbf{E} \approx E_r \hat{r} - (k_x/k_z)E_z \hat{z}$, where $k_z = i\sqrt{k_T^2 - k_0^2}$, $k_r = \sqrt{k_x^2 + k_y^2}$ is the plasmonic wavenumber in the direction of \hat{r} , \hat{r} is the in-plane direction of \mathbf{k} , and k_0 is the free-space wave number given by ω/c , where c is the speed of light in a vacuum^{14,27}. Because the SPPs are evanescent perpendicular to the surface, k_z is imaginary and the field rotates along \hat{r} . Near the centre of the Brillouin zone ($k_x = 0$), we have $k_r \approx k_y \approx k_0$, and the SPP wavelength λ_{SPP} in our structures is similar to the far-field wavelength λ (Supplementary Fig. 14 and see discussion below). As k_x increases, however, k_r continuously increases due to highly anisotropic dispersion relation, and for $k_r \gg k_0$ the modes become circularly polarized in the x - z plane. Near the edge of the Brillouin zone, modes of opposite circular polarization hybridize, and the polarization effects in the x - z plane vanish. These considerations indicate that when projected on the x - z plane, an SPP mode with $k_x < 0$ ($k_x > 0$) exhibits σ^+ (σ^-) polarization (note that an SPP with $k_x = 0$ will exhibit electric field rotation in the y - z plane¹⁵). The direction of SPP propagation is, however, governed by the group velocity vector that is perpendicular to the isofrequency contour. The small angular spread of the right- and leftward SPP beams is a consequence of the shape of this isofrequency contour, which reflects the optical anisotropy of our silver/air grating. As shown in Fig. 4b, this simple consideration explains our experimental observations. Specifically, when the device exhibits elliptical dispersion ($\lambda > \lambda_T$), the σ^+ (σ^-)-polarized SPPs deflect to the left (right) because the leftward (rightward) group velocity vector is associated with $k_x < 0$ ($k_x > 0$). In contrast, in the hyperbolic dispersion regime ($\lambda < \lambda_T$), the reverse is true, leading to the switching of the deflection directions for σ^+ (σ^-)-polarized SPPs.

A key improvement of our approach is the dramatic reduction in optical losses in comparison to bulk metamaterials. To directly characterize the optical performance of HMS, we fabricated silver/air gratings of varying lengths with identical light in- and out-coupling structures, and measured the out-coupled light intensity as a function of the grating length at the same in-coupling intensity. By fitting the intensity-length curve by a single exponential at a given λ , we then

determined L_p in our devices, ranging from 6 μm at $\lambda = 490$ nm up to 29 μm at $\lambda = 610$ nm (blue stars in Fig. 2c; for discussion see Supplementary Fig. 15). These propagation length L_p values are one to two orders of magnitude larger than those reported in bulk visible-frequency hyperbolic metamaterials^{3,4}.

To analyse our observations quantitatively, we carried out detailed finite-difference time-domain (FDTD) simulations of SPP propagation in our device geometries (D1 through D3). These FDTD simulations are in good agreement with the experimental observations in Figs 2–4: negative refraction for $\lambda < \lambda_T$ (Fig. 2b, solid line), diffraction-free propagation at λ_T (Supplementary Fig. 12), and the dispersion-dependent PSHE (Supplementary Fig. 16). The FDTD simulations also indicate that the local polarization of the SPP field reaches 87% for left- and right-propagating circularly polarized SPPs, larger than experimentally observed values of 80%, due to the imperfect polarization conversion of our out-coupling structure (Supplementary Fig. 17). The simulated propagation lengths (black line in Fig. 2c; for discussion see Supplementary Information) in the HMS are $\sim 30\%$ larger than the experimentally determined ones, probably owing to residual nanoscale roughness introduced during the fabrication procedure. Owing to increasing SPP confinement, the sensitivity to surface roughness increases at lower wavelengths, resulting in greater scattering losses. Despite these imperfections, the measured propagation distances indicate that the low-loss, two-dimensional nature of our devices offers a substantial improvement over conventional bulk metamaterials in terms of optical loss, thereby opening the door for a wide array of high-performance plasmonic nanostructures.

Although our demonstrations focused on one particular family of metasurfaces, that is, a silver/air grating, the fabrication strategy is general and compatible with other bottom-up and top-down semiconductor and metal processing techniques. Our method thus opens up the possibility of realizing low-dimensional transformation optics and metamaterial-based devices^{28,29}. The same method can be used to generate integrated metamaterial circuits that combine HMSs on-chip with other optoelectronic and plasmonic devices. The HMSs can enable quantum optics applications as well. Because of their small mode volumes and increased plasmonic density of states^{10,11}, HMSs can be used for enhancing interactions of SPPs with individual quantum emitters—a new pathway for realizing solid-state quantum nonlinear optical circuits. Moreover, the frequency-dependent spin-orbit interaction enables the exploration of a new class of solid-state quantum optical phenomena that involve chiral optical interfaces with quantum emitters. By extending recent demonstrations involving such interactions with one-dimensional waveguides¹⁵ into two dimensions, this could enable spin-dependent routing of single photons as well as non-trivial topological phenomena that combine spin-orbit interactions with single photon nonlinearities associated with quantum emitters³⁰.

Received 7 December 2014; accepted 10 April 2015.

- Pendry, J. B. Negative refraction makes a perfect lens. *Phys. Rev. Lett.* **85**, 3966–3969 (2000).
- Shelby, R. A., Smith, D. R. & Schultz, S. Experimental verification of a negative index of refraction. *Science* **292**, 77–79 (2001).
- Yao, J. *et al.* Optical negative refraction in bulk metamaterials of nanowires. *Science* **321**, 930 (2008).
- Naik, G. V. *et al.* Epitaxial superlattices with titanium nitride as a plasmonic component for optical hyperbolic metamaterials. *Proc. Natl Acad. Sci. USA* **111**, 7546–7551 (2014).
- Esfandiyarpour, M., Garnett, E. C., Cui, Y., McGehee, M. D. & Brongersma, M. L. Metamaterial mirrors in optoelectronic devices. *Nature Nanotechnol.* **9**, 542–547 (2014).
- Salandrino, A. & Engheta, N. Far-field subdiffraction optical microscopy using metamaterial crystals: theory and simulations. *Phys. Rev. B* **74**, 075103 (2006).
- Liu, Z. W., Lee, H., Xiong, Y., Sun, C. & Zhang, X. Far-field optical hyperlens magnifying sub-diffraction-limited objects. *Science* **315**, 1686 (2007).
- Shalaev, V. M. Optical negative-index metamaterials. *Nature Photon.* **1**, 41–48 (2007).
- Poddubny, A., Iorsh, I., Belov, P. & Kivshar, Y. Hyperbolic metamaterials. *Nature Photon.* **7**, 948–957 (2013).

10. Kildishev, A. V., Boltasseva, A. & Shalae, V. M. Planar photonics with metasurfaces. *Science* **339**, 1232009 (2013).
11. Liu, Y. M. & Zhang, X. Metasurfaces for manipulating surface plasmons. *Appl. Phys. Lett.* **103**, 141101 (2013).
12. Lin, J. *et al.* Polarization-controlled tunable directional coupling of surface plasmon polaritons. *Science* **340**, 331–334 (2013).
13. Rodriguez-Fortuno, F. J. *et al.* Near-field interference for the unidirectional excitation of electromagnetic guided modes. *Science* **340**, 328–330 (2013).
14. Kapitanova, P. V. *et al.* Photonic spin Hall effect in hyperbolic metamaterials for polarization-controlled routing of subwavelength modes. *Nature Commun.* **5**, 3226 (2014).
15. Petersen, J., Volz, J. & Rauschenbeutel, A. Chiral nanophotonic waveguide interface based on spin-orbit interaction of light. *Science* **346**, 67–71 (2014).
16. Baski, A. A. & Fuchs, H. Epitaxial growth of silver on mica as studied by AFM and STM. *Surf. Sci.* **313**, 275–288 (1994).
17. Park, J. H. *et al.* Single-crystalline silver films for plasmonics. *Adv. Mater.* **24**, 3988–3992 (2012).
18. Johnson, P. B. & Christy, R. W. Optical constants of noble metals. *Phys. Rev. B* **6**, 4370–4379 (1972).
19. Palik, E. D. *Handbook of Optical Constants of Solids* Vol. 3 353–357 (Academic Press, 1998).
20. Wu, Y. *et al.* Intrinsic optical properties and enhanced plasmonic response of epitaxial silver. *Adv. Mater.* **26**, 6106–6110 (2014).
21. Fan, X. B., Wang, G. P., Lee, J. C. W. & Chan, C. T. All-angle broadband negative refraction of metal waveguide arrays in the visible range: theoretical analysis and numerical demonstration. *Phys. Rev. Lett.* **97**, 073901 (2006).
22. Smith, D. R. & Schurig, D. Electromagnetic wave propagation in media with indefinite permittivity and permeability tensors. *Phys. Rev. Lett.* **90**, 077405 (2003).
23. Lee, S. Y. *et al.* Role of magnetic induction currents in nanoslit excitation of surface plasmon polaritons. *Phys. Rev. Lett.* **108**, 213907 (2012).
24. Huang, L. L. *et al.* Helicity dependent directional surface plasmon polariton excitation using a metasurface with interfacial phase discontinuity. *Light Sci. Appl.* **2**, e70 (2013).
25. Bychkov, Y. A. & Rashba, E. I. Oscillatory effects and the magnetic susceptibility of carriers in inversion layers. *J. Phys. C* **17**, 6039–6045 (1984).
26. Onoda, M., Murakami, S. & Nagaosa, N. Hall effect of light. *Phys. Rev. Lett.* **93**, 083901 (2004).
27. Raether, H. *Surface Plasmons on Smooth and Rough Surfaces and on Gratings* Ch. 1 (Springer, 1988).
28. Silva, A. *et al.* Performing mathematical operations with metamaterials. *Science* **343**, 160–163 (2014).
29. Huang, K. C. Y. *et al.* Electrically driven subwavelength optical nanocircuits. *Nature Photon.* **8**, 244–249 (2014).
30. Hafezi, M., Demler, E. A., Lukin, M. D. & Taylor, J. M. Robust optical delay lines with topological protection. *Nature Phys.* **7**, 907–912 (2011).

Supplementary Information is available in the online version of the paper.

Acknowledgements We acknowledge support from ONR-MURI (FA9550-12-1-0024), NSF-AMO (PHY-0969816), NSF-CUA (PHY-1125846) and DARPA SPARQC (W31P4Q-12-1-0017). We carried out all film deposition and device fabrication at the Harvard Center for Nanoscale Systems. J.P. acknowledges I. R. Hooper for useful discussions.

Author Contributions A.A.H. and H.P. conceived the study, and A.A.H., R.C.D., M.D.L. and H.P. designed the experiments. A.A.H., R.C.D., A.D. and N.P.d.L. developed the fabrication procedure. A.A.H., R.C.D., A.D. and M.P. performed experiments. A.A.H., R.C.D., D.S.W. and J.P. performed computational analyses and simulations. A.A.H., R.C.D., D.S.W., J.P., N.P.d.L., M.D.L. and H.P. contributed to theoretical descriptions. A.A.H., R.C.D., D.S.W., J.P., M.D.L. and H.P. wrote the manuscript, with extensive input from all authors.

Author Information Reprints and permissions information is available at www.nature.com/reprints. The authors declare no competing financial interests. Readers are welcome to comment on the online version of the paper. Correspondence and requests for materials should be addressed to H.P. (hongkun_park@harvard.edu) and M.D.L. (lukin@physics.harvard.edu).

Bipolar seesaw control on last interglacial sea level

G. Marino¹, E. J. Rohling^{1,2}, L. Rodríguez-Sanz¹, K. M. Grant¹, D. Heslop¹, A. P. Roberts¹, J. D. Stanford³ & J. Yu¹

Our current understanding of ocean–atmosphere–cryosphere interactions at ice-age terminations relies largely on assessments of the most recent (last) glacial–interglacial transition^{1–3}, Termination I (T-I). But the extent to which T-I is representative of previous terminations remains unclear. Testing the consistency of termination processes requires comparison of time series of critical climate parameters with detailed absolute and relative age control. However, such age control has been lacking for even the penultimate glacial termination (T-II), which culminated in a sea-level highstand during the last interglacial period that was several metres above present⁴. Here we show that Heinrich Stadial 11 (HS11), a prominent North Atlantic cold episode^{5,6}, occurred between 135 ± 1 and 130 ± 2 thousand years ago and was linked with rapid sea-level rise during T-II. Our conclusions are based on new and existing^{6–9} data for T-II and the last interglacial that we collate onto a single, radiometrically constrained chronology. The HS11 cold episode^{5,6} punctuated T-II and coincided directly with a major deglacial meltwater pulse, which predominantly entered the North Atlantic Ocean and accounted for about 70 per cent of the glacial–interglacial sea-level rise^{8,9}. We conclude that, possibly in response to stronger insolation and CO₂ forcing earlier in T-II, the relationship between climate and ice-volume changes differed fundamentally from that of T-I. In T-I, the major sea-level rise clearly post-dates^{3,10,11} Heinrich Stadial 1. We also find that HS11 coincided with sustained Antarctic warming, probably through a bipolar seesaw temperature response¹², and propose that this heat gain at high southern latitudes promoted Antarctic ice-sheet melting that fuelled the last interglacial sea-level peak.

Late Quaternary glacial–interglacial cycles exemplify the response of Earth's climate to combined insolation and CO₂ forcing⁴. Their overall 'sawtooth' structure consists of gradual global cooling and ice-volume build-up during glaciations, followed by rapid warming and melting during glacial terminations^{4,9,13}. Millennial-scale episodes of North Atlantic cooling and ice-rafted-debris (IRD) deposition, commonly referred to as Heinrich events¹⁴, punctuated each of the last five terminations^{15,16}. During T-I, North Atlantic cooling and IRD events occurred during Heinrich Stadial 1 (HS1, ~18–14.6 kyr ago, ka) and the Younger Dryas (YD, ~12.8–11.5 ka), which coincided with weakened Atlantic Meridional Overturning Circulation (AMOC), drought in the boreal tropics, and heat build-up and strengthening of wind-driven upwelling in the Southern Ocean¹. These developments were coupled with a bipolar temperature 'seesaw' and CO₂ release from the (Southern) ocean into the atmosphere¹. Neither HS1 nor the YD appear to correspond to periods with high rates of deglacial sea-level rise¹¹ (so-called meltwater pulses, MWPs). This raises the question of whether the North Atlantic climate and sea-level change were decoupled only during T-I, or if this decoupling applied also to other terminations with different forcing histories. Accordingly, we need detailed assessments of the relative phasing between bipolar seesaw, atmospheric CO₂, and sea level through older terminations, while the absolute timing of these processes allows the resolution of their relationship with insolation forcing.

Absolute chronologies for terminations older than T-I hinge on radiometric (U-series) dating of speleothems and corals, while marine sediment cores lack such independent age control. Pioneering studies

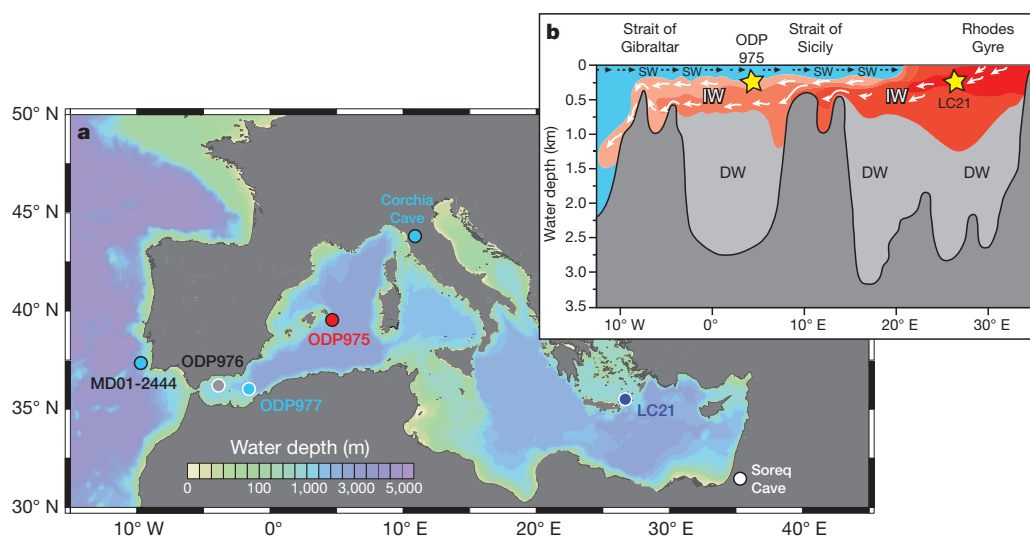


Figure 1 | Location of the palaeoclimate archives discussed here, and the Mediterranean circulation pattern. **a**, Bathymetric map of the Mediterranean Sea with locations of the marine and continental records discussed in the text. **b**, West–east cross-section across the Mediterranean Sea with a sketch of the basin's anti-estuarine circulation: surface inflow (black dashed arrows) through the Strait of Gibraltar and subsurface circulation and outflow

(white arrows) into the Atlantic Ocean (Methods). Yellow stars indicate the upper intermediate-water depth habitat of *N. pachyderma* (d) (Methods) at the location of core LC21 ($35^{\circ} 40' \text{ N}$, $26^{\circ} 35' \text{ E}$, water depth 1,522 m) and Ocean Drilling Program (ODP) Site 975 ($38^{\circ} 53.8' \text{ N}$, $4^{\circ} 30.6' \text{ E}$, water depth 2,415 m). SW, surface water (blue); IW, intermediate water (red); DW, deep water (grey).

¹Research School of Earth Sciences, The Australian National University, Canberra, Australian Capital Territory 2601, Australia. ²Ocean and Earth Science, University of Southampton, National Oceanography Centre, Southampton SO14 3ZH, UK. ³Department of Geography, Wallace Building, Swansea University, Singleton Park, Swansea SA2 8PP, UK.

placed pre-T-I terminations on radiometrically constrained timescales using: (i) correlation between North Atlantic deep-sea benthic stable oxygen isotopes ($\delta^{18}\text{O}_{\text{benthic}}$) and coral sea-level benchmarks¹⁷, (ii) inferred similarity between North Atlantic sea surface temperature (SST) and an Italian speleothem $\delta^{18}\text{O}$ ($\delta^{18}\text{O}_{\text{speleothem}}$) record interpreted in terms of precipitation change⁷, and (iii) inferred synchronicity of North Atlantic cold events and Asian Monsoon weak episodes, archived in $\delta^{18}\text{O}_{\text{speleothem}}$ time series^{16,18}. However, deep-sea hydrographic changes complicate interpretation of North Atlantic $\delta^{18}\text{O}_{\text{benthic}}$ records in terms of sea-level change¹⁹, and factors other than precipitation may affect $\delta^{18}\text{O}_{\text{speleothem}}$ in the Mediterranean region⁸. Finally, the relationship between North Atlantic climate and Asian Monsoon intensity may not be straightforward on millennial timescales²⁰. Hence, these studies laid critical foundations, but did not deliver a conclusive, quantitative (with uncertainties) chronological framework for pre-T-I terminations. Among these, T-II is noteworthy because its overall insolation forcing considerably exceeded that of T-I (Extended Data Fig. 1), and it culminated in an interglacial that was warmer than the Holocene^{4,21}, with sea level above present⁴.

To advance the debate, we present a new radiometrically constrained chronology for North Atlantic records of climate variability across T-II and the last interglacial period. We use records that are co-registered in single sediment-sample series (that is, phase relationships are unambiguous), and well-understood land-sea climate relationships to transfer—with rigorous uncertainty propagation—radiometric (U-series) ages to marine records. We exploit the well-documented intermediate-water connectivity between the eastern and western Mediterranean Sea (Methods), and the relationship between marine surface water microfossil $\delta^{18}\text{O}$ and U-series-dated regional $\delta^{18}\text{O}_{\text{speleothem}}$ records^{7,8} (Extended Data Fig. 2). We generated centennially resolved $\delta^{18}\text{O}$ and $\delta^{13}\text{C}$ records for Mediterranean surface- and intermediate-water dwelling planktic foraminifera *Globigerina bulloides* and *Neoglobobulimina pachyderma* (dextral) (Methods), respectively, from western Mediterranean Ocean Drilling Program (ODP) Site 975 (ODP975, Fig. 1). Next, we synchronized the ODP975 $\delta^{18}\text{O}_{\text{N. pachyderma}}$ (d) record to the $\delta^{18}\text{O}_{\text{N. pachyderma}}$ (d) record of eastern Mediterranean core LC21 (Fig. 2a; Methods). The latter was placed previously⁸ on a radiometric timescale by relating its co-registered surface $\delta^{18}\text{O}$ signal to Soreq Cave $\delta^{18}\text{O}_{\text{speleothem}}$. Finally, we use the co-registered $\delta^{18}\text{O}_{\text{G. bulloides}}$ of ODP975 to further transfer the radiometrically constrained timescale to the $\delta^{18}\text{O}_{\text{G. bulloides}}$ record of nearby ODP Sites 976 (ODP976) and 977, and to core MD01-2444 and, in turn, to the SST and/or IRD records of North Atlantic climate variability that are archived in these sediment cores (Extended Data Figs 2, 3, Methods).

Comparison of $\delta^{18}\text{O}_{\text{G. bulloides}}$ from ODP975 and ODP976 on their new radiometrically constrained timescale with the Corchia Cave $\delta^{18}\text{O}_{\text{speleothem}}$ record on its own radiometric chronology (Methods) reveals a striking similarity with respect to both timing and magnitude of $\delta^{18}\text{O}$ shifts, notably between ~140 and ~129 ka (Fig. 2b). Possible correlation between western Mediterranean and Corchia Cave $\delta^{18}\text{O}$ signals was contemplated before⁷, but—at that stage—an alternative coupling of North Atlantic warming with increased precipitation over central Italy was favoured. The two interpretations lead to substantially (up to ~4 kyr) different timings for HS11. The approach used here is independent of assumptions about the phasing between North Atlantic climate and $\delta^{18}\text{O}_{\text{speleothem}}$. Instead, it diagnostically indicates a source-water control on Corchia Cave $\delta^{18}\text{O}_{\text{speleothem}}$; negative $\delta^{18}\text{O}$ anomalies in North Atlantic and western Mediterranean surface waters—during Heinrich events¹⁴ (see below)—were transmitted via the hydrological cycle to the cave catchment. The $\delta^{18}\text{O}$ similarity between ODP975 and Corchia Cave provides strong and independent validation of the LC21-based radiometric chronology for ODP975, and thus to the LC21–Soreq Cave synchronization used previously to provide radiometric age constraints to sea-level records⁸. Validation of the LC21–Soreq Cave synchronization was obtained using U-series-dated Asian monsoon records⁹, so the T-II chronology

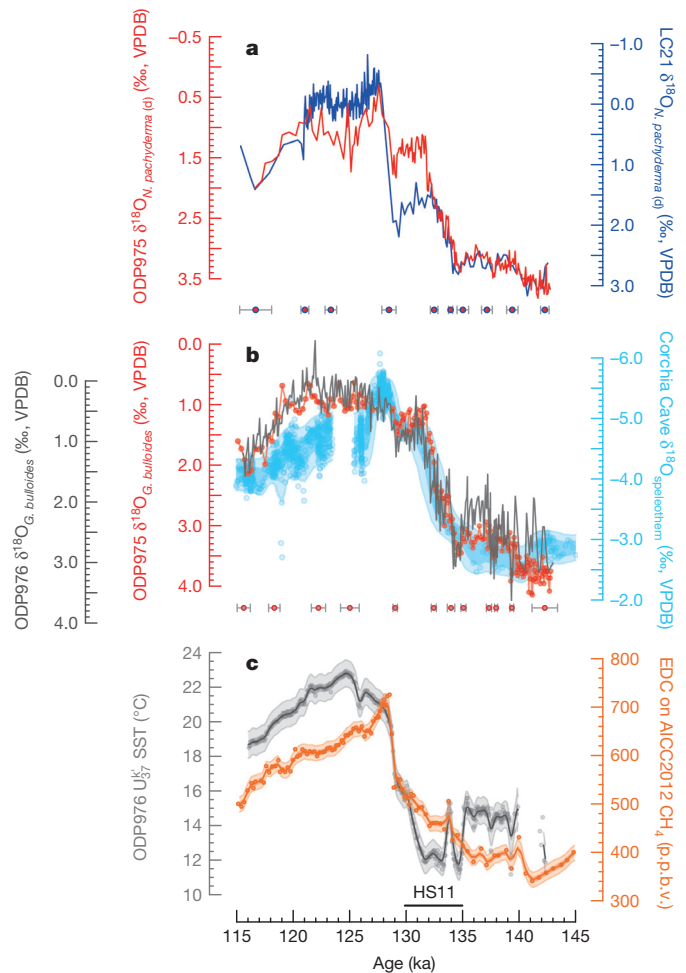


Figure 2 | Construction and validation of a radiometrically constrained chronology for western Mediterranean Sea ODP975 and ODP976.

a, Synchronization of *N. pachyderma* (d) $\delta^{18}\text{O}$ from ODP975 (red line) to its counterpart from eastern Mediterranean core LC21 (blue line; Methods), which was placed on a radiometric chronology by ref. 8. Red filled circles and grey error bars depict the tie points used to synchronize ODP975 to LC21 and the 2σ synchronization uncertainties, respectively (Methods, Extended Data Table 1). **b**, Synchronization of *G. bulloides* $\delta^{18}\text{O}$ from ODP976 (grey line; after ref. 6) to its counterpart from nearby ODP975 (red line) on its radiometrically constrained chronology. Grey filled circles and error bars depict the tie points used to synchronize ODP976 to ODP975 and the 2σ synchronization uncertainties, respectively (Methods, Extended Data Table 2). Comparison of $\delta^{18}\text{O}_{\text{G. bulloides}}$ from ODP975 and ODP976 with the speleothem $\delta^{18}\text{O}$ ($\delta^{18}\text{O}_{\text{speleothem}}$) from Corchia Cave⁷ (Italy) is made to validate (not to constrain) the chronology of the western Mediterranean cores. Confidence limits (95% lighter sky blue, 68% darker blue) for the Corchia Cave $\delta^{18}\text{O}_{\text{speleothem}}$ data (sky blue circles) result from Monte Carlo analysis (Methods) of the chronological and $\delta^{18}\text{O}_{\text{speleothem}}$ uncertainties (ref. 7). **c**, Comparison of the western Mediterranean ODP976 sea surface temperature (SST) data⁶ (grey circles) on the radiometrically constrained chronology developed in this study with the Antarctic atmospheric methane (CH_4) record²³ (orange circles) on the AICC2012 timescale²², supporting consistency between the two independent chronologies. Confidence limits for the ODP976 SST (95% light grey, probability maximum with 95% uncertainty, heavier grey line and envelope) and atmospheric CH_4 concentrations (95% light orange, probability maximum with 95% uncertainty, heavier orange line and envelope) result from Monte Carlo analysis of their chronological and proxy related uncertainties, employing Gaussian filters of 0.2 and 0.4 kyr, respectively (Methods). Black bar indicates the timing of Heinrich Stadial 11 (HS11).

of sea-level change now involves agreement between three independent, radiometrically constrained approaches.

Investigation of the interhemispheric climate relationships requires first an assessment of consistency between our new radiometrically

constrained chronology and the AICC2012 timescale for the Antarctic EPICA Dome C (EDC) ice core²². Building on the notion that atmospheric methane (CH_4) concentrations and Greenland/North Atlantic temperatures covaried on millennial timescales²³, we compare the western Mediterranean SST record (reflecting North Atlantic climate⁶) on our new chronology with the EDC CH_4 record²³ on AICC2012 (Fig. 2c). The remarkable signal similarity between 131 and 128 ka supports consistency between the two independent chronologies across this interval. Such consistency plausibly extends back to ~ 134 ka, when a distinct SST maximum coincided with a CH_4 peak. Although the latter is documented by a single data point in EDC, the

Vostok Antarctic ice core CH_4 record²⁴ appears to corroborate the occurrence of a CH_4 peak at this time.

In the following we examine in millennial-scale detail the relative timing between insolation, North Atlantic climate, sea level, Antarctic temperatures, and atmospheric CO_2 across HS11 and the transition into the last interglacial period (Fig. 3a–f). T-II contains two major meltwater pulses⁹ (MWP-2A and MWP-2B), which are centred on 139 ± 1 and 133 ± 1 ka (2σ uncertainties⁸) and coincided within uncertainties with two North Atlantic cooling episodes (Fig. 3c, d). MWP-2A indicates an early phase of ice-sheet retreat. Similar to its T-I counterpart³ at ~ 19 ka, it coincided with a short-lived ($\sim 2^\circ\text{C}$) North Atlantic cooling. MWP-2B is more convincingly resolved and marks a steep ~ 70 m sea-level rise ($\sim 70\%$ of the glacial–interglacial change) at rates of 28 ± 8 m kyr⁻¹ (refs 8, 9). It lagged 4 ± 1 kyr behind the boreal summer insolation rise and coincided with the prominent North Atlantic cold phase, HS11 (Fig. 3b–d). Our new chronology places the initiation and termination of HS11 at 135 ± 1 and 130 ± 2 ka (2σ uncertainties), respectively, and the ~ 0.5 -kyr warm interlude⁶ that briefly interrupted it at 134 ± 1 ka (Fig. 3c), in overall agreement with the ‘synthetic’ Greenland record¹⁶ (Extended Data Fig. 3). HS11 also coincided with over half of the glacial–interglacial atmospheric CO_2 increase, and with $\sim 9^\circ\text{C}$ Antarctic warming¹³ (Fig. 3e, f). Only $\sim 5^\circ\text{C}$ of this warming can be ascribed to radiative forcing²¹, which leaves $\sim 4^\circ\text{C}$ of ‘residual’ warming that we interpret as the Southern Ocean bipolar temperature seesaw response¹² to meltwater-forced AMOC collapse and attendant North Atlantic cooling (Fig. 3c, d).

An intense seesaw response with strong North Atlantic cooling suggests that the meltwater entered the North Atlantic. This inference is supported by major North Atlantic IRD deposition (Fig. 3b), the large magnitude (~ 70 m) sea-level rise associated with MWP-2B (maximum freshwater flux of 0.3 ± 0.04 Sv; Fig. 4a) that requires intense reduction of the large northern ice-sheets, and the distinct source-water-related negative shift in $\delta^{18}\text{O}$ of precipitation ($\Delta\delta^{18}\text{O}_{\text{precipitation}}$) at Corchia Cave (Fig. 4b), interpreted here as a reflection of meltwater-based freshening of the wider North Atlantic (Methods). The seesaw response at the time of HS11 is also corroborated by its agreement with the established relationship between magnitudes of Antarctic warming and North Atlantic stadial duration during the last glacial cycle (Extended Data Fig. 4). Finally, HS11 coincided with a weak Asian monsoon event¹⁸ and South American monsoon intensification²⁵, both archived in radiometrically dated speleothems and interpreted in terms of a southward shift of the Intertropical Convergence Zone (ITCZ) in response to AMOC weakening. The relative timing between ITCZ dynamics, AMOC, and North Atlantic climate is well documented across T-I and within the

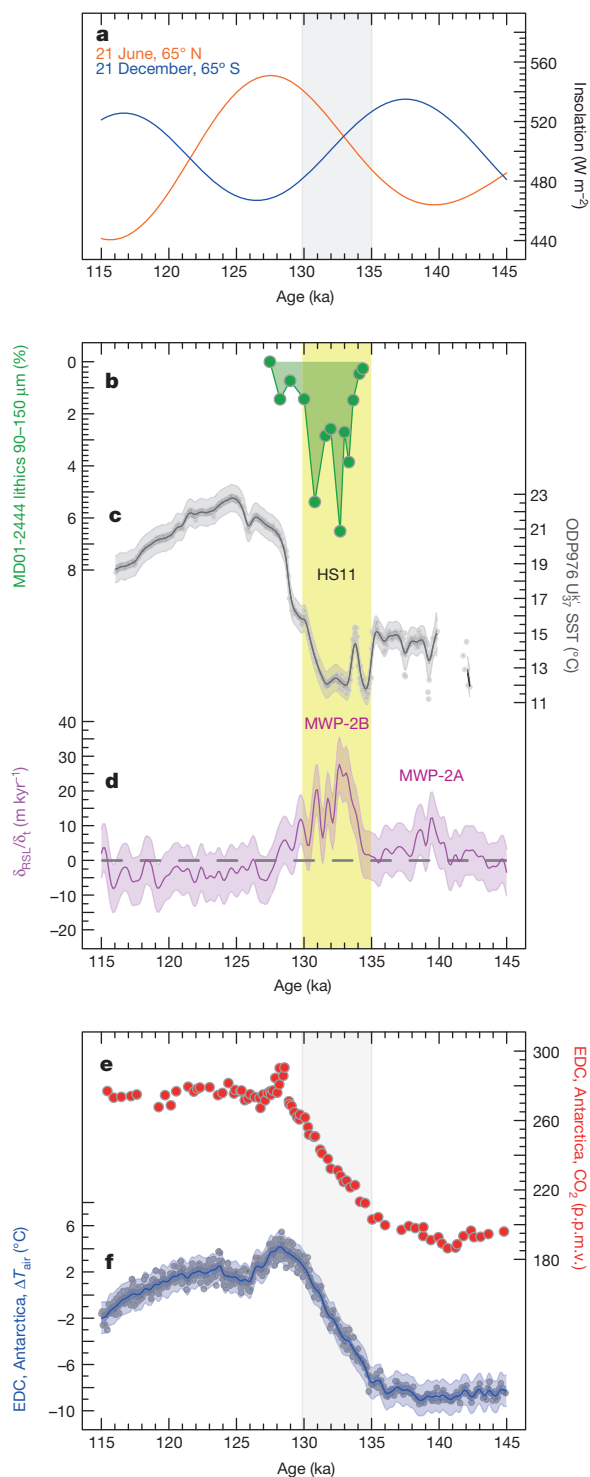


Figure 3 | Interhemispheric records of climate change across glacial Termination II. a, Boreal and austral summer insolation curves; age is

calculated using astronomical solutions³¹. b, Ice-rafted-debris (IRD) record from core MD01-2444, Iberian Margin¹⁹ (North Atlantic). c, Sea surface temperature (SST) record from ODP976, western Mediterranean Sea⁶. The 95% confidence limits (light grey envelope) and probability maximum (heavier grey line) with 95% uncertainty (heavier grey envelope) of the SST data (grey circles) are based on a Monte Carlo analysis of chronological and SST uncertainties, employing a 0.2 kyr Gaussian filter (Methods). Profiles in b and c are on the radiometrically constrained chronology developed in this study (Methods). d, Rates of relative sea-level change ($\delta_{\text{RSL}}/\delta_t$) with associated 95% confidence limits (magenta shaded envelopes) of the probability maximum (magenta solid line) from Monte Carlo analysis of uncertainties in the relative sea-level reconstructions and chronology⁹. e, Composite atmospheric CO_2 concentrations from EPICA Dome C (EDC) (Methods). f, Antarctic air temperatures¹³ (ΔT_{air}) from EDC. The 95% confidence limits (light blue envelope) and probability maximum (heavier blue line) and its associated 95% uncertainty (heavier blue envelope) for the ΔT data (blue circles) are based on a Monte Carlo analysis of chronological and ΔT uncertainties, employing a 0.2 kyr Gaussian filter (Methods). Data in e and f are plotted on the AICC2012 timescale²² (Methods). HS11, Heinrich Stadial 11; MWP, meltwater pulse.

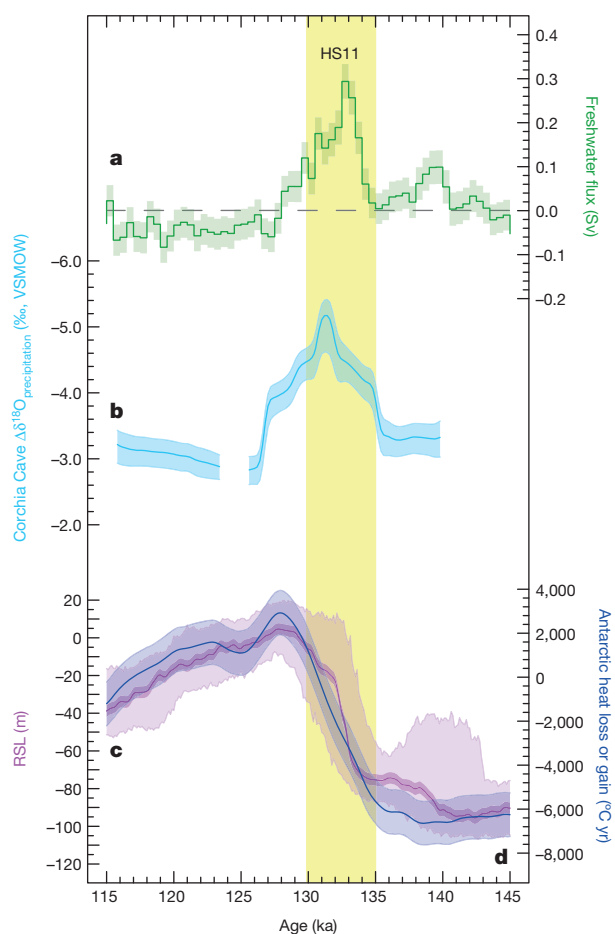


Figure 4 | Origin and impacts of meltwater pulses during glacial termination II. **a**, Freshwater fluxes calculated (Supplementary Information) from rates of sea-level change⁹. **b**, Ice-volume and temperature corrected $\delta^{18}\text{O}$ of Corchia Cave speleothem (Methods), indicating isotopic anomalies of precipitation in the cave catchment. Envelopes are the 95% confidence limits of the probability maximum (solid line) obtained from a Monte Carlo approach that takes into account proxy related and chronological uncertainties of the various records (Methods). **c**, Relative Sea Level (RSL)⁹. The 95% confidence limits (light magenta) and the probability maximum with 95% uncertainty (heavy magenta line and shading) were presented in ref. 9. **d**, Antarctic heat loss/gain obtained by integrating the Antarctic temperatures¹³ over a period of 0.75 ± 0.15 kyr, using a Monte Carlo approach employing a 0.8 kyr Gaussian filter of the data (blue).

last glacial cycle²⁶. Similar scenarios were suggested for previous terminations¹⁸ (including T-II), but required assumptions about timing relationships between records. By placing all records on a single radiometrically constrained chronology, our results overcome this limitation, and independently corroborate the scenario for T-II.

Since $\sim 70\%$ of the glacial–interglacial sea-level rise (MWP-2B) occurred during a phase of weak AMOC (HS11; Fig. 3b–d), T-II fundamentally differed from T-I. During T-I, $\sim 75\%$ of the sea-level rise¹¹ post-dated the major deglacial cooling phase in the North Atlantic (HS1), and the largest meltwater pulse (MWP-1A; 15–20% of the deglacial sea-level rise) peaked when the North Atlantic was warm (or warming) and AMOC was relatively strong (or strengthening)^{3,10,27}. This fuelled arguments that Antarctic ice sheets contributed substantially to MWP-1A (ref. 10). In contrast, we find that MWP-2B was more than three times larger than MWP-1A, and was tied directly to circum-North-Atlantic ice-sheet reduction and attendant North Atlantic cooling. This fundamentally different relationship between North Atlantic climate and sea-level change during the last two terminations indicates that during T-II, Northern Hemisphere ice

sheets collapsed early in the termination, possibly in response to a combination of overall stronger (and more rapidly rising¹⁸) boreal summer insolation and higher atmospheric CO_2 (Extended Data Fig. 1).

Our reconstructed phasing of interhemispheric climate developments through HS11 is consistent with a southward shift and/or possible strengthening of Southern Ocean westerlies²⁸, and associated subsurface oceanic warming around Antarctica²⁹. This provides a mechanism for conveying the oceanic heat related to the bipolar seesaw to Antarctica. The attendant excess warming of $\sim 4^\circ\text{C}$ in Antarctica²¹ (see above) during HS11 would have then affected the Antarctic ice sheet stability through processes such as under-ice melting and grounding line retreat of ice-shelves³⁰. To account for relatively long (but poorly known) adjustment timescales of this major ice sheet to warming, including the excess 4°C , we approximate heat gain/loss by integrating the Antarctic temperature record over time¹³. We find that the timings of maximum heat gain and the last interglacial sea-level peak⁸ match best for an overall integration timescale of 0.75 ± 0.15 kyr (Fig. 4c).

Securing records to a single, radiometrically constrained chronology reveals the sequence of events through T-II. An initial (minor but significant) ice-sheet reduction caused MWP-2A during a Northern Hemisphere insolation minimum. Next followed the main phase of northern ice-sheet reduction (MWP-2B), ~ 4 kyr after the onset of insolation rise, which caused AMOC collapse, with attendant North Atlantic cooling and (seesaw) Southern Ocean warming. We infer that resultant Antarctic heating drove continuation of sea-level rise well after MWP-2B, up to several metres above present⁴, which predominantly reflects Antarctic ice reduction.

Online Content Methods, along with any additional Extended Data display items and Source Data, are available in the online version of the paper; references unique to these sections appear only in the online paper.

Received 26 November 2014; accepted 15 April 2015.

- Denton, G. H. *et al.* The last glacial termination. *Science* **328**, 1652–1656 (2010).
- Clark, P. U. *et al.* Global climate evolution during the last deglaciation. *Proc. Natl Acad. Sci. USA* **109**, E1134–E1142 (2012).
- Carlson, A. E. & Clark, P. U. Ice sheet sources of sea level rise and freshwater discharge during the last deglaciation. *Rev. Geophys.* **50**, RG4007 (2012).
- Masson-Delmotte, V. *et al.* in *Climate Change 2013: The Physical Science Basis* (eds Stocker, T. F.) Ch. 5 383–464 (Cambridge Univ. Press, 2013).
- Oppo, D. W., McManus, J. F. & Cullen, J. L. Evolution and demise of the Last Interglacial warmth in the subpolar North Atlantic. *Quat. Sci. Rev.* **25**, 3268–3277 (2006).
- Martrat, B., Jimenez-Amat, P., Zahn, R. & Grimalt, J. O. Similarities and dissimilarities between the last two deglaciations and interglaciations in the North Atlantic region. *Quat. Sci. Rev.* **99**, 122–134 (2014).
- Drysdale, R. N. *et al.* Evidence for obliquity forcing of glacial termination II. *Science* **325**, 1527–1531 (2009).
- Grant, K. M. *et al.* Rapid coupling between ice volume and polar temperature over the past 150,000 years. *Nature* **491**, 744–747 (2012).
- Grant, K. M. *et al.* Sea-level variability over five glacial cycles. *Nature Commun.* **5**, 5076 (2014).
- Clark, P. U., Mitrovica, J. X., Milne, G. A. & Tamisiea, M. E. Sea-level fingerprinting as a direct test for the source of global meltwater pulse 1A. *Science* **295**, 2438–2441 (2002).
- Lambeck, K., Rouby, H., Purcell, A., Sun, Y. & Sambridge, M. Sea level and global ice volumes from the Last Glacial Maximum to the Holocene. *Proc. Natl Acad. Sci. USA* **111**, 15296–15303 (2014).
- Stocker, T. F. & Johnsen, S. J. A minimum thermodynamic model for the bipolar seesaw. *Paleoceanography* **18**, 1087 (2003).
- Jouzel, J. *et al.* Orbital and millennial Antarctic climate variability over the past 800,000 years. *Science* **317**, 793–796 (2007).
- Hemming, S. R. Heinrich events: massive late Pleistocene detritus layers of the North Atlantic and their global climate imprint. *Rev. Geophys.* **42**, RG1005 (2004).
- McManus, J. F., Oppo, D. W. & Cullen, J. L. A 0.5-million-year record of millennial-scale climate variability in the North Atlantic. *Science* **283**, 971–975 (1999).
- Barker, S. *et al.* 800,000 years of abrupt climate variability. *Science* **334**, 347–351 (2011).
- Shackleton, N. J., Sanchez-Goni, M. F., Pailler, D. & Lancelot, Y. Marine isotope sub-stage 5e and the Eemian interglacial. *Glob. Planet. Change* **36**, 151–155 (2003).
- Cheng, H. *et al.* Ice age terminations. *Science* **326**, 248–252 (2009).
- Skinner, L. C. & Shackleton, N. J. Deconstructing Terminations I and II: revisiting the glacioeustatic paradigm based on deep-water temperature estimates. *Quat. Sci. Rev.* **25**, 3312–3321 (2006).

20. Rohling, E. J. *et al.* Controls on the East Asian monsoon during the last glacial cycle, based on comparison between Hulu Cave and polar ice-core records. *Quat. Sci. Rev.* **28**, 3291–3302 (2009).
21. Masson-Delmotte, V. *et al.* EPICA Dome C record of glacial and interglacial intensities. *Quat. Sci. Rev.* **29**, 113–128 (2010).
22. Bazin, L. *et al.* An optimized multi-proxy, multi-site Antarctic ice and gas orbital chronology (AICC2012): 120–800 ka. *Clim. Past* **9**, 1715–1731 (2013).
23. Loulergue, L. *et al.* Orbital and millennial-scale features of atmospheric CH₄ over the past 800,000 years. *Nature* **453**, 383–386 (2008).
24. Delmotte, M. *et al.* Atmospheric methane during the last four glacial-interglacial cycles: Rapid changes and their link with Antarctic temperature. *J. Geophys. Res. D* **109**, D12104 (2004).
25. Wang, X. F. *et al.* Wet periods in northeastern Brazil over the past 210 kyr linked to distant climate anomalies. *Nature* **432**, 740–743 (2004).
26. Schneider, T., Bischoff, T. & Haug, G. H. Migrations and dynamics of the intertropical convergence zone. *Nature* **513**, 45–53 (2014).
27. Weaver, A. J., Saenko, O. A., Clark, P. U. & Mitrovica, J. X. Meltwater pulse 1A from Antarctica as a trigger of the Bølling-Allerød warm interval. *Science* **299**, 1709–1713 (2003).
28. Toggweiler, J. R., Russell, J. L. & Carson, S. R. Midlatitude westerlies, atmospheric CO₂, and climate change during the ice ages. *Paleoceanography* **21**, PA2005 (2006).
29. Spence, P. *et al.* Rapid subsurface warming and circulation changes of Antarctic coastal waters by poleward shifting winds. *Geophys. Res. Lett.* **41**, 4601–4610 (2014).
30. Joughin, I., Alley, R. B. & Holland, D. M. Ice-sheet response to oceanic forcing. *Science* **338**, 1172–1176 (2012).
31. Laskar, J. *et al.* A long-term numerical solution for the insolation quantities of the Earth. *Astron. Astrophys.* **428**, 261–285 (2004).

Supplementary Information is available in the online version of the paper.

Acknowledgements We thank the International Ocean Discovery Program for providing samples from Leg 161 and W. Hale for sampling assistance. M. Charidemou contributed to a pilot study on ODP975, J. Amies to preliminary stratigraphic assessment, and J. Cali to stable isotope analyses. We thank M. Bar-Matthews for providing the updated version of the Soreq Cave chronology table, R. N. Drysdale and J. Hellstrom for helpful discussions, and B. Martrat and L. Skinner for making published data available. This study was supported by Australian Research Council Australian Laureate Fellowship FL120100050 and by UK-NERC project NE/I009906/1 (E.J.R.).

Author Contributions G.M. and E.J.R. designed the study. G.M. prepared the foraminiferal samples for stable isotope analyses and together with E.J.R. and D.H. performed the statistical analysis. L.R.S. performed the stable isotope analyses. K.M.G. and J.D.S. oversaw early stratigraphic assessment. All authors contributed to interpretation and preparation of the final manuscript.

Author Information Reprints and permissions information is available at www.nature.com/reprints. The authors declare no competing financial interests. Readers are welcome to comment on the online version of the paper. Correspondence and requests for materials should be addressed to G.M. (Gianluca.Marino@anu.edu.au).

METHODS

Core material. Ocean Drilling Program (ODP) Site 975 was drilled by RV *Joides Resolution* in the western Mediterranean Sea (Fig. 1; 38° 53.8' N, 4° 30.6' E; water depth 2,415 m). ODP Site 975 is located on the Menorca Rise³², along the path of the Atlantic surface water entering the Mediterranean Sea through the Strait of Gibraltar and flowing eastward across the basin^{33–36}. Sections 2H4 to 2H6 from ODP Site 975 Hole C were sampled using u-channels, and subsequently sliced at 1 cm resolution. Data were generated for this study at a resolution of 1 to 2 cm.

Stable oxygen ($\delta^{18}\text{O}$) and carbon ($\delta^{13}\text{C}$) isotopes. For ODP Site 975, 20–30 individuals of *G. bulloides* (300–355 μm size fraction) and 10–20 individuals of *N. pachyderma* (d) (212–250 μm size fraction) were picked. For core LC21, 10–15 individuals of *N. pachyderma* (d) (250–300 μm size fraction) were picked to increase the resolution and spliced together with previously published records^{8,37} between 143 and 129 ka. To avoid complications arising from size-dependent vital effects in planktic foraminifera^{38,39}, we constrained the size window of the picked foraminifera from ODP Site 975 and core LC21 to a maximum of $\sim 55 \mu\text{m}$. This compromised the continuity of the *G. bulloides* $\delta^{18}\text{O}$ and $\delta^{13}\text{C}$ records between 129 and 127 ka in ODP Site 975, as *G. bulloides* abundance drops significantly in that interval, and insufficient numbers were available in one strict size window.

Prior to analysis, foraminiferal samples were crushed, cleaned and ultrasonicated briefly in methanol. The cleaned samples were then analysed ($\delta^{18}\text{O}$ and $\delta^{13}\text{C}$) at the Australian National University with a Thermo Finnigan Delta Advantage mass spectrometer coupled to a Kiel IV carbonate device, in which samples react with 105% phosphoric acid at 75 °C. Results were normalized to the Vienna Pee Dee Belemnite (VPDB) scale with the NBS-19 ($\delta^{18}\text{O} = -2.20\text{‰}$, $\delta^{13}\text{C} = 1.95\text{‰}$) and NBS-18 ($\delta^{18}\text{O} = -23.20\text{‰}$, $\delta^{13}\text{C} = -5.014\text{‰}$) carbonate standards. External reproducibility (1σ) of a carbonate standard (NBS-19) was better than $\pm 0.08\text{‰}$ for $\delta^{18}\text{O}$ and $\pm 0.06\text{‰}$ for $\delta^{13}\text{C}$.

Chronology for ODP Site 975. Synchronization of western Mediterranean ODP Site 975 to eastern Mediterranean core LC21 exploits the strong oceanographic connectivity between the two Mediterranean sub-basins at intermediate depths. Vigorous intermediate circulation transports water westward from the Rhodes Gyre (nearby core LC21, Fig. 1), to the western Mediterranean, and eventually through the Strait of Gibraltar as Mediterranean outflow into the Atlantic Ocean (for example, refs 33–36). Data⁴⁰ and numerical modelling⁴¹ indicate that this intermediate-water connection is an enduring feature of Mediterranean circulation through time. Accordingly, characterization of past geochemical property changes in intermediate waters across the Mediterranean provides a valuable tool for synchronizing sediment cores from different sectors of the basin. To characterize variability of the intermediate waters at ODP Site 975 and core LC21, we use new (see above) and existing^{8,37} $\delta^{18}\text{O}$ and $\delta^{13}\text{C}$ data for the upper intermediate-water dwelling³⁸ planktic foraminifer *N. pachyderma* (d).

Based on the enduring intermediate-water connection, the $\delta^{18}\text{O}_{\text{N. pachyderma (d)}}$ profile of ODP Site 975 is synchronized with that of LC21 (Fig. 2a, Extended Data Figs 2, 5), for which a radiometrically constrained chronology was recently developed, based on a strong surface-water $\delta^{18}\text{O}$ relationship with $\delta^{18}\text{O}$ in speleothems ($\delta^{18}\text{O}_{\text{speleothem}}$) in Soreq Cave (Israel)⁸. Specifically, we identified ten $\delta^{18}\text{O}_{\text{N. pachyderma (d)}}$ shifts, each represented by multiple (ranging from 3 to 34) data points, and used their mid-points to place the ODP Site 975 records onto the LC21 chronology of ref. 8 (Fig. 2a, Extended Data Fig. 5a). We linearly interpolated ages between age control points, assuming constant sedimentation rates between them. We adopted this approach because there is no evidence to suggest highly variable sedimentation rates at ODP Site 975. In addition, this assumption does not affect the age of the individual tie-points and hence our conclusions, given that the timing of HS11 is constrained by four age control points.

The ODP Site 975 and LC21 $\delta^{18}\text{O}_{\text{N. pachyderma (d)}}$ profiles are virtually identical between ~ 143 and ~ 132 ka. An abrupt shift to lighter values at ~ 132 ka follows at ODP Site 975, while it is not observed in LC21. Next, the ODP Site 975 $\delta^{18}\text{O}_{\text{N. pachyderma (d)}}$ stabilizes at values of $\sim 1.6\text{‰}$ before shifting again at 129 ka (as does its LC21 counterpart) to reach a distinct minimum 128 kyr ago. The interval between 132 and 130 ka coincides with the strongest phase of Heinrich Stadial 11, when, according to our analysis, the meltwater discharge into the North Atlantic Ocean reached its maximum (see main text). This delivered large volumes of isotopically light freshwater to the North Atlantic and (via the Strait of Gibraltar) to the western Mediterranean Sea. Similar to (smaller) events during the last glacial cycle⁴², such influxes would have affected intermediate levels of the water column, for example, through winter mixing in the north-western Mediterranean⁴³, where ODP Site 975 is located (Fig. 1). Between 128 and 121 ka, the ODP Site 975 and LC21 $\delta^{18}\text{O}_{\text{N. pachyderma (d)}}$ records diverge somewhat (although both become more positive at 126–123 ka). This is probably due to enhanced stratification in the eastern Mediterranean during the monsoon-related freshwater inputs along the North African Margin^{36–38,44–46}.

From ~ 121 to ~ 117 ka, there is a similar magnitude positive shift in the ODP Site 975 and LC21 $\delta^{18}\text{O}_{\text{N. pachyderma (d)}}$ records.

Our inferred synchronization of marine sediment records and the accuracy of the radiometrically constrained chronology we derived for ODP Site 975 can be independently validated (Extended Data Fig. 2). First, we did not use the $\delta^{13}\text{C}_{\text{N. pachyderma (d)}}$ profiles for ODP975 and core LC21 to constrain the synchronization between the two sites but use those data on the synchronized age model for validation purposes (Extended Data Fig. 5b). There is a remarkable agreement between the ODP975 and LC21 $\delta^{13}\text{C}_{\text{N. pachyderma (d)}}$ profiles particularly between 129 and 126 ka and between 123 and 120 ka, when both records have considerably lighter values than in the preceding glacial and deglacial periods (Extended Data Fig. 5b). The $\delta^{13}\text{C}_{\text{N. pachyderma (d)}}$ minimum is a characteristic feature of intervals of sapropel deposition in the eastern Mediterranean and testifies to subsurface accumulation of isotopically light respiration products in response to decreased deep sea ventilation^{36–38,45,47}. With an isotopic shift in excess of -3‰ , this feature is particularly prominent during last interglacial sapropel S5 (ref. 38), which is well-documented^{37,46,48,49} and precisely dated⁸ (~ 128 to ~ 121 ka) in core LC21. Contemporaneous $\delta^{13}\text{C}_{\text{N. pachyderma (d)}}$ minima in both core LC21 and ODP Site 975 during S5, therefore, supports our synchronization, in that they indicate that a low- $\delta^{13}\text{C}$ anomaly has been effectively transferred via intermediate waters from the eastern to the western Mediterranean basin, in line with previous studies⁴⁰. The ~ 2 kyr shift to heavier $\delta^{13}\text{C}_{\text{N. pachyderma (d)}}$ values between 126 and 124 ka at ODP Site 975 reflects an interval of potentially weakened sapropel conditions in the eastern Mediterranean during which deep-sea ventilation may have intermittently resumed^{37,44,45} and the transport of low- $\delta^{13}\text{C}$ water to the western basin interrupted. Second, between 140 and 129 ka there is a strong similarity between changes in the ODP Site 975 $\delta^{18}\text{O}_{\text{G. bulloides}}$ and $\delta^{18}\text{O}_{\text{speleothem}}$ from Corchia Cave (Fig. 2b). This indicates that the large negative shift in the $\delta^{18}\text{O}_{\text{speleothem}}$ between ~ 135 and ~ 130 ka resulted mostly from a ^{18}O -depletion of similar magnitude in the source of precipitation for Corchia, which at present⁵⁰ and on glacial-interglacial timescales⁵¹ is the wider North Atlantic Ocean/western Mediterranean Sea. Note that source water influence on $\delta^{18}\text{O}_{\text{speleothem}}$ is a common feature of the Mediterranean cave records^{8,36,52,53}. This interpretation is further corroborated by the fact that increase in speleothem growth rates and decrease in speleothem $\delta^{13}\text{C}$ did not occur before ~ 130 ka⁷ and by a similarly timed growth rate increase in a nearby cave⁵⁴. Concurrence of these climate signals in the mid-latitude speleothems indicates a transition from drier/colder to wetter/warmer conditions⁷ that therefore occurred at the end of the large negative $\delta^{18}\text{O}_{\text{speleothem}}$ shift, that is, after 130 ka.

Chronology for ODP Sites 976 and 977 and core MD01-2444. The $\delta^{18}\text{O}_{\text{G. bulloides}}$ record for core ODP Site 975 is used to transfer our new radiometrically constrained chronology of ODP Site 975 to $\delta^{18}\text{O}_{\text{G. bulloides}}$ in other western Mediterranean (ODP Sites 976 and 977) and Iberian Margin (North Atlantic, MD01-2444) sediment cores (Fig. 2b, Extended Data Figs 2, 3a, c). Alignment of co-registered (same sample series) alkenone-based sea surface temperature (SST) records from ODP Site 977 and core MD01-2444 with that from ODP Site 976 lends credence to the robustness of the $\delta^{18}\text{O}_{\text{G. bulloides}}$ -based synchronization (Extended Data Fig. 5b, d).

Propagation of chronological uncertainties. Propagation of chronological uncertainties through the various synchronization steps used in this study to transfer the chronology of core LC21 (ref. 8) to ODP Site 975 and then to ODP Site 976, ODP Site 977, and core MD01-2444 follows the exact same approach used by Grant *et al.* (ref. 8). The steps are outlined below.

(i) From core LC21 to ODP Site 975. For LC21 the chronological uncertainty at each depth level was obtained by linearly interpolating the uncertainties between the tie-points used for transferring the radiometric chronology of Soreq Cave to LC21 (ref. 8). Next we calculate root-mean-square errors (MSE) that propagate all the chronological uncertainties involved in the synchronization of ODP Site 975 to LC21. Specifically, we include the dating error associated with the LC21 chronology of Grant *et al.* (ref. 8), the sample spacing of the $\delta^{18}\text{O}_{\text{N. pachyderma (d)}}$ record in core LC21, the sample spacing of $\delta^{18}\text{O}_{\text{N. pachyderma (d)}}$ in ODP Site 975, and extra uncertainty (2 or 3 times the sample spacing) for more ambiguous tie-points (indicated in red in the Extended Data Table 1).

(ii) From ODP Site 975 to ODP Site 976. For ODP Site 975, the chronological uncertainty at each depth level was obtained by linearly interpolating the uncertainties between the tie-points used for transferring the radiometrically constrained chronology of LC21 to ODP Site 975. Next we use MSE that propagate all the chronological uncertainties involved in the synchronization of ODP Site 975 to ODP Site 976. This includes the ODP Site 975 chronological uncertainty from (i), the sample spacing of $\delta^{18}\text{O}_{\text{G. bulloides}}$ in ODP Site 975, the sample spacing of $\delta^{18}\text{O}_{\text{G. bulloides}}$ in ODP Site 976, and extra uncertainty (2 or 3 times the sample spacing) for more ambiguous tie-points (Extended Data Table 2).

(iii) From ODP Site 975 to ODP Sites 977. We include the ODP Site 975 chronological uncertainty (as reported in (ii)), the sample spacing of $\delta^{18}\text{O}_{\text{G. bulloides}}$ in ODP Site 975, the sample spacing of $\delta^{18}\text{O}_{\text{G. bulloides}}$ in ODP Site 977, and extra uncertainty (2 or 3 times the sample spacing) for more ambiguous tie-points. These uncertainties were propagated as root-mean-square errors (MSE) (Extended Data Table 3).

(iv) From ODP Site 975 to core MD01-2444. We include the ODP Site 975 chronological uncertainty from (as reported in (ii)), the sample spacing of $\delta^{18}\text{O}_{\text{G. bulloides}}$ in ODP Site 975, the sample spacing of $\delta^{18}\text{O}_{\text{G. bulloides}}$ in core MD01-2444, and extra uncertainty (2 or 3 times the sample spacing) for more ambiguous tie-points. These uncertainties were propagated as root-mean-square errors (MSE) (Extended Data Table 4).

Records of atmospheric CO_2 and CH_4 and Antarctic temperatures. Existing records of atmospheric CO_2 and CH_4 concentrations and Antarctic atmospheric temperatures were placed on the latest ice-core chronology (AICC2012)^{22,55}. For atmospheric CO_2 concentrations (Fig. 3e), a composite was made of the records by Landais *et al.* (ref. 56) and Schneider *et al.* (ref. 57).

Probabilistic assessment of the time series. We performed a probabilistic assessment of uncertainties for several of the new and previously published proxy records discussed in our study (for example, Figs 2b, c, 3c, f) in order to evaluate their confidence levels, taking into full account the uncertainties associated with both their chronologies (X) and proxy measurements/calibrations (Y). This analysis of the time series relies on Monte Carlo-style simulations of the input data using MATLAB. For each time series, all individual data points are separately and randomly sampled 10,000 times within their X- and Y-uncertainties. The 'Y-uncertainties', related to the proxy reconstructions (for example, sea surface temperature), are taken from the original source (for example, Martrat *et al.*, refs 6, 58, 59). The 'X-uncertainties', related to the chronologies of the various records, are either taken from the error propagation discussed above (Mediterranean and North Atlantic records) or from the original source (Corchia Cave⁷, sea-level^{8,9}, and Antarctic ice core records^{22,55}). Each of the 10,000 iterations was then either linearly interpolated (for example, Fig. 2b) or smoothed using a Gaussian filter of defined time window (for example, Fig. 2c). Next, the probability distribution of the 10,000 iterations was assessed per time step, which allowed determination of the 68% (16th–84th percentile) and 95% (2.5th–97.5th percentile) probability intervals for the data. Finally, we determined the probability maximum (modal value) at each time step, and its uncertainties (notably, the 95% probability interval for the probability maximum). For details on this approach, see refs 8, 60.

Calculation of freshwater fluxes from rates of sea-level change. *Code availability.* Freshwater fluxes shown in Fig. 4a were calculated from rates of sea-level change⁹, using a script that was developed in MATLAB and is available in the Supplementary Information.

Relationships between sea level and seawater oxygen isotopes. The response of $\delta^{18}\text{O}$ in planktic foraminifera from the eastern Mediterranean Sea to sea-level change has recently been quantified⁶⁰. This builds on the notion that sea level controls water exchange between the Mediterranean Sea and the Atlantic Ocean through the Strait of Gibraltar and, in turn, the residence time of waters in the basin^{60–62}. Because of the highly evaporative conditions over the Mediterranean region, a longer residence time of water leads to higher salinity and $\delta^{18}\text{O}$ of seawater, which is, in turn, archived in the $\delta^{18}\text{O}$ of foraminiferal calcite^{38,60,62}. Here we use results from the model of ref. 60 to decipher the 'glacial ^{18}O -enrichment' in eastern Mediterranean seawater, which is approximated by a second-order polynomial regression (Extended Data Fig. 6). Note that the generous uncertainties associated with the regression are mostly systematic⁶⁰ and therefore have minor impacts on the relative seawater $\delta^{18}\text{O}$ ($\delta^{18}\text{O}_{\text{seawater}}$) shifts assessed here. Next, we (re)calculate the relationship between sea-level lowering and mean open-ocean $\delta^{18}\text{O}_{\text{seawater}}$ due to freshwater loss from the ocean to the continental ice sheets during glacial times. This was done before⁶³, but here we use the latest sea-level assessment for the last glacial maximum¹¹ (LGM) and the contemporaneous oceanic $\delta^{18}\text{O}_{\text{seawater}}$ value reconstructed from pore water analyses of deep-sea cores⁶³. Finally, we evaluate the response of western Mediterranean $\delta^{18}\text{O}_{\text{seawater}}$ to sea-level change by employing a linear mixing model of the open ocean ($30 \pm 5\%$) and eastern Mediterranean ($70 \pm 5\%$) end-members at each sea-level value that probabilistically evaluates the uncertainties in the various regressions. This mixing ratio is consistent with the range of salinity gradients across the Mediterranean Sea under present-day and LGM boundary conditions⁶⁴.

Corchia Cave palaeoprecipitation $\delta^{18}\text{O}$ changes and source-water effect. To obtain a time series of the $\delta^{18}\text{O}$ anomaly of precipitation ($\Delta\delta^{18}\text{O}_{\text{precipitation}}$) in the catchment area of Corchia Cave between 145 and 115 ka (shown in Fig. 4b), we 'deconstructed' the $\delta^{18}\text{O}_{\text{speleothem}}$ into its main components. These include the cave temperature that controls the isotopic fractionation between dripping water and inorganic (speleothem) calcite^{65,66} and the $\delta^{18}\text{O}$ of precipitation ($\delta^{18}\text{O}_{\text{precipitation}}$). The latter reflects the interplay of two independent factors:

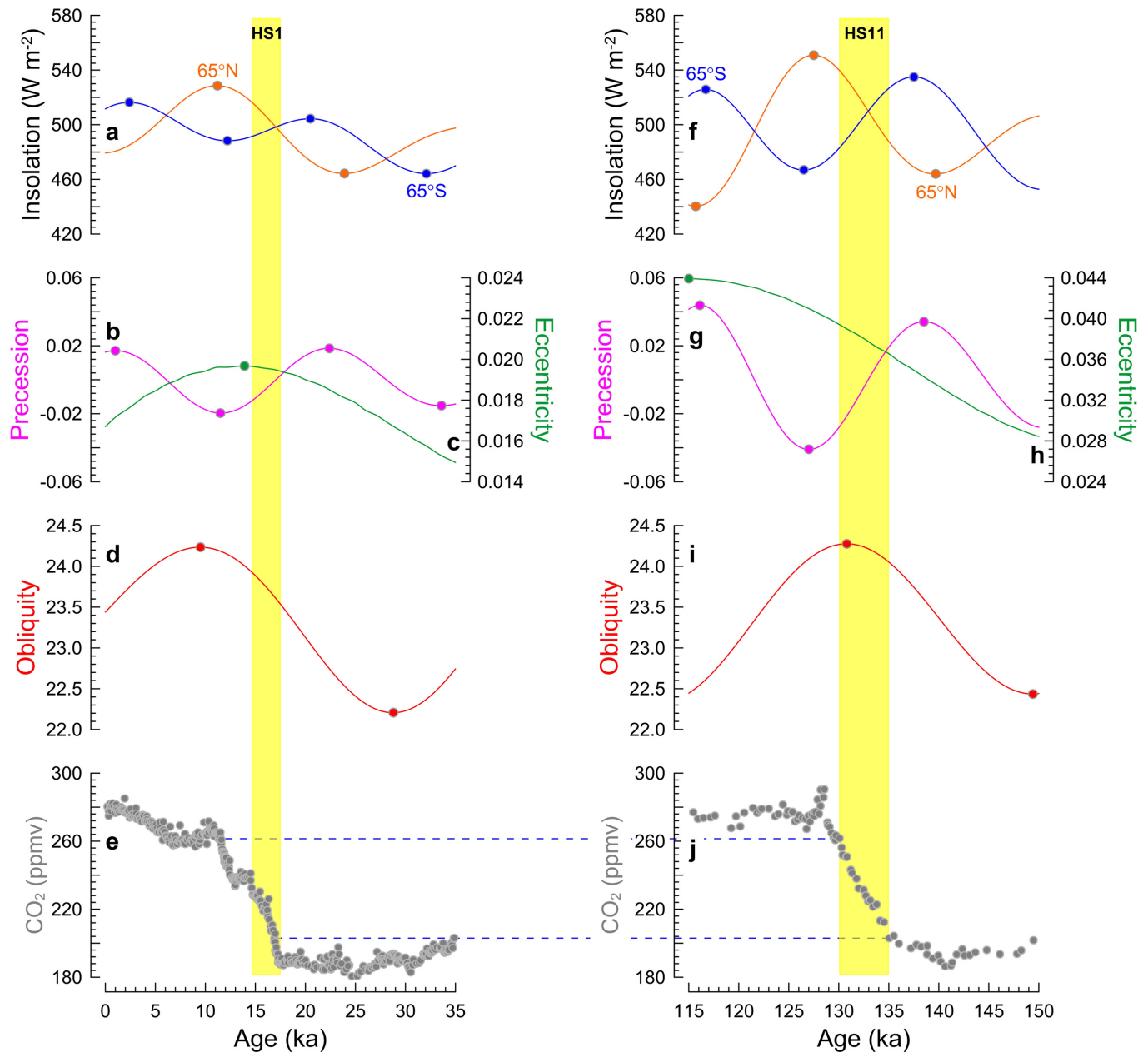
(i) the $\delta^{18}\text{O}$ of the mean marine source of precipitation, for which variability depends on the glacial ^{18}O -enrichment (see above), and (ii) the residual, here referred to as $\Delta\delta^{18}\text{O}_{\text{precipitation}}$ component, which reflects variations in the isotopic composition of precipitation either due to inputs of isotopically light freshwater to the North Atlantic and (via Gibraltar) to the western Mediterranean Sea (for example, from melting ice sheets) or due to changes in the amount of precipitation⁶⁷.

Our approach relies on the assumption that the temperature change within the cave reflects mean annual temperature changes in the regional climate⁷, as reflected in the western Mediterranean SST. We also consider the propagated chronological uncertainties of the three records used to derive the $\Delta\delta^{18}\text{O}_{\text{precipitation}}$ time series. To probabilistically evaluate the impacts of these assumptions and uncertainties on $\Delta\delta^{18}\text{O}_{\text{precipitation}}$, we have used a Monte Carlo approach (see above), in which the SST record⁶, the sea-level driven mean ocean $\delta^{18}\text{O}_{\text{seawater}}$ and $\delta^{18}\text{O}_{\text{speleothem}}$ from Corchia Cave are given as input data along with the propagated chronological uncertainties. Note that calculation of the $\Delta\delta^{18}\text{O}_{\text{precipitation}}$ using a glacial mean ocean ^{18}O -enrichment and a western Mediterranean ^{18}O -enrichment are statistically indistinguishable across the interval of interest. This analysis is possible here for the first time because we placed all relevant records on the same timescale with rigorous assessment of the propagated uncertainties.

The negative $\Delta\delta^{18}\text{O}_{\text{precipitation}}$ shift in Corchia Cave during HS11 had a magnitude of $\sim 1.5\text{‰}$ (Fig. 4b). An order of magnitude mass-balance assessment suggests that a ^{18}O -depletion by 1.5‰ in the wider North Atlantic and western Mediterranean source areas for precipitation to Corchia Cave⁶⁸ is consistent with addition of ~ 0.3 Sverdrup (Sv, $10^{-6} \text{ m}^3 \text{ s}^{-1}$; Fig. 4a) of isotopically light (assumed -40‰) meltwater to a 80-m-deep mixed layer with $\delta^{18}\text{O}$ of 1‰ (ref. 69). This implies a mixing ratio between marine and meltwater end-members of 40:1 and scales the marine flux in the Subtropical Atlantic to approximately 12 Sv. Despite the roughness of our calculation this overall agrees with a complete collapse of the thermohaline component of the Gulf Stream in the Subtropical North Atlantic during HS11 and with the persistence of only the wind-driven marine transport, which today accounts for ~ 17 Sv (ref. 70).

32. Comas, M. C., Zahn, R. & Klaus, A. Mediterranean Sea II: The Western Mediterranean. *Proc. ODP Init. Rep.* **161**, <http://dx.doi.org/10.2973/odp.proc.ir.161.1996> (1996).
33. Pinardi, N. & Masetti, E. Variability of the large scale general circulation of the Mediterranean Sea from observations and modelling: a review. *Palaeogeogr. Palaeoclimatol. Palaeoecol.* **158**, 153–173 (2000).
34. Pinardi, N. *et al.* Mediterranean Sea large-scale low-frequency ocean variability and water mass formation rates from 1987 to 2007: a retrospective analysis. *Prog. Oceanogr.* **132**, 318–332 (2015).
35. Malanotte-Rizzoli, P. *et al.* Physical forcing and physical/biochemical variability of the Mediterranean Sea: a review of unresolved issues and directions for future research. *Ocean Sci.* **10**, 281–322 (2014).
36. Rohling, E. J., Marino, G. & Grant, K. M. Mediterranean climate and oceanography, and the periodic development of anoxic events (sapropels). *Earth Sci. Rev.* **143**, 62–97 (2015).
37. Marino, G. *et al.* Aegean Sea as driver of hydrographic and ecological changes in the eastern Mediterranean. *Geology* **35**, 675–678 (2007).
38. Rohling, E. J. *et al.* Reconstructing past planktic foraminiferal habitats using stable isotope data: a case history for Mediterranean sapropel S5. *Mar. Micropaleontol.* **50**, 89–123 (2004).
39. Friedrich, O. *et al.* Influence of test size, water depth, and ecology on Mg/Ca, Sr/Ca, $\delta^{18}\text{O}$ and $\delta^{13}\text{C}$ in nine modern species of planktic foraminifers. *Earth Planet. Sci. Lett.* **319–320**, 133–145 (2012).
40. Incarbona, A., Sprovieri, M., Lirer, F. & Sprovieri, R. Surface and deep water conditions in the Sicily channel (central Mediterranean) at the time of sapropel S5 deposition. *Palaeogeogr. Palaeoclimatol. Palaeoecol.* **306**, 243–248 (2011).
41. Myers, P. G., Haines, K. & Rohling, E. J. Modeling the paleocirculation of the Mediterranean: the last glacial maximum and the Holocene with emphasis on the formation of sapropel S1. *Paleoceanography* **13**, 586–606 (1998).
42. Rogerson, M. *et al.* Enhanced Mediterranean-Atlantic exchange during Atlantic freshening phases. *Geochim. Geophys. Geosyst.* **11**, Q08013 (2010).
43. Rohling, E. J. *et al.* Abrupt cold spells in the northwest Mediterranean. *Paleoceanography* **13**, 316–322 (1998).
44. Rohling, E. J. *et al.* African monsoon variability during the previous interglacial maximum. *Earth Planet. Sci. Lett.* **202**, 61–75 (2002).
45. Rohling, E. J., Hopmans, E. C. & Damste, J. S. S. Water column dynamics during the last interglacial anoxic event in the Mediterranean (sapropel S5). *Paleoceanography* **21**, PA2018 (2006).
46. van der Meer, M. T. J. *et al.* Hydrogen isotopic compositions of long-chain alkenones record freshwater flooding of the Eastern Mediterranean at the onset of sapropel deposition. *Earth Planet. Sci. Lett.* **262**, 594–600 (2007).
47. Casford, J. S. L. *et al.* A dynamic concept for eastern Mediterranean circulation and oxygenation during sapropel formation. *Palaeogeogr. Palaeoclimatol. Palaeoecol.* **190**, 103–119 (2003).
48. Osborne, A. H., Marino, G., Vance, D. & Rohling, E. J. Eastern Mediterranean surface water Nd during Eemian sapropel S5: monitoring northerly (mid-latitude) versus

- southerly (sub-tropical) freshwater contributions. *Quat. Sci. Rev.* **29**, 2473–2483 (2010).
49. Grelaud, M., Marino, G., Ziveri, P. & Rohling, E. J. Abrupt shoaling of the nutricline in response to massive freshwater flooding at the onset of the last interglacial sapropel event. *Paleoceanography* **27**, PA3208 (2012).
 50. Piccini, L. *et al.* The environmental features of the Monte Corchia cave system (Apuan Alps, central Italy) and their effects on speleothem growth. *Int. J. Speleol.* **37**, 153–172 (2008).
 51. Bard, E. *et al.* Hydrological conditions over the western Mediterranean basin during the deposition of the cold Sapropel 6 (ca. 175 kyr BP). *Earth Planet. Sci. Lett.* **202**, 481–494 (2002).
 52. Marino, G. *et al.* Early and middle Holocene in the Aegean Sea: interplay between high and low latitude climate variability. *Quat. Sci. Rev.* **28**, 3246–3262 (2009).
 53. Badertscher, S. *et al.* Pleistocene water intrusions from the Mediterranean and Caspian seas into the Black Sea. *Nature Geosci.* **4**, 236–239 (2011).
 54. Regattieri, E. *et al.* A continuous stable isotope record from the penultimate glacial maximum to the Last Interglacial (159–121 ka) from Tana Che Urla Cave (Apuan Alps, central Italy). *Quat. Res.* **82**, 450–461 (2014).
 55. Veres, D. *et al.* The Antarctic ice core chronology (AICC2012): an optimized multi-parameter and multi-site dating approach for the last 120 thousand years. *Clim. Past* **9**, 1733–1748 (2013).
 56. Landais, A. *et al.* Two-phase change in CO₂, Antarctic temperature and global climate during Termination II. *Nature Geosci.* **6**, 1062–1065 (2013).
 57. Schneider, R., Schmitt, J., Koehler, P., Joos, F. & Fischer, H. A reconstruction of atmospheric carbon dioxide and its stable carbon isotopic composition from the penultimate glacial maximum to the last glacial inception. *Clim. Past* **9**, 2507–2523 (2013).
 58. Martrat, B. *et al.* Abrupt temperature changes in the Western Mediterranean over the past 250,000 years. *Science* **306**, 1762–1765 (2004).
 59. Martrat, B. *et al.* Four climate cycles of recurring deep and surface water destabilizations on the Iberian margin. *Science* **317**, 502–507 (2007).
 60. Rohling, E. J. *et al.* Sea-level and deep-sea-temperature variability over the past 5.3 million years. *Nature* **508**, 477–482 (2014).
 61. Rohling, E. J. & Bryden, H. L. Estimating past changes in the eastern Mediterranean fresh-water budget, using reconstructions of sea-level and hydrography. *Proc. Kon. Ned. Akad. B* **97**, 201–217 (1994).
 62. Rohling, E. J. Environmental control on Mediterranean salinity and $\delta^{18}\text{O}$. *Paleoceanography* **14**, 706–715 (1999).
 63. Schrag, D. P. *et al.* The oxygen isotopic composition of seawater during the Last Glacial Maximum. *Quat. Sci. Rev.* **21**, 331–342 (2002).
 64. Mikolajewicz, U. Modeling Mediterranean Ocean climate of the Last Glacial Maximum. *Clim. Past* **7**, 161–180 (2011).
 65. Kim, S. T. & O'Neil, J. R. Equilibrium and nonequilibrium oxygen isotope effects in synthetic carbonates. *Geochim. Cosmochim. Acta* **61**, 3461–3475 (1997).
 66. Lachniet, M. S. Climatic and environmental controls on speleothem oxygen-isotope values. *Quat. Sci. Rev.* **28**, 412–432 (2009).
 67. Dansgaard, W. Stable isotopes in precipitation. *Tellus* **16**, 436–468 (1964).
 68. Drysdale, R. N. *et al.* Palaeoclimatic implications of the growth history and stable isotope ($\delta^{18}\text{O}$ and $\delta^{13}\text{C}$) geochemistry of a Middle to Late Pleistocene stalagmite from central-western Italy. *Earth Planet. Sci. Lett.* **227**, 215–229 (2004).
 69. LeGrande, A. N. & Schmidt, G. A. Global gridded data set of the oxygen isotopic composition in seawater. *Geophys. Res. Lett.* **33**, L12604 (2006).
 70. Lynch-Stieglitz, J., Curry, W. B. & Slowey, N. Weaker Gulf Stream in the Florida straits during the last glacial maximum. *Nature* **402**, 644–648 (1999).
 71. Berger, A. L. Long-term variations of daily insolation and Quaternary climatic changes. *J. Atmos. Sci.* **35**, 2362–2367 (1978).
 72. Berger, A. L. Long-term variations of caloric insolation resulting from Earth's orbital elements. *Quat. Res.* **9**, 139–167 (1978).
 73. Berger, A. & Loutre, M. F. Long-term variations in insolation and their effects on climate, the LLN experiments. *Surv. Geophys.* **18**, 147–161 (1997).
 74. Monnin, E. *et al.* Atmospheric CO₂ concentrations over the last glacial termination. *Science* **291**, 112–114 (2001).
 75. Schmitt, J. *et al.* Carbon isotope constraints on the deglacial CO₂ rise from ice cores. *Science* **336**, 711–714 (2012).
 76. Ahn, J. & Brook, E. J. Siple Dome ice reveals two modes of millennial CO₂ change during the last ice age. *Nature Commun.* **5**, 3723 (2014).
 77. Andersen, K. K. *et al.* High-resolution record of Northern Hemisphere climate extending into the last interglacial period. *Nature* **431**, 147–151 (2004).
 78. Stenni, B. *et al.* The deuterium excess records of EPICA Dome C and Dronning Maud Land ice cores (East Antarctica). *Quat. Sci. Rev.* **29**, 146–159 (2010).
 79. Clark, P. U. *et al.* The Last Glacial Maximum. *Science* **325**, 710–714 (2009).

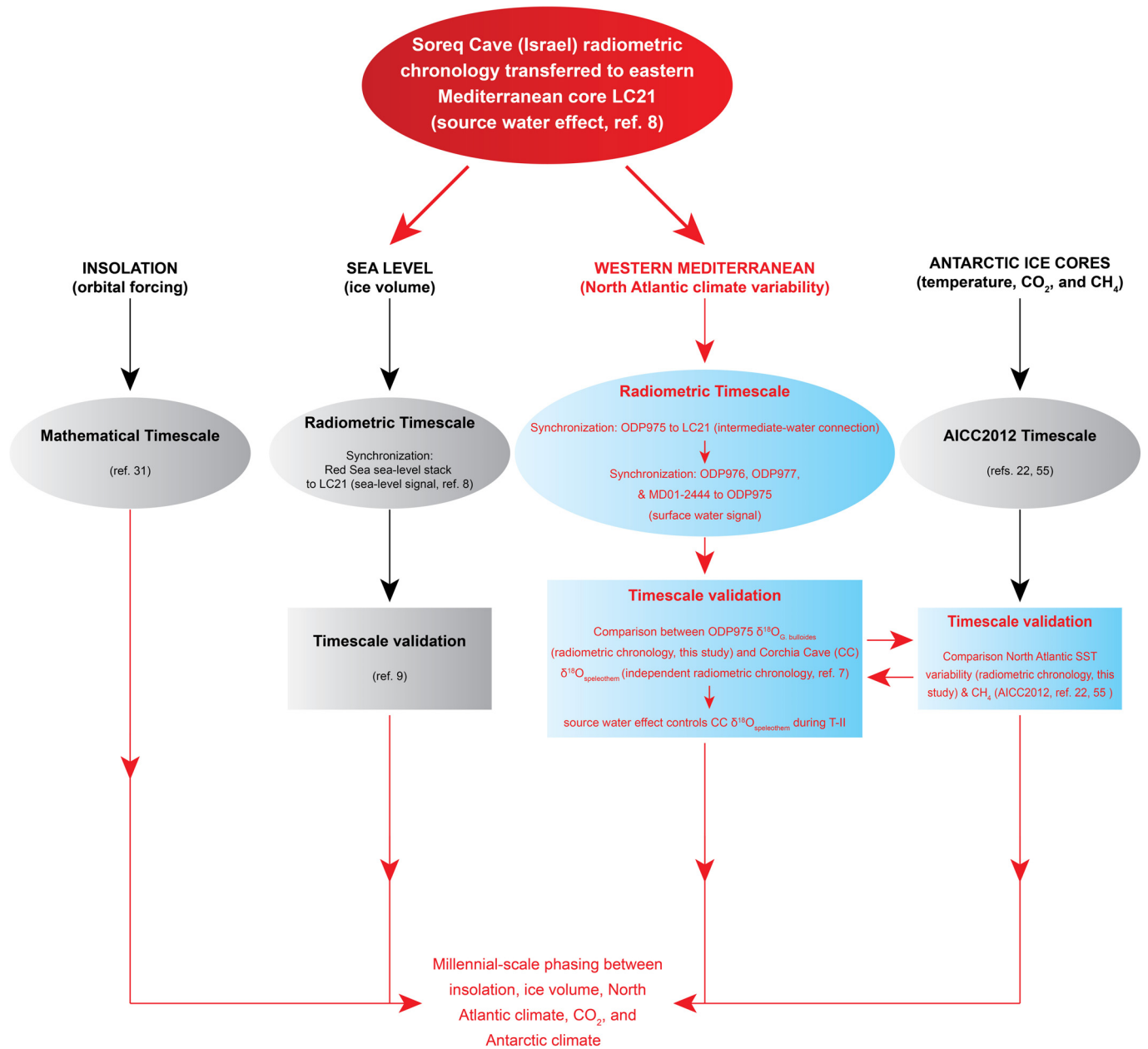


Extended Data Figure 1 | Orbital parameters, insolation forcing, and atmospheric CO₂ concentrations during the last two glacial-interglacial transitions. **a, f**, Incoming solar radiation on 21 June and 21 December at 65° N (orange) and 65° S (blue), for T-I (**a**) and T-II (**f**)³¹. **b, g**, Precession of the Earth's axis³¹ for T-I (**b**) and T-II (**g**). **c, h**, as **b, g**, but for eccentricity of the Earth's orbit³¹. Note the different axis scales in **c** and **h**. **d, i**, Obliquity of the Earth's axis³¹ for T-I (**d**) and T-II (**i**). Different orbital configurations during glacial terminations I (T-I) and II (T-II) led to markedly different insolation

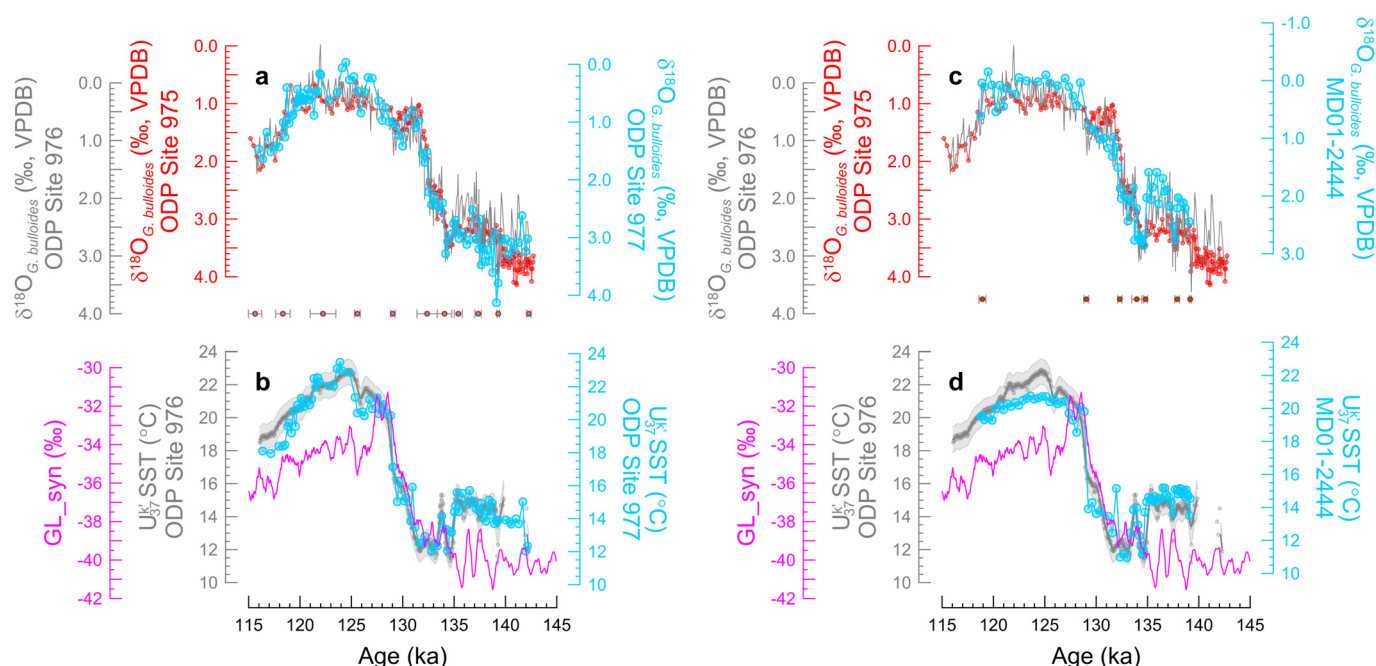
forcing^{31,71–73}, with the summer 65° N insolation increase during T-II larger by ~35% (~23 W m⁻²), and occurring at faster rates¹⁸, than that during T-I. **e, j**, atmospheric CO₂ concentrations during T-I (refs 74–76) and T-II (ref. 56). Yellow bands illustrate the timing of Heinrich stadial 1 (HS1) and 11 (HS11), following previous literature¹ and this study, respectively. Dashed blue lines highlight that atmospheric CO₂ concentrations were systematically higher during T-II than during T-I. Symbols indicate the maxima and/or minima in insolation, precession, eccentricity, and obliquity cycles.

Legend

- Timescale construction (previous study)
- Timescale construction (this study)
- Timescale validation (previous study)
- Timescale validation (this study)

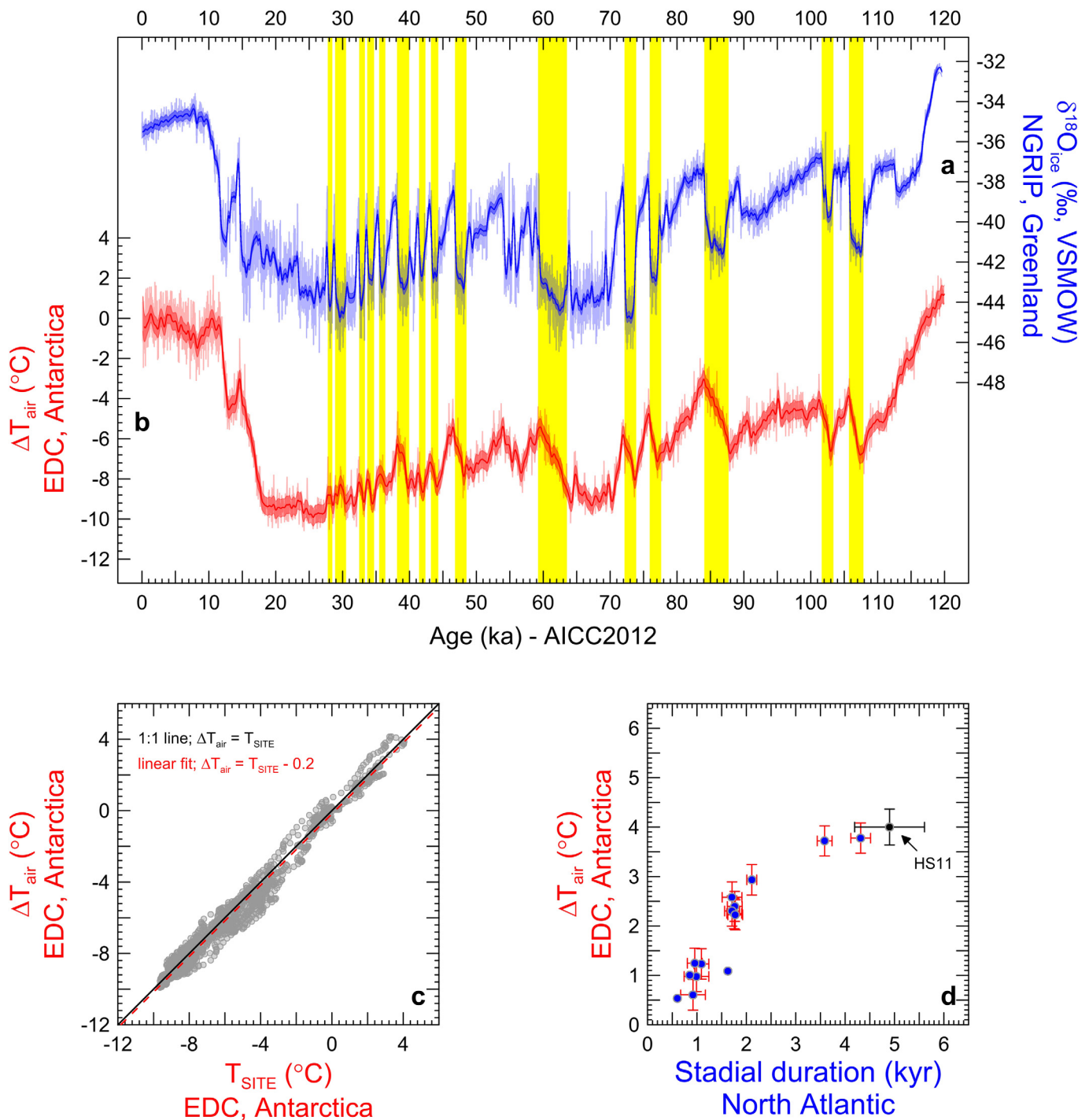


Extended Data Figure 2 | Flowchart of the approach used to construct and validate chronologies of the various records. See main text and Methods for details.



Extended Data Figure 3 | Synchronization of western Mediterranean Sea ODP975 to ODP977 and Iberian Margin core MD01-2444. **a**, Synchronization of *G. bulloides* $\delta^{18}\text{O}$ from western Mediterranean ODP977 to its counterpart from nearby ODP975. Circles and error bars depict tie points and 2σ synchronization errors, respectively (Methods, Extended Data Table 3). The *G. bulloides* $\delta^{18}\text{O}$ from ODP976 is only shown for comparison and is not used to transfer our new, radiometrically constrained chronology, to ODP977 (Methods). **b**, Validation of the synchronization exercise shown in **a** by comparing the alkenone-based sea surface temperature (SST) records from ODP977 and ODP976, on their new, radiometrically constrained chronology. The 95% confidence intervals (light grey envelope) and probability maximum (heavier grey line) and its associated 95% confidence intervals (heavier grey envelope) of the ODP976 SST data (grey circles) are based on a Monte Carlo

analysis of chronological and SST uncertainties, employing a 0.2 kyr Gaussian filter (Methods). The synthetic record of Greenland climate variability¹⁶ is also shown. **c**, Synchronization of the *G. bulloides* $\delta^{18}\text{O}$ from Iberian Margin (Atlantic Ocean) core MD01-2444 to its counterpart from ODP975 (Western Mediterranean, Methods). Circles and error bars depict tie points and 2σ synchronization errors, respectively (Methods, Extended Data Table 3). The *G. bulloides* $\delta^{18}\text{O}$ from ODP976 is shown for comparison and is not used to transfer the MD01-2444 records to our new, radiometrically constrained chronology (Methods). **d**, Validation of the synchronization exercise shown in **c** by comparing alkenone-based SST records from core MD01-2444 and ODP976 (shaded envelopes and circles as in **b**), on their new radiometrically constrained chronology. The synthetic record of Greenland climate variability¹⁶ is also shown.

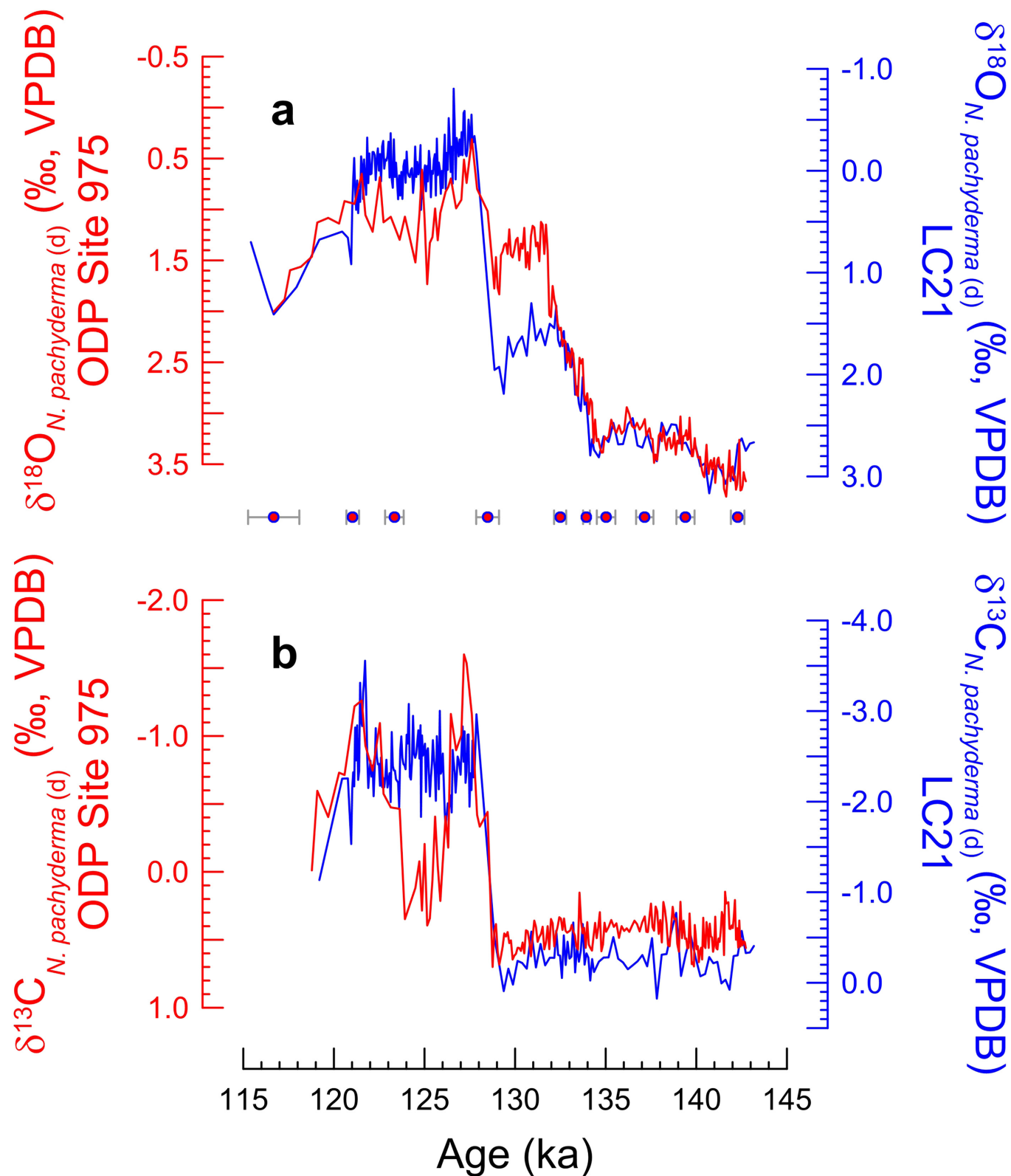


Extended Data Figure 4 | Relationship between the duration of the North Atlantic cold phases (stadials) and the magnitude of Antarctic warming.

a, $\delta^{18}\text{O}_{\text{ice}}$ time series from North Greenland Ice Core Project (NGRIP)⁷⁷ (light blue). The probability maximum (solid blue line) and associated 95% confidence bounds (shaded blue envelope) of the $\delta^{18}\text{O}_{\text{ice}}$ record result from 10,000 Monte Carlo simulations, employing a 0.15 kyr Gaussian filter through the data and their chronological and $\delta^{18}\text{O}_{\text{ice}}$ uncertainties (see Methods).

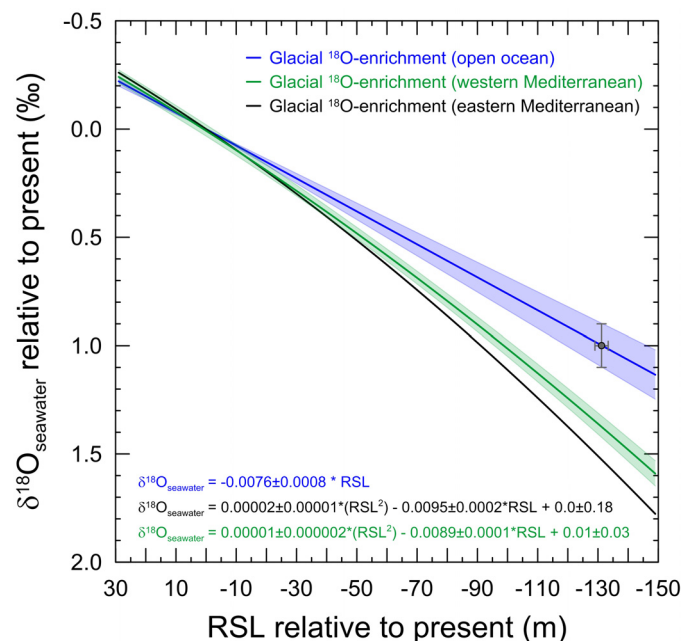
b, EPICA Dome C (EDC) temperature reconstructions (ΔT) based on δD_{ice} data¹³ (light red). The probability maximum (solid red line) and associated 95% confidence bounds (shaded red envelope) of the temperature record result from

10,000 Monte Carlo simulations, employing a 0.2 kyr Gaussian filter through the data and their chronological and ΔT uncertainties. **c**, Comparison between Antarctic temperature reconstructions from EDC using the methods of Jouzel *et al.* (ΔT , ref. 13) and Stenni *et al.* (T_{SITE} , ref. 78), revealing no difference in the amplitude of the estimated Antarctic temperature shifts. **d**, Relationship between duration of Greenland stadials and Antarctic warming for bipolar seesaw events highlighted in **a** and **b** by yellow bands. Greenland and Antarctic records are on the latest ice core chronology AICC2012 (ref. 55). Error bars depict 1σ uncertainty in the magnitude and duration of North Atlantic cooling.



Extended Data Figure 5 | Synchronization of western Mediterranean Sea ODP975 to eastern Mediterranean core LC21. **a**, Synchronization of the *N. pachyderma* (d) $\delta^{18}\text{O}$ from ODP975 to its counterpart from eastern Mediterranean core LC21 (Methods), which was placed on a radiometric chronology by ref. 8. Red filled circles and error bars depict the tie points used to

synchronize ODP975 to LC21 and the 2σ synchronization uncertainties, respectively. **b**, Validation of the synchronization exercise shown in **a** by comparing the respective co-registered *N. pachyderma* (d) $\delta^{13}\text{C}$ profiles from the same cores.



Extended Data Figure 6 | Glacial ^{18}O -enrichment in oceanic and Mediterranean seawater. Blue (open ocean), black (eastern Mediterranean Sea) and green (western Mediterranean Sea) lines illustrate the relationship between seawater $\delta^{18}\text{O}$ ($\delta^{18}\text{O}_{\text{seawater}}$) and relative sea level (RSL). The open ocean relationship has been re-calculated here using the latest assessment (grey symbol) of the sea-level lowstand¹¹ of the Last Glacial Maximum (26.5–19 ka, ref. 79) and the mean ocean $\delta^{18}\text{O}_{\text{seawater}}$ value derived from porewater analyses

in a suite of deep-sea cores⁶³. The eastern Mediterranean relationship is derived from the model presented in ref. 60. The western Mediterranean relationship (green line) reflects linear mixing between eastern Mediterranean (black line) and open ocean (blue line) end-members, assuming that the residence time effect^{60,62} on $\delta^{18}\text{O}_{\text{seawater}}$ (and salinity) in the western Mediterranean is $70 \pm 5\%$ of that in eastern Mediterranean⁶⁴. Shaded envelopes are 1σ confidence bounds, derived from probabilistic analysis of uncertainties.

Extended Data Table 1 | Synchronization of ODP975 to LC21

Age (ka BP)	ODP975 sample spacing (kyr)	LC21 sample spacing (kyr)	MSE synchronization (kyr)	MSE age uncertainty (kyr)
116.68	0.50	0.50	0.71	1.52
121.04	0.04	0.04	0.17	1.76
123.34	0.07	0.05	0.26	1.56
128.48	0.22	0.22	0.31	1.20
132.49	0.12	0.12	0.17	1.17
133.94	0.04	0.08	0.09	0.59
135.02	0.16	0.20	0.26	0.56
137.16	0.09	0.22	0.24	0.93
139.40	0.08	0.24	0.25	1.33
142.28	0.11	0.15	0.19	1.50

Sample spacing (1σ) uncertainties in ODP975 and LC21 and dating (1σ) uncertainties of LC21 (ref. 7) are combined in mean squared estimates (MSE). Tie-points in red include extra uncertainty (3 times the sample spacing).

Extended Data Table 2 | Synchronization of ODP976 to ODP975

Age (ka BP)	ODP976 sample spacing (kyr)	ODP975 sample spacing (kyr)	MSE synchronization	MSE age uncertainty (kyr)
115.63	0.18	0.23	0.29	1.54
118.33	0.03	0.25	0.25	1.59
122.24	0.26	0.18	0.31	1.76
125.02	0.21	0.36	0.41	1.52
129.04	0.06	0.08	0.10	1.20
132.45	0.07	0.08	0.11	1.18
133.98	0.14	0.08	0.16	0.76
135.08	0.07	0.09	0.11	0.58
137.34	0.08	0.08	0.12	0.92
137.97	0.02	0.06	0.07	1.06
139.36	0.06	0.06	0.08	1.30
142.28	0.54	0.16	0.56	1.57

Sample spacing (1σ) uncertainties in ODP976 and ODP975 and dating uncertainties of ODP975 (see Extended Data Table 1) are combined in mean squared estimates (MSE). Tie-points in red include extra uncertainty (3 times the sample spacing).

Extended Data Table 3 | Synchronization of ODP977 to ODP975

Age (ka BP)	ODP977 sample spacing (kyr)	ODP975 sample spacing (kyr)	MSE synchronization	MSE age uncertainty (kyr)
115.63	0.23	0.23	0.32	1.55
118.33	0.25	0.25	0.35	1.65
122.24	0.60	0.18	0.63	1.77
125.59	0.10	0.10	0.14	1.41
129.04	0.08	0.08	0.11	1.20
132.38	0.49	0.08	0.50	1.20
134.07	0.34	0.08	0.35	0.72
135.41	0.16	0.12	0.20	0.67
137.34	0.13	0.08	0.16	0.98
139.30	0.03	0.06	0.06	1.31
142.28	0.09	0.05	0.10	1.47

Sample spacing (1σ) uncertainties in ODP977 and ODP975 and dating uncertainties of ODP975 (see Extended Data Table 1) are combined in mean squared estimates (MSE).

Extended Data Table 4 | Synchronization of core MD01-2444 to ODP975.

Age (ka BP)	MD01-2444 sample spacing (kyr)	ODP975 sample spacing (kyr)	MSE synchronization	MSE age uncertainty (kyr)
118.930	0.075	0.150	0.168	1.640
129.035	0.079	0.092	0.121	1.203
132.300	0.077	0.077	0.108	1.177
133.955	0.227	0.101	0.249	0.718
134.810	0.065	0.065	0.092	0.576
137.885	0.108	0.043	0.116	1.031
139.165	0.015	0.045	0.047	1.281

Sample spacing (1σ) uncertainties in MD01-2444 and ODP975 and dating uncertainties of ODP975 (see Extended Data Table 1) are combined in mean squared estimates (MSE).

Experimental constraints on the electrical anisotropy of the lithosphere–asthenosphere system

Anne Pommier^{1,2}, Kurt Leinenweber³, David L. Kohlstedt⁴, Chao Qi⁴, Edward J. Garnero², Stephen J. Mackwell⁵ & James A. Tyburczy²

The relative motion of lithospheric plates and underlying mantle produces localized deformation near the lithosphere–asthenosphere boundary¹. The transition from rheologically stronger lithosphere to weaker asthenosphere may result from a small amount of melt or water in the asthenosphere, reducing viscosity^{1–3}. Either possibility may explain the seismic and electrical anomalies that extend to a depth of about 200 kilometres^{4,5}. However, the effect of melt on the physical properties of deformed materials at upper-mantle conditions remains poorly constrained⁶. Here we present electrical anisotropy measurements at high temperatures and quasi-hydrostatic pressures of about three gigapascals on previously deformed olivine aggregates and sheared partially molten rocks. For all samples, electrical conductivity is highest when parallel to the direction of prior deformation. The conductivity of highly sheared olivine samples is ten times greater in the shear direction than for undeformed samples. At temperatures above 900 degrees Celsius, a deformed solid matrix with nearly isotropic melt distribution has an electrical anisotropy factor less than five. To obtain higher electrical anisotropy (up to a factor of 100), we propose an experimentally based model in which layers of sheared olivine are alternated with layers of sheared olivine plus MORB or of pure melt. Conductivities are up to 100 times greater in the shear direction than when perpendicular to the shear direction and reproduce stress-driven alignment of the melt. Our experimental results and the model reproduce mantle conductivity–depth profiles for melt-bearing geological contexts. The field data are best fitted by an electrically anisotropic asthenosphere overlain by an isotropic, high-conductivity lowermost lithosphere. The high conductivity could arise from partial melting associated with localized deformation resulting from differential plate velocities relative to the mantle, with subsequent upward melt percolation from the asthenosphere.

Electromagnetic profiles of the lithosphere–asthenosphere system reveal zones of high electrical conductivity and electrical anisotropy, which vary with depth (Fig. 1)^{5,7,8}. High conductivity can be attributed to several factors, including the presence of an interconnected fluid phase⁹. Regions of electrical anisotropy are usually attributed to mantle deformation that can result from the motion of rigid lithospheric plates relative to the underlying convecting mantle^{3,4}. Experimental investigations under controlled laboratory conditions allow a direct assessment of the effect of deformation and chemistry on electrical conductivity, an important step in investigating the dynamic coupling of tectonic plates with the underlying mantle.

The current laboratory-derived database of electrical anisotropy of mantle materials consists principally of measurements of electrical conductivity σ for different crystallographic orientations of dry and hydrous olivine single crystals^{10,11}. Only one set of measurements has been made for σ of melt-bearing olivine aggregates during torsion¹², and these experiments were performed at low crustal pressure

(0.3 GPa) and only to low shear strain ($\gamma < 0.5$ –1), limiting the formation of noticeable melt bands. Recently, new electrical measurements on melt + olivine aggregates were performed during simple shear at 3 GPa, but only small strains ($\gamma < 1.8$) were reached¹³.

Here we report the results of laboratory experiments at asthenospheric pressure (about 3 GPa) and on samples previously deformed to high strains ($\gamma \approx 9$). These experiments were designed to investigate electrical anisotropy in deformed mantle materials, in order to develop an electrical model of the upper mantle to be compared with field results. The electrical anisotropy of mantle materials was investigated by measuring the electrical conductivity of previously deformed sam-

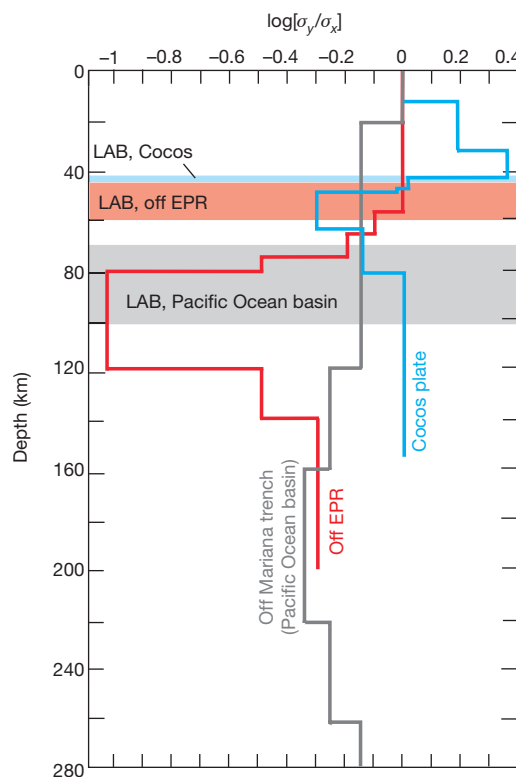
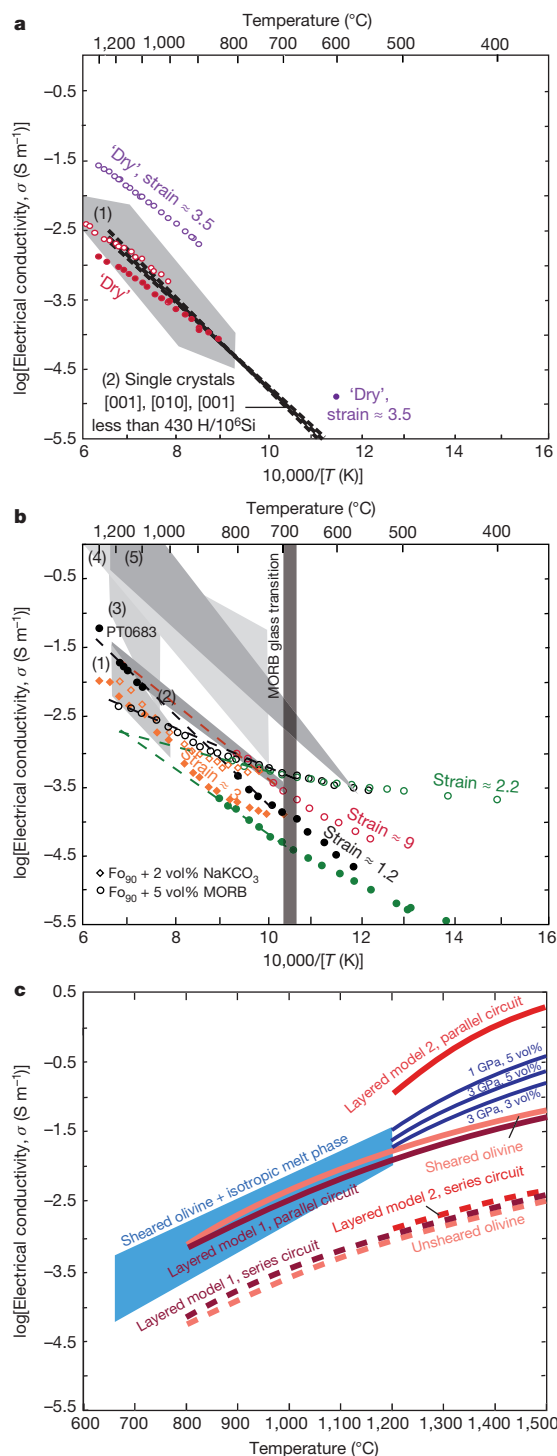


Figure 1 | Anisotropic conductivity models obtained from inversion of electromagnetic data in different geological contexts. The conductivity ratio is for perpendicular directions σ_y and σ_x , with σ_x the direction of highest conductivity in the asthenosphere. Electrical profiles are for the Pacific Ocean Basin (off the Mariana Trench) in grey, the East Pacific Rise (EPR, 200 km off the ridge axis) in red, and the Cocos plate (250 km off trench) in blue^{5,7,8}. Anisotropy in the lithosphere under the Cocos plate is not well constrained. All profiles present a sublithospheric or asthenospheric region of high anisotropy, topped with a low-anisotropy layer.

¹University of California San Diego, Scripps Institution of Oceanography, Institute of Geophysics and Planetary Physics, La Jolla, California 92093, USA. ²School of Earth and Space Exploration, Arizona State University, Tempe, Arizona 85287, USA. ³Department of Chemistry and Biochemistry, Arizona State University, Tempe, Arizona 85287, USA. ⁴Department of Earth Sciences, University of Minnesota, Minneapolis, Minnesota 55455, USA. ⁵Lunar and Planetary Institute, Universities Space Research Association, Houston, Texas 77058, USA.

ples in a multi-anvil apparatus at about 3 GPa and up to 1,300 °C in two perpendicular directions using impedance spectroscopy (Extended Data Fig. 1).

Dry polycrystalline olivine samples (Fo_{90}), a $\text{Fo}_{90} + 5 \text{ vol\% MORB}$ sample, and a $\text{Fo}_{90} + 2 \text{ vol\% NaKCO}_3$ melt sample were used. These samples were initially deformed in triaxial compression or in simple shear (Methods and Extended Data Table 1) at a confining pressure $P = 0.3 \text{ GPa}$ and a temperature $T = 1,200\text{--}1,250 \text{ °C}$ in a gas-medium apparatus. The parts of the samples that had experienced maximum shear strain were extracted and placed in a conductivity cell in the multi-anvil apparatus (Extended Data Table 1) for measurements of electrical properties at a pressure representative of the pressure of the asthenosphere.



Measurements were primarily conducted under quasi-hydrostatic conditions at temperatures not exceeding 900 °C with a few experiments at temperatures near 1,300 °C (Methods). In the low-temperature conductivity runs, melt-enriched sheets (bands in two dimensions) formed during deformation runs are preserved as previously observed^{14,15}, whereas after the high-temperature conductivity experiments the melt-rich bands are no longer detected (Extended Data Fig. 2). Instead, melt-bearing samples quenched from high-temperature measurements ($>1,100 \text{ °C}$) exhibited a sheared solid matrix with an approximately homogeneous (meaning a lack of melt-rich bands) and isotropic melt distribution, because in the high-temperature conductivity experiments, surface tension relatively quickly redistributes the melt, both in terms of dissipation of the melt-rich bands and in terms of randomization of the orientation of melt-filled triple junctions, thus removing the melt preferred orientation introduced by deformation^{16,17}.

Nonetheless, a small degree of heterogeneity in melt distribution remained, with some areas showing slightly higher melt concentrations than others. This observation suggests that some structural anisotropy associated with the deformation-induced lattice preferred orientation persists for the duration of our conductivity measurements, in agreement with previous observations on sheared samples that were statically annealed after large strain deformation¹⁸. Chemical analyses of run products are consistent with starting compositions (Extended Data Table 2).

Because the temperature of the lithosphere–asthenosphere system is not well constrained, our experiments investigated the electrical properties of mantle analogues over a wide range of temperature. For olivine samples, a single Arrhenius relationship can satisfactorily reproduce the electrical data over the investigated temperature range (Fig. 2a; Extended Data Table 3). For both MORB-bearing and carbonate-bearing samples, a slight bowing in the trend of electrical conductivity with temperature is observed at about 870–900 °C, possibly caused by textural changes. Electrical data are therefore best reproduced by two Arrhenius equations, one on either side of this temperature (Fig. 2b; Extended Data Table 4). For experiments performed at low temperature ($<900 \text{ °C}$) on melt-bearing samples, values of σ at

Figure 2 | Electrical conductivity–temperature diagrams of experimental results. **a**, Results for olivine aggregates at low and high shear strains. Open and closed circles represent data parallel to and perpendicular to the main deformation direction, respectively. Our data agree well with grey zone (1), which corresponds to σ of olivine aggregates under pressure^{26,27}. Electrical data on olivine single crystal in different crystallographic directions (zone (2), with water content less than 430 H atoms per 10^6 Si atoms) are from ref. 10. **b**, Results for the melt-bearing systems. Open and closed symbols represent data parallel to and perpendicular to the main deformation direction, respectively. Only the electrical measurements of carbonate-bearing samples (diamonds) and of the MORB-bearing sample with a strain of 1.2 in the direction parallel to the main deformation (open black circles) were performed over a large temperature range from high to low temperature. All other experiments were performed either at high ($>1,100 \text{ °C}$) or at low ($<900 \text{ °C}$) temperature (Extended Data Table 4). Good agreement is obtained with data from zone (1)¹². The slight difference in the results from zone (2) at 0.1 MPa (ref. 28) is consistent with the effect of pressure. The conductivities from refs 29 and 30 (zones (3), (4), and (5)) are higher than the ones measured in this study, possibly owing to melt chemistry effects. The dashed lines are Arrhenius relations for conductivity in the post-glass transition temperature range. Electrical anisotropy decreases with increasing temperature to become negligible at high temperature. **c**, Laboratory-based isotropic (blue colours) and anisotropic (red colours) models of the electrical conductivity of deformed mantle materials. Models are based on Arrhenius equations and on extrapolations of our results from low- to high-temperature experiments. Isotropic models for MORB-bearing samples at $>1,200 \text{ °C}$ are based on the Hashin–Shtrikman upper bound. Layered model 1 considers layers of polycrystalline olivine alternating with layers of sheared $\text{Fo}_{90} + 5 \text{ vol\% MORB}$, and layered model 2 considers layers of polycrystalline olivine alternating with layers of basalt²² (see Methods).

higher T can be calculated by extrapolating electrical data collected above the glass transition (at about 670 °C) (dashed lines in Fig. 2b; Extended Data Table 4). Although this extrapolation to high temperature does not account for the slight bowing in the slope observed at around 870–900 °C for high-temperature samples, it provides a constraint with the least amount of uncertainty on conductivity–strain relationships because the melt phase did not redistribute in these low-temperature experiments. It also satisfactorily reproduces the measurements of high-temperature samples performed up to 1,300 °C (sample PT0683, Fig. 2b). In fact, the electrical conductivity of melts with a low degree of polymerization shows no major change in activation energy at temperatures above the glass transition temperature to 1,300 °C (ref. 19), and previous experimental studies have demonstrated that a single activation energy describes the electrical conductivity of olivine over the temperature range of interest, 700–1,300 °C (ref. 20).

Our results, which quantify the effects of deformation and partial melt on the electrical conductivity of mantle rocks, are summarized as follows. (1) Deformation affects the electrical response of all the systems investigated, including both melt-free olivine compacts and melt + olivine samples (Fig. 2). This observation contrasts with results from a previous study¹³ that did not show anisotropy in sheared melt-free samples, possibly because the shear strains were too low ($\gamma < 1.8$). The effect on conductivity anisotropy of a relatively small amount of strain in triaxial compression of olivine aggregates is small (a factor of < 2) but detectable (Fig. 2a). Simple shear deformation in torsion of olivine aggregates to a relatively large shear strain ($\gamma \approx 3.5$) results in an enhancement by a factor of about ten in electrical conductivity parallel to the direction of shear compared to an undeformed sample. For this sample (PT0264), the lattice preferred orientation of olivine is defined by [100] subparallel to the shear direction, and by (010) subparallel to the shear plane (also called type-A fabric)²¹. The lattice preferred orientation of the olivine grains is unlikely to explain the high bulk conductivity of this sheared sample, because electrical anisotropy in olivine single crystals is only about a factor of two at 1,200 °C (ref. 10), much smaller than our measured factor of ten. The high conductivity in the high-strain sample may be due to the contribution of grain boundaries, as the grain size in the sheared samples is smaller than in an undeformed sample owing to dynamic recrystallization and

the grain boundaries are sympathetically oriented in the shear samples. The decrease in activation energy observed for most samples at high temperature (more than about 1,040 °C) may be an indication that the stress regime preserved from the deformation experiment has relaxed to a greater degree during the electrical experiment. However, the deformed texture of the sample was preserved during the entire experiment (Extended Data Fig. 2a). No systematic effect of shear strain (for $1.2 < \gamma < 9$) on conductivity was observed for melt-bearing samples (Fig. 2b).

(2) The addition of a few volume per cent of basaltic or carbonate melt to a polycrystalline olivine slightly increases the bulk electrical conductivity (by 10%–30%). For all melt-bearing samples, electrical anisotropy is large at low T in the glass region and above the glass transition temperature T_g up to 900 °C, but decreases at temperatures greater than 900 °C, consistent with the disappearance of melt-rich bands in the run products during the high-temperature conductivity experiments (Extended Data Fig. 2). This low electrical anisotropy at high temperature indicates a reorganization of the melt network in the multi-anvil apparatus, despite the persistence of some degree of structural anisotropy: the crystallographic preferred orientation of the olivine grains was maintained, but the melt preferred orientation weakened (controlled by anisotropy in the melt–solid interfacial energy rather than by stress) and the melt-rich bands dissipated in response to surface tension, leaving a nearly isotropic melt distribution. Samples with 5 vol% MORB and 2 vol% carbonate yield similar values for conductivity at a given temperature. From their electrical response alone, all investigated materials can potentially explain high conductivities in the upper mantle (typically $\geq 0.03 \text{ S m}^{-1}$), emphasizing that electrical conductivity alone cannot discriminate between the effect of bulk composition and deformation textures.

On the basis of the results of our experiments, we propose models for the electrical conductivity in both anisotropic and predominantly isotropic environments (Fig. 2c). Melt-bearing samples provide analogues of a melt-bearing isotropic mantle and of melt-rich bands in a highly anisotropic mantle. The bulk electrical conductivity of a banded mantle is calculated using a layered model that consists of either series or parallel circuit equations, depending on the direction considered (Methods). In this model, melt-rich layers correspond to either a MORB-bearing material using our conductivity measurements or a basaltic material

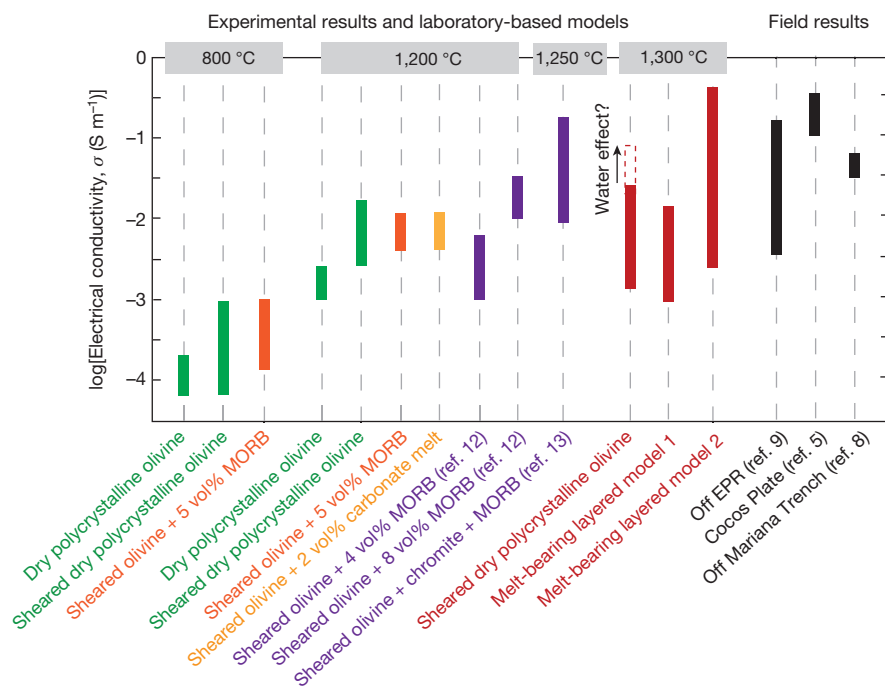


Figure 3 | Comparison between the electrical anisotropy of deformed materials measured in laboratory experiments and that determined from field measurements. Experimental results are from this study and refs 12 and 13, and field results are the same as in Fig. 1^{5,7,8}. Calculations using the laboratory-based layered model are explained in Methods. Large anisotropies are well reproduced with the layered model and sheared olivine. The addition of water may increase the electrical anisotropy of sheared olivine. High temperatures are needed to match the highest conductivity values ($\sigma > 0.1 \text{ S m}^{-1}$) observed in the field. Electrical results at 800 °C are not shown for the carbonate-bearing material because this sample was first taken to high temperature (before being cooled down), where the melt homogenized and damaged the anisotropic texture.

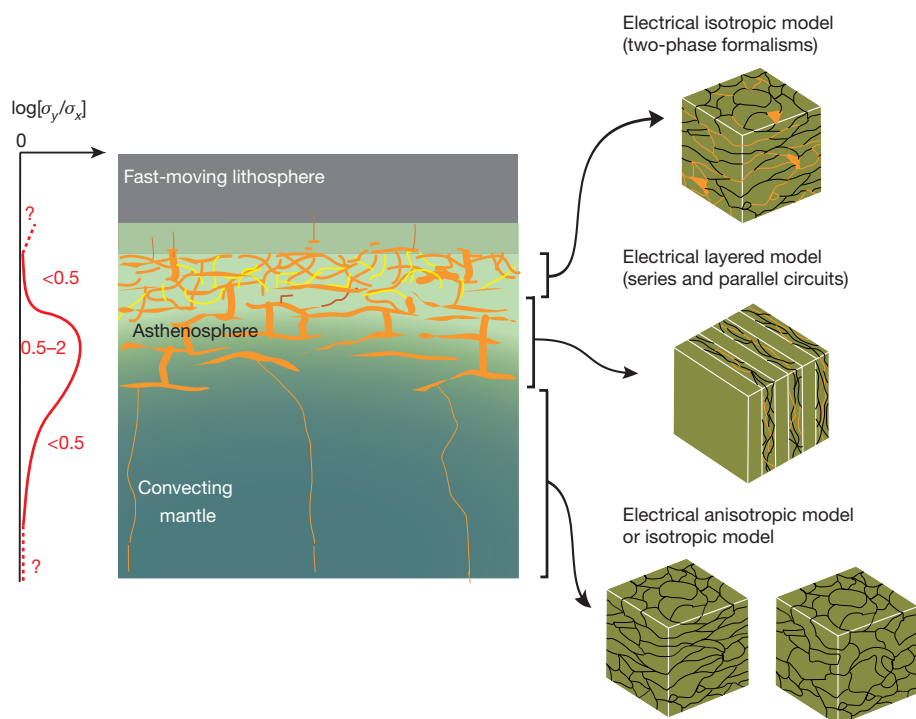


Figure 4 | Cross-section portrayal of the electrical conductivity of the uppermost mantle in a melt-bearing context. The corresponding conductivity ratio for the direction of lowest (σ_y) to the highest (σ_x) conductivity is shown in red. Melt reaches the asthenosphere from the deeper mantle. The geometry and the distribution of melt pathways in the deeper mantle do not significantly affect electrical anisotropy. In the asthenosphere, the horizontal alignment (of sheets, tubules, and so on) is the dominant process and results from mantle flow so electrical anisotropy is enhanced as a result of plate motion. Vertical melt migration has an insignificant influence on the geophysical response. Melt accumulates at the bottom of the lithosphere because the lithosphere is less permeable, and becomes well interconnected in all directions despite a deformed solid matrix. This melt is isolated from mantle flow, cooling and crystallizing.

based on published conductivity results²²; melt-free layers correspond to either undeformed or sheared polycrystalline Fo_{90} .

Our results reproduce both the magnitude and the anisotropy of electrical conductivity in various melt-bearing contexts (Fig. 3). Near the East Pacific Rise, where a few volume per cent of melt is expected, the high anisotropy ($\sigma_{\text{max}}/\sigma_{\text{min}} > 50$, Fig. 3) detected at a depth of 80–120 km is best reproduced by a laboratory-based layered model (melt-bearing layered model 2 in Fig. 3) that is consistent with plate-motion-related strains in the asthenosphere that induce alignment of melt and formation of melt-enriched sheets in the direction of plate motion.

Under the Cocos plate, the main conductivity anomaly in the asthenosphere (45–60 km) has a small anisotropy ($\sigma_{\text{max}}/\sigma_{\text{min}} \approx 3$, Fig. 3) despite the fact that the high speed of the plate (8.5 cm yr^{-1}) is expected to be accompanied by substantial strain in the underlying asthenosphere. Our layered models are too anisotropic to be comparable to field observations under the Cocos plate (Fig. 3), suggesting that the geometric configuration of the melt phase under the Cocos plate is almost electrically isotropic. In highly deformed rocks, a low degree of anisotropy of the melt phase may appear paradoxical. However, this possibility can be reconciled at high temperatures, where stresses are lower and thus deformation produces a weaker crystallographic preferred orientation and melt preferred orientation than at lower T where stress is higher (to maintain the same strain rate). Temperatures exceeding $1,400^\circ\text{C}$ with a few volume per cent of hydrous melt have been previously suggested to explain these high conductivities⁵. Our experiments demonstrate that a temperature of around $1,300^\circ\text{C}$ is sufficient to explain the observed conductivities and that the weak anisotropy is reproduced by a sheared material in which melt pathways exist in all directions.

Under the Pacific Ocean basin, at more than 100 km east of the Mariana Trench and at a depth of 150–250 km, the weak electrical anisotropy ($\sigma_{\text{max}}/\sigma_{\text{min}} \approx 1.8$, Fig. 3) has been attributed to mantle flow in the Mariana Trough⁷. As for the Cocos plate, the field data are best reproduced by an isotropic melt phase interconnected in a sheared solid matrix at high temperature ($>1,200^\circ\text{C}$). The extrapolation of Arrhenian equations based on our data on sheared olivine + 5 vol% MORB (Fig. 2b; Extended Data Table 4) to $1,350^\circ\text{C}$ reproduces the

electrical field data off the Mariana Trench, with electrical conductivity values of $6.4 \times 10^{-2} \text{ S m}^{-1}$ in the direction of deformation and $2.7 \times 10^{-2} \text{ S m}^{-1}$ in the direction perpendicular to deformation.

Regions of high anisotropy embedded between layers of low anisotropy that have been observed beneath mid-ocean ridges and oceanic plates (Fig. 1) can be related to vertical stratification in mantle rheology and fluid distribution (Fig. 4). Deep regions of low anisotropy are observed under the East Pacific Rise, the Cocos plate, and the Pacific Ocean basin (at depths of 140 km, 80 km and 250 km, respectively), consistent with an isotropic distribution of mantle phases and possibly scattered melt pathways towards shallower asthenospheric depths. At shallower depths, the decrease in electrical anisotropy and conductivity observed for the regions considered (less than about 80 km depth off the East Pacific Rise, 40–45 km depth under the Cocos plate, and less than about 120 km depth off the Mariana Trench, Fig. 1) may involve processes associated with the coupling of tectonic plate motion and flow in the underlying mantle. Layers of low electrical anisotropy are consistent with a more isotropically distributed melt phase that governs the bulk conductivity. An interconnected liquid phase with a weak melt preferred orientation in a deformed matrix may also explain why some electromagnetic studies in other locations observe high conductivities but do not detect electrical anisotropy²³. This melt distribution may arise from its accumulation at the lithosphere–asthenosphere boundary and possible upward migration through dikes that propagate buoyantly into the lithosphere^{24,25}. It is also possible that asthenospheric melt percolates into the bottom of the lithosphere, eventually cooling and crystallizing. If the long-term rheological behaviour of crystallizing melt-rich structures results in increasing the viscosity in a zone at the base of the lithosphere, it can then reduce the efficiency of viscous coupling between the tectonic plates and the underlying flow of the mantle through time.

Online Content Methods, along with any additional Extended Data display items and Source Data, are available in the online version of the paper; references unique to these sections appear only in the online paper.

Received 16 June 2014; accepted 21 April 2015.

1. Holtzman, B. K. & Kendall, J.-M. Organized melt, seismic anisotropy, and plate boundary lubrication. *Geochem. Geophys. Geosyst.* **11**, Q0AB06 (2010).

2. Höink, T., Lenardic, A. & Richards, M. Depth-dependent viscosity and mantle stress amplification: implications for the role of the asthenosphere in maintaining plate tectonics. *Geophys. J. Int.* **191**, 30–41 (2012).
3. Karato, S.-i. On the origin of the asthenosphere. *Earth Planet. Sci. Lett.* **321–322**, 95–103 (2012).
4. Kawakatsu, H. *et al.* Seismic evidence for sharp lithosphere–asthenosphere boundaries of oceanic plates. *Science* **324**, 499–502 (2009).
5. Naif, S., Key, K., Constable, S. & Evans, R. L. Melt-rich channel observed at the lithosphere–asthenosphere boundary. *Nature* **495**, 356–359 (2013).
6. Hirschmann, M. M. Partial melt in the oceanic low velocity zone. *Phys. Earth Planet. Inter.* **179**, 60–71 (2010).
7. Matsuno, T. *et al.* Upper mantle electrical resistivity structure beneath the central Mariana subduction system. *Geochem. Geophys. Geosyst.* **11**, Q09003 (2010).
8. Baba, K., Chave, A. D., Evans, R. L., Hirth, G. & Mackie, R. L. Mantle dynamics beneath the East Pacific Rise at 17°S: insights from the Mantle Electromagnetic and Tomography (MELT) experiment. *J. Geophys. Res.* **111**, B02101 (2006).
9. Reynard, B., Mibe, K. & Van de Moortèle, B. Electrical conductivity of the serpentinised mantle and fluid flow in subduction zones. *Earth Planet. Sci. Lett.* **307**, 387–394 (2011).
10. Yoshino, T., Takuya, M., Yamashita, S. & Katsura, T. Hydrous olivine unable to account for conductivity anomaly at the top of the asthenosphere. *Nature* **443**, 973–976 (2006).
11. Poe, B. T., Romano, C., Nestolo, F. & Smyth, J. R. Electrical conductivity anisotropy of dry and hydrous olivine at 8 GPa. *Phys. Earth Planet. Inter.* **181**, 103–111 (2010).
12. Caricchi, L., Gaillard, F., Mecklenburgh, J. & Le Trong, E. Experimental determination of electrical conductivity during deformation of melt-bearing olivine aggregates: implications for electrical anisotropy in the oceanic low velocity zone. *Earth Planet. Sci. Lett.* **302**, 81–94 (2011).
13. Zhang, B., Yoshino, T., Yamazaki, D., Manthilake, G. & Katsura, T. Electrical conductivity anisotropy in partially molten peridotite under shear deformation. *Earth Planet. Sci. Lett.* **405**, 98–109 (2014).
14. Holtzman, B. K. *et al.* Melt segregation and strain partitioning: implications for seismic anisotropy and mantle flow. *Science* **301**, 1227–1230 (2003).
15. King, D. S., Kohlstedt, D. L. & Zimmerman, M. E. Stress-driven melt segregation in partially molten rocks deformed in torsion. *J. Petrol.* **51**, 21–42 (2010).
16. Parsons, R. A., Nimmo, F., Hustoft, J., Holtzman, B. K. & Kohlstedt, D. L. An experimental and numerical study of surface tension-driven melt flow. *Earth Planet. Sci. Lett.* **267**, 548–557 (2008).
17. King, D. S. H., Hier-Majumder, S. & Kohlstedt, D. L. An experimental study of the effects of surface tension in homogenizing perturbations in melt fraction. *Earth Planet. Sci. Lett.* **307**, 349–360 (2011).
18. Kohlstedt, D. L. & Zimmerman, M. E. Rheology of partially molten mantle rocks. *Annu. Rev. Earth Planet. Sci.* **24**, 41–62 (1996).
19. Pommier, A., Gaillard, F., Pichavant, M. & Scaillet, B. Laboratory measurements of electrical conductivities of hydrous and dry Mount Vesuvius melts under pressure. *J. Geophys. Res.* **113**, B05205 (2008).
20. Constable, S. SE03: a new model of olivine electrical conductivity. *Geophys. J. Int.* **166**, 435–437 (2006).
21. Jung, H., Katayama, I., Jiang, Z., Hiraga, T. & Karato, S. Effect of water and stress on the lattice-preferred orientation of olivine. *Tectonophysics* **421**, 1–22 (2006).
22. Ni, H., Keppler, H. & Behrens, H. Electrical conductivity of hydrous basaltic melts: implications for partial melting in the upper mantle. *Contrib. Mineral. Petrol.* **162**, 637–650 (2011).
23. Evans, R. L., Wannamaker, P. E., McGary, R. S. & Elsenbeck, J. Electrical structure of the central Cascadia subduction zone: the EMSLAB Lincoln Line revisited. *Earth Planet. Sci. Lett.* **402**, 265–274 (2014).
24. Havlin, C., Parmentier, E. M. & Hirth, G. Dike propagation driven by melt accumulation at the lithosphere–asthenosphere boundary. *Earth Planet. Sci. Lett.* **376**, 20–28 (2013).
25. Sakamaki, T. *et al.* Ponded melt at the boundary between the lithosphere and asthenosphere. *Nature Geosci.* **6**, 1041–1044 (2013).
26. Dai, L., Li, H., Li, C., Hu, H. & Shan, S. The electrical conductivity of dry polycrystalline olivine compacts at high temperatures and pressures. *Mineral. Mag.* **74**, 849–857 (2010).
27. Xu, Y. S., Shankland, T. J. & Duba, A. G. Pressure effect on electrical conductivity of mantle olivine. *Phys. Earth Planet. Inter.* **118**, 149–161 (2000).
28. Roberts, J. J. & Tyburczy, J. A. Partial-melt electrical conductivity: influence of melt composition. *J. Geophys. Res.* **104**, 7055–7065 (1999).
29. Yoshino, T., Laumonier, M., McIsaac, E. & Katsura, T. Electrical conductivity of basaltic and carbonatite melt-bearing peridotites at high pressures: implications for melt distribution and melt fraction in the upper mantle. *Earth Planet. Sci. Lett.* **295**, 593–602 (2010).
30. Yoshino, T., McIsaac, E., Laumonier, M. & Katsura, T. Electrical conductivity of partial molten carbonate peridotite. *Earth Planet. Sci. Lett.* **194–195**, 1–9 (2012).

Acknowledgements This work benefited from funding by the NSF through Cooperative Studies of the Earth's Deep Interior (CSEDI) projects number 1461594 to the University of California San Diego, number 1265395 to Arizona State University, and number 1265428 to the University of Minnesota. This research was partially supported by COMPRES (the Consortium for Materials Properties Research in Earth Sciences) under National Science Foundation (NSF) Cooperative Agreement EAR 11-57758 (cell assembly development project). We thank A. von der Handt (University of Minnesota) and H. Cathey (Arizona State University) for their assistance with the electron microprobe and scanning electron microscope imaging, respectively. A.P. appreciates help with calibration experiments from staff and scientists at Bayerisches Geoinstitut (BGI). This paper is Lunar and Planetary Institute (LPI) contribution number 1840.

Author Contributions A.P. proposed and led the project, performed the conductivity experiments and the electron microprobe analyses, interpreted the results, wrote the first draft and made the figures. K.L. and A.P. developed the conductivity setup at Arizona State University. D.L.K. and C.Q. synthesized the deformed starting materials and provided some of the scanning electron microscope images. E.J.G., S.J.M. and D.L.K. contributed to the data interpretation and discussion. All authors commented on the manuscript and provided editorial assistance.

Author Information Reprints and permissions information is available at www.nature.com/reprints. The authors declare no competing financial interests. Readers are welcome to comment on the online version of the paper. Correspondence and requests for materials should be addressed to A.P. (pommier@ucsd.edu).

METHODS

Starting materials. Electrical measurements were performed on three anhydrous starting materials: polycrystalline olivine (Fo₉₀), Fo₉₀ + 5 vol.% MORB, and Fo₉₀ + 2 vol.% NaKCO₃ melt. These samples were deformed in triaxial compression to a strain of approximately 0.1 or in simple shear to shear strains from 1.2 to 9 (Extended Data Table 1) at a confining pressure of 0.3 GPa and temperatures of 1,200 °C–1,250 °C in a gas-medium apparatus. The parts of the samples that had experienced maximum shear strain were extracted and placed in a conductivity cell in the multi-anvil apparatus (Extended Data Fig. 1a) for electrical measurements. Simultaneous monitoring of the deformation and the electrical response is not required to investigate the effect of deformation on the electrical conductivity and anisotropy in σ of polycrystalline materials, as long as the same starting material is used to do the measurements in the different orientations. Note that the gas-medium apparatus used to deform the samples is operated at low pressure (0.3 GPa), whereas the multi-anvil apparatus can reproduce asthenospheric conditions (in our case, about 3 GPa).

Multi-anvil experiments. All electrical experiments were performed at about 3 GPa in a multi-anvil apparatus using tungsten carbide cubes with a corner-truncation edge length of 8 mm and mullite octahedral pressure media with an edge length of 14 mm. Graphite heaters were used, placed inside an outer zirconia sleeve that provided thermal insulation. Experimental samples were 2 mm in diameter and 0.8–1.5 mm in length, and were placed at the centre of the cylindrical heater inside an MgO sleeve. Two molybdenum disks (outer diameter 2 mm) were in contact with the sample, serving as electrodes. The temperature was monitored with a W₉₅Re₅–W₇₄Re₂₆ (C-type) thermocouple inserted within an MgO sleeve with the junction in contact with the top of one of the molybdenum disks (Extended Data Fig. 1b). A single tungsten–rhenium (W–Re) wire was connected to the other molybdenum disk.

The conductivity cell (Extended Data Fig. 1b) was connected to a 1260 Solartron Impedance/Gain-Phase Analyzer for electrical impedance measurements. Redox conditions (oxygen fugacity) were not controlled during the experiments. However, the presence of a graphite furnace implies a reducing environment with an oxygen fugacity near the fayalite–magnetite–quartz buffer³¹.

To preserve the influence of deformation and chemistry on conductivity, heating duration in the multi-anvil conductivity experiments did not exceed 2 h, and measurements were preferentially conducted at temperatures <900 °C. As illustrated by Extended Data Fig. 2c and f, melt-rich bands were preserved at temperatures slightly above the glass transition. This observation is consistent with previous experimental work on sheared melt-bearing materials, which demonstrated that annealing at about 1,100 °C and below causes essentially no melt redistribution over laboratory timescales^{16,32}.

Electrical conductivity cell calibration. Our electrical cell has been tested using a hot-pressed polycrystalline olivine sample (wet Fo₇₅) by performing σ experiments under the same conditions (same sample, pressure and temperature) in two different laboratories (Arizona State University and Bayerisches GeoInstitut). The cell used at BGI was different from the one used at ASU, in terms of both materials and part dimensions. Electrical conductivity data were collected at 3 GPa and at temperatures up to 700 °C. All data from both laboratories fitted into a 3% error in $\log\sigma$, confirming that our cell was measuring the sample's response without interference from any other part of the cell assembly. A short-circuit experiment performed at 4 GPa and at temperature up to 1,900 °C showed that our cell has a resistance of about 7 Ω (ref. 33), which is negligible compared to the resistance of our samples (>3,000 Ω).

Electrical conductivity measurements. The complex impedance was collected during cooling over different temperature ranges (Extended Data Tables 3 and 4) in the frequency range 1 Hz to 5 MHz. The reproducibility of electrical measurements was validated by performing a few measurements during heating. For melt-free samples and melt-bearing samples at low temperature, the electrical response consisted of an impedance arc (Extended Data Fig. 1c). For MORB-bearing samples at high temperature, the impedance arc was not observed and the electrical response consisted of a noisy part at high frequency and a vertical line at low frequency intersecting with the real axis of the complex plane. For all samples, the electrical resistance of the sample corresponds to the real part of the complex impedance, identified in the real versus imaginary component plot as the intercept of the spectrum with the real axis.

Data reduction and uncertainties. For each sample, the electrical conductivity was calculated using the measured electrical resistance and sample geometric factor G (ref. 34)

$$\sigma = 1/(RG) \quad (1)$$

where $G = \pi r^2/L$, σ is the electrical conductivity (in units of S m⁻¹), R is the electrical resistance (in ohms), r is the radius of the cylindrical sample (in metres), and L is the thickness of the sample (in metres). Relative errors on values of σ

(Extended Data Tables 3 and 4) were calculated on the basis of errors on the geometrical factor (that is, considering errors on r and L) as well as propagated errors on each measured value of resistance R . As an example, uncertainties on electrical conductivity values are provided in Extended Data Table 5 for each temperature of the experiment on sample PT0683-2.

Analytical techniques. All the recovered run products were mounted in epoxy resin and then ground and polished (using ethanol for the carbonate-bearing samples to preserve the carbonate phase, and using water for all the other samples) for analytical investigations. Scanning electron microscope imaging and electron microprobe analyses were performed after each experiment to characterize the texture and chemistry of the samples. The chemical compositions of melt and mineral phases were obtained using a JEOL JXA-8900 Electron Probe Microanalyzer equipped with five wavelength-dispersive spectrometers. Electron microprobe analyses were conducted at 15 keV and 10 nA, with 10 s counting on peak elements and a beam size of 100 $\mu\text{m} \times 100 \mu\text{m}$.

Electrical conductivity results. The dependence of electrical conductivity on temperature for each sample was fitted using an Arrhenius law

$$\sigma = \sigma_0 \times \exp[-E_a/(kT)]$$

with σ_0 being the pre-exponential factor (in units of S m⁻¹), E_a the activation energy (in electronvolts), k the Boltzmann constant (8.617×10^{-5} eV K⁻¹), and T the temperature (in kelvin). Values calculated for the pre-exponential factor and activation energy are presented in Extended Data Tables 3 and 4.

Electrical conductivity layered model. In this electrical model, the material considered alternating layers of sheared polycrystalline olivine and of olivine + 5 vol.% MORB (layered model 1) or of basalt only (layered model 2). Electrical anisotropy can be modelled using series and parallel circuits, depending on the horizontal direction (x and y) of the electrical current. The vertical z direction is not considered since the magnetotelluric technique does not detect vertical anisotropy³⁵.

Series circuit. The direction of the electrical current is perpendicular to the shear plane. The equivalent resistance of the circuit, R_{eq} , corresponds to the sum of the resistances of each layer, R_i

$$R_{\text{eq}} = \sum_i R_i \quad (2)$$

The resistance R_i is calculated from values for σ from our study (sheared samples of polycrystalline olivine and of olivine + MORB) and from ref. 22 (basalt) using the relationship

$$R_i = \frac{1}{\sigma_i \times G_i} \quad (3)$$

with G_i the geometric factor of layer i (surface area divided by thickness). The bulk equivalent electrical conductivity is obtained using

$$\sigma_{\text{eq}} = \frac{1}{R_{\text{eq}} \times G} \quad (4)$$

where G is the geometric factor for the sample.

Application. We consider a cubic and layered material of size $L = 1.5$ mm ($G = 1.5 \times 10^{-3}$ m) made of five layers, two of olivine and three of olivine + MORB or of basalt. The dimensions of each olivine layer are 1.5 mm \times 1.5 mm \times 0.525 mm (geometric factor of 4.3×10^{-3} m), and the dimensions of each melt-bearing layer are 1.5 mm \times 1.5 mm \times 0.15 mm (geometric factor of 1.5×10^{-2} m). At 1,200 °C, the equivalent value of σ is 1.31×10^{-3} S m⁻¹ ($\log\sigma = -2.88$) for the material with basalt layers and 2.99×10^{-4} S m⁻¹ ($\log\sigma = -3.52$) for the material with 5 vol.% MORB layers. At 1,300 °C, the equivalent value of σ is 2.13×10^{-3} S m⁻¹ ($\log\sigma = -2.67$) for the material with basalt layers and 1.08×10^{-3} S m⁻¹ ($\log\sigma = -2.97$) for the material with 5 vol.% MORB layers.

Parallel circuit. In this case, the electrical current is parallel to the shear plane. The reciprocal of equivalent resistance equals the sum of the reciprocals of the resistance values

$$\frac{1}{R_{\text{eq}}} = \sum_i \frac{1}{R_i} \quad (5)$$

The resistance R_i is calculated from values of σ measured in our study (undeformed polycrystalline olivine and olivine + MORB) and reported in ref. 22 (for basalt).

The bulk equivalent electrical conductivity is obtained using the relationship

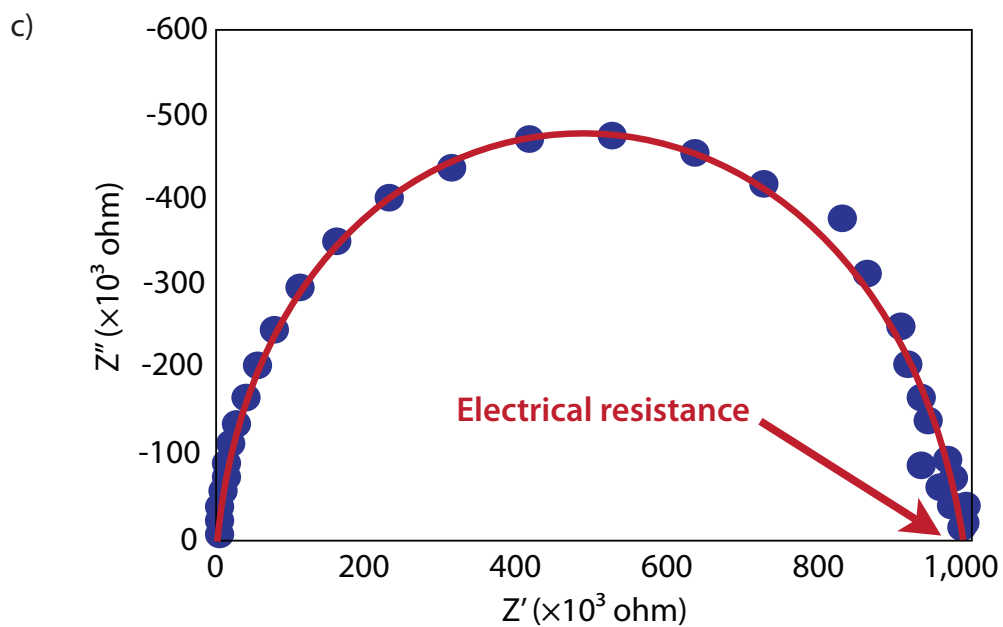
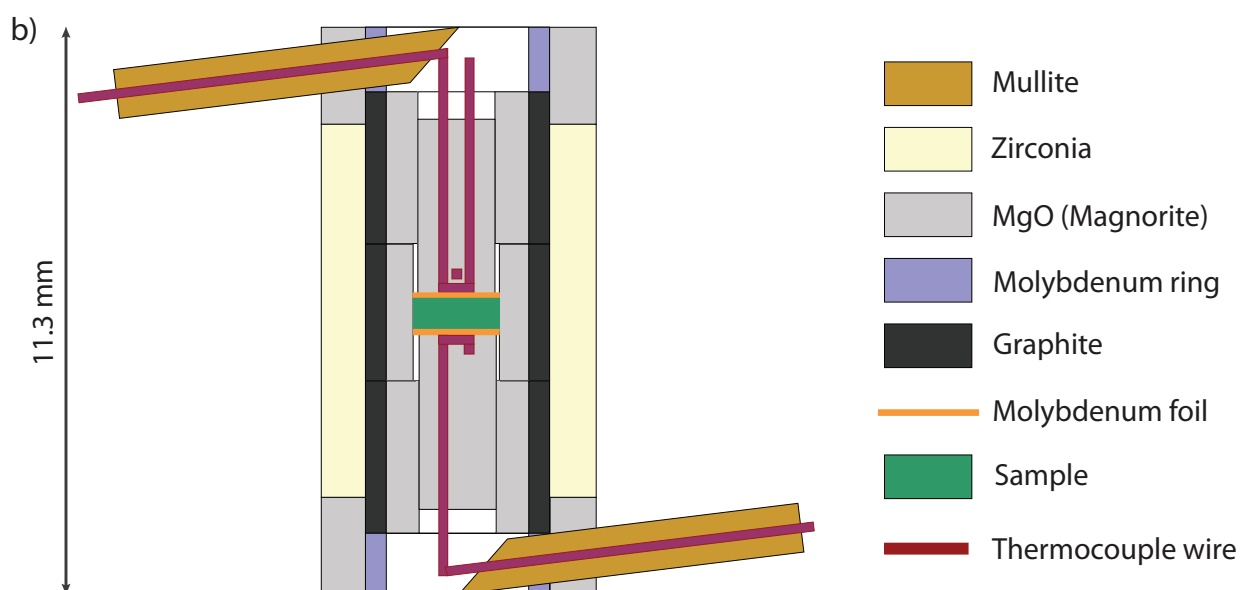
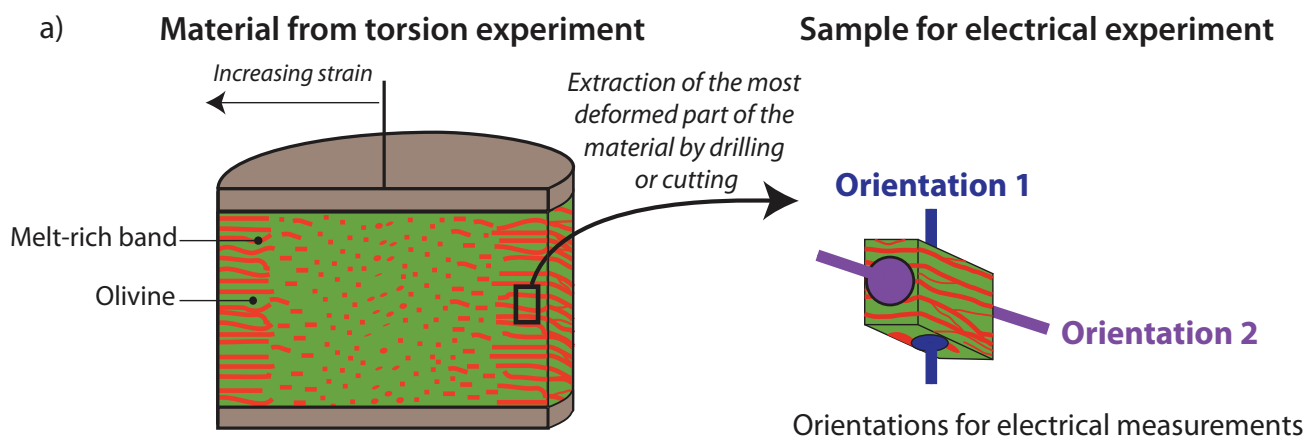
$$\sigma_{\text{eq}} = \frac{1}{R_{\text{eq}} \times G} \quad (6)$$

Application. We consider the same cubic material as above. With this direction for the current flow, the geometric factor of each olivine layer is 5.25×10^{-4} m and of each melt-bearing layer is 1.5×10^{-4} m. At 1,200 °C, the equivalent value of σ is 0.11 S m⁻¹ ($\log\sigma = -0.96$) for the material with basalt layers and 6.59×10^{-3} S m⁻¹ ($\log\sigma = -2.18$) for the material with 5 vol.% MORB layers.

At 1,300 °C, the equivalent value of σ is 0.44 S m^{-1} ($\log \sigma = -0.36$) for the material with basalt layers and $1.40 \times 10^{-2} \text{ S m}^{-1}$ ($\log \sigma = -1.85$) for the material with 5 vol% MORB layers.

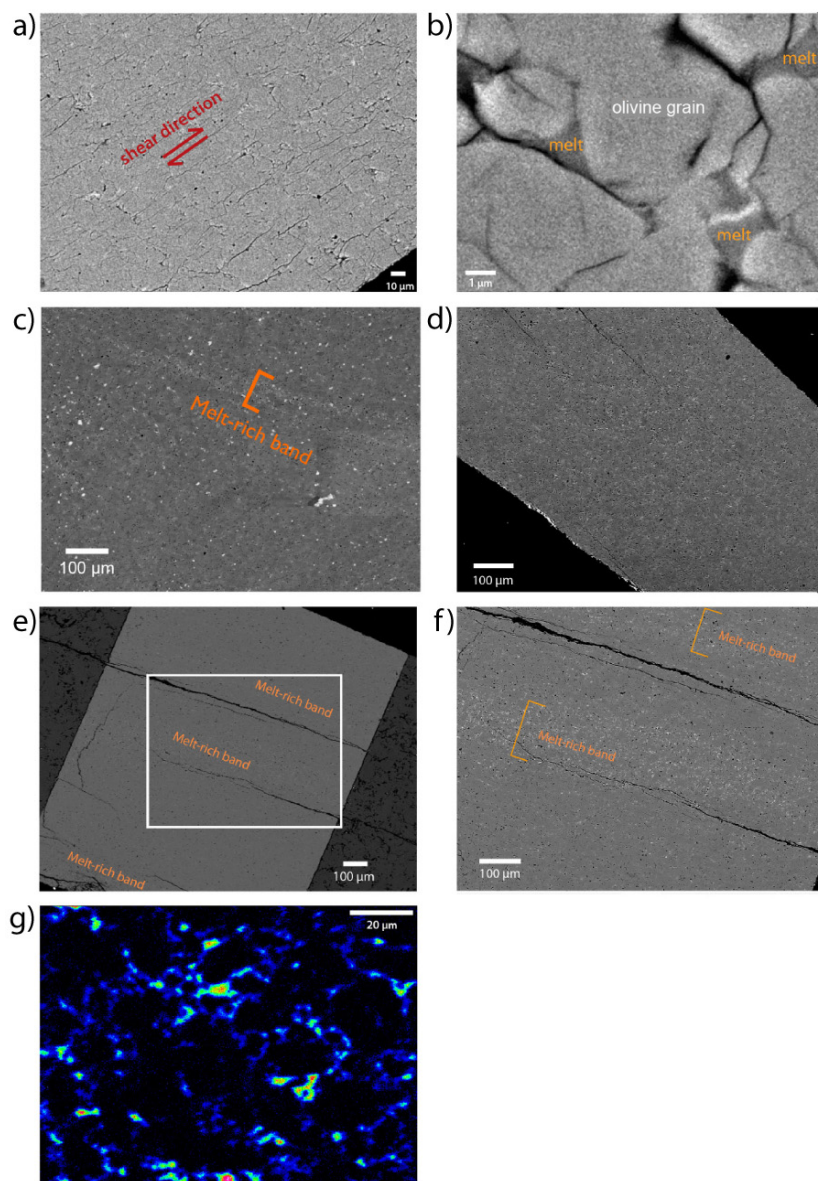
Electrical anisotropy. Electrical anisotropy is the ratio of electrical conductivity for the parallel circuits to electrical conductivity for the series circuits (that is, $\sigma_{\text{parallel circuit}}/\sigma_{\text{series circuit}}$). For the material containing 5 vol% MORB layers, electrical anisotropy is $22.0 (\pm 2.0)$ and $13.0 (\pm 0.1)$ at 1,200 °C and 1,300 °C, respectively. For the material containing basalt layers, higher values for electrical anisotropy of $82.9 (\pm 7.5)$ and $207 (\pm 29)$ at 1,200 °C and 1,300 °C, respectively, are obtained.

31. Stagno, V. & Frost, D. Carbon speciation in the asthenosphere: experimental measurements of the redox conditions at which carbonate-bearing melts coexist with graphite or diamond in peridotite assemblages. *Earth Planet. Sci. Lett.* **300**, 72–84 (2010).
32. King, D. S. H., Hier-Majumder, S. & Kohlstedt, D. L. An experimental study of the effects of surface tension in homogenizing perturbations in melt fraction. *Earth Planet. Sci. Lett.* **307**, 349–360 (2011).
33. Pommier, A., Leinenweber, K. & Tasaka, M. Experimental investigation of the electrical behavior of olivine during partial melting under pressure and application to the lunar mantle. *Earth Planet. Sci. Lett.* (in the press).
34. Ni, H., Keppler, H., Manthilake, M. A. & Katsura, T. Electrical conductivity of dry and hydrous $\text{NaAlSi}_3\text{O}_8$ glasses and liquids at high pressures. *Contrib. Mineral. Petrol.* **162**, 501–513 (2011).
35. Martí, A. The role of electrical anisotropy in magnetotelluric responses: from modelling and dimensionality analysis to inversion and interpretation. *Surv. Geophys.* **35**, 179–218 (2014).



Extended Data Figure 1 | Experimental protocol. **a**, Starting material preparation. Deformed material is synthesized in a gas-medium apparatus at 300 MPa (left), and its outer part is extracted for electrical measurements in the multi-anvil apparatus at about 3 GPa (right). Two orientations of the sample are considered, leading to vertical (blue) and tangential (purple) electrical measurements. **b**, Cross-section of the electrical conductivity cell (14/8 multi-anvil assembly, that is, the corner-truncation edge length is 8 mm and the pressure media edge length is 14 mm). Both electrodes are made of W-Re

thermocouple wire with one electrode also serving as a thermocouple. **c**, Example of a complex impedance spectrum (real part Z' versus imaginary part Z'') for a sheared sample of olivine + 5 vol% MORB sample at 750 °C and approximately 3 GPa. The intersection between the response of the sample (blue dots, each dot corresponding to one frequency) with the real axis corresponds to the electrical resistance of the sample. The corresponding electrical conductivity value is obtained using the geometric factor (the surface of the electrode divided by thickness of the sample).



Extended Data Figure 2 | Texture and melt geometry. **a**, Back-scattered electron image of sheared sample PT0683-2 after electrical measurements, showing that deformation-induced melt texture was preserved during the experiment in the multi-anvil apparatus. **b**, Back-scattered electron image of sheared sample PT0756-2 after electrical measurements, illustrating the location of melt amongst the olivine grains. **c**, Starting material PT0683 showing the presence of melt-rich bands. **d**, Back-scattered electron image of sheared sample PT0683-1HT after electrical measurements at high temperature (up to 1,573 K). The absence of pronounced melt-rich bands suggests a loss in structural anisotropy, attributed to the effect of high temperature. These observations are consistent with electrical data that showed

a noticeable decrease in electrical anisotropy with increasing temperature. **e**, Back-scattered electron image of sheared sample PT0683-1LT after electrical measurements at low temperature (<1,073 K), showing several light-coloured zones identified as melt-rich bands. The rectangle corresponds to the location of image **f** below. **f**, Zoom on melt-rich bands in sample PT0683-1LT. Melt is also present between the melt-rich zones as pockets amongst the olivine grains. **g**, Map of sodium distribution in sample PT0742-2 after electrical measurements. Colours correspond to the number of counts. Warm colours (reddish) correspond to high sodium concentration and are interpreted as pockets of carbonatite melt between olivine grains.

Extended Data Table 1 | Description of the starting materials.

Sample*	Composition	Av. grain size (micron)	Starting material synthesis						
			Deformation type	P (GPa)	T (K)	Stress (GPa)	Shear strain	Shear stress (GPa)	Shear strain rate (10 ⁻⁴ s ⁻¹)
<i>Dry polycrystalline olivine</i>									
PI1543-1	FO ₉₀	16	compression	0.3	1523	0.44	-	-	-
PI1543-2	FO ₉₀	16	compression	0.3	1523	0.44	-	-	-
PT0264-1	FO ₉₀	4-10	torsion	0.3	1473	-	3.5	0.24	3.5
PT0264-2	FO ₉₀	4-10	torsion	0.3	1473	-	3.5	0.24	3.5
<i>Dry polycrystalline olivine + MORB</i>									
PT0683-1LT	FO ₉₀ +5% MORB	15	torsion	0.3	1473	-	1.2	0.12-0.15	4.6
PT0683-1HT	FO ₉₀ +5% MORB	15	torsion	0.3	1473	-	1.2	0.12-0.15	4.6
PT0683-2	FO ₉₀ +5% MORB	15	torsion	0.3	1473	-	1.2	0.12-0.15	4.6
PT0705-2	FO ₉₀ +5% MORB	15	torsion	0.3	1473	-	9	0.12-0.15	1.5
PT0756-1	FO ₉₀ +5% MORB	15	torsion	0.3	1473	-	2.16	0.12-0.15	5.5
PT0756-2	FO ₉₀ +5% MORB	15	torsion	0.3	1473	-	2.16	0.12-0.15	5.5
<i>Dry polycrystalline olivine + carbonate melt</i>									
PT0742-1	FO ₉₀ +2%NaKCO ₃ melt	5-10	torsion	0.3	1473	-	3	0.12-0.15	1.1
PT0742-2	FO ₉₀ +2%NaKCO ₃ melt	5-10	torsion	0.3	1473	-	3	0.12-0.15	1.1
PT0742-3	FO ₉₀ +2%NaKCO ₃ melt	5-10	torsion	0.3	1473	-	3	0.12-0.15	1.1

* Extension: Electrical conductivity σ measurements perpendicular to deformation (-1), parallel to deformation (-2) and undeformed (centre of column) (-3), respectively. LT, low temperature; HT, high temperature.

Extended Data Table 2 | Electron microprobe analyses of most of the run products

Sample	Phase	SiO ₂	TiO ₂	Al ₂ O ₃	Cr ₂ O ₃	FeOtot	MnO	MgO	CaO	Na ₂ O	K ₂ O	NiO	Mg#	Sum									
PT0683-1LT	ol(9) ^a	40.7	(16) ^b	-	-	10.4	(11)	0.11	(2)	48.8	(32)	-	-	0.35	(3)	0.89	100.5						
	gl(1)	46.7	0.29	13.2	0.04	5.78	0.05	22.9	5.21	2.64	0.06	-	0.88	96.9									
PT0683-2	gl(1)	47.0	0.22	16.0	0.01	5.23	0.05	22.9	6.26	2.24	0.12	-	0.89	99.9									
PT0683-2bis	ol(17)	40.9	(48)	-	-	9.67	(11)	0.12	(2)	48.8	(31)	-	-	0.37	(3)	0.90	99.9						
	gl(1)	47.4	1.62	12.6	0.02	6.82	0.11	21.4	7.1	2.15	0.15	-	0.85	99.3									
PT0705-2	ol(17)	40.9	(19)	-	-	9.25	(14)	0.12	(3)	48.4	(23)	-	-	0.37	(4)	0.90	99.1						
	gl(1)	45.7	0.34	13.4	0.02	5.03	0.17	26.7	5.42	1.85	0.07	-	0.90	98.7									
PT0756-1	ol(12)	40.9	(16)	-	-	9.64	(13)	0.12	(2)	49.4	(29)	-	-	0.35	(4)	0.90	100.3						
PT0756-2	ol(10)	41.0	(29)	-	-	10.0	(19)	0.14	(2)	48.0	(34)	-	-	0.37	(2)	0.90	99.5						
	gl(3)	47.3	(9)	0.14	(10)	17.0	(24)	0.04	(1)	5.08	(17)	0.05	(1)	21.1	(68)	6.82	(24)	2.37	(19)	0.05	(1)	-	0.88
PT0742-1	ol(29)	41.0	(15)	-	-	8.44	(47)	0.12	(3)	50.5	(36)	-	-	-	0.36	(4)	0.91	100.3					
PT0742-3	ol(10)	41.4	(30)	-	-	8.48	(53)	0.11	(2)	50.1	(52)	-	-	-	0.31	(8)	0.91	100.4					

Contents are in weight per cent. Ol, olivine; gl, glass. A dash indicates 'not measured'. ^aThe number of microprobe analyses is shown in parentheses. ^bOne standard deviation in terms of least unit cited is shown in italics and parentheses; for example, 46.11(123) indicates a standard deviation of 1.23wt% on the value of 46.11wt%.

Extended Data Table 3 | Electrical results for polycrystalline olivine materials

Sample	Composition	Electrical conductivity experiments				Arrhenius equation parameters ♦			
		P (GPa)	T (K)	Duration (hr)*	Rel. error on σ (%)	Ea (eV)	Error (eV)	Ln(σ_0), (σ_0 in S/m)	Error (S/m)
PI1543-1	Fe _{0.90}	2.8	1121-1575	2.0	7.5-10.5	0.959	0.005	0.56	0.003
PI1543-2	Fe _{0.90}	2.8	1274-1623	1.9	2.1-7.1	0.879	0.010	0.64	0.007
PT0264-1	Fe _{0.90}	2.8	873	0.5	2.2	-	-	-	-
PT0264-2	Fe _{0.90}	2.8	1173-1570	1.0	2.0-11.5	1.042	0.001	4.1	0.003

*Time spent in heating and cooling cycles.
♦ $\ln \sigma = \ln \sigma_0 - E_a/kT$.

Extended Data Table 4 | Electrical results for melt-bearing materials

Sample	Composition	Electrical conductivity experiments				Arrhenius equation parameters at T<-870°C ♦				Arrhenius equation parameters at T>-870°C ♦				Extrapolation of low-T data to T>T _g ^a		
		P (GPa)	T (K)	Duration (hr)*	Rel. error on σ (%)	E _a (eV)	Error (eV)	Ln(σ ₀), (σ ₀ in S/m)	Error (S/m)	E _a (eV)	Error (eV)	Ln(σ ₀), (σ ₀ in S/m)	Error (S/m)	Slope a	Intercept b	R ²
Dry polycrystalline olivine + MORB																
PT0683-1LT	F ₉₀ +5% MORB	2.8	847-1,073	1.0	0.8-1.6	1.047	0.030	3.5	0.100	-	-	-	-	-0.571	1.942	0.967
PT0683-1HT	F ₉₀ +5% MORB	2.8	1,395-1,466	1	4.1-5.1	-	-	-	-	1.223	0.047	6.0	0.667	-	-	-
PT0683-2	F ₉₀ +5% MORB	2.8	825-1,479	1.3	2.5-10.7	0.335	0.003	-3.6	0.028	0.691	0.010	0.14	0.002	-	-	-
PT0705-2	F ₉₀ +5% MORB	2.8	822-1,076	1.0	1.6-3.1	1.109	0.010	5.1	0.480	-	-	-	-	-0.542	2.023	0.984
PT0756-1	F ₉₀ +10% MORB	2.8	725-1,120	2.5	5.0-5.7	0.942	0.004	1.3	0.005	-	-	-	-	-0.499	0.775	0.995
PT0756-2	F ₉₀ +10% MORB	2.8	671-1,078	1.2	6.4-6.8	0.728	0.022	0.55	0.117	-	-	-	-	-0.178	-1.523	0.904
Dry polycrystalline olivine + carbonate melt																
PT0742-1	F ₉₀ +2% NaKCO ₃ melt	2.8	1,023-1,473	2.0	1.6-4.2	0.381	0.018	-3.3	0.160	1.254	0.010	5.3	0.043	-	-	-
PT0742-3	F ₉₀ +2% NaKCO ₃ melt	2.8	968-1,576	1.6	1.6-4.2	0.509	0.032	-3.1	0.196	1.358	0.013	5.6	0.053	-	-	-

*Time spent in heating and cooling cycles.

♦ $\ln \sigma = \ln \sigma_0 - E_a/kT$.■ $\log \sigma_0 = a \times 10,000/T + b$.

Extended Data Table 5 | Uncertainties on electrical conductivity values for the experiment on sample PT0683-2

Temperature (K)	Resistance (ohm)	Electrical conductivity (S/m)	Error on conductivity (%)	Upper value (S/m)	Lower value (S/m)
825	1800000	0.00027	2.5	0.00028	0.00026
848	1680000	0.00029	2.5	0.00030	0.00028
878	1500000	0.00032	2.6	0.00034	0.00031
899	1320000	0.00037	2.8	0.00039	0.00035
922	1200000	0.00041	2.9	0.00043	0.00038
945	1100000	0.00044	3.0	0.00047	0.00042
975	1000000	0.00049	3.1	0.00052	0.00046
1001	860000	0.00057	3.4	0.00060	0.00053
1024	780000	0.00062	3.6	0.00067	0.00058
1050	700000	0.00070	3.8	0.00075	0.00064
1078	640000	0.00076	4.0	0.00082	0.00070
1098	590000	0.00083	3.3	0.00088	0.00077
1126	520000	0.00094	3.6	0.00100	0.00087
1144	480000	0.00101	3.7	0.00109	0.00094
1176	420000	0.00116	4.0	0.00125	0.00107
1196	360000	0.00135	4.4	0.00147	0.00123
1221	294000	0.00166	5.0	0.00182	0.00149
1245	260000	0.00187	5.5	0.00208	0.00167
1277	220000	0.00221	6.2	0.00249	0.00194
1321	172000	0.00283	7.5	0.00325	0.00241
1378	136000	0.00358	9.0	0.00423	0.00294
1422	116000	0.00420	10.3	0.00506	0.00334
1479	110000	0.00443	10.7	0.00538	0.00348

Massive migration from the steppe was a source for Indo-European languages in Europe

Wolfgang Haak^{1*}, Iosif Lazaridis^{2,3*}, Nick Patterson³, Nadin Rohland^{2,3}, Swapan Mallick^{2,3,4}, Bastien Llamas¹, Guido Brandt⁵, Susanne Nordenfelt^{2,3}, Eadaoin Harney^{2,3,4}, Kristin Stewardson^{2,3,4}, Qiaomei Fu^{2,3,6,7}, Alissa Mittnik⁸, Eszter Bánffy^{9,10}, Christos Economou¹¹, Michael Francken¹², Susanne Friederich¹³, Rafael Garrido Pena¹⁴, Fredrik Hallgren¹⁵, Valery Khartanovich¹⁶, Aleksandr Khokhlov¹⁷, Michael Kunst¹⁸, Pavel Kuznetsov¹⁷, Harald Meller¹³, Oleg Mochalov¹⁷, Vayacheslav Moiseyev¹⁶, Nicole Nicklisch^{5,13,19}, Sandra L. Pichler²⁰, Roberto Risch²¹, Manuel A. Rojo Guerra²², Christina Roth⁵, Anna Szécsényi-Nagy^{5,9}, Joachim Wahl²³, Matthias Meyer⁶, Johannes Krause^{8,12,24}, Dorcas Brown²⁵, David Anthony²⁵, Alan Cooper¹, Kurt Werner Alt^{5,13,19,20} & David Reich^{2,3,4}

We generated genome-wide data from 69 Europeans who lived between 8,000–3,000 years ago by enriching ancient DNA libraries for a target set of almost 400,000 polymorphisms. Enrichment of these positions decreases the sequencing required for genome-wide ancient DNA analysis by a median of around 250-fold, allowing us to study an order of magnitude more individuals than previous studies^{1–8} and to obtain new insights about the past. We show that the populations of Western and Far Eastern Europe followed opposite trajectories between 8,000–5,000 years ago. At the beginning of the Neolithic period in Europe, ~8,000–7,000 years ago, closely related groups of early farmers appeared in Germany, Hungary and Spain, different from indigenous hunter-gatherers, whereas Russia was inhabited by a distinctive population of hunter-gatherers with high affinity to a ~24,000-year-old Siberian⁶. By ~6,000–5,000 years ago, farmers throughout much of Europe had more hunter-gatherer ancestry than their predecessors, but in Russia, the Yamnaya steppe herders of this time were descended not only from the preceding eastern European hunter-gatherers, but also from a population of Near Eastern ancestry. Western and Eastern Europe came into contact ~4,500 years ago, as the Late Neolithic Corded Ware people from Germany traced ~75% of their ancestry to the Yamnaya, documenting a massive migration into the heartland of Europe from its eastern periphery. This steppe ancestry persisted in all sampled central Europeans until at least ~3,000 years ago, and is ubiquitous in present-day Europeans. These results provide support for a steppe origin⁹ of at least some of the Indo-European languages of Europe.

Genome-wide analysis of ancient DNA has emerged as a transformative technology for studying prehistory, providing information that is comparable in power to archaeology and linguistics. Realizing its promise, however, requires collecting genome-wide data from an adequate number of individuals to characterize population changes over time, which means not only sampling a succession of archaeological cultures², but also multiple individuals per culture. To make analysis of large numbers of ancient DNA samples practical, we used in-solution hybridization capture^{10,11} to enrich next generation sequencing libraries for a

target set of 394,577 single nucleotide polymorphisms (SNPs) ('390k capture'), 354,212 of which are autosomal SNPs that have also been genotyped using the Affymetrix Human Origins array in 2,345 humans from 203 populations^{4,12}. This reduces the amount of sequencing required to obtain genome-wide data by a minimum of 45-fold and a median of 262-fold (Supplementary Data 1). This strategy allows us to report genomic scale data on more than twice the number of ancient Eurasians as has been presented in the entire preceding literature^{1–8} (Extended Data Table 1).

We used this technology to study population transformations in Europe. We began by preparing 212 DNA libraries from 119 ancient samples in dedicated clean rooms, and testing these by light shotgun sequencing and mitochondrial genome capture (Supplementary Information section 1, Supplementary Data 1). We restricted the analysis to libraries with molecular signatures of authentic ancient DNA (elevated damage in the terminal nucleotide), negligible evidence of contamination based on mismatches to the mitochondrial consensus¹³ and, where available, a mitochondrial DNA haplogroup that matched previous results using PCR^{4,14,15} (Supplementary Information section 2). For 123 libraries prepared in the presence of uracil-DNA-glycosylase¹⁶ to reduce errors due to ancient DNA damage¹⁷, we performed 390k capture, carried out paired-end sequencing and mapped the data to the human genome. We restricted analysis to 94 libraries from 69 samples that had at least 0.06-fold average target coverage (average of 3.8-fold) and used majority rule to call an allele at each SNP covered at least once (Supplementary Data 1). After combining our data (Supplementary Information section 3) with 25 ancient samples from the literature — three Upper Paleolithic samples from Russia^{1,6,7}, seven people of European hunter-gatherer ancestry^{2,4,5,8}, and fifteen European farmers^{2,3,4,8} — we had data from 94 ancient Europeans. Geographically, these came from Germany ($n = 41$), Spain ($n = 10$), Russia ($n = 14$), Sweden ($n = 12$), Hungary ($n = 15$), Italy ($n = 1$) and Luxembourg ($n = 1$) (Extended Data Table 2). Following the central European chronology, these included 19 hunter-gatherers (~43,000–2,600 BC), 28 Early Neolithic farmers (~6,000–4,000 BC), 11 Middle Neolithic farmers (~4,000–3,000 BC) including

¹Australian Centre for Ancient DNA, School of Earth and Environmental Sciences & Environment Institute, University of Adelaide, Adelaide, South Australia 5005, Australia. ²Department of Genetics, Harvard Medical School, Boston, Massachusetts 02115, USA. ³Broad Institute of Harvard and MIT, Cambridge, Massachusetts 02142, USA. ⁴Howard Hughes Medical Institute, Harvard Medical School, Boston, Massachusetts 02115, USA. ⁵Institute of Anthropology, Johannes Gutenberg University of Mainz, D-55128 Mainz, Germany. ⁶Max Planck Institute for Evolutionary Anthropology, D-04103 Leipzig, Germany. ⁷Key Laboratory of Vertebrate Evolution and Human Origins of Chinese Academy of Sciences, IVPP, CAS, Beijing 100049, China. ⁸Institute for Archaeological Sciences, University of Tübingen, D-72070 Tübingen, Germany. ⁹Institute of Archaeology, Research Centre for the Humanities, Hungarian Academy of Science, H-1014 Budapest, Hungary. ¹⁰Römisch Germanische Kommission (RGK) Frankfurt, D-60325 Frankfurt, Germany. ¹¹Archaeological Research Laboratory, Stockholm University, 114 18 Stockholm, Sweden. ¹²Departments of Paleoanthropology and Archaeogenetics, Senckenberg Center for Human Evolution and Paleoenvironment, University of Tübingen, D-72070 Tübingen, Germany. ¹³State Office for Heritage Management and Archaeology Saxony-Anhalt and State Museum of Prehistory, D-06114 Halle, Germany. ¹⁴Departamento de Prehistoria y Arqueología, Facultad de Filosofía y Letras, Universidad Autónoma de Madrid, E-28049 Madrid, Spain. ¹⁵The Cultural Heritage Foundation, Västerås 722 12, Sweden. ¹⁶Peter the Great Museum of Anthropology and Ethnography (Kunstkamera) RAS, St Petersburg 199034, Russia. ¹⁷Volga State Academy of Social Sciences and Humanities, Samara 443099, Russia. ¹⁸Deutsches Archäologisches Institut, Abteilung Madrid, E-28002 Madrid, Spain. ¹⁹Danube Private University, A-3500 Krems, Austria. ²⁰Institute for Prehistory and Archaeological Science, University of Basel, CH-4003 Basel, Switzerland. ²¹Departamento de Prehistòria, Universitat Autònoma de Barcelona, E-08193 Barcelona, Spain. ²²Departamento de Prehistòria y Arqueología, Universidad de Valladolid, E-47002 Valladolid, Spain. ²³State Office for Cultural Heritage Management Baden-Württemberg, Osteology, D-78467 Konstanz, Germany. ²⁴Max Planck Institute for the Science of Human History, D-07745 Jena, Germany. ²⁵Anthropology Department, Hartwick College, Oneonta, New York 13820, USA.

*These authors contributed equally to this work.

the Tyrolean Iceman³, 9 Late Copper/Early Bronze Age individuals (Yamnaya: ~3,300–2,700 BC), 15 Late Neolithic individuals (~2,500–2,200 BC), 9 Early Bronze Age individuals (~2,200–1,500 BC), two Late Bronze Age individuals (~1,200–1,100 BC) and one Iron Age individual (~900 BC). Two individuals were excluded from analyses as they were related to others from the same population. The average number of SNPs covered at least once was 212,375 and the minimum was 22,869 (Fig. 1).

We determined that 34 of the 69 newly analysed individuals were male and used 2,258 Y chromosome SNPs targets included in the capture to obtain high resolution Y chromosome haplogroup calls (Supplementary Information section 4). Outside Russia, and before the Late Neolithic period, only a single R1b individual was found (early Neolithic Spain) in the combined literature ($n = 70$). By contrast, haplogroups R1a and R1b were found in 60% of Late Neolithic/Bronze Age Europeans outside Russia ($n = 10$), and in 100% of the samples from European Russia from all periods (7,500–2,700 BC; $n = 9$). R1a and R1b are the most common haplogroups in many European populations today^{18,19}, and our results suggest that they spread into Europe from the East after 3,000 BC. Two hunter-gatherers from Russia included in our study belonged to R1a (Karelia) and R1b (Samara), the earliest documented ancient samples of either haplogroup discovered to date. These two hunter-gatherers did not belong to the derived lineages M417 within R1a and M269 within R1b that are predominant in Europeans today^{18,19}, but all 7 Yamnaya males did belong to the M269 subclade¹⁸ of haplogroup R1b.

Principal components analysis (PCA) of all ancient individuals along with 777 present-day West Eurasians⁴ (Fig. 2a, Supplementary Information section 5) replicates the positioning of present-day Europeans between the Near East and European hunter-gatherers^{4,20}, and the clustering of early farmers from across Europe with present day Sardinians^{3,4}, suggesting that farming expansions across the Mediterranean to Spain and via the Danubian route to Hungary and Germany descended from a common stock. By adding samples from later periods and additional locations, we also observe several new patterns. All samples from Russia have affinity to the ~24,000-year-old MA1 (ref. 6), the type specimen for

the Ancient North Eurasians (ANE) who contributed to both Europeans⁴ and Native Americans^{4,6,8}. The two hunter-gatherers from Russia (Karelia in the northwest of the country and Samara on the steppe near the Urals) form an ‘eastern European hunter-gatherer’ (EHG) cluster at one end of a hunter-gatherer cline across Europe; people of hunter-gatherer ancestry from Luxembourg, Spain, and Hungary sit at the opposite ‘western European hunter-gatherer’²⁴ (WHG) end, while the hunter-gatherers from Sweden^{4,8} (SHG) are intermediate. Against this background of differentiated European hunter-gatherers and homogeneous early farmers, multiple population turnovers transpired in all parts of Europe included in our study. Middle Neolithic Europeans from Germany, Spain, Hungary, and Sweden from the period ~4,000–3,000 BC are intermediate between the earlier farmers and the WHG, suggesting an increase of WHG ancestry throughout much of Europe. By contrast, in Russia, the later Yamnaya steppe herders of ~3,000 BC plot between the EHG and the present-day Near East/Caucasus, suggesting a decrease of EHG ancestry during the same time period. The Late Neolithic and Bronze Age samples from Germany and Hungary² are distinct from the preceding Middle Neolithic and plot between them and the Yamnaya. This pattern is also seen in ADMIXTURE analysis (Fig. 2b, Supplementary Information section 6), which implies that the Yamnaya have ancestry from populations related to the Caucasus and South Asia that is largely absent in 38 Early or Middle Neolithic farmers but present in all 25 Late Neolithic or Bronze Age individuals. This ancestry appears in Central Europe for the first time in our series with the Corded Ware around 2,500 BC (Supplementary Information section 6, Fig. 2b). The Corded Ware shared elements of material culture with steppe groups such as the Yamnaya although whether this reflects movements of people has been contentious²¹. Our genetic data provide direct evidence of migration and suggest that it was relatively sudden. The Corded Ware are genetically closest to the Yamnaya ~2,600 km away, as inferred both from PCA and ADMIXTURE (Fig. 2) and F_{ST} (0.011 ± 0.002) (Extended Data Table 3). If continuous gene flow from the east, rather than migration, had occurred, we would expect successive cultures in Europe to become increasingly differentiated from the Middle Neolithic, but

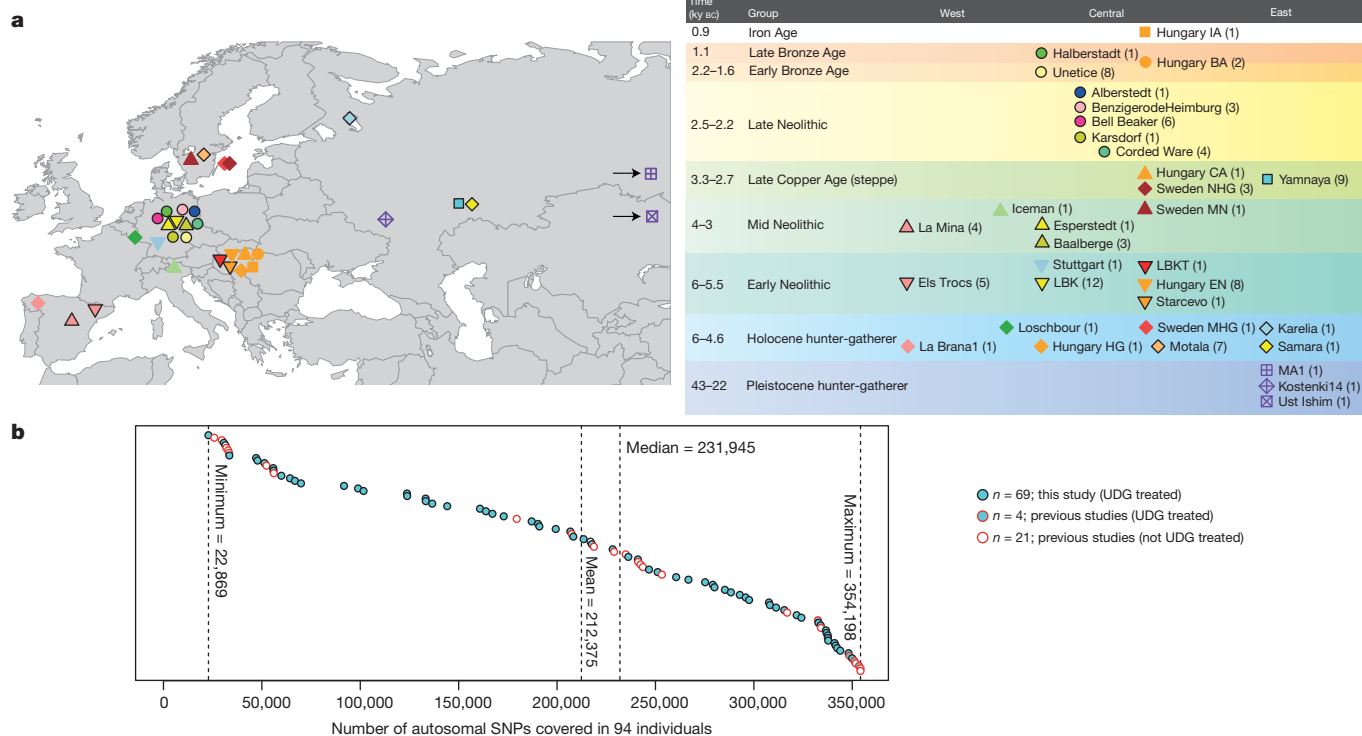


Figure 1 | Location and SNP coverage of samples included in this study. **a**, Geographic location and time-scale (central European chronology) of the 69 newly analysed ancient individuals from this study (black outline) and 25 from

the literature for which shotgun sequencing data was available (no outline). **b**, Number of SNPs covered at least once in the analysis data set of 94 individuals.

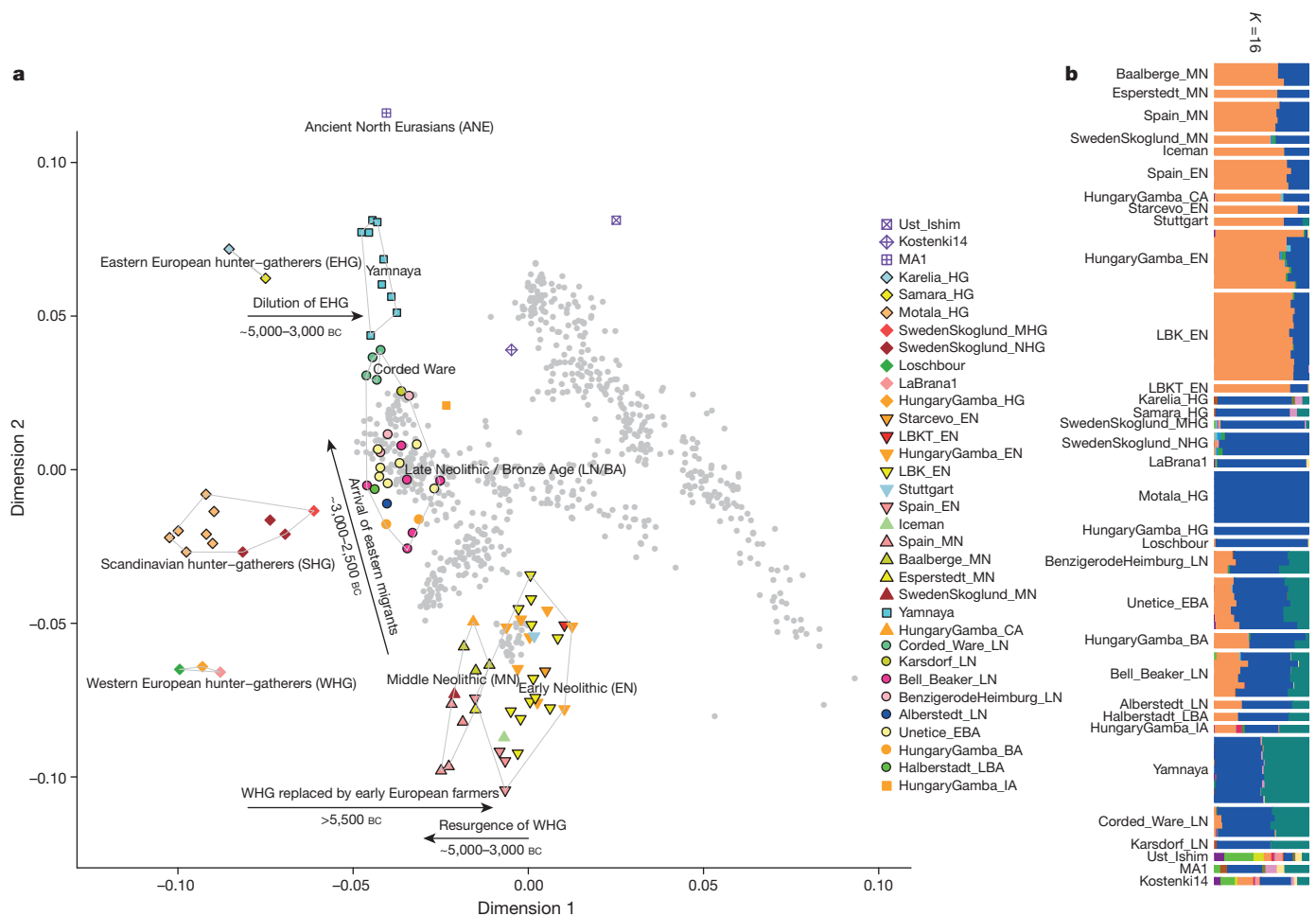


Figure 2 | Population transformations in Europe. **a**, PCA analysis. **b**, ADMIXTURE analysis. The full ADMIXTURE analysis including present-day humans is shown in Supplementary Information section 6.

instead, the Corded Ware are both the earliest and most strongly differentiated from the Middle Neolithic population.

'Outgroup' f_3 statistics⁶ (Supplementary Information section 7), which measure shared genetic drift between a pair of populations (Extended Data Fig. 1), support the clustering of hunter-gatherers, Early/Middle Neolithic, and Late Neolithic/Bronze Age populations into different groups as in the PCA (Fig. 2a). We also analysed f_4 statistics, which allow us to test whether pairs of populations are consistent with descent from common ancestral populations, and to assess significance using a normally distributed Z score. Early European farmers from the Early and Middle Neolithic were closely related but not identical. This is reflected in the fact that Loschbour, a WHG individual from Luxembourg⁴, shared more alleles with post-4,000 BC European farmers from Germany, Spain, Hungary, Sweden and Italy than with early farmers of Germany, Spain, and Hungary, documenting an increase of hunter-gatherer ancestry in multiple regions of Europe during the course of the Neolithic. The two EHG form a clade with respect to all other present-day and ancient populations ($|Z| < 1.9$), and MA1 shares more alleles with them ($|Z| > 4.7$) than with other ancient or modern populations, suggesting that they may be a source for the ANE ancestry in present Europeans^{4,12,22} as they are geographically and temporally more proximate than Upper Paleolithic Siberians. The Yamnaya differ from the EHG by sharing fewer alleles with MA1 ($|Z| = 6.7$) suggesting a dilution of ANE ancestry between 5,000–3,000 BC on the European steppe. This was likely due to admixture of EHG with a population related to present-day Near Easterners, as the most negative f_3 statistic in the Yamnaya (giving unambiguous evidence of admixture) is observed when we model them as a mixture of EHG and present-day Near Eastern populations like Armenians ($Z = -6.3$;

Supplementary Information section 7). The Late Neolithic/Bronze Age groups of central Europe share more alleles with Yamnaya than the Middle Neolithic populations do ($|Z| = 12.4$) and more alleles with the Middle Neolithic than the Yamnaya do ($|Z| = 12.5$), and have a negative f_3 statistic with the Middle Neolithic and Yamnaya as references ($Z = -20.7$), indicating that they were descended from a mixture of the local European populations and new migrants from the east. Moreover, the Yamnaya share more alleles with the Corded Ware ($|Z| \geq 3.6$) than with any other Late Neolithic/Early Bronze Age group with at least two individuals (Supplementary Information section 7), indicating that they had more eastern ancestry, consistent with the PCA and ADMIXTURE patterns (Fig. 2).

Modelling of the ancient samples shows that while Karelia is genetically intermediate between Loschbour and MA1, the topology that considers Karelia as a mixture of these two elements is not the only one that can fit the data (Supplementary Information section 8). To avoid biasing our inferences by fitting an incorrect model, we developed new statistical methods that are substantial extensions of a previously reported approach⁴, which allow us to obtain precise estimates of the proportion of mixture in later Europeans without requiring a formal model for the relationship among the ancestral populations. The method (Supplementary Information section 9) is based on the idea that if a Test population has ancestry related to reference populations $Ref_1, Ref_2, \dots, Ref_N$ in proportions $\alpha_1, \alpha_2, \dots, \alpha_N$, and the references are themselves differentially related to a triple of outgroup populations A, B, C , then:

$$f_4(\text{Test}; A, B, C) = \sum_{i=1}^N \alpha_i f_4(Ref_i; A, B, C)$$

By using a large number of outgroup populations we can fit the admixture coefficients α_i and estimate mixture proportions (Supplementary Information section 9, Extended Data Fig. 2). Using 15 outgroups from Africa, Asia, Oceania and the Americas, we obtain good fits as assessed by a formal test (Supplementary Information section 10), and estimate that the Middle Neolithic populations of Germany and Spain have ~18–34% more WHG-related ancestry than Early Neolithic populations and that the Late Neolithic and Early Bronze Age populations of Germany have ~22–39% more EHG-related ancestry than the Middle Neolithic ones (Supplementary Information section 9). If we model them as mixtures of Yamnaya-related and Middle Neolithic populations, the inferred degree of population turnover is doubled to 48–80% (Supplementary Information sections 9 and 10).

To distinguish whether a Yamnaya or an EHG source fits the data better, we added ancient samples as outgroups (Supplementary Information section 9). Adding any Early or Middle Neolithic farmer results in EHG-related genetic input into Late Neolithic populations being a poor fit to the data (Supplementary Information section 9); thus, Late Neolithic populations have ancestry that cannot be explained by a mixture of EHG and Middle Neolithic. When using Yamnaya instead of EHG, however, we obtain a good fit (Supplementary Information sections 9 and 10). These results can be explained if the new genetic material that arrived in Germany was a composite of two elements: EHG and a type of Near Eastern ancestry different from that which was introduced by early farmers (also suggested by PCA and ADMIXTURE; Fig. 2, Supplementary Information sections 5 and 6). We estimate that these two elements each contributed about half the ancestry of the Yamnaya (Supplementary Information sections 6 and 9), explaining why the population turnover inferred using Yamnaya as a source is about twice as high compared to the undiluted EHG. The estimate of Yamnaya-related ancestry in the Corded Ware is consistent when using either present populations or ancient Europeans as outgroups (Supplementary Information sections 9 and 10), and is $73.1 \pm 2.2\%$ when both sets are combined (Supplementary Information section 10). The best proxies for ANE ancestry in Europe⁴ were initially Native Americans^{12,22}, and then the Siberian MA1 (ref. 6), but both are geographically and temporally too remote for what appears to be a recent migration into Europe⁴. We can now add three new pieces to the puzzle of how ANE ancestry was transmitted to Europe: first by the EHG, then the Yamnaya formed by mixture between EHG and a Near Eastern related population, and then the Corded Ware who were formed by a mixture of the Yamnaya with Middle Neolithic Europeans. We caution that the sampled Yamnaya individuals from Samara might not be directly ancestral to Corded Ware individuals from Germany. It is possible that a more western Yamnaya population, or an earlier (pre-Yamnaya) steppe population may have migrated into central Europe, and future work may uncover more missing links in the chain of transmission of steppe ancestry.

By extending our model to a three-way mixture of WHG, Early Neolithic and Yamnaya, we estimate that the ancestry of the Corded Ware was 79% Yamnaya-like, 4% WHG, and 17% Early Neolithic (Fig. 3). A small contribution of the first farmers is also consistent with uniparentally inherited DNA: for example, mitochondrial DNA haplogroup N1a and Y chromosome haplogroup G2a, common in early central European farmers^{14,23}, almost disappear during the Late Neolithic and Bronze Age, when they are largely replaced by Y haplogroups R1a and R1b (Supplementary Information section 4) and mtDNA haplogroups I, T1, U2, U4, U5a, W, and subtypes of H^{14,23,24} (Supplementary Information section 2). The uniparental data not only confirm a link to the steppe populations but also suggest that both sexes participated in the migrations (Supplementary Information sections 2 and 4 and Extended Data Table 2). The magnitude of the population turnover that occurred becomes even more evident if one considers the fact that the steppe migrants may well have mixed with eastern European agriculturalists on their way to central Europe. Thus, we cannot exclude a scenario in which the Corded Ware arriving in today's Germany had no ancestry at all from local populations.

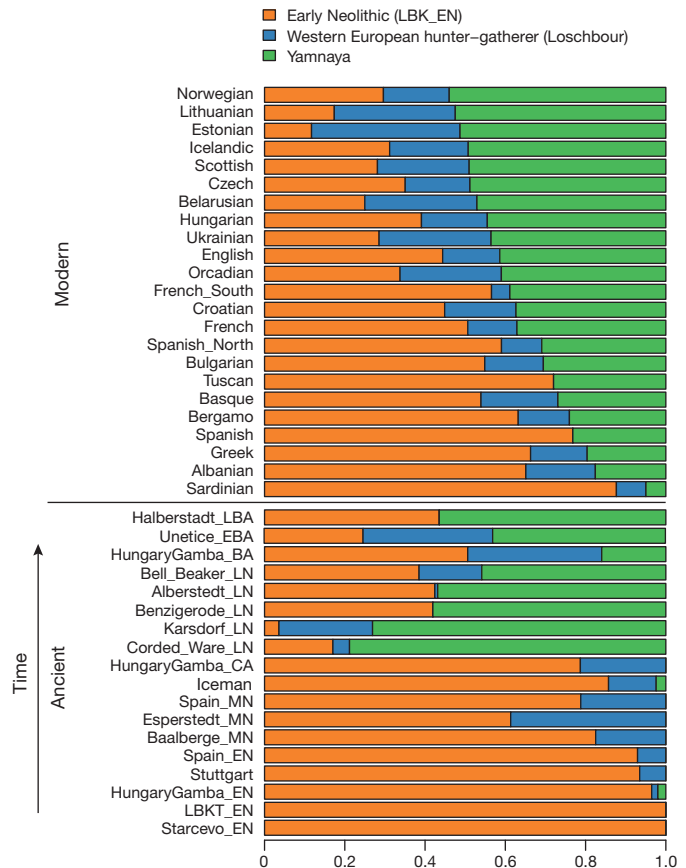


Figure 3 | Admixture proportions. We estimate mixture proportions using a method that gives unbiased estimates even without an accurate model for the relationships between the test populations and the outgroup populations (Supplementary Information section 9). Population samples are grouped according to chronology (ancient) and Yamnaya ancestry (present-day humans).

Our results support a view of European pre-history punctuated by two major migrations: first, the arrival of the first farmers during the Early Neolithic from the Near East, and second, the arrival of Yamnaya pastoralists during the Late Neolithic from the steppe. Our data further show that both migrations were followed by resurgences of the previous inhabitants: first, during the Middle Neolithic, when hunter-gatherer ancestry rose again after its Early Neolithic decline, and then between the Late Neolithic and the present, when farmer and hunter-gatherer ancestry rose after its Late Neolithic decline. This second resurgence must have started during the Late Neolithic/Bronze Age period itself, as the Bell Beaker and Unetice groups had reduced Yamnaya ancestry compared to the earlier Corded Ware, and comparable levels to that in some present-day Europeans (Fig. 3). Today, Yamnaya related ancestry is lower in southern Europe and higher in northern Europe, and all European populations can be modelled as a three-way mixture of WHG, Early Neolithic, and Yamnaya, whereas some outlier populations show evidence for additional admixture with populations from Siberia and the Near East (Extended Data Fig. 3, Supplementary Information section 9). Further data are needed to determine whether the steppe ancestry arrived in southern Europe at the time of the Late Neolithic/Bronze Age, or is due to migrations in later times from northern Europe^{25,26}.

Our results provide new data relevant to debates on the origin and expansion of Indo-European languages in Europe (Supplementary Information section 11). Although the findings from ancient DNA are silent on the question of the languages spoken by preliterate populations, they do carry evidence about processes of migration which are invoked by theories on Indo-European language dispersals. Such theories make predictions about movements of people to account for the spread of

languages and material culture (Extended Data Fig. 4). The technology of ancient DNA makes it possible to reject or confirm the proposed migratory movements, as well as to identify new movements that were not previously known. The best argument for the 'Anatolian hypothesis'²⁷ that Indo-European languages arrived in Europe from Anatolia ~8,500 years ago is that major language replacements are thought to require major migrations, and that after the Early Neolithic when farmers established themselves in Europe, the population base was likely to have been so large that later migrations would not have made much of an impact^{27,28}. However, our study shows that a later major turnover did occur, and that steppe migrants replaced ~75% of the ancestry of central Europeans. An alternative theory is the 'steppe hypothesis', which proposes that early Indo-European speakers were pastoralists of the grasslands north of the Black and Caspian Seas, and that their languages spread into Europe after the invention of wheeled vehicles⁹. Our results make a compelling case for the steppe as a source of at least some of the Indo-European languages in Europe by documenting a massive migration ~4,500 years ago associated with the Yamnaya and Corded Ware cultures, which are identified by proponents of the steppe hypothesis as vectors for the spread of Indo-European languages into Europe. These results challenge the Anatolian hypothesis by showing that not all Indo-European languages in Europe can plausibly derive from the first farmer migrations thousands of years earlier (Supplementary Information section 11). We caution that the location of the proto-Indo-European^{9,27,29,30} homeland that also gave rise to the Indo-European languages of Asia, as well as the Indo-European languages of southeastern Europe, cannot be determined from the data reported here (Supplementary Information section 11). Studying the mixture in the Yamnaya themselves, and understanding the genetic relationships among a broader set of ancient and present-day Indo-European speakers, may lead to new insight about the shared homeland.

Online Content Methods, along with any additional Extended Data display items and Source Data, are available in the online version of the paper; references unique to these sections appear only in the online paper.

Received 29 December 2014; accepted 12 February 2015.

Published online 2 March 2015.

1. Fu, Q. *et al.* Genome sequence of a 45,000-year-old modern human from western Siberia. *Nature* **514**, 445–449 (2014).
2. Gamba, C. *et al.* Genome flux and stasis in a five millennium transect of European prehistory. *Nature Commun.* **5**, 5257 (2014).
3. Keller, A. *et al.* New insights into the Tyrolean Iceman's origin and phenotype as inferred by whole-genome sequencing. *Nature Commun.* **3**, 698 (2012).
4. Lazaridis, I. *et al.* Ancient human genomes suggest three ancestral populations for present-day Europeans. *Nature* **513**, 409–413 (2014).
5. Olalde, I. *et al.* Derived immune and ancestral pigmentation alleles in a 7,000-year-old Mesolithic European. *Nature* **507**, 225–228 (2014).
6. Raghavan, M. *et al.* Upper Palaeolithic Siberian genome reveals dual ancestry of Native Americans. *Nature* **505**, 87–91 (2014).
7. Seguin-Orlando, A. *et al.* Genomic structure in Europeans dating back at least 36,200 years. *Science* **346**, 1113–1118 (2014).
8. Skoglund, P. *et al.* Genomic diversity and admixture differs for Stone-Age Scandinavian foragers and farmers. *Science* **344**, 747–750 (2014).
9. Anthony, D. W. *The Horse, the Wheel, and Language: How Bronze-Age Riders from the Eurasian Steppes Shaped the Modern World* (Princeton Univ. Press, 2007).
10. Fu, Q. *et al.* DNA analysis of an early modern human from Tianyuan Cave, China. *Proc. Natl Acad. Sci. USA* **110**, 2223–2227 (2013).
11. Rohland, N., Harney, E., Mallick, S., Nordenfelt, S. & Reich, D. Partial uracil–DNA-glycosylase treatment for screening of ancient DNA. *Phil. Trans. R. Soc. Lond. B* **370**, 20130624 (2015).
12. Patterson, N. *et al.* Ancient admixture in human history. *Genetics* **192**, 1065–1093 (2012).
13. Fu, Q. *et al.* A revised timescale for human evolution based on ancient mitochondrial genomes. *Curr. Biol.* **23**, 553–559 (2013).
14. Brandt, G. *et al.* Ancient DNA reveals key stages in the formation of central European mitochondrial genetic diversity. *Science* **342**, 257–261 (2013).
15. Der Sarkissian, C. *et al.* Ancient DNA reveals prehistoric gene-flow from Siberia in the complex human population history of North East Europe. *PLoS Genet.* **9**, e1003296 (2013).
16. Briggs, A. W. *et al.* Removal of deaminated cytosines and detection of *in vivo* methylation in ancient DNA. *Nucleic Acids Res.* **38**, e87 (2010).
17. Briggs, A. W. *et al.* Patterns of damage in genomic DNA sequences from a Neandertal. *Proc. Natl Acad. Sci. USA* **104**, 14616–14621 (2007).
18. Myres, N. M. *et al.* A major Y-chromosome haplogroup R1b Holocene era founder effect in Central and Western Europe. *Eur. J. Hum. Genet.* **19**, 95–101 (2011).
19. Underhill, P. A. *et al.* The phylogenetic and geographic structure of Y-chromosome haplogroup R1a. *Eur. J. Hum. Genet.* **23**, 124–131 (2015).
20. Skoglund, P. *et al.* Origins and genetic legacy of Neolithic farmers and hunter-gatherers in Europe. *Science* **336**, 466–469 (2012).
21. Czebreszuk, J. in *Ancient Europe, 8000 B.C. to A.D. 1000: Encyclopedia of the Barbarian World* (eds Bogucki, P. I. & Crabtree, P. J.) 467–475 (Charles Scribners & Sons, 2003).
22. Lipson, M. *et al.* Efficient moment-based inference of admixture parameters and sources of gene flow. *Mol. Biol. Evol.* **30**, 1788–1802 (2013).
23. Szécsényi-Nagy, A. *et al.* Tracing the genetic origin of Europe's first farmers reveals insights into their social organization. Preprint at *bioRxiv* <http://dx.doi.org/10.1101/008664> (2014).
24. Haak, W. *et al.* Ancient DNA from European early Neolithic farmers reveals their Near Eastern affinities. *PLoS Biol.* **8**, e1000536 (2010).
25. Hellenthal, G. *et al.* A genetic atlas of human admixture history. *Science* **343**, 747–751 (2014).
26. Ralph, P. & Coop, G. The geography of recent genetic ancestry across Europe. *PLoS Biol.* **11**, e1001555 (2013).
27. Renfrew, C. *Archaeology and Language: The Puzzle of Indo-European Origins* (Pimlico, 1987).
28. Bellwood, P. *First Farmers: The Origins of Agricultural Societies* (Wiley-Blackwell, 2004).
29. Gamkrelidze, T. V. & Ivanov, V. V. The early history of Indo-European languages. *Sci. Am.* **262**, 110–116 (1990).
30. Mallory, J. P. In *Search of the Indo-Europeans: Language, Archaeology and Myth* (Thames and Hudson, 1991).

Supplementary Information is available in the online version of the paper.

Acknowledgements We thank P. Bellwood, J. Burger, P. Heggarty, M. Lipson, C. Renfrew, J. Diamond, S. Pääbo, R. Pinhasi and P. Skoglund for critical comments, and the Initiative for the Science of the Human Past at Harvard for organizing a workshop around the issues touched on by this paper. We thank S. Pääbo for support for establishing the ancient DNA facilities in Boston, and P. Skoglund for detecting the presence of two related individuals in our data set. We thank L. Orlando, T. S. Korneliusen, and C. Gamba for help in obtaining data. We thank Agilent Technologies and G. Frommer for help in developing the capture reagents. We thank C. Der Sarkissian, G. Valverde, L. Papac and B. Nickel for wet laboratory support. We thank archaeologists V. Dresely, R. Ganslmeier, O. Balanovsky, J. Ignacio Royo Guillén, A. Oszás, V. Majerik, T. Paluch, K. Somogyi and V. Voicsek for sharing samples and discussion about archaeological context. This research was supported by an Australian Research Council grant to W.H. and B.L. (DP130102158), and German Research Foundation grants to K.W.A. (AI 287/7-1 and 7-3, AI 287/10-1 and AI 287/14-1) and to H.M. (Me 3245/1-1 and 1-3). D.R. was supported by US National Science Foundation HOMINID grant BCS-1032255, US National Institutes of Health grant GM100233, and the Howard Hughes Medical Institute.

Author Contributions W.H., N.P., N.R., J.K., K.W.A. and D.R. supervised the study. W.H., E.B., C.E., M.F., S.F., R.G.P., F.H., V.K., A.K., M.K., P.K., H.M., O.M., V.M., N.N., S.L.P., R.R., M.A.R.G., C.R., A.S.-N., J.W., J.K., D.B., D.A., A.C., K.W.A. and D.R. assembled archaeological material, W.H., I.L., N.P., N.R., S.M., A.M. and D.R. analysed genetic data. I.L., N.P. and D.R. developed methods using *f* statistics for inferring admixture proportions. W.H., N.R., B.L., G.B., S.N., E.H., K.S. and A.M. performed wet laboratory ancient DNA work. I.L., N.R., S.M., B.L., Q.F., M.M. and D.R. developed the 390k capture reagent. W.H., I.L. and D.R. wrote the manuscript with help from all co-authors.

Author Information The aligned sequences are available through the European Nucleotide Archive under accession number PRJEB8448. The Human Origins genotype dataset including ancient individuals can be found at (http://genetics.med.harvard.edu/reichlab/Reich_Lab/Datasets.html). Reprints and permissions information is available at www.nature.com/reprints. The authors declare no competing financial interests. Readers are welcome to comment on the online version of the paper. Correspondence and requests for materials should be addressed to D.R. (reich@genetics.med.harvard.edu).

METHODS

Screening of libraries (shotgun sequencing and mitochondrial capture). The 212 libraries screened in this study (Supplementary Information section 1) from a total of 119 samples (Supplementary Information section 3) were produced at Adelaide ($n = 151$), Tübingen ($n = 16$), and Boston ($n = 45$) (Supplementary Data 1).

The libraries from Adelaide and Boston had internal barcodes directly attached to both sides of the molecules from the DNA extract so that each sequence begins with the barcode¹⁰. The Adelaide libraries had 5 base pair (bp) barcodes on both sides, while the Boston libraries had 7 bp barcodes. Libraries from Tübingen had no internal barcodes, but were differentiated by the sequence of the indexing primer³¹.

We adapted a reported protocol for enriching for mitochondrial DNA¹⁰, with the difference that we adjusted the blocking oligonucleotides and PCR primers to fit our libraries with shorter adapters. Over the course of this project, we also lowered the hybridization temperature from 65 °C to 60 °C and performed stringent washes at 55 °C instead of 60 °C³².

We used an aliquot of approximately 500 ng of each library for target enrichment of the complete mitochondrial genome in two consecutive rounds³², using a bait set for human mtDNA³². We performed enrichment in 96-well plates with one library per well, and used a liquid handler (Evolution P3, Perkin Elmer) for the capture and washing steps³³. We used blocking oligonucleotides in hybridization appropriate to the adapters of the truncated libraries. After either of the two enrichment rounds, we amplified the enriched library molecules with the primer pair that keeps the adapters short (PreHyb) using Herculase Fusion II PCR Polymerase. We performed an indexing PCR of the final capture product using one or two indexing primers³¹. We cleaned up all PCR reactions using SPRI technology³⁴ and the liquid handler. Libraries from Tübingen were amplified with the primer pair IS5/IS6³¹.

For libraries from Boston and Adelaide, we used a second aliquot of each library for shotgun sequencing after performing an indexing PCR³¹. We used unique index combinations for each library and experiment, allowing us to distinguish shotgun sequencing and mitochondrial DNA capture data, even if both experiments were in the same sequencing run. We sequenced shotgun libraries and mtDNA captured libraries from Tübingen in independent sequencing runs since the index was already attached at the library preparation stage.

We quantified the sequencing pool with the BioAnalyzer (Agilent) and/or the KAPA Library Quantification kit (KAPA Biosystems) and sequenced on Illumina MiSeq, HiSeq2500 or NextSeq500 instruments for 2 × 75, 2 × 100 or 2 × 150 cycles along with the indexing read(s).

Enrichment for 394,577 SNP targets ('390k capture'). The protocol for enrichment for SNP targets was similar to the mitochondrial DNA capture, with the exception that we used another bait set (390k) and about twice as much library (up to 1,000 ng) compared to the mtDNA capture.

The specific capture reagent used in this study is described for the first time here. To target each SNP, we used a different oligonucleotide probe design compared to ref. 10. We used four 52 base pair probes for each SNP target. One probe ends just before the SNP, and one starts just after. Two probes are centred on the SNP, and are identical except for having the alternate alleles. This probe design avoids systematic bias towards one SNP allele or another. For the template sequence for designing the San and Yoruba panels baits, we used the sequence that was submitted for these same SNPs during the design of the Affymetrix Human Origins SNP array¹². For SNPs that were both in the San and Yoruba panels, we used the Yoruba template sequence in preference. For all other SNPs, we used the human genome reference sequence as a template. Supplementary Data 2a–d gives the list of SNPs that we targeted, along with details of the probes used. The breakdown of SNPs into different classes is as follows.

124,106 'Yoruba SNPs': all SNPs in 'panel 5' of the Affymetrix Human Origins array (discovered as heterozygous in a Yoruba male: HGDP00927)¹² that passed the probe design criteria specified in ref. 11.

146,135 'San SNPs': all SNPs in 'panel 4' of the Affymetrix Human Origins array (discovered as heterozygous in a San male: HGDP01029)¹² that passed probe design criteria¹¹. The full Affymetrix Human Origins array panel 4 contains several tens of thousands of additional SNPs overlapping those from panel 5, but we did not wish to redundantly capture panel 5 SNPs.

98,166 'compatibility SNPs': SNPs that overlap between the Affymetrix Human Origins, the Affymetrix 6.0, and the Illumina 610 Quad arrays, which are not already included in the 'Yoruba SNPs' or 'San SNPs' lists¹² and that also passed the probe design design criteria¹¹.

26,170 'miscellaneous SNPs': SNPs that did not overlap the Human Origins array. The subset analysed in this study were 2,258 Y chromosome SNPs (http://isogg.org/tree/ISOGG_YDNA_SNP_Index.html) that we used for Y haplogroup determination.

Processing of sequencing data. We restricted analysis to read pairs that passed quality control according to the Illumina software ('PF reads').

We assigned read pairs to libraries by searching for matches to the expected index and barcode sequences (if present, as for the Adelaide and Boston libraries). We allowed no more than 1 mismatch per index or barcode, and zero mismatches if there was ambiguity in sequence assignment or if barcodes of 5 bp length were used (Adelaide libraries).

We used Seqprep (<https://github.com/jstjohn/SeqPrep>) to search for overlapping sequence between the forward and reverse read, and restricted to molecules where we could identify a minimum of 15 bp of overlap. We collapsed the two reads into a single sequence, using the consensus nucleotide if both reads agreed, and the read with higher base quality in the case of disagreement. For each merged nucleotide, we assigned the base quality to be the higher of the two reads. We further used Seqprep to search for the expected adaptor sequences at either ends of the merged sequence, and to produce a trimmed sequence for alignment.

We mapped all sequences using BWA-0.6.1 (ref. 35). For mitochondrial analysis we mapped to the mitochondrial genome RSRS³⁶. For whole-genome analysis we mapped to the human reference genome hg19. We restricted all analyses to sequences that had a mapping quality of MAPQ ≥ 37.

We sorted all mapped sequences by position, and used a custom script to search for mapped sequences that had the same orientation and start and stop positions. We stripped all but one of these sequences (keeping the best quality one) as duplicates.

Mitochondrial sequence analysis and assessment of ancient DNA authenticity. For each library for which we had average coverage of the mitochondrial genome of at least tenfold after removal of duplicated molecules, we built a mitochondrial consensus sequence, assigning haplogroups for each library as described in Supplementary Information section 2.

We used contamMix-1.0.9 to search for evidence of contamination in the mitochondrial DNA¹³. This software estimates the fraction of mitochondrial DNA sequences that match the consensus more closely than a comparison set of 311 worldwide mitochondrial genomes. This is done by taking the consensus sequence of reads aligning to the RSRS mitochondrial genome, and requiring a minimum coverage of 5 after filtering bases where the quality was <30. Raw reads are then realigned to this consensus. In addition, the consensus is multiply aligned with the other 311 mitochondrial genomes using kalign (2.0.4)³⁷ to build the necessary inputs for contamMix, trimming the first and last 5 bases of every read to mitigate against the confounding factor of ancient damage. This software had difficulty running on data sets with higher coverage, and for these data sets, we downsampled to 50,000 reads.

For all sequences mapping to the mitochondrial DNA for which the consensus mitochondrial DNA sequence had a cytosine at the terminal nucleotide, we measured the proportion of sequences with a thymine at that position. For population genetic analysis, we only used partially UDG-treated libraries with a minimum of 3% C→T substitutions as recommended by ref. 33. In cases where we used a fully UDG-treated library for 390k analysis, we examined mitochondrial capture data from a non-UDG-treated library made from the same extract, and verified that the non-UDG library had a minimum of 10% C→T at the first nucleotide as recommended by ref. 38. Metrics for the mitochondrial DNA analysis on each library are given in Supplementary Data 1.

390k capture, sequence analysis and quality control. For 390k analysis, we restricted to reads that not only mapped to the human reference genome hg19 but that also overlapped the 354,212 autosomal SNPs genotyped on the Human Origins array⁴. We trimmed the last two nucleotides from each sequence because we found that these are highly enriched in ancient DNA damage even for UDG-treated libraries. We further restricted analyses to sites with base quality ≥ 30.

We made no attempt to determine a diploid genotype at each SNP in each sample. Instead, we used a single allele—randomly drawn from the two alleles in the individual—to represent the individual at that site^{20,39}. Specifically, we made an allele call at each target SNP using majority rule over all sequences overlapping the SNP. When each of the possible alleles was supported by an equal number of sequences, we picked an allele at random. We set the allele to 'no call' for SNPs at which there was no read coverage.

We restricted population genetic analysis to libraries with a minimum of 0.06-fold average coverage on the 390k SNP targets, and for which there was an unambiguous sex determination based on the ratio of X to Y chromosome reads (Supplementary Information section 4 and Supplementary Data 1). For individuals for whom there were multiple libraries per sample, we performed a series of quality control analysis. First, we used the ADMIXTURE software^{40,41} in supervised mode, using Kharia, Onge, Karitiana, Han, French, Mbuti, Ulchi and Eskimo as reference populations. We visually inspected the inferred ancestry components in each individual, and removed individuals with evidence of heterogeneity in inferred ancestry components across libraries. For all possible pairs of libraries for each sample, we also computed statistics of the form $D(Library_1, Library_2; Probe, Mbuti)$, where *Probe* is any of a panel of the same set of eight reference

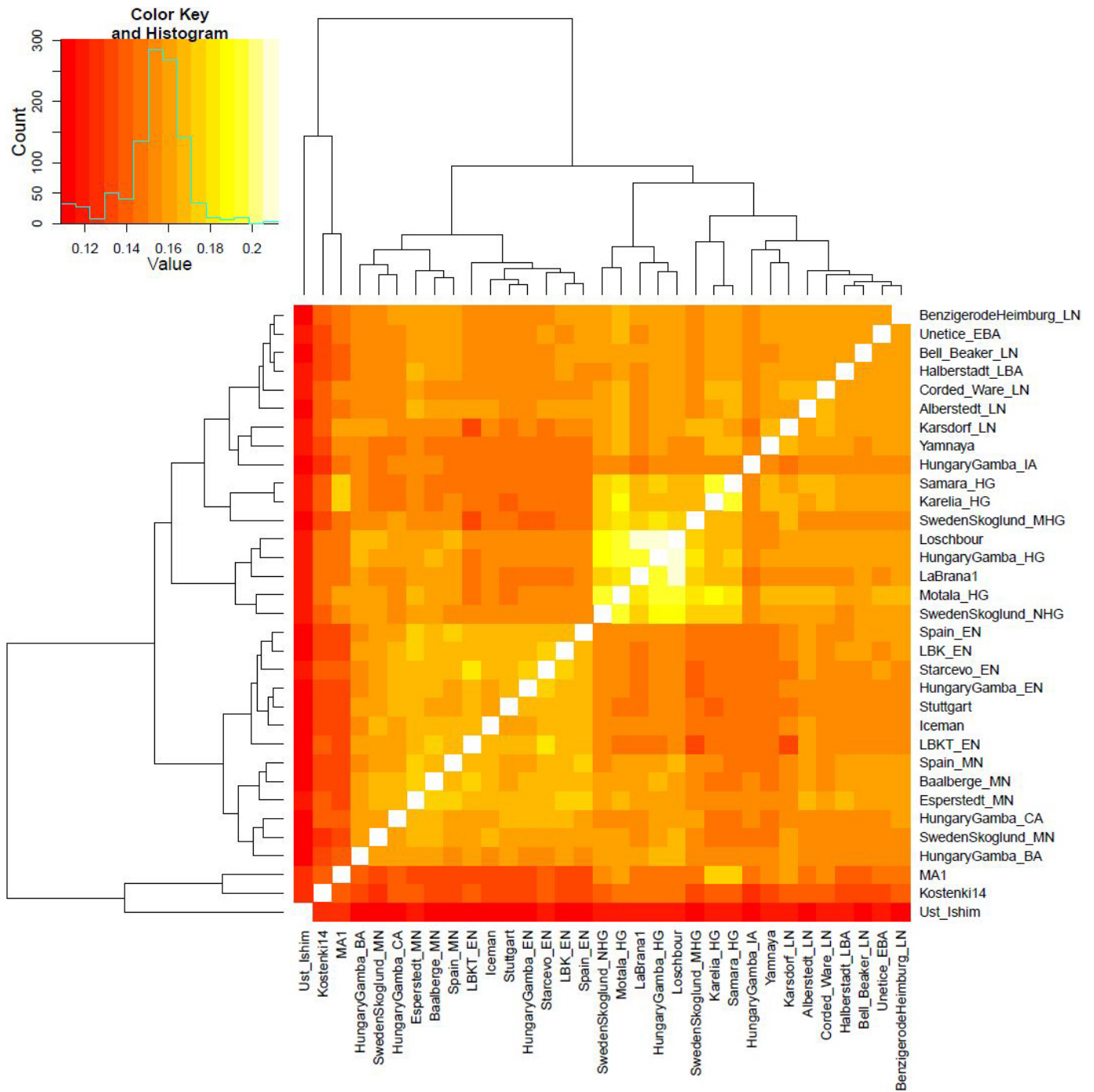
populations), to determine whether there was significant evidence of the *Probe* population being more closely related to one library from an ancient individual than another library from that same individual. None of the individuals that we used had strong evidence of ancestry heterogeneity across libraries. For samples passing quality control for which there were multiple libraries per sample, we merged the sequences into a single BAM.

We called alleles on each merged BAM using the same procedure as for the individual libraries. We used ADMIXTURE⁴¹ as well as PCA as implemented in EIGENSOFT⁴² (using the *lsqproject*: YES option to project the ancient samples) to visualize the genetic relationships of each set of samples with the same culture label with respect to 777 diverse present-day West Eurasians⁴. We visually identified outlier individuals, and renamed them for analysis either as outliers or by the name of the site at which they were sampled (Extended Data Table 1). We also identified two pairs of related individuals based on the proportion of sites covered in pairs of ancient samples from the same population that had identical allele calls using PLINK⁴³. From each pair of related individuals, we kept the one with the most SNPs.

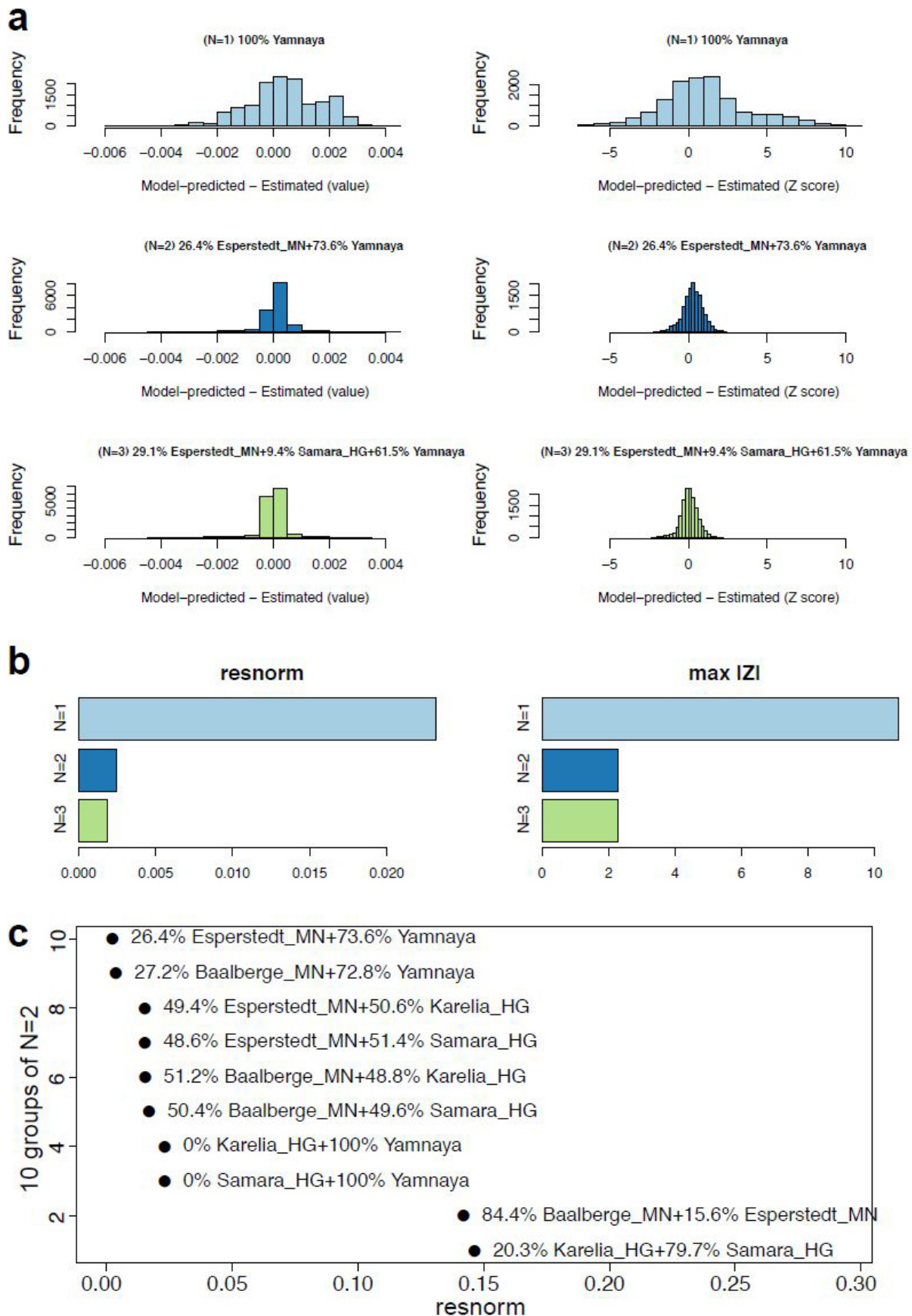
Population genetic analyses. We determined genetic sex using the ratio of X and Y chromosome alignments⁴⁴ (Supplementary Information section 4), and Y chromosome haplogroup for the male samples (Supplementary Information section 4). We studied population structure (Supplementary Information sections 5 and 6). We used *f* statistics to carry out formal tests of population relationships (Supplementary Information section 6) and built explicit models of population history consistent with the data (Supplementary Information section 7). We estimated mixture proportions in a way that was robust to uncertainty about the exact population history that applied (Supplementary Information section 8). We estimated the minimum number of streams of migration into Europe needed to explain the data (Supplementary Information sections 9 and 10). The estimated mixture proportions shown in Fig. 3 were obtained using the *lsqin* function of Matlab and the optimization method described in Supplementary Information section 9 with 15 world outgroups.

Sample size. No statistical methods were used to predetermine sample size.

31. Kircher, M., Sawyer, S. & Meyer, M. Double indexing overcomes inaccuracies in multiplex sequencing on the Illumina platform. *Nucleic Acids Res.* **40**, e3 (2012).
32. Meyer, M. *et al.* A mitochondrial genome sequence of a hominin from Sima de los Huesos. *Nature* **505**, 403–406 (2014).
33. Rohland, N., Harney, E., Mallick, S., Nordenfelt, S. & Reich, D. Partial uracil–DNA–glycosylase treatment for screening of ancient DNA. *Phil. Trans. R. Soc. Lond. B* **370**, 20130624 (2015).
34. Rohland, N. & Reich, D. Cost-effective, high-throughput DNA sequencing libraries for multiplexed target capture. *Genome Res.* **22**, 939–946 (2012).
35. Li, H. & Durbin, R. Fast and accurate short read alignment with Burrows–Wheeler transform. *Bioinformatics* **25**, 1754–1760 (2009).
36. Behar, D. M. *et al.* A “Copernican” reassessment of the human mitochondrial DNA tree from its root. *Am. J. Hum. Genet.* **90**, 675–684 (2012).
37. Lassmann, T. & Sonnhammer, E. L. L. Kalign—an accurate and fast multiple sequence alignment algorithm. *BMC Bioinformatics* **6**, 298 (2005).
38. Sawyer, S., Krause, J., Guschanski, K., Savolainen, V. & Pääbo, S. Temporal patterns of nucleotide misincorporations and DNA fragmentation in ancient DNA. *PLoS ONE* **7**, e34131 (2012).
39. Green, R. E. *et al.* A draft sequence of the Neandertal genome. *Science* **328**, 710–722 (2010).
40. Alexander, D. H. & Lange, K. Enhancements to the ADMIXTURE algorithm for individual ancestry estimation. *BMC Bioinformatics* **12**, 246 (2011).
41. Alexander, D. H., Novembre, J. & Lange, K. Fast model-based estimation of ancestry in unrelated individuals. *Genome Res.* **19**, 1655–1664 (2009).
42. Reich, D., Price, A. L. & Patterson, N. Principal component analysis of genetic data. *Nature Genet.* **40**, 491–492 (2008).
43. Purcell, S. *et al.* PLINK: a tool set for whole-genome association and population-based linkage analyses. *Am. J. Hum. Genet.* **81**, 559–575 (2007).
44. Skoglund, P., Storå, J., Götherström, A. & Jakobsson, M. Accurate sex identification of ancient human remains using DNA shotgun sequencing. *J. Archaeol. Sci.* **40**, 4477–4482 (2013).

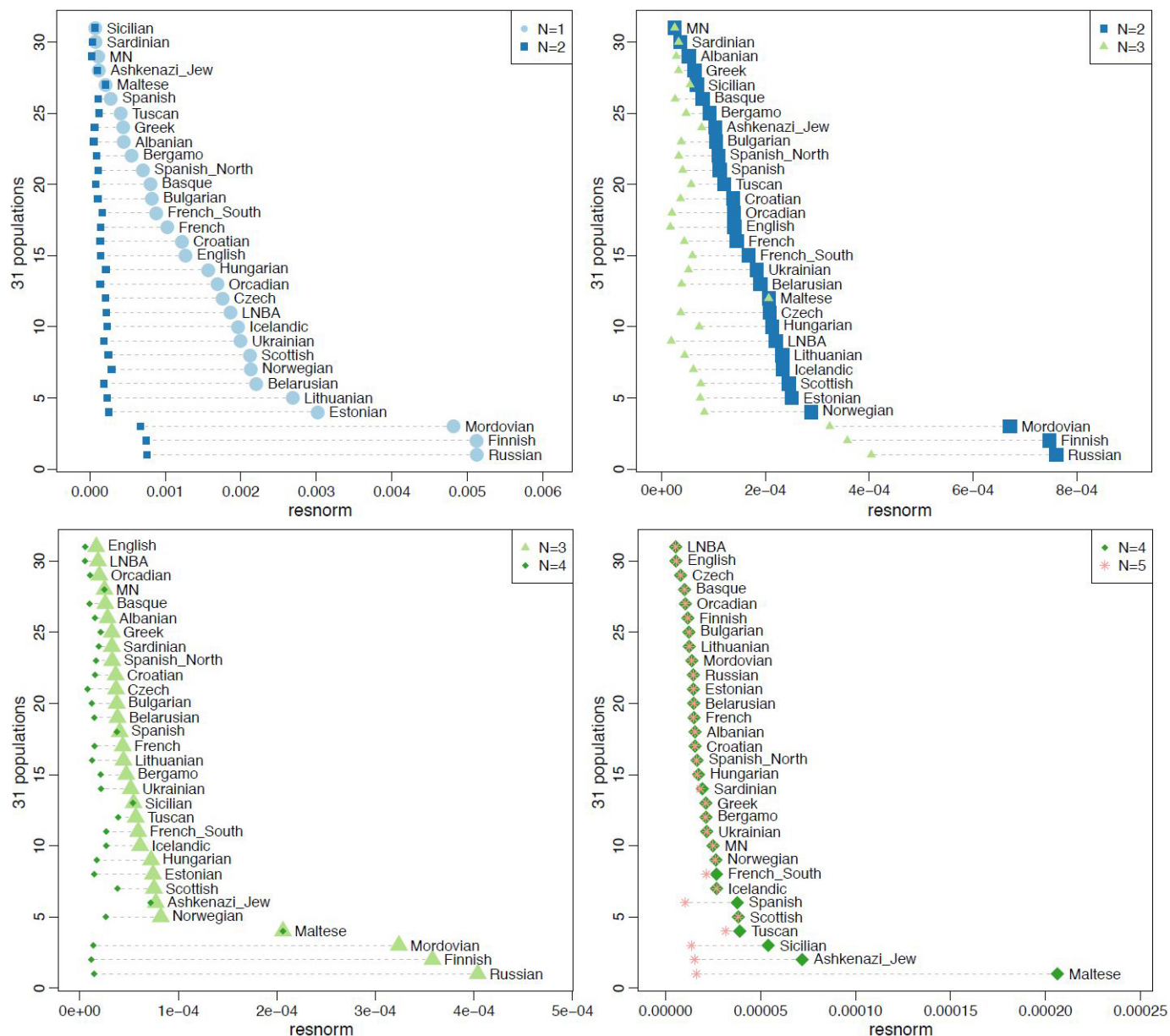


Extended Data Figure 1 | Outgroup f_3 statistic $f_3(\text{Dinka}; X, Y)$, measuring the degree of shared drift among pairs of ancient individuals.



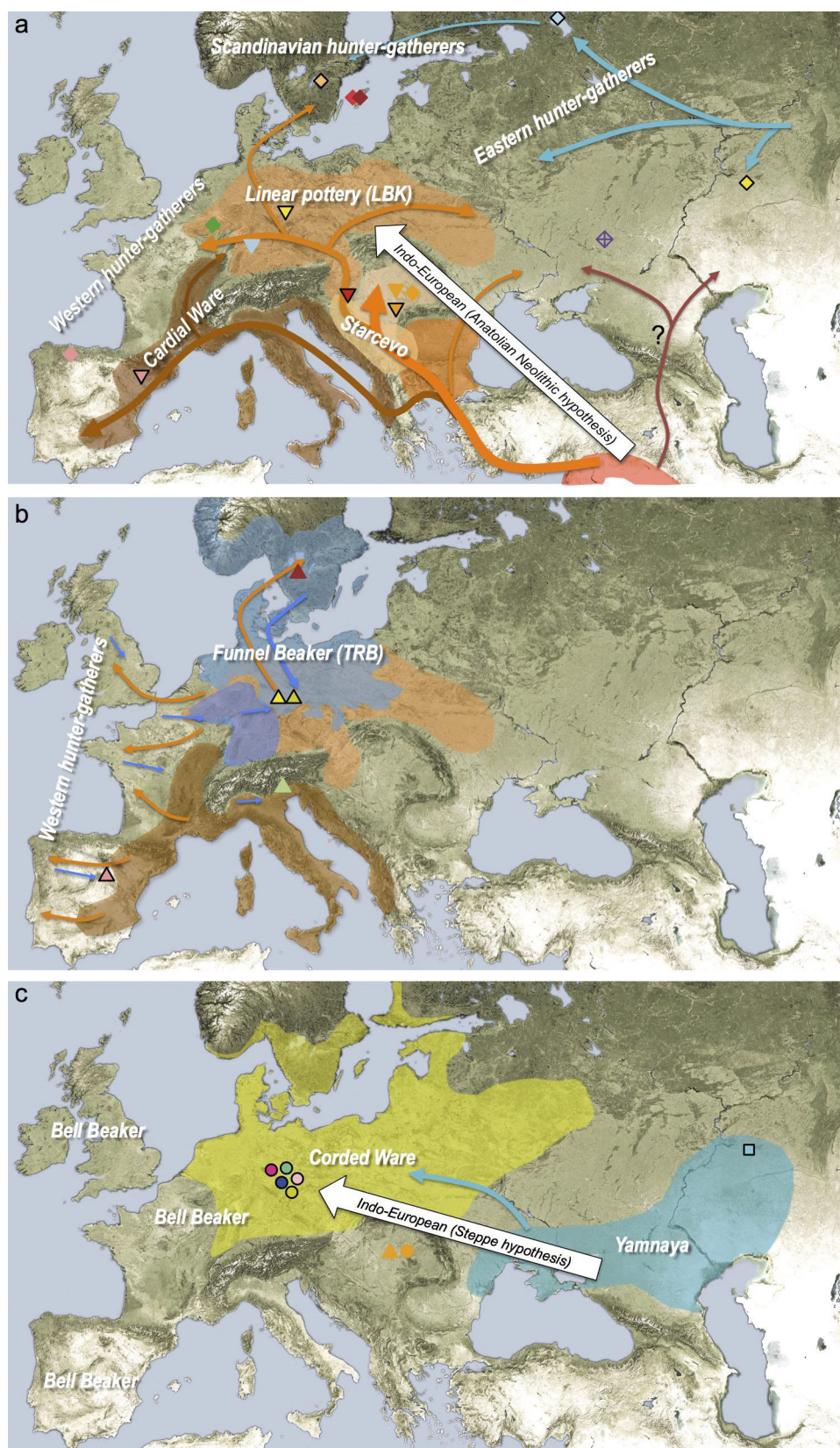
Extended Data Figure 2 | Modelling Corded Ware as a mixture of $N = 1, 2$, or 3 ancestral populations. **a**, The left column shows a histogram of raw f_4 statistic residuals and on the right Z-scores for the best-fitting (lowest squared 2-norm of the residuals, or *resnorm*) model at each N . **b**, The data on

the left show *resnorm* and on the right show the maximum $|Z|$ score change for different N . **c**, *resnorm* of different $N = 2$ models. The set of outgroups used in this analysis in the terminology of Supplementary Information section 9 is 'World Foci 15 + Ancients'.



Extended Data Figure 3 | Modelling Europeans as mixtures of increasing complexity: $N=1$ (EN), $N=2$ (EN, WHG), $N=3$ (EN, WHG, Yamnaya), $N=4$ (EN, WHG, Yamnaya, Nganasan), $N=5$ (EN, WHG, Yamnaya,

Nganasan, BedouinB). The residual norm of the fitted model (Supplementary Information section 9) and its changes are indicated.



Extended Data Figure 4 | Geographic distribution of archaeological cultures and graphic illustration of proposed population movements / turnovers discussed in the main text. a, Proposed routes of migration by early farmers into Europe ~9,000–7,000 years ago. b, Resurgence of hunter-gatherer

ancestry during the Middle Neolithic 7,000–5,000 years ago. c, Arrival of steppe ancestry in central Europe during the Late Neolithic ~4,500 years ago. White arrows indicate the two possible scenarios of the arrival of Indo-European language groups. Symbols of samples are identical to those in Fig. 1.

Extended Data Table 1 | Number of ancient Eurasian modern human samples screened in genome-wide studies to date

First author	Description	No. samples at $\geq 0.05\times$ coverage (enough for Procrustes analysis)	No. samples at $>0.25\times$ coverage (enough to analyze in pairs)
Keller ³	Tyrolean Iceman	1	1
Raghavan ⁶	Upper Paleolithic Siberians	2	1
Olalde ⁵	Mesolithic Iberian from LaBrana	1	1
Skoglund ⁸	Farmers and hunter-gatherers from Sweden	5	2
Lazaridis ⁴	Early European farmer from Germany & Mesolithic hunter-gatherers from Luxembourg and Sweden	7	4
Gamba ²	Neolithic, Bronze Age, Iron Age Hungary	13	9
Fu ¹	Upper Paleolithic Siberian from Ust-Ishim	1	1
Seguin-Orlando ⁷	Upper Paleolithic European from Kostenki	1	1
<i>Total before study</i>		31	20
This study	Hunter-gatherers and pastoralists from Russia, Mesolithic hunter-gatherers from Sweden, Early Neolithic from Germany, Hungary, and Spain, Middle Neolithic from Germany & Spain, Late Neolithic / Bronze Age from Germany	69	58

Only studies that produced at least one sample at $\geq 0.05\times$ coverage are listed.

Extended Data Table 2 | Summary of the archaeological context for the 69 newly reported samples

Reich ID	Pop Label for Analysis	Culture	Group	Location and sample details (e.g. sample, grave and museum ID)	Date (lab no.)	Country	Sex	mt-hg	Y-hg	Autosomal SNPs
10061	Karelia_HG	Russian Mesolithic	EHG	Yuzhnyy Oleni Ostrov, Karelia, Russia, UzOO74, grave 142, MAE RAS 5773-74	5600-5000 BC	Russia	M	C1g (formerly C1f)	R1a1	341554
10124	Samara_HG	Russian Neolithic HG	EHG	Sok River, Samara, Russia, SVP44	5650-5555 cal BC (Beta – 392490)	Russia	M	U5a1d	R1b1	206748
10011	Motala_HG	Swedish Mesolithic	SHG	Motala, Sweden, Motala 1	5898-5531 cal BC	Sweden	F	U5a1		228271
10012	Motala_HG	Swedish Mesolithic	SHG	Motala, Sweden, Motala 2	5898-5531 cal BC	Sweden	M	U2e1	I2c2	292853
10013	Motala_HG	Swedish Mesolithic	SHG	Motala, Sweden, Motala 3	5898-5531 cal BC	Sweden	M	U5a1	I2a1b	251108
10014	Motala_HG	Swedish Mesolithic	SHG	Motala, Sweden, Motala 4	5898-5531 cal BC	Sweden	F	U5a2d		311299
10015	Motala_HG	Swedish Mesolithic	SHG	Motala, Sweden, Motala 6	5898-5531 cal BC	Sweden	M	U5a2d	I2a1	285307
10016	Motala_HG	Swedish Mesolithic	SHG	Motala, Sweden, Motala 9	5898-5531 cal BC	Sweden	M	U5a2	I2a1	275233
10017	Motala_HG	Swedish Mesolithic	SHG	Motala, Sweden, Motala 12	5898-5531 cal BC	Sweden	M	U2e1	I2a1b	337794
10174	Starcevo_EN	Starcevo	EN	Aisönyék-Bálaszék, Mémőkői telep, Hungary; BAM25a, feature 1532	5710-5550 cal BC (MAMS 11939)	Hungary	M	N1a1a1b	H2	101653
10176	LBK1_EN	LBK1	EN	Szemely-Hegyes, Hungary; SZE4b, feature 1001	5210-4940 cal BC (Beta - 310038)	Hungary	M	N1a1a1a3		30718
10046	LBK_EN	LBK	EN	Halberstadt-Sonntagsfeld, Germany; HAL5, grave 2, feature 241.1	5206-5004 cal BC (MAMS 21479)	Germany	F	T2c1de1f		296764
10048	LBK_EN	LBK	EN	Halberstadt-Sonntagsfeld, Germany; HAL25, grave 28, feature 861	5206-5052 cal BC (MAMS 21482)	Germany	M	K1a	G2a2a	123628
10056	LBK_EN	LBK	EN	Halberstadt-Sonntagsfeld, Germany; HAL14, grave 15, feature 430	5206-5052 cal BC (MAMS 21480)	Germany	M	T2b(8)	G2a2a	136578
10057	LBK_EN	LBK	EN	Halberstadt-Sonntagsfeld, Germany; HAL34, grave 38, feature 992	5207-5067 cal BC (MAMS 21483)	Germany	F	N1a1a1		55802
10100	LBK_EN	LBK	EN	Halberstadt-Sonntagsfeld, Germany; HAL4, grave 1, feature 139	5032-4946 cal BC (KIA40341)	Germany	F	N1a1a1a		342342
10059	LBK_EN	LBK	EN	Halberstadt-Sonntagsfeld, Germany; HAL2, grave 35, feature 999	5079-4997 cal BC (KIA40350)	Germany	M	N1a1a	G2a2a1	191007
				5066-4979 cal BC (KIA30408)						
10821	LBK_EN	LBK	EN	Halberstadt-Sonntagsfeld, Germany; HAL24, grave 27, feature 867	5034-4942 cal BC (KIA40348)	Germany	M	Pre-X2d1	G2a2a1	55914
10795	LBK_EN	LBK	EN	Karsdorf, Germany; KAR6a, feature 170	5207-5070 cal BC (MAMS 22523)	Germany	M	H1	T1a	47804
10054	LBK_EN	LBK	EN	Oberwiederstedt-Untenwiederstedt, UWS4, Germany, grave 6, feature 1 14	5209-5070 cal BC (MAMS 21485)	Germany	F	J1c17		337625
10022	LBK_EN	LBK	EN	Viesenhäuser Hof, Stuttgart-Mühlhausen, Germany; LBK1976	5500-4800 BC	Germany	F	T2e		160852
10025	LBK_EN	LBK	EN	Viesenhäuser Hof, Stuttgart-Mühlhausen, Germany; LBK1992	5500-4800 BC	Germany	F	T2b		307686
10026	LBK_EN	LBK	EN	Viesenhäuser Hof, Stuttgart-Mühlhausen, Germany; LBK2155	5500-4800 BC	Germany	F	T2b		315494
10409	Spain_EN	Els Trocs	EN	Els Trocs, Spain; Troc1	5311-5218 cal BC (MAMS 16159)	Spain	F	J1c3		172903
10410	Spain_EN	Els Trocs	EN	Els Trocs, Spain; Troc3	5178-5086 cal BC (MAMS 16161)	Spain	M	pre-T2c1d2	R1b1	297595
10411	Spain_EN	Els Trocs	EN	Els Trocs, Spain; Troc4	5177-5088 cal BC (MAMS 16162)	Spain	M	K1a2a	F*	31507
10412	Spain_EN	Els Trocs	EN	Els Trocs, Spain; Troc5	5310-5206 cal BC (MAMS 16164)	Spain	M	N1a1a1	I2a1b1	333940
10413	Spain_EN	Els Trocs	EN	Els Trocs, Spain; Troc7	5303-5204 cal BC (MAMS 16166)	Spain	F	V		295844
10405	Spain_MN	La Mina	MN	La Mina, Spain; Mina1	3900-3600 BC	Spain	M	K1a1b1	I2a1a1/H2?	133230
10406	Spain_MN	La Mina	MN	La Mina, Spain; Mina4	3900-3600 BC	Spain	M	H1	I2a2a1	324169
10407	Spain_MN	La Mina	MN	La Mina, Spain; Mina9b	3900-3600 BC	Spain	F	K1b1a1		236225
10408	Spain_MN	La Mina	MN	La Mina, Spain; Mina18a	3900-3600 BC	Spain	F	pre-U5b1f		321761
10558	Esperstedt_MN	Salzmünde/Bernburg	MN	Esperstedt, Germany; ESP24, feature 1841	3360-3086 cal BC (Er86699)	Germany	M	T2b	I2a1b1a	279147
10559	Baalberge_MN	Baalberge	MN	Quedlinburg, Germany; QLB15D, feature 21033	3645-3537 cal BC (MAMS 22818)	Germany	M	Hv617	R7?	64304
10560	Baalberge_MN	Baalberge	MN	Quedlinburg, Germany; QLB18A, feature 21039	3640-3510 cal BC (Er7856)	Germany	F	T2e1		133305
10607	Baalberge_MN	Baalberge	MN	Esperstedt, Germany; ESP30, feature 6220	3887-3797 cal BC (Er7784)	Germany	M	H1e1a	F*	33481
10231	Yamnaya	Yamnaya	EBA	Ekaterinovka, Southern Steppe, Samara, Russia, SVP3	2910-2875 cal BC (Beta 392487)	Russia	M	U4a1	R1b1a2a2	348142
10357	Yamnaya	Yamnaya	EBA	Lopatino I, Sok River, Samara, Russia; SVP5 same sample as SVP37	3090-2910 cal BC (Beta 392489)	Russia	F	W6		163845
10370	Yamnaya	Yamnaya	EBA	Ishkinovka I, Eastern Orenburg, Pre-Ural steppe, Samara, Russia; SVP10	3000-2700 BC	Russia	M	H13a1a1a	R1b1a2a2	199345
10429	Yamnaya	Yamnaya	EBA	Lopatino I, Sok River, Samara, Russia; SVP39	3339-2917 cal BC (AA47804)	Russia	M	T2c1a2	R1b1a2a2	217594
10438	Yamnaya	Yamnaya	EBA	Luzhki I, Samara River, Samara, Russia; SVP50	3021-2635 cal BC (AA47807)	Russia	M	U5a1a1	R1b1a2a2	213493
10439	Yamnaya	Yamnaya	EBA	Lopatino I, Sok River, Samara, Russia; SVP52	3305-2925 cal BC (Beta 392491)	Russia	M	U5a1a1	R1b1a	98900
10441	Yamnaya	Yamnaya	EBA	Kurmanavskii II, Buzuluk, Samara, Russia; SVP54	3010-2622 cal BC (AA47805)	Russia	F	H2b		51326
10443	Yamnaya	Yamnaya	EBA	Lopatino II, Sok River, Samara, Russia; SVP57	3300-2700 BC	Russia	M	W3a1a	R1b1a2a	343890
10444	Yamnaya	Yamnaya	EBA	Kutuluk I, Kutuluk River, Samara, Russia; SVP58	3300-2700 BC	Russia	M	H6a1b	R1b1a2a2	187126
10560	Karsdorf_LN	unknown	LN	Karsdorf, Germany; KAR22a, feature 191	2564-2475 cal BC (MAMS 22344)	Germany	F	T1a1		59907
10103	Corded_Ware_LN	Corded Ware	LN	Esperstedt, Germany; ESP16, feature 6236	2566-2477 cal BC (MAMS 21488)	Germany	F	W6a		336918
10049	Corded_Ware_LN	Corded Ware	LN	Esperstedt, Germany; ESP22, feature 6140	2454-2291 cal BC (MAMS 21489)	Germany	F	X2b4		167170
10106	Corded_Ware_LN	Corded Ware	LN	Esperstedt, Germany; ESP26, feature 6233.1	2454-2291 cal BC (MAMS 21490)	Germany	F	T2a1b1		69886
10104	Corded_Ware_LN	Corded Ware	LN	Esperstedt, Germany; ESP11, feature 6216	2473-2348 cal BC (MAMS 21487)	Germany	M	U4b1a1a1	R1a1a1	336637
10059	Benzingerode-Heimburg_LN	Bell Beaker?	LN	Benzingerode-Heimburg, Germany; BZH6, grave 2, feature/ind 1287/1036	2286-2153 cal BC (MAMS 21486)	Germany	F	H1/H1b1ad		241081
10058	Benzingerode-Heimburg_LN	Bell Beaker	LN	Benzingerode-Heimburg, Germany; BZH4, grave 7, feature 4607	2283-2146 cal BC (MAMS 21491)	Germany	F	H1e		246728
10171	Benzingerode-Heimburg_LN	Bell Beaker?	LN	Benzingerode-Heimburg, Germany; BZH12, grave 3, feature 6256	2294-2136 cal BC (KIA27952)	Germany	F	U5a1a2a		66900
10112	Bell_Beaker_LN	Bell Beaker	LN	Quedlinburg XII, Germany; QUEX16, feature 6256	2340-2190 cal BC (Er7038)	Germany	F	H13a1a2		341003
10113	Bell_Beaker_LN	Bell Beaker	LN	Quedlinburg XII, Germany; QUEX14, feature 6255.1	2290-2130 cal BC (Er7283)	Germany	F	J1c5		190352
10108	Bell_Beaker_LN	Bell Beaker	LN	Rothenschimbach, Germany; ROT6, feature 10044	2497-2436 cal BC (Er8710)	Germany	F	H5a3		200528
10111	Bell_Beaker_LN	Bell Beaker	LN	Rothenschimbach, Germany; ROT4, feature 10142	2414-2333 cal BC (Er8712)	Germany	F	H3new		208256
10060	Bell_Beaker_LN	Bell Beaker	LN	Rothenschimbach, Germany; ROT3, feature 10011	2294-2206 cal BC (MAMS 22819)	Germany	F	K1a2c		47085
10806	Bell_Beaker_LN	Bell Beaker	LN	Quedlinburg VII 2, Germany; QLB28b, feature 19617	2296-2206 cal BC (MAMS 22820)	Germany	M	H1	R1b1a2a1a2	91757
10118	Alberstedt_LN	unknown	LN	Alberstedt, Germany; ALB3, feature 7144.2	2459-2345 cal BC (MAMS 21492)	Germany	F	Hv617		349656
10114	Unetice_EBA_relative_of_10117	Unetice	EBA	Esperstedt, Germany; ESP2, feature 3340.1	2131-1979 cal BC (MAMS 21493)	Germany	M	I3a	I2a2	217031
10115	Unetice_EBA	Unetice	EBA	Esperstedt, Germany; ESP3, feature 1559.1	1931-1780 cal BC (MAMS 21494)	Germany	F	U5a1		123744
10116	Unetice_EBA	Unetice	EBA	Esperstedt, Germany; ESP4, feature 3322/3323	2118-1981 cal BC (MAMS 21495)	Germany	M	W3a1	I2c2	308158
10117	Unetice_EBA	Unetice	EBA	Esperstedt, Germany; ESP29, feature 3332/3333	2166-2064 cal BC (MAMS 21496)	Germany	F	I3a		278696
10164	Unetice_EBA	Unetice	EBA	Quedlinburg VIII, Germany; QUEVIII6, feature 3580	2012-1919 cal BC (MAMS 21497)	Germany	F	pre-U5b2a1b		332832
10803	Unetice_EBA	Unetice	EBA	Eulau, Germany; EUL41A, feature 882	2115-1996 cal BC (MAMS 22822)	Germany	F	H4a1a1		144186
10804	Unetice_EBA	Unetice	EBA	Eulau, Germany; EUL57B, feature1911.5	2131-1882 cal BC (MAMS 22821)	Germany	M	H3	I2	22869
10047	Unetice_EBA	Unetice	EBA	Halberstadt-Sonntagsfeld, Germany; HAL16, grave 19, feature 613.1	2022-1937 cal BC (MAMS 21481)	Germany	F	V		288353
10099	Halberstadt_LBA	Late Bronze Age	LBA	Halberstadt-Sonntagsfeld, Germany; HAL36c, grave 40, feature 1114	1113-1021 cal BC (MAMS 21484)	Germany	M	H23	R1a1a1b1a2	337566

Samples with direct radiocarbon dates are indicated by a calibrated date “cal bc” along with associated laboratory numbers. Dates that are estimated based on faunal elements associated with the samples are not indicated with ‘cal’ (although they are still calibrated, absolute dates).

Extended Data Table 3 | Pairwise F_{ST} for all ancient groups with ≥ 2 individuals, present-day Europeans with ≥ 10 individuals, and selected other groups

	Amerindian	Baalberge_LN	Basque	BedouinB	Belarusian	Bell_Beaker_LN	BenzingerdeHeimbürg_LN	Bergamo	Bulgarian	Corded_Ware_LN	Croatian	Czech	EHG	English	Estonian	French	Greek	Han	Hungarian	HungaryGamba_BA	HungaryGamba_EN	Icelandic	Iraqi_Jew	Kanishia	LBK_EN	Lezgin	Lithuanian	Mala	Moldavia	Moldia_HG	Norwegian	Onge	Orcadian	Papuan	Russian	Sardinian	Sicilian	Sindhi	Spain_EN	Spain_LN	Spanish	SwedenSkoglund_NHG	Turkish	Unetice_EBA	WHG	Yamaya	Yoruba		
Amerindian	0.004	0.000	0.001	0.001	0.001	0.002	0.000	0.000	0.001	0.000	0.000	0.000	0.002	0.000	0.001	0.000	0.000	0.001	0.000	0.002	0.001	0.000	0.001	0.002	0.001	0.000	0.001	0.001	0.001	0.000	0.001	0.000	0.002	0.000	0.000	0.000	0.000	0.001	0.001	0.000	0.003	0.000	0.001	0.002	0.001	0.001			
Baalberge_LN	0.023	0.003	0.004	0.004	0.005	0.006	0.004	0.004	0.005	0.004	0.003	0.003	0.007	0.004	0.004	0.003	0.003	0.004	0.003	0.008	0.005	0.004	0.004	0.005	0.004	0.004	0.004	0.004	0.004	0.003	0.004	0.003	0.003	0.003	0.003	0.003	0.005	0.005	0.003	0.013	0.003	0.004	0.005	0.004	0.004				
Basque	0.017	0.019	0.001	0.000	0.001	0.002	0.000	0.000	0.001	0.000	0.000	0.002	0.000	0.000	0.000	0.000	0.000	0.001	0.000	0.002	0.001	0.000	0.002	0.001	0.000	0.001	0.000	0.001	0.000	0.001	0.000	0.001	0.000	0.002	0.000	0.000	0.000	0.000	0.001	0.001	0.000	0.003	0.000	0.001	0.002	0.001	0.001		
BedouinB	0.025	0.047	0.041	0.001	0.001	0.002	0.001	0.001	0.001	0.001	0.001	0.001	0.002	0.001	0.001	0.001	0.000	0.000	0.001	0.001	0.002	0.001	0.001	0.001	0.001	0.001	0.001	0.001	0.001	0.001	0.001	0.001	0.001	0.001	0.001	0.001	0.001	0.001	0.001	0.001	0.001	0.001	0.001	0.001	0.001				
Belarusian	0.014	0.026	0.012	0.041	0.001	0.002	0.000	0.000	0.001	0.000	0.000	0.002	0.000	0.000	0.000	0.000	0.000	0.001	0.000	0.002	0.001	0.000	0.002	0.001	0.000	0.000	0.001	0.000	0.001	0.000	0.001	0.000	0.001	0.000	0.002	0.000	0.000	0.000	0.001	0.001	0.000	0.003	0.000	0.001	0.002	0.001	0.001		
Bell_Beaker_LN	0.017	0.020	0.012	0.042	0.008	0.002	0.001	0.001	0.002	0.001	0.001	0.003	0.001	0.001	0.001	0.001	0.001	0.002	0.001	0.003	0.002	0.001	0.001	0.001	0.001	0.001	0.001	0.001	0.001	0.001	0.002	0.001	0.001	0.001	0.001	0.001	0.001	0.001	0.001	0.001	0.001	0.001	0.001	0.001	0.001	0.001			
BenzingerdeHeimbürg_LN	0.019	0.021	0.017	0.047	0.011	0.004	0.002	0.002	0.003	0.002	0.002	0.004	0.002	0.002	0.002	0.002	0.002	0.002	0.002	0.004	0.003	0.002	0.002	0.003	0.002	0.002	0.002	0.002	0.002	0.002	0.002	0.002	0.002	0.003	0.002	0.002	0.002	0.002	0.002	0.003	0.003	0.002	0.006	0.002	0.002	0.003	0.002	0.002	
Bergamo	0.007	0.015	0.008	0.032	0.007	0.008	0.012	0.000	0.001	0.000	0.000	0.002	0.000	0.000	0.000	0.000	0.000	0.001	0.000	0.002	0.001	0.000	0.002	0.001	0.000	0.000	0.001	0.000	0.001	0.000	0.001	0.000	0.001	0.000	0.002	0.000	0.000	0.000	0.000	0.001	0.001	0.000	0.003	0.000	0.001	0.002	0.001	0.001	
Bulgarian	0.006	0.019	0.009	0.031	0.003	0.008	0.010	0.002	0.001	0.000	0.000	0.002	0.000	0.000	0.000	0.000	0.000	0.001	0.000	0.002	0.001	0.000	0.002	0.001	0.000	0.001	0.000	0.001	0.000	0.001	0.000	0.001	0.000	0.002	0.000	0.000	0.000	0.000	0.001	0.001	0.000	0.003	0.000	0.001	0.002	0.001	0.001		
Corded_Ware_LN	0.023	0.032	0.025	0.052	0.015	0.008	0.007	0.019	0.017	0.001	0.001	0.003	0.001	0.001	0.001	0.001	0.001	0.002	0.001	0.003	0.002	0.001	0.002	0.002	0.001	0.001	0.002	0.001	0.001	0.002	0.001	0.001	0.001	0.001	0.001	0.001	0.001	0.001	0.001	0.001	0.001	0.001	0.001	0.001	0.001	0.001	0.001		
Croatian	0.009	0.019	0.010	0.035	0.002	0.007	0.011	0.004	0.001	0.015	0.000	0.002	0.000	0.000	0.000	0.000	0.000	0.001	0.000	0.002	0.001	0.000	0.001	0.002	0.001	0.000	0.001	0.000	0.001	0.000	0.002	0.000	0.001	0.000	0.002	0.000	0.000	0.000	0.000	0.001	0.001	0.000	0.003	0.000	0.001	0.002	0.001	0.001	
Czech	0.011	0.024	0.009	0.037	0.001	0.007	0.010	0.005	0.002	0.015	0.001	0.002	0.000	0.000	0.000	0.000	0.000	0.001	0.000	0.002	0.001	0.000	0.001	0.002	0.001	0.000	0.001	0.000	0.001	0.000	0.002	0.000	0.001	0.000	0.002	0.000	0.000	0.000	0.000	0.001	0.001	0.000	0.003	0.000	0.001	0.002	0.001	0.001	
EHG	0.067	0.082	0.060	0.093	0.042	0.041	0.038	0.057	0.051	0.034	0.048	0.043	0.002	0.002	0.002	0.002	0.003	0.002	0.004	0.003	0.002	0.003	0.003	0.003	0.002	0.002	0.002	0.002	0.002	0.002	0.002	0.003	0.002	0.003	0.002	0.002	0.002	0.002	0.002	0.003	0.003	0.002	0.006	0.002	0.003	0.003	0.002	0.002	
English	0.011	0.020	0.008	0.038	0.004	0.006	0.009	0.004	0.003	0.014	0.003	0.002	0.045	0.000	0.000	0.000	0.001	0.000	0.002	0.001	0.000	0.001	0.002	0.001	0.000	0.001	0.000	0.001	0.000	0.001	0.000	0.001	0.000	0.002	0.000	0.000	0.000	0.000	0.001	0.001	0.000	0.003	0.000	0.001	0.002	0.001	0.001		
Estonian	0.017	0.027	0.014	0.045	0.002	0.009	0.011	0.010	0.006	0.016	0.005	0.002	0.040	0.005	0.000	0.000	0.001	0.000	0.002	0.001	0.000	0.001	0.002	0.001	0.001	0.000	0.001	0.000	0.001	0.000	0.001	0.000	0.001	0.000	0.001	0.000	0.001	0.000	0.001	0.000	0.003	0.000	0.001	0.002	0.001	0.001			
French	0.009	0.018	0.006	0.035	0.004	0.006	0.008	0.002	0.002	0.015	0.002	0.001	0.048	0.001	0.005	0.000	0.001	0.000	0.002	0.001	0.000	0.001	0.009	0.000	0.002	0.001	0.000	0.000	0.001	0.000	0.001	0.000	0.001	0.000	0.002	0.000	0.000	0.000	0.000	0.001	0.001	0.000	0.003	0.000	0.001	0.002	0.001	0.001	
Greek	0.004	0.018	0.010	0.028	0.007	0.010	0.014	0.002	0.000	0.019	0.003	0.004	0.057	0.005	0.009	0.003	0.001	0.000	0.002	0.001	0.000	0.000	0.002	0.001	0.000	0.000	0.001	0.000	0.001	0.000	0.001	0.000	0.001	0.000	0.002	0.000	0.000	0.000	0.000	0.000	0.001	0.001	0.000	0.003	0.000	0.001	0.002	0.001	0.001
Han	0.106	0.136	0.120	0.128	0.110	0.114	0.117	0.113	0.108	0.118	0.110	0.111	0.135	0.113	0.110	0.110	0.110	0.001	0.003	0.002	0.001	0.001	0.002	0.001	0.001	0.001	0.001	0.001	0.001	0.001	0.001	0.001	0.001	0.001	0.001	0.001	0.001	0.001	0.001	0.001	0.001	0.001	0.001	0.001	0.001	0.001	0.001	0.001	
Hungarian	0.009	0.019	0.009	0.036	0.001	0.007	0.009	0.003	0.001	0.014	0.002	0.000	0.046	0.001	0.003	0.001	0.003	0.108	0.002	0.001	0.000	0.001	0.002	0.001	0.000	0.000	0.001	0.000	0.001	0.000	0.001	0.000	0.001	0.000	0.001	0.000	0.001	0.000	0.001	0.000	0.003	0.000	0.001	0.002	0.001	0.001			
HungaryGamba_BA	0.016	0.021	0.010	0.039	0.005	0.008	0.010	0.008	0.005	0.016	0.005	0.005	0.046	0.007	0.006	0.005	0.007	0.115	0.005	0.003	0.002	0.002	0.003	0.002	0.002	0.002	0.002	0.002	0.002	0.002	0.002	0.002	0.003	0.002	0.002	0.002	0.002	0.002	0.002	0.003	0.003	0.002	0.006	0.002	0.003	0.003	0.003	0.002	
HungaryGamba_EN	0.016	0.009	0.018	0.037	0.021	0.020	0.025	0.009	0.012	0.037	0.015	0.018	0.081	0.018	0.028	0.014	0.010	0.129	0.016	0.014	0.001	0.001	0.002	0.001	0.001	0.001	0.001	0.001	0.001	0.001	0.001	0.001	0.001	0.001	0.001	0.001	0.001	0.001	0.001	0.001	0.001	0.001	0.001	0.001	0.001	0.001	0.001		
Icelandic	0.015	0.025	0.011	0.041	0.005	0.008	0.011	0.006	0.005	0.014	0.006	0.003	0.045	0.002	0.006	0.003	0.008	0.113	0.004	0.007	0.021	0.001	0.002	0.001	0.000	0.000	0.001	0.000	0.001	0.000	0.001	0.000	0.001	0.000	0.001	0.000	0.001	0.000	0.001	0.000	0.003	0.000	0.001	0.002	0.001	0.001			
Iraqi_Jew	0.005	0.031	0.021	0.026	0.020	0.022	0.024	0.011	0.010	0.029	0.014	0.017	0.073	0.016	0.023	0.014	0.009	0.112	0.015	0.018	0.020	0.021	0.002	0.001	0.001	0.001	0.001	0.001	0.001	0.001	0.001	0.001	0.001	0.001	0.001	0.001	0.001	0.001	0.001	0.001	0.001	0.001	0.001	0.001	0.001	0.001	0.001		
Kanishia	0.210	0.234	0.218	0.230	0.205	0.208	0.208	0.212	0.206	0.209	0.207	0.206	0.206	0.209	0.205	0.208	0.209	0.180	0.205	0.214	0.229	0.209	0.002	0.002	0.002	0.002	0.002	0.002	0.002	0.002	0.002	0.002	0.002	0.002	0.002	0.002	0.002	0.002	0.002	0.002	0.002	0.002	0.002	0.002	0.002	0.002	0.002	0.002	
LBK_EN	0.023	0.009	0.024	0.043	0.029	0.021	0.025	0.017	0.018	0.035	0.022	0.024	0.084	0.024	0.033	0.020	0.016	0.137	0.022	0.018	0.006	0.029	0.029	0.237	0.001	0.001	0.0																						

Reducing the energy cost of human walking using an unpowered exoskeleton

Steven H. Collins^{1*}, M. Bruce Wiggin^{2*} & Gregory S. Sawicki^{2*}

With efficiencies derived from evolution, growth and learning, humans are very well-tuned for locomotion¹. Metabolic energy used during walking can be partly replaced by power input from an exoskeleton², but is it possible to reduce metabolic rate without providing an additional energy source? This would require an improvement in the efficiency of the human-machine system as a whole, and would be remarkable given the apparent optimality of human gait. Here we show that the metabolic rate of human walking can be reduced by an unpowered ankle exoskeleton. We built a lightweight elastic device that acts in parallel with the user's calf muscles, off-loading muscle force and thereby reducing the metabolic energy consumed in contractions. The device uses a mechanical clutch to hold a spring as it is stretched and relaxed by ankle movements when the foot is on the ground, helping to fulfil one function of the calf muscles and Achilles tendon. Unlike muscles, however, the clutch sustains force passively. The exoskeleton consumes no chemical or electrical energy and delivers no net positive mechanical work, yet reduces the metabolic cost of walking by $7.2 \pm 2.6\%$ for healthy human users under natural conditions, comparable to savings with powered devices. Improving upon walking economy in this way is analogous to altering the structure of the body such that it is more energy-effective at walking. While strong natural pressures have already shaped human locomotion, improvements in efficiency are still possible. Much remains to be learned about this seemingly simple behaviour.

Humans are skilled walkers. Over generations, our bodies have evolved muscular¹, skeletal³ and neural⁴ systems well-suited to locomotion. We learn and embed walking coordination strategies over our lifetimes⁵ and adapt to new locomotor environments in minutes or seconds⁶. We take about 10,000 steps per day⁷, or hundreds of millions of steps in a lifetime, exceeding the approximately 10,000 h of practice thought to be needed to attain expertise⁸ by adulthood. We naturally keep energy expenditure low during walking, choosing, for example, step length⁹ and even arm motions¹⁰ that minimize energy cost. Nearly any change to the human musculoskeletal system or its pattern of coordination increases metabolic rate. Despite this skill and efficiency, getting about is still expensive. People expend more energy during walking than any other activity of daily life¹¹, and fatigue can limit mobility. Herein lies the challenge: reducing the effort of normal walking could garner substantial benefits, but humans are already so energy-effective that making improvements is extremely difficult.

Since at least the 1890s¹², engineers have designed machines intended to make walking easier^{13–15}. A survey of these designs can be found in the Supplementary Discussion. It is only recently that any attempt at reducing the energy cost of walking with an external device has met with success. The first machine to do so used off-board pneumatic pumps and valves to replace human joint work with exoskeleton work², overcoming the surprisingly tricky challenge of coordinating assistance with the human neuromuscular system. More recently still, a powered and untethered device using similar control strategies succeeded in

reducing energy cost¹⁶, overcoming the additional challenge of autonomous packaging.

Reducing the energy cost of walking with an unpowered device requires a different approach. Instead of adding a robotic energy source to replace metabolic sources, one must, in a sense, change the human body such that it is more efficient at locomotion (Extended Data Fig. 1). For the task of carrying heavy loads while walking, such improvements have been demonstrated using a spring-mounted backpack¹⁷ and by training people to balance the weight on their head in just the right way¹⁸. But is there room for a similar improvement in the already expert task of normal walking?

The possibility of unpowered assistance is made more likely by the fact that level walking at steady speed requires no power input in theory, and therefore all energy used in this activity is, in a sense, wasted. Simulation models with spring-loaded legs illustrate this idea¹⁹; their springs store and return energy during each step, but no mechanical work is done by actuators, capitalizing on the fact that the kinetic and potential energy

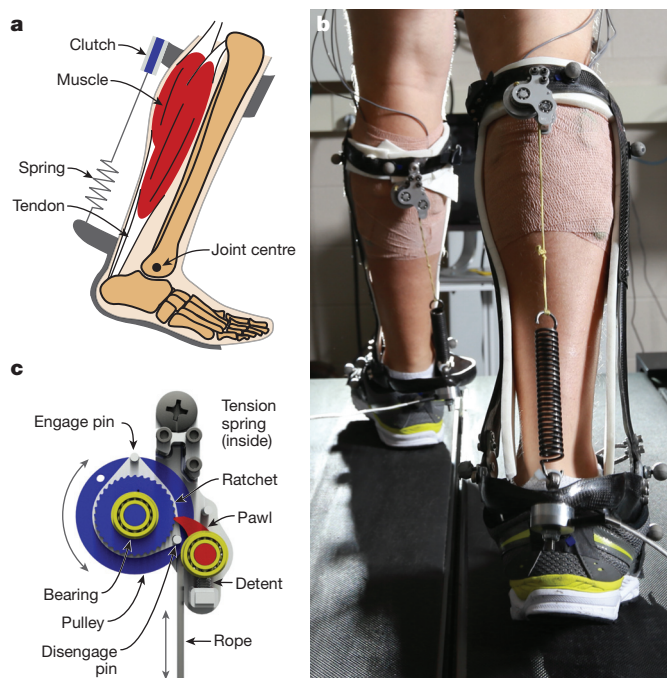


Figure 1 | Unpowered exoskeleton design. **a**, The exoskeleton comprises rigid sections attached to the human shank and foot and hinged at the ankle. A passive clutch mechanism and series spring act in parallel with the calf muscles and Achilles tendon. **b**, Participant walking with the device. Load cells measured spring force. **c**, The passive clutch mechanism has no electronics, but instead uses a ratchet and pawl that mechanically engage the spring when the foot is on the ground and disengage it when the foot is in the air.

¹Department of Mechanical Engineering, Carnegie Mellon University, 5000 Forbes Avenue, Pittsburgh, Pennsylvania 15213, USA. ²Joint Department of Biomedical Engineering, North Carolina State University and the University of North Carolina at Chapel Hill, 911 Oval Drive, Raleigh, North Carolina 27695, USA.

*All authors contributed equally to this work.

of the body remain constant on average. Humans expend metabolic energy during walking in part to restore energy that has been dissipated, in passive motions of soft tissues²⁰ for example, but the greatest portion of waste occurs in muscles. Muscles consume metabolic energy to perform positive work, as required by conservation of energy, but they also use metabolic energy to produce force isometrically and to perform negative work²¹. This places a metabolic cost on body weight support²² and on holding tendons as they stretch and recoil²³. By contrast, mechanical clutches require no energy to produce force.

We designed a lightweight exoskeleton that provides some of the functions of the calf muscles and tendons during walking, but uses more efficient structures for those tasks. It has a spring in parallel with the Achilles tendon (Fig. 1a) connected to the leg using a lightweight composite frame with a lever about the ankle joint (Fig. 1b and Extended Data Fig. 2). A mechanical clutch in parallel with the calf muscles engages the spring when the foot is on the ground and disengages it to allow free motion when the foot is in the air (Fig. 1c and Supplementary Video 1). This design was inspired by ultrasound imaging studies suggesting clutch-like behaviour of muscle fascicles to hold the spring-like Achilles tendon²⁴, the recoil of which leads to the largest burst of positive mechanical power at any joint during walking. The exoskeleton clutch, described in detail in the Supplementary Methods and Supplementary Video 2, has no motor, battery or computer control, and weighs 0.057 kg. The entire exoskeleton has a mass of between 0.408 and 0.503 kg per leg,

depending on participant size (Extended Data Tables 1 and 2). On the basis of simulation studies of walking with elastic ankles^{19,25}, we expected an intermediate stiffness to minimize energy cost and performed tests with a range of springs.

We conducted experiments with healthy participants ($N = 9$) wearing an exoskeleton on each leg while walking at a normal speed (1.25 m s^{-1}) on a treadmill. The exoskeleton produced a pattern of torque similar to that produced by the biological ankle, but with lower magnitude (Fig. 2a). This reduced the ankle moment produced by calf muscles (Fig. 2b) and reduced calf muscle activation, particularly in the soleus (Fig. 2c). Joint angles changed little across conditions (Fig. 2d), confirming that the exoskeleton did not interfere with other normal ankle functions, such as toe clearance during leg swing (60–100% stride).

The exoskeleton reduced human metabolic energy consumption when using moderate-stiffness springs (Fig. 3). Wearing a lightweight exoskeleton on each ankle without springs did not measurably increase energy cost compared with normal walking. With increasing spring stiffness, metabolic rate first decreased then increased, supporting the hypothesis that an intermediate stiffness would be optimal. The 180 N m rad^{-1} spring reduced the metabolic cost of walking to $2.67 \pm 0.14 \text{ W kg}^{-1}$ (mean \pm standard error), down from $2.88 \pm 0.10 \text{ W kg}^{-1}$ for normal walking, a reduction of $7.2 \pm 2.6\%$ (paired t -test: $P = 0.023$). Metabolic energy used for walking, or net metabolic rate, is calculated as total metabolic rate minus the rate for quiet standing, which was

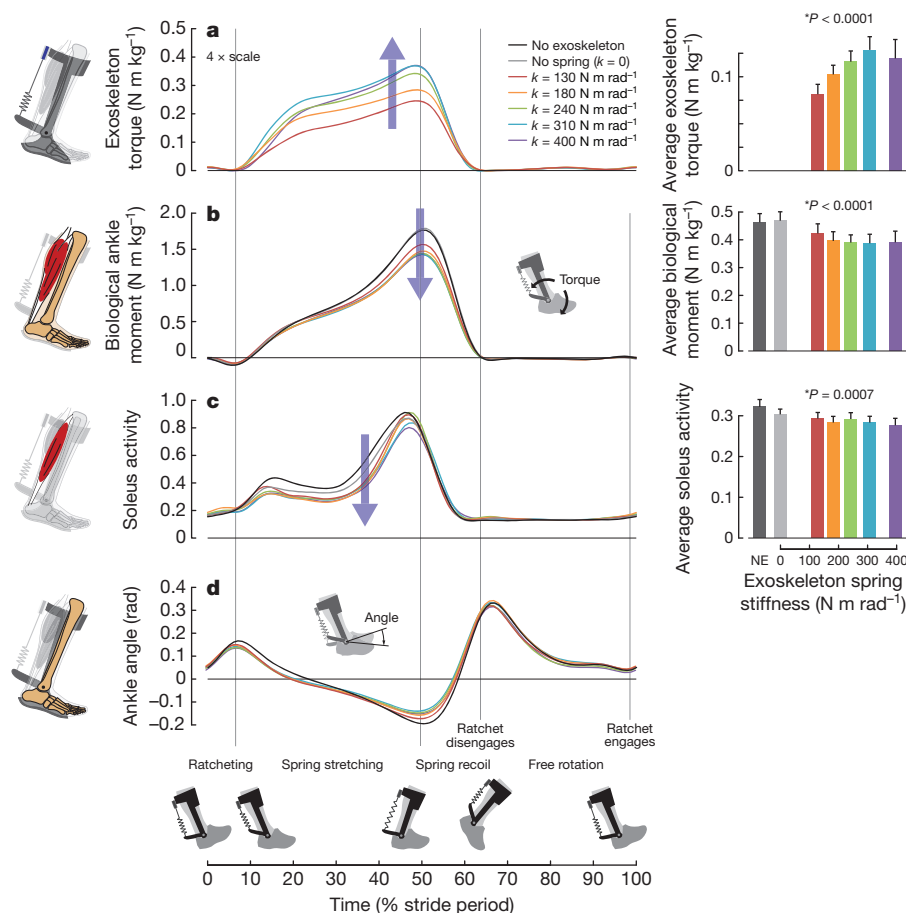


Figure 2 | Mechanics and muscle activity. **a**, Exoskeleton torque (normalized to body mass) in time (normalized to stride period) for each spring, averaged across participants. Bars at right are the averages of these trajectories in time; $N = 9$; error bars, s.e.m.; P values indicate the results of analysis of variance (ANOVA) tests for an effect of spring stiffness; NE, no exoskeleton. Exoskeleton torque increased with spring stiffness (except with the stiffest spring, which tended to be engaged later in stance). **b**, Time course of the biological contributions to ankle moment, which decreased with increasing

spring stiffness. **c**, Time course of electrical activity in the soleus muscle, an ankle plantarflexor, which decreased with increasing spring stiffness. **d**, Time course of ankle joint angle, which triggered passive clutch engagement and disengagement. The ratchet was engaged at heel strike, took up slack through foot flat, held the spring as it stretched and recoiled through mid- and late stance, and disengaged to allow toe clearance during leg swing. The average stride period was $1.15 \pm 0.08 \text{ s}$ (mean \pm s.d.).

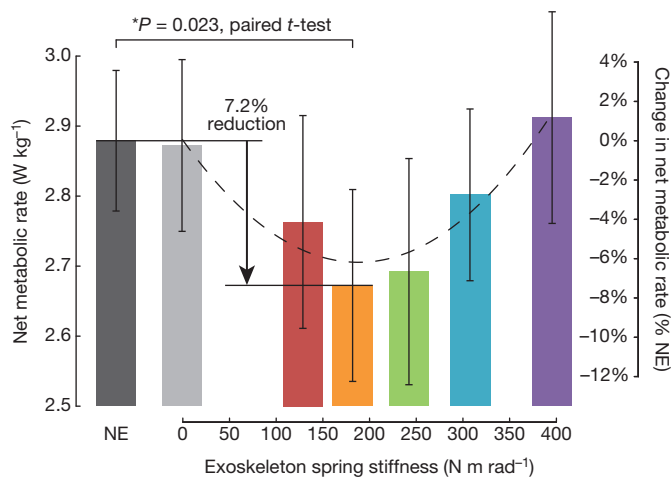


Figure 3 | Human metabolic rate. Spring stiffness affected metabolic rate ($N = 9$; ANOVA with second-order model; $P_{\text{stiffness}} = 0.016$, $P_{\text{stiffness}^2} = 0.008$). Net metabolic rate, with the value for quiet standing subtracted out, was $7.2 \pm 2.6\%$ (mean \pm s.e.m.) lower with the 180 N m rad^{-1} spring (orange bar) than during normal walking (dark grey bar; paired two-sided t -test with correction for multiple comparisons; $P = 0.023$). The dashed line is a quadratic best fit to mean data from exoskeleton conditions ($R^2 = 0.91$, $P = 0.029$). Wearing the exoskeleton with the spring removed (light grey bar, $k = 0$) did not increase energy cost compared with normal walking (paired t -test; $P = 0.9$). Error bars, s.e.m., dominated by inter-participant variability.

$1.47 \pm 0.1 \text{ W kg}^{-1}$ in this study. The observed reduction is similar to improvements with high-powered devices^{2,16} and equivalent to the effect of taking off a 4 kg backpack for an average person²⁶.

It is difficult to attribute changes in whole-body metabolic rate to a particular change in muscle mechanics²⁷, but with this device there is an association with reduced muscle forces at the assisted ankle joints. Muscles consume energy whenever active, even when producing force without performing mechanical work. Simply reducing muscle force can therefore save metabolic energy. For all exoskeleton springs, we measured reductions in the biological component of ankle moment and the activity of major plantarflexor muscles, both indicative of reduced force. Reductions occurred primarily during early and mid-stance (0–40% stride, Fig. 2b, c) when muscle fascicles are nearly isometric and therefore perform little mechanical work²⁴. Simulation models estimate that plantarflexor muscle energy use primarily occurs during this period and accounts for about 27% of the metabolic energy used for walking²⁷. With the 180 N m rad^{-1} spring, the biological component of average ankle moment was reduced by 14% and mid-stance soleus electrical activity was reduced by 22% compared with normal walking. Extrapolating from these values, one might expect about a 4–6% reduction in overall metabolic rate, comparable to the observed 7% reduction.

Biological contributions to ankle joint work were also partly replaced by the exoskeleton, but it is unlikely that these changes were responsible for reductions in metabolic rate. The connections between joint work, musculotendon work, muscle fascicle work and metabolic rate are complex. Much of the mechanical work at the ankle joint during walking is the result of elastic stretch and recoil of the Achilles tendon²⁴, which does not directly consume metabolic energy. Because of tendon compliance, using an exoskeleton to reduce cyclic musculotendon work can actually preserve or increase the mechanical work performed by muscle fascicles²⁸—reducing tendon force reduces its stretch, which can lead to increased excursion of the muscle itself and more muscle work. Even if reduced joint work had been the result of reduced muscle fascicle work, under these circumstances such a change would probably not have reduced metabolic cost. It has recently been shown that for contraction cycles similar to those of the calf muscles during normal walking, where muscle fascicles undergo stretch–shorten cycles with nearly zero net work, making equal and opposite changes to both negative

and positive work has no effect on metabolic energy use per unit force²⁹. Our understanding of the relationship between muscle activity and metabolic rate remains imperfect, but reduced muscle work does not seem to provide a good explanation for reduced metabolic cost in this study.

Metabolic rate increased back to normal levels when using high-stiffness exoskeleton springs, apparently the result of several factors. Humans tend to select coordination patterns with similar net ankle moments across a range of exoskeleton torques^{2,30}, a trend also observed here. With stiff springs, tibialis anterior activity counteracting exoskeleton torque in early and mid-stance appeared to increase, possibly reducing changes in total joint moment. Knee muscle activity to prevent hyperextension during mid- and late stance may also have contributed to increases in metabolic cost. Unexpectedly, some of the increase in metabolic rate appears to be associated with increased plantarflexor activity at the end of stance. Furthermore, despite being more active during this period, plantarflexor muscles produced lower joint moments. These reduced moments probably reflect increased contraction velocity, because muscle force drops rapidly as the rate of shortening increases. These two observations suggest that exoskeleton support during mid-stance led to inefficient, rapid shortening of plantarflexor muscles during the usual burst of positive work at the end of the step. Also unexpectedly, it does not appear that the increase in metabolic rate with high-stiffness springs is well explained by simple dynamic models of walking, which predict changes in centre-of-mass work that were not observed here^{19,25}. These and other interpretations are presented in expanded form in the Supplementary Discussion and can be explored using joint mechanics, muscle activity and centre-of-mass mechanics data presented in Extended Data Figs 3–8.

The complexity of the neuromuscular system can impede useful application of simple ideas from mechanics and robotics to human locomotion. For example, it is tempting to equate joint work or centre-of-mass work with metabolic energy use. However, the benefits derived from reduced muscle activity with this unpowered exoskeleton would not have been discovered using joint-level power estimates as a guide, since these draw attention towards terminal stance and away from early and mid-stance when joint power is negative and of low magnitude. The increased metabolic rate at higher exoskeleton spring stiffness found here also cannot be explained using mechanical power, because human contributions decreased or remained suppressed with increasing stiffness. The complex neuromuscular factors underlying these changes make effective integration of assistive devices very challenging and may explain why the threshold of reducing the metabolic rate of normal walking, with^{2,16} or without additional power input, has taken more than a century to cross. Much remains to be learned about human coordination, even in this seemingly uncomplicated activity.

We have demonstrated that net energy input is not a fundamental requirement for reducing the metabolic cost of human walking. Reducing calf muscle forces—while also fulfilling normal ankle functions and minimizing penalties associated with added mass or restricted motions—can provide a benefit. Passive clutch-like structures are feasible in nature, making the use of this type of device analogous to a change in anatomy that improves walking economy. Similar morphological changes might augment other lower-limb musculature or locomotion in other animals. While evolution, growth and learning have driven efficiency, improvements are yet possible.

Online Content Methods, along with any additional Extended Data display items and Source Data, are available in the online version of the paper; references unique to these sections appear only in the online paper.

Received 11 December 2014; accepted 6 February 2015.

Published online 1 April 2015.

- Alexander, R. M. *Principles of Animal Locomotion* Chs 1 and 7 (Princeton Univ. Press, 2003).
- Malcolm, P., Derave, W., Galle, S. & De Clercq, D. A simple exoskeleton that assists plantarflexion can reduce the metabolic cost of human walking. *PLoS ONE* **8**, e56137 (2013).

3. Lovejoy, C. O. The natural history of human gait and posture: part 1. Spine and pelvis. *Gait Posture* **21**, 95–112 (2005).
4. Dietz, V. Spinal cord pattern generators for locomotion. *Clin. Neurophysiol.* **114**, 1379–1389 (2003).
5. Forssberg, H. Ontogeny of human locomotor control I. Infant stepping, supported locomotion and transition to independent locomotion. *Exp. Brain Res.* **57**, 480–493 (1985).
6. Davidson, P. R. & Wolpert, D. M. Widespread access to predictive models in the motor system: a short review. *J. Neural Eng.* **2**, S313–S319 (2005).
7. Tudor-Locke, C., Johnson, W. D. & Katzmarzyk, P. T. Accelerometer-determined steps per day in US adults. *Med. Sci. Sports Exerc.* **41**, 1384–1391 (2009).
8. Ericsson, K. A. & Charness, N. Expert performance: its structure and acquisition. *Am. Psychol.* **49**, 725–747 (1994).
9. Zarrugh, M. Y., Todd, F. N. & Ralston, H. J. Optimization of energy expenditure during level walking. *Eur. J. Appl. Physiol. Occup. Physiol.* **33**, 293–306 (1974).
10. Collins, S. H., Adamczyk, P. G. & Kuo, A. D. Dynamic arm swinging in human walking. *Proc. R. Soc. B* **276**, 3679–3688 (2009).
11. Westerterp, K. R. Physical activity and physical activity induced energy expenditure in humans: measurement, determinants, and effects. *Front. Physiol.* **4**, 90 (2013).
12. Yagn, N. Apparatus for facilitating walking, running and jumping. US patent 420,179 (1890).
13. Grabowski, A. M. & Herr, H. M. Leg exoskeleton reduces the metabolic cost of human hopping. *J. Appl. Physiol.* **107**, 670–678 (2009).
14. van Dijk, W., van der Kooij, H. & Hekman, E. A passive exoskeleton with artificial tendons: design and experimental evaluation. *Proc. IEEE Int. Conf. Rehabil. Rob.* <http://dx.doi.org/10.1109/ICORR.2011.5975470> (2011).
15. Zoss, A. & Kazerooni, H. Design of an electrically actuated lower extremity exoskeleton. *Adv. Robot.* **20**, 967–988 (2006).
16. Mooney, L. M., Rouse, E. J. & Herr, H. M. Autonomous exoskeleton reduces metabolic cost of human walking. *J. Neuroeng. Rehabil.* **11**, 1–6 (2014).
17. Rome, L. C., Flynn, L. & Yoo, T. D. Biomechanics: rubber bands reduce the cost of carrying loads. *Nature* **444**, 1023–1024 (2006).
18. Heglund, N. C., Willems, P. A., Penta, M. & Cavagna, G. A. Energy-saving gait mechanics with head-supported loads. *Nature* **375**, 52–54 (1995).
19. Zelik, K. E., Huang, T. W. P., Adamczyk, P. G. & Kuo, A. D. The role of series ankle elasticity in bipedal walking. *J. Theor. Biol.* **346**, 75–85 (2014).
20. Zelik, K. E. & Kuo, A. D. Human walking isn't all hard work: evidence of soft tissue contributions to energy dissipation and return. *J. Exp. Biol.* **213**, 4257–4264 (2010).
21. Ryschon, T. W., Fowler, M. D., Wysong, R. E., Anthony, A. & Balaban, R. S. Efficiency of human skeletal muscle *in vivo*: comparison of isometric, concentric, and eccentric muscle action. *J. Appl. Physiol.* **83**, 867–874 (1997).
22. Grabowski, A., Farley, C. T. & Kram, R. Independent metabolic costs of supporting body weight and accelerating body mass during walking. *J. Appl. Physiol.* **98**, 579–583 (2005).
23. Roberts, T. J. The integrated function of muscles and tendons during locomotion. *Comp. Biochem. Physiol. A* **133**, 1087–1099 (2002).
24. Ishikawa, M., Komi, P. V., Grey, M. J., Lepola, V. & Brüggemann, G. P. Muscle-tendon interaction and elastic energy usage in human walking. *J. Appl. Physiol.* **99**, 603–608 (2005).
25. Bregman, D. J. *et al.* The effect of ankle foot orthosis stiffness on the energy cost of walking: a simulation study. *Clin. Biomech.* **26**, 955–961 (2011).
26. Browning, R. C., Modica, J. R., Kram, R. & Goswami, A. The effects of adding mass to the legs on the energetics and biomechanics of walking. *Med. Sci. Sports Exerc.* **39**, 515–525 (2007).
27. Umberger, B. R. & Rubenson, J. Understanding muscle energetics in locomotion: new modeling and experimental approaches. *Exerc. Sport Sci. Rev.* **39**, 59–67 (2011).
28. Farris, D. J., Robertson, B. D. & Sawicki, G. S. Elastic ankle exoskeletons reduce soleus muscle force but not work in human hopping. *J. Appl. Physiol.* **115**, 579–585 (2013).
29. Holt, N. C., Roberts, T. J. & Askew, G. N. The energetic benefits of tendon springs in running: is the reduction of muscle work important? *J. Exp. Biol.* **217**, 4365–4371 (2014).
30. Kao, P. C., Lewis, C. L. & Ferris, D. P. Invariant ankle moment patterns when walking with and without a robotic ankle exoskeleton. *J. Biomech.* **43**, 203–209 (2010).

Supplementary Information is available in the online version of the paper.

Acknowledgements We thank A. Westbrook for data collection, K. Takahashi and R. Nuckols for stiffness characterizations, B. Reich for discussions on statistical analysis, R. Jackson for data collection and manuscript editing, and J. Caputo, P. Collins, S. Diller, N. Donahue, A. Kuo, I. Lau, L. Lau, C. Majidi, J. Malen, T. Roberts, A. Robinson, A. Ruina, P. Taggart, K. Witte, M. Wu and others for editorial suggestions. The photograph in Fig. 1b is by S. Thrift. Funding for this research was provided by grants to G.S.S. from the North Carolina State Faculty Research and Professional Development Fund; the North Carolina State Chancellors Innovation Fund; grant number 2011152 from the United States - Israel Binational Science Foundation; and award number R01NR014756 from the National Institute of Nursing Research of the National Institutes of Health. This material is based upon work supported by the National Science Foundation under grant number IIS-1355716 to S.H.C. The content is solely the responsibility of the authors and does not necessarily represent the official views of the National Institutes of Health or other funding agencies listed.

Author Contributions G.S.S. and S.H.C. contributed equally to study design and direction; M.B.W., S.H.C. and G.S.S. designed the device; M.B.W. fabricated the device; M.B.W. and G.S.S. conducted human locomotion experiments; M.B.W., S.H.C. and G.S.S. analysed data; S.H.C., M.B.W. and G.S.S. drafted the manuscript; S.H.C. and G.S.S. edited the manuscript. All authors approved the final manuscript.

Author Information Source data are available at <https://www.bme.ncsu.edu/labs/hpl/NaturePassiveExoData/>. Reprints and permissions information is available at www.nature.com/reprints. The authors declare competing financial interests: details are available in the online version of the paper. Readers are welcome to comment on the online version of the paper. Correspondence and requests for materials should be addressed to S.H.C. (stevecollins@cmu.edu) or G.S.S. (greg_sawicki@ncsu.edu).

METHODS

Participants. Nine healthy adults ($N = 9$, 2 female, 7 male; age = 23.0 ± 3.7 years; mass = 77.4 ± 9.2 kg; height = 1.84 ± 0.10 m; mean \pm s.d.) participated in the study. One additional participant dropped out before completing the protocol, in part owing to hardware malfunctions during training sessions. Sample size was chosen on the basis of data from previous studies; no statistical methods were used to predetermine sample size. All participants provided written informed consent before participation and separately provided written consent to publish de-identified photographs (as applicable). The study protocol was approved and overseen by the Institutional Review Board of the University of North Carolina at Chapel Hill.

Exoskeleton hardware. Custom frames were fabricated for each participant using modified orthotics methods. A flexible cast was used to create a positive plaster mould of the foot, ankle and shank, upon which a thin, selectively reinforced carbon fibre frame was formed. Shank and foot segments were removed from the mould and connected using an aluminium hinge joint with a plain bearing (Extended Data Fig. 2). The custom mechanical clutch^{31,32} (Fig. 1c and Supplementary Methods) was then integrated with the frame. Part drawings and CAD files are provided as Supplementary Data 1 and 2, a detailed accounting of component mass and comparisons with other systems are provided in Extended Data Tables 1 and 2, and a demonstration of clutch function can be found in Supplementary Video 2.

We used five sets of steel coil extension springs with stiffnesses of 5.6, 7.9, 10.5, 13.3 and 17.2 kN m⁻¹ and masses of 0.059, 0.061, 0.068, 0.092 and 0.098 kg, respectively. Spring stiffnesses were determined in experiments where springs were stretched to several displacements using a fixture and forces were measured using a load cell. Springs were attached to a lever arm on the foot frame with an average radius of 0.152 m, resulting in average exoskeleton rotational stiffnesses of 130, 180, 240, 310 and 400 N m rad⁻¹. This spans the range of reported ankle joint quasi-stiffnesses for walking³³. To measure force, a single-axis load cell (LC8125-312-500, Omega Engineering) was placed in series with the spring. Exoskeleton joint torque was calculated as the product of spring force and the lever arm, assuming constant leverage.

The effective stiffness experienced by participants was lower than that indicated by the springs themselves. In a follow-up experiment with a single participant, quasi-static loading of the exoskeleton, and additional markers on the exoskeleton frame, compliance in the frame and rope led to about an 18% decrease in effective stiffness, while compliance at the human–exoskeleton interface led to an additional decrease of about 15%. The effective mechanical stiffness of the exoskeleton, when clutched, was therefore probably about 33% lower than indicated by the springs alone. Such effects probably varied across participants, being dependent both on frame construction and on individual human characteristics.

Walking trials. Participants walked on a treadmill at 1.25 m s⁻¹ under seven conditions: normal walking without the exoskeleton (No Exoskeleton or NE); walking with the complete exoskeleton but no spring connected (No Spring or $k = 0$); and walking with each of the springs attached (exoskeleton spring stiffness $k = 130, 180, 240, 310$ and 400 N m rad⁻¹). In previous studies, humans have taken about 20 min to adapt fully to tethered pneumatic ankle exoskeletons³⁴. To allow sufficient time for learning, participants completed 21 min of training under each condition over three or four walking sessions before data collection. During training, participants walked under each condition for 7 min. Mechanical failure of the clutch occurred for some conditions during some training sessions, resulting in more collection sessions for some participants, but an equal amount of training (21 min) with a functioning exoskeleton for all participants and conditions. Data were collected during minutes 5–7 of a final 7 min session, or minutes 26–28 of the multi-day experiment. The order of presentation of conditions was randomized for each participant on the first collection day and then held constant for that participant over the remainder of the experiment. This ensured that each participant's training progress was not confounded by ordering effects. Blinding was not practical in this protocol.

Biomechanics and energetics measurements. Body segment motions were measured using a reflective marker motion capture system (eight T-Series cameras, Vicon). Ground reaction forces were measured using a treadmill instrumented with load cells (Bertec). Ankle muscle activity (soleus, medial and lateral gastrocnemius, tibialis anterior) was measured using a wired electromyography system (SX230, Biometrics). Whole-body oxygen consumption and carbon dioxide production were measured using an indirect calorimetry system (Oxycon Mobile, CareFusion).

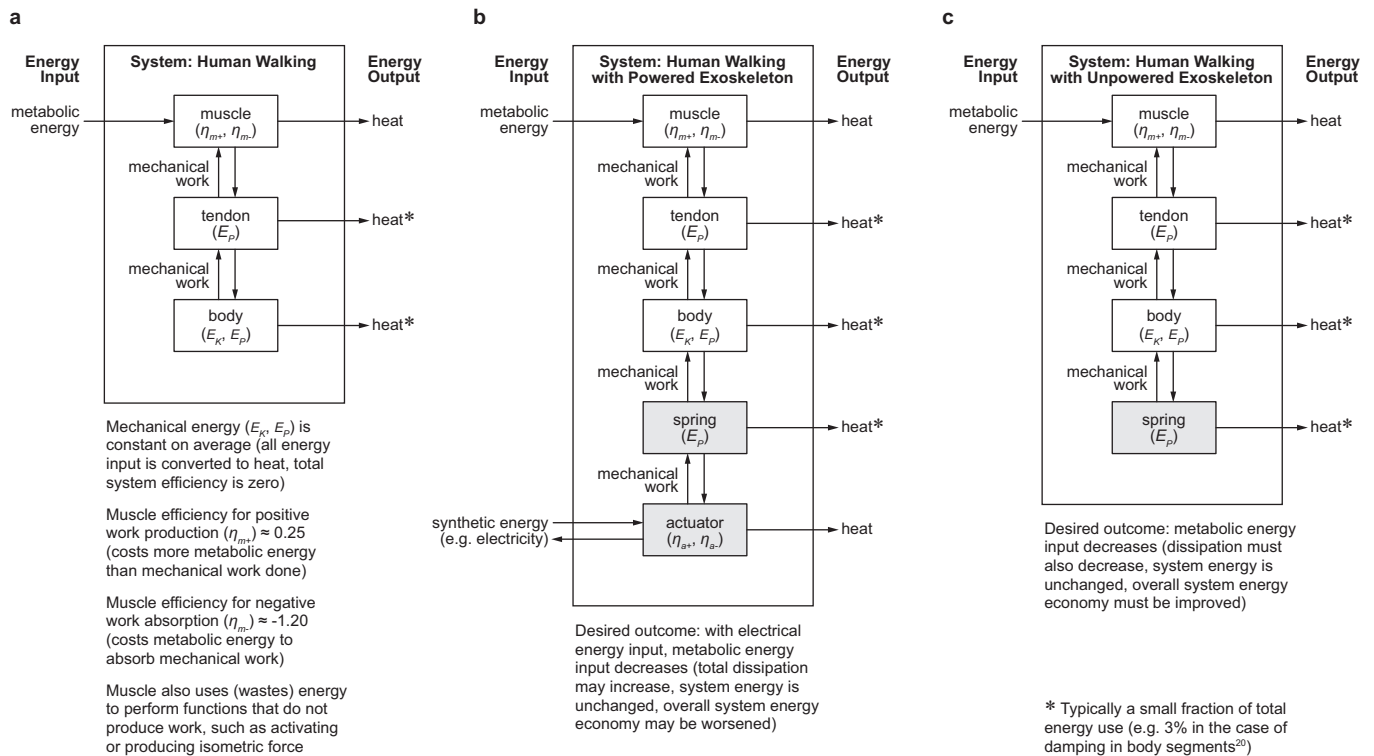
Data analysis. Joint angles, moments and powers were calculated from body motions and ground reaction forces using inverse kinematics and inverse dynamics analyses³⁵ (Visual 3D, C-Motion). Components of joint moment and power attributed to the human (biological component) were calculated^{36,37} by subtracting the exoskeleton torque or power, measured using onboard sensors, from the total ankle joint moment or power, estimated using inverse dynamics. Centre-of-mass power was calculated from ground reaction forces using the individual limbs method³⁸. Muscle activity was band-pass filtered (20–460 Hz) in hardware and then conditioned by rectifying

and low-pass filtering with a cutoff frequency of 6 Hz in software. Medial and lateral gastrocnemius signals were combined to simplify analysis and interpretation. Metabolic rate was estimated from average rates of oxygen consumption (\dot{V}_{O_2}) and carbon dioxide production (\dot{V}_{CO_2}) during the collection window using a standard formula³⁹. The metabolic rate during quiet standing was subtracted from gross metabolic rate to obtain the net value attributable to the energetic demands of walking^{2,10,16,22,26}. Net metabolic rate values were then normalized to participant body mass.

Mechanics data and muscle activity from each condition were broken into strides, determined as the period between subsequent heel strikes of a single leg, and an average stride for each participant and condition was obtained. These average strides were used to calculate values of average moment, mechanical power and muscle activity for each participant and condition. Average moment and power values were calculated as the time integral of moment and power time series data divided by stride period. Positive and negative average joint moments and powers were separated out using time integrals of periods of positive or negative moment or power, respectively. Average net power was calculated as the time integral of power over the whole stride period. Average moment and power values were normalized to participant body mass. Average muscle activity was calculated as the time integral of muscle activity divided by stride period. Average muscle activity during additional periods of interest was calculated as the time integral of muscle activity during those periods divided by stride period (for example, early and mid-stance, defined as 0–40% stride, and late stance, defined as 40–60% stride). Muscle activity was normalized to the maximum value observed during normal walking for each muscle and for each participant. For each condition, study-wide average trajectories of lower-limb joint angles, moments and powers were calculated by averaging across participants, used for display purposes in Fig. 2 and Extended Data Figs 3–8.

Statistics. For each condition, means and standard errors of net metabolic rate, average moment, average mechanical power and average muscle activity outcomes were calculated across participants, with standard error indicating inter-participant variability. On the basis of the expectation that user performance would be a non-linear function of exoskeleton stiffness²⁵, we conducted a mixed-model, three-factor ANOVA (random effect: participant; fixed effects: spring stiffness and square of spring stiffness) to test for an effect of spring stiffness across exoskeleton conditions (significance level $\alpha = 0.05$; JMP Pro, SAS). For the primary outcome measure, net metabolic rate, stiffness had a significant effect. We used paired *t*-tests with a Šidák–Holm correction for multiple comparisons⁴⁰ to compare spring conditions with each other and with the 'No Exoskeleton' condition to identify which exoskeleton springs exacted a significant change in metabolic rate. We used a Jarque–Bera two-sided goodness-of-fit test to confirm applicability of tests that assume a normal distribution. For the primary outcome measure, net metabolic rate, we also used a least-squares regression to fit a second-order polynomial (quadratic) function relating mean outcome data to exoskeleton spring stiffness. Additional two-factor ANOVA analyses (random effect: participant; fixed effect: spring stiffness) were performed to test for an effect of spring stiffness across exoskeleton conditions for secondary outcomes in joint mechanics, centre-of-mass mechanics and muscle activity. These results are compiled in Supplementary Table 1.

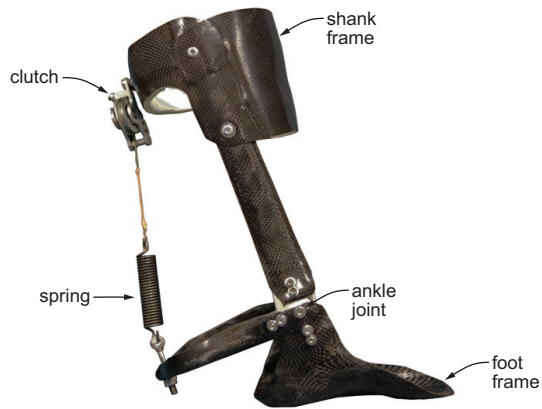
- Wiggin, M. B., Collins, S. H. & Sawicki, G. S. An exoskeleton using controlled energy storage and release to aid ankle propulsion. *Proc. IEEE Int. Conf. Rehabil. Robot.* <http://dx.doi.org/10.1109/ICORR.2011.5975342> (2011).
- Wiggin, M. B., Sawicki, G. S. & Collins, S. H. Apparatus and clutch for using controlled storage and release of mechanical energy to aid locomotion. US patent 2013/0046218 (2013).
- Shamaei, K., Sawicki, G. S. & Dollar, A. M. Estimation of quasi-stiffness and propulsive work of the human ankle in the stance phase of walking. *PLoS ONE* **8**, e59935 (2013).
- Galle, S., Malcolm, P., Derave, W. & De Clercq, D. Adaptation to walking with an exoskeleton that assists ankle extension. *Gait Posture* **38**, 495–499 (2013).
- Winter, D. A. *Biomechanics and Motor Control of Human Movement* Ch. 7 (John Wiley, 2009).
- Farris, D. J. & Sawicki, G. S. Linking the mechanics and energetics of hopping with elastic ankle exoskeletons. *J. Appl. Physiol.* **113**, 1862–1872 (2012).
- Sawicki, G. S. & Ferris, D. P. Mechanics and energetics of level walking with powered ankle exoskeletons. *J. Exp. Biol.* **211**, 1402–1413 (2008).
- Donelan, J. M., Kram, R. & Kuo, A. D. Simultaneous positive and negative external mechanical work in human walking. *J. Biomech.* **35**, 117–124 (2002).
- Brockway, J. M. Derivation of formulae used to calculate energy expenditure in man. *Hum. Nutr. Clin. Nutr.* **41**, 463–471 (1987).
- Glantz, S. A. *Primer of Biostatistics* 65 (McGraw-Hill, 2005).
- Tucker, V. A. The energetic cost of moving about: walking and running are extremely inefficient forms of locomotion. Much greater efficiency is achieved by birds, fish—and bicyclists. *Am. Sci.* **63**, 413–419 (1975).
- Donelan, J. M. et al. Biomechanical energy harvesting: generating electricity during walking with minimal user effort. *Science* **319**, 807–810 (2008).
- Collins, S. H. & Kuo, A. D. Recycling energy to restore impaired ankle function during human walking. *PLoS ONE* **5**, e9307 (2010).



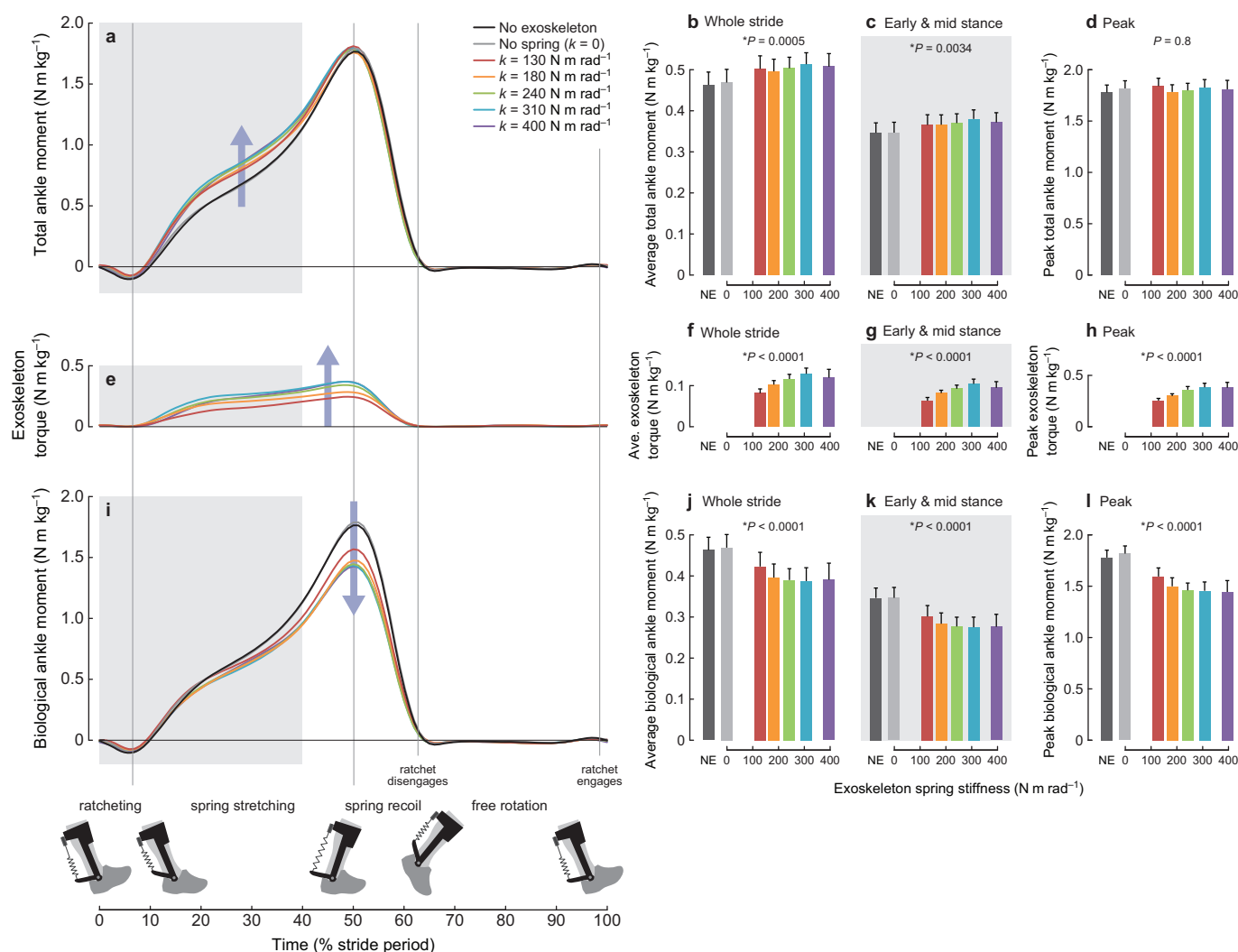
Extended Data Figure 1 | Energy diagrams for human-exoskeleton walking.

Each diagram includes energy inputs, outputs, storage and transfers within the mechanical system, depicted for steady-state walking. In each case, all chemical or electrical energy input is eventually output as heat, since the mechanical energy of the system is constant on average and no useful work is performed on the body or the environment. Energy efficiency, strictly defined, is therefore zero in all cases, and so energy effectiveness or energy economy is instead characterized in terms of 'cost of transport', which is the energy used per unit weight per unit distance travelled⁴¹. **a**, Energy diagram for normal human walking. Muscles consume metabolic energy both to produce mechanical work and to absorb it (and to perform a variety of other functions, such as activating or producing force), and so metabolic energy flows only into the system. Energy loss in muscle manifests as heat. Inside the mechanical system, tendons exchange energy with both the muscle and the body, while kinetic and gravitational potential energy are exchanged within the body segments, all at high mechanical efficiency. Body segment mechanical energy is dissipated only in damping in soft tissues, for example during collisions, which is small (about 3% of the total metabolic energy input²⁰), and in friction from slipping of the feet against the ground, deformation of the ground or air resistance, all of which are negligible under typical conditions. All of these mechanical losses manifest as heat. **b**, Energy diagram for walking with a powered exoskeleton. An additional energy input is provided in the form of, for example, electricity. The total energy input (and corresponding eventual dissipation) of the system can therefore increase, even if a smaller

portion is borne by the human, resulting in poorer overall energy economy. This has been the case with the two powered devices that have reduced the metabolic energy cost of human walking^{2,16}. In theory, overall energy economy could still be improved with a powered device in three ways. First, positive mechanical work from muscles could be replaced by work done by a motor with higher efficiency. Second, negative mechanical work could be replaced by generation done by a motor with higher (than -120%) efficiency, thereby usefully recapturing energy that would otherwise be dissipated as heat. In fact, because muscle expends metabolic energy to absorb mechanical work, it is theoretically possible to simultaneously reduce metabolic rate and capture electrical energy with zero electrical input⁴², although this has yet to be demonstrated in practice. Third, the powered device could approximate an unpowered device, with negligible amounts of electricity used only to control the timing of mechanical elements such as clutches⁴³. **c**, Energy diagram for walking with an unpowered exoskeleton. No additional energy supply is provided; so, unlike the powered case, the only way to decrease metabolic energy use is to reduce total system energy dissipation, or, equivalently, to improve the energy economy of the system as a whole. Note that the only difference from normal human walking, in terms of energy flow, is the addition of elements such as springs that store and transfer mechanical energy within the system. In this sense, reducing metabolic rate with a passive exoskeleton is akin to changing the person's morphology such that it is more energy-effective at locomotion.

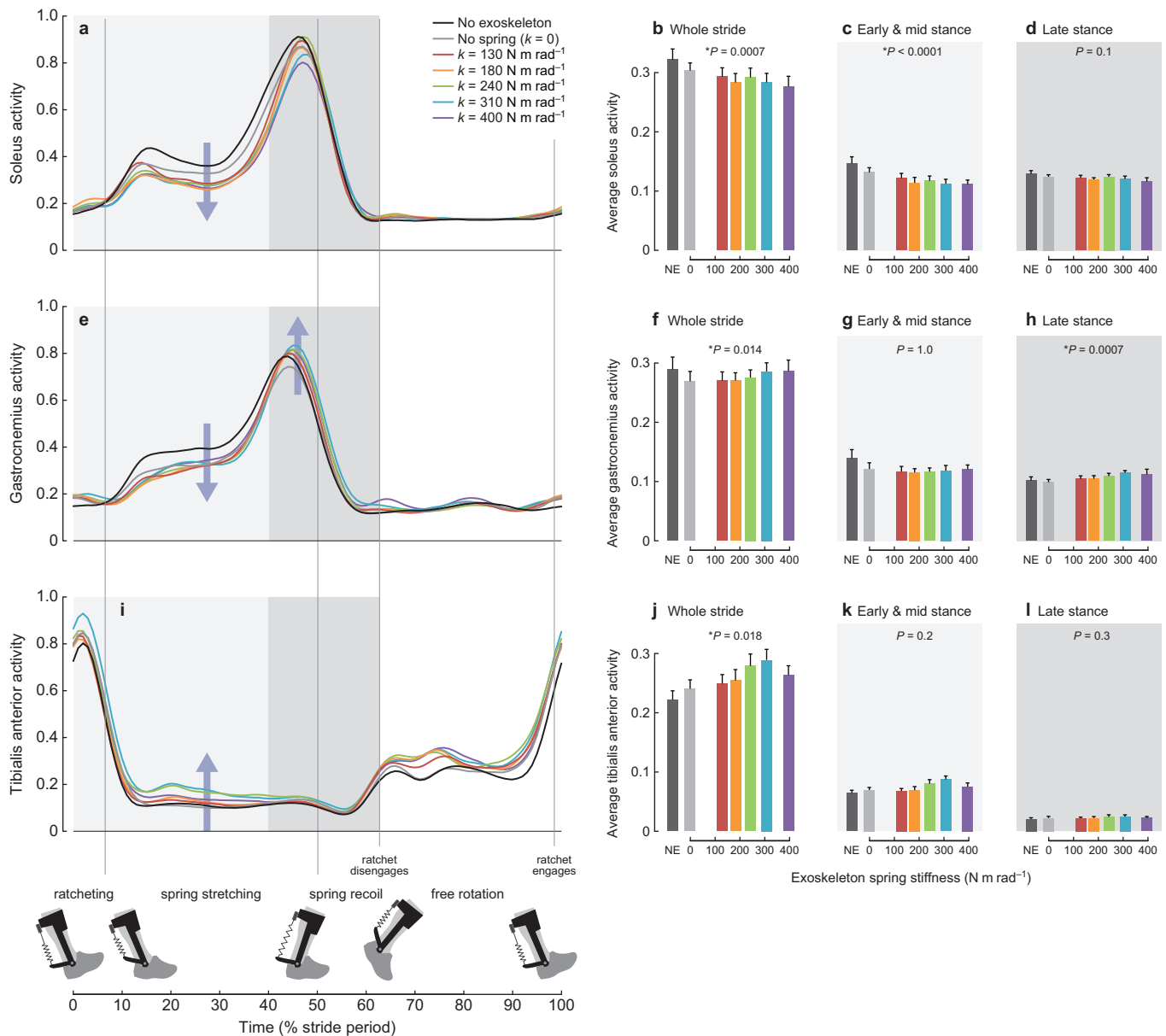


Extended Data Figure 2 | Exoskeleton frame design. A rigid carbon fibre shank frame and foot frame were custom-made for each participant. The shank section clamps onto the user's lower leg just below the knee and connects to the foot frame through a rotary joint at the ankle. The foot frame includes a lever arm protruding to the rear of the heel, to which the parallel spring is connected. The clutch is mounted to the shank frame posterior to the calf muscles.



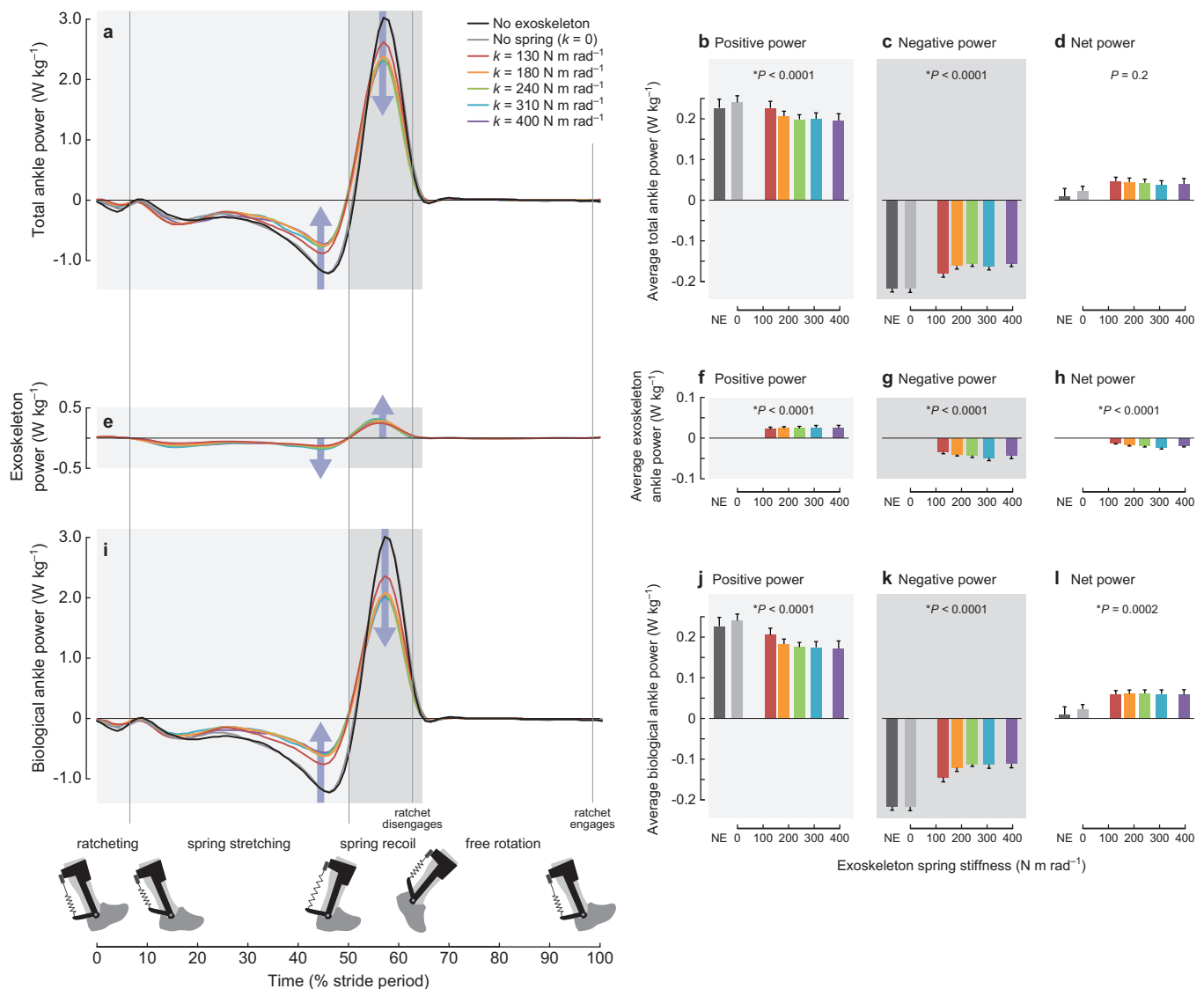
Extended Data Figure 3 | Ankle moment contributions. **a**, Total ankle moment, measured using a motion capture system. Average total ankle moment (**b**) during the entire stride and (**c**) during early and mid-stance, defined as 0–40% stride, and (**d**) peak ankle moment. All spring conditions increased average total joint moment slightly during early stance, but peak total joint moment was maintained across conditions. **e**, Exoskeleton torque contribution, as measured using onboard sensors. Average exoskeleton torque (**f**) during the entire stride and (**g**) during early and mid-stance, defined as 0–40% stride, and (**h**) peak exoskeleton torque. Average and peak

exoskeleton torque increased with increasing exoskeleton spring stiffness, except with the highest stiffness spring. **i**, Biological contributions to ankle moment, calculated as the subtraction of the exoskeleton moment from the total moment. Average biological ankle moment (**j**) during the entire stride and (**k**) during early and mid-stance, defined as 0–40% stride, and (**l**) peak ankle moment. Ankle moments arising from muscle activity decreased with increasing exoskeleton spring stiffness, but with diminishing returns at high spring stiffness. $N = 9$; bars, mean; error bars, s.e.m.; P values, two-factor ANOVA (random effect: participant; fixed effect: spring stiffness).



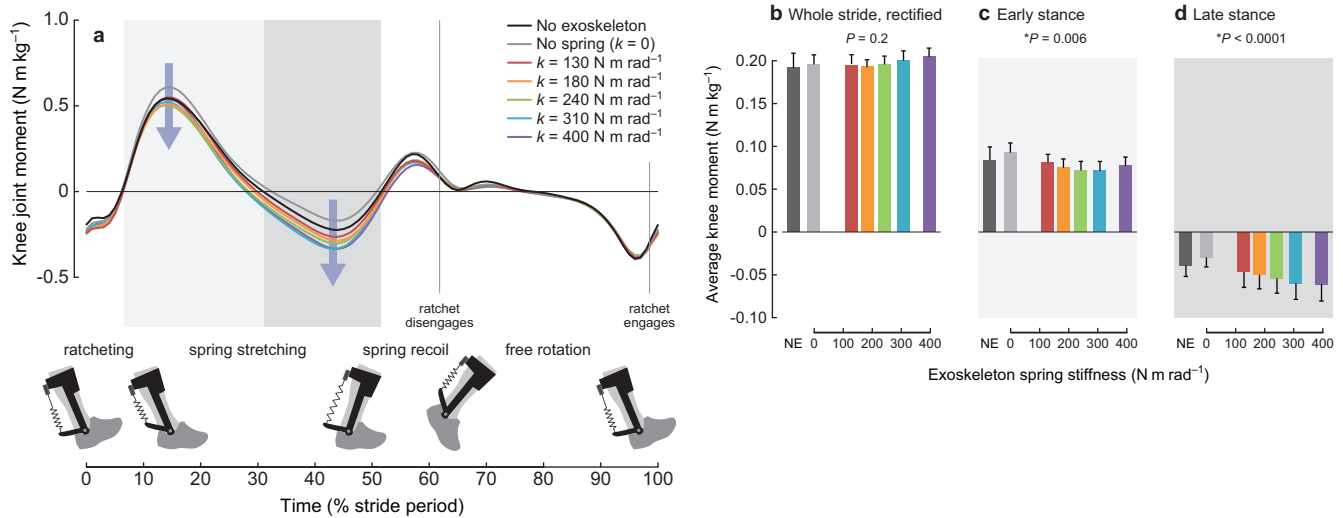
Extended Data Figure 4 | Ankle muscle activity. **a**, Activity in the soleus, a mono-articular muscle group that acts to plantarflex the ankle. Average soleus activity over **(b)** the whole stride, **(c)** early and mid-stance, defined as 0–40% stride, and **(d)** late stance, defined as 40–60% stride. Soleus activity decreased with increasing spring stiffness. **e**, Activity in the gastrocnemius, a biarticular muscle group that acts to plantarflex the ankle and flex the knee. Average gastrocnemius activity over **(f)** the whole stride, **(g)** early and mid-stance, defined as 0–40% stride, and **(h)** late stance, defined as 40–60% stride. Gastrocnemius activity was reduced compared with the ‘No Exoskeleton’ condition during early and mid-stance, but increased with

increasing spring stiffness during late stance. **i**, Activity in the tibialis anterior, a mono-articular muscle group that acts to dorsiflex the ankle. Average tibialis anterior activity over **(j)** the whole stride, **(k)** early and mid-stance, defined as 0–40% stride, and **(l)** late stance, defined as 40–60% stride. Tibialis anterior activity seemed to increase during early and mid-stance, and was unchanged during late stance. All values were measured using electromyography and normalized to maximum activity during normal walking. $N = 8$; bars, mean; error bars, s.e.m.; P values, two-factor ANOVA (random effect: participant; fixed effect: spring stiffness).



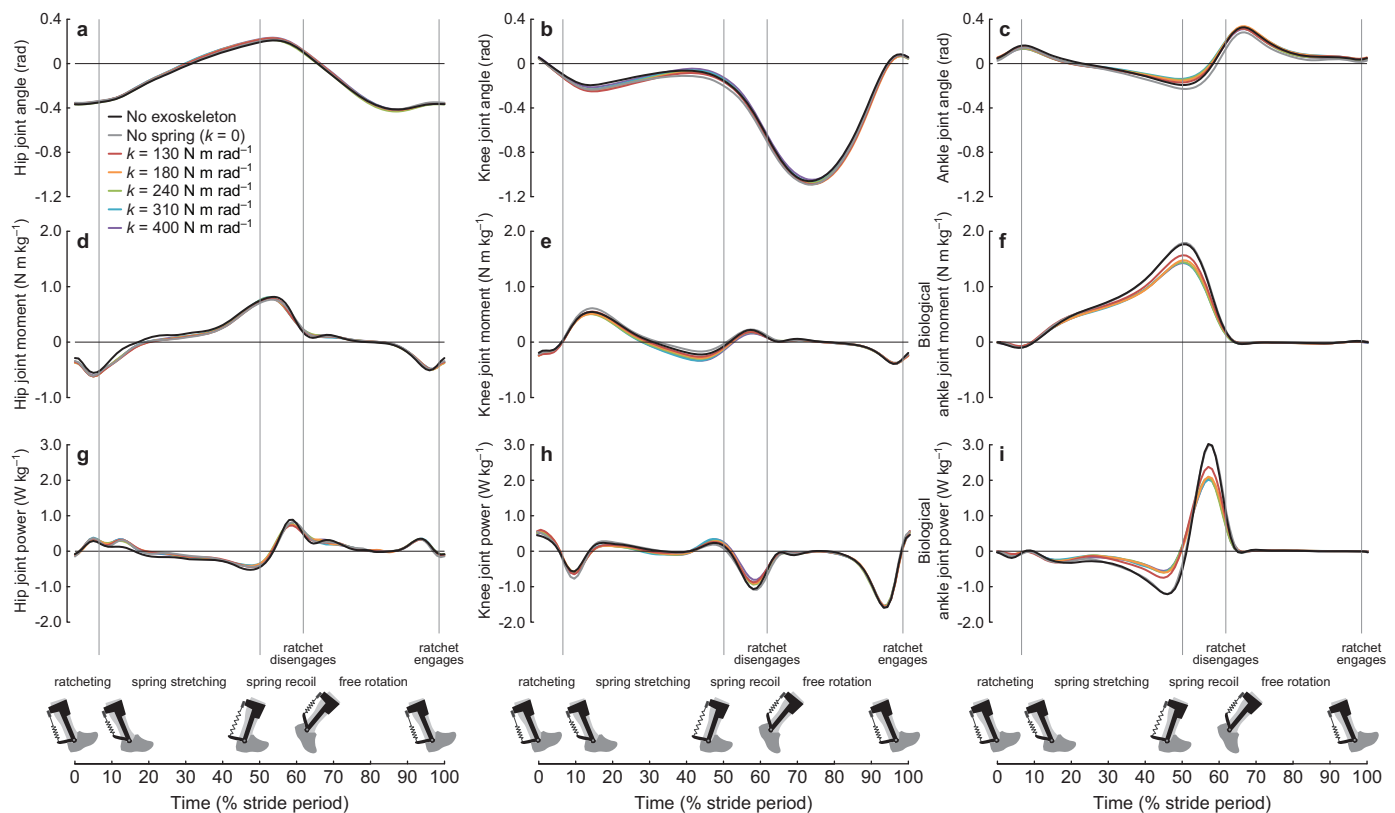
Extended Data Figure 5 | Ankle power contributions. **a**, Mechanical power of the combined human–exoskeleton system, measured using a motion capture system, **(b)** average positive power, defined as positive work divided by stride time, **(c)** average negative power, defined as negative work divided by stride time, and **(d)** average net power, equivalent to average power, defined as the sum of positive and negative work divided by stride time. Total positive ankle joint power decreased with increasing stiffness, while net joint power increased. **e**, Exoskeleton power, measured using onboard sensors for torque and motion capture for joint velocity, **(f)** average positive exoskeleton

power, **(g)** average negative exoskeleton power and **(h)** average net exoskeleton power. Net exoskeleton power was always negative. **i**, Biological ankle power, defined as the subtraction of exoskeleton power from total ankle power, **(j)** average positive biological power, **(k)** average negative biological power and **(l)** average net biological power. Net biological power increased with the exoskeleton compared with normal walking. $N = 9$; bars, mean; error bars, s.e.m.; P values, two-factor ANOVA (random effect: participant; fixed effect: spring stiffness).



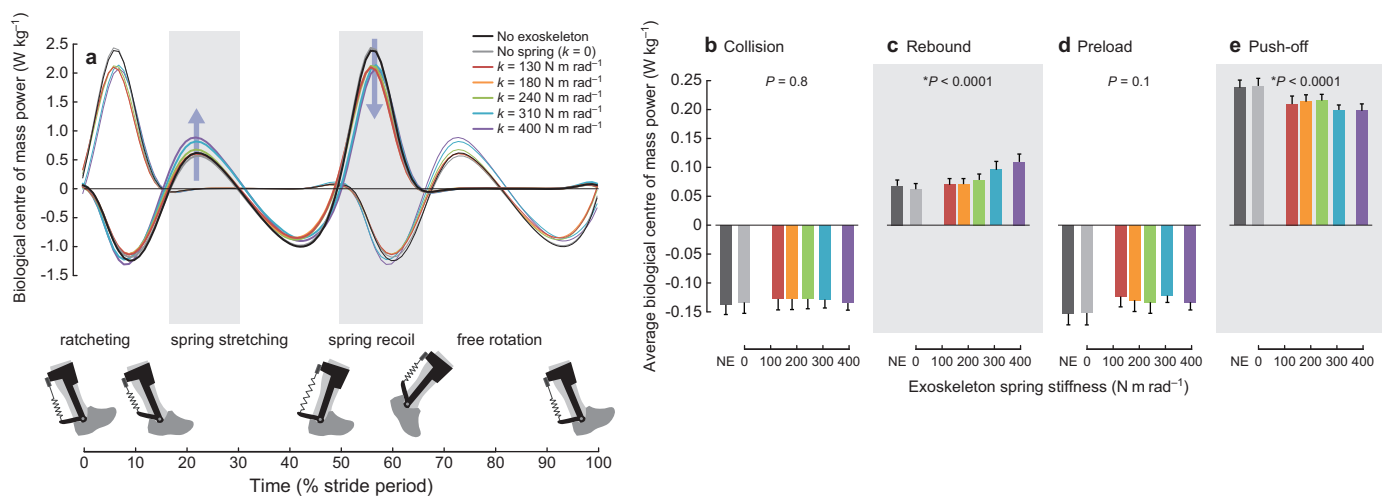
Extended Data Figure 6 | Knee moment. **a**, Knee moment in time as measured by motion capture, **(b)** average absolute knee moment over the entire stride, **(c)** average knee moment during early stance, defined as the positive impulse within approximately 10–30% stride divided by stride period, and **(d)** average knee moment during late stance, defined as the negative impulse

within approximately 30–50% stride divided by stride period. Average knee moment during late stance increased in magnitude with the highest stiffness springs. Positive values denote knee extension. $N = 9$; bars, mean; error bars, s.e.m.; P values, two-factor ANOVA (random effect: participant; fixed effect: spring stiffness).



Extended Data Figure 7 | Hip, knee and ankle joint mechanics. Joint angles, moments and powers are presented at the same scale to facilitate comparisons across joints. **a**, Hip joint angle, **(b)** knee joint angle and **(c)** ankle joint angle. Joint angle trajectories did not appear to change substantially across conditions. **d**, Hip moment, **(e)** knee moment and **(f)** biological component of ankle moment. Hip moment did not appear to change substantially across conditions, while knee moment and ankle moment showed trends detailed in

Extended Data Figs 6 and 3, respectively. **g**, Hip joint power, **(h)** knee joint power and **(i)** the biological component of ankle joint power. Hip and knee power did not appear to change substantially across conditions, while biological ankle power showed trends detailed in Extended Data Fig. 5. Positive values denote hip extension, knee extension and ankle plantarflexion with respect to standing posture. $N = 9$.



Extended Data Figure 8 | Centre-of-mass mechanics. **a**, The biological contribution to centre-of-mass power for each individual limb, defined as the dot product of ground reaction force with centre-of-mass velocity, both determined from force plate data, minus the ankle exoskeleton power.

b, Average collision power, defined as the negative work performed during the first half of stance divided by stride time. **c**, Average rebound power, defined as the positive work performed during mid-stance divided by stride time.

d, Average preload power, defined as the negative work performed during mid-stance divided by stride time. **e**, Average push-off power, defined as the positive work performed during late stance divided by stride time. With increasing spring stiffness, the human contribution to push-off work decreased, while the human contribution to rebound work increased substantially. $N = 9$; thin lines, contralateral limb; bars, mean; error bars, s.e.m.; P values, two-factor ANOVA (random effect: participant; fixed effect: spring stiffness).

Extended Data Table 1 | Passive ankle exoskeleton mass by component

Segment	US Size 8	US Size 13
Carbon Fiber Foot Section	130 g	160 g
Aluminum Ankle Joints (x2)	40 g	40 g
Carbon Fiber Shank Section	105 g	170 g
Frame Mass	275 g	370 g
Average Spring	76 g	76 g
Mechanical Clutch	57 g	57 g
Total Mass	408 g	503 g

Extended Data Table 2 | Comparison of ankle exoskeleton masses

Author	Mass of Exoskeleton (per leg)
Mooney <i>et al.</i> ¹⁶	2,000 g
Sawicki <i>et al.</i> ³⁷	1,210 g*
Malcolm <i>et al.</i> ²	760 g*
Passive Elastic (US size 13)	503 g
Passive Elastic (US size 8)	408 g

*Does not include tethered hardware.

Drug-based modulation of endogenous stem cells promotes functional remyelination *in vivo*

Fadi J. Najm¹, Mayur Madhavan¹, Anita Zaremba², Elizabeth Shick¹, Robert T. Karl¹, Daniel C. Factor¹, Tyler E. Miller^{1,3,4}, Zachary S. Nevin¹, Christopher Kantor², Alex Sargent², Kevin L. Quick⁵, Daniela M. Schlatter⁶, Hong Tang⁷, Ruben Papoian^{7†}, Kyle R. Brimacombe⁸, Min Shen⁸, Matthew B. Boxer⁸, Ajit Jadhav⁸, Andrew P. Robinson⁹, Joseph R. Podojil⁹, Stephen D. Miller⁹, Robert H. Miller^{2†} & Paul J. Tesar^{1,2}

Multiple sclerosis involves an aberrant autoimmune response and progressive failure of remyelination in the central nervous system. Prevention of neural degeneration and subsequent disability requires remyelination through the generation of new oligodendrocytes, but current treatments exclusively target the immune system. Oligodendrocyte progenitor cells are stem cells in the central nervous system and the principal source of myelinating oligodendrocytes¹. These cells are abundant in demyelinated regions of patients with multiple sclerosis, yet fail to differentiate, thereby representing a cellular target for pharmacological intervention². To discover therapeutic compounds for enhancing myelination from endogenous oligodendrocyte progenitor cells, we screened a library of bioactive small molecules on mouse pluripotent epiblast stem-cell-derived oligodendrocyte progenitor cells^{3–5}. Here we show seven drugs function at nanomolar doses selectively to enhance the generation of mature oligodendrocytes from progenitor cells *in vitro*. Two drugs, miconazole and clobetasol, are effective in promoting precocious myelination in organotypic cerebellar slice cultures, and *in vivo* in early postnatal mouse pups. Systemic delivery of each of the two drugs significantly increases the number of new oligodendrocytes and enhances remyelination in a lysolecithin-induced mouse model of focal demyelination. Administering each of the two drugs at the peak of disease in an experimental autoimmune encephalomyelitis mouse model of chronic progressive multiple sclerosis results in striking reversal of disease severity. Immune response assays show that miconazole functions directly as a remyelinating drug with no effect on the immune system, whereas clobetasol is a potent immunosuppressant as well as a remyelinating agent. Mechanistic studies show that miconazole and clobetasol function in oligodendrocyte progenitor cells through mitogen-activated protein kinase and glucocorticoid receptor signalling, respectively. Furthermore, both drugs enhance the generation of human oligodendrocytes from human oligodendrocyte progenitor cells *in vitro*. Collectively, our results provide a rationale for testing miconazole and clobetasol, or structurally modified derivatives, to enhance remyelination in patients.

As repair of damaged myelin may provide therapeutic benefit in multiple sclerosis (MS) and other demyelinating disorders^{6–12}, we set out to identify drugs that could be re-purposed as remyelinating therapeutics. We selected the US National Institutes of Health (NIH) Clinical Collection I and II libraries comprising 727 drugs with a history of safe use in clinical trials, to test for maturation of oligodendrocyte progenitor cell (OPCs) into myelinating oligodendrocytes.

Using mouse epiblast stem cell (EpiSC)-derived OPCs, we developed an *in vitro* phenotypic screen that accurately quantified differentiation into mature oligodendrocytes by high content imaging of myelin protein expression (Fig. 1a).

Two batches (>100 million cells each) of pure OPCs were generated from independent mouse pluripotent EpiSC lines of opposite sex (Extended Data Fig. 1a). EpiSC-derived OPCs shared virtually all defining molecular and cellular properties, including gene expression profiles with *in vivo* isolated OPCs, but provided the key advantage of being highly scalable (Extended Data Fig. 1b)³. For *in vitro* screening, the seeding density, endpoint assays, and dimethylsulphoxide (DMSO) (vehicle) tolerance were optimized in pilot studies to assure accurate and reproducible measurement of OPC differentiation in a 96-well format (Extended Data Fig. 1c).

For the primary screen, OPCs were treated with vehicle alone (0.05% (v/v) DMSO) as a negative control, thyroid hormone (a known OPC differentiation inducer) as a positive control¹³, or drug dissolved in DMSO at a concentration of 5 μ M. After 72 h, cells were fixed and labelled with antibodies to myelin basic protein (MBP) and the length and intensity of MBP labelled oligodendrocyte processes measured (Fig. 1a). These features were reliable indicators of alteration in cellular phenotype, as indicated by consistency and high signal to background ratio of positive and vehicle controls across all screening plates (Extended Data Fig. 1d–g). We then normalized the experimental data for the tested drugs against thyroid hormone (set value of 100) on a per plate basis. On the basis of this analysis, we identified the 22 drugs that enhanced oligodendrocyte formation greater than five standard deviations above DMSO treatment and outperformed thyroid hormone in the measured parameters (Fig. 1b). Notably, one of the top 22 drugs was benztropine, a muscarinic receptor antagonist recently shown to induce OPC differentiation and remyelination^{8,9}.

To validate and prioritize the 22 drug hits, the assay was repeated using alternative OPCs, reagents, and parameters to eliminate screen-specific artefacts (see Methods). Drugs were ranked by their dose-dependent ability to induce oligodendrocyte generation from OPCs without toxicity (Extended Data Fig. 2a). To demonstrate reproducibility, an independent laboratory tested selected drug hits using distinct equipment, plate format (1,536-well), personnel, and imaging/analysis scripts (see Methods). Of the 16 hits tested at the external screening site, 14 were validated as potent inducers of oligodendrocyte differentiation (Extended Data Fig. 2a, b).

We next tested whether the drug hits could promote the maturation of native OPCs in central nervous system (CNS) tissue. Cerebellar

¹Department of Genetics and Genome Sciences, Case Western Reserve University School of Medicine, Cleveland, Ohio 44106, USA. ²Department of Neurosciences, Case Western Reserve University School of Medicine, Cleveland, Ohio 44106, USA. ³Department of Pathology, Case Western Reserve University School of Medicine, Cleveland, Ohio 44106, USA. ⁴Department of Stem Cell Biology and Regenerative Medicine, Lerner Research Institute, Cleveland Clinic, Cleveland, Ohio 44195, USA. ⁵PerkinElmer, 940 Winter Street, Waltham, Massachusetts 02451, USA. ⁶Center for Proteomics and Bioinformatics, Case Western Reserve University School of Medicine, Cleveland, Ohio 44106, USA. ⁷Drug Discovery Center, University of Cincinnati College of Medicine, Cincinnati, Ohio 45237, USA. ⁸National Center for Advancing Translational Sciences, National Institutes of Health, 9800 Medical Center Drive, Rockville, Maryland 20850, USA. ⁹Department of Microbiology-Immunology and Interdepartmental Immunobiology Center, Feinberg School of Medicine, Northwestern University, 303 E. Chicago Avenue, Chicago, Illinois 60611, USA. †Present addresses: Department of Neurology & Rehabilitation Medicine, University of Cincinnati College of Medicine, Cincinnati, Ohio 45229, USA (R.P.); Department of Anatomy & Regenerative Biology, George Washington University School of Medicine and Health Sciences, Washington DC 20037, USA (R.H.M.).

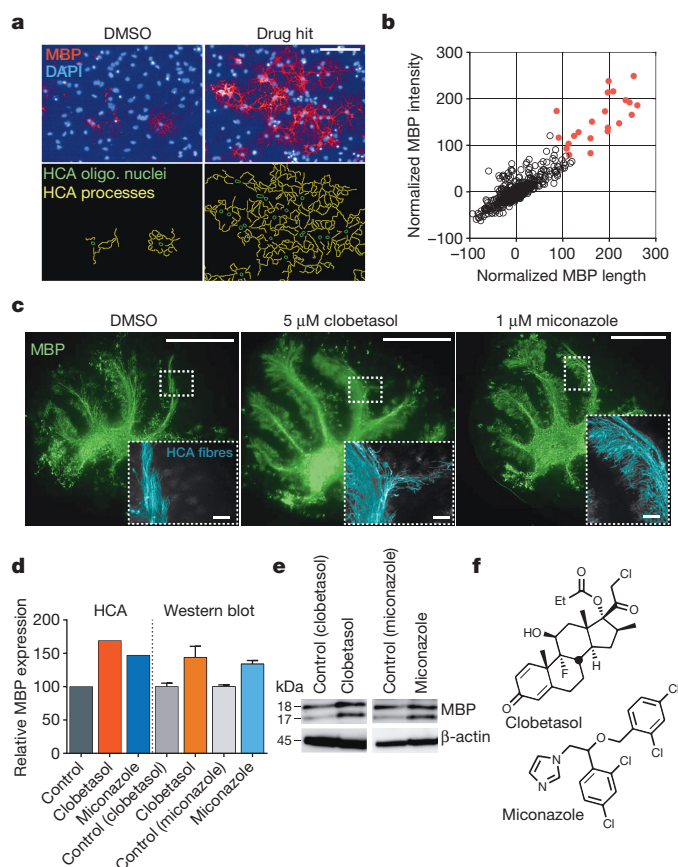


Figure 1 | A pluripotent stem-cell-based phenotypic screening platform to identify modulators of OPC differentiation and maturation.

a, Representative images of vehicle- and drug-hit-treated mouse EpiSC-derived OPCs from the primary screen. Nuclear (DAPI (4',6-diamidino-2-phenylindole), blue) and MBP (red) staining along with HCA to identify oligodendrocyte (oligo.) nuclei (green) and MBP⁺ processes (yellow). Scale bar, 100 μ m. **b**, Scatter plot of primary screen results displayed as normalized values of MBP process length and intensity for all 727 drugs with the 22 hits marked in red. Baseline (vehicle) was set at zero and thyroid hormone (positive control) was set at 100. **c**, Montaged images of whole postnatal day 7 mouse cerebellar slices treated with drug or vehicle for 5 days and stained for MBP (green). Insets show a representative example of the HCA script used to identify and quantify MBP⁺-aligned fibres (light blue). Scale bars, 1 mm for whole slices and 100 μ m for insets. **d**, Relative quantification of HCA and western blot data from cerebellar slices treated for 5 days. For HCA screen, $n = 1$ with 6–12 slices averaged per group (also see Extended Data Fig. 2a). For western blot, $n = 3$ independent replicates of 12 slices per group. Values are mean for HCA and mean \pm s.e.m. for western blot. **e**, Representative western blot of MBP isoforms and β -actin (loading control) of cerebellar slices treated for 5 days. Full blots are available in Supplementary Fig. 1. **f**, Chemical structures of clobetasol and miconazole. Source data are provided for Fig. 1b, d.

slices were generated from mice at postnatal day 7—a time that precedes widespread myelination—and treated *ex vivo* with drug or DMSO (vehicle) for 5 days and labelled with anti-MBP antibodies (Fig. 1c)^{6,7}. We screened 11 of the top drugs and used a high content analysis (HCA) algorithm developed in house to rank them on the basis of their ability to increase the extent of MBP⁺ aligned fibres in whole cerebellar slices. The 'high' performing group consisted of four drugs that increased the number of MBP⁺ aligned fibres $\sim 150\%$ or greater (Fig. 1d and Extended Data Fig. 2a). We validated the accuracy of our high content screen by semi-quantitative western blotting of MBP protein isoforms in independent slice culture experiments (Fig. 1d, e)^{14,15}.

Analysis of structure–activity relationships revealed that the top hits from the primary screen segregated into two specific classes containing

either a 1,3-diazole with mono-substitution at the 1-position or a sterane base structure (Extended Data Fig. 3a–d). We selected miconazole and clobetasol, the top overall performing hits in each of the imidazole and sterane classes respectively, for further mechanistic and functional testing after confirming that both drugs readily crossed the blood–brain barrier in mice (Fig. 1f, Extended Data Fig. 2a and Supplementary Table 1). Miconazole is a topical antifungal agent functioning through cytochrome P450 inhibition, and clobetasol is a potent topical corticosteroid, but their functions in OPCs were unknown.

To test whether miconazole or clobetasol enhance remyelination *in vivo*, we used a toxin-induced model whereby focal demyelinated lesions are generated in dorsal white matter of the spinal cord of adult mice by localized injection of lyssolecithin (lysophosphatidylcholine (LPC)). In lesioned animals, demyelination is complete within 4 days, after which OPCs are recruited into the lesion. Widespread remyelination does not normally start until 14–21 days post lesion (d.p.l.), which provides a defined window from days 4 to 14 to test the efficacy of drugs to enhance the extent and rate of remyelination¹⁶. Both miconazole (10 or 40 mg per kg (body weight)) and clobetasol (2 mg per kg) treatment induced a marked improvement within the lesions of treated mice compared with vehicle-treated controls. At 8 d.p.l. both drugs induced a significant increase in the number of newly generated CC1⁺ oligodendrocytes in the lesion core (Fig. 2a, b). This was coincident with extensive MBP staining in the lesions of miconazole- and clobetasol- but not vehicle-treated animals at both 8 and 12 d.p.l. (Fig. 2a). Electron micrographs and tissue sections stained with toluidine blue demonstrated that miconazole and clobetasol each induced a striking increase in the extent of remyelination (Fig. 2c, d and Extended Data Fig. 4a, b). At 12 d.p.l., lesions of vehicle-treated mice consisted mostly of unmyelinated axons (6% myelinated) while those of clobetasol- and miconazole-treated mice contained $>70\%$ remyelinated axons throughout the extent of the lesion (Fig. 2d). Analysis of myelin thickness relative to axon diameter (g ratio) at 12 d.p.l. revealed that miconazole- and clobetasol-induced myelin was thinner than intact myelin, a defining characteristic of remyelination (Fig. 2d).

We also evaluated whether miconazole or clobetasol could promote precocious myelination during development, in the absence of injury or disease. We treated mice at postnatal day 2—a time point that precedes widespread CNS myelination—daily for 4 days with drug or vehicle. In miconazole- and clobetasol-treated mice, we found a significant increase in the number of CC1⁺ oligodendrocytes in the lateral corpus callosum compared with vehicle-treated mice (Extended Data Fig. 5a). Additionally, we found a significantly larger portion of the corpus callosum was populated by MBP⁺ fibre tracts in miconazole- and clobetasol-treated mice (Extended Data Fig. 5b). This suggests that clobetasol and miconazole enhance myelination in the absence of damage or disease. Collectively, the LPC demyelination and developmental mouse models demonstrate that miconazole and clobetasol each function to induce the differentiation of endogenous OPCs in the CNS and promote enhanced myelination.

To determine whether the drugs were working at a particular stage of the OPC differentiation process, we seeded OPCs in differentiation conditions and treated them with either miconazole or clobetasol at different time points (0, 16, 24, or 48 h), and assayed MBP expression at 72 h. For both miconazole and clobetasol, the number of MBP⁺ oligodendrocytes present at 72 h was dependent on drug treatment within the first 24 h of differentiation (Fig. 3a). In agreement with these data, treatment of differentiating OPCs with either drug for different durations (24, 48, 56, and 72 h) induced a progressive, time-dependent increase in the number of MBP⁺ oligodendrocytes (Fig. 3b). These data suggest that both drugs function directly on OPCs early in the differentiation process. Additionally, neither drug showed a significant impact on astrocyte formation from OPCs *in vitro*, suggesting they probably function as direct inducers of oligodendrocyte differentiation (Fig. 3c).

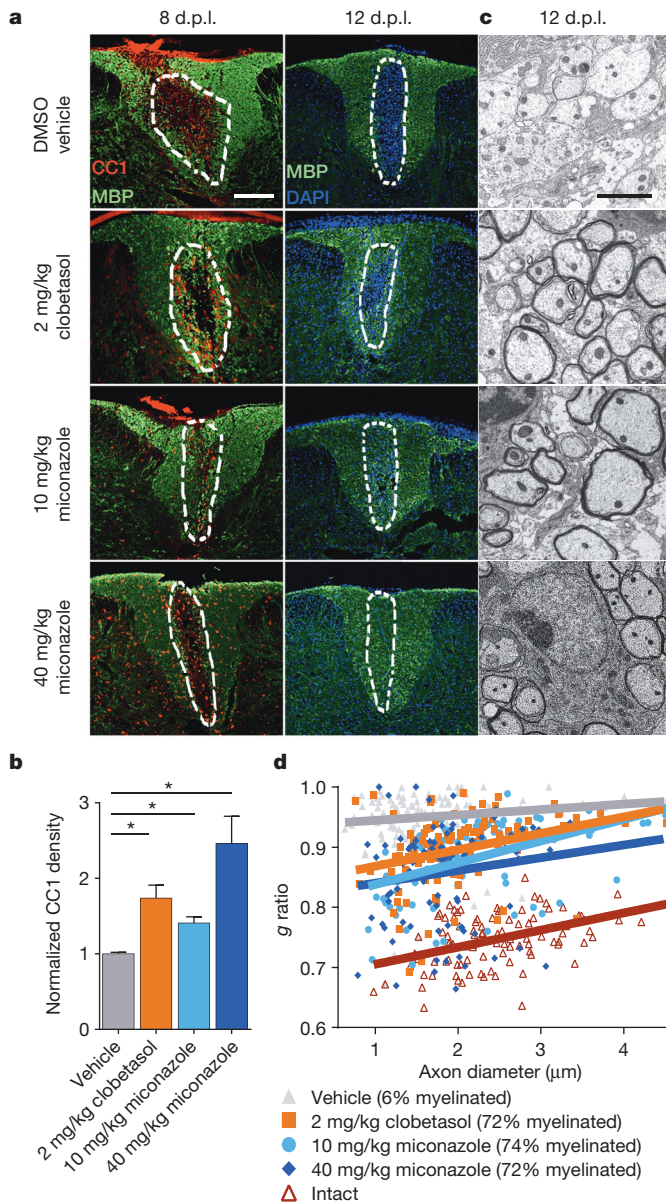


Figure 2 | Miconazole and clobetasol each enhance remyelination in the LPC lesion mouse model. **a**, Representative immunohistochemical images of treated mice showing newly generated oligodendrocytes (CC1, red) and MBP (green) within the lesion (approximated by white dashed outline) at eight and 12 d.p.i. Scale bar, 200 μm . **b**, Quantification of CC1⁺ oligodendrocytes per lesion area at 8 d.p.i. Values are mean \pm s.e.m.; $n = 3$ mice per group. Two-tailed t -test, $*P < 0.05$. **c**, Representative electron micrographs showing remyelinated axons within lesions of drug-treated mice at 12 d.p.i. Scale bar, 2 μm . **d**, Scatter plot of g ratios of lesion axons at 12 d.p.i.; $n = 100$ calculated from two mice per group compared to wild-type intact axons. Percentage of lesion axons myelinated is indicated in the legend. Source data are provided for Fig. 2b, d.

Muscarinic receptor antagonists such as benztropine and clemastine have recently been identified as remyelinating agents^{8,9}. Therefore we tested whether miconazole or clobetasol function through the muscarinic acetylcholine pathway using functional cellular reporter assays of all muscarinic receptor subtypes (M1–M5). Neither miconazole nor clobetasol inhibited any of the five muscarinic receptor subtypes (Fig. 3d). We then profiled whether clobetasol or miconazole biochemically inhibited the activity of 414 different kinase isoforms. Neither clobetasol nor miconazole inhibited any of the kinases tested, suggesting their activity is not based on direct inhibition of protein kinases (Supplementary Table 2).

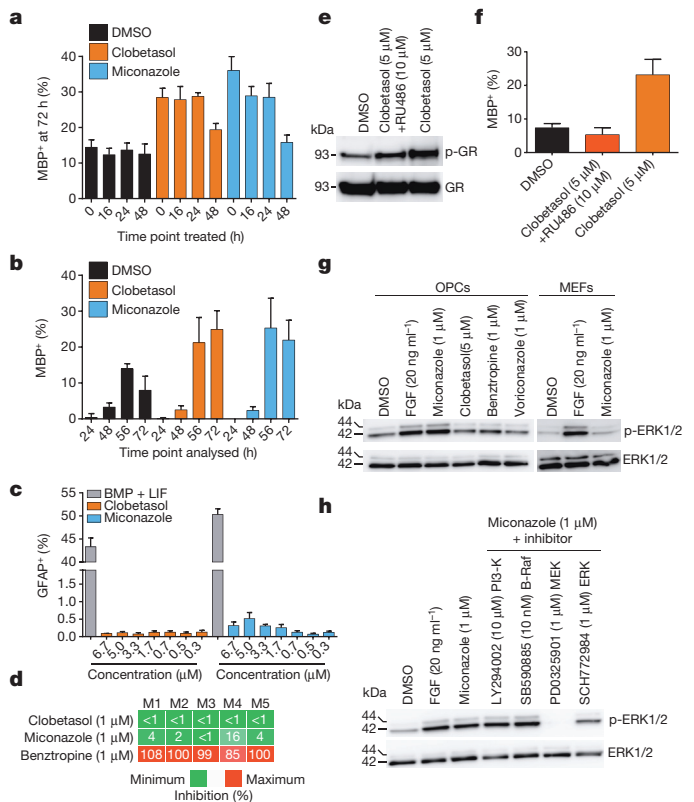


Figure 3 | Cellular and molecular effects of miconazole and clobetasol on mouse OPCs. **a**, Percentage MBP⁺ oligodendrocytes generated from OPCs at 72 h with treatments initiated at time points indicated; $n = 6$ wells per condition with $>6,000$ cells scored per well. **b**, Percentage MBP⁺ oligodendrocytes generated from OPCs treated simultaneously and analysed at time points indicated; $n = 8$ wells per condition with $>1,700$ cells scored per well. **c**, Percentage GFAP⁺ astrocytes generated from OPCs at 72 h of treatment; $n = 4$ wells per condition $>2,900$ cells scored per well. **d**, Heat map depicting biochemical inhibition of muscarinic receptors M1–M5 displayed as percentage inhibition with minimum (green) and maximum (red). **e**, Western blot of total glucocorticoid receptor and its phosphorylation at Ser220 (p-GR) in OPCs treated for 1 h. **f**, Percentage MBP⁺ oligodendrocytes generated from OPCs 72 h after treatment; $n = 6$ wells per condition with $>1,400$ cells scored per well. **g**, Western blot of total ERK1/2 and their phosphorylation at Thr202/Tyr204 or Thr185/Tyr187 (p-ERK1/2) in cells (OPCs or mouse embryonic fibroblasts) treated for 1 h. FGF served as a positive control for p-ERK1/2 induction. **h**, Western blot of total ERK1/2 and p-ERK1/2 in OPCs treated for 1 h in the presence of the indicated pathway inhibitors. All graphs depict mean \pm s.e.m. Full western blots are available in Supplementary Fig. 2. Source data are provided for Fig. 3a–d, f.

To explore the signalling pathways in OPCs influenced by these drugs, we performed genome-wide RNA sequencing and phosphoproteomic analyses on mouse OPCs treated with drug or vehicle (Extended Data Fig. 6a–c and Supplementary Table 3). Miconazole or clobetasol treatment altered OPC transcript expression and phosphoproteins within hours, and influenced expression of genes in signalling pathways involved in oligodendrocyte maturation and myelination. Clobetasol potentially modulated genes downstream of multiple nuclear hormone receptors, including glucocorticoid receptor, which are known to be important regulators of myelin gene expression^{13,17}. Since glucocorticoid receptor signalling is also known to enhance Schwann-cell-mediated myelination in the peripheral nervous system¹⁸, we tested whether the activity of clobetasol on OPCs was mediated by glucocorticoid receptor signalling. Treatment of OPCs with clobetasol for 1 h increased the phosphorylation of glucocorticoid receptor at Ser220, an activating post-translational modification (Fig. 3e). RU486, a competitive glucocorticoid receptor

antagonist, blocked clobetasol-induced glucocorticoid receptor phosphorylation and oligodendrocyte differentiation (Fig. 3e, f) suggesting that the activity of clobetasol in OPCs is mediated through the glucocorticoid receptor signalling axis.

For miconazole, pathway analyses showed that proteins in the mitogen-activated protein (MAP) kinase pathway were most strongly affected (Extended Data Fig. 7a, b and Supplementary Table 3). Most prominent was the strong and sustained phosphorylation of both extracellular signal-regulated kinases ERK1 and ERK2 (ERK1/2) at canonical activation sites, which we validated by western blotting (Fig. 3g). In mice, genetic loss of ERK1/2 in the oligodendrocyte lineage results in normal numbers of OPCs and oligodendrocytes but widespread hypomyelination, while constitutive activation of ERK1/2 results in a profound increase in the extent of remyelination after toxin-induced demyelinating injury^{19,20}. In contrast to miconazole, treatment of OPCs with clobetasol or benzotropine did not induce ERK1/2 phosphorylation (Fig. 3g). Miconazole treatment of a non-neural cell type, mouse fibroblasts, also showed no increase of ERK1/2 phosphorylation, indicating potential cell-type specificity (Fig. 3g). PD0325901, a small molecule inhibitor of ERK's upstream MAP-kinase kinase (MEK), blocked the ability of miconazole to induce ERK1/2 phosphorylation, suggesting that miconazole functions through a MEK-dependent mechanism in OPCs (Fig. 3h). We also treated mouse OPCs with voriconazole, a triazole-containing antifungal cytochrome P450 inhibitor with 80% structural similarity to miconazole, which failed to induce changes in ERK1/2 phosphorylation (Fig. 3g). This was consistent with the observation that voriconazole did not promote the differentiation of OPCs into oligodendrocytes (Extended Data Fig. 7c). Taken together, these results suggest that the effect of miconazole on OPCs is independent of cytochrome P450 inhibition.

We then assessed whether clobetasol and miconazole treatment would enhance the differentiation of human OPCs into oligodendrocytes. We generated human OPCs from human embryonic stem cells (hESCs) and human-induced pluripotent stem cells (hiPSCs) (Extended Data Fig. 8a–c)^{21,22}. We then treated human OPCs with DMSO, clobetasol, or miconazole for 21 days followed by staining for MBP, imaging, and HCA (Extended Data Fig. 8d–g). Both drugs enhanced human OPC differentiation, with miconazole exhibiting the most reproducible and potent effects.

To interpret the potential impact of clobetasol or miconazole as therapeutics in immune-mediated MS models, we tested effects on immune cell survival and function. We found that only clobetasol, as expected from its known corticosteroid properties, altered naive T-cell differentiation and both the proliferation and secretion of cytokines by proteolipid protein (PLP_{139–151})- or myelin oligodendrocyte glycoprotein (MOG_{35–55})-sensitized lymph node cells (Extended Data Fig. 9a–j). As such, only clobetasol, but not the solely remyelinating drugs miconazole or benzotropine, showed efficacy in reducing disease severity in the immune-driven relapsing–remitting PLP_{139–151} experimental autoimmune encephalomyelitis (EAE) model (Fig. 4a). The positive effect of clobetasol in this model resulted from its immunosuppressive effects as evidenced by the severe reduction of T cells within the spleen (Fig. 4b).

We also used a second EAE mouse model, MOG_{35–55}-induced, in which the immune response was relatively controlled and disease pathology recapitulated chronic progressive demyelination. We used a therapeutic, rather than prophylactic, treatment regimen to evaluate whether drugs could reverse, rather than prevent, disease. Miconazole- and clobetasol-treated animals all exhibited a marked improvement in function, with nearly all animals regaining use of one or both hind limbs (Fig. 4c, d). In contrast, vehicle-treated mice exhibited chronic hindlimb paralysis over the treatment period. Benzotropine treatment also resulted in functional improvement, but to a lesser extent than miconazole and clobetasol (Fig. 4c, d). Overt functional recovery of miconazole- and clobetasol-treated mice correlated with histological improvements in the spinal cord. Specifically, drug-treated mice

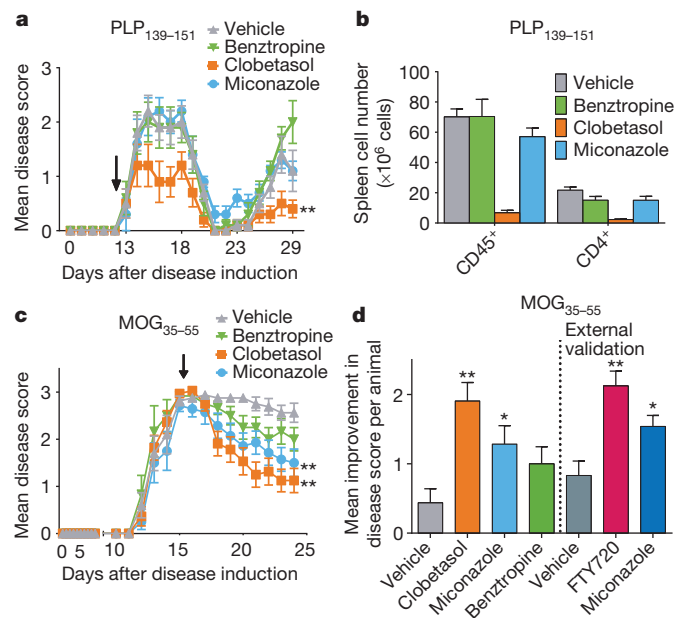


Figure 4 | Therapeutic efficacy of miconazole and clobetasol in mouse models of MS. **a**, Scoring of disease severity in relapsing remitting PLP_{139–151}-induced EAE mice treated beginning on day 13 (black arrow) and ending on day 29; $n = 10$ mice per group. Graph depicts mean daily disease score \pm s.e.m. **b**, Flow-cytometric-based quantification of spleen cell numbers at day 29 from the PLP_{139–151} EAE cohort in **a**. Values are mean \pm s.e.m.; $n = 4$ or 5 mice per group. **c**, Scoring of disease severity in chronic progressive MOG_{35–55}-induced EAE mice treated daily for 10 days beginning at the peak of disease on day 15 (black arrow); $n = 12$ –16 mice per group. Graph depicts mean daily disease score \pm s.e.m. **d**, Mean improvement in disease score per animal (peak score minus ending score) of MOG_{35–55} EAE cohort in **c**. Also shown are external validation results in MOG_{35–55} EAE from an independent contract laboratory. $n = 12$ mice per group. For all EAE experiments, drugs were dosed daily by intraperitoneal injection: clobetasol (2 mg/kg), miconazole (10 mg/kg), benzotropine (10 mg/kg), or FTY720 (1 mg/kg). All EAE disease scoring was as follows: 0, no abnormality; 1, limp tail; 2, limp tail and hind limb weakness; 3, hind limb paralysis; 4, hind limb paralysis and forelimb weakness; and 5, moribund. Two-tailed t -test, $*P < 0.05$ and $**P < 0.01$ for drug-treated groups compared with their respective vehicle-treated group. Source data are provided for Fig. 4a–d.

showed restoration of MBP expression and a reduction in the extent of demyelination in the spinal cord, whereas vehicle-treated mice showed sustained areas of white matter disruption (Extended Data Fig. 10a–e).

Although the immunosuppressive effect of clobetasol makes it challenging to evaluate its remyelinating potential in EAE directly, its consistent and robust induction of OPC differentiation *in vitro*, and enhancement of remyelination in non-immune-driven *in vivo* assays, suggests that it serves a role in both immunomodulation and promotion of myelination. In contrast, miconazole did not modulate immune cell function and our data indicate that it acts as a direct remyelinating agent. Given the potential of miconazole as a remyelinating therapeutic, we contracted a separate laboratory to provide independent validation of its efficacy in the MOG_{35–55}-induced EAE preclinical model. The laboratory independently validated the preclinical efficacy of miconazole in MOG_{35–55}-induced EAE to reduce disease severity in treated mice (Fig. 4d).

Since the approval in 1993 of interferon (IFN)- β -1b for the treatment of MS, therapeutic development has centred on the generation of additional immunomodulatory agents. Despite the effectiveness of many of these drugs to modulate CNS inflammation in patients with MS, none of them prevent chronic progressive disease and disability—largely because of their inability to stop or reverse the failure of remyelination in the CNS. We developed an advanced high throughput

screening platform to discover effective remyelinating therapeutics. This pluripotent stem-cell-based system provides unprecedented scalability, purity, and genotypic flexibility to screen for compounds that enhance OPC differentiation and myelination. Using this platform we identified two drugs approved by the US Food and Drug Administration, miconazole and clobetasol, with newly discovered functions to modulate OPC differentiation directly, enhance remyelination, and significantly reduce disease severity in mouse models of MS. Since miconazole and clobetasol are currently only approved for topical administration in humans, significant optimization of dosing, delivery, and potentially chemical structure will be required to enhance the on-target pharmacology in OPCs while diminishing any potential off-target side effects. However, the ability of miconazole and clobetasol to cross the blood–brain barrier raises the exciting possibility that these drugs, or modified derivatives, could advance into clinical trials for the currently untreatable chronic progressive phase of MS.

Online Content Methods, along with any additional Extended Data display items and Source Data, are available in the online version of the paper; references unique to these sections appear only in the online paper.

Received 1 April 2014; accepted 18 February 2015.

Published online 20 April 2015.

- Goldman, S. A., Nedergaard, M. & Windrem, M. S. Glial progenitor cell-based treatment and modeling of neurological disease. *Science* **338**, 491–495 (2012).
- Chang, A., Tourtellotte, W. W., Rudick, R. & Trapp, B. D. Premyelinating oligodendrocytes in chronic lesions of multiple sclerosis. *N. Engl. J. Med.* **346**, 165–173 (2002).
- Najm, F. J. *et al.* Rapid and robust generation of functional oligodendrocyte progenitor cells from epiblast stem cells. *Nature Methods* **8**, 957–962 (2011).
- Tesar, P. J. *et al.* New cell lines from mouse epiblast share defining features with human embryonic stem cells. *Nature* **448**, 196–199 (2007).
- Brons, I. G. *et al.* Derivation of pluripotent epiblast stem cells from mammalian embryos. *Nature* **448**, 191–195 (2007).
- Mi, S. *et al.* Promotion of central nervous system remyelination by induced differentiation of oligodendrocyte precursor cells. *Ann. Neurol.* **65**, 304–315 (2009).
- Bai, L. *et al.* Hepatocyte growth factor mediates mesenchymal stem cell-induced recovery in multiple sclerosis models. *Nature Neurosci.* **15**, 862–870 (2012).
- Deshmukh, V. A. *et al.* A regenerative approach to the treatment of multiple sclerosis. *Nature* **502**, 327–332 (2013).
- Mei, F. *et al.* Micropillar arrays as a high-throughput screening platform for therapeutics in multiple sclerosis. *Nature Med.* **20**, 954–960 (2014).
- Fancy, S. P. *et al.* Overcoming remyelination failure in multiple sclerosis and other myelin disorders. *Exp. Neurol.* **225**, 18–23 (2010).
- Franklin, R. J. & Ffrench-Constant, C. Remyelination in the CNS: from biology to therapy. *Nature Rev. Neurosci.* **9**, 839–855 (2008).
- Dubois-Dalcq, M., Ffrench-Constant, C. & Franklin, R. J. Enhancing central nervous system remyelination in multiple sclerosis. *Neuron* **48**, 9–12 (2005).
- Barres, B. A., Lazar, M. A. & Raff, M. C. A novel role for thyroid hormone, glucocorticoids and retinoic acid in timing oligodendrocyte development. *Development* **120**, 1097–1108 (1994).
- Woodruff, R. H. & Franklin, R. J. The expression of myelin basic protein exon 1 and exon 2 containing transcripts during myelination of the neonatal rat spinal cord – an in situ hybridization study. *J. Neurocytol.* **27**, 683–693 (1998).
- Woodruff, R. H. & Franklin, R. J. The expression of myelin protein mRNAs during remyelination of lysolecithin-induced demyelination. *Neuropathol. Appl. Neurobiol.* **25**, 226–235 (1999).
- Jeffery, N. D. & Blakemore, W. F. Remyelination of mouse spinal cord axons demyelinated by local injection of lysolecithin. *J. Neurocytol.* **24**, 775–781 (1995).
- Kumar, S., Cole, R., Chiappelli, F. & de Vellis, J. Differential regulation of oligodendrocyte markers by glucocorticoids: post-transcriptional regulation of both proteolipid protein and myelin basic protein and transcriptional regulation of glycerol phosphate dehydrogenase. *Proc. Natl Acad. Sci. USA* **86**, 6807–6811 (1989).
- Morisaki, S. *et al.* Endogenous glucocorticoids improve myelination via Schwann cells after peripheral nerve injury: an *in vivo* study using a crush injury model. *Glia* **58**, 954–963 (2010).
- Ishii, A., Fyffe-Maricich, S. L., Furusho, M., Miller, R. H. & Bansal, R. ERK1/ERK2 MAPK signaling is required to increase myelin thickness independent of oligodendrocyte differentiation and initiation of myelination. *J. Neurosci.* **32**, 8855–8864 (2012).
- Fyffe-Maricich, S. L., Schott, A., Karl, M., Krasno, J. & Miller, R. H. Signaling through ERK1/2 controls myelin thickness during myelin repair in the adult central nervous system. *J. Neurosci.* **33**, 18402–18408 (2013).
- Hu, B. Y., Du, Z. W. & Zhang, S. C. Differentiation of human oligodendrocytes from pluripotent stem cells. *Nature Protocols* **4**, 1614–1622 (2009).
- Wang, S. *et al.* Human iPSC-derived oligodendrocyte progenitor cells can myelinate and rescue a mouse model of congenital hypomyelination. *Cell Stem Cell* **12**, 252–264 (2013).

Supplementary Information is available in the online version of the paper.

Acknowledgements This research was supported by grants from the US NIH NS085246 (P.J.T. and R.H.M.), NS030800 (R.H.M.), and NS026543 (S.D.M.); New York Stem Cell Foundation (P.J.T.); Myelin Repair Foundation (P.J.T., R.H.M., and S.D.M.); Mt. Sinai Health Care Foundation (P.J.T.); and NIH predoctoral training grants T32GM008056 (R.T.K.) and F30CA183510 (T.E.M.). Additional support was provided by the Cytometry & Imaging Microscopy, Proteomics, and Genomics core facilities of the Case Comprehensive Cancer Center (P30CA043703), the CWRU Council to Advance Human Health, and philanthropic support from the Goodman, Long, and Geller families. P.J.T. is a New York Stem Cell Foundation–Robertson Investigator. We are grateful to M. Hitomi, W. Harte, D. Adams, W. Seibel, M. Haag, P. Scacheri, J. Wanta, C. Fang, H. Olsen, T. LaFramboise, J. Song, F. Van den Akker, and M. Shoham for technical assistance and discussion, A. Lager and M. Elitt for comments on the manuscript, B. Trapp for the PLP1 antibody, and B. Barres and B. Zuchero for RNA from *in vivo* isolated OPCs.

Author Contributions F.J.N., R.H.M., and P.J.T. designed the overall screening strategy; F.J.N. and P.J.T. generated mouse OPCs and performed the primary screen; F.J.N., K.Q., H.T., and R.P. designed analysis scripts for the primary screen; K.R.B., M.S., M.B.B., and A.J. performed 1,536-well external validation of primary screen; M.M., F.J.N., A.Z., E.S., C.K., and A.S. performed organotypic slice culture and *in vivo* assays; F.J.N. and K.Q. designed analysis scripts for the slice cultures; A.P.R., J.R.P., and S.D.M. designed and performed PLP EAE and immune cell experiments; R.T.K., Z.S.N., and F.J.N. generated and tested human OPCs; D.C.F., F.J.N., T.E.M., and P.J.T. generated and analysed RNAseq data; D.M.S., F.J.N., and P.J.T. generated and analysed the proteomics data; F.J.N., M.M., R.H.M., and P.J.T. analysed all of the data and wrote the paper. All authors edited and approved the final manuscript.

Author Information RNAseq datasets have been deposited in GEO under accession number GSE63804. Reprints and permissions information is available at www.nature.com/reprints. The authors declare no competing financial interests. Readers are welcome to comment on the online version of the paper. Correspondence and requests for materials should be addressed to P.J.T. (paul.tesar@case.edu) or R.H.M. (rhm3@gwu.edu).

METHODS

No statistical methods were used to predetermine sample size.

Mouse OPC preparation. OPCs used in this study were generated from two separate EpiSC lines, EpiSC9 (female) and 129O1 (male), using *in vitro* differentiation protocols and culture conditions described previously²³. Cultures were regularly tested and shown to be mycoplasma free. To ensure uniformity throughout all *in vitro* screening experiments, EpiSC-derived OPCs were sorted to purity by fluorescent activated cell sorting at passage five with conjugated CD140a-APC (eBioscience, 17-1401; 1:80) and NG2-AF488 (Millipore, AB5320A4; 1:100) antibodies. Sorted batches of OPCs were expanded and frozen down in aliquots. OPCs were thawed into growth conditions for one passage before use in screening assays.

***In vitro* phenotypic screening of OPCs.** EpiSC-derived OPCs were seeded onto poly-D-lysine 96-well Viewplate or CellCarrier plates (PerkinElmer) coated with laminin (Sigma, L2020; 10 µg ml⁻¹) using electronic multichannel pipetors. For the primary screen, 30,000 cells were seeded per well in screening medium (DMEM/F12 supplemented with N2 (R&D Systems), B-27 (Life Technologies), neurotrophin 3 (R&D Systems; 10 ng ml⁻¹), cAMP (Sigma; 50 µM), IGF-1 (R&D Systems; 100 ng ml⁻¹), noggin (R&D Systems; 100 ng ml⁻¹)) and allowed to attach for 2 h before addition of drug. NIH Clinical Collection I and II (<http://www.nihclinicalcollection.com>) drugs were added to assay plates with 0.1 µl pin replicators (Molecular Devices, Genetix; X5051), resulting in a final primary screening concentration of 5 µM. Thyroid-hormone-positive controls and DMSO vehicle controls were included in each assay plate. Cells were incubated under standard conditions (37 °C, 5% CO₂) for 3 days and fixed with 4% paraformaldehyde (PFA) in phosphate buffered saline (PBS). Fixed plates were permeabilized with 0.1% Triton X-100 and blocked with 10% donkey serum (v/v) in PBS for 2 h. Cells were labelled with MBP antibodies (Abcam, ab7349; 1:100) for 1 h at room temperature (~22 °C) followed by detection with Alexa Fluor-conjugated secondary antibodies (1:500) for 45 min. Nuclei were visualized by DAPI staining (Sigma; 1 µg ml⁻¹). All plates for the primary screen were processed and analysed simultaneously to eliminate variability. Donepezil was identified in the primary screen; however, the drug was not available at the time of dose-response testing and was excluded from further testing.

Dose-response testing of drug hits followed the same procedure with the following modifications to eliminate any artefacts in the primary screen: independently sourced drugs; a distinct batch of EpiSC-derived OPCs from a mouse of opposite sex; multi-dose testing; cytotoxicity analysis; an alternative marker of mature oligodendrocytes proteolipid protein 1 (PLP1, antibody clone AA3 provided by B. Trapp; 1:5,000); and an alternative high content assay endpoint parameter (percentage of oligodendrocytes differentiated instead of process intensity and length parameters). All drugs were tested in quadruplicate at seven different doses (ranging from 333 nM to 6.7 µM) and classified into tiers on the basis of their half-maximum effective concentration (EC₅₀) to induce OPC maturation, and their toxicity (concentration at which 50% of the cells were lost). Tier A drugs ($n = 3$) consisted of nanomolar dose effectors with little to no detectable toxicity at doses tested. Tier B drugs ($n = 4$) showed nanomolar effects but demonstrated toxicity at high doses. Tier C and D drugs required high doses to see an effect, demonstrated toxicity at low doses, or failed to show a dose-dependent response.

HCA of *in vitro* screen. For the 5 µM *in vitro* screen, stained plates were imaged on the Opera confocal imaging system (PerkinElmer) and a set of 24 × 10 fields were collected from each well, resulting in an average of 10,000 cells being scored per well. For the dose-response (6.7 µM, 5 µM, 3.3 µM, 1.7 µM, 666 nM, 500 nM, and 333 nM) *in vitro* assays, plates were imaged on the Operetta High Content Imaging and Analysis system (PerkinElmer) and a set of 14 × 20 fields captured from each well resulting in an average of 3,300 cells being scored per well. Analysis (PerkinElmer Acapella, Harmony, and Columbus software) began by identifying intact nuclei stained by DAPI; that is, those traced nuclei that were larger than 50 µm² in surface area and possessed intensity levels that were typical and less than the threshold brightness of pyknotic cells. Each traced nucleus region was then expanded by 50% and cross-referenced with the mature myelin protein (MBP or PLP1) stain to identify oligodendrocyte nuclei, and from this the percentage of oligodendrocytes was calculated. Processes emanating from oligodendrocyte nuclei were identified using the CSIRO2 analysis module within a custom Acapella script. Maximum mean process length (denoted 'process length') and mean process intensity (denoted 'process intensity') were generated on a per well basis. For the 5 µM *in vitro* screen, values were calculated and normalized to 100 for thyroid hormone (positive control)-treated wells and to 0 for DMSO (vehicle)-treated wells, on a per plate basis.

Phenotypic validation testing of OPCs. Briefly, OPCs were grown and expanded in laminin-coated flasks before harvesting for plating. Cells were dispensed in screening media (see above for details) using a Multidrop Combi dispenser (Thermo Fisher) into laminin/poly-L-ornithine-coated sterile, 1,536-well, black

clear-bottom tissue culture plates (Brooks Automation), to a final density of 2,000 cells per well. Plates were sealed with gasketed stainless steel lids with holes for gas exchange (Wako USA). Following cell attachment, library compounds were transferred by pintool (Wako USA) using 10 nl slotted pins. Library compounds were serially diluted in DMSO, and were added to plates to yield final concentrations of 0 (DMSO only), 4, and 20 µM compound. After incubation for 72 h at 37 °C, cells were fixed, washed, and stained similar to the 96-well OPC assay protocol, although all aspiration steps were performed using a Biotek EL406 Microplate Washer Dispenser (Biotek) equipped with a 1,536-well aspiration manifold. Dispense steps were performed with both peristaltic pump cassettes (for gentle reagent additions) and syringe pump manifolds (for faster bulk dispenses). Cells were stained with DAPI (Sigma; 1 µg ml⁻¹) and MBP antibody (Abcam, ab7349; 1:100). Plates were then imaged using an InCell 2000 Analyzer High Content Imager (GE Healthcare Bio-Sciences). Well images were analysed using InCell Analyzer Workstation software, and the MBP signal was quantified with a process detection algorithm, using total process skeleton length to qualify activity.

***Ex vivo* cerebellar slice cultures.** Whole cerebellum was collected from C57BL/6 mice at postnatal day 7 and embedded in agarose. Sagittal slices were cut on a microtome (Leica) at 300 µm. Slices were cultured in a DMEM-Basal Medium Eagle's base with 15% heat-inactivated horse serum, modified N2, and PDGF-AA. After 1 day in culture, slices were treated daily for 5 days with test drugs or vehicle (DMSO). Drugs tested were clobetasol (5 µM), hydroxyzine (5 µM), clotrimazole (2 µM), miconazole (1 µM), ketoconazole (1 µM), vesamicol (5 µM), propafenone (2 µM), dicyclomine (5 µM), benztropine (2 µM), haloperidol (5 µM), and medroxyprogesterone (5 µM). The identity of the drugs was blinded to the experimenter. Slices were then lysed for western blot or fixed in 4% PFA and processed for HCA as detailed below.

Immunohistochemistry. Immunohistochemistry was performed as previously described³. In short, tissue sections or whole slices were washed three times in PBS, blocked in PBS containing Triton X-100 (0.1%) and normal donkey serum (NDS, 2% for sections and 10% for cerebellar slices) and incubated with primary antibody overnight. For MBP immunohistochemistry, the primary antibody solution consisted of 2% NDS, 2% bovine serum albumin, and 0.1% saponin. For all other antibodies, the primary antibody solution consisted of 2% NDS and 0.1% Triton X-100. Primary antibodies used included rat anti-MBP (Abcam, ab7349; 1:100), mouse anti-APC CC1 clone (Millipore, MABC200; 1:500), and rabbit anti-IBA1 (Wako Chemicals, 019-19741; 1:1,000). The tissue was then washed in PBS and incubated in secondary antibodies for 2 h. Secondary detection was performed with Alexa Fluor-conjugated secondary antibodies (1:500) for 1 h. Luxol fast blue staining was performed as previously described⁷.

High content screen of cerebellar slices. MBP-stained cerebellar slices were analysed by confocal image on an Operetta system using Phenologic machine-learning technology within Harmony software. The software was trained to identify elongated fibres more characteristic of axonal ensheathment and to exclude regions of small fibres or diffuse background fluorescence on the basis of texture features. MBP-positive surface area was collected and normalized to the total surface area for the group of slices treated with each drug. A minimum of six slices were treated per drug, which included an equal distribution of medial and lateral slices.

Western blotting of cerebellar slices. Cerebellar slices (each biological replicate using 12 slices per condition; six each from two separate animals) were collected in PBS and centrifuged. The PBS was aspirated and the pellet resuspended in 100 µL lysis buffer (20 mM Tris, 137 mM NaCl, 5.0 mM EDTA pH 8.0, 10% glycerol, 1% NP40, pH to 8.0 with HCl), incubated on ice for 20 min, centrifuged, and the supernatant collected. Protein concentration was determined by a Pierce BCA protein assay kit (Thermo Fisher). Equal amounts of protein were applied to NuPAGE 12% Bis-TRIS gels (Life Technologies), and electrophoretically transferred onto a PVDF membrane (Life Technologies). The membranes were incubated with rabbit anti-MBP (Millipore, AB980; 1:500) and consequently probed with horseradish peroxidase (HRP)-conjugated goat anti-rabbit (1:5,000) or incubated with HRP-conjugated mouse anti-β-actin (Sigma, A3854; 1:10,000) to ensure even loading of samples. Enhanced chemiluminescence was performed with a West Pico kit (Thermo Fisher) and relative optical density was measured using ImageJ (NIH).

Cheminformatics. Structure-activity searches of azoles and steranes were performed with Canvas program (Schrodinger Software, release 2014-1: Canvas, version 1.9). Tanimoto similarity between voriconazole and miconazole was calculated by ROCS (OpenEye Scientific Software).

Pharmacokinetics. C57BL/6 adult female mice were dosed intraperitoneally with miconazole (10 mg/kg or 40 mg/kg) or clobetasol (10 mg/kg). After 1 or 6 h, 100 µL of plasma was collected then each animal was perfused with PBS. Brains were collected, weighed, and rinsed with PBS. Water (0.5 ml) was added to the brain

samples, which were then homogenized. Plasma and brain samples were each diluted fivefold with blank rat plasma. Three hundred microlitres of internal standard solution was added to the samples, vortexed, and centrifuged. Five microlitres of each sample was injected into an API-4000Qtrap mass spectrometer and quantified (Climax Labs).

Focal demyelination and drug treatment. Focal demyelination in the spinal cord was induced by the injection of 1% LPC solution. Ten- to 12-week-old C57BL/6 female mice were anaesthetized using isoflurane and a T10 laminectomy was performed. One microlitre of 1% LPC was infused into the dorsal column at a rate of 15 ml h^{-1} . The animals were euthanized either at day 8 or day 12 after the laminectomy ($n = 6\text{--}9$ per group). Animals that were euthanized at day 8 received vehicle or drug daily by intraperitoneal injection between days 3 and 7. Animals used in the day 12 experiments received vehicle or drug daily by intraperitoneal injection between days 4 and 11. Drugs were dissolved in DMSO and then diluted with sterile saline for injection. Mice were deeply anaesthetized using ketamine/xylazine rodent cocktail and then euthanized by transcardial perfusion with 4% PFA for histological analysis or 4% PFA, 2% glutaraldehyde, and 0.1 M sodium cacodylate for electron microscopy. PFA fixed tissue was equilibrated in 30% sucrose, embedded in OCT, and cryosectioned at $20 \mu\text{m}$ thickness and processed for CC1 and MBP immunohistochemistry. ImageJ was used to measure area of the lesion and CC1⁺ cells within the lesion were scored manually. For CC1 scoring, sections were taken from the centre of each lesion to control for lesion variability.

Electron microscopy. Samples were processed as previously described^{3,24}. In short, samples were osmicated, stained *en bloc* with uranyl acetate, and embedded in EMbed 812, an Epon-812 substitute (EMS). Sections ($1 \mu\text{m}$) were cut and stained with toluidine blue and visualized on a light microscope (Leica DM5500B). Additional thin sections were cut, carbon-coated and imaged either on a JEOL JEM-1200-EX electron microscope or a T12 electron microscope (FEI).

Developmental myelination. Mouse pups of strain CD1 were administered 2 mg/kg clobetasol, 10 mg/kg miconazole, or vehicle (DMSO in saline) by daily intraperitoneal injections from postnatal day 2–6. Some clobetasol treated animals exhibited sickness on the basis of this treatment, with low body weight, and some animals of the cohort died before end of treatment. On postnatal day 6 the pups were anaesthetized using ketamine and xylazine and euthanized by transcardial perfusion with 4% PFA. Tissue was fixed overnight in 4% PFA, equilibrated in 30% sucrose, and embedded in OCT. Sections ($20 \mu\text{m}$) were cut and processed for CC1 and MBP immunohistochemistry. ImageJ was then used to count and measure area of the corpus callosum as well as measure the extent of the corpus callosum length covered by MBP⁺ processes. Eight coronal sections containing corpus callosum rostral to the hippocampus from at least three animals per group were used for these analyses. To quantitate extent of MBP in the corpus callosum, a line was drawn through the centre of the corpus callosum from the lateral tip to the dorsal most extent of MBP expression in the corpus callosum. The length of this line was measured and then the dorsal-most point of the line was extended to the dorsal tip of the corpus callosum and measured to yield the length of the lateral callosum. The two numbers were divided to get the MBP/corpus callosum proportion. A two-tailed *t*-test was used to compare drug- with vehicle-treated groups.

Muscarinic receptor antagonism. Miconazole, clobetasol, and benztropine (all at $1 \mu\text{M}$ in DMSO) were sent to Select Screen (Life Technologies) with identities coded. GeneBLAzer or Tango assays were performed to determine level of acetylcholine muscarinic receptor M1, M3, M5 (GeneBLAzer), M2 and M5 (Tango) antagonism.

Kinase profiling. LanthaScreen, Z'-LYTE, and Adapta kinase assays were performed by Select Screen (Life Technologies). LanthaScreen Eu kinase assays were performed in Greiner low-volume 384-well plates. Assay buffer consisted of 50 mM HEPES pH 7.5, 0.01% BRIJ-35, 10 mM MgCl_2 , 1 mM EGTA. Each well consisted of this mixture: $4.0 \mu\text{l}$ of $4 \mu\text{M}$ test drug in assay buffer, $8 \mu\text{l}$ of $2\times$ kinase/Eu antibody mixture, and $4 \mu\text{l}$ of $4\times$ Alexa Fluor 647 tracer. Plates were incubated for 60 min at room temperature ($\sim 22^\circ\text{C}$), then Alexa Fluor 647 emission (665 nm) and Europium emission (615 nm) read on a fluorescent plate reader. Data were analysed by generating the emission ratio (665 nm/615 nm) for each test point and normalizing 0% to control wells with no known inhibitor and 100% to control wells with highest concentration of known inhibitor.

Z'-LYTE assays were performed in Corning, low volume 384-well plates. Assay buffer consisted of 50 mM HEPES pH 7.5, 0.01% BRIJ-35, 10 mM MgCl_2 , 1 mM EGTA. Each well consisted of this mixture: $2.5 \mu\text{l}$ of $4\times$ of $4 \mu\text{M}$ drug in assay buffer, $5 \mu\text{l}$ of $2\times$ peptide/kinase mixture, $2.5 \mu\text{l}$ of $4\times$ ATP solution. Plates were then incubated at room temperature ($\sim 22^\circ\text{C}$) for 60 min. Then $5 \mu\text{l}$ of a development reagent that contained a protease that selectively digested the non-phosphorylated peptide was added and the plates incubated for 60 min. Coumarin emission (445 nm) and fluorescein emission (520 nm) were read on a fluorescent plate reader. Data were analysed by normalizing out background fluorescence then generating the emission ratio (445 nm/520 nm) for each test point. Data were

further normalized to 0% in control wells with no ATP and 100% in control wells with synthetically phosphorylated peptide of the same sequence.

Adapta assays were performed in Corning, low volume 384-well plates. Assay buffer consisted of 30 mM HEPES. Each well consisted of this mixture: $2.5 \mu\text{l}$ of $4\times$ of $4 \mu\text{M}$ drug in assay buffer, $2.5 \mu\text{l}$ of $4\times$ ATP solution, $5 \mu\text{l}$ of $2\times$ substrate/kinase mixture. Plates were then incubated at room temperature ($\sim 22^\circ\text{C}$) for 60 min. Then $5 \mu\text{l}$ of a development reagent that contained europium-anti-ADP antibody and ADP tracer were added and the plate incubated for 60 min. Alexa Fluor 647 emission (665 nm) and europium emission (615 nm) were read on a fluorescent plate reader. Data were analysed by generating the emission ratio (665 nm/615 nm) for each test point and normalizing 0% to control wells with no ATP in the kinase reaction and 100% to control wells with ADP.

Raw data from all kinase assays can be found in Supplementary Table 2.

HCA of astrocyte induction. For the astrocyte experiments in Fig. 3c, the experimental setup was identical to the PLP1-based primary validation screen except plates were stained for GFAP (DAKO, Z0334; 1:5,000). BMP4 (R&D Systems; 50 ng ml^{-1}) and LIF (Millipore; 10^3 U ml^{-1}) were used as the positive control for astrocyte induction. Assay plates were imaged on the Operetta High Content Imaging and Analysis system and a set of 14×20 fields captured. Columbus Data Management and Analysis System software (PerkinElmer) was used to quantify the percentage of GFAP⁺ astrocytes in each well using a method similar to that developed for oligodendrocytes.

Global phosphoproteomics. Quantitative global phosphorylation studies were performed on OPCs across two different time points (1 and 5 h after treatment) with miconazole, clobetasol, or DMSO treatment using a label-free ultra-high-performance liquid chromatography–tandem mass spectrometry (LC-MS/MS) workflow without fractionation. Briefly, for each sample 30 million cells were lysed with 2% SDS solution with protease and phosphatase inhibitor (Thermo Fisher), and detergent was removed on $200 \mu\text{l}$ of the cell lysate using the FASP cleaning procedure²⁵. Each sample was digested by a two-step Lys-C/trypsin proteolytic cleavage and subjected to phospho-enrichment using a commercially available TiO_2 enrichment spin tips (Thermo Fisher). LC-MS/MS analysis used a UPLC system (NanoAcquity, Waters) that was interfaced to an Orbitrap ProVelo Elite MS system (Thermo Fisher). Fold-change calculations were determined from peptide intensities for each drug versus DMSO at each time point. Phosphopeptides with greater than twofold change were imported into Ingenuity Pathway Analysis to elucidate signalling pathways perturbed with drug treatment.

RNA sequencing and analysis. Cells were lysed directly in 1 ml TRIzol (Invitrogen) and stored at -80°C . Once all samples were collected, samples were thawed on ice and separated with chloroform using Phase Lock Gel tubes (5 PRIME). RNA was isolated using the miRNeasy Plus Mini Kit (Qiagen) according to the manufacturer's protocol. One microgram of each sample was then poly-A selected, fragmented, and library prepared using the TruSeq RNA Sample Prep Kit (Illumina) according to the manufacturer's protocol. Samples were indexed using TruSeq adapters. One hundred base-pair paired-end reads were generated for each sample on an Illumina HiSeq 2500 instrument at the Case Western Reserve University Genomics Core facility. Between 5 million and 13 million reads were generated per sample for drug time course experiments. EpiSC RNaseq data were previously published (GEO accession number GSE57403)²⁶. EpiSCs, EpiSC OPCs, and *in vivo* OPCs were sequenced to depths of 51,271,458 reads, 61,072,460 reads, and 62,530,709 reads, respectively. For *in vivo* isolated OPCs, CD140a⁺ cells were immunopanned from the CNS of mouse pups at postnatal day 7 as described previously²⁷. Cells were then cultured for 5 days in identical culture conditions to EpiSC-derived OPCs before analysis.

Reference genome files were retrieved from Illumina iGenomes (<http://cufflinks.cbcb.umd.edu/igenomes.html>). Reads were aligned to the mm9 genome using Tophat version 2.0.8 with default settings²⁸. Expression values of known RefSeq genes were calculated in units of fragments per kilobase per million reads (FPKM) using Cufflinks version 2.0.2 (ref. 29). Expression values were tabled to eliminate background signal by converting all values below 0.25 to 0, and subsequently adding 0.25 to all values. FPKMs were quantile normalized to correct for inter-sample variation. To identify genes whose expression was perturbed by drug treatments, duplicate samples of OPCs were treated with drug or vehicle for 2, 6, or 12 h. RNA sequencing data were tested for differential expression by comparing treatments to vehicle at each time point using Cuffdiff version 2.0.2 (ref. 30). The collective list of changed genes for each drug was evaluated with Ingenuity Pathway Analysis (application build 261899, content version 18030641).

Western blotting of mouse OPCs. EpiSC-derived OPCs were seeded into poly-L-ornithine/laminin coated six-well plates and allowed to attach for 2 h in DMEM/F12 without additional factors. Cells were treated with indicated inhibitors or DMSO for 1 h—SCH727984 (ChemieTek, $1 \mu\text{M}$), SB590885 (Tocris, 10 nM), LY294002 (Tocris, $10 \mu\text{M}$), and PD0325901 (Stemgent, $1 \mu\text{M}$). Cells were then stimulated with drug or FGF2 (R&D Systems; 20 ng ml^{-1}) for 1 h and then lysed in

200 µL RIPA buffer (0.15 M NaCl, 0.05 M Tris, pH = 8.0, 1 mM EDTA, 1% Triton X-100, 0.1% SDS, 10% glycerol, HALT protease and phosphatase inhibitor (Thermo Fisher) added just before use) and incubated on ice for 20 min. Lysates were centrifuged at 4 °C and supernatant collected. Protein concentrations were determined by Pierce BCA protein assay kit (Thermo Fisher). Equal amounts of protein were resolved in a reduced manner on NuPAGE 4–12% Bis-Tris gels (Life Technologies) and transferred onto PVDF membranes (Life Technologies). Blots were blocked in either 5% BSA (phosphoprotein) or 5% milk (non-phosphoprotein). Primary antibodies were all from the same vendor (Cell Signaling) and included phospho-Erk1/2 (4370S, clone D13.14.4E; 1:2,000), ERK1/2 (9107S, clone 3A7; 1:2,000), phospho-glucocorticoid receptor (4161S; 1:1,000), and glucocorticoid receptor (12041, clone D6H2L; 1:1,000) followed by incubation with HRP-conjugated secondary antibodies and chemiluminescent enhancement by West Pico substrate (Thermo Fisher).

Generation and screening of human OPCs. Human OPCs were generated from skin fibroblast-derived human iPSC line (CWRU43, Tesar laboratory) and hESC lines H7 (NIH Human Embryonic Stem Cell Registry WA07; NIH approval number NIHhESC-10-0061) and H9 (NIH Human Embryonic Stem Cell Registry WA09; NIH approval number NIHhESC-10-0062) as previously described^{21,22}. iPSC- and hESC-derived OPCs were characterized by Sox10 (R&D Systems, AF2864; 1:100) staining, and then seeded in 96-well plates at 40,000 cells per well for drug testing. Cells were cultured with 1 µM miconazole, 5 µM clobetasol, or vehicle (DMSO) for 21 days, with fresh media changes with drug or vehicle every 2 days. Plates were fixed and stained with MBP (Abcam, ab7349; 1:100) then imaged on the Operetta system. We analysed results with slight modification to HCA Acapella scripts used for mouse oligodendrocytes.

Naive CD4⁺ T-cell assays. Naive CD4⁺ T cells (CD4⁺ L-selectin^{hi} cells) were purified using AutoMacs Magnetic Bead cell separation technology (Miltenyi Biotech) from total lymph node cells isolated from unprimed mice with purity ranging from 98 to 99.9%. For *in vitro* activation, 5×10^5 naive CD4⁺ T cells were activated in the presence of plate-bound anti-CD3 (1 µg ml⁻¹) plus Th1- (200 U ml⁻¹ interleukin-2 (IL-2), 40 U ml⁻¹ IL-12, 10 µg ml⁻¹ anti-IL-4) or Th17- (10 ng ml⁻¹ TGF-β1, 50 ng ml⁻¹ IL-6, 1 µg ml⁻¹ anti-IFN-γ, 1 µg ml⁻¹ anti-IL-4, 1 µg ml⁻¹ anti-IL-2) promoting conditions. On day 4, the cultured T cells were collected and the percentage of viable cytokine positive cells assessed by flow cytometry. The cells were stained with a LIVE/DEAD Fixable Violet Dead Cell Stain Kit, for 405 nm excitation (Life Technologies), anti-CD4-APC/Cy7 (clone RM4-5), anti-IFN-γ-PerCP/Cy5.5 (clone XMG1.2), and anti-IL-17-APC (clone eBio17B7) (eBioscience). Viable cells (5×10^5) were analysed per individual sample using a BD Canto II cytometer (BD Biosciences), and the data were analysed using FloJo version 9.5.2 software (Tree Star).

Ex vivo lymphocyte recall assays. Female SJL/J (Harlan Laboratories) or C57BL/6 mice were housed under SPF conditions. Six- to seven-week-old female mice were immunized subcutaneously with 100 µL of an emulsion containing 200 µg of *Mycobacterium tuberculosis* H37Ra (BD Biosciences) and 50 µg of PLP_{139–151} (SJL/J) or MOG_{35–55} (C57BL/6) distributed over three sites on the flank. For *ex vivo* culture draining, lymph nodes on day 8 were collected and cells were activated in the presence of anti-CD3 (1 µg ml⁻¹) in the absence or presence of clobetasol, miconazole, or benztropine (10^{-9} – 10^{-5} M). To assess total cellular proliferation, cultures were pulsed with tritiated thymidine (1 µCi) at 24 h and cultures were harvested at 72 h. In replicate wells, culture supernatants were harvested at 72 h after culture, and the level of IFN-γ and IL-17 were assessed via Luminex assay (Millipore).

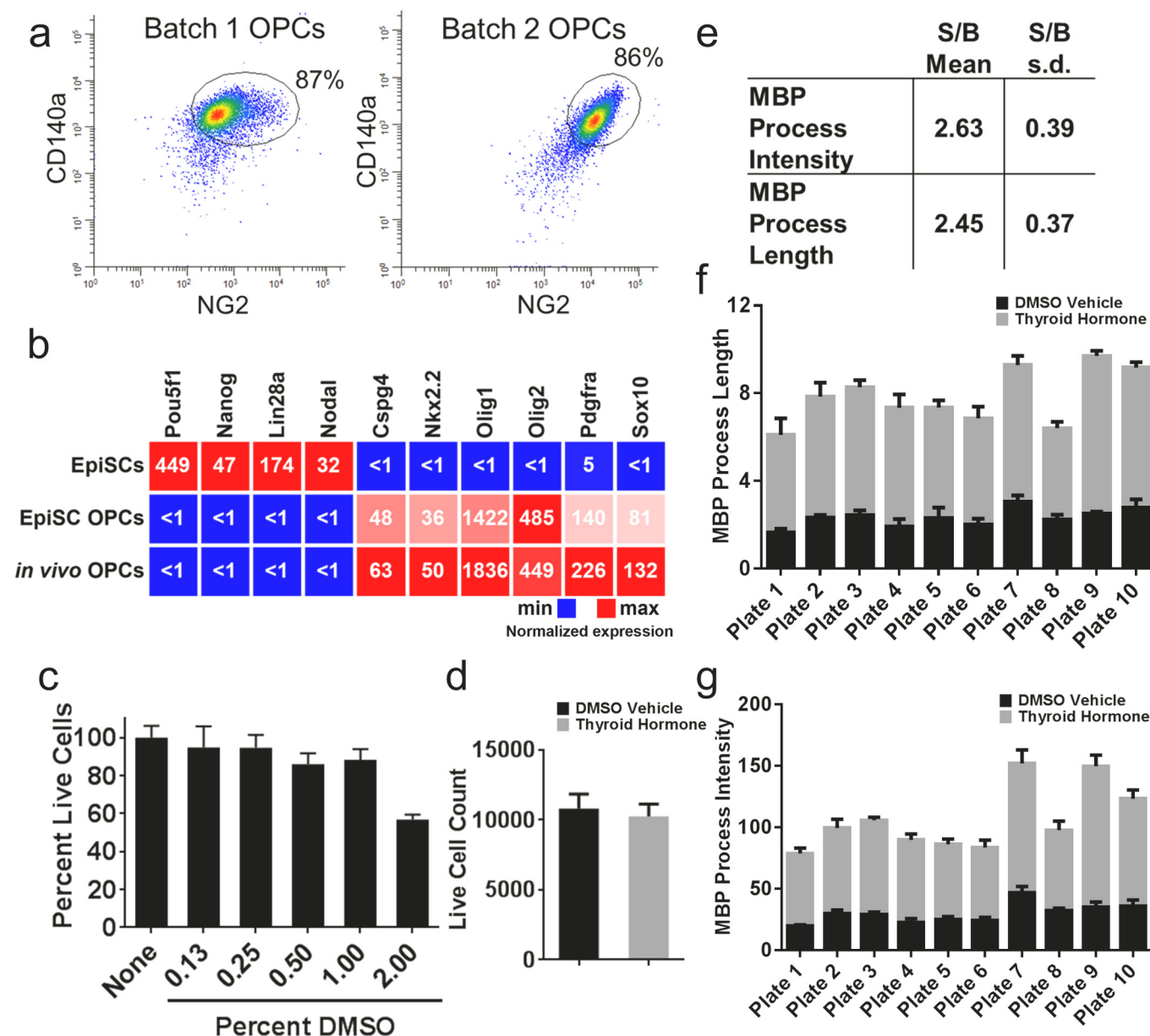
PLP_{139–151}-induced relapsing remitting EAE. Six- to seven-week-old female SJL/J mice were induced with PLP_{139–151} as for *ex vivo* recall assays. Mice were allowed to progress to disease onset at day 13 before being randomized into

treatment groups ($n = 10$ mice per group). Mice were then monitored for paralysis and treated daily by intraperitoneal injection with vehicle (DMSO in sterile saline), benztropine (10 mg/kg), clobetasol (2 mg/kg), or miconazole (10 mg/kg) beginning on day 13 and ending on day 29. This period fully encompassed the acute phase of disease onset followed by remission and the primary disease relapse. Treatments were blinded to the experimenters performing the assays. Mice were followed for disease severity in a blinded fashion with disease scoring as follows: 0, no abnormality; 1, limp tail; 2, limp tail and hind limb weakness; 3, hind limb paralysis; 4, hind limb paralysis and forelimb weakness; and 5, moribund.

MOG_{35–55} chronic progressive EAE model. EAE was induced by immunizing 10-week-old C57BL/6 female mice with 100 µL injection of MOG_{35–55}/complete Freund's adjuvant emulsion (Hooke Laboratories). One hour after immunization, mice were given 100 ng of pertussis toxin by 100 µL intraperitoneal injection. A second dose of pertussis toxin was administered the next day. EAE onset was monitored daily and scored using a clinical scale where 0 represented no abnormality; 1, limp tail; 2, limp tail and hind limb weakness; 3, hind limb paralysis; 4, hind limb paralysis and forelimb weakness; and 5, moribund. Mice that appeared moribund or exhibited forelimb paralysis were immediately euthanized and not used for the study. Once mice reached peak of disease (~day 15; clinical score = 3) they were randomized into treatment groups, and drug or vehicle (DMSO in saline) was administered intraperitoneally daily for 10 days ($n = 12$ –16 mice per group). Doses for each drug were miconazole (10 mg/kg), clobetasol (2 mg/kg), and benztropine (10 mg/kg). At these doses, no drugs showed any overt evidence of toxicity to any of the animals. Experimenters were blinded to the identity of the treatments and animals were scored daily. Cumulative disease scores for each animal were calculated during the treatment period, and a two-tailed *t*-test compared drug- with vehicle-treated groups. The extent of recovery for each animal was calculated as the difference between the peak disease score and the score at the end of each experiment, and a two-tailed *t*-test was used to compare each treatment with vehicle. External validation of MOG_{35–55} EAE experiments ($n = 12$ mice per group) was performed at Hooke Laboratories with experimenters blinded to the identity of the substances. FTY720 (fingolimod, 1 mg/kg), a known immunomodulatory drug, was used as a positive control during external validation of miconazole (10 mg/kg).

Animal welfare. All animal experiments were performed in accordance with protocols approved by the Case Western Reserve University and Northwestern University Institutional Animal Care and Use Committees.

23. Najm, F. J. *et al.* Isolation of epiblast stem cells from preimplantation mouse embryos. *Cell Stem Cell* **8**, 318–325 (2011).
24. Najm, F. J. *et al.* Transcription factor-mediated reprogramming of fibroblasts to expandable, myelinogenic oligodendrocyte progenitor cells. *Nature Biotechnol.* **31**, 426–433 (2013).
25. Wisniewski, J. R., Nagaraj, N., Zougman, A., Gnäd, F. & Mann, M. Brain phosphoproteome obtained by a FASP-based method reveals plasma membrane protein topology. *J. Proteome Res.* **9**, 3280–3289 (2010).
26. Factor, D. C. *et al.* Epigenomic comparison reveals activation of “seed” enhancers during transition from naive to primed pluripotency. *Cell Stem Cell* **14**, 854–863 (2014).
27. Cahoy, J. D. *et al.* A transcriptome database for astrocytes, neurons, and oligodendrocytes: a new resource for understanding brain development and function. *J. Neurosci.* **28**, 264–278 (2008).
28. Trapnell, C., Pachter, L. & Salzberg, S. L. TopHat: discovering splice junctions with RNA-Seq. *Bioinformatics* **25**, 1105–1111 (2009).
29. Trapnell, C. *et al.* Transcript assembly and quantification by RNA-Seq reveals unannotated transcripts and isoform switching during cell differentiation. *Nature Biotechnol.* **28**, 511–515 (2010).
30. Trapnell, C. *et al.* Differential analysis of gene regulation at transcript resolution with RNA-seq. *Nature Biotechnol.* **31**, 46–53 (2013).



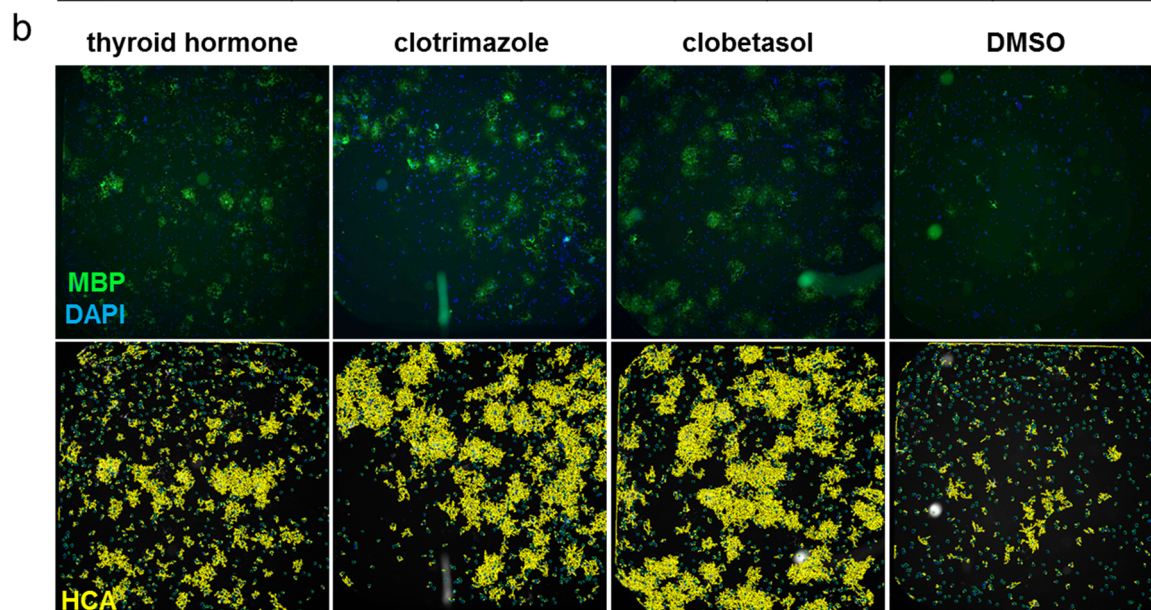
Extended Data Figure 1 | Performance of the primary screen.

a, Representative flow cytometry plots showing co-expression of NG2 and CD140a in both batches of EpiSC-derived OPCs used for this study. The batches of EpiSC-derived OPCs were sorted to purity (circled areas of plots) before use in this study. **b**, RNaseq expression heat map showing downregulation of pluripotent stem cell transcripts and upregulation of OPC transcripts when EpiSCs were differentiated into OPCs. Fragments per kilobase exon per million reads (FPKM) for each transcript are shown compared with *in vivo* isolated mouse OPCs. **c**, Quantification of DMSO (v/v) tolerance of EpiSC-derived OPCs in 96-well plates shown as mean \pm s.e.m. For reference, 0.05% (v/v) DMSO was used as vehicle for all *in vitro* experiments in this study; $n = 16$

wells per group with >690 cells scored per well. **d**, Quantification of cell viability of thyroid hormone (positive control) and DMSO vehicle treatments per well across all ten assay plates shown as mean \pm s.e.m.; $n = 80$ wells per group with $>6,800$ cells scored per well. **e**, Signal to background (S/B) mean values with standard deviation (s.d.) of controls from the entire screen; $n = 80$ wells per group. **f**, Raw data of MBP process length from the primary screen for thyroid hormone treatment and DMSO vehicle across all plates shown as mean \pm s.d.; $n = 8$ wells per group with $>6,800$ cells scored per well. **g**, Raw data of MBP process intensity from the primary screen for thyroid hormone treatment and DMSO vehicle shown as mean \pm s.d.; $n = 8$ wells per group with $>6,800$ cells scored per well.

a

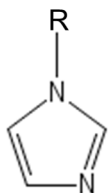
	Single Dose Rank	EC ₅₀ (μM)	50% Tox (μM)	Primary Screen Tier	External Validation	Brain Slice Percent MBP of Control	Brain Slice Group
Drugs	<i>in vitro</i>	<i>in vitro</i>	<i>in vitro</i>	<i>in vitro</i>	<i>in vitro</i>	<i>ex vivo</i>	<i>ex vivo</i>
clobetasol	7	0.4	>6.7	A	Yes	169	High
miconazole	5	0.5	>6.7	A	NT	148	High
hydroxyzine	13	0.6	>6.7	A	NT	168	High
oxiconazole	10	0.6	5.7	B	Yes	NT	NT
propafenone	18	0.5	5	B	Yes	112	Medium
benztropine	22	0.6	4.2	B	Yes	96	Low
clotrimazole	6	0.6	4.1	B	Yes	148	High
tamoxifen	12	0.4	2	C	Yes	NT	NT
ketoconazole	4	0.5	2.4	C	NT	117	Medium
dicyclomine	15	1.1	>6.7	C	Yes	105	Medium
vesamicol	8	2.5	>6.7	C	NT	117	Medium
haloperidol	20	3.6	>6.7	C	Yes	81	Low
medroxyprogesterone	2	4.4	>6.7	C	Yes	76	Low
megestrol	11	>6.7	>6.7	D	Yes	NT	NT
ifenprodil	16	>6.7	>6.7		Yes		
oxybutinin	1	FAIL	>6.7		NT		
bifonazole	9	FAIL	>6.7		No		
cinanserin	17	FAIL	>6.7		No		
betamethasone	19	FAIL	>6.7		Yes		
methylprednisolone	21	FAIL	>6.7		Yes		
econazole	3	FAIL	3		Yes		
donepezil	14	NT	NT	NT	NT		



Extended Data Figure 2 | Drug hit ranking and validation. **a**, Chart ranking the 22 primary drug hits (single dose rank) into four tiers on the basis of calculation of EC₅₀ to induce PLP1⁺ oligodendrocytes from OPCs and the concentration at which 50% of the cells were lost (50% Tox) calculated from a seven-point dose treatment; *n* = 4 wells per dose per drug using independently sourced drug and separate OPC batch from the primary screen. Tiers ranged from the most potent and least toxic effectors to the least potent and most toxic: tier a (green), tier b (grey), tier c (orange), and tier d (red). The 1,536-well

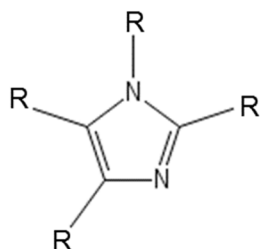
format external validation of 14 out of 16 tested hits is also shown. Drugs were further ranked into groups of high (green), medium (grey), and low (orange) on the basis of their ability to increase MBP⁺ axonal ensheathment in mouse cerebellar brain slices relative to vehicle (DMSO)-treated controls as measured by HCA. NT, not tested. **b**, External validation whole 1,536-well images of MBP⁺ (green) oligodendrocytes generated from OPCs after 72 h of treatment. GE InCell HCA is shown with processes traced in yellow and nuclei in blue.

a



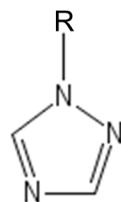
(1,3) Diazoles, mono-substituted at the 1-position	Primary Screen Rank
econazole	3
ketoconazole	4
miconazole	5
clotrimazole	6
bifonazole	9
oxiconazole	10
ozagrel	428
1-benzylimidazole	616

b



(1,3) Diazoles, poly-substituted	Primary Screen Rank
telithromycin	27
metronidazole	60
ondansetron	116
azathioprine	315
(+)-etomidate	322
ornidazole	327
pilocarpine	473
methimazole	483
tinidazole	589

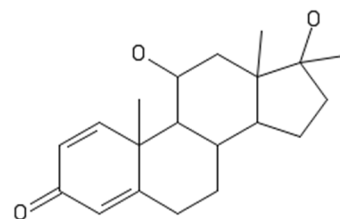
c



(1,2,4) Triazoles, mono-substituted at the 1-position	Primary Screen Rank
rizatriptan	214
voriconazole	219
letrozole	271
itraconazole	413
fluconazole	414
anastrozole	571

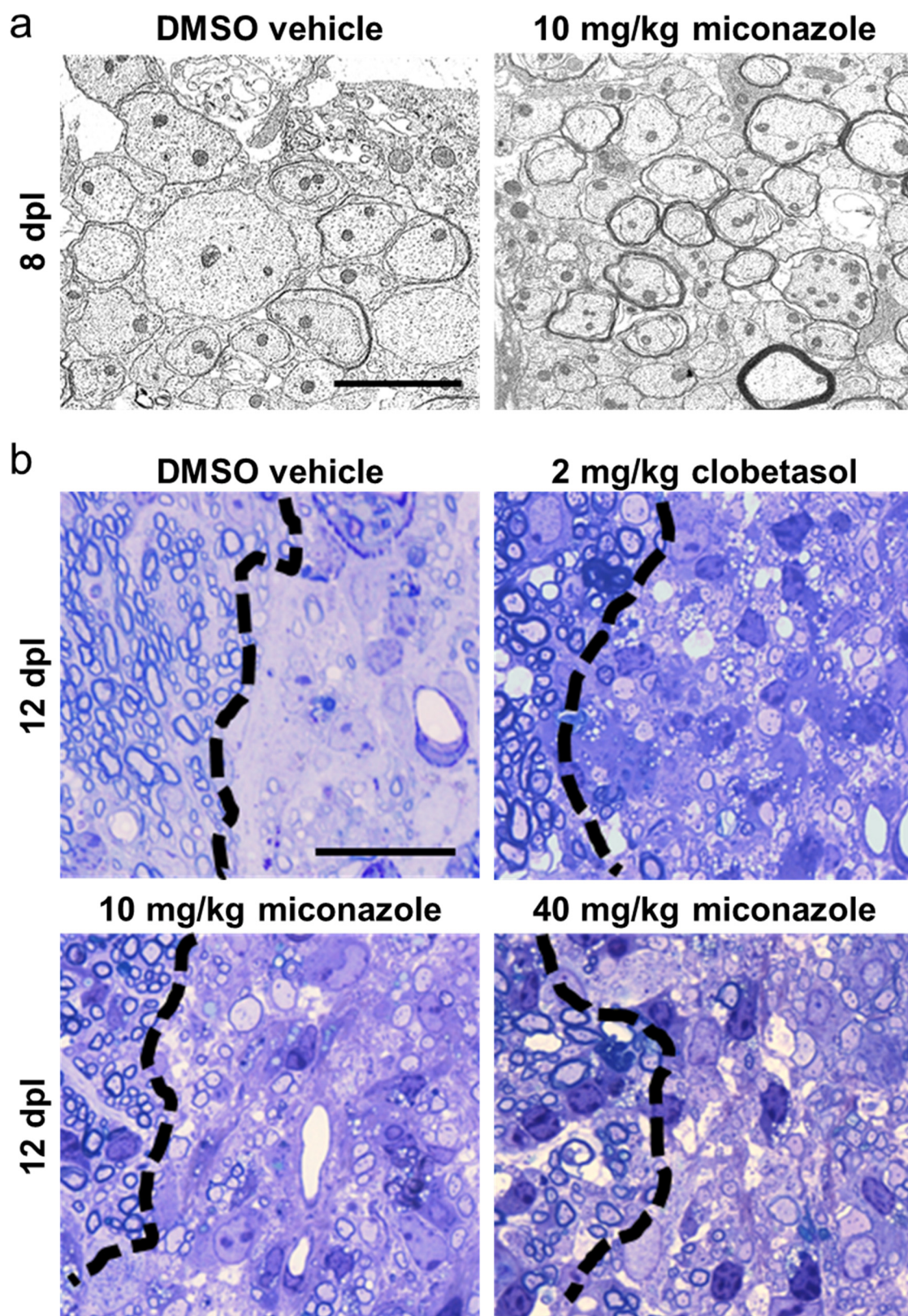
d

Steroids	Primary Screen Rank
clobetasol	7
betamethasone	19
methylprednisolone	21
budesonide	28
triamcinolone	29
amcinonide	35
fluticasone	37
fluorometholone	38
depo-medrol	41
beclomethasone	44
loteprednol	45
fluocinolone	47
dexamethasone	49
hydrocortisone	50
halometasone	52
flucinonide	57
prednisolone	67
desoximetasone	100
dehydrocholic Acid	188
mestanolone	198
exemestane	212
flunisolide	259
prednisone	528



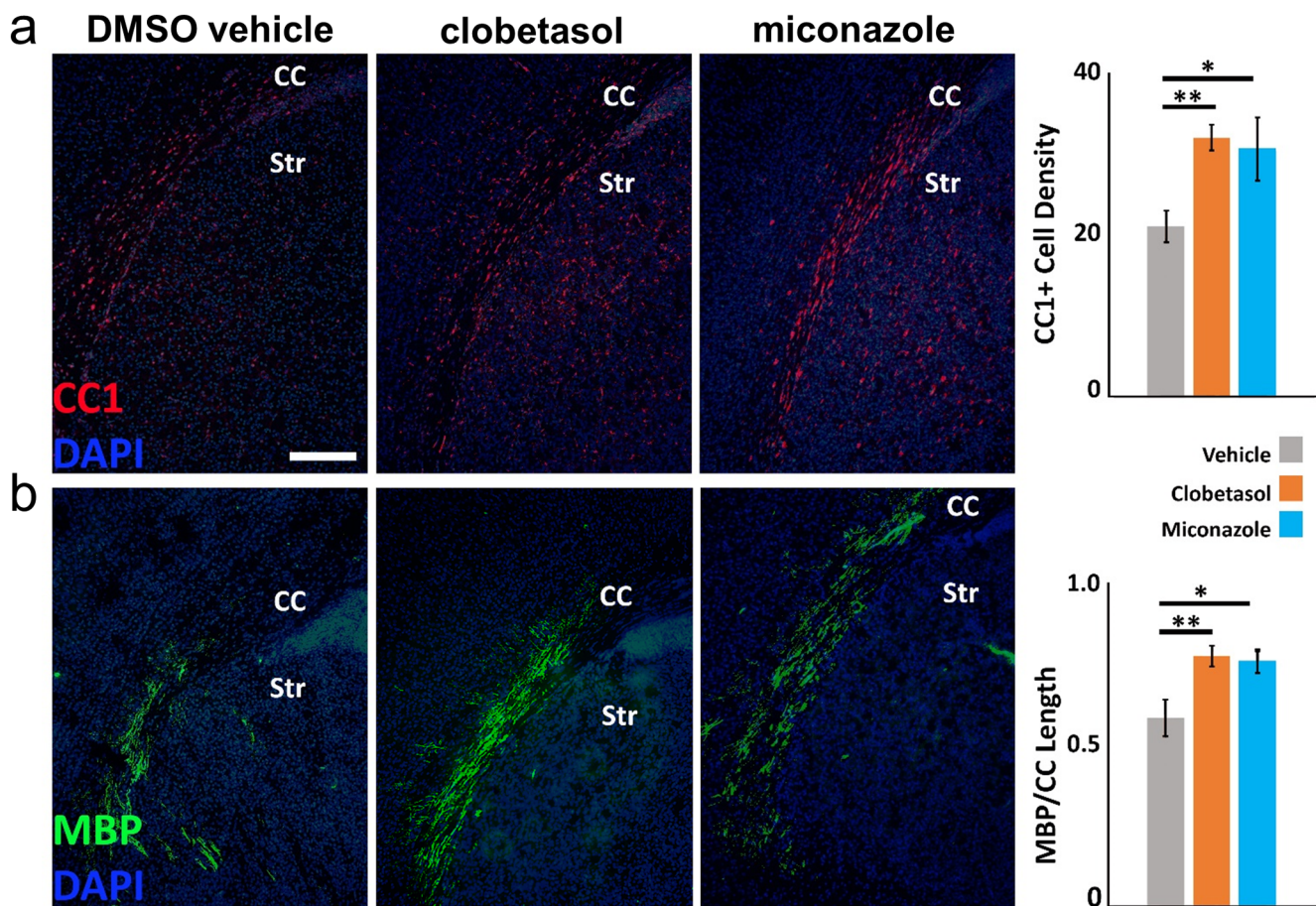
Extended Data Figure 3 | Primary screen structure–activity analysis. Chemoinformatic identification of two substructures consistently enriched in high-performing drugs in the OPC assay. Numerical activity rank in the primary screen is indicated with the top 22 shown in green, 23–50 shown in grey, and >51 in red. **a**, 1,3-Diazoles, mono-substituted at the 1-position

showed consistent activity on OPCs. **b**, **c**, 1,3-Diazoles, poly-substituted at two or more of the R groups (**b**), or 1,2,4-triazoles, mono-substituted at the 1-position (**c**) showed no activity on OPCs. **d**, The sterane base structure showed enrichment in the top performing hits.



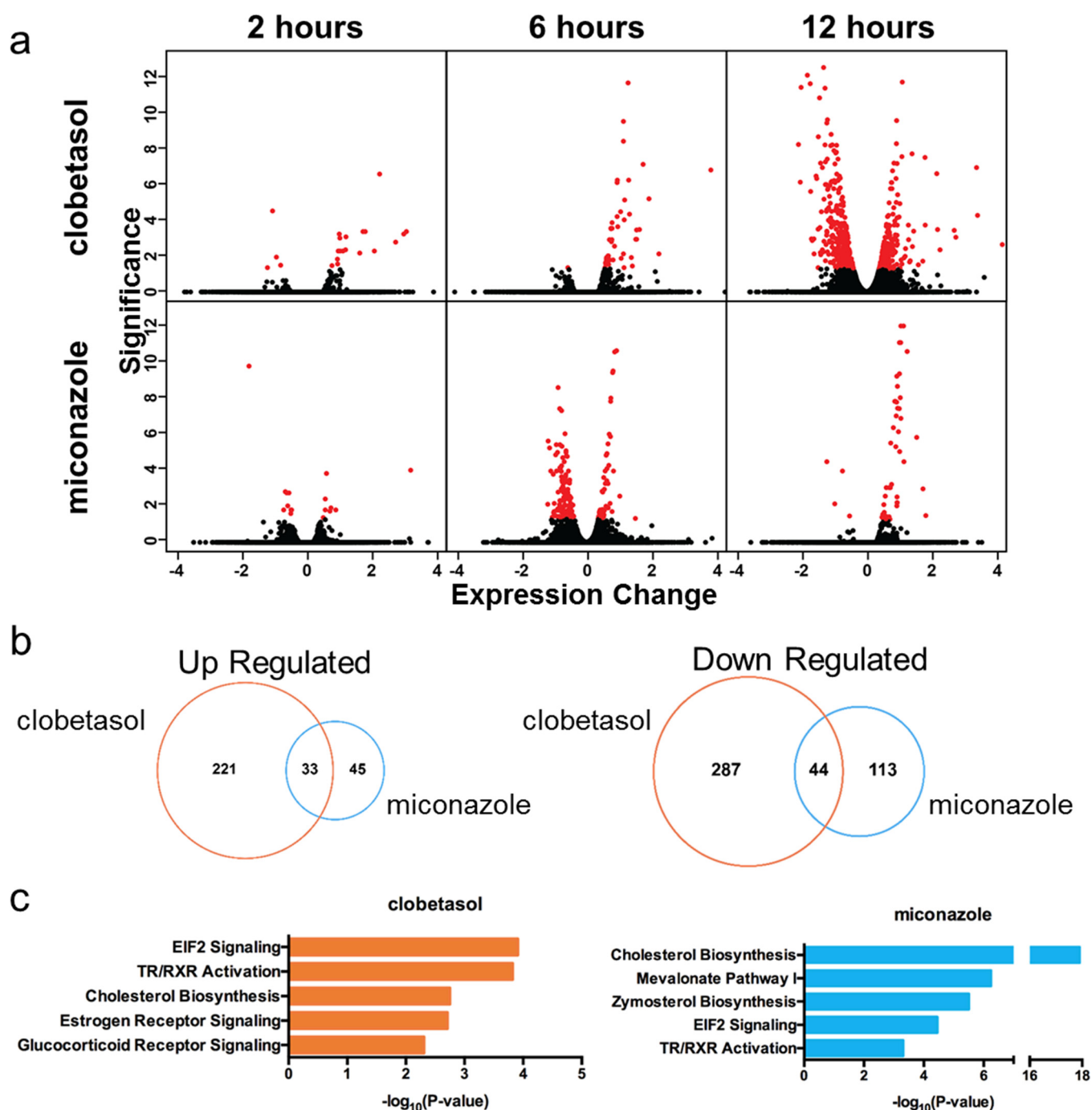
Extended Data Figure 4 | Histological assessment of remyelination in the LPC-induced model of demyelination. **a**, Representative electron micrographs showing remyelinated axons within lesions of miconazole treated mice at 8 d.p.l. Scale bar, 2 μ m. **b**, Histological sections stained with toluidine

blue showing the extent of remyelination in the lesions of treated animals at 12 d.p.l. Normal uninjured myelin appears to the left of the black dashed line demarcating the definitive lesion edge. Scale bar, 20 μ m.



Extended Data Figure 5 | Miconazole and clobetasol enhance myelination *in vivo*. **a, b,** Representative immunohistochemical images of the lateral corpus callosum (CC) of postnatal day 6 mouse pups that had been injected intraperitoneally daily for 4 days previously starting on postnatal day 2 with vehicle, clobetasol (2 mg/kg), or miconazole (10 mg/kg). CC1 (red) marks newly generated oligodendrocytes (**a**) and MBP (green) shows the extent of

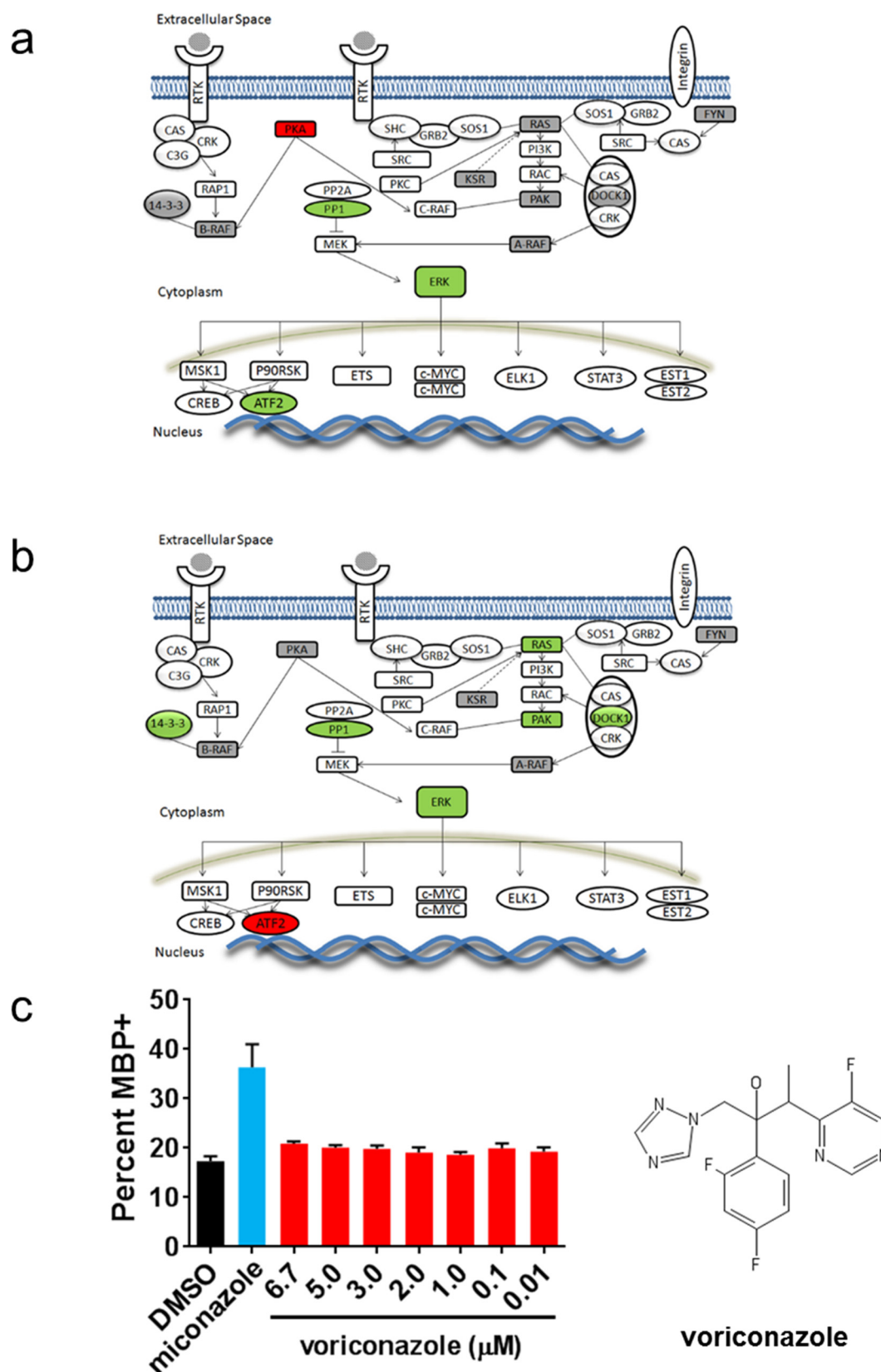
developmental myelination (**b**). Clobetasol and miconazole treatment each induce a marked increase in the number of CC1-positive oligodendrocytes in the lateral corpus callosum (**a**) and a significant increase in the length of the corpus callosum covered with aligned MBP⁺ fibres (**b**). Scale bar, 200 μ m. Two-tailed *t*-test, * $P \leq 0.05$ and ** $P \leq 0.01$. Str, striatum. All graphs are presented as mean \pm s.e.m.



Extended Data Figure 6 | RNaseq time course of drug-treated OPCs.

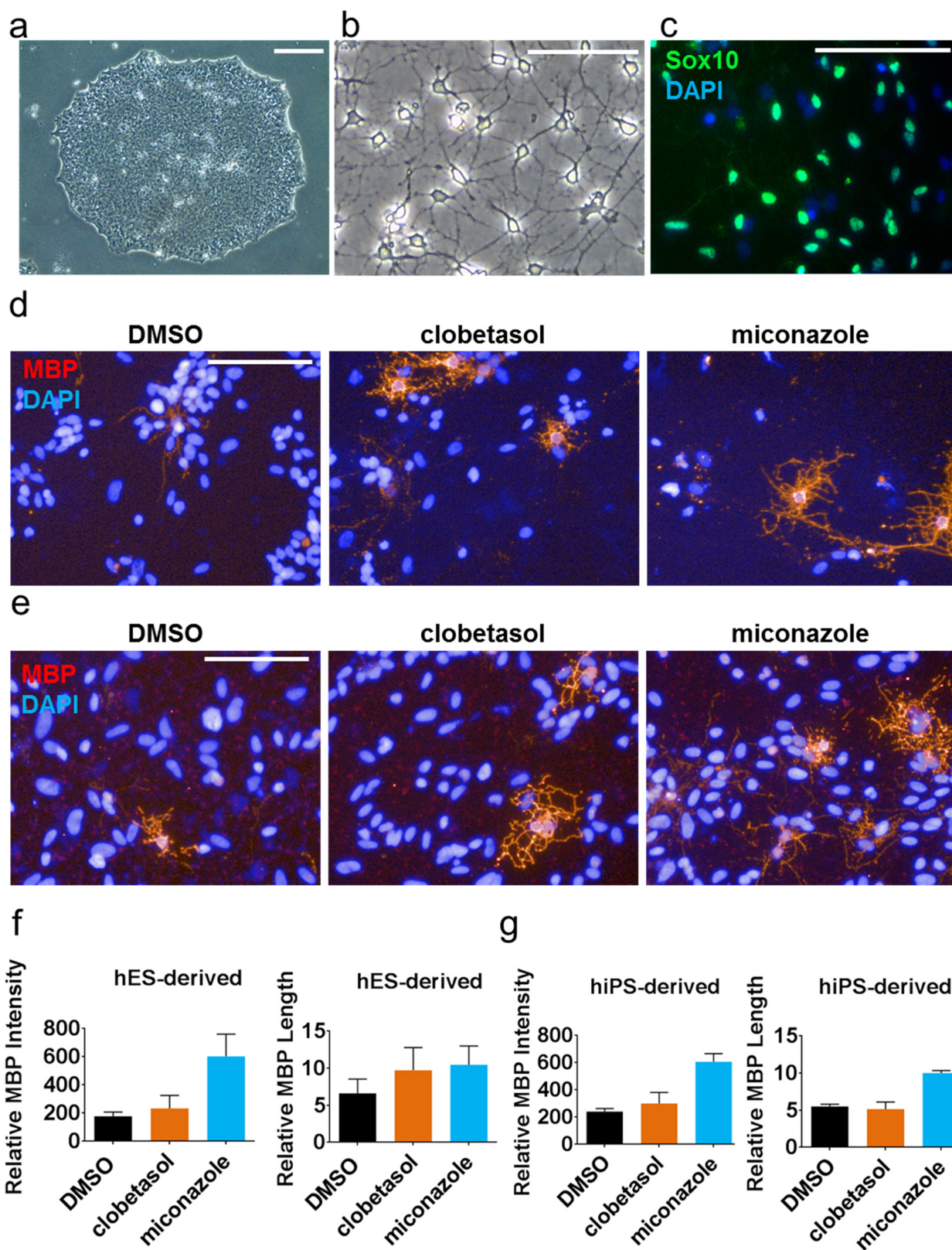
a, Volcano plots of all genes from OPCs treated with clobetasol or miconazole relative to vehicle control, with differentially expressed genes highlighted (red). Significance (measured as $-\log_{10}[q \text{ value}]$) is plotted in relation to expression change ($\log_2[\text{treatment/vehicle}]$). Time course was after 2, 6, and 12 h of drug

treatment. **b**, Venn diagrams depicting the overlap of genes differentially expressed at any time point and increased in treatments versus vehicle (left), as well as those decreased in treatments versus vehicle (right). **c**, Significant canonical pathways perturbed by each drug treatment according to Ingenuity Pathway Analysis.



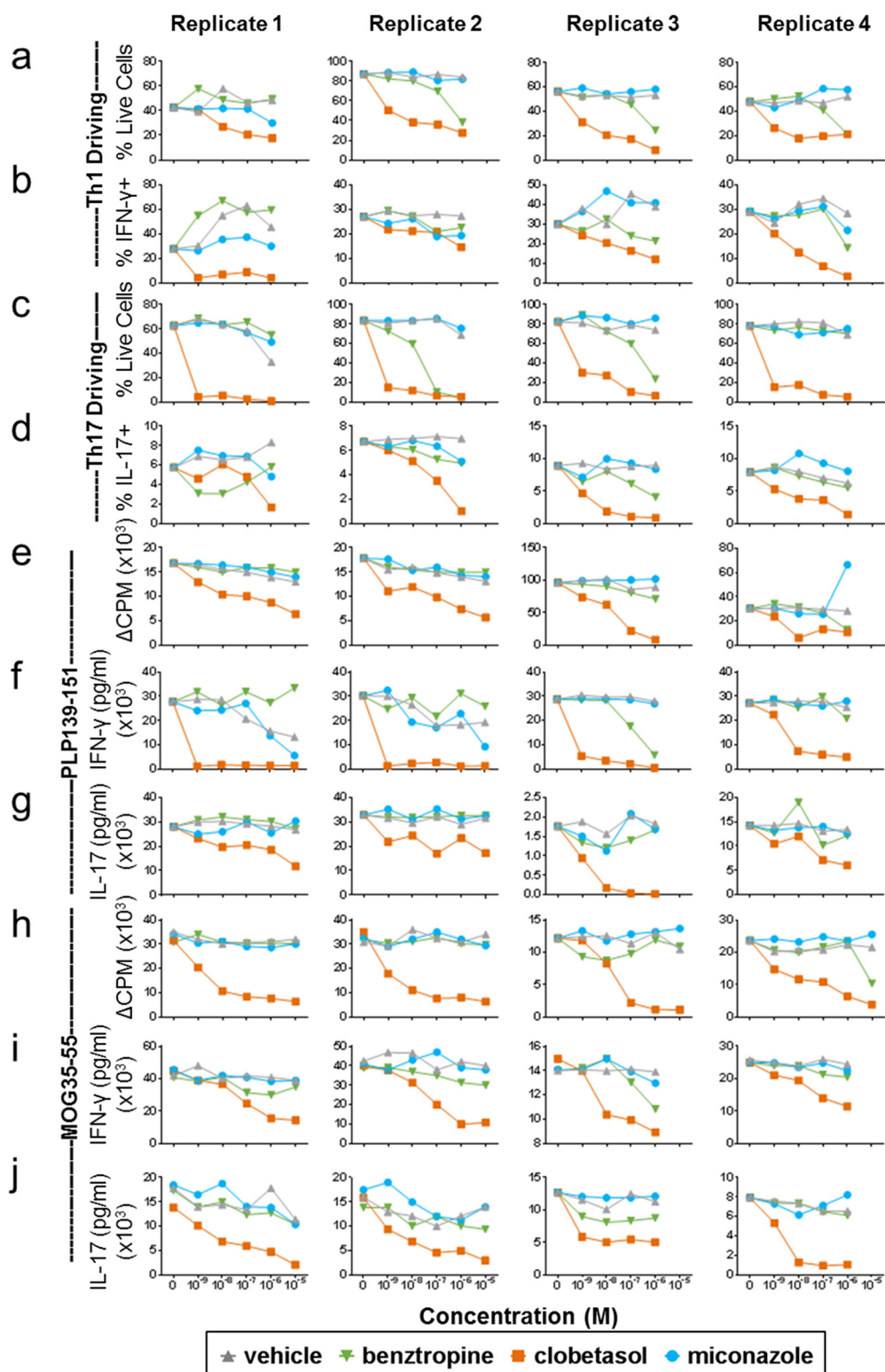
Extended Data Figure 7 | Global phosphoproteomic analysis of miconazole-treated OPCs. **a, b,** OPCs treated with miconazole for (a) 1 h or (b) 5 h followed by global phosphoproteomic analysis. Proteins highlighted in green were observed to have a two-fold or greater increase in phosphorylation whereas those highlighted in red were observed to have a two-fold or greater decrease in phosphorylation compared with time-point-matched vehicle-treated controls. Proteins highlighted in grey were detected in the analysis but

were not changed compared with vehicle control. See Supplementary Table 3 for the full phosphoproteomic data set. **c,** Quantification of the percentage of MBP⁺ oligodendrocytes differentiated from mouse OPCs after 72 h of treatment with DMSO, miconazole (1 μM), or voriconazole (seven doses, 0.01–6.7 μM); *n* = 6 wells per condition with >6,000 cells scored per well. Graph presented as mean ± s.e.m. The chemical structure of voriconazole is shown.



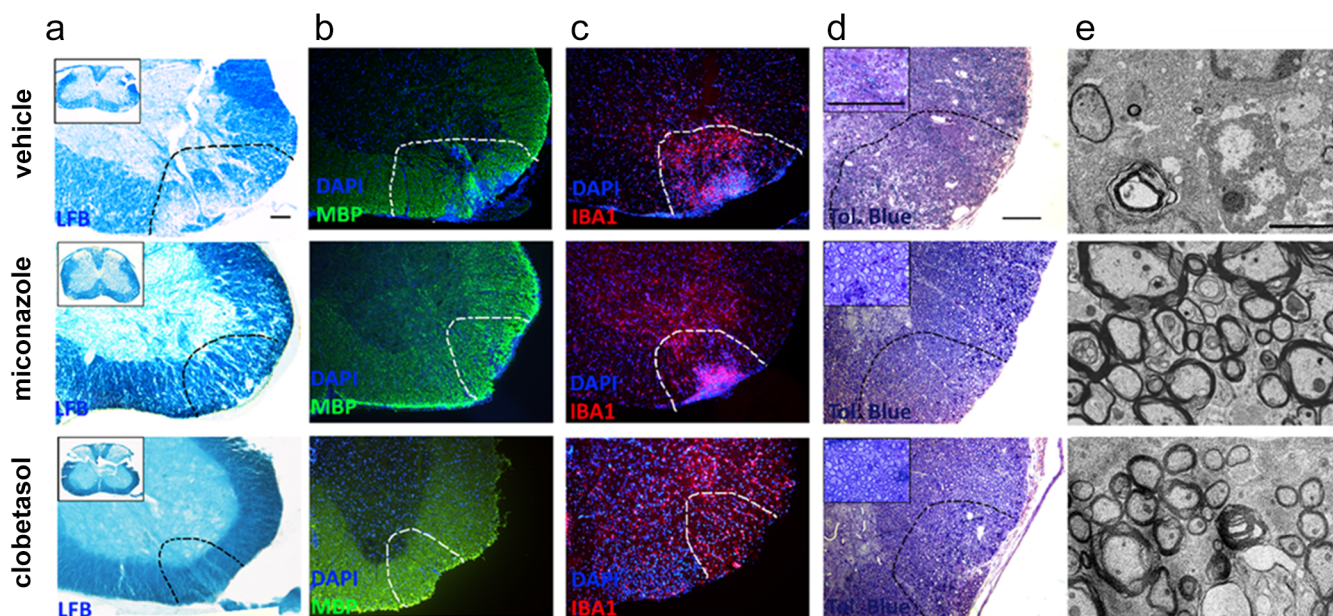
Extended Data Figure 8 | Miconazole and clobetasol enhance human OPC differentiation. **a**, Representative phase contrast image of a hESC colony cultured on matrigel. **b**, Representative phase contrast image of hESC-derived OPCs. **c**, hESC-derived OPCs stain positive for Sox10. **d**, **e**, Representative images of hESC-derived OPCs (**d**) and hiPSC-derived OPCs (**e**) treated with

vehicle (DMSO), miconazole (1 μ M), or clobetasol (5 μ M) for 21 days stained for MBP (red). **f**, **g**, HCA of hESC-derived (**f**) and hiPSC-derived (**g**) OPCs differentiated in the presence of drugs or vehicle over 21 days; $n = 3-5$ wells per condition with >120 cells scored per well. Graphs presented as mean \pm s.e.m. Scale bars, 100 μ m.



Extended Data Figure 9 | Effects of miconazole and clobetasol on immune cell survival and function. a–d, Quantification of cell proliferation (a, c) and differentiation (b, d) of naive CD4⁺ T cells from unprimed SJL/J mice after activation with plate-bound anti-CD3 under Th1 (a, b) or Th17 (c, d) cell driving conditions. e–j, *Ex vivo* recall assays quantifying cell proliferation

(ΔCPM) (e, h), with IFN-γ (f, i) and IL-17 (g, j) cytokine production from lymphocytes of mice primed with PLP_{139–151} (e–g) or MOG_{35–55} (h–j). Cultures were treated with vehicle (DMSO), benzotropine, clobetasol, or miconazole (10^{−9}–10^{−5} M) and analysed after 4 days. Four independent replicates are shown for each assay.



Extended Data Figure 10 | Histological improvements in MOG₃₅₋₅₅ EAE spinal cords after treatment with miconazole or clobetasol. **a**, **b**, Representative images of luxol fast blue (LFB) staining (**a**) demonstrated a clear decrease in areas of white matter disruption in the spinal cords of drug-treated animals which coincides with increased MBP staining (**b**). **c**, IBA1 staining showed a small reduction of immune cell infiltration into the lesion

areas, especially in clobetasol-treated animals, but not an abrogation. **d**, **e**, Representative images stained with toluidine blue (**d**) and electron micrographs (**e**) revealed a reduction in the areas of demyelination in drug-treated animals. Lesioned areas are outlined with black dotted lines. Insets in toluidine blue staining show higher magnification of myelination in the corresponding spinal cords. Scale bars, 100 μm (**a-c**, **d**) and 2 μm (**e**).

Intrinsic retroviral reactivation in human preimplantation embryos and pluripotent cells

Edward J. Grow¹, Ryan A. Flynn², Shawn L. Chavez^{3,4,5}, Nicholas L. Bayless⁶, Mark Wossidlo^{1,3,4}, Daniel J. Wesche³, Lance Martin², Carol B. Ware⁷, Catherine A. Blish⁸, Howard Y. Chang², Renee A. Reijo Pera^{1,3,4,9} & Joanna Wysocka^{3,10,11}

Endogenous retroviruses (ERVs) are remnants of ancient retroviral infections, and comprise nearly 8% of the human genome¹. The most recently acquired human ERV is HERVK(HML-2), which repeatedly infected the primate lineage both before and after the divergence of the human and chimpanzee common ancestor^{2,3}. Unlike most other human ERVs, HERVK retained multiple copies of intact open reading frames encoding retroviral proteins⁴. However, HERVK is transcriptionally silenced by the host, with the exception of in certain pathological contexts such as germ-cell tumours, melanoma or human immunodeficiency virus (HIV) infection^{5–7}. Here we demonstrate that DNA hypomethylation at long terminal repeat elements representing the most recent genomic integrations, together with transactivation by OCT4 (also known as POU5F1), synergistically facilitate HERVK expression. Consequently, HERVK is transcribed during normal human embryogenesis, beginning with embryonic genome activation at the eight-cell stage, continuing through the emergence of epiblast cells in preimplantation blastocysts, and ceasing during human embryonic stem cell derivation from blastocyst outgrowths. Remarkably, we detected HERVK viral-like particles and Gag proteins in human blastocysts, indicating that early human development proceeds in the presence of retroviral products. We further show that overexpression of one such product, the HERVK accessory protein Rec, in a pluripotent cell line is sufficient to increase IFITM1 levels on the cell surface and inhibit viral infection, suggesting at least one mechanism through which HERVK can induce viral restriction pathways in early embryonic cells. Moreover, Rec directly binds a subset of cellular RNAs and modulates their ribosome occupancy, indicating that complex interactions between retroviral proteins and host factors can fine-tune pathways of early human development.

Given the substantial contribution of transposons to the human genome and their emerging roles in shaping host regulatory networks^{8,9}, understanding the dynamic expression and function of these genomic elements is important for dissecting both human- and primate-specific aspects of gene regulation and development. We used published single-cell RNA-sequencing (RNA-seq) data sets to analyse the expression of major transposon classes at various stages of human preimplantation embryogenesis¹⁰, a developmental period associated with dynamic changes in DNA methylation and transposon expression¹¹. This analysis revealed two major clusters, one primarily consisting of repeats that begin to be transcribed at the onset of embryonic genome activation (EGA), which in humans occurs around the eight-cell stage, and a second cluster of repeats, whose transcripts can be detected in the embryo before EGA, indicating maternal deposition (Extended Data Fig. 1a). Within each cluster, more discrete stage-

specific changes in repeat transcription could be observed, such that analysis of the repetitive transcriptome alone was able to distinguish pre- and post-EGA cells, as well as eight-cell/morula cells from blastocyst cells (Extended Data Fig. 1a). For example, HERVK and its regulatory element, long terminal repeat (LTR)5HS, were both induced in eight-cell stage embryos, morulae, and continued to be expressed in epiblast cells of blastocysts (Fig. 1a–c and Extended Data Fig. 1a). We further observed that although HERVK was expressed in blastocyst outgrowths (passage 0 human embryonic stem (ES) cells), it was downregulated by passage 10 (Fig. 1d). In contrast, transcripts of another HERV, HERVH, and of its regulatory element LTR7, were detected before EGA and throughout preimplantation development, including in all blastocyst lineages and human ES cells (Extended Data Fig. 1a–c).

Recent studies have reported conditions for capturing a human naive pluripotent state *in vitro*^{12–16}, and we used RNA-seq to analyse the repetitive transcriptome of ELF1, a cell line derived from an eight-cell-stage human embryo under naive culture conditions, and compared it to the repeat expression in ELF1 cells matured *in vitro* into a primed state¹⁴. Surprisingly, although many transposon classes (for example, HERVH and LINE1-HS) were highly expressed in both cell states, only a few showed differential levels between the two (Fig. 1e). In particular, transcripts corresponding to HERVK proviruses and their regulatory elements, LTR5HS (but not the older LTR5a or LTR5b; see later), were among the most strongly induced in naive versus primed ELF1 cells (Fig. 1e and Extended Data Fig. 1d). Similar results were obtained by analysing available transcriptomes of primed H1 human ES cells and naive 3iL cells derived from them, as well as of primed H9 human ES cells and those ‘reset’ to the naive state by *NANOG* and *KLF2* transgene expression^{12,15} (Fig. 1e). Therefore, naive-state-specific upregulation of HERVK is consistent across multiple genetic backgrounds, derivation methods or culture conditions.

From an evolutionary perspective, HERVK is especially interesting, as it is the most recently acquired HERV from which multiple insertions have retained protein-coding potential¹⁷ (Extended Data Fig. 2a). While HERVK is present in all Old World primates, nearly a third of its proviruses in the human genome represent human-specific insertions, and 48% of those show polymorphisms in the human population, suggesting that HERVK was active within the last 200,000 years¹⁸ (Extended Data Fig. 2a). All human-specific and human-polymorphic HERVK elements are regulated by a specific LTR subgroup, LTR5HS, whereas insertions representing older integrations typically have regulatory elements of the LTR5a or LTR5b subtype⁴ (Extended Data Fig. 2a). Interestingly, during human preimplantation development and in the naive state, transcripts originating from LTR5HS, but not LTR5a or LTR5b, are preferentially expressed

¹Department of Genetics, Stanford University School of Medicine, Stanford, California 94305, USA. ²Howard Hughes Medical Institute and Program in Epithelial Biology, Stanford University School of Medicine, Stanford, California 94305, USA. ³Institute for Stem Cell Biology & Regenerative Medicine, Stanford University School of Medicine, Stanford University, Stanford, California 94305, USA.

⁴Department of Obstetrics and Gynecology, Stanford University School of Medicine, Stanford University, Stanford, California 94305, USA. ⁵Division of Reproductive and Developmental Sciences, Oregon National Primate Research Center, Oregon Health & Science University, Beaverton, Oregon 97006, USA. ⁶Stanford Immunology, Stanford University School of Medicine, Stanford, California 94305, USA.

⁷Department of Comparative Medicine, University of Washington, Seattle, Washington 98195-8056, USA. ⁸Department of Medicine, Stanford University School of Medicine, Stanford, California 94305, USA. ⁹Department of Cell Biology and Neurosciences, Montana State University, Bozeman, Montana 59717, USA. ¹⁰Department of Chemical and Systems Biology, Stanford University School of Medicine, Stanford, California 94305, USA. ¹¹Department of Developmental Biology, Stanford University School of Medicine, Stanford, California 94305, USA.

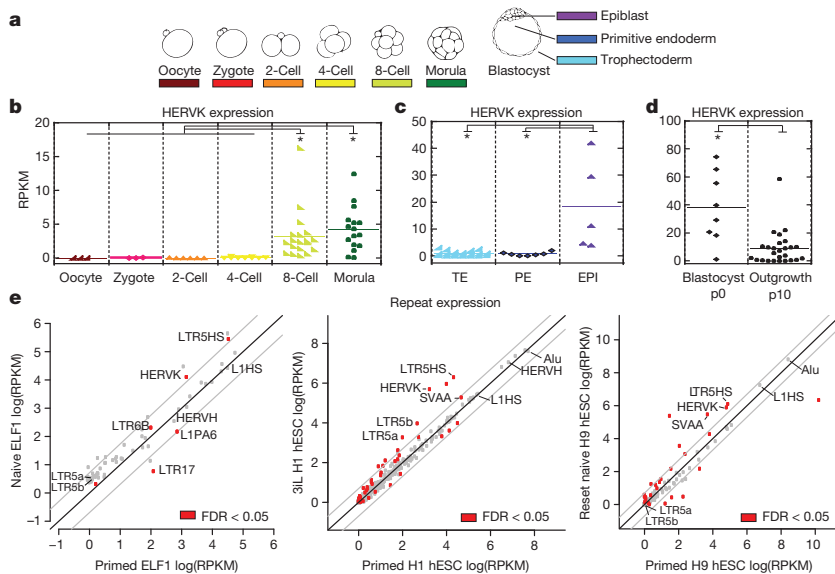


Figure 1 | Transcriptional reactivation of HERVK in human preimplantation embryos and naive human ES cells. **a**, Schematic of human preimplantation development. **b**, HERVK expression in single cells of human embryos at indicated stages. Solid line indicates mean. Oocyte ($n = 3$), zygote ($n = 3$), 2-cell ($n = 6$), 4-cell ($n = 11$), 8-cell ($n = 19$), morula ($n = 16$). **b–d**, Data are taken from ref. 10. * P value < 0.05, non-paired Wilcoxon test. RPKM, reads per kilobase per million. **c**, HERVK expression in single cells of human blastocysts, grouped by lineage. Solid line indicates mean. Trophoblast (TE; $n = 18$), primitive endoderm (PE; $n = 7$), epiblast (EPI; $n = 5$). **d**, HERVK expression in single cells of blastocyst outgrowths (passage (p)0 or human ES cells at passage (p)10). Solid line indicates mean. p0 ($n = 8$), p10 ($n = 26$). **e**, Analysis of the repetitive transcriptomes of three, genetically matched naive/primed human ES cell pairs. Left, naive/primed ELF1 human ES cells (data from this study) ($n = 3$ biological replicates for both conditions). Middle, 3iL/primed H1 human ES cells (data are taken from ref. 12) ($n = 3$ biological replicates for both conditions). Right, naive/primed H9 human ES cells (data are taken from ref. 15) ($n = 3$ biological replicates for both conditions). Significant repeats indicated in red at false discovery rate (FDR) < 0.05, DESeq. hESC, human ES cells.

(Fig. 1e), and we observed an upregulation of human-specific proviruses compared to evolutionarily older elements (Fig. 2a). We hypothesized that this differential regulation can be explained by *cis*-regulatory change in LTR5HS. Indeed, sequence analysis uncovered an OCT4 motif at position 693–699 base pairs (bp) of LTR5HS, which was conserved across diverse LTR5HS sequences, but not present in LTR5a/LTR5b, despite their overall high (~88%) sequence homology with LTR5HS (Fig. 2b and Extended Data Fig. 2a). To test whether OCT4 binding contributes to the transcriptional activation of LTR5HS, we used pluripotent NCCIT human embryonic carcinoma (EC) cells, which express OCT4, but, in contrast to human ES cells, are permissive for HERVK expression^{5,19} (Extended Data Fig. 2b–d). Chromatin immunoprecipitation with quantitative polymerase chain reaction (ChIP-qPCR) analysis of human EC cells showed preferential occupancy of OCT4, p300 and histone marks of active chromatin at LTR5HS elements, as compared to LTR5a/LTR5b (Fig. 2c). In contrast, we did not detect OCT4 or p300 binding at LTR5HS in primed human ES cells (Extended Data Fig. 2f). Consistent with a functional role in HERVK activation, knockdown of OCT4 or SOX2, but not of NANOG, led to a significant decrease in viral transcripts in human EC cells (Extended Data Fig. 2e and Extended Data Fig. 3a). Furthermore, the activity of transcriptional reporters driven by LTR5HS was impaired by mutations in the OCT4 motif (Fig. 2d and Extended Data Fig. 3b).

The aforementioned observations are consistent with transactivation by OCT4 being a driver of LTR5HS regulatory activity, but do not explain the differential transcriptional status of HERVK in primed versus naive human ES cells and in human EC cells, as all three express OCT4. We hypothesized that DNA methylation may contribute an additional layer of regulation, and indeed we observed HERVK hypomethylation of solo and proviral LTR5HS (but not the Gag open reading frame (ORF)) in human EC cells and naive ES cells, as compared to primed human ES cells and human induced pluripotent stem cells (iPSCs) (Fig. 2e and Extended Data Fig. 3c, d). Strong and preferential demethylation of LTR5HS was also observed in recently published DNA methylation maps from human preimplantation embryos, whereas HERVK coding sequences remained more highly methylated¹¹. Importantly, treatment of primed human ES cells with a

DNA methylation inhibitor, 5-aza-2'-deoxycytidine, for 24 h induced HERVK transcription, with 8–12-fold upregulation of an early transcript encoding an accessory protein, Rec (Fig. 2f). In addition, inhibition of DNA methylation, together with overexpression of OCT4 and SOX2, jointly facilitated HERVK transcription in HEK293 cells (Fig. 2g and Extended Data Fig. 3e), indicating that DNA hypomethylation and transactivation by OCT4 synergistically promote HERVK expression.

A defining characteristic of HERVK is that multiple proviruses have retained ORFs encoding full-length retroviral proteins⁴. Consequently, HERVK reactivation in pathological conditions has been associated with the presence of HERVK proteins^{5–7}, prompting us to examine whether retroviral proteins are also present in human embryos. We used a well-characterized monoclonal antibody recognizing the HERVK Gag precursor and its proteolytically processed form Capsid, which detects cytoplasmic signal with a characteristic punctate pattern in human EC cells and in a subset of naive ELF1 cells, but shows no staining in primed human ES cells and loss of signal in human EC cells after gag short interfering RNA (siRNA) knockdown (Extended Data Fig. 4a–d). In human blastocysts, Gag/Capsid staining was also detected in dense cytoplasmic puncta resembling those seen in human EC cells and naive ELF1 cells (Fig. 3a and Extended Data Fig. 4a, d, e), with all analysed blastocysts ($n = 19/19$) showing a robust signal. Several HERVK-positive human EC cell lines have been shown to produce viral-like particles (VLPs)²⁰. Remarkably, heavy metal staining transmission electron microscopy (TEM) of blastocysts revealed the presence of cytoplasmic, electron-dense particles of approximately 100 nm in diameter—the reported size of reconstructed HERVK VLPs—with electron-lucent cores^{21,22} (Fig. 3b). Additionally, human blastocyst cells also contained cytosolic vesicles enclosing 50 or more smaller, highly electron-dense particles of approximately 75 nm in size, which resembled the immature VLPs also seen in human EC cells (Fig. 3c and Extended Data Fig. 5a). The presence of HERVK-derived particles in human blastocysts was further supported by immuno-gold TEM staining, which detected VLPs (or vesicles with multiple VLPs) labelled by Gag/Capsid antibodies either within embryonic cells or on the cell surface, similar to those seen in immuno-gold TEM staining of human EC cells (Fig. 3d, e and

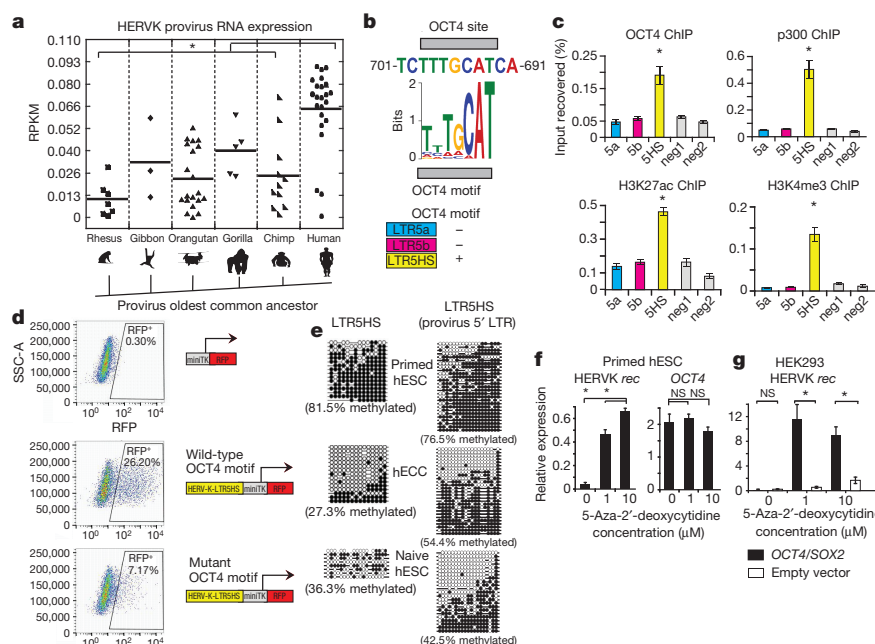


Figure 2 | Transactivation by OCT4 and DNA hypomethylation of LTR5HS synergistically regulate HERVK transcription. **a**, Expression of different HERVK proviral sequences, grouped according to the oldest common ancestor, as defined previously⁴. **P* value < 0.05, non-paired Wilcoxon test. Solid line indicates mean. RNA-seq data set used for the analysis was from 3iL naive H1 cells¹²; *n* = 3 biological replicates. **b**, Conserved OCT4 site in LTR5HS with position weight matrix of the corresponding motif shown for comparison (top). Presence/absence of OCT4 motif in distinct LTR5 sequences is indicated (bottom); more detailed sequence information is in Extended Data Fig. 2a. **c**, ChIP-qPCR analyses from human EC cells (NCCIT) using antibodies indicated on top of each graph. Signals were quantified using primer sets specific to LTR5HS (5HS), LTR5a (5a) and LTR5b (5b) consensus sequences or two 'negative' intergenic, non-repetitive regions (neg1, neg2). **P* value < 0.05 compared to negative control, one-sided *t*-test. *n* = 4 biological replicates, error bars are ± 1 standard deviation (s.d.). **d**, Flow cytometry analysis of human EC cells with integrated LTR5HS fluorescent reporters, either wild type (middle) or with OCT4 motif mutation (bottom). Red fluorescent protein (RFP)-positive

population was gated using side-scatter area (SSC-A) and cells with integrated negative control reporter (top) containing minimal thymidine kinase (miniTK) promoter. Shown is a representative result of two independent experiments. **e**, Bisulfite conversion quantification of LTR5HS 5-methyl-cytosine levels measured using LTR5HS-specific primer pairs anchored in the LTR5HS consensus sequence (left) or provirus-specific 5' LTR5HS (right) for human EC cells (hECC; NCCIT), human ES cells (hESC; H9) or naive human ES cells (ELF1). Filled circles depict modified cytosines, open circles depict unmodified cytosines. Human EC cells (NCCIT) and naive human ES cells (ELF1) are less methylated than primed human ES cells (H9). *P* < 0.05, non-paired Wilcoxon test. **f**, qPCR with reverse transcription (RT-qPCR) analysis of human ES cells (H9) treated with indicated concentrations of 5-aza-2'-deoxycytidine for 24 hours. **P* value < 0.05, one-sided *t*-test. *n* = 3 biological replicates, error bars ± 1 s.d. **g**, RT-qPCR analysis of HERVK *rec* RNA levels in HEK293 cells treated with indicated concentrations of 5-aza-2'-deoxycytidine, followed by transfection with OCT4/SOX2 expression constructs. **P* value < 0.05, one-sided *t*-test; NS, not significant. *n* = 4 biological replicates, error bars ± 1 s.d.

Extended Data Fig. 5b); control blastocyst staining showed no signal from secondary antibody (Extended Data Fig. 5c). Altogether, these data demonstrate that human preimplantation development proceeds in the presence of retroviral proteins and VLPs (summarized in Extended Data Fig. 5d).

Recent studies highlight the ability of TEs to contribute regulatory sequences to mammalian genomes^{9,23,24}. For example, MERV-L elements in mouse have been reported to function as alternative promoters, driving expression of many two-cell stage-specific chimaeric transcripts²³. However, we did not detect robust evidence for HERVK-associated chimaeric transcription (Extended Data Fig. 6a, b and Supplementary Table 1), suggesting that LTR5HS is unlikely to contribute promoter activity to nearby host genes. Alternatively, LTR sequences derived from ERVs could be co-opted to act as long-distance enhancers for the host²⁴. In agreement with such a possibility, LTR5HS elements were marked by p300 and H3K27ac (Fig. 2c), while genes located in their vicinity showed a strong bias for naive-state-enriched expression, regardless of their upstream or downstream position in relation to the LTR5HS (Extended Data Fig. 6c–e). However, we cannot rule out that this result could be a consequence of preferential HERVK integration near genes active in the naive state.

HERVK encodes a small accessory protein, Rec, homologous to HIV Rev, which binds to and promotes nuclear export and translation of viral RNAs²⁵. *rec*, an early viral transcript derived through alternative splicing of the *env* gene (Extended Data Fig. 2a), is expressed in

naive ES cells and human blastocysts, and is rapidly induced in primed human ES cells exposed to 5-aza-2'-deoxycytidine (Extended Data Fig. 7a and Fig. 2f). We hypothesized that Rec-mediated nuclear export of viral RNAs into the cytoplasm might ultimately lead to the induction of innate antiviral responses, which typically rely on cytosolic detection of viral RNA/DNA and protein. We noted a striking induction of messenger RNA encoding an interferon-induced viral restriction factor IFITM1 (ref. 26; also known as FRAGILIS2) in human epiblast cells¹⁰, as well as upregulation of *IFITM1* transcripts and surface protein levels in human naive versus primed human ES cells (Extended Data Fig. 7b, c, f and Supplementary Table 6). Furthermore, expression of a *rec* transgene in human EC cells was sufficient to elevate surface-localized IFITM1 protein levels (Fig. 4a). This was at least in part mediated through an effect on *IFITM1* mRNA transcription or stability, as *Rec* overexpression or knockdown had, respectively, increased or decreased *IFITM1* mRNA levels (Extended Data Fig. 7d). Of note, although the minimal components of the JAK/STAT interferon pathway are present in human EC cells, many other interferon-induced genes are not upregulated or expressed, indicating that HERVK triggers a precise antiviral response in host cells (Supplementary Table 2). To test whether HERVK expression provides viral resistance, we infected control wild-type human EC cells, control human EC cells expressing a green fluorescent protein (GFP) transgene, or two independent clonal Rec human EC cell lines (Rec-hECCs) with influenza H1N1(PR8) virus. Interestingly, the Rec-hECCs exhibited substantially attenuated infec-

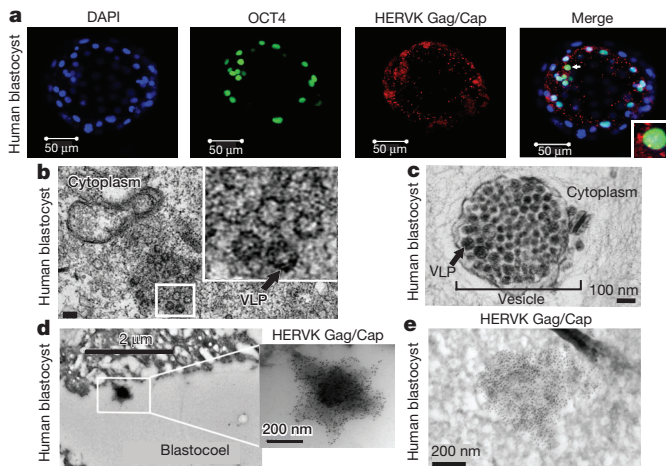


Figure 3 | Human blastocysts contain HERVK proteins and viral-like particles. **a**, Immunofluorescence of human blastocysts (days post-fertilization (DPF) 5–6) stained with 4',6-diamidino-2-phenylindole (DAPI; blue), OCT4 antibody (green), and HERVK Gag/Capsid antibody (red). Images show a representative example ($n = 19$ embryos). Scale bar = 50 μm . White arrow indicates an OCT4⁺ nucleus, surrounded by cytoplasmic Gag/Capsid (Cap), which is shown with higher magnification in an inset. **b**, Heavy metal staining TEM of a human blastocyst. Arrow indicates putative VLP (found in $n = 2/3$ blastocysts, DPF 5–6). Higher magnification of indicated region is shown in inset. Scale bar = 200 nm. **c**, Heavy metal staining TEM of human blastocyst. Arrow indicates putative immature VLP, bracket indicates vesicle filled with putative VLP (found in $n = 2/3$ blastocysts, DPF 5–6). Scale bar = 100 nm. **d, e**, Immuno-TEM of human blastocysts with Gag/Capsid staining; region of higher magnification is boxed. Representative examples of budding (**d**) and cell-internal (**e**) particles are shown; $n = 3$ blastocysts (DPF 5–6), $n = 3$ labelled particles in two embryos.

tion levels as compared to the control GFP-hECCs (Fig. 4b) or wild-type human EC cells (Extended Data Fig. 7e).

Retroviral accessory proteins often masterfully manipulate host cell factors to achieve optimal replicative efficiency. To examine whether, beyond reported binding to HERVK 3' LTRs^{25,27}, Rec can also associate with cellular RNAs, we performed tandem affinity purification

iCLIP-seq in human EC cells expressing Flag-GFP (GFP) or Flag-GFP-tagged *rec* transgene (Extended Data Fig. 8a, b). We did not detect associated RNA in the control Flag-eGFP purifications, indicating low nonspecific RNA recovery of our assay (Extended Data Fig. 8b). In contrast, parallel Rec purifications from two Flag-GFP Rec expressing clones yielded ultraviolet-crosslinked RNAs, sequencing of which demonstrated that *in vivo*, Rec robustly binds LTR5HS, but only in the region previously defined as containing the highly structured Rec-responsive element^{25,28} (Fig. 4c and Extended Data Fig. 8b, c). In addition, Rec directly interacts with ~1,600 host mRNAs, preferentially in their 3' untranslated regions (UTRs), a positional preference analogous to that observed in the viral RNA (Fig. 4d, e, Extended Data Fig. 9a and Supplementary Table 3). We did not detect specific RNA sequence motifs enriched at Rec-bound sites; however, multiple examined Rec iCLIP targets were predicted to fold into stable secondary structures (Extended Data Fig. 9b). This is reminiscent of the interaction of Rec with its HERVK LTR response element, which is mediated by RNA secondary structure, rather than a discrete specific binding site²⁸. We also observed Rec association with mRNAs encoding surface receptor molecules and ligands (for example, *FGFR1*, *FGF13*, *FGFR3*, *KLRG2*, *IGF1R*, *FZD7*, *GDF3*) and chromatin regulators (for example, *DNMT1*, *CHD4*) (Extended Data Fig. 9a and Supplementary Table 3).

Given that Rec binding to viral RNAs promotes their nuclear export and translation, we next examined if endogenous mRNAs bound by Rec are also more efficiently targeted to ribosomes^{22,25}. Ribosome profiling of Rec-hECCs, in comparison to wild-type human EC cells, revealed both increases and decreases in ribosomal occupancy, with differential enrichment of 941 mRNAs, of which 134 were also Rec iCLIP targets, representing a significant overlap (P value < 0.05, hypergeometric test) (Fig. 4f and Supplementary Table 5). Notably, mRNAs bound by Rec in 3' UTRs or coding sequences were more likely to be upregulated in their ribosomal occupancy than expected by chance (P value < 0.05, hypergeometric test), but we did not observe such enrichment for mRNAs bound in their 5' UTRs. We also noticed that several Rec-bound transcripts (for example, *RPL22*, *RPL31*, *RPS13*, *RPS20*, *EIF4G1*) encoding ribosome components and translation regulators had increased occupancy in Rec-hECCs,

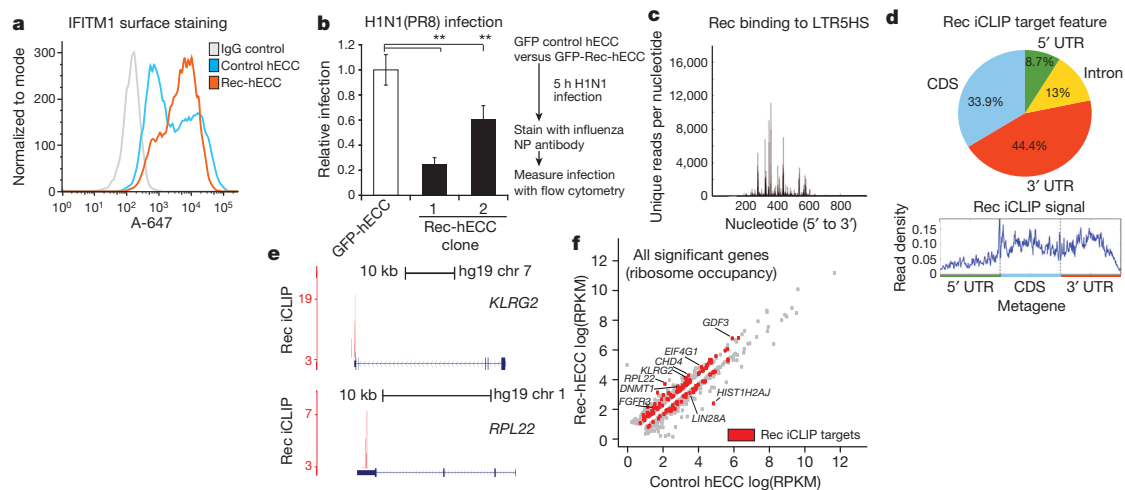


Figure 4 | HERVK accessory protein Rec upregulates viral restriction pathway and engages cellular mRNAs. **a**, Flow cytometry histograms of IFITM1 surface staining in control human EC cells or Rec-hECC cells; histogram of negative control cells stained with isotype IgG⁺ Alexa-647 secondary antibody (A-647) is shown for comparison. Shown is a representative result of two independent experiments. **b**, H1N1(PR8) influenza infection of control GFP-hECC cells or two clonal lines of Rec-hECCs. Control cells were set as 100%, shown is aggregate results from two independent experiments, $n = 8$ total biological replicates for each condition. Error bars are

± 1 s.d. ** P value < 0.005, one-sided t -test. **c**, Rec iCLIP reads mapped to the LTR5HS sequence, $n = 2$ biological replicates. **d**, Distribution of Rec binding sites on endogenous mRNAs (top) and aggregate Rec iCLIP-seq signal on a metagene (bottom), $n = 2$ biological replicates. CDS, coding DNA sequence. **e**, Distribution of Rec iCLIP reads at representative target mRNAs *KLRG2* (top), *RPL22* (bottom); y-axis, iCLIP score, at cut-off = 3 (see Methods for details). **f**, Ribosome profiling signal for all significant genes (FDR < 0.05 Cuffdiff) in wild-type human EC cells versus Rec-hECCs, $n = 4$ biological replicates. Rec iCLIP targets are coloured in red.

potentially contributing to additional indirect translational effects of Rec overexpression (Fig. 4e, f and Supplementary Table 5).

Altogether, our results demonstrate that early human development is accompanied by the stage-specific transcriptional activation of HERVK, translation of its ORFs, and assembly of VLPs (Extended Data Fig. 10a). Beyond preimplantation development, we predict that HERVK reactivation occurs in human primordial germ cells (PGCs), which are also characterized by the presence of OCT4 and genome-wide DNA hypomethylation²⁹. HERVK protein products have the potential to engage host machinery, as exemplified here by modulation of cellular mRNAs by Rec. This fine-tuning of cellular functions by HERVK proteins may contribute to human-specific or even individual-specific aspects of early development, as the retroviral ORFs are preferentially expressed from the human-specific proviruses, many of which are polymorphic in the human population^{4,18}. Finally, our data raise the intriguing possibility that HERVK provides an immunoprotective effect for human embryos against different classes of viruses sensitive to the IFITM1-type restriction. Although *IFITM* family members were first described as interferon-induced genes, they are also classical naive-state and PGC markers in the mouse, which nonetheless appear to be dispensable for development³⁰. These observations suggest that IFITM1-mediated restriction may be a evolutionarily conserved mechanism protecting both embryos and germ cells from either reinfection from infectious ERVs or exogenous viral infection (Extended Data Fig. 10a).

Online Content Methods, along with any additional Extended Data display items and Source Data, are available in the online version of the paper; references unique to these sections appear only in the online paper.

Received 4 March 2014; accepted 10 February 2015.

Published online 20 April 2015.

- Stoye, J. P. Studies of endogenous retroviruses reveal a continuing evolutionary saga. *Nature Rev. Microbiol.* **10**, 395–406 (2012).
- Belshaw, R. et al. Long-term reinfection of the human genome by endogenous retroviruses. *Proc. Natl Acad. Sci. USA* **101**, 4894–4899 (2004).
- Barbulescu, M. et al. Many human endogenous retrovirus K (HERVK) proviruses are unique to humans. *Curr. Biol.* **9**, 861–868 (1999).
- Subramanian, R. P., Wildschutte, J. H., Russo, C. & Coffin, J. M. Identification, characterization, and comparative genomic distribution of the HERVK (HML-2) group of human endogenous retroviruses. *Retrovirology* **8**, 90 (2011).
- Herbst, H., Sauter, M. & Mueller-Lantzsch, N. Expression of human endogenous retrovirus K elements in germ cell and trophoblastic tumors. *Am. J. Pathol.* **149**, 1727–1735 (1996).
- Muster, T. et al. An endogenous retrovirus derived from human melanoma cells. *Cancer Res.* **63**, 8735–8741 (2003).
- Contreras-Galindo, R. et al. Human endogenous retrovirus K (HML-2) elements in the plasma of people with lymphoma and breast cancer. *J. Virol.* **82**, 9329–9336 (2008).
- Pace, J. K. & Feschotte, C. The evolutionary history of human DNA transposons: evidence for intense activity in the primate lineage. *Genome Res.* **17**, 422–432 (2007).
- Kunars, G. et al. Transposable elements have rewired the core regulatory network of human embryonic stem cells. *Nature Genet.* **42**, 631–634 (2010).
- Yan, L. et al. Single-cell RNA-seq profiling of human preimplantation embryos and embryonic stem cells. *Nature Struct. Mol. Biol.* **20**, 1131–1139 (2013).
- Smith, Z. D. et al. DNA methylation dynamics of the human preimplantation embryo. *Nature* **511**, 611–615 (2014).
- Chan, Y.-S. et al. Induction of a human pluripotent state with distinct regulatory circuitry that resembles preimplantation epiblast. *Cell Stem Cell* **13**, 663–675 (2013).
- Gafni, O. et al. Derivation of novel human ground state naive pluripotent stem cells. *Nature* **504**, 282–286 (2013).
- Ware, C. B. et al. Derivation of naive human embryonic stem cells. *Proc. Natl Acad. Sci. USA* **111**, 4484–4489 (2014).
- Takahashi, Y. et al. Resetting transcription factor control circuitry toward ground-state pluripotency in human. *Cell* **158**, 1254–1269 (2014).
- Theunissen, T. W. et al. Systematic identification of culture conditions for induction and maintenance of naive human pluripotency. *Cell Stem Cell* **15**, 471–487 (2014).
- Hohn, O., Hanke, K. & Bannert, N. HERVK(HML-2), the best preserved family of HERVs: endogenization, expression, and implications in health and disease. *Front. Oncol.* **3**, 246 (2013).
- Shin, W. et al. Human-specific HERVK insertion causes genomic variations in the human genome. *PLoS ONE* **8**, e60605 (2013).
- Boller, K. et al. Evidence that HERVK is the endogenous retrovirus sequence that codes for the human teratocarcinoma-derived retrovirus HTDV. *Virology* **196**, 349–353 (1993).
- Bieda, K., Hoffmann, A. & Boller, K. Phenotypic heterogeneity of human endogenous retrovirus particles produced by teratocarcinoma cell lines. *J. Gen. Virol.* **82**, 591–596 (2001).
- Dewannieux, M. et al. Identification of an infectious progenitor for the multiple-copy HERVK human endogenous retroelements. *Genome Res.* **16**, 1548–1556 (2006).
- Lee, Y. N. & Bieniasz, P. D. Reconstitution of an infectious human endogenous retrovirus. *PLoS Pathog.* **3**, e10 (2007).
- Macfarlan, T. S. et al. Embryonic stem cell potency fluctuates with endogenous retrovirus activity. *Nature* **487**, 57–63 (2012).
- Chuong, E. B., Rumi, M. A. K., Soares, M. J. & Baker, J. C. Endogenous retroviruses function as species-specific enhancer elements in the placenta. *Nature Genet.* **45**, 325–329 (2013).
- Löwer, R., Tönjes, R. R., Korbacher, C., Kurth, R. & Löwer, J. Identification of a Rev-related protein by analysis of spliced transcripts of the human endogenous retroviruses HTDV/HERVK. *J. Virol.* **69**, 141–149 (1995).
- Brass, A. L. et al. The IFITM proteins mediate cellular resistance to influenza A H1N1 virus, West Nile virus, and dengue virus. *Cell* **139**, 1243–1254 (2009).
- Hanke, K. et al. Staufen-1 interacts with the human endogenous retrovirus family HERVK(HML-2) Rec and Gag proteins and increases virion production. *J. Virol.* **87**, 11019–11030 (2013).
- Magin-Lachmann, C. et al. Rec (formerly Corf) function requires interaction with a complex, folded RNA structure within its responsive element rather than binding to a discrete specific binding site. *J. Virol.* **75**, 10359–10371 (2001).
- Gkoutela, S. et al. The ontogeny of cKIT⁺ human primordial germ cells proves to be a resource for human germ line reprogramming, imprint erasure and *in vitro* differentiation. *Nature Cell Biol.* **15**, 113–122 (2013).
- Lange, U. C. et al. Normal germ line establishment in mice carrying a deletion of the *Ifitm/Fragilis* gene family cluster. *Mol. Cell. Biol.* **28**, 4688–4696 (2008).

Supplementary Information is available in the online version of the paper.

Acknowledgements We thank P. Bieniasz for the HERVK-con plasmid, P. Lovelace for assistance with FACS, M. Teruel for recombinant *Giardia* DICER, J. Perrino for TEM assistance, T. Swigut for ideas and input on data analysis, B. Gu for assistance with bisulfite sequencing, A. Moore for assistance with influenza experiments, J. Skowronski and members of the Wysocka laboratory for invaluable comments on the manuscript. This work was supported by the National Institutes of Health (NIH) P01 GM099130 and R01 GM112720 (J.W.); Stanford Genome Sciences Training Program and National Science Foundation Graduate Research Fellowship Program (E.J.G.); NIH F30 (1F30CA189514-01) (R.A.F.); NIH DP2AI11219301 (C.A.B.); Smith Family Stanford Graduate Fellowship (N.L.B.); CIRM RB4-05763 and NIH P50-HG007735 (H.Y.C.); CIRM RB3-02209, March of Dimes 6-FY10-351 and U01 HL100397 (R.A.R.P.) grants and NIH equipment grants 1S10RR02933801 (Institute for Stem Cell Biology and Regenerative Medicine FACS core) and 1S10RR02678001 (electron microscopy core facility).

Author Contributions E.J.G. and J.W. conceived the project, designed experiments and wrote the manuscript, with input from all authors. E.J.G. carried out the majority of the experiments and data analyses. S.L.C., M.W. and E.J.G. performed human blastocyst handling and immunofluorescence with expertise and resources provided by R.A.R.P. R.A.F., L.M. and H.Y.C. performed and analysed iCLIP experiments. R.A.F. provided assistance with ribosome profiling experiments and analysis. N.L.B. and C.A.B. contributed influenza infection experiments. C.B.W. provided human naive cells and reagents. D.J.W. performed expression analysis of LTR5HS-associated genes.

Author Information Sequencing data sets generated for this study are deposited under in the Gene Expression Omnibus under accession number GSE63570. Reprints and permissions information is available at www.nature.com/reprints. The authors declare no competing financial interests. Readers are welcome to comment on the online version of the paper. Correspondence and requests for materials should be addressed to J.W. (wysocka@stanford.edu).

METHODS

DNA and RNA isolation at reverse transcription. Genomic DNA was isolated using phenol:chloroform:isoamyl (100:100:1; PCI) (Invitrogen). Briefly, cells were digested in 10 mM Tris-HCl (pH = 8.0), 0.1 M EDTA, 0.5% SDS for 37 °C for 1 h, then proteinase K was added to final concentration of 100 µg ml⁻¹ and then incubated for 3 h at 50 °C. DNA was PCI extracted, ethanol precipitated, and resuspended in TE. RNA was extracted using Trizol (Invitrogen) according to the manufacturer's instructions. DNase treatment with Turbo DNase (Ambion) was performed for 30 min at 37 °C, PCI extracted, ethanol precipitated, and resuspended in water. Reverse transcription was performed with SuperScript III (Invitrogen) using ~500 ng of DNase treated total RNA following the manufacturer's instructions. No reverse transcriptase controls were performed where necessary.

Cell lines and culture. NCCIT and HEK293 cells were obtained from ATCC. NCCIT cells were maintained in 10% FBS (Omega), 1× Glutamax-I supplement (100× stock, Invitrogen), 1× non-essential amino acids (100× stock, Invitrogen), and basal media RPMI 1640 (Hyclone). HEK293 cells were maintained in 10% FBS, 1× NEAA, 1× glutamax in DMEM-high glucose (Hyclone). Human ES cells (H9 line female, Wi-Cell) were used at passage 60–67 and were expanded in feeder-free, serum-free medium (mTeSR-1) from StemCell technologies. HESC HSF-1 (male) and HSF-8 (male) human ES cells were used at passage 20–28, cultured as described earlier and their characterization is described elsewhere³¹. Cells were passaged 1:7 every 5–6 days by incubation with accutase (Invitrogen) and the resultant small cell clusters (50–200 cells) were subsequently re-plated on tissue culture dishes coated overnight with growth-factor-reduced matrigel (BD Biosciences). ELFI naive human ES cells were obtained from C.W. and cultured as previously described¹⁴, with 10 ng ml⁻¹ human recombinant LIF (R&D). Cell cultures were routinely tested and found negative for mycoplasma infection (MycoAlert, Lonza).

ChIP. ChIP assays were performed from approximately 10⁷ cells per experiment, according to previously described protocol with slight modifications^{32,33}. Briefly, cells were crosslinked with 1% formaldehyde for 10 min at room temperature and formaldehyde was quenched by addition of glycine to a final concentration of 0.125 M. Chromatin was sonicated to an average size of 0.5–2 kb, using Bioruptor (Diagenode). 50–75 µl of protein G dynal beads (Invitrogen) were used to capture 3–5 µg of antibody in phosphate citrate buffer pH 5.0 (2.4 mM citric acid, 5.16 mM Na₂HPO₄) for 30 min at 27 °C. Antibody bead complexes were rinsed two times with PBS and added to sonicated chromatin and rotated at 4 °C overnight. Ten per cent of chromatin was reserved as 'input' DNA. Magnetic beads were washed and chromatin eluted, followed by reversal of the crosslinkings and DNA purification. Resultant ChIP DNA was dissolved in TE.

Flow cytometry. Cells were trypsinized and analysed on a CS&T-calibrated BD FACS Aria II SORP flow cytometer on a 561 nm laser line for turboRFP, with 582/15BP. For IFITM1 flow cytometry, cells were allowed to recover after trypsinization for 2 h at 37 °C in media. Then, 2.5 × 10⁵ cells were washed with PBS/10% FBS/0.1% sodium azide and stained with 1:100 IFITM1 antibody (rabbit pAb, ProteinTech, #50556193) for 30 min at 4 °C. Washed cells were then incubated with chick, anti-mouse A647 secondary for 30 min at room temperature. Control stainings using rabbit IgG (santa cruz) and anti-mouse A647 were also performed.

Bisulfite sequencing. EpiTect Plus Bisulphite conversion kit (Qiagen) was used to bisulfite convert 1 µg genomic DNA as per manufacturer's instructions. Approximately 20 ng of BS-treated DNA was used as a template for 35–40 cycles with Platinum taq (Invitrogen, 10966) as per manufacturer's instructions. A-tailed PCR fragments were gel purified and inserted into pGEM-T. 5' LTR provirus = specific BS-PCR was conducted with primers including NcoI and NotI sites to facilitate cloning into pGEM-T. Approximately 15 clones were Sanger sequenced for both forward and reverse strands. BiQ software was used to align and quantify CpG methylation.

Protein extraction and immunoblotting. Proteins were extracted using previously described protocols³³. Briefly, cells were resuspended in buffer A (10 mM HEPES, pH 7.9, 10 mM KCl, 1.5 mM MgCl₂, 0.34 M sucrose, 10% glycerol) and fresh protease inhibitors (Complete EDTA-free, Roche), 1 mM PMSF and 0.1% Triton-X 100 were added. Cytoplasmic extract was further clarified by centrifugation at 13,000 r.p.m. at 4 °C for 10 min, and total protein concentration was assayed with Bradford reagent (Biorad). Equal amounts of protein were run on SDS-PAGE gels and then transferred onto Hybond ECL membranes (Amersham). Membranes were blocked using 5% milk, PBS, 0.1% Tween-20 for 1 h at 27 °C. Primary antibodies (see Supplementary Table 10) were used in blocking solution overnight at 4 °C. Horseradish peroxidase (HRP)-conjugated secondary antibodies were used and chemoluminescence was assayed using Lumi-light plus (Roche).

qPCR. All primers used in qPCR analyses are shown in Supplementary Table 10. qPCR was performed using SensiFAST SYBR No-Rox Kit (Bioline) in a Light

Cycler 480II machine (Roche), using technical triplicates. ChIP-qPCR signals were calculated as percentage of input and unless, indicated, qRT-PCR signal was normalized to 18S rRNA. Standard deviations were measured from the averages of the technical repeats for each biological replicates and represented as error bars ±1 s.d.

Plasmid and constructs. HERVK LTR5_HS sequence from HERVK-con²² was cloned upstream of a miniTK promoter driving turboRFP and inserted into piggy-back transposon (SystemBio). Motif mutations for OCT4 or SOX2 were produced by replacing the respective motif with a NotI site. 2.5 µg of reporter vector along with 0.5 µg of piggy-back transposase were transfected into cells using 18 µl lipofectamine2000 (Invitrogen) in 6-well plates. 400 µg ml⁻¹ G418 (Amresco) was used to select for integrants. Cells were analysed >10 days later to minimize signal from non-integrated reporter expression. Complementary DNAs encoding OCT4 or SOX2 were cloned into pcDNA containing carboxy-terminal or amino-terminal Flag-haemagglutinin (HA) tags, respectively. The same LTR regulatory regions were cloned into pGL3 firefly luciferase reporters, and constructs were co-transfected with Renilla luciferase for perform dual luciferase assays. SV40 promoter/enhancer firefly luciferase was used as a positive control. Transgene constructs for Rec expression in NCCIT cells were used with *eifla* promoter, N-terminal Flag-eGFP-tagged Rec cloned into a piggy-back construct with a puromycin selectable marker. Control construct using Flag-eGFP alone (vector only control) was also used in parallel. Transgene constructs were cotransfected with piggy-back transposase plasmid to generate stable lines. Clones were selected and expanded. Flag-eGFP-Rec clone #1 has ~30× endogenous expression of *rec* mRNA (as measured by qPCR) and Flag-eGFP-Rec clone #2 has ~14× endogenous expression of *rec* mRNA (qPCR), data not shown.

siRNA knockdown. siRNA was generated using baculovirus-produced *Giardia* DICER as described³⁴. Briefly, 1 µg of PCR product was *in vitro* transcribed using Megascript T7 (Ambion) and digested using DICER at 37 °C for 16 h. siRNA was purified using Purelink RNA mini Kit (Ambion) and the absence of >22 nucleotides RNA was verified using gel electrophoresis and ethidium bromide staining. NCCIT cells were plated onto Matrigel-coated 24-well plates, transfected using 1.5 µl of RNAi-max (Invitrogen) in opti-mem (Gibco) with 25 nM siRNA concentrations for 4 h before addition of fresh media. siRNA knockdowns were performed for three consecutive days, cells were harvested 24 h after final transfection. Two independent siRNA pools were generated for OCT4, NANOG and SOX2, one each for turboRFP (non-targeting control) and *rec*, which overlaps the *env* ORF. Primers used to generate double-stranded RNA (dsRNA) templates are listed in Supplementary Table 10.

Human embryo source and procurement. Human embryos were obtained as previously described³⁵. Approximately 25 supernumerary human blastocysts from successful IVF cycles, subsequently donated for non-stem-cell research, were obtained with written informed consent from the Stanford University RENEW Biobank. De-identification was performed according to the Stanford University Institutional Review Board-approved protocol #10466 entitled 'The RENEW Biobank' and the molecular analysis of the embryos was in compliance with institutional regulations. Approximately 25% of the embryos were from couples that used donor gametes and the most common cause of infertility was unexplained at 35% of couples. No protected health information was associated with any of the embryos.

Human embryo thawing and culture. Human embryos cryopreserved at the blastocyst stage were thawed by a two-step rapid thawing protocol using Quinn's Advantage Thaw Kit (CooperSurgical) as previously described^{35,36}. In brief, either cryotrays or vials were removed from the liquid nitrogen and exposed to air before incubating in a 37 °C water bath. Once thawed, embryos were transferred to a 0.5 mol l⁻¹ sucrose solution for 10 min followed by a 0.2 mol l⁻¹ sucrose solution for an additional 10 min. The embryos were then washed in Quinn's advantage medium with HEPES (CooperSurgical) plus 5% serum protein substitute (CooperSurgical) and each transferred to a 25 µl microdrop of Quinn's advantage blastocyst medium (CooperSurgical) supplemented with 10% serum protein substitute under mineral oil (Sigma). The embryos were cultured at 37 °C with 6% CO₂, 5% O₂ and 89% N₂ under standard human embryo culture conditions in accordance with current clinical IVF practice. Embryos used in this study were DPF 5–6.

Immunofluorescence. Cells were grown on Matrigel-coated glass coverslips, fixed using EM-grade 4% PFA (Electron Microscopy Sciences) for 15 min at 27 °C, washed three times with PBS, blocked and permeabilized with 1% BSA, 0.3% Triton-X 100 in PBS (antibody buffer) supplemented with 5% serum for species-matched secondary antibody for 1 h at 27 °C. Primary antibodies were resuspended in antibody buffer and incubated at 4 °C overnight. Washes were performed three times using 0.1% Triton-X 100 in PBS, and secondary antibodies were added for 1 h at 27 °C in the dark. Cells were mounted using Prolong-fade gold (Invitrogen) with DAPI and imaged on Zeiss LSM 700 confocal.

For embryo immunostaining, the zona pellucida (ZP) was removed from each embryo by treatment with acidified Tyrode's solution (Millipore) and ZP-free embryos were washed in PBS plus 0.1% BSA and 0.1% Tween-20 (PBS-T; Sigma-Aldrich) before fixation in 4% paraformaldehyde for 20 min at room temperature. Once fixed, the embryos were washed three times in PBS-T to remove any residual fixative and permeabilized in 1% Triton X-100 (Sigma-Aldrich) for 1 h at room temperature. Following permeabilization, the embryos were washed three times in PBS-T and then blocked in 4% of chicken or goat serum in PBS-T overnight at 4 °C. The embryos were incubated with primary antibodies in PBS-T with 1% serum sequentially for 1 h each at room temperature at the following dilutions: 1:200 OCT4, 1:100 Gag/Capsid. Primary signals were detected using the appropriate 488- or 647-conjugated Alexa Fluor secondary antibody (Invitrogen) at a 1:250 dilution at room temperature for 1 h in the dark and subsequently DAPI stained. Immunofluorescence was visualized by sequential imaging, whereby the channel track was switched each frame to avoid cross-contamination between channels, using a Zeiss LSM510 Meta inverted laser scanning confocal microscope. The instrument settings, including the laser power, pinhole and gain, were kept constant for each channel to facilitate semi-quantitative comparisons between embryos.

DNA demethylation treatment. HEK293 cells were plated on Matrigel-coated 24-well plates, and treated with 0, 1 or 10 μ M 5-aza-2'-deoxycytidine (Calbiochem) freshly prepared every 24 h. Cells were then transfected with 1 μ g each of pcDNA3.1-OCT4 and pcDNA3.1-SOX2 expression plasmids. Media was changed 24 h later, and cells were harvested 3 days after transfection for RNA analysis. Human ES cells (H9) were grown as described earlier, except mTeSR was supplemented with Rock inhibitor (γ -27632, Sigma) at 5 μ M, and treated with 0, 1 or 10 μ M 5-aza-2'-deoxycytidine (Calbiochem) for 24 h.

RNA-seq library construction. Libraries were constructed as described³³, using ~10 μ g of total RNA followed by poly-A selection with oligo-dT beads, ligation and ten cycles of PCR with NEBnext kit oligonucleotides, and sequenced using Illumina Hi-Seq2000 at the Stanford Sequencing Facility or ELIM Bio.

Sequence analysis. For RNA-seq repeat analysis of data from embryo and human ES cell libraries (for Fig. 1 and Extended Data Fig. 1), FASTQ files were aligned to rebase consensus sequences (downloaded from RepBase) with bowtie using the command "bowtie -q -p 8 -S -n 2 -e 70 -l 28 -maxbts 800 -k 1 -best". These bowtie parameters ensure that only the best alignment (highest scores) is reported, furthermore only one alignment per read is reported, that is, these settings do not allow multiple-matching. For Fig. 2a analysis of HERVK proviruses, RNA-seq reads were aligned to hg19 using the same parameters described earlier, and the overlap between the manually curated HERVK provirus data set⁵ is reported. For RefSeq analysis for RNA-seq libraries generated for this paper (ELF1 naive or primed human ES cells; from human EC cell siRNA RNA-seq, or Rec-hECC versus wild-type human EC cell experiments), reads were processed using DNAnexus software to obtain read counts and RPKM. Reads were counted and where indicated normalized to repeat length and library size using RPKM. Differential expression in RNA-seq experiments described earlier was performed using DESeq, with reported FDR using Benjamini-Hochberg correction.

Interferon-induced gene set analysis. Genes were defined as interferon induced if they were induced fivefold in interferon-treated cells/tissues for experimentally deposited data sets found in Interferome database³⁷ (<http://interferome.its.monash.edu.au/interferome/home.jsp>).

LTR5HS-associated gene analysis. RefSeq genes were classified as associated or not associated with LTR5HS (downloaded from UCSC genome browser table) using Great Analysis Software (Bejerano laboratory, Stanford University) with a cut-off of 100 kb distance from the TSS. These classified RefSeq genes were then compared using the RPKM and DESeq analysis as described earlier. Differential enrichment of LTR5HS-associated transcripts in naive/primed upregulated versus naive/primed downregulated was analysed using non-paired Wilcoxon test, and significance is reported at P value < 0.05. Higher average naive/primed RPKM of LTR5HS-associated versus non-LTR5HS-associated genes was tested using non-paired Wilcoxon test.

Chimaeric transcript identification. One-hundred base-pair paired-end RNA-seq reads generated with ELF1 naive versus primed human ES cells (see earlier) were analysed using a published pipeline²². Briefly, Cufflinks software was used to perform *de novo* identification of transcript models. These transcript models were then used to identify splice junctions in which one side of the transcript model overlapped the GTF file (for hg19 from UCSC), cataloguing known genes and long noncoding RNAs (lincRNAs), and the other side of the transcript model aligned to hg19 classified as a repeat (UCSC genome browser, repeat track). Transcripts that fulfilled these criteria were classified as chimaeric transcripts, and are reported in Supplementary Table 1.

Clustering. Hierarchical clustering was performed using Gene-e software (<http://www.broadinstitute.org/cancer/software/GENE-E/index.html>) using K -means clustering of log₂-transformed RPKM.

Statistical tests. A list of the statistical tests, multiple-hypothesis testing corrections, and normality criteria for parametric tests is reported in Supplementary Table 7.

Electron microscopy. Samples were fixed using 4% PFA and 0.01% glutaraldehyde for 15 min at 27 °C. Routine heavy metal staining was conducted where indicated. Immuno-TEM with 1:100 dilution of anti-HERVK Gag/Capsid using overnight incubation at 4 °C and labelling was visualized using 5 nm gold-labelled anti-mouse secondary antibody. Secondary only controls demonstrated specificity of the antibody for this application. TEM was performed at the Electron Microscopy core at Stanford University using a Jeol JEM-1400 electron microscope.

iCLIP and data analysis. The iCLIP method was performed as described before with the specific modifications below³⁸. Flag-GFP-Rec (FG-Rec)-expressing NCC cells were UV-C crosslinked to a total of 0.3 J cm⁻². Each iCLIP experiment was normalized for total protein amount, typically 1 mg, and partially digested with RNaseI (Life Technologies) for 10 min at 37 °C and quenched on ice. FG-Rec was isolated with anti-Flag agarose beads (Sigma) for 3 h at 4 °C on rotation. Samples were washed sequentially in 1 ml for 5 min each at 4 °C: 2 \times high stringency buffer (15 mM Tris-HCl pH 7.5, 5 mM EDTA, 2.5 mM EGTA, 1% Triton X-100, 1% Na-deoxycholate, 120 mM NaCl, 25 mM KCl), 1 \times high salt buffer (15 mM Tris-HCl pH 7.5, 5 mM EDTA, 2.5 mM EGTA, 1% Triton X-100, 1% Na-deoxycholate, 1 M NaCl), 1 \times NT2 buffer (50 mM Tris-HCl pH 7.5, 150 mM NaCl, 1 mM MgCl₂, 0.05% NP-40). Purified FG-Rec was then eluted from anti-Flag agarose beads using competitive Flag peptide elution. Each sample was resuspended in 500 μ l of Flag elution buffer (50 mM Tris-HCl pH 7.5, 250 mM NaCl, 0.5% NP-40, 0.1% Na-deoxycholate, 0.5 mg ml⁻¹ Flag peptide) and rotated at 4 °C for 30 min. The Flag elution was repeated once for a total of 1 ml elution. FG-Rec was then captured using anti-GFP antibody (Life Technologies, A-11122) conjugated to Protein A dynabeads (Life Technologies) for 3 h at 4 °C on rotation. Samples were then washed as described previously in the anti-Flag agarose beads. 3'-End RNA dephosphorylation, 3'-end single-stranded RNA (ssRNA) ligation, 5' labelling, SDS-PAGE separation and transfer, autoradiograph, RNP isolation, Proteinase K treatment and overnight RNA precipitation took place as previously described³⁸. The 3'-ssRNA ligation adaptor was modified to contain a 3' biotin moiety as a blocking agent. The iCLIP library preparation was performed as described elsewhere^{38,39}. Final library material was quantified on the BioAnalyzer High Sensitivity DNA chip (Agilent) and then sent for deep sequencing on the Illumina HiSeq 2500 machine for 1 \times 75 bp cycle run. iCLIP data analysis was performed as previously described³⁹. For analysis of repetitive noncoding RNAs, custom annotation files were built from the Rfam database. For analysis of endogenous retroviral elements, custom annotation files were built from the rebase database. iCLIP reads were filtered for quality, barcode split, PCR-duplicate removed, trimmed (5' and 3' ends), and mapped for unique matches under parameters previously described^{38,39}. Bioinformatic pipeline used for iCLIP data analysis is described previously³⁹. Briefly, RT stops were used to map nucleotide resolution of Rec binding, and only nucleotides supported with three independent RT stops in two replicates (with at least one RT stop in each replicate) were reported as binding events, and are reported in Supplementary Table 3.

Ribosome profiling. Human EC cells (NCCIT) were cultured as described earlier. Total RNA was extracted using Trizol (Life Technologies) and used as input material for the ARTseq Ribosome Profiling Kit—Mammalian (Epicentre) following the manufacturer's protocol with the following modifications. The 3' RNA ligation adaptor and cDNA synthesis primers from the iCLIP protocol were for library construction. Final library material was quantified as in the iCLIP experiments and sequenced on the Illumina HiSeq 2500 machine for 1 \times 75 bp cycle run. Sequencing reads were preprocessed (quality filter, PCR duplicate removal, and trimming) as in the iCLIP protocol. Mapping was performed using an established pipeline previously described⁴⁰. Briefly, reads were aligned to 45 s rDNA repeat sequence with bowtie to remove residual rRNA reads from libraries. Non-aligning reads (non-rRNA) were then aligned to hg19 with TopHat2 and differential expression was identified using default parameters for CuffDiff/Cufflinks software with significance at FDR < 0.05.

Influenza infection experiments. Human EC cells (NCCIT) were plated in duplicate (1.5 \times 10⁵ cells per well) on a 96-well flat-bottom plate in 100 μ l Virus Diluent (DMEM, Gibco, supplemented with 1% BSA, 1 \times antibiotics and 20 mM HEPES). Cells were incubated at 37 °C and 5% CO₂ for 1.5 h. Wild-type human EC cells and REC-hECCs were then infected with virus (influenza A/H1N1/PR8/1934, diluted 1:10 into 100 μ l virus diluent, increasing total volume to 200 μ l). Cells were incubated at 37 °C for 1 h. FBS (Hyclone) was added to the wells to a final concentration of 10% FBS. Cells were incubated at 37 °C for 5 h. 20 mM EDTA (20 μ l) was added to all wells and mixed thoroughly to stop infection. Cells were washed with 200 μ l 1 \times PBS (Hyclone), re-suspended in

100 µl 1× BD FACS Lysing Solution (BD Biosciences) and stored at -80°C for later processing.

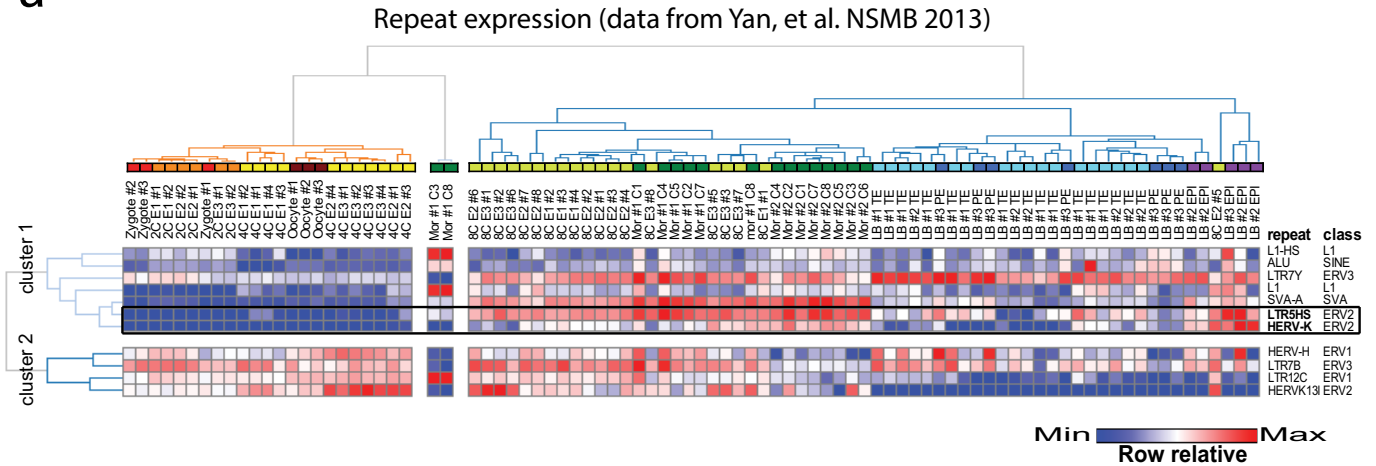
For staining and analysis, cells were thawed in 37°C for 20 min. One-hundred microlitres FACS wash (1× HyClone DPBS with 2% FBS) was added to each well and plate was centrifuged. Cell pellets were re-suspended in 200 µl BD FACS Permeabilizing Solution II (BD Biosciences). Cells were incubated at room temperature in the dark for 10 min. Plate was centrifuged and cells were washed twice with 200 µl FACS wash. Cells were stained with primary antibody (mouse anti-influenza A nucleoprotein, C43 clone, Abcam) diluted to $2\text{ }\mu\text{g ml}^{-1}$. Cells were incubated in the dark at room temperature for 30 min and washed twice. Cell pellets were resuspended in $2\text{ }\mu\text{g ml}^{-1}$ of secondary antibody (chicken anti-mouse Alexa647, Invitrogen) in 50 µl FACS wash and incubated in the dark at room temperature for 30 min. Cells were washed twice and cell pellets were resuspended in 1% PFA (Electron Microscopy Sciences). Cells were analysed on the MACSQuant Analyzer (Miltenyi Biotec). MACSQuant Calibration Beads (Miltenyi Biotec) were used for calibration of the cytometer. Compensation controls were run using 1:1 mixture of CompBead Plus Anti-mouse Igκ (BD) and negative control beads. Single stained cellular controls were run in parallel to infected and uninfected samples. Data were analysed by FlowJo 9.7.6 (TreeStar). Cells were gated to exclude dead cells and debris. Infection levels were background subtracted using uninfected wells, and normalized to infection levels in GFP-hECC for each run.

RNA-seq data sets. Data sets used in this study can be accessed from: Array Express Database (accession number E-MATB-2031)¹²; Gene Expression Omnibus (accession number GSE36552)¹⁰; Gene Expression Omnibus (accession number GSE44183)⁴¹; Array Express (accession number E-MTAB-2857)¹⁵. Sequencing data sets generated for this study are deposited under in the Gene

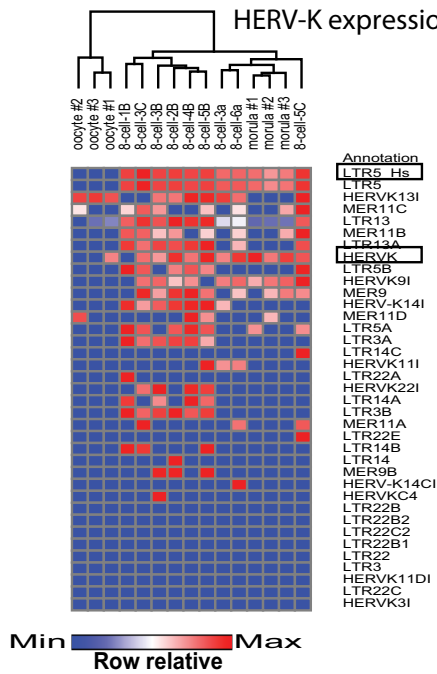
Expression Omnibus under accession number GSE63570, and are summarized in Supplementary Table 8.

31. Chavez, S. L., Meneses, J. J., Nguyen, H. N., Kim, S. K. & Pera, R. A. R. Characterization of six new human embryonic stem cell lines (HSF7, -8, -9, -10, -12, and -13) derived under minimal-animal component conditions. *Stem Cells Dev.* **17**, 535–546 (2008).
32. Boyer, L. A. *et al.* Core transcriptional regulatory circuitry in human embryonic stem cells. *Cell* **122**, 947–956 (2005).
33. Peng, J. C. *et al.* Jarid2/Jumonji coordinates control of PRC2 enzymatic activity and target gene occupancy in pluripotent cells. *Cell* **139**, 1290–1302 (2009).
34. Myers, J. W. & Ferrell, J. E. Jr. in *RNA Silencing* (ed. Carmichael, G. G.) 93–196 (Humana Press, 2005).
35. Chavez, S. L. *et al.* Dynamic blastomere behaviour reflects human embryo ploidy by the four-cell stage. *Nature Commun.* **3**, 1251 (2012).
36. Wong, C., Chen, A. A., Behr, B. & Shen, S. Time-lapse microscopy and image analysis in basic and clinical embryo development research. *Reprod. Biomed. Online* **26**, 120–129 (2013).
37. Rusinova, I. *et al.* INTERFEROME v2.0: an updated database of annotated interferon-regulated genes. *Nucleic Acids Res.* **41**, D1040–D1046 (2013).
38. Huppertz, I. *et al.* iCLIP: protein-RNA interactions at nucleotide resolution. *Methods* **65**, 274–287 (2014).
39. Flynn, R. A. *et al.* Dissecting noncoding and pathogen RNA–protein interactomes. *RNA* **21**, 135–143 (2015).
40. Ingolia, N. T., Lareau, L. F. & Weissman, J. S. Ribosome profiling of mouse embryonic stem cells reveals the complexity and dynamics of mammalian proteomes. *Cell* **147**, 789–802 (2011).
41. Xue, Z. *et al.* Genetic programs in human and mouse early embryos revealed by single-cell RNA sequencing. *Nature* **500**, 593–597 (2013).

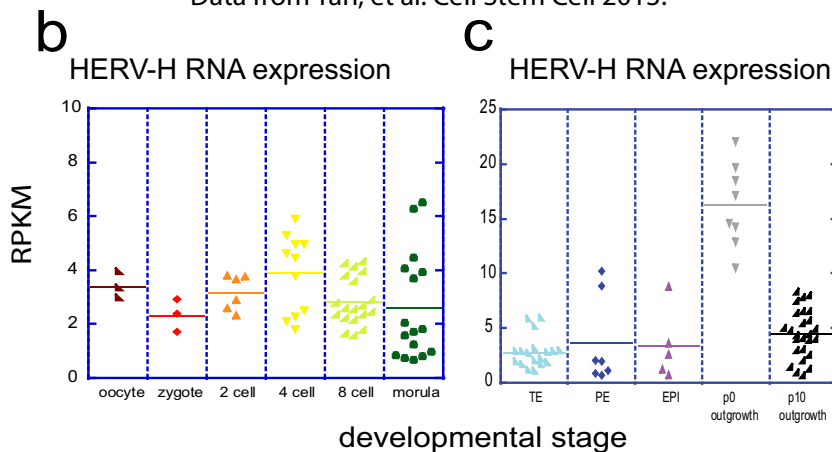
a



HERV-K expression (Data from Xue, et al. Nature, 2013)

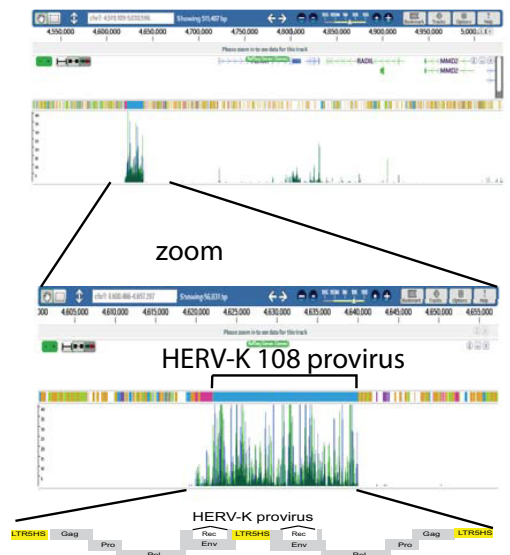


Data from Yan, et al. Cell Stem Cell 2013.



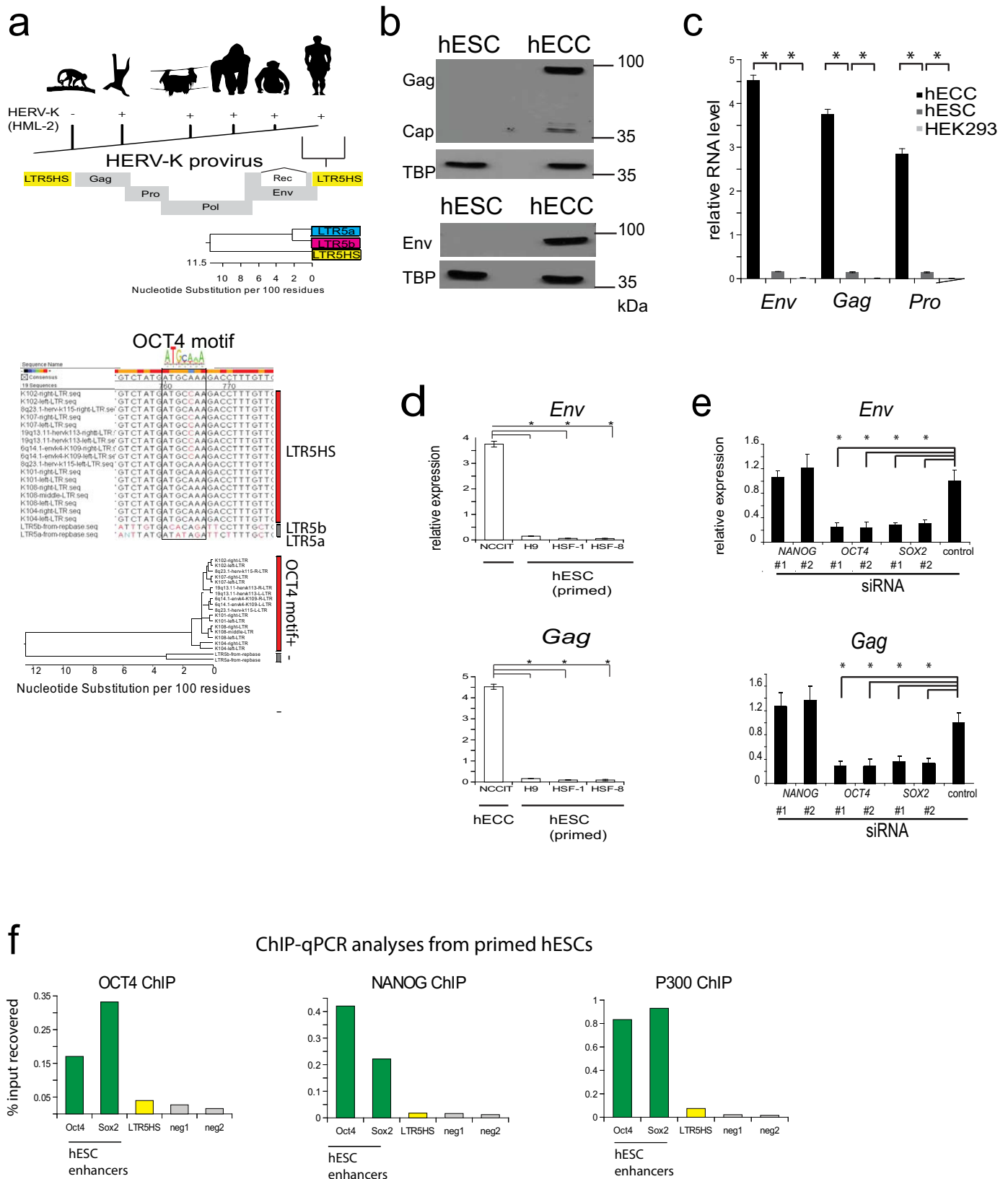
Data from this study

d naive hESC RNA-seq



Extended Data Figure 1 | Additional single-cell RNA-seq data analyses from preimplantation human embryos (supporting Fig. 1). **a**, Heat map and hierarchical *K*-means clustering of highly expressed (average RPKM > 6 across 89 embryo libraries) repetitive elements in single cells of human preimplantation embryos at indicated developmental stages (top) and HERVK expression (bottom) using indicated data sets. **b**, HERVH expression (RPKM) in single cells of human embryos at indicated preimplantation stages. Solid

line indicates mean. RNA-seq data are taken from ref. 10. **c**, HERVH expression (RPKM) in single cells of human blastocysts, grouped by lineage. Solid line indicates mean. Oocyte ($n = 3$), zygote ($n = 3$), 2-cell ($n = 6$), 4-cell ($n = 11$), 8-cell ($n = 19$), morula ($n = 16$), TE ($n = 18$), PE ($n = 7$), EPI ($n = 5$), p0 ($n = 8$), p10 ($n = 26$). RNA-seq data set was from ref. 10. **d**, Genome browser snapshot showing 100 bp PE-RNA-seq reads from ELF1 naive human EScells aligning at the HERVK 108 provirus on chromosome 7.

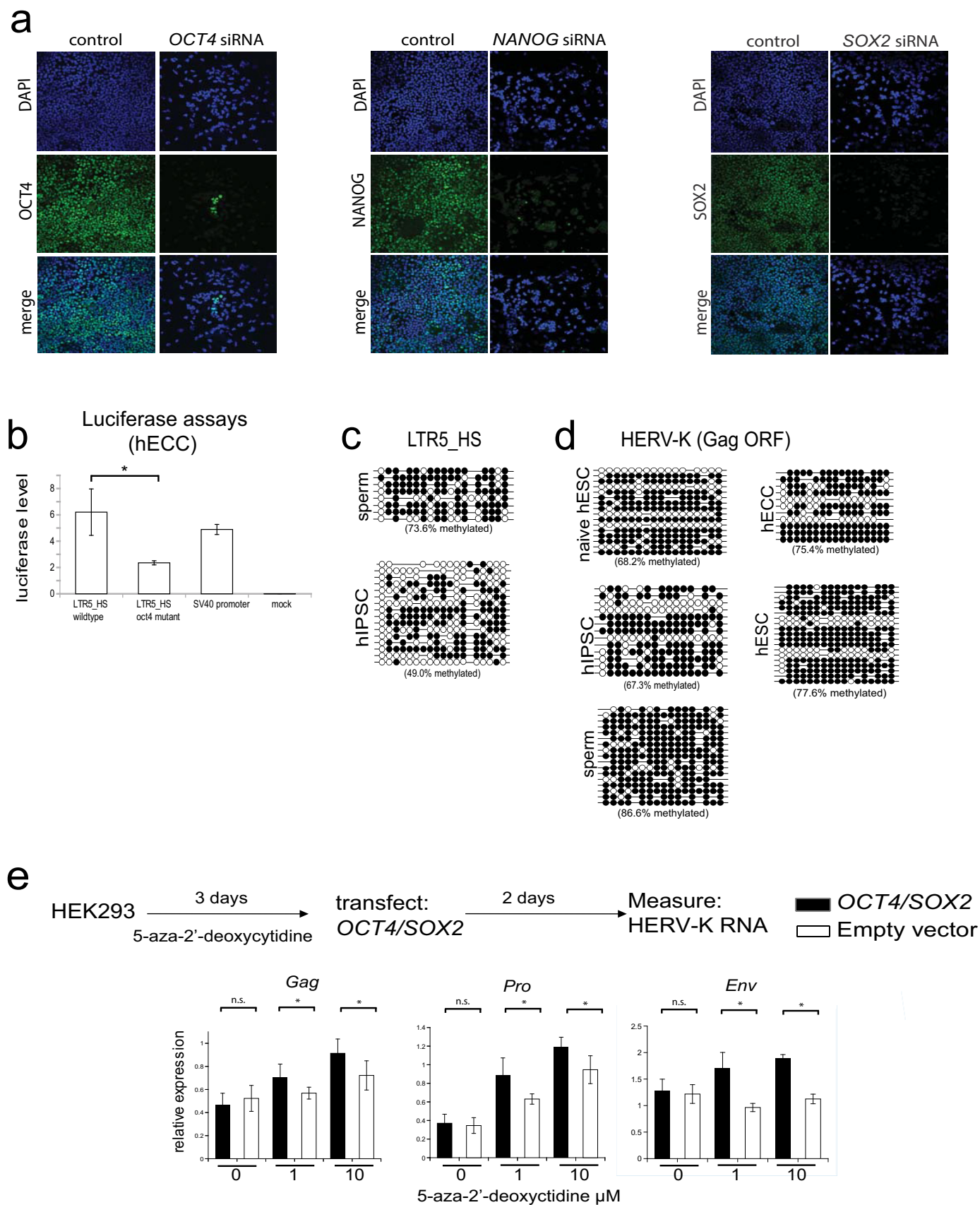


Extended Data Figure 2 | LTR5 alignments, HERVK expression data in cell lines, and control ChIP-qPCR analyses in primed human ES cells (supporting Fig. 2).

a, Top, presence of HERVK(HML-2) sequences in Old World primates, but absence in New World primates. Middle, schematic of HERVK proviral genome; all human-specific insertions contain LTR5HS. Bottom, phylogenetic relationship of HERVK LTR subclasses showing high degree of sequence similarity. Pro, protease; Pol, polymerase; Gag, group-specific antigen; Env, envelope. Bottom, ClustLW multiple sequence alignment of indicated HERVK LTR sequences (top), region around OCT4 motif is boxed, phylogenetic tree (bottom) indicating presence/absence of OCT4 motif.

b, HERVK protein expression in human EC cells and human ES cells. Protein extracts from human EC cells (NCCIT) and human ES cells (H9) were analysed by immunoblotting with an antibody detecting HERVK Gag precursor and the processed Capsid (top), or the glycosylated, unprocessed form of the HERVK envelope protein Env (bottom). Tata-binding protein (TBP) was used as a loading control. Shown is a representative result of three independent

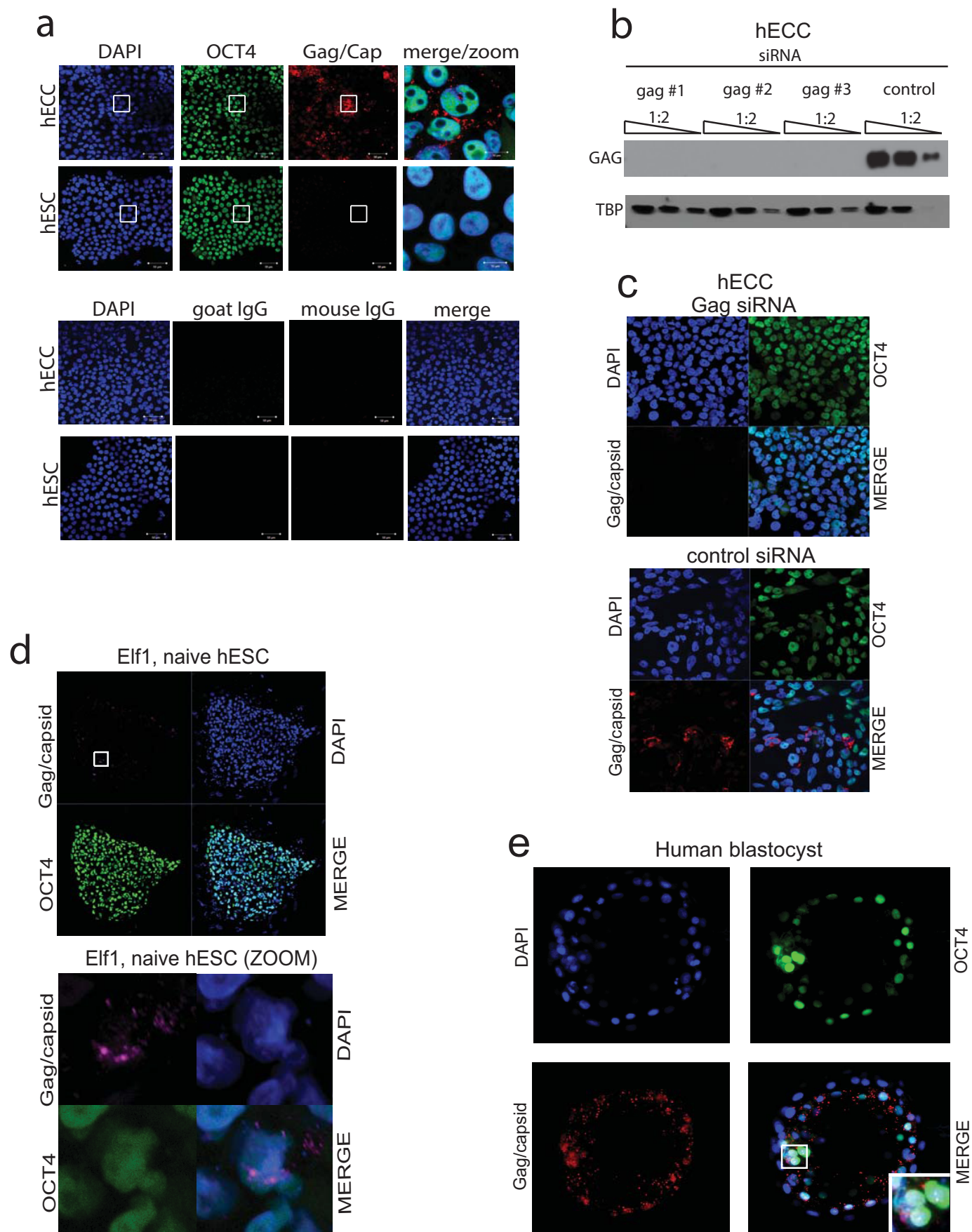
experiments. **c**, RT-qPCR analysis of HERVK RNA expression in human EC cell line NCCIT, human ES cell line H9, and HEK293 cells. Three distinct qPCR amplicons, corresponding to *env*, *gag* and *pro* are shown. Samples were normalized to 18S ribosomal RNA levels. **P* value < 0.05, one-sided *t*-test. Error bars are ± 1 s.d., *n* = 3 biological replicates. **d**, HERVK *gag* or *env* expression in male human ES cell lines HSF-1, HSF-8, female human ES cell line H9 and human EC cell line NCCIT. **P* value < 0.05, one sided *t*-test compared to control siRNA, *n* = 3 biological replicates. Error bars are ± 1 s.d. **e**, RT-qPCR analysis of HERVK transcripts after siRNA knockdown of NANOG, OCT4 or SOX2 in human EC cells (NCCIT). Signals were normalized to 18S rRNA. **P* value < 0.05, one sided *t*-test compared to control siRNA, *n* = 3 biological replicates. Error bars are ± 1 s.d. **f**, ChIP-qPCR analyses of human ES cells (H9) with indicated antibodies. Signals were interrogated with primer sets for positive control regions (active human ES cell *OCT4* and *SOX2* enhancers), LTR5HS, or non-repetitive, intergenic negative regions, as indicated at the bottom. Shown is a representative result of two biological replicates.



Extended Data Figure 3 | HERVK regulation by OCT4 and DNA

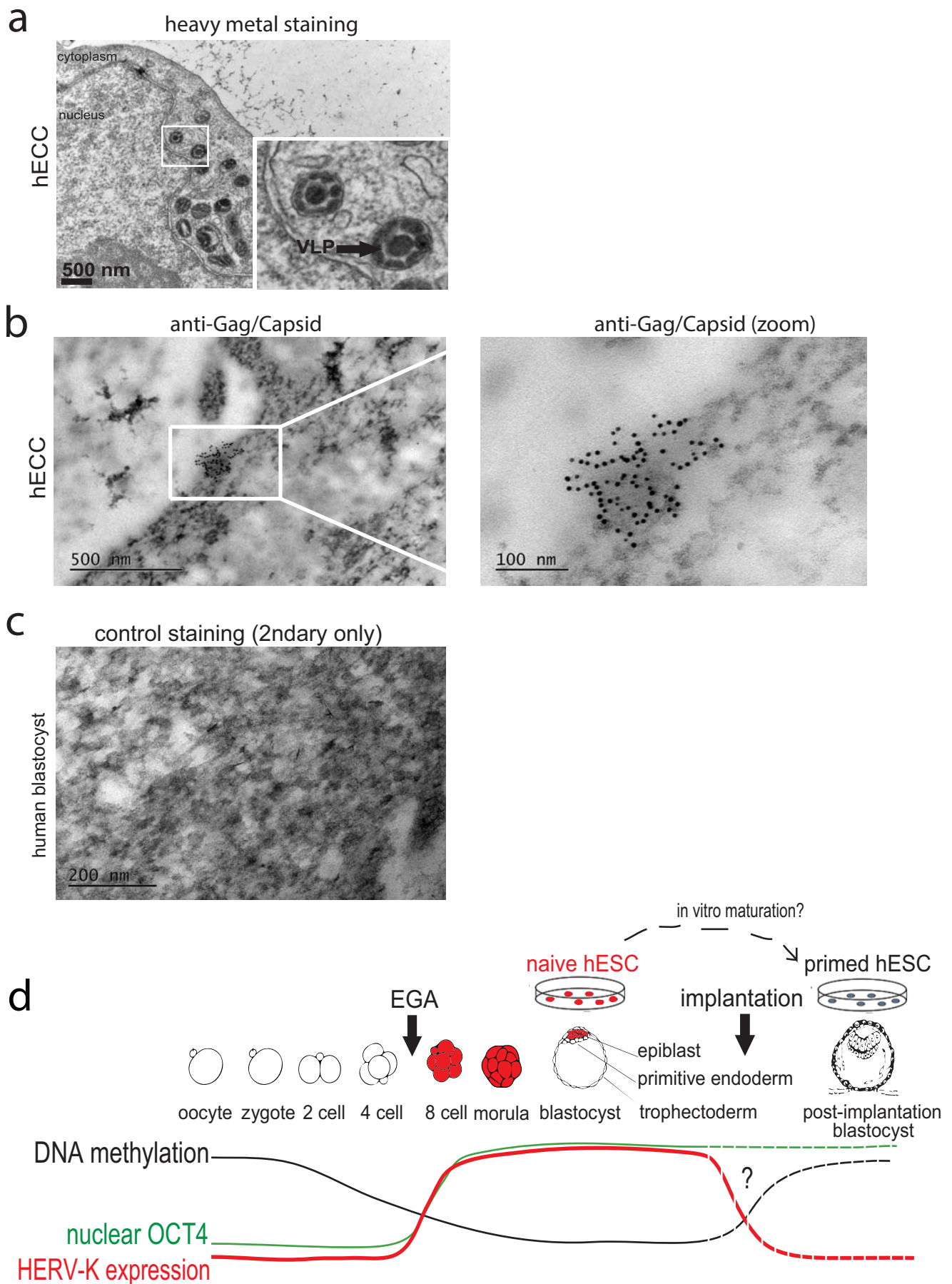
methylation (supporting Fig. 2). **a**, Transcription factor knockdown in human EC cells (NCCIT). Cells were transfected with siRNA pools targeting indicated transcription factors and protein depletion was measured by immunofluorescence with respective antibodies in comparison with control, mock-transfected cells. DAPI (blue), OCT4 (green, left), NANOG (green, middle), SOX2 (green, right). Shown is one of three representative fields of view at $\times 20$ magnification. **b**, Dual luciferase assays with indicated reporter constructs in human EC cells (NCCIT) showing that mutation of OCT4 site decreases reporter activity. $N = 3$ biological replicates, error-bars ± 1 s.d. * P value < 0.05 , one-sided t -test. SV40 enhancer/promoter construct was used as a positive control. **c**, Bisulfite sequencing for

indicated cell types (WT33 human iPSC) analysing consensus LTR5HS-specific amplicon as in Fig. 2e. **d**, Bisulfite sequencing analysis of HERVK proviral consensus amplicon containing 3' end of LTR, primer binding site, and 5' region of Gag ORF (see Extended Data Fig. 2a) in indicated cell types: ELF1 naive, human ES cell, WT33 human iPSC, NCCIT human EC cell, or H9 human ES cell. **e**, RT-qPCR analysis of HERVK RNA levels in HEK293 cells treated with indicated concentrations of 5-aza-2'-deoxycytidine for 3 days, followed by transfection with *OCT4*/*SOX2* expression constructs and RNA collection 48 h after transfection. qPCR primer sets were designed to three independent amplicons of HERVK. * P value < 0.05 , one-sided t -test. $n = 4$ biological replicates, error bars ± 1 s.d.



Extended Data Figure 4 | HERVK Gag/Capsid antibody validation and staining (supporting Fig. 3). **a**, Immunofluorescence analysis of human EC cells (NCCIT) and human ES cells (H9) stained with DAPI (blue), OCT4 (green), Gag/Capsid (red), or IgG control (bottom). White boxes indicate regions shown in higher magnification/merge (right). Shown are representative fields of three independent experiments. **b**, Sensitivity of HERVK Gag/Capsid antibody immunoblot signal to HERVK knockdown. Human EC cells were transfected with one of three independent siRNA pools targeting HERVK Gag or with a control, non-targeting pool (synthesized against RFP) and total protein was analysed by immunoblotting with anti-Env and anti-Gag/Capsid antibodies. 1:2 serial dilution of total protein was loaded, as indicated. Blots were stripped

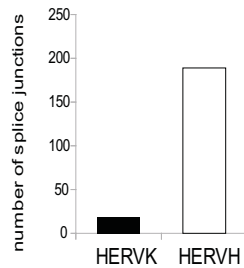
and re-probed with TBP as a loading control. Shown is a representative result of two independent experiments. **c**, Sensitivity of HERVK Gag/Capsid antibody immunofluorescence signal to siRNA knockdown of Gag/Capsid (top) or control siRNA targeting RFP (bottom). Shown is a representative result of three fields of view. Magnification: 20X **d**, Immunofluorescence of naive ELF1 human ES cells with antibodies against OCT4 (green), HERVK Gag/Capsid (pink), DAPI in blue. Region marked with white box on left is shown with larger magnification (bottom). Magnification = 20x, 40x respectively. **e**, Another representative example of immunofluorescence of human blastocysts with DAPI (blue), OCT4 (green) and Gag/Capsid (red) shown ($n = 19$ blastocysts; DPF 5–6). Original magnification, $\times 40$.



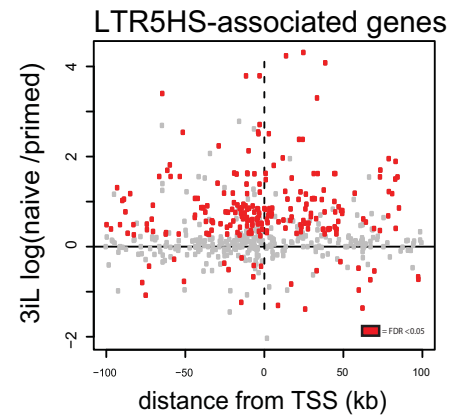
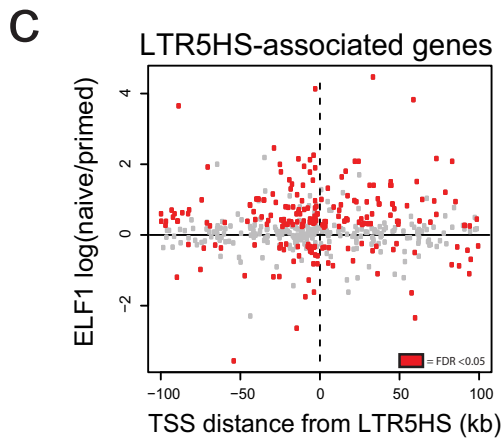
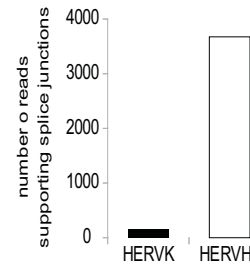
Extended Data Figure 5 | TEM analyses of human EC cells and control embryo staining (supporting Fig. 3). **a**, TEM analysis of human EC cells (NCCIT) with heavy metal staining; arrow indicates VLPs. Boxed region is shown with higher magnification in an inset. Scale bar = 500 nm. Shown is a representative example of two independent experiments. **b**, TEM immuno-gold labelling of human EC cells (NCCIT) with Gag/Capsid antibodies. Shown is a representative example from two independent experiments. **c**, Secondary

antibody only control for immuno-gold labelling of human blastocysts. Shown is a representative example from eight fields of view. **d**, Model figure summarizing HERVK transcriptional regulation in human embryos and *in vitro* cultured pluripotent cells. Dashed lines indicate inference of OCT4, DNA methylation and HERVK level changes at implantation from those observed between naive and primed human ES cells, in the absence of data from actual postimplantation human embryos.

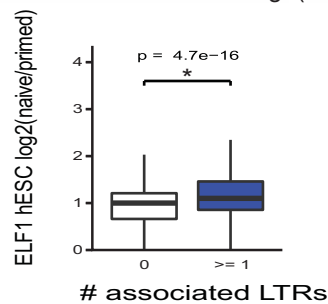
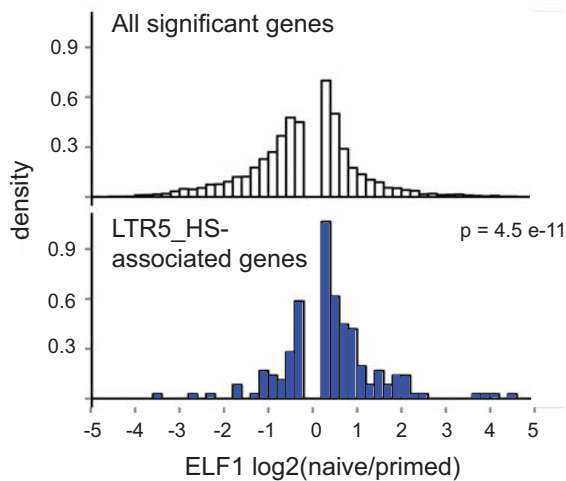
a Chimeric transcript identification
(Cufflinks analysis ELF1 naive hESC)



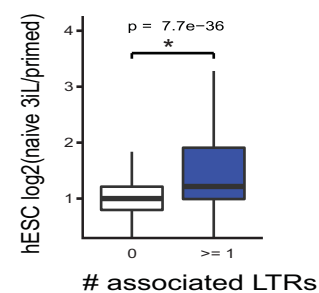
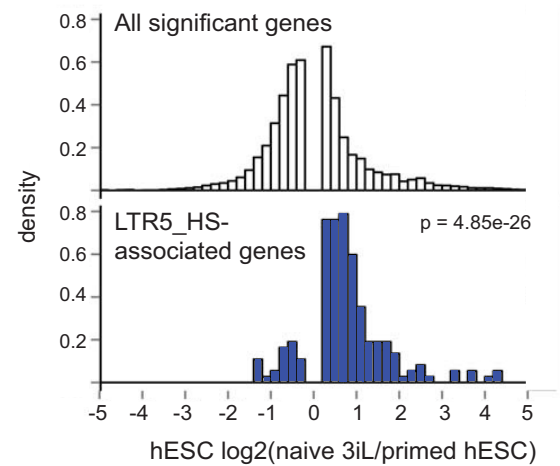
b Chimeric transcript identification
(Cufflinks analysis ELF1 naive hESC)



d ELF1 hESC, naive vs primed
(This study, Ware, et al. 2013)

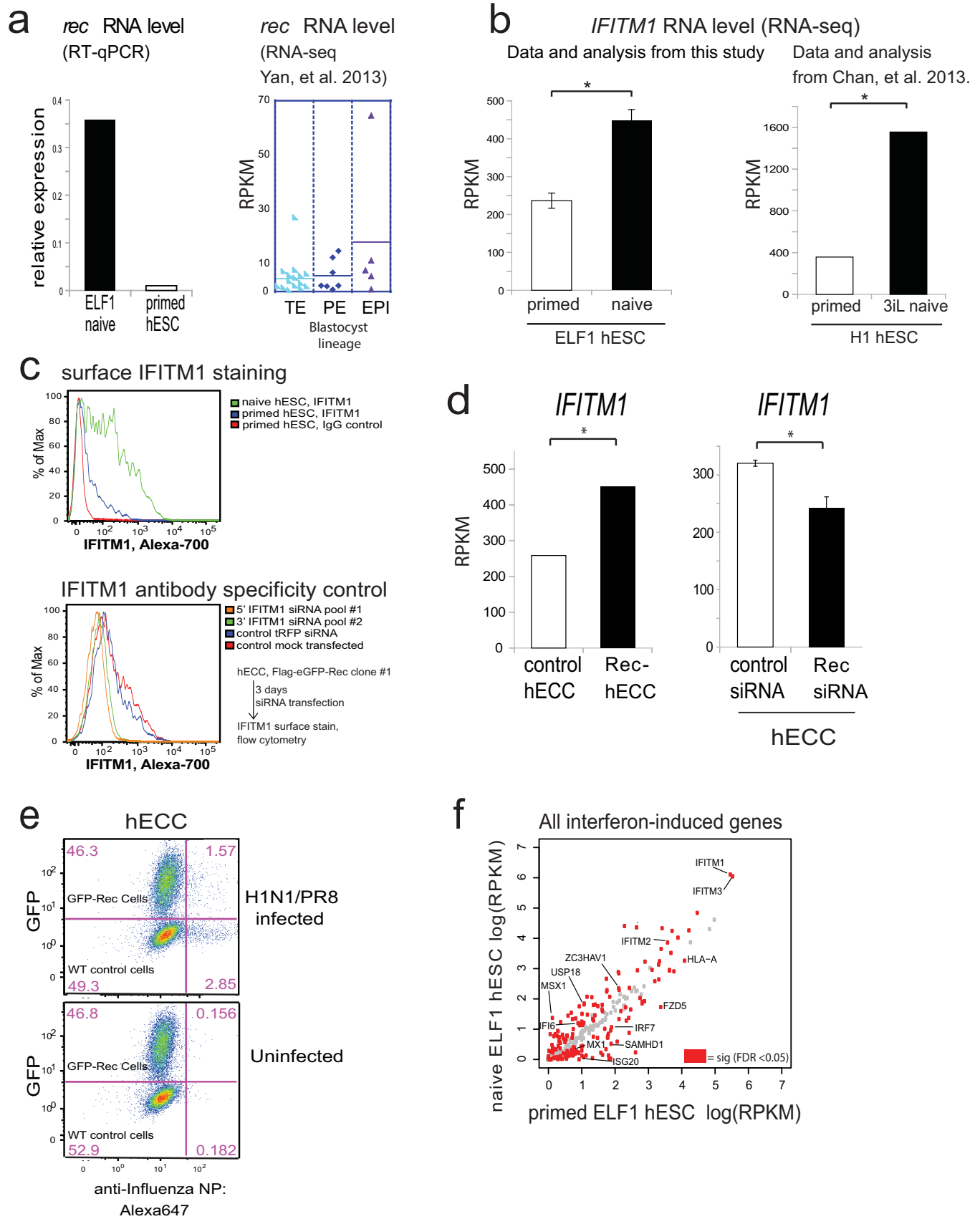


e 3iL naive hESC vs primed H1 hESC
(Chan, et al. 2013)



Extended Data Figure 6 | Correlation of HERVK LTR5HS elements with gene expression (supporting Fig. 4). **a**, Number of splice junctions identified linking indicated HERV class to annotated RefSeq genes. Analysis was done using RNA-seq data set from ELF1 naive human ES cells, $n = 3$ biological replicates. **b**, Number of reads supporting chimaeric transcripts from indicated HERV class in ELF1 naive human ES cells, $n = 3$ biological replicates. **c**, Expression of LTR5HS linked genes plotted as a function of distance to the gene's transcription start site (TSS). x -axis: distance of TSS to the nearest LTR5HS in kb; y -axis: fold change in expression of the linked gene in ELF1 naive versus primed human ES cells (this study, left) or expression of the linked gene in 3iL versus primed H1 human ES cells (right, ref. 12). **d**, Top, histograms showing expression of all genes that significantly change in expression between naive and primed ELF1 human ES cells (top histogram, white) or significantly changed genes that are LTR5HS associated (bottom histogram, blue); expression values from naive versus primed ELF1 human ES cell RNA-seq data

sets ($FDR < 0.05$ DESeq). Fischer's exact test gives stated P value, indicating enrichment of LTR5HS-linked genes in naive upregulated category. Bottom, quantification of average expression of LTR5HS-linked (blue) or unlinked (white) genes. Non-paired Wilcoxon test with stated P value indicating that genes linked to 1 or more LTR5HS have significantly higher mean expression. **e**, Top, histograms showing expression of all genes that significantly change in expression between 3iL and primed H1 human ES cells (top histogram, white) or significantly changed genes that are LTR5_HS associated (bottom histogram, blue); expression values from RNA-seq data sets reported previously¹², $FDR < 0.05$ DESeq. Fischer's exact test gives stated P value indicating enrichment of LTR5HS-linked genes in naive upregulated category. Bottom, quantification of average expression of LTR5HS-linked (blue) or unlinked (white) genes. Non-paired Wilcoxon test with stated P value indicating that genes linked to 1 or more LTR5HS have significantly higher mean expression.

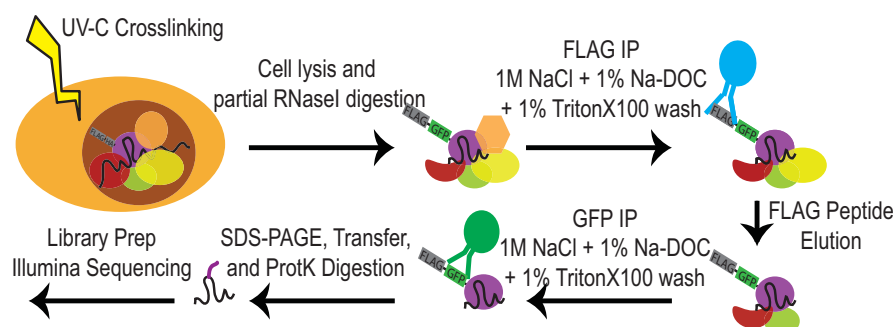


Extended Data Figure 7 | *rec* and *IFITM1* expression in naive human ES cells, and effect of *Rec* expression on H1N1(PR8) infection

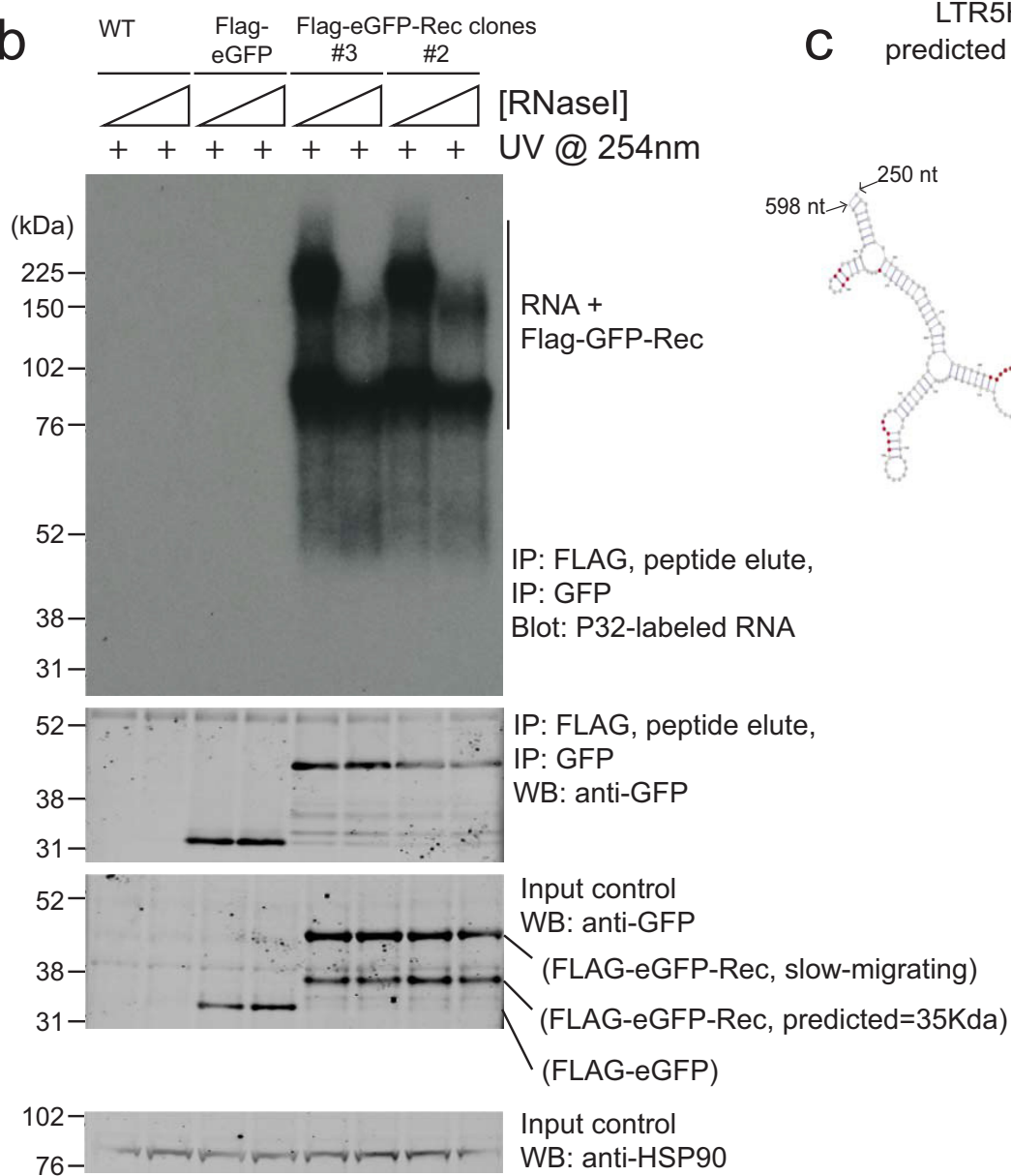
(supporting Fig. 4). **a**, Left, RT-qPCR analysis of HERVK *rec* expression levels in ELF1 naive human ES cells ($n = 3$ biological replicates) or H9 primed human ES cells (one biological replicate). Normalized to 18S rRNA. Right, *Rec* RNA levels in indicated blastocyst lineages. Solid line indicates mean; data are from ref. 10. **b**, RNA-seq quantification of *IFITM1* RNA levels in naive or primed ELF1 human ES cells (left, this study) or 3iL human ES cells versus primed H1 human ES cells from ref. 12 (right). $n = 3$ biological replicates for each condition, error bars are ± 1 s.d. Asterisk indicates significance at $FDR < 0.05$, DESeq. **c**, Flow cytometry for surface-localized IFITM1 staining in the indicated H9 human ES cells or naive ELF1 human ES cells (top) or, as a control for IFITM1 antibody specificity, knockdown of *IFITM1* with two independent *IFITM1* siRNA pools compared to control siRNA-treated cells in Flag-eGFP-Rec-hECCs (bottom). **d**, Left, *IFITM1* expression in control human EC cell versus

Rec-hECC (NCCIT) RNA-seq data sets. $n = 2$ biological replicates. Significance = $FDR < 0.05$, DESeq. Right, *IFITM1* expression in control siRNA versus Rec siRNA-treated human EC cells (NCCIT) RNA-seq. $n = 3$ biological replicates, error bars are ± 1 s.d. Significance = $FDR < 0.05$, DESeq. **e**, Flow-cytometry profiles for indicated cell types in H1N1(PR8) infected (top) or non-infected (bottom) wild-type (WT) control human EC cells or Flag-GFP-Rec-hECCs, clone #1. Shown is one representative example of four independent experiments showing a co-plating experiment in which GFP-Rec cells and wild-type control (GFP negative) cells are infected in the same well, stained in the same tube and identified by GFP fluorescence after gating for FSC and SSC. **f**, Scatterplot of ELF1 naive versus primed human ES cell RNA-seq showing all interferon-induced genes, with differentially regulated genes ($FDR < 0.05$ DESeq, $n = 3$ biological replicates each) highlighted in red. There is a significant overlap between differentially regulated genes and interferon-induced genes as measured by a hypergeometric test (P value < 0.05).

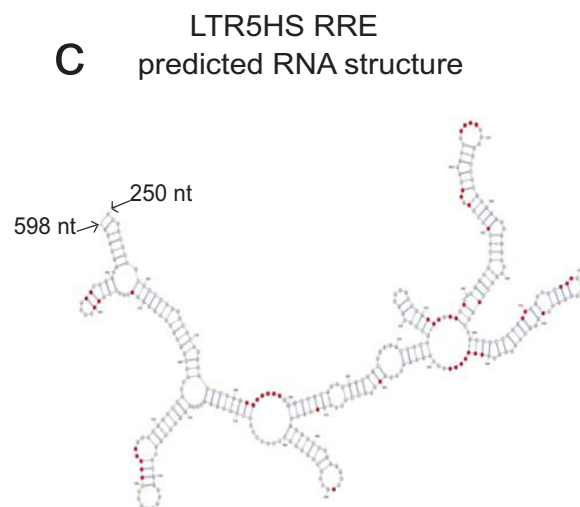
a Diagram of iCLIP-seq procedure



b



c

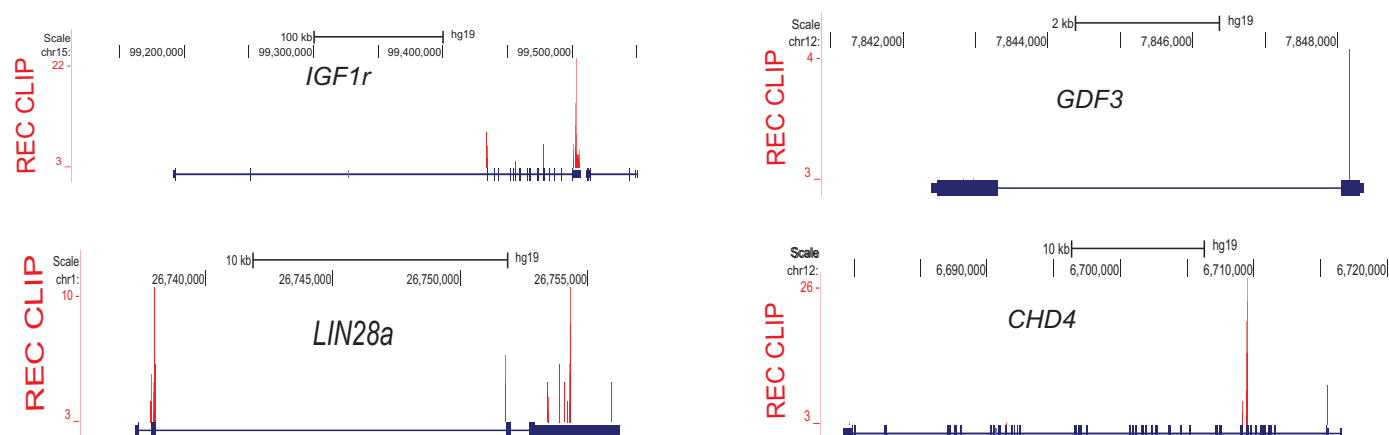
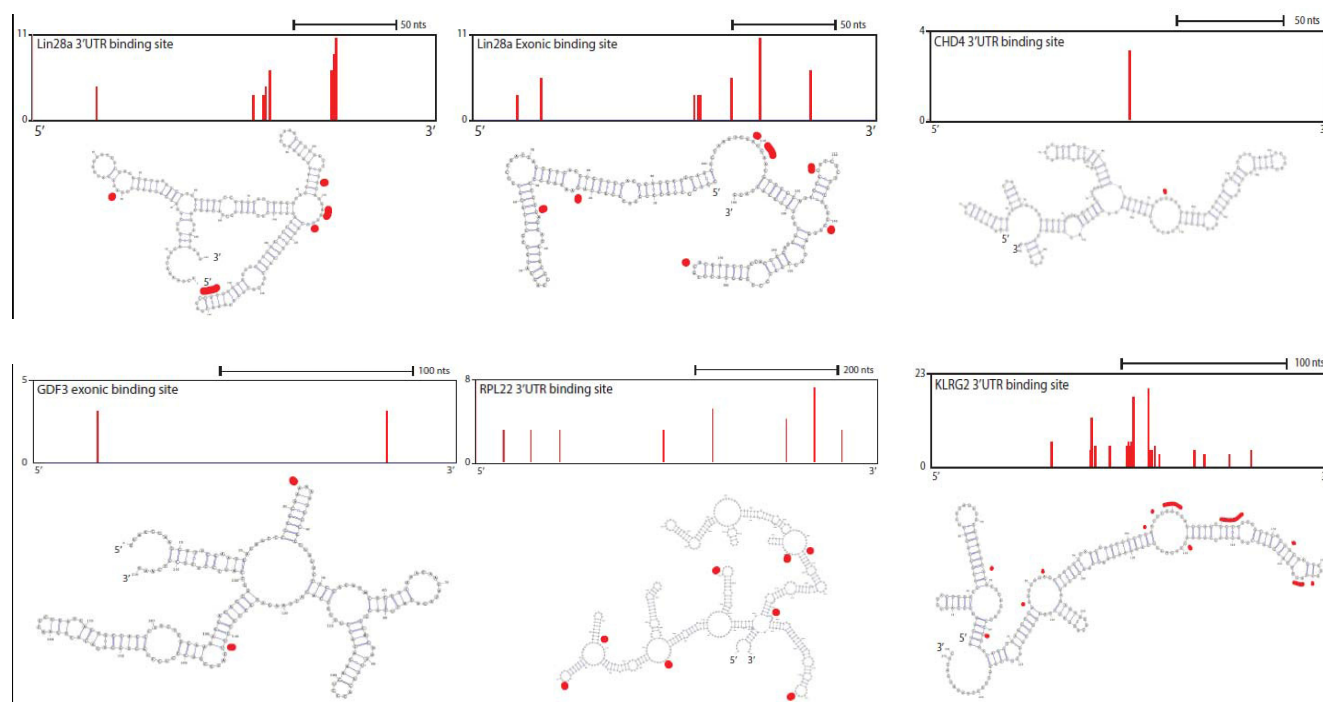


Extended Data Figure 8 | iCLIP analysis of Rec-associated RNAs

(supporting Fig. 4). **a**, Diagram of iCLIP-seq procedure (see Methods for details). Briefly, cells are crosslinked using ultraviolet, lysed and digested with RNase to trim RNAs. Sequential immunopurification is performed using Flag M2, peptide elution, and GFP immunoprecipitation (IP). After stringent washing, RNAs are recovered and either radiolabelled (shown in **b**) or reverse transcribed and prepared for Illumina HTS libraries.

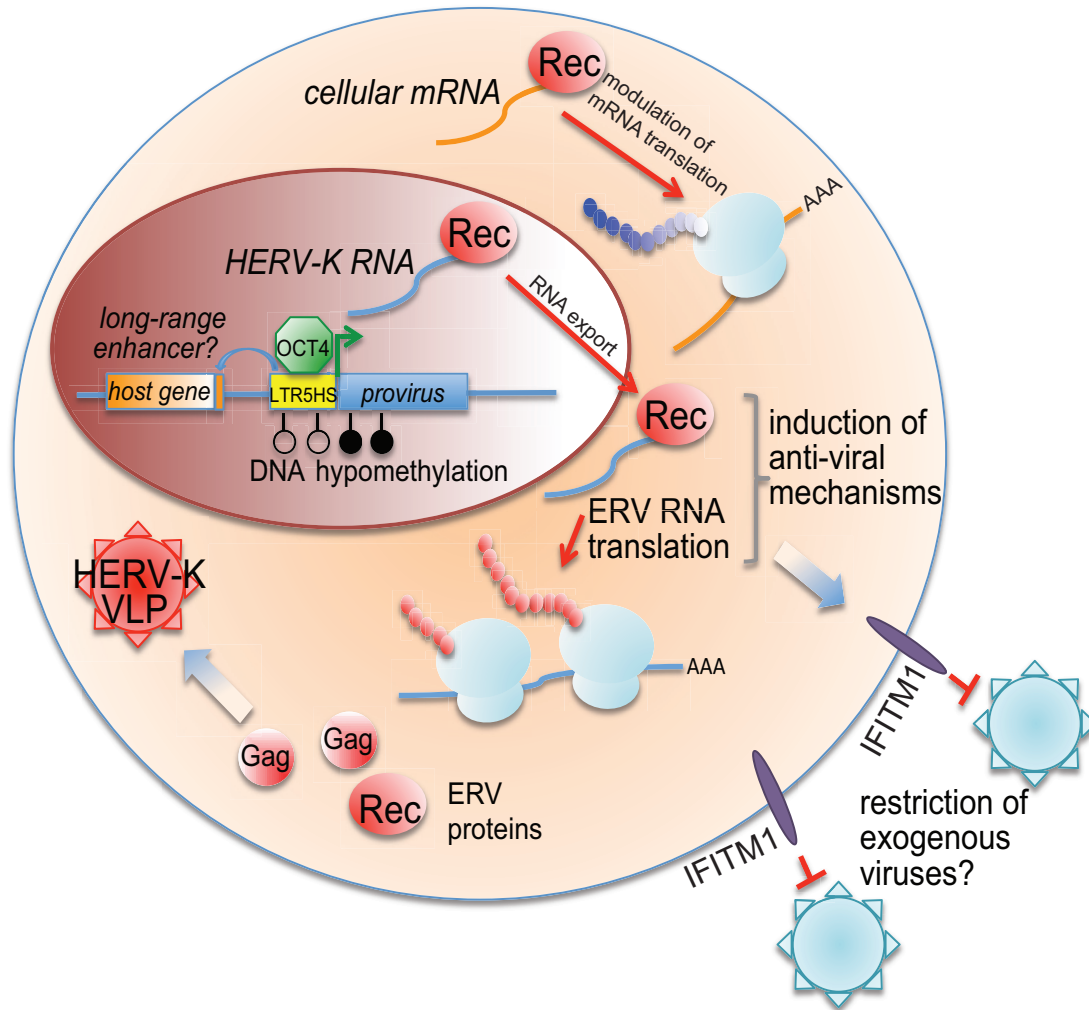
b, Autoradiogram of labelled RNAs (top) recovered from ultraviolet-crosslinked cells using sequential Flag-eGFP immunoprecipitation from: wild-type human EC cells (lanes 1, 2), Flag-eGFP control human EC cells (lanes 3, 4), or two independent Rec-hECC transgenic lines (lanes 5–8), separated on an SDS–polyacrylamide gel electrophoresis (SDS–PAGE) gel. Free Rec protein runs as a ~35 kDa band, while Rec protein crosslinked to

RNA molecules show lower electrophoretic mobility. Please note that: (1) Rec-bound RNAs are resistant to even high concentrations of RNaseI, probably indicating extensive secondary RNA structures, and (2) low/no background of contaminating RNAs in control immunoprecipitation from wild-type human EC cells or Flag-eGFP control human EC cells. Western blots with anti-GFP antibody were also performed to confirm the presence of tagged protein in Flag-eGFP control and Flag-eGFP–Rec cells, both in input and immunoprecipitation fractions (middle). HSP90 was used as a loading control (bottom). **c**, Computationally predicted (using mFold) secondary structure of LTR5HS sequence around the Rec response element (identified experimentally *in vitro* previously²⁵). Single nucleotide resolution Rec ultraviolet-crosslinking sites determined by iCLIP are shaded in red; $n = 2$ biological replicates.

a genome browser snapshots of Rec binding**b** Rec targets predicted RNA secondary structure

Extended Data Figure 9 | Rec target mRNA analysis (supporting Fig. 4).
a, Genome browser representations of the Rec iCLIP read ($n = 2$ biological replicates) distribution at indicated mRNA targets. **b**, Computationally predicted (using mFold) secondary structures of indicated Rec iCLIP-seq

targets. Single-nucleotide resolution Rec ultraviolet-crosslinking sites determined by iCLIP are shaded in red; to orient the reader, browser representation of the folded fragment is shown above each respective cartoon.



Extended Data Figure 10 | Model of HERVK regulation and function.

Epicardial regeneration is guided by cardiac outflow tract and Hedgehog signalling

Jinhu Wang^{1*}, Jingli Cao^{1*}, Amy L. Dickson¹ & Kenneth D. Poss¹

In response to cardiac damage, a mesothelial tissue layer enveloping the heart called the epicardium is activated to proliferate and accumulate at the injury site. Recent studies have implicated the epicardium in multiple aspects of cardiac repair: as a source of paracrine signals for cardiomyocyte survival or proliferation; a supply of perivascular cells and possibly other cell types such as cardiomyocytes; and as a mediator of inflammation^{1–9}. However, the biology and dynamism of the adult epicardium is poorly understood. To investigate this, we created a transgenic line to ablate the epicardial cell population in adult zebrafish. Here we find that genetic depletion of the epicardium after myocardial loss inhibits cardiomyocyte proliferation and delays muscle regeneration. The epicardium vigorously regenerates after its ablation, through proliferation and migration of spared epicardial cells as a sheet to cover the exposed ventricular surface in a wave from the chamber base towards its apex. By reconstituting epicardial regeneration *ex vivo*, we show that extirpation of the bulbous arteriosus—a distinct, smooth-muscle-rich tissue structure that distributes outflow from the ventricle—prevents epicardial regeneration. Conversely, experimental repositioning of the bulbous arteriosus by tissue recombination initiates epicardial regeneration and can govern its direction. Hedgehog (Hh) ligand is expressed in the bulbous arteriosus, and treatment with a Hh signalling antagonist arrests epicardial regeneration and blunts the epicardial response to muscle injury. Transplantation of Sonic hedgehog (Shh)-soaked beads at the ventricular base stimulates epicardial regeneration after bulbous arteriosus removal, indicating that Hh signalling can substitute for the influence of the outflow tract. Thus, the ventricular epicardium has pronounced regenerative capacity, regulated by the neighbouring cardiac outflow tract and Hh signalling. These findings extend our understanding of tissue interactions during regeneration and have implications for mobilizing epicardial cells for therapeutic heart repair.

To assess the homeostatic properties of the epicardium, we used an inducible cell ablation system in adult zebrafish. Targeted expression of bacterial nitroreductase (NTR) depletes specific cell types via conversion of a non-toxic substrate, metronidazole (Mtz), to a cytotoxin^{10–12}. We used *tcf21* regulatory sequences, which in zebrafish drive the most widespread epicardial expression of known DNA elements², to create an NTR transgenic line for lesioning this tissue without direct myocardial damage. After treatment of adult *tcf21:NTR*; *tcf21:nucGFP* animals with Mtz, ~90% of enhanced green fluorescent protein (eGFP)⁺ epicardial nuclei on average were ablated from the ventricular surface in large patches (Fig. 1a, b, f).

To determine whether epicardial depletion affects the well-documented capacity of the zebrafish heart to regenerate¹³, we transiently incubated *tcf21:NTR* zebrafish with Mtz after resection of the ventricular apex. Mtz treatment reduced epicardial cell number in the 7 days post-amputation (dpa) injury site by ~45%, while reducing cardiomyocyte proliferation indices by ~33% (Fig. 1c, d and Extended Data Figs 1a, b, 3c). Myofibroblasts were represented similarly in

vehicle- and Mtz-treated clutchmates by 14 dpa (Extended Data Fig. 1c). Injured ventricles of Mtz-treated animals displayed reduced vascularization and muscularization by 30 dpa (Fig. 1e and Extended Data Fig. 1d, e), associated with fibrin and collagen retention (Fig. 1e). By 60 dpa, ventricles from Mtz-treated zebrafish consistently showed normal muscularization and a large complement of *tcf21:nucGFP*⁺ cells, along with minor collagen deposits (Extended Data Fig. 1f). Thus, depletion of epicardial tissue inhibits cardiomyocyte proliferation and vascularization after resection injury, reducing the efficacy of heart regeneration.

These experiments suggested a high capacity of epicardial cells to regenerate after major depletion. To test this directly, we examined otherwise uninjured hearts at different times after epicardial ablation. Ventricular epicardial cells typically have a low proliferation index (Extended Data Fig. 2a). However, within 3 days of Mtz treatment (3 days post-incubation (dpi)), many spared epicardial cells entered the cell cycle (Extended Data Fig. 2b, c). At 7 dpi, ventricles displayed quantifiable epicardial recovery that was more prominent at the chamber base (Fig. 1b). By 14 dpi, and as early as 7 dpi, ventricles were fully covered to their apices with *tcf21:nucGFP*⁺ epicardial cells (Fig. 1b, f). The temporal variation in recovery probably reflects variation in the location/pattern of epicardial cells spared by ablation among clutchmates, or in chamber size (Extended Data Fig. 3a). To examine the origins of the regenerated epicardium, we used inducible Cre-based genetic fate-mapping to label *tcf21*-expressing cells and their progeny permanently before injury². Labelling and subsequent fate-mapping experiments indicated that pre-existing epicardial cells, and not a *tcf21*-negative precursor, are a primary source for regeneration (Fig. 1g, h). In sum, these experiments reveal that adult epicardium regenerates after substantial genetic ablation, through a mechanism of expansion by spared epicardial cells.

To expand our range of experimental manipulations, we refined protocols such that freshly dissected hearts contracted for several weeks *ex vivo* (Supplementary Video 1)^{14,15}. When Mtz was added transiently to the culture medium for 1 day, ventricular epicardial cells were potentially ablated. Epicardial layers of the atrium and the bulbous arteriosus (alternatively referred to as the outflow tract) were less effectively depleted (Fig. 2a), probably owing to differential expression of the NTR transgene among cardiac chambers (Extended Data Fig. 3b). Daily imaging of these hearts confirmed observations from *in vivo* experiments, demonstrating regeneration of the epicardium from base to apex that was typically completed in 2 weeks (Fig. 2a). Hearts from animals given partial ventricular resections *in vivo* showed a similar pattern of epicardial regeneration after *ex vivo* ablation (Extended Data Fig. 4a). Cardiac muscle regeneration was ineffective in explanted hearts in our experiments. Increases in cell number occurred concomitantly with movement across the myocardial surface during epicardial regeneration, with spared epicardial cell patches away from the leading edge eventually incorporated into the sheet (Fig. 2a).

To identify possible intrinsic differences in epicardial cells from different ventricular regions, we examined behaviours of basal or

¹Department of Cell Biology and Howard Hughes Medical Institute, Duke University Medical Center, Durham, North Carolina 27710, USA.

*These authors contributed equally to this work.

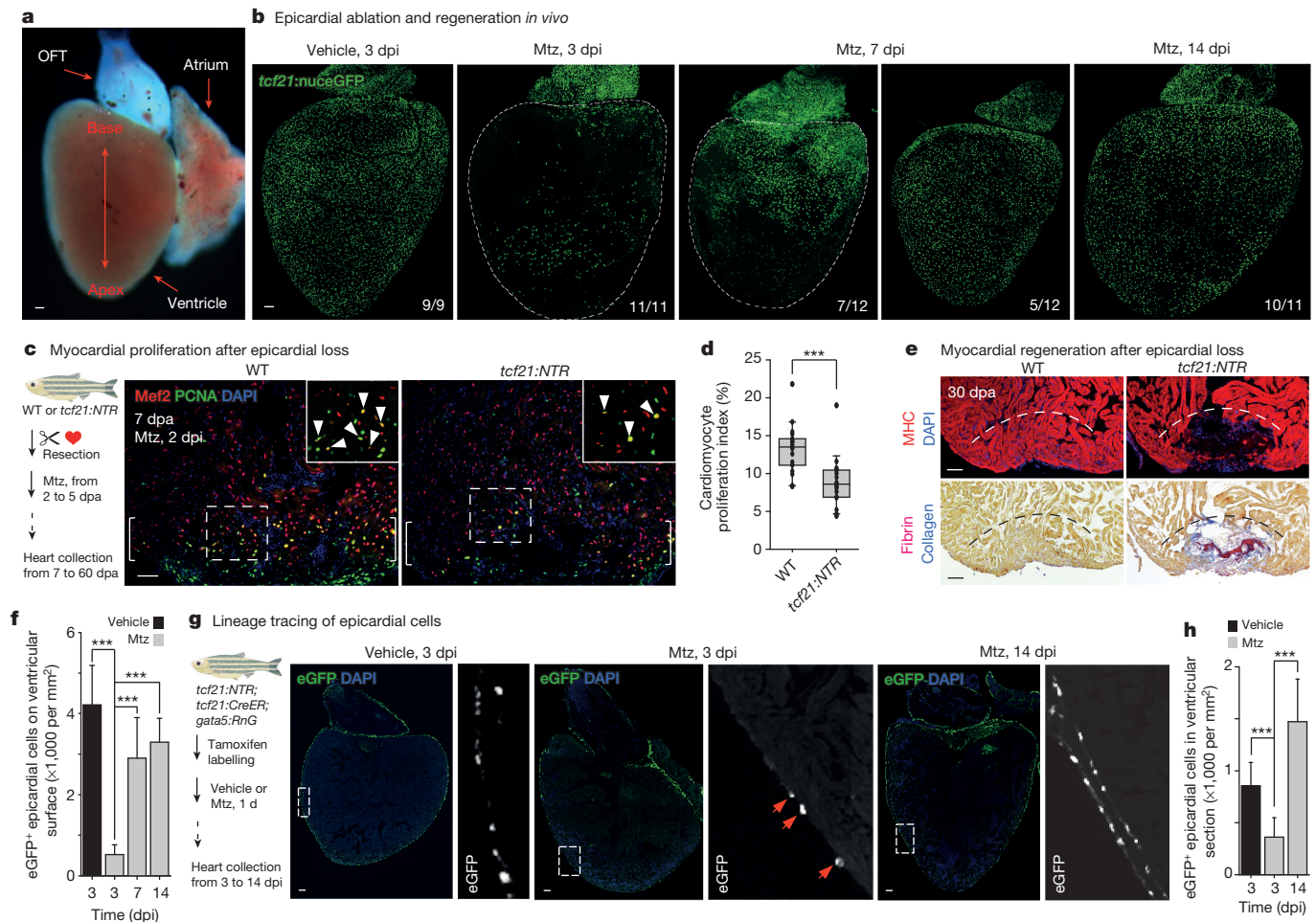


Figure 1 | Epicardial ablation and regeneration. **a**, Adult zebrafish heart. OFT, outflow tract. **b**, *tcf21:NTR*; *tcf21:nucGFP* adults were incubated with Mtz or vehicle, and hearts were collected by random sampling at 3, 7 or 14 dpi. White dashed lines delineate ventricle. Numbers in bottom right corners are proportion of total animals with indicated phenotype. All 3 dpi ventricles showed major ablation, averaging ~90% loss. **c**, Left, schematic for tests of epicardial ablation on muscle regeneration. Right, ventricular cardiomyocyte proliferation at 7 dpi. Brackets indicate injury site. Arrowheads indicate proliferating cardiomyocytes. DAPI, 4',6-diamidino-2-phenylindole; WT, wild type. **d**, Quantified PCNA⁺ cardiomyocyte indices in injury sites in experiments from **c**. ****P* < 0.001, Mann-Whitney rank sum test; *n* = 18 (wild type) and 19 (*tcf21:NTR*) animals from two experiments. **e**, Section images of

ventricles at 30 dpi, assessed for muscle recovery (MHC) and scar indicators (fibrin, collagen). One of eleven *tcf21:nucGFP* and 8 of 12 *tcf21:NTR*; *tcf21:nucGFP* ventricles showed myocardial gaps. Dashed line indicates approximate resection plane. ****P* < 0.01, Fisher Irwin exact test. **f**, Quantified eGFP⁺ nuclei from experiments in **b**. ****P* < 0.001, Student's two-tailed *t*-test. **g**, Left, CreER-based strategy for permanent labelling of *tcf21*⁺ progeny. Right, section images of lineage-labelled eGFP⁺ epicardial progeny up to 14 dpi, indicating derivation from pre-existing epicardium. Arrows indicate eGFP⁺ cells spared by epicardial ablation. **h**, Quantified eGFP⁺ cells from experiments in **g**. ****P* < 0.001, Student's two-tailed *t*-test; *n* = 10 (vehicle, 3 dpi), 13 (Mtz, 3 dpi) and 15 (Mtz, 14 dpi). **c**, **g**, Insets, high magnifications of boxed areas. Scale bars, 50 μ m. Error bars indicate standard deviation (s.d.).

apical epicardial tissue patches transplanted to ablated ventricles. In these experiments, transplanted cells of either origin consistently repopulated the ventricular surface in a base-to-apex direction after transplantation (Extended Data Fig. 5a–d), revealing no proliferative bias in ventricular epicardial cells that could explain the directional flow of regeneration. To assess potential extrinsic influences on epicardial regeneration, we removed the atrium or bulbous arteriosus from its attachment at the ventricular base before epicardial ablation. Atrial extirpation did not noticeably affect the regeneration of ventricular epicardium (Fig. 2b and Supplementary Video 2). By contrast, removal of outflow tract tissue blocked epicardial cell recovery, an arrest that persisted for at least 2 weeks (Fig. 2c, d and data not shown). To test whether this arrest was solely a consequence of mechanical tissue disruption, we ablated the epicardium after host bulbous arteriosus removal, before grafting a non-transgenic bulbous arteriosus to the ventricular base 2 days later. In most of these tissue recombination procedures (13 of 21), host *tcf21:nucGFP*⁺ epicardium regenerated to cover the ventricle (Fig. 3a). This effect was not observed when a portion of donor ventricular apex was inverted and transplanted to

the host ventricular base (Extended Data Fig. 5e). Complementary grafting experiments indicated that bulbous arteriosus could contribute epicardial cells to the ventricular surface, as a potential supplement to expansion of the ventricular epicardial cell pool (Extended Data Fig. 5f). Thus, our experiments indicate that outflow tract provides an essential interaction for regeneration from existing ventricular epicardial cells.

To test whether outflow tract tissue is sufficient to stimulate epicardial regeneration, we ectopically positioned experimentally manipulated cardiac structures. Co-culture of several outflow tracts in a transwell assay with an epicardially ablated ventricle did not restore regeneration in the absence of host bulbous arteriosus (Extended Data Fig. 6a). Similarly, a bulbous arteriosus graft placed at the ventricular apex showed no evidence of directing regeneration of basally located host epicardial cells towards the apex (Extended Data Fig. 6b). Thus, we could not detect bulbous arteriosus effects requiring long-range diffusion through tissue or culture medium. Next, we transplanted a *tcf21:nucGFP*⁺ epicardial cell patch to the apex of an ablated host ventricle, after which we grafted a wild-type bulbous arteriosus to the

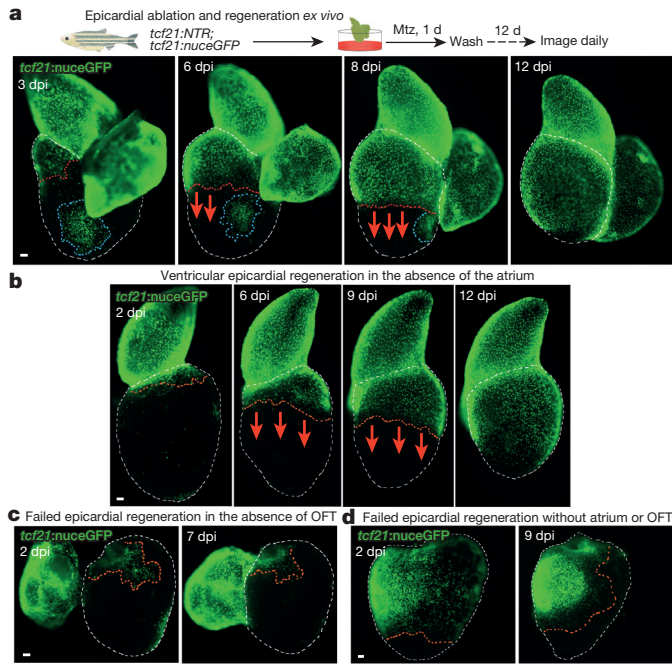


Figure 2 | Cardiac outflow tract is required for regeneration of adjacent ventricular epicardium. **a**, Top, schematic for epicardial ablation and regeneration in hearts cultured *ex vivo*. Bottom, regeneration occurs in a base-to-apex direction (arrows). Isolated patches (circled by blue dashed lines) do not participate in regeneration until contacted by the leading edge. **b**, Ventricular epicardium regenerates in the absence of the atrium ($n = 19$; behaviour seen in all samples). Arrows indicate direction of regeneration. **c**, **d**, Ventricular epicardium fails to regenerate in the absence of the bulbous arteriosus. Ventricular epicardium showed defective regeneration in these experiments with (**c**) ($n = 6$; all samples) or without atrium (**d**) ($n = 14$; all samples), even when, in rare cases, many basal epicardial cells were spared (**d**). Red dashed lines delineate epicardium or epicardial leading edge. White dashed lines delineate ventricle. OFT, outflow tract. Scale bars, 50 μm .

apex (Fig. 3b). Remarkably, the apical bulbous arteriosus was capable of stimulating apex-to-base regeneration from the nearby epicardial patch in a high proportion (21 of 32) of experiments, effectively reversing the stereotypical direction of recovery (Fig. 3c, d). Together, these experiments indicate that the cardiac outflow tract is necessary and sufficient for epicardial regeneration, and that this neighbouring tissue provides a short-range influence(s) that directs regeneration from base to apex.

To pursue the molecular nature of interactions between outflow tract and ventricular epicardium, we applied a small panel of signalling pathway effectors to epicardially ablated hearts cultured *ex vivo*. Among several compounds (Extended Data Fig. 7), the Smoothened (Smo) antagonist cyclopamine (CyA) blocked regeneration; nonetheless, regeneration initiated normally after drug washout (Fig. 4a). CyA treatment reduced spontaneous epicardial cell 5-ethynyl-2'-deoxyuridine (EdU) incorporation occurring in the first 2 days of explant culture, suggesting that intact Hh signalling promotes epicardial proliferation (Extended Data Fig. 8a, b). CyA also disrupted *in vivo* epicardial regeneration, not only in adults but in larvae, an additional developmental setting in which we identified base-to-apex regeneration (Fig. 4b, c and Extended Data Fig. 9a–c). CyA treatment from 2 to 4 days post-fertilization also reduced the initial epicardial occupancy of the larval ventricle (Extended Data Fig. 9d–f), indicating that epicardial regeneration recapitulates at least one pathway influential in morphogenesis. Finally, we observed inhibitory effects of CyA on the epicardial proliferative response to muscle resection *in vivo*, and in coverage of these injuries *ex vivo* (Extended Data Fig. 4b and Extended Data Fig. 8c, d).

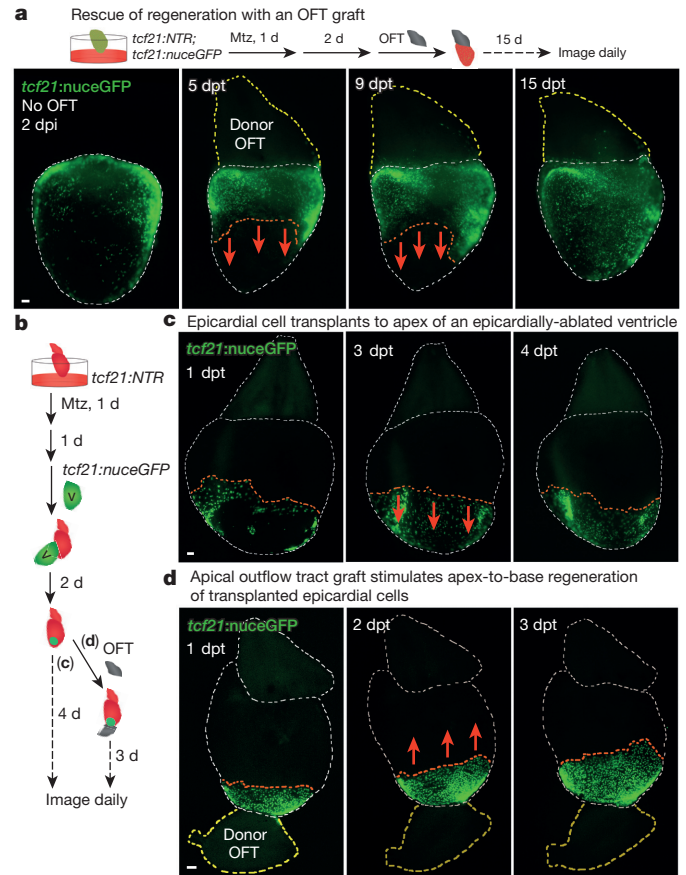


Figure 3 | Outflow tract tissue is sufficient to initiate and redirect epicardial regeneration. **a**, Top, a non-transgenic donor outflow tract (OFT) was transplanted to a transgenic ventricular base after epicardial ablation *ex vivo*. Bottom, base-to-apex epicardial regeneration (arrows) was observed from host tissue in 13 of 21 ventricles. dpt, days post-transplantation. **b**, Experimental design in **c**, **d**. **c**, **d**, *tcf21:nucGFP*⁺ epicardial cells transplanted to an epicardially ablated ventricular apex were static or regenerated (arrows) towards the apex ($n = 12$, all samples), but not towards the base. **d**, *tcf21:nucGFP*⁺ epicardial cells were transplanted to the apex of an epicardially ablated ventricle, followed by apical grafting of a donor bulbous arteriosus. *tcf21:nucGFP*⁺ cells regenerated in a reversed apex-to-base direction (arrows) in 9 of 14 ventricles. Twelve of eighteen host ventricles with the host bulbous arteriosus removed before donor bulbous arteriosus grafting also showed apex-to-base regeneration. **a**, **c**, **d**, Red dashed lines delineate epicardial sheet edge; white dashed lines delineate ventricle and host bulbous arteriosus. **a**, **d**, Yellow dashed lines indicate donor bulbous arteriosus. Scale bars, 50 μm .

Smo is an effector for several Hh family ligands, which have potent short-range effects in multiple contexts of embryonic development^{16–21}. Quantitative polymerase chain reaction (qPCR) revealed *shha*, *ihhb* and *dhh* ligand transcripts in adult atrium, ventricle and bulbous arteriosus, where *in situ* hybridization detected *shha* and *dhh* transcript signals in smooth muscle tissue (Extended Data Fig. 10a–d). Epicardial ablation injury boosted bulbous arteriosus and ventricular *shha* levels, as well as levels of *ptch1* and *gli2a* in purified epicardial cells (Fig. 4d, e). Moreover, a *shha:eGFP* reporter strain visualized *shha* regulatory-sequence-driven fluorescence in smooth muscle and epicardial tissues of the bulbous arteriosus (Extended Data Fig. 10e). No additional *in situ* hybridization or *shha:eGFP* fluorescence patterns were detectable after epicardial ablation; however, apical resection injury induced fluorescence in ventricular epicardial tissue by 2 dpa (Extended Data Fig. 10d, f). To test whether local Hh ligand delivery is sufficient to substitute for the bulbous arteriosus, we removed atrium and bulbous arteriosus from cardiac explants, ablated epicardial cells, and applied

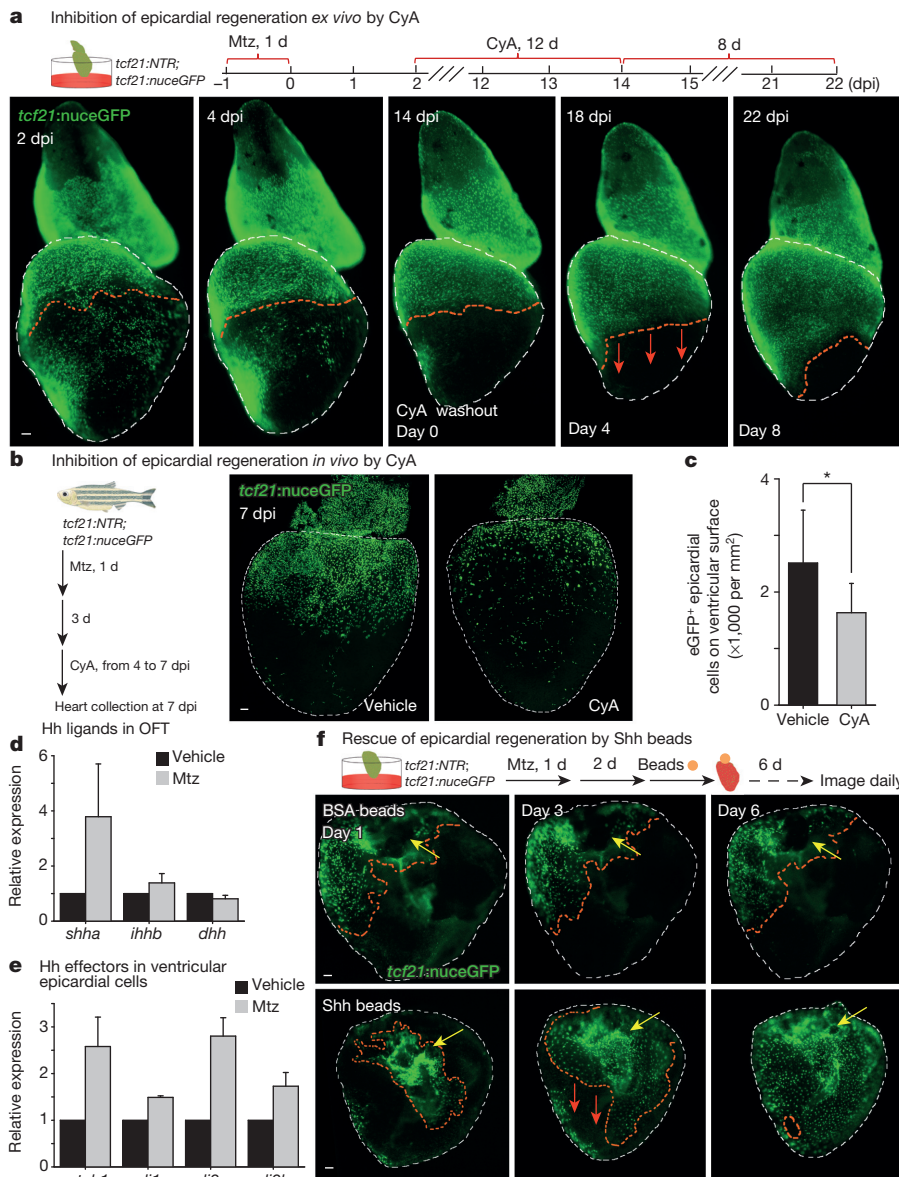


Figure 4 | Hh signalling controls epicardial regeneration. **a**, Top, experimental schematic. Bottom, CyA arrested regeneration while present (*n* = 7; all samples), and regeneration initiated (arrows) after CyA removal (6 of 7 ventricles). **b**, tcf21:NTR; tcf21:nucGFP adults were incubated with Mtz and randomly separated into two groups for treatment with CyA or vehicle. **c**, Quantified tcf21:nucGFP⁺ epicardial cells from experiments in **b**. **P* < 0.05, Student's two-tailed *t*-test; *n* = 13 (vehicle) and 12 (CyA). **d**, Quantitative RT-PCR detecting *shha* and *ihhb* expression in outflow tract (OFT) after epicardial ablation (3 dpi), from 3 separate experiments on pooled tissues using 90 total zebrafish. **e**, RT-qPCR of fluorescence-activated cell sorting (FACS)-purified ventricular epicardial cells showed increased *ptch1* and *gli2a* expression after epicardial ablation (7 dpi), from 2 separate experiments using 209 zebrafish. **f**, Top, BSA- or recombinant Shh-soaked beads were grafted to the base of epicardially ablated ventricles 2 days after 24 h Mtz treatment. Bottom, Shh-soaked beads stimulated one-half or greater coverage (red arrows) in 9 of 32 ventricles, whereas BSA-soaked beads (middle) did not (0 of 27). Yellow arrows indicate transplanted beads. **a**, **f**, Red dashed lines delineate epicardium or epicardial leading edge; white dashed lines delineate ventricle. Scale bars, 50 μ m. Error bars indicate s.d.

beads soaked with Shh protein to the exposed ventricular base. Shh-soaked beads stimulated epicardial regeneration (one-half or greater coverage) in 9 of 32 ventricles, whereas this level of recovery never occurred after transplantation of BSA-soaked beads (0 of 27 ventricles; Fig. 4f). We speculate that these effects of Hh on the epicardial sheet might involve cytoplasmic extensions or a factor transport system^{22,23}. Together, our findings support a model in which Hh ligand from the outflow tract, and possibly additional tissues, guides the base-to-apex regeneration of ventricular epicardium.

In conclusion, we have identified a requirement for the mesothelial covering of the zebrafish heart for proficient muscle regeneration. Moreover, we show that the ventricular epicardium itself has high endogenous renewal capacity, vigorously regenerating as a sheet from the base of the chamber to its apex after genetic depletion. Our results point to the outflow tract as an unexpected signalling centre and source of Hh, and possibly additional influences, that can promote epicardial regeneration. It is likely that tissue regeneration is similarly regulated in *trans* in other contexts; for example, to maintain the mesothelium that lines abdominal organs. As a mediator of epicardial regeneration, Hh signalling can be integrated into new strategies to modulate repair of the damaged heart.

Online Content Methods, along with any additional Extended Data display items and Source Data, are available in the online version of the paper; references unique to these sections appear only in the online paper.

Received 16 July 2014; accepted 12 February 2015.

Published online 4 May 2015.

- Huang, G. N. *et al.* C/EBP transcription factors mediate epicardial activation during heart development and injury. *Science* **338**, 1599–1603 (2012).
- Kikuchi, K. *et al.* tcf21⁺ epicardial cells adopt non-myocardial fates during zebrafish heart development and regeneration. *Development* **138**, 2895–2902 (2011).
- Smart, N. *et al.* De novo cardiomyocytes from within the activated adult heart after injury. *Nature* **474**, 640–644 (2011).
- Zhou, B. *et al.* Adult mouse epicardium modulates myocardial injury by secreting paracrine factors. *J. Clin. Invest.* **121**, 1894–1904 (2011).
- Wang, J., Karra, R., Dickson, A. L. & Poss, K. D. Fibronectin is deposited by injury-activated epicardial cells and is necessary for zebrafish heart regeneration. *Dev. Biol.* **382**, 427–435 (2013).
- Smart, N. *et al.* Thymosin β 4 induces adult epicardial progenitor mobilization and neovascularization. *Nature* **445**, 177–182 (2007).
- Lepilina, A. *et al.* A dynamic epicardial injury response supports progenitor cell activity during zebrafish heart regeneration. *Cell* **127**, 607–619 (2006).
- Song, K. *et al.* Heart repair by reprogramming non-myocytes with cardiac transcription factors. *Nature* **485**, 599–604 (2012).
- Qian, L. *et al.* In vivo reprogramming of murine cardiac fibroblasts into induced cardiomyocytes. *Nature* **485**, 593–598 (2012).

10. Pisharath, H., Rhee, J. M., Swanson, M. A., Leach, S. D. & Parsons, M. J. Targeted ablation of β cells in the embryonic zebrafish pancreas using *E. coli* nitroreductase. *Mech. Dev.* **124**, 218–229 (2007).
11. Curado, S. *et al.* Conditional targeted cell ablation in zebrafish: a new tool for regeneration studies. *Dev. Dyn.* **236**, 1025–1035 (2007).
12. Singh, S. P., Holdway, J. E. & Poss, K. D. Regeneration of amputated zebrafish fin rays from *de novo* osteoblasts. *Dev. Cell* **22**, 879–886 (2012).
13. Poss, K. D., Wilson, L. G. & Keating, M. T. Heart regeneration in zebrafish. *Science* **298**, 2188–2190 (2002).
14. Kikuchi, K. *et al.* Retinoic acid production by endocardium and epicardium is an injury response essential for zebrafish heart regeneration. *Dev. Cell* **20**, 397–404 (2011).
15. Kim, J., Rubin, N., Huang, Y., Tuan, T. L. & Lien, C. L. *In vitro* culture of epicardial cells from adult zebrafish heart on a fibrin matrix. *Nature Protocols* **7**, 247–255 (2012).
16. Riddle, R. D., Johnson, R. L., Laufer, E. & Tabin, C. Sonic hedgehog mediates the polarizing activity of the ZPA. *Cell* **75**, 1401–1416 (1993).
17. Roelink, H. *et al.* Floor plate and motor neuron induction by different concentrations of the amino-terminal cleavage product of sonic hedgehog autoproteolysis. *Cell* **81**, 445–455 (1995).
18. Fan, C. M. & Tessier-Lavigne, M. Patterning of mammalian somites by surface ectoderm and notochord: evidence for sclerotome induction by a hedgehog homolog. *Cell* **79**, 1175–1186 (1994).
19. Roelink, H. *et al.* Floor plate and motor neuron induction by vhh-1, a vertebrate homolog of hedgehog expressed by the notochord. *Cell* **76**, 761–775 (1994).
20. Echelard, Y. *et al.* Sonic hedgehog, a member of a family of putative signaling molecules, is implicated in the regulation of CNS polarity. *Cell* **75**, 1417–1430 (1993).
21. Johnson, R. L., Laufer, E., Riddle, R. D. & Tabin, C. Ectopic expression of Sonic hedgehog alters dorsal-ventral patterning of somites. *Cell* **79**, 1165–1173 (1994).
22. Guerrero, I. & Kornberg, T. B. Hedgehog and its circuitous journey from producing to target cells. *Semin. Cell Dev. Biol.* **33**, 52–62 (2014).
23. Sanders, T. A., Llagostera, E. & Barna, M. Specialized filopodia direct long-range transport of SHH during vertebrate tissue patterning. *Nature* **497**, 628–632 (2013).

Supplementary Information is available in the online version of the paper.

Acknowledgements We thank J. Burris, N. Lee, A. Dunlap and S. Davies for fish care, and M. Bagnat, B. Hogan, J. Kang and R. Karra for comments on the manuscript. This work was funded by postdoctoral fellowships from the American Heart Association to J.W. and J.C., and grants from the National Institutes of Health (HL081674) and American Federation for Aging Research to K.D.P.

Author Contributions J.W., J.C. and K.D.P. designed the experimental strategy, analysed data, and prepared the manuscript. J.W. generated the transgenic system for epicardial cell ablation and performed *in vivo* regeneration experiments and analysis. J.C. developed the *ex vivo* culture assay and performed *ex vivo* regeneration experiments and analysis. A.L.D. performed histology and data analysis. All authors commented on the manuscript.

Author Information Reprints and permissions information is available at www.nature.com/reprints. The authors declare no competing financial interests. Readers are welcome to comment on the online version of the paper. Correspondence and requests for materials should be addressed to K.D.P. (kenneth.poss@duke.edu).

METHODS

Zebrafish maintenance and procedures. Adult zebrafish of the Ekkwill and Ekkwill/AB strains were maintained as described and resection injuries were performed as described^{13,24}. Animals between 4 and 12 months of both sexes were used. Transgenic lines used in this study were *Tg(tcf21:mCherry-NTR)^{pd108}* (*tcf21:NTR*, described later), *Tg(tcf21:nucGFP)^{pd41}* (ref. 24), *Tg(tcf21:CreER)^{pd42}* (ref. 2), *Tg(gata5:loxP-mCherry-loxP-nucGFP)^{pd40}* (ref. 25), *Tg(fli1a:eGFP)^{y1}* (ref. 26) and *Tg(shha:eGFP)^{sb15}* (ref. 27). All transgenic strains were analysed as hemizygotes. For epicardial ablation experiments in adults, animals were bathed for 24 h in 10 mM Mtz (Sigma) as described and returned to water¹². If ablation was performed after ventricular resection, we used a protocol of daily changes of 1 mM Mtz solution for 3 days that had similar ablation effects (Extended Data Fig. 3c). This period corresponds with the early epicardial proliferative response to resection injury⁷ (data not shown), and was intended to extend the ablation window and improve animal survival. For larval epicardial ablation, 6 hours post-fertilization (hpf) embryos were bathed for 48 h in 10 mM Mtz before washout. For *ex vivo* epicardial ablation, dissected hearts were bathed for 24 h in 1 mM Mtz before washout. Cyclopamine (CyA; Selleckchem) was dissolved in ethanol to a final concentration of 20 mM. CyA was used at 10 μ M for *in vivo* treatment of adult animals and 5 μ M for *ex vivo* culture and embryo treatments. For EdU incorporation experiments that followed epicardial ablation, animals were injected with 10 mM EdU 4 h before collection. Experiments with uninjured animals used three daily 10 mM EdU injections. For lineage tracing, strains carrying *tcf21:NTR*; *tcf21:CreER* and *gata5:loxP-mCherry-loxP-nucGFP* transgenes were placed in a small beaker of aquarium water containing 5 μ M tamoxifen. Fish were maintained for 24 h, rinsed with fresh aquarium water, and returned to a recirculating aquatic system for 24 h, before repeating this incubation twice. After 3 days of rinsing, Mtz was added for an additional 24 h. As is common when using Cre-based tools, we could not genetically label all epicardial cells in these experiments or rule out minor contributions by *tcf21*-negative cells. Animal procedures were performed in accordance with Duke University guidelines.

Construction of *tcf21:NTR* zebrafish. The translational start codon of *tcf21* in the bacterial artificial chromosome (BAC) clone DKEYP-79F12 was replaced with the *mCherry-NTR* cassette by Red/ET recombineering technology (Gene Bridges)¹². The 5' and 3' homologous arms for recombination were a 50-base pair (bp) fragment upstream and downstream of the start codon, and were included in PCR primers to flank the *mCherry-NTR* cassette. To avoid aberrant recombination between the *mCherry-NTR* cassette and the endogenous *loxP* site in the BAC vector, we replaced the vector-derived *loxP* site with an I-SceI site using the same technology. The final BAC was purified with Nucleobond BAC 100 kit (Clontech) and co-injected with I-SceI into one-cell-stage zebrafish embryos.

Ex vivo cardiac explants. Adult hearts were rinsed several times in PBS after collection and cultured in dishes with DMEM medium (Life Technologies) plus 2 mM L-glutamine (Life Technologies), 10% fetal bovine serum (HyClone, Thermo), 1% MEM non-essential amino acids (Life Technologies), 100 U ml⁻¹ penicillin, 100 μ g ml⁻¹ streptomycin (Life Technologies) and 50 μ M 2-mercaptoethanol (Life Technologies), while rotating at 150 r.p.m. Primocin (InvivoGen) was added to prohibit microbial contaminants during the first 3 days primary culture. For transplantation experiments, outflow tract or ventricular tissues were grafted by mounting in 1% low-melting-point agarose with ablated hearts in culture dishes, and covering with medium. After 2 days of culturing, attached tissues were released from the agarose; if transplanting an epicardial patch, the ventricular donor tissue was removed carefully using forceps. Fluorescent transgenes in these cardiac explants were monitored using a Leica MZ05FA stereo-fluorescence microscope.

Recombinant mouse Shh (C25II), N terminus protein (R & D Systems) was reconstituted at 100 μ g ml⁻¹ in PBS containing 0.1% BSA. Affi-Gel Blue beads (Bio-Rad) were prepared by thoroughly washing the beads in PBS, then incubating them in the Shh solution for 2 h at room temperature. A solution with the same concentration of BSA protein was used as the control. The beads were then applied to the base of ventricular explants that were settled in low-melting-point agarose in serum-free DMEM supplemented as described earlier. After 24 h, the ventricles were released from the agarose with the attached beads and cultured in supplemented, serum-free DMEM. Under these *ex vivo* culture conditions we observed no increase in cardiomyocyte proliferation upon resection injury.

Preparation of outflow tract and ventricular epicardial cells and RT-qPCR. Adult hearts were dissected from *tcf21:NTR* or *tcf21:nucGFP* animals 3 and 7 days post-treatment with vehicle or Mtz. Outflow tracts were frozen in liquid nitrogen. Ventricular nucGFP⁺ epicardial cells were isolated as described previously²⁸ with modifications. Briefly, ventricles were collected on ice and washed several times to remove blood cells. Ventricles were digested in an

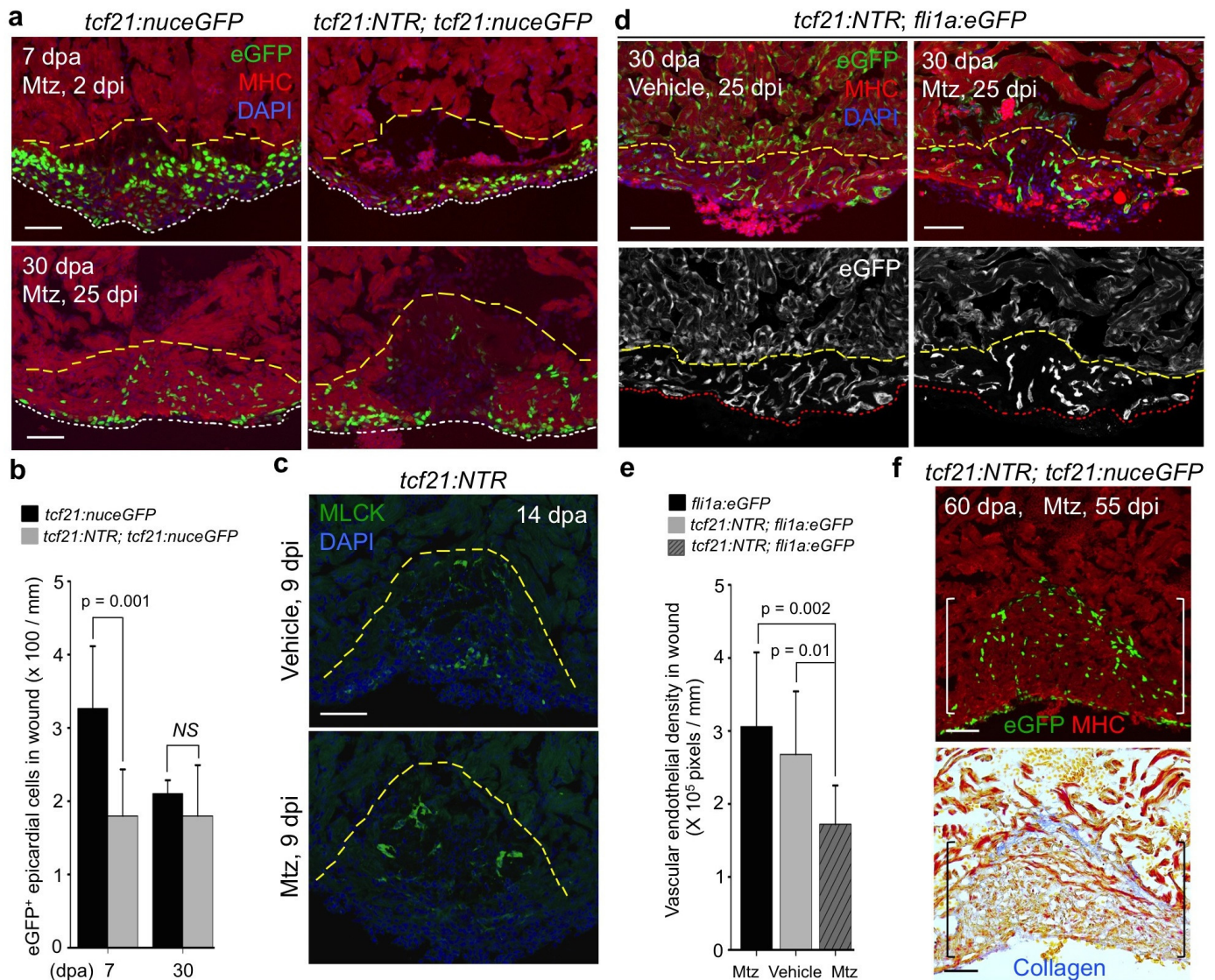
Eppendorf tube with 0.5 ml HBSS plus 0.13 U ml⁻¹ Liberase DH (Roche) and 1% sheep serum at 37 °C, while stirring gently with a Spinbar magnetic stirring bar (Bel-Art Products). Supernatants were collected every 5 min and neutralized with sheep serum. Dissociated cells were spun down and sorted using a BD FACS Vantage SE sorter for eGFP-positive cells. Total RNA was extracted using an RNeasy-Micro isolation kit (Ambion) according to the manufacturer's instructions. Reverse transcription was carried out using a SuperScript III First-Strand synthesis kit (Life Technologies). qPCR was carried out in triplicate using a Roche LightCycler 480 II system with the LightCycler 480 Probes Master Mix and the Universal Probe Library (UPL) (Roche). *rpl13a* served as the control. Primers and the UPL numbers used in this study were: *shha*-f, AAGCCACATTCAT TGCTCT, and *shha*-r, CCTTCTGTCTCCGTCCTG, UPL #54; *shhb*-f, GCAAG TATGGGATGCTATCCAG, and *shhb*-r, TCCTGATTAGCAGCCACTG, UPL #16; *ihha*-f, TGGGTCTACTATGAGTCCAAAGC, and *ihha*-r, GGTTTATGCA GCCACAGAGTG, UPL #86; *ihhb*-f, TCTTGTATGCTGCGGTGAA, and *ihhb*-r, AAGCGTAGAGGTGCAAAAGC, UPL #140; *dhh*-f, CGTGCACTGCTCTGT CAAA, and *dhh*-r, AAACATGACATGGGCTTTGT, UPL #156; *ptch1*-f, TG GCTTAAGGGCAGCTAATC, and *ptch1*-r, GCCGTGTGACTTGAGTTCCT, UPL #87; *ptch2*-f, CCATGACATCAACTGGAATGA, and *ptch2*-r, GAATGCT CCCATGAACAACC, UPL #6; *gli1*-f, CTGCAGCAAAGAGTTCGACA, and *gli1*-r, CTCCGTGGATGTGCTCATTA, UPL #68; *gli2a*-f, CCTCACCCACC ACAGCAT, and *gli2a*-r, CGATCGGGATTGGTGTGT, UPL #39; *gli2b*-f, CCTGCCAGAATACTTACATCA, and *gli2b*-r, CTCACCTGGGCGTCA TAC, UPL #48; *rpl13a*-f, GCGGACCGATTCAATAAGG, and *rpl13a*-r, GAAAGACGACCGAGGAGATG, UPL #147.

Histology. Analyses of cardiomyocyte proliferation were performed as previously described by counting Mef2⁺ and PCNA⁺ nuclei in wound sites¹⁴. To quantify vascular endothelial cells in the wound site by 30 dpa with *fli1a:eGFP* or *tcf21:NTR*; *fli1a:eGFP* animals, three medial, longitudinal sections were selected from each heart. Images of single optical slices of green fluorescence in the wound site were acquired using a $\times 20$ objective (1,024 \times 1,024 pixels). eGFP⁺ areas were quantified in pixels by ImageJ software, and the ratio of eGFP⁺ area versus the length of the outlined apical wound was calculated for each heart. To quantify *tcf21*⁺ epicardial cells in the wound site at 7 and 30 dpa with *tcf21:nucGFP* or *tcf21:NTR*; *tcf21:nucGFP* animals, three medial, longitudinal sections were selected from each heart. eGFP⁺ cells were counted in the wound area, and the ratio of eGFP⁺ cells versus the length of the outlined apical wound was calculated for each heart. Acid Fuchsin-Orange G and immunostaining were performed as described¹³. Primary antibodies used in this study were anti-myosin heavy chain (MHC; F59, mouse; Developmental Studies Hybridoma Bank), anti-GFP (rabbit; Invitrogen), anti-Mef2 (rabbit; Santa Cruz Biotechnology), anti-MLCK (mouse, K36; Sigma) and anti-PCNA (mouse; Sigma). Secondary antibodies (Invitrogen) used in this study were: Alexa Fluor 488 goat anti-rabbit; Alexa Fluor 594 goat anti-rabbit, goat anti-rat and goat anti-mouse; and Alexa 633 goat anti-mouse. EdU was detected through a click reaction as described previously²⁹ with fluorescent azide (Alexa Fluor 594 or 647; Invitrogen). Whole-mounted and sectioned ventricular tissues were imaged using a Zeiss 700 confocal microscope.

Data collection and statistics. Clutchmates (or hearts collected from clutchmates) were randomized into different treatment groups for each experiment. No animal or sample was excluded from the analysis unless the animal died during the procedure. All experiments were performed with at least two biological replicates, using appropriate numbers of samples for each replicate. Sample sizes were chosen on the basis of previous publications and experiment types, and are indicated in each figure legend. For expression patterns, at least six fish were examined. For assessment of epicardial ablation and consequences on muscle regeneration, at least nine fish were examined. At least 12 hearts of each group were pooled for RNA purification and subsequent RT-qPCR. For *ex vivo* epicardial ablation experiments, at least six hearts were used for each treatment. An exception was the small compound screen, where at least four hearts were used for each drug. Quantification of cell proliferation and calculation of statistical outcomes were assessed by a person blinded to the treatments. All statistical values are displayed as mean \pm standard deviation. Sample sizes, statistical tests, and *P* values are indicated in the figures or the legends. Student's *t*-tests (two-tailed) were applied when normality and equal variance tests were passed. The Mann-Whitney rank sum test was used when these failed. Fisher Irwin exact tests or chi-squared tests were used where appropriate.

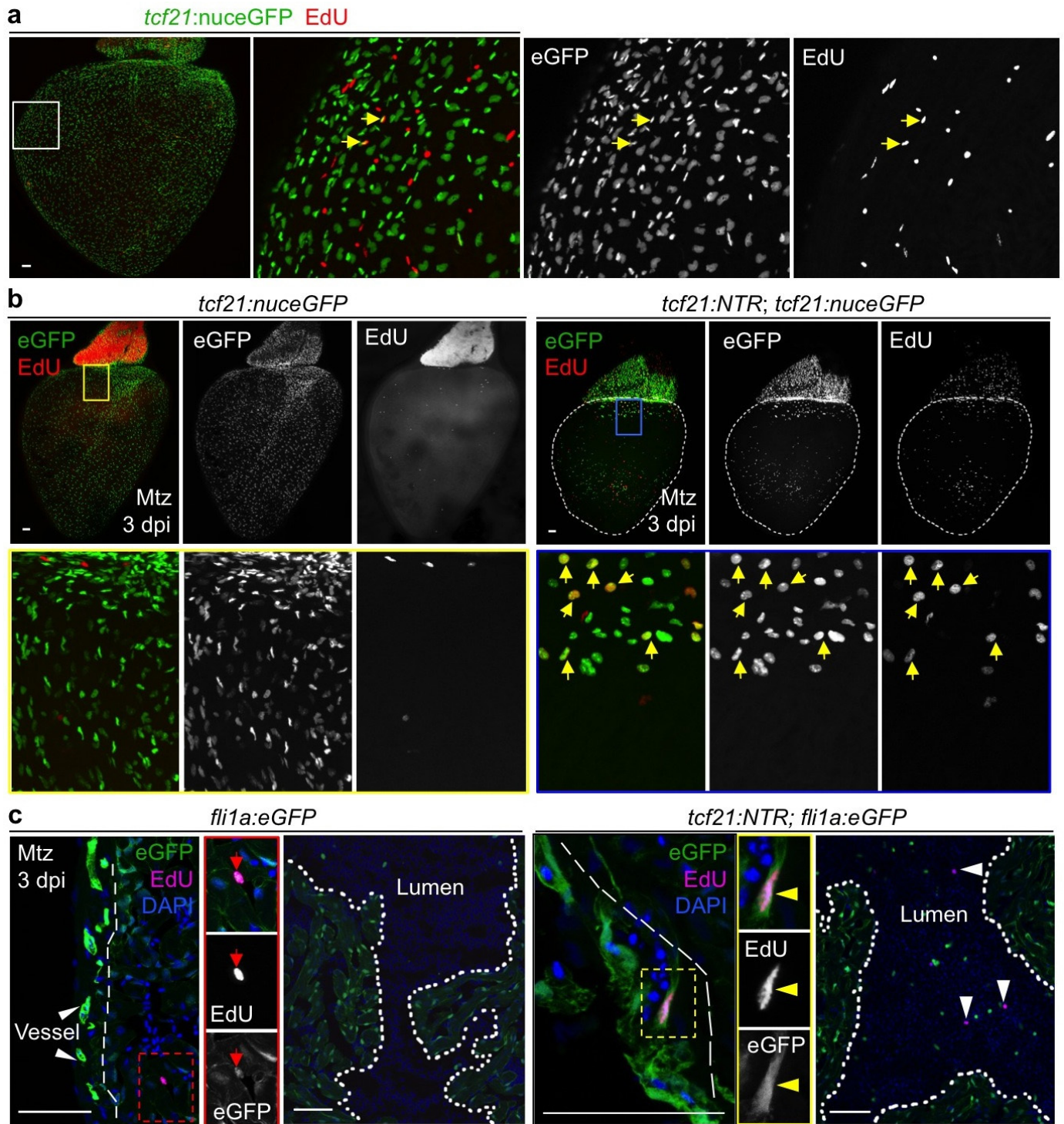
24. Wang, J. et al. The regenerative capacity of zebrafish reverses cardiac failure caused by genetic cardiomyocyte depletion. *Development* **138**, 3421–3430 (2011).
25. Kikuchi, K. et al. Primary contribution to zebrafish heart regeneration by *gata4*⁺ cardiomyocytes. *Nature* **464**, 601–605 (2010).

26. Lawson, N. D. & Weinstein, B. M. *In vivo* imaging of embryonic vascular development using transgenic zebrafish. *Dev. Biol.* **248**, 307–318 (2002).
27. Shkumatava, A., Fischer, S., Muller, F., Strahle, U. & Neumann, C. J. Sonic hedgehog, secreted by amacrine cells, acts as a short-range signal to direct differentiation and lamination in the zebrafish retina. *Development* **131**, 3849–3858 (2004).
28. Zhou, B. & Pu, W. T. Isolation and characterization of embryonic and adult epicardium and epicardium-derived cells. *Methods Mol. Biol.* **843**, 155–168 (2012).
29. Salic, A. & Mitchison, T. J. A chemical method for fast and sensitive detection of DNA synthesis *in vivo*. *Proc. Natl Acad. Sci. USA* **105**, 2415–2420 (2008).



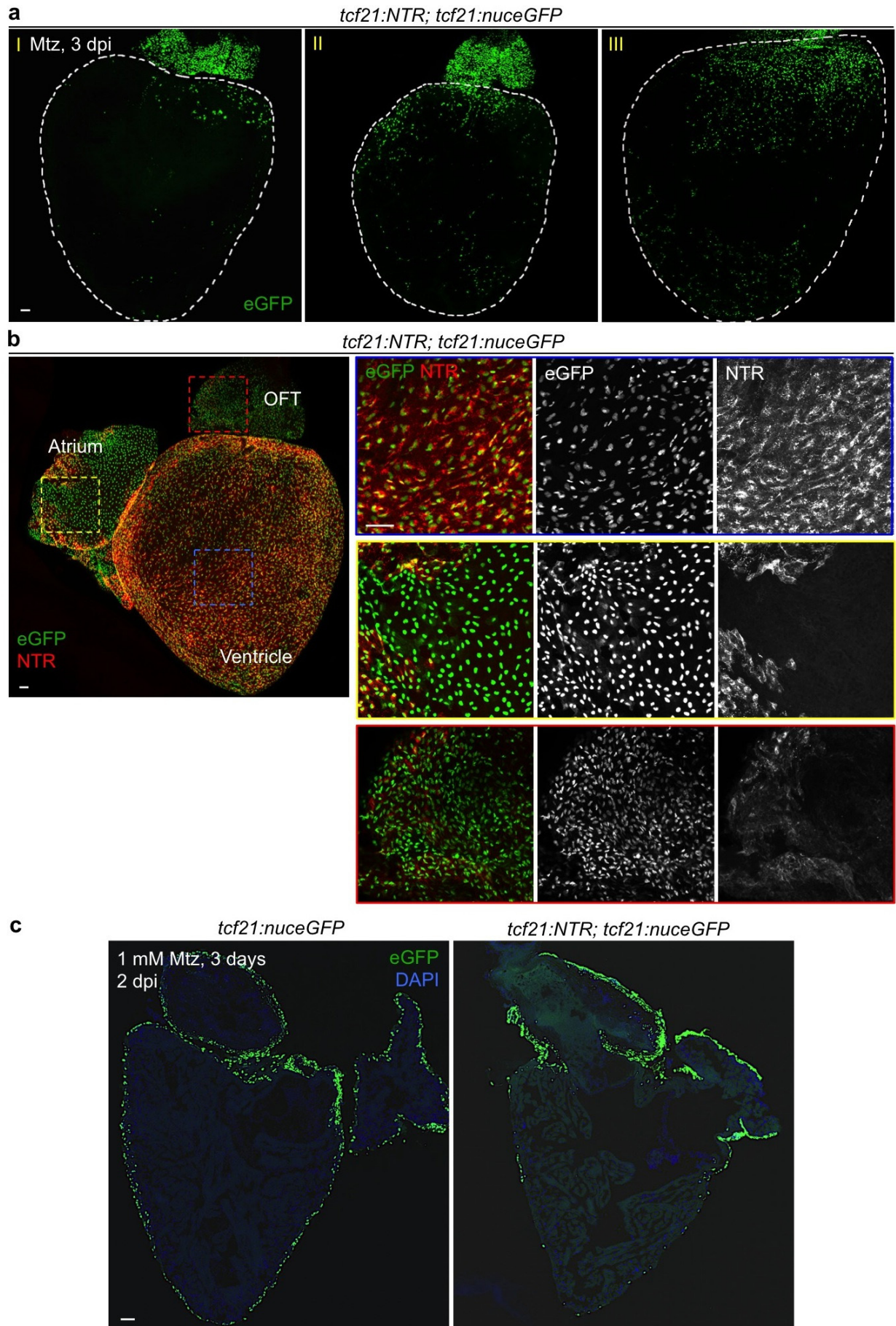
Extended Data Figure 1 | Epicardial ablation and responses to resection injury. **a**, *tcf21:nuceGFP* or *tcf21:NTR; tcf21:nuceGFP* clutchmates underwent resection injury and were treated for 3 days with 1 mM Mtz, before collection of ventricles at 7 ($n = 8$ animals per group) and 30 dpa ($n = 11$). *tcf21:NTR; tcf21:nuceGFP* wounds had fewer epicardial cells at 7 dpa and comparable occupancy by 30 dpa compared with *tcf21:nuceGFP* wounds. White dashed lines indicate wound edge. **b**, Quantification of eGFP⁺ epicardial cells at 7 and 30 dpa with respect to wound edge lengths from **a**. NS, not significant; Mann-Whitney rank sum test. **c**, *tcf21:NTR* clutchmates underwent resection injury and were treated for 3 days with 1 mM Mtz or vehicle with random separation into two groups for treatment. MLCK⁺ cells, indicating myofibroblasts, had comparable presence in both groups at 14 dpa ($n = 7$ for each group).

d, *tcf21:NTR; fli1a:eGFP* clutchmates underwent resection injury and were treated for 3 days with 1 mM Mtz or vehicle with random separation into two groups for treatment. Epicardial ablation led to lower vascular density in 30 dpa wounds compared with controls. Red dashed lines indicate wound edge. **e**, Quantification of eGFP⁺ vascular endothelial pixel area in wounds of *tcf21:NTR; fli1a:eGFP* zebrafish treated with Mtz ($n = 12$) or vehicle ($n = 6$), or of *fli1a:eGFP* zebrafish treated with Mtz ($n = 6$), with respect to the wound edge lengths. Student's two-tailed t -test. **f**, By 60 dpa, 55 days after epicardial ablation protocols, muscularization (top) and wound collagen deposition (bottom) were grossly normal ($n = 23$). Brackets indicate area of regeneration. **a**, **c**, **d**, Yellow dashed lines indicate the approximate amputation plane. Scale bars, 50 μ m. Error bars indicate s.d.



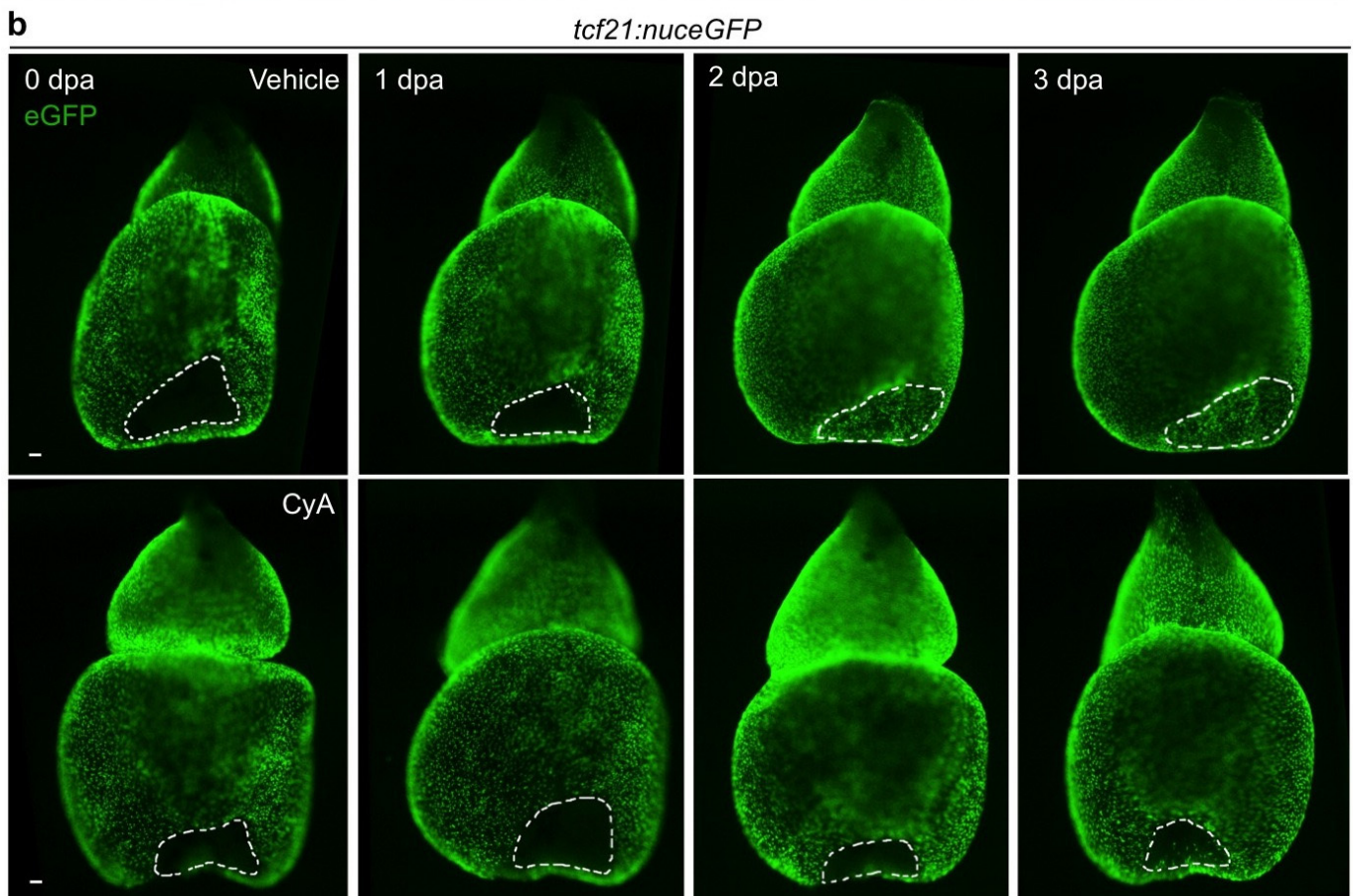
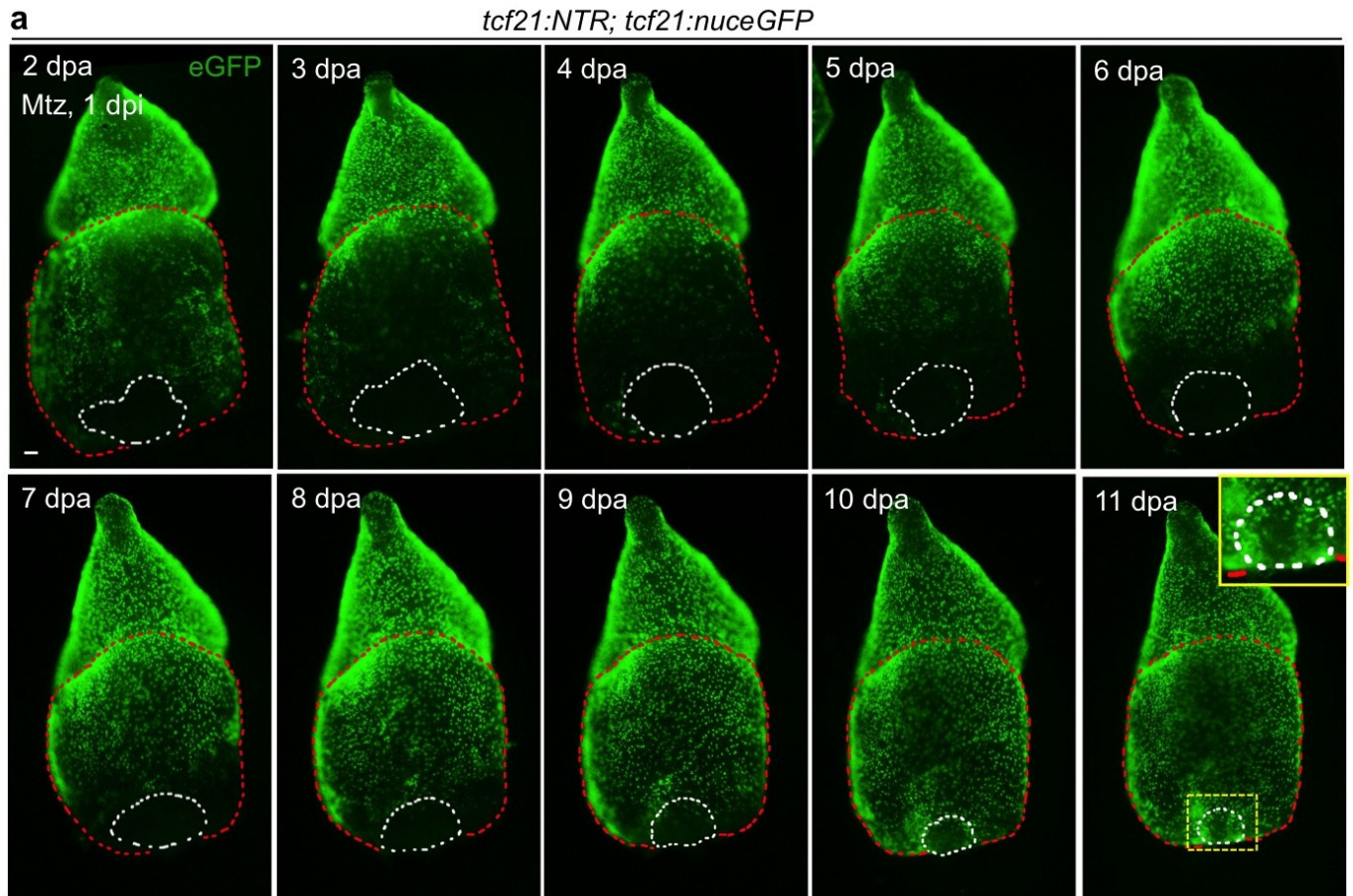
Extended Data Figure 2 | Epicardial cell proliferation without injury and after epicardial ablation. **a**, Limited epicardial cell proliferation on the ventricular surface. *tcf21:nuceGFP* fish were injected with 10 mM EdU once daily for 3 days and collected 1 day after the last injection. 10^5 ventricular *nucGFP*⁺ cells were assessed for EdU reactivity in 15 animals, from which 608 cells were positive (a 0.6% rate for 4 days EdU labelling). Whole-mount image is shown, and arrows in enlarged boxed area indicate *eGFP*⁺EdU⁺ nuclei. **b**, *tcf21:nucGFP* or *tcf21:NTR; tcf21:nucGFP* fish were injected with 10 mM EdU at 3 days post-Mtz treatment, and hearts were collected 4 h later. Boxed

areas in images of whole-mounted hearts show magnified views. **a**, **b**, Yellow arrows indicate representative *eGFP*⁺ (green) EdU⁺ (red) nuclei. **c**, *fli1a:eGFP* or *tcf21:NTR; fli1a:eGFP* fish were injected with 10 mM EdU at 3 days post-Mtz treatment, and hearts were collected 4 h later. Red arrows indicate representative *eGFP*⁺ (green) EdU⁺ (magenta) endocardial cell nuclei; yellow arrowheads, representative *eGFP*⁺ (green) EdU⁺ (magenta) vascular endothelial cell nuclei; white arrowheads, EdU⁺ (magenta) nuclei within the ventricular lumen, ostensibly erythrocyte nuclei. Scale bars, 50 μ m.



Extended Data Figure 3 | Mosaic NTR expression and patterns of spared epicardial cells after ablation. **a**, Whole-mounted examples of varied location/pattern of spared epicardial cells in ventricles from *tcf21:NTR*; *tcf21:nucEGFP* adult clutchmates 3 days after incubation with 10 mM Mtz. White dashed lines delineate ventricle. **b**, Differential expression of the NTR transgene among cardiac chambers. In adult *tcf21:NTR*; *tcf21:nucEGFP* hearts, eGFP expression is comparable in epicardial tissue covering the atrium, outflow tract (OFT) and

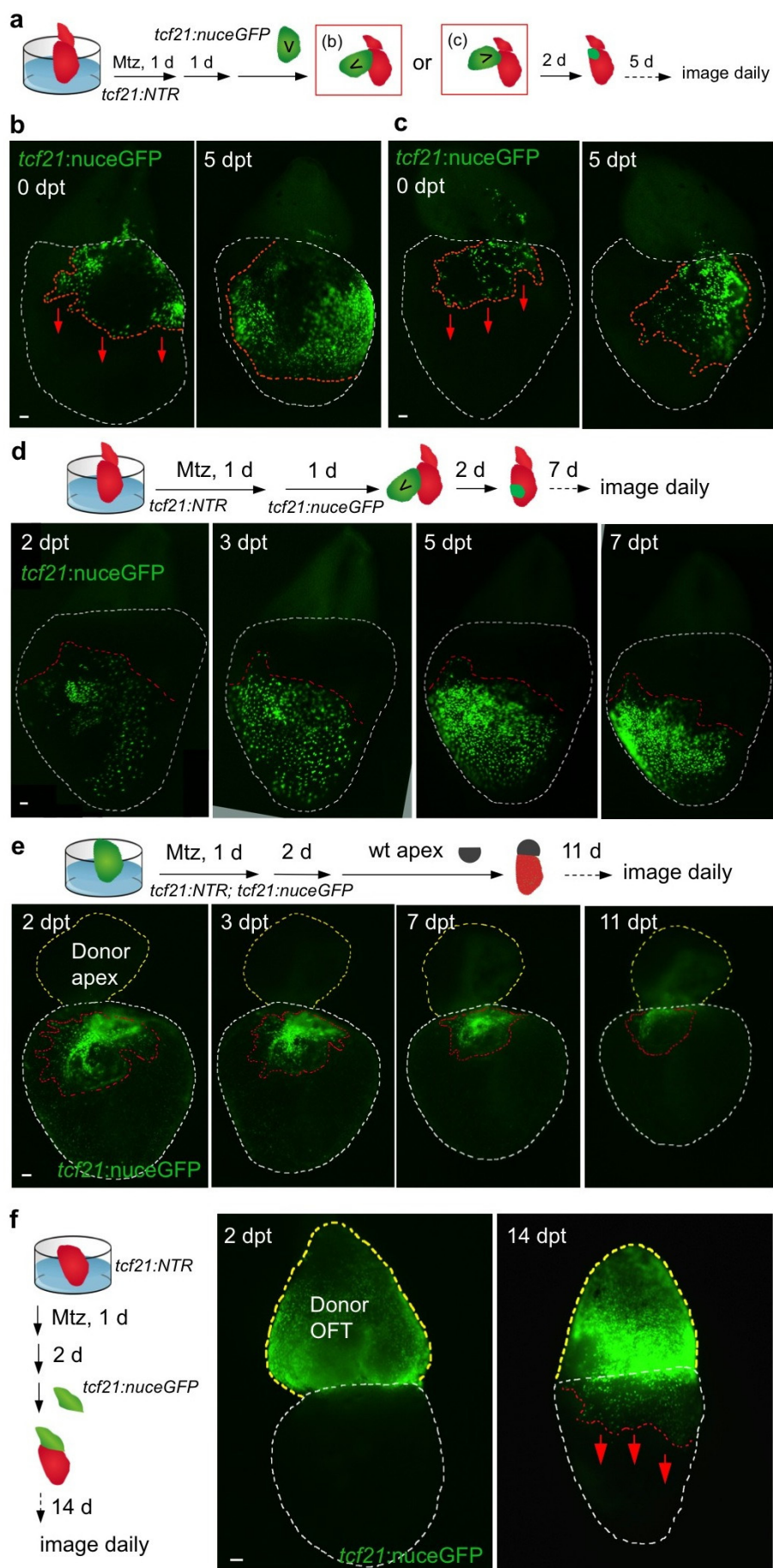
ventricle. By contrast, NTR (red, indicated by mCherry) expression is patchy and/or weak in the atrium and outflow tract compared with ventricular expression. **c**, Section images of ventricles from *tcf21:nucEGFP* (left) or *tcf21:NTR*; *tcf21:nucEGFP* zebrafish (right) treated with 1 mM Mtz (right) for 3 days, and collected 2 days later. Ventricular epicardium was ablated effectively in these experiments. Scale bars, 50 μ m.



Extended Data Figure 4 | Epicardial regeneration after ventricular

resection. **a**, Hearts were removed from *tcf21:NTR; tcf21:nucGFP* fish immediately after ventricular resection injuries, followed by 24 h of Mtz and a 24 h washout *ex vivo*. A base-to-apex pattern of epicardial regeneration was observed, in this example covering the apical wound by 11 dpa ($n = 18$; behaviour seen in all samples). Epicardial coverage of resection injuries in these ablation experiments is delayed compared to ventricles recovering with an

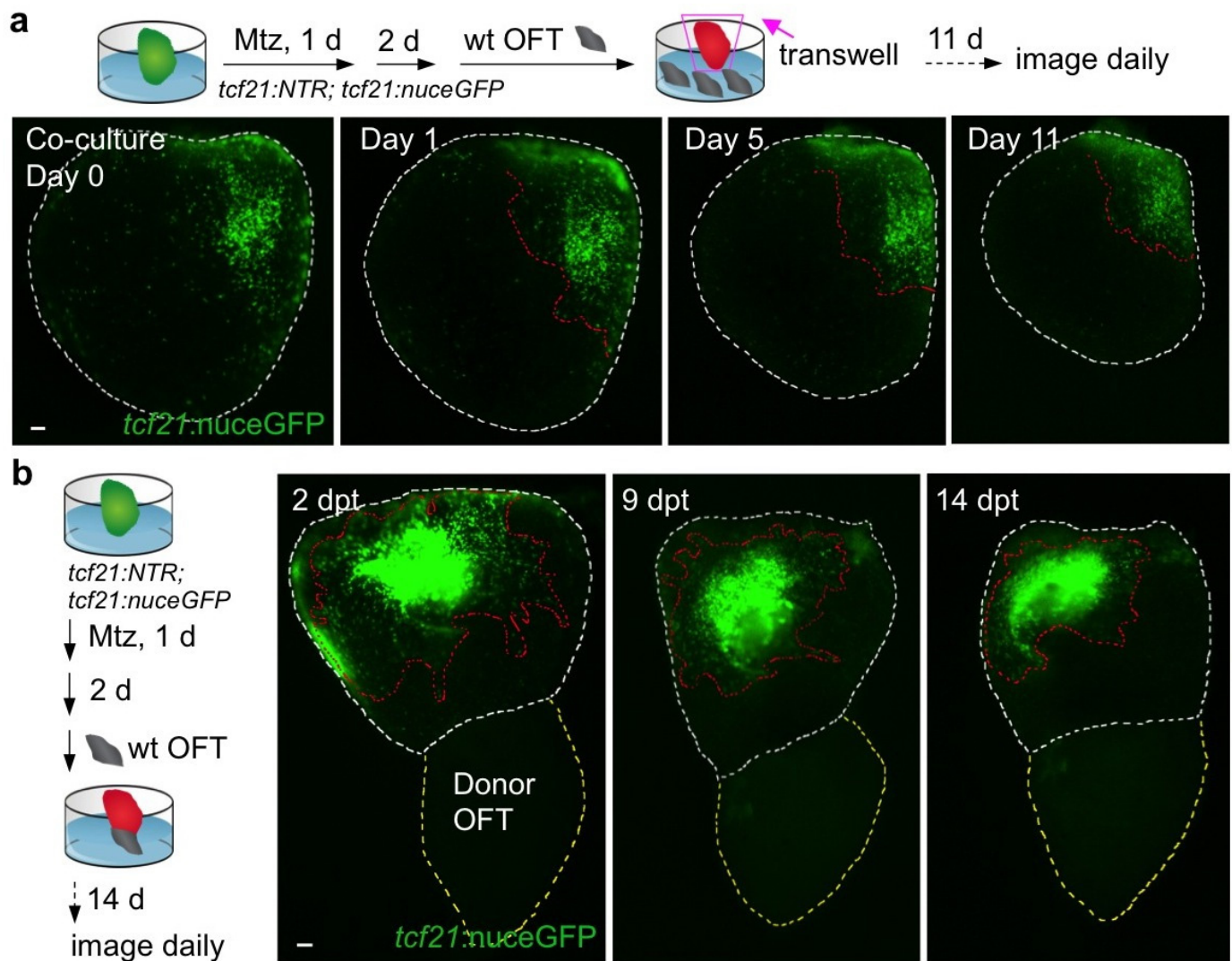
intact epicardium (**b**, top). Yellow boxed area, magnified view of the apical wound. Red dashed lines delineate ventricle. **b**, Hearts were removed from *tcf21:nucGFP* clutchmates immediately after apical resection injury and cultured *ex vivo*, before random separation into two treatment groups. Epicardial cells covered the wound area by 3 dpa ($n = 11$; behaviour seen in all samples), unless treated with CyA ($n = 26$; failed coverage in 20 of 26 ventricles). **a**, **b**, White dashed lines indicate apical wounds. Scale bars, 50 μm .



Extended Data Figure 5 | *Ex vivo* grafts and epicardial regeneration.

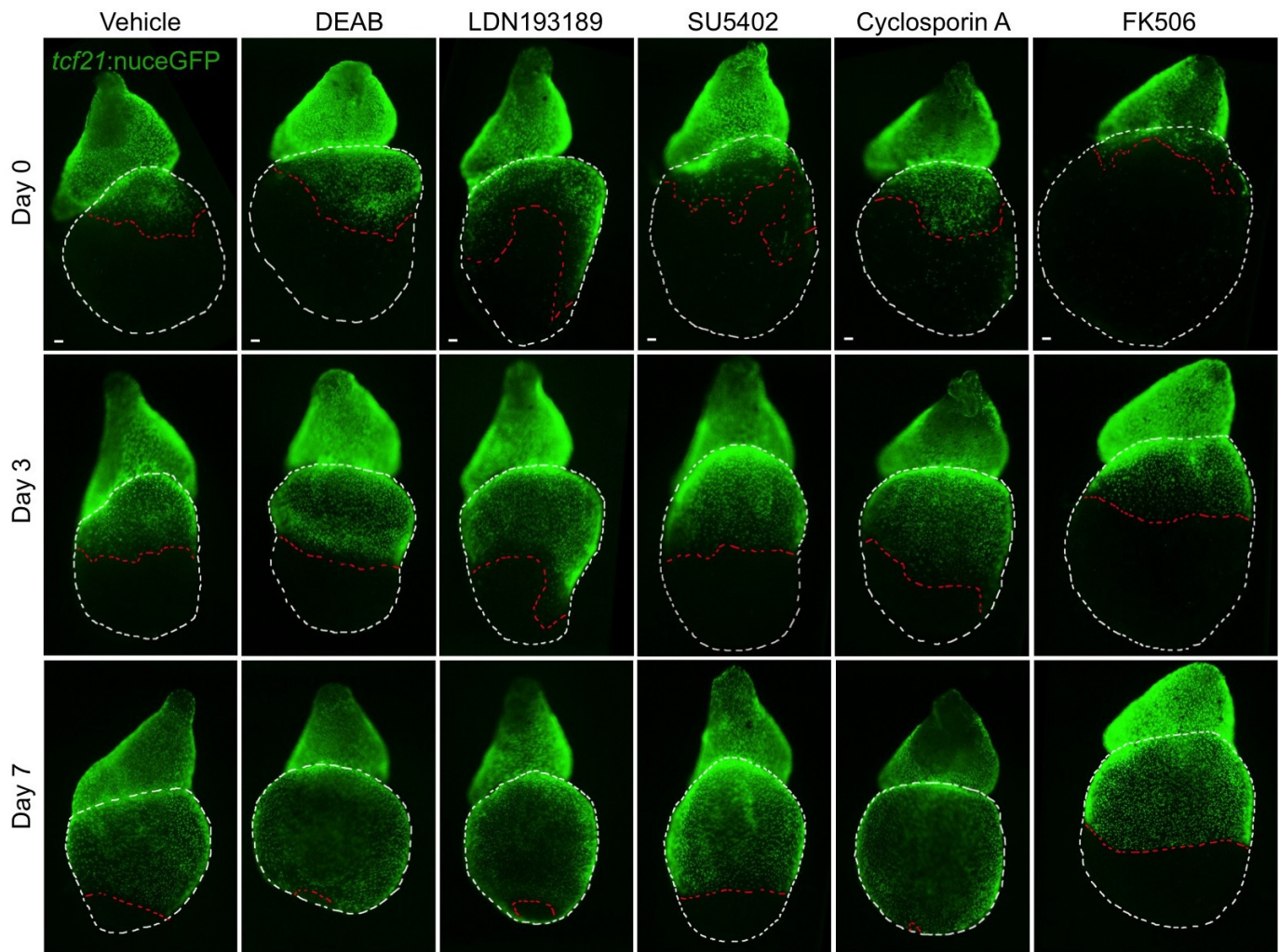
a, Schematic of the experimental design. **b, c**, Epicardial cells transplanted at the base of an epicardially ablated host regenerated towards the apex regardless of basal (**b**) ($n = 25$, behaviour seen in all samples) or apical (**c**) ($n = 27$, all samples) origin. **d**, Top, epicardial cells from the base of a transgenic donor ventricle were transplanted to the chamber midpoint of an epicardially ablated host ventricle and observed for regeneration. Bottom, transplanted cells eventually migrated towards the apex, not the base ($n = 13$; all samples). **e**, Top, after epicardial ablation, the host bulbous arteriosus was replaced with a non-

transgenic donor ventricular apex and observed for regeneration. Bottom, ventricular epicardium showed little or no regeneration in these experiments ($n = 7$; behaviour seen in all samples). **f**, Left, after *ex vivo* epicardial ablation in a host *tcf21:NTR* ventricle, the host bulbous arteriosus was replaced with a donor *tcf21:nucGFP* bulbous arteriosus. Right, the host ventricular surface contained different amounts of eGFP⁺ nuclei in these ventricles ($n = 3$; behaviour seen in all samples). **b–f**, Red dashed lines indicate epicardium or epicardial leading edge; white dashed lines delineate ventricle. **e, f**, Yellow dashed lines indicate donor apex (**e**) or bulbous arteriosus (**f**). Scale bars, 50 μ m.



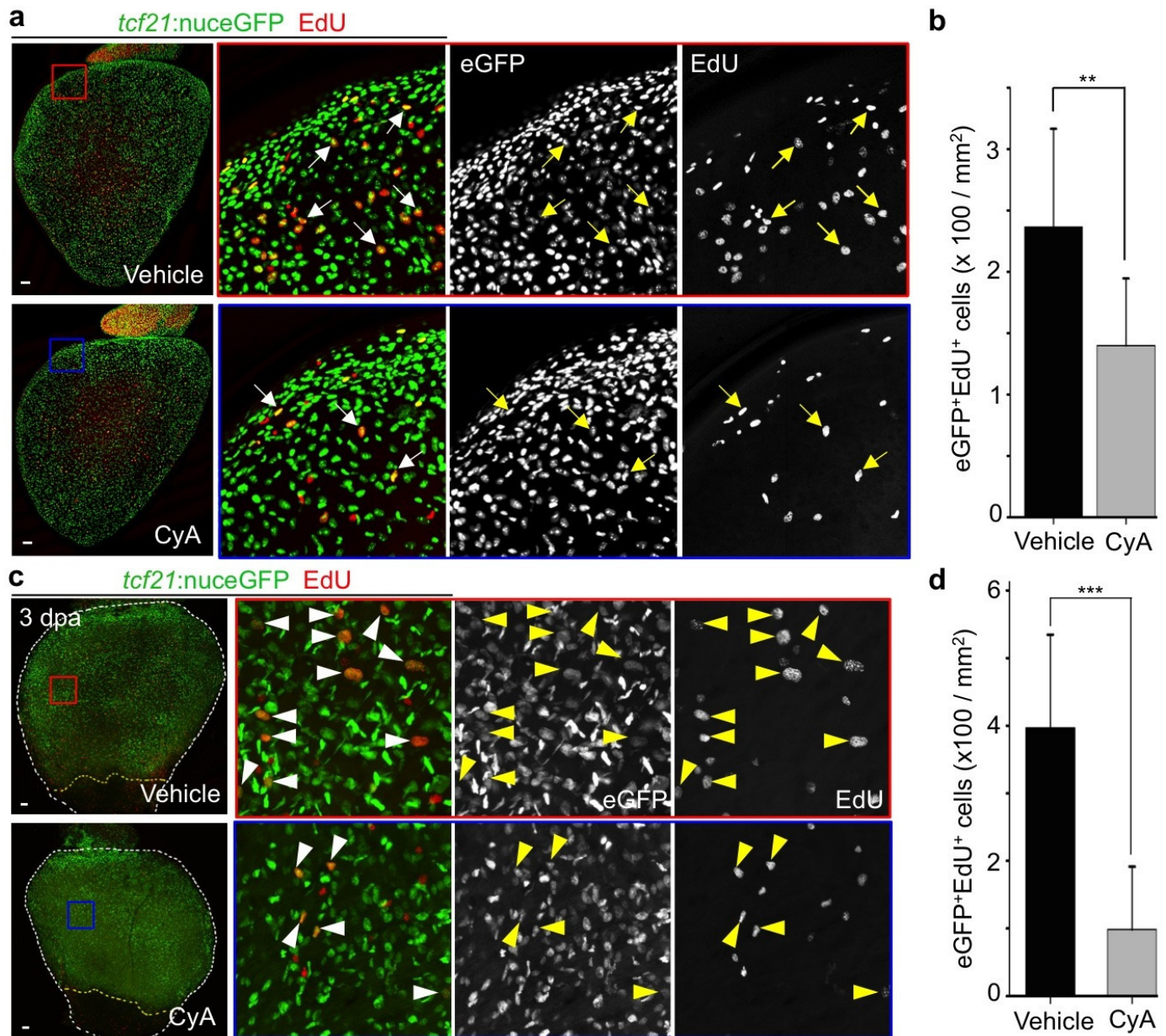
Extended Data Figure 6 | Context-specific effects of outflow tract on epicardial regeneration. **a**, Top, after *ex vivo* epicardial ablation and bulbous arteriosus removal, ventricles were co-cultured with ten outflow tracts in a transwell assay and observed for regeneration. Bottom, no evidence for epicardial regeneration was observed in these experiments ($n = 9$; behaviour seen in all samples). **b**, Left, after *ex vivo* epicardial ablation and bulbous

arteriosus removal, a non-transgenic bulbous arteriosus (labelled as donor OFT) was transplanted to the apex and observed for regeneration. Right, no evidence for regeneration of $eGFP^+$ epicardium from apex to base was observed in these experiments ($n = 10$; behaviour seen in all samples). Red dashed lines delineate epicardium; white dashed lines delineate ventricle; yellow dashed lines delineate donor outflow tract. Scale bars, 50 μm .



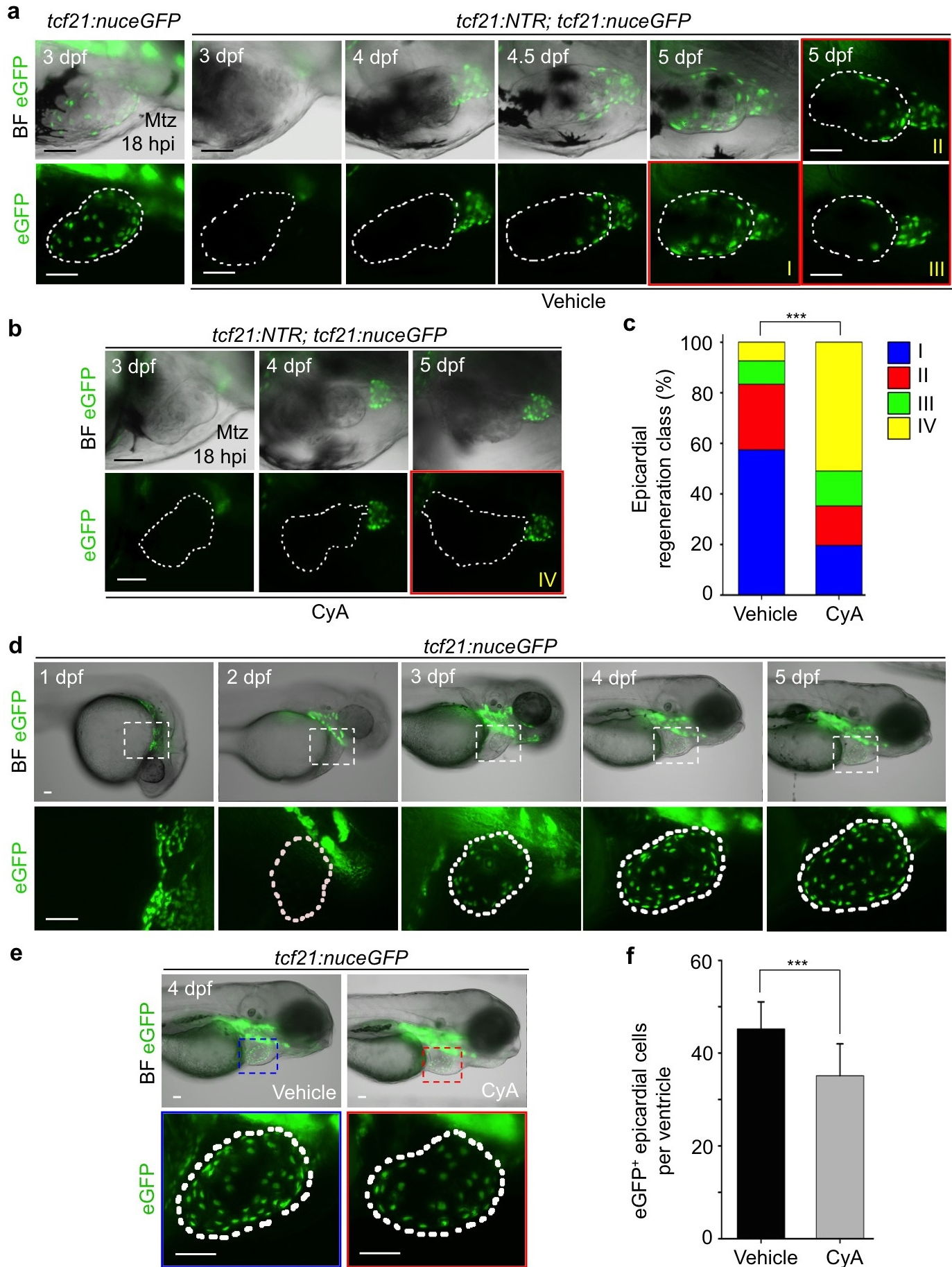
Extended Data Figure 7 | Small-scale screen for compounds that inhibit epicardial regeneration. *Ex vivo* ablation and regeneration of *tcf21:NTR*; *tcf21:nucGFP* ventricles over 7 days. Mtz was added for 24 h to freshly isolated hearts, washed out, and compounds were added after 2 days (day 0). Hearts were treated with vehicle ($n > 10$), 10 μM DEAB ($n = 5$; Sigma-Aldrich), 100 nM LDN193189 ($n = 4$; Cayman Chemical), 10 μM SU5402 ($n = 5$; Santa Cruz

Biotechnology), 1 μM cyclosporin A ($n = 4$; Sigma-Aldrich), or 0.1 $\mu\text{g ml}^{-1}$ FK506 ($n = 5$; Sigma-Aldrich), in each case showing base-to-apex recovery (behaviour seen in all samples). The dissected hearts were randomly separated into groups for drug treatment. Red dashed lines indicate epicardial leading edge; white dashed lines delineate ventricle. Scale bars, 50 μm .



Extended Data Figure 8 | Epicardial proliferation is regulated by Hh signalling. **a**, Freshly dissected *tcf21:nucGFP* hearts were randomly separated into two groups and cultured for 47 h with vehicle ($n = 11$) or 5 μ M CyA ($n = 8$). Then, 25 μ M EdU was added to the medium for 1 h before collection at 48 h. CyA treatment decreases epicardial cell proliferation *ex vivo*. Arrows indicate representative eGFP⁺ (green) EdU⁺ (red) nuclei. **b**, Quantification of eGFP⁺EdU⁺ nuclei per mm² on the ventricular surface, from hearts in **a**. $**P < 0.01$, Student's two-tailed *t*-test. **c**, *tcf21:nucGFP* adult fish were subjected to partial ventricular resection surgery, and randomly separated into

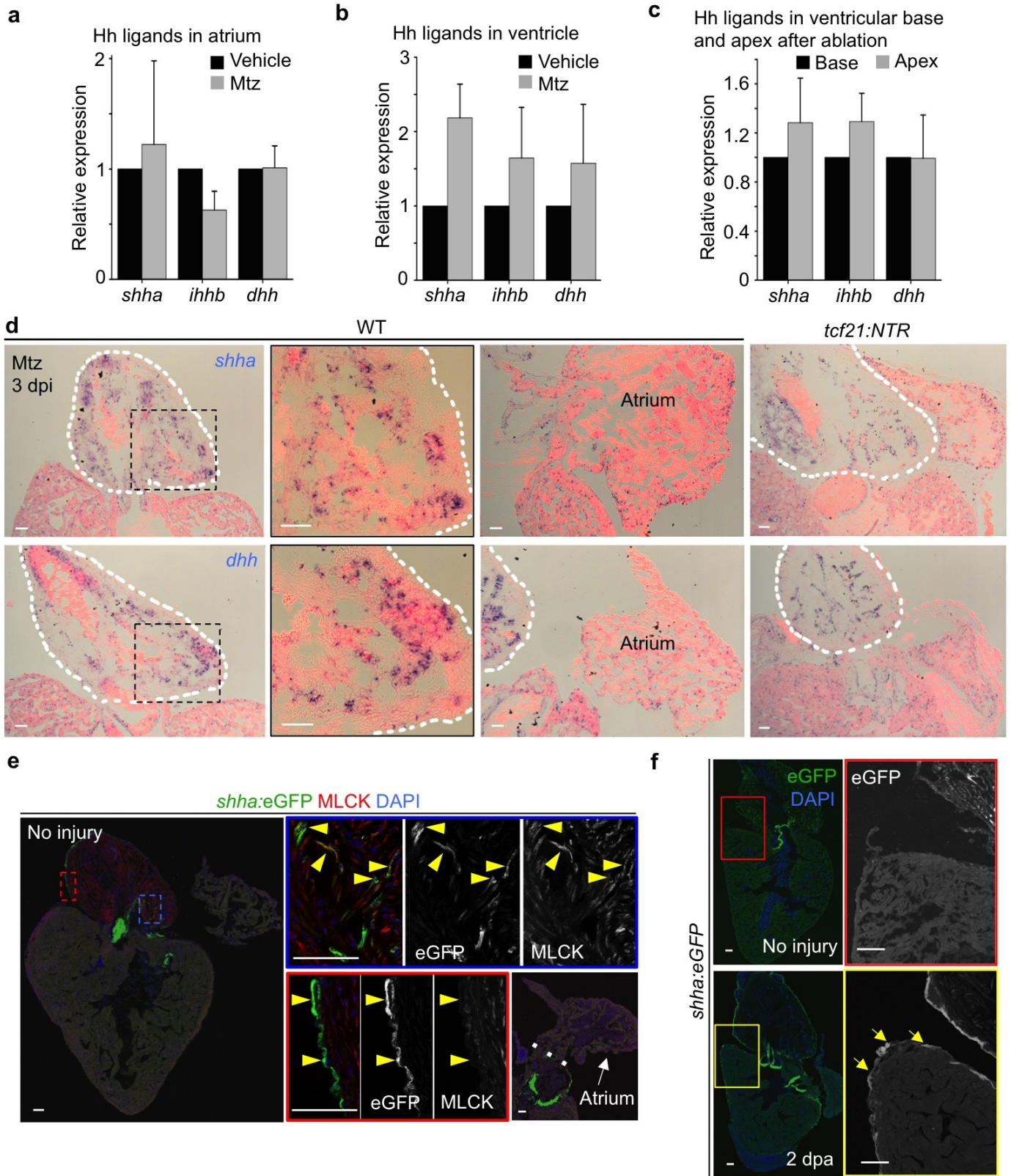
two groups for treatment with vehicle ($n = 8$) or 10 μ M CyA ($n = 10$) from 2 to 3 dpa. Then, 10 mM EdU was injected intraperitoneally 1 h before collection. CyA treatment decreases epicardial cell proliferation *in vivo*. Arrowheads indicate representative eGFP⁺ (green) EdU⁺ (red) nuclei. **d**, Quantification of eGFP⁺EdU⁺ nuclei per mm² on the ventricular surface, from hearts in **c**. $***P < 0.001$; Mann-Whitney rank sum test. **c**, Yellow dashed lines indicate resection plane; white dashed lines delineate ventricle. **a**, **c**, Boxed areas, magnified views. Scale bars, 50 μ m. Error bars indicate s.d.



Extended Data Figure 9 | Larval epicardial development and regeneration.

a, *tcf21:nucGFP* or *tcf21:NTR*; *tcf21:nucGFP* larval clutchmates were treated with 10 mM Mtz from 6 hpf to 54 hpf, and then imaged at different times from 3 to 5 dpf. *tcf21:nucGFP* larvae show normal ventricular epicardial coverage at 3 dpf, while *tcf21:NTR*; *tcf21:nucGFP* coverage is sparse. *tcf21:NTR*; *tcf21:nucGFP* larvae with confirmed full ablation were imaged from 3 to 5 dpf, covering first the ventricular base and then the apex. Three different extents of regeneration at 5 dpf are shown: class I, greater than two-thirds coverage; class II, one-third to two-thirds coverage; and class III, some cells but less than one-third coverage. **b**, A subset of *tcf21:NTR*; *tcf21:nucGFP* larvae with confirmed full ablations were randomly separated and treated with vehicle or CyA, which limited regeneration in most cases (class IV, no ventricular epicardial cells).

c, Quantification of extents of regeneration from experiments in **a** and **b**. *** $P < 0.001$, chi-squared test; $n = 54$ embryos for vehicle, 51 for CyA. **d**, Epicardial morphogenesis visualized in *tcf21:nucGFP* larvae. No epicardial cells are evident at or before 2 dpf. By 3 dpf, ventricles contained 17.6 ± 6 epicardial cells on average ($n = 23$), whereas 4 dpf larvae contained 45.2 ± 5.8 cells ($n = 21$). **e**, *tcf21:nucGFP* larval clutchmates were randomly separated into two groups for treatment with vehicle or 5 μ M CyA from 2 to 4 dpf. **f**, Quantification of ventricular eGFP⁺ epicardial cells from groups in **e**. *** $P < 0.001$, Student's two-tailed t -test; $n = 21$ for each group. **a**, **b**, **d**, **e**, White dashed lines delineate ventricle. **d**, **e**, Boxed areas, magnified views. Scale bars, 50 μ m. Error bars indicate s.d.



Extended Data Figure 10 | Hh ligand expression. **a–c**, Quantitative RT–PCR revealing *shha*, *ihhb* and *dhh* expression in atrium (**a**) or ventricle (**b**) in uninjured hearts and 3 days post-ablation, or in separated ventricular basal (the basal third of the chamber) and apical (the apical third) tissue after ablation (**c**). Three separate quantitative RT–PCR experiments on pooled tissues were performed, using a total of 90 zebrafish for experiments shown in **a** and **b**, and another 90 fish for **c**. *shhb* and *ihha* were not detected in these tissues. **d**, *In situ* hybridization (ISH) for *shha* or *dhh* in wild-type (WT) or *tcf21:NTR* clutchmate hearts at 3 days after Mtz treatment, indicating expression in outflow tract but not ventricle or atrium. Outflow tract of uninjured and epicardially ablated hearts showed comparable *shha* and *dhh* signals by ISH, a qualitative/

semiquantitative assay. **e**, Section of adult *shha:eGFP* heart, indicating fluorescence in outflow tract tissues. Smooth muscle cells (MLCK, red) and epicardial cells (outer layer) in outflow tract showed clear eGFP signals, while there is no obvious eGFP fluorescence in ventricle and atrium. Valve mesenchyme also displays eGFP fluorescence. Arrowheads indicate eGFP signals in smooth muscle cells and epicardium. **f**, Ventricular resection induces *shha:eGFP* fluorescence in the basal ventricular epicardium at 2 dpa. Arrows indicate ventricular epicardial fluorescence. **d**, **e**, White dashed line indicate outflow tract (**d**) or atrioventricular junction (**e**). **d–f**, Boxed areas, magnified views. Scale bars, 50 μ m. Error bars indicate s.d.

Spastin and ESCRT-III coordinate mitotic spindle disassembly and nuclear envelope sealing

Marina Vietri^{1,2}, Kay O. Schink^{1,2*}, Coen Campsteijn^{1,2*}, Catherine Sem Wegner^{1,2}, Sebastian W. Schultz^{1,2}, Liliane Christ^{1,2}, Sigrid B. Thoresen^{1,2}, Andreas Brech^{1,2}, Camilla Raiborg^{1,2} & Harald Stenmark^{1,2,3}

At the onset of metazoan cell division the nuclear envelope breaks down to enable capture of chromosomes by the microtubule-containing spindle apparatus¹. During anaphase, when chromosomes have separated, the nuclear envelope is reassembled around the forming daughter nuclei^{1,2}. How the nuclear envelope is sealed, and how this is coordinated with spindle disassembly, is largely unknown. Here we show that endosomal sorting complex required for transport (ESCRT)-III, previously found to promote membrane constriction and sealing during receptor sorting, virus budding, cytokinesis and plasma membrane repair^{3–6}, is transiently recruited to the reassembling nuclear envelope during late anaphase. ESCRT-III and its regulatory AAA (ATPase associated with diverse cellular activities) ATPase VPS4 are specifically recruited by the ESCRT-III-like protein CHMP7 to sites where the reforming nuclear envelope engulfs spindle microtubules. Subsequent association of another ESCRT-III-like protein, IST1, directly recruits the AAA ATPase spastin to sever microtubules. Disrupting spastin function impairs spindle disassembly and results in extended localization of ESCRT-III at the nuclear envelope. Interference with ESCRT-III functions in anaphase is accompanied by delayed microtubule disassembly, compromised nuclear integrity and the appearance of DNA damage foci in subsequent interphase. We propose that ESCRT-III, VPS4 and spastin cooperate to coordinate nuclear envelope sealing and spindle disassembly at nuclear envelope-microtubule intersection sites during mitotic exit to ensure nuclear integrity and genome safeguarding, with a striking mechanistic parallel to cytokinetic abscission⁷.

Previous studies have shown that ESCRT-III is recruited to the membrane bridge connecting daughter cells during cytokinesis^{5,8}. Interestingly, cell lines stained with an antibody against the ESCRT-III subunit chromatin modifying protein (CHMP)4B showed a specific staining around chromatin discs during late anaphase (Fig. 1a and Extended Data Fig. 1a, c). Similar anaphase localization was observed in HeLa cells stably expressing haemagglutinin (HA)-tagged CHMP4B (Extended Data Fig. 1d). This recruitment appeared transient as it was not observed during early anaphase or telophase (Fig. 1a). Live-cell microscopy of HeLa cells stably expressing CHMP4B fused to enhanced green fluorescent protein (CHMP4B-eGFP)⁹ revealed CHMP4B-eGFP localization around chromatin discs between 6 and 12 min after anaphase onset (Fig. 1b and Supplementary Video 1).

As the main constituent, CHMP4B assembles with other ESCRT-III subunits into membrane-deforming helical filaments¹⁰, and we found that ESCRT-III subunits CHMP2A, CHMP3 and CHMP4A were also recruited around chromatin discs, as were the ESCRT-III associated proteins CHMP1A, CHMP1B and IST1 (Extended Data Fig. 1e). Lack of co-localization with markers for early (EEA1-positive), multivesicular (Hrs-positive) or late (LAMP1-positive) endosomes around chromatin discs argues against an endosomal nature of this ESCRT-III localization³ (Extended Data Fig. 1f, g).

CHMP4B recruitment occurs at a mitotic stage similar to reassembly of the nuclear lamina, and nuclear pore complex reformation¹¹ (Extended Data Fig. 1h, i); however, there was little co-localization with the nucleoporin Nup153 (Extended Data Fig. 1j). Since direct association of ESCRT-III with membranes is essential for its role in membrane constriction and scission¹², we compared CHMP4B dynamics with nuclear envelope (NE) reassembly. We found that CHMP4B-eGFP localized prominently to punctate sites where the NE is reassembled from mobilized endoplasmic reticulum¹, and was largely absent from regions lacking apparent nuclear membranes (Fig. 1c, Extended Data Fig. 2a and Supplementary Video 2). As reported for CHMP1A¹³, CHMP4B localization was nuclease resistant (Extended Data Fig. 2b), whereas mutations in the amino (N)-terminal helix (4DE) of CHMP4B, critical for membrane association¹⁴, largely abolished its recruitment around anaphase chromatin (Fig. 1d, Extended Data Fig. 2c and Supplementary Video 3). This suggests that CHMP4B localization does not require chromatin and rather indicates that ESCRT-III is recruited to discrete sites of the nuclear membrane during the NE reassembly process.

In other ESCRT-dependent processes, CHMP4B recruitment depends on upstream regulators such as CEP55, ESCRT-0 (Hrs), ESCRT-I (TSG101), or the BRO-domain proteins ALIX, BROX and HD-PTP¹⁵. However, these proteins showed no enrichment at the reforming NE, and depletion of these factors did not appreciably affect CHMP4B recruitment to the reforming NE (Extended Data Fig. 2d). In striking contrast, depletion of the poorly characterized ESCRT-III-like protein CHMP7¹⁶ effectively abolished CHMP4B localization to nuclear membranes without apparent effect on CHMP4B localization to the midbody (Fig. 1e, Extended Data Fig. 2e, f and Supplementary Video 4). Our data identify CHMP7 as a novel and essential recruiter of ESCRT-III during NE reformation.

VPS4 is critical to ESCRT-III function, with its inactivation causing persistent localization of ESCRT-III to membrane necks and preventing membrane sealing¹⁷. Like CHMP4B, eGFP-VPS4A transiently localized around chromatin discs during late anaphase (Extended Data Fig. 3a). Importantly, upon depletion of VPS4, CHMP3 or CHMP2A a dramatic increase in the residence time of CHMP4B foci was observed (Fig. 2a and Supplementary Video 5), indicative of defective ESCRT-III function and recycling. This specific phenotype (Extended Data Fig. 3b) was particularly striking upon CHMP2A knockdown, resulting in the persistence of anaphase CHMP4B foci long into following cell cycles (Supplementary Video 6). Taken together, this suggests that ESCRT-III and VPS4, which mediate cytokinetic membrane scission⁷, also cooperate during NE reassembly.

Disruption of ESCRT-III function did not affect markers for general NE reassembly, nuclear pore complex accumulation or reestablishment of nuclear import (Fig. 2b and Extended Data Fig. 3c–e). As CHMP4B localized only to a limited number of foci during anaphase, we asked whether ESCRT-III functions at specific nuclear membrane

¹Centre for Cancer Biomedicine, Faculty of Medicine, University of Oslo, Montebello, N-0379 Oslo, Norway. ²Department of Molecular Cell Biology, Institute for Cancer Research, Oslo University Hospital, Montebello, N-0379 Oslo, Norway. ³Centre of Molecular Inflammation Research, Faculty of Medicine, Norwegian University of Science and Technology, N-7491 Trondheim, Norway.

*These authors contributed equally to this work.

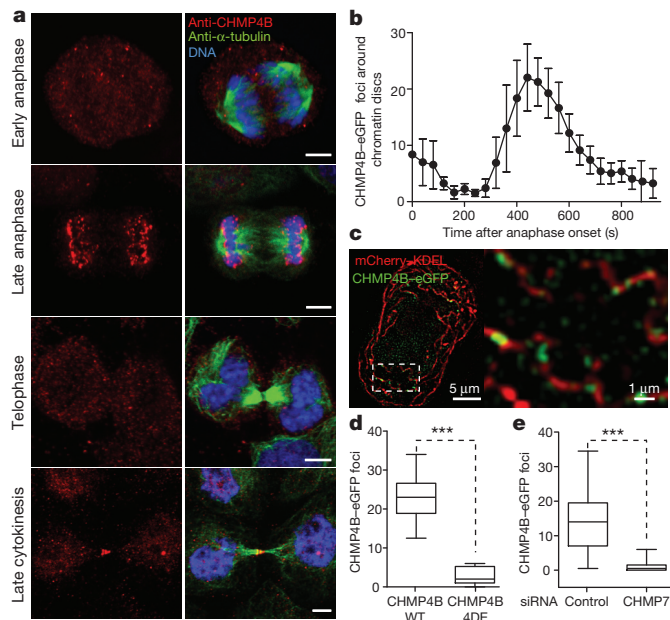


Figure 1 | ESCRT-III is transiently recruited around chromatin discs during nuclear envelope reformation. **a**, Confocal images of fixed HeLa cells in different phases of mitotic exit. Scale bars, 5 μ m. Representative confocal images of at least five captures for each stage. **b**, Number of CHMP4B foci around chromatin discs in HeLa cells stably expressing CHMP4B-eGFP. $n = 10$ cells. Bars, mean with 95% confidence intervals. **c**, Deconvolved wide-field image of a living HeLa anaphase cell expressing CHMP4B-eGFP and mCherry-KDEL. Representative image from wide-field live cell imaging of at least ten cells. **d**, Number of CHMP4B foci appearing around anaphase chromatin discs in HeLa cells expressing wild-type (WT) CHMP4B-eGFP or CHMP4B-eGFP 4DE, depleted for endogenous CHMP4B. Whiskers illustrate the minima and maxima of samples. $n = 18$ cells for wild-type CHMP4B-eGFP; $n = 25$ cells for CHMP4B-eGFP 4DE. $***P < 0.0001$ derived from unpaired t -test. **e**, Number of CHMP4B foci appearing around anaphase chromatin discs in HeLa cells expressing CHMP4B-eGFP decreases dramatically upon CHMP7 knockdown. Whiskers illustrate the minima and maxima of samples. $n = 35$ cells for control short interfering RNA (siRNA); $n = 19$ cells for CHMP7 siRNA. $***P < 0.0001$ derived from unpaired t -test.

sites. Correlative light and electron microscopy (CLEM) analyses revealed overlap of CHMP4B foci with areas of the NE that are not fully closed and that could also contain electron dense contact sites between chromatin and microtubules (MTs) (Fig. 2c and Extended Data Figs 3f and 4, arrows).

Structured illumination microscopy (SIM) highlighted a striking association of CHMP4B with MTs traversing holes in the reforming NE (Fig. 2d and Extended Data Fig. 5a), indicating that ESCRT-III functions at sites of intersection between nuclear membranes and MTs¹⁸. Such intersections were found for polar MTs at the rim of the chromatin disc and kinetochore MT bundles at its core regions (Extended Data Fig. 5b, c). Live tracking of CHMP4B-eGFP in cells co-expressing the kinetochore marker mCherry-CENP-A showed CHMP4B foci transiently at the rim of chromatin discs; however, as anaphase progressed, CHMP4B foci appeared prominently at the core regions of the chromatin disc to sites juxtapositioned with CENP-A, before disappearing from the chromatin discs at the end of anaphase (Fig. 2e, Extended Data Fig. 5d and Supplementary Video 7). Since NE reassembly initiates from the rim of chromatin discs and subsequently envelopes the central part of the chromatin disc¹⁹, our data suggest that ESCRT-III foci are formed progressively at NE-MT intersections as the nuclear membrane engulfs spindle attachments along the chromatin disc. The dependence on MTs is further supported by the fact that CHMP4B foci were readily observed during NE reassembly upon mitotic slippage in Taxol-treated cells, while they

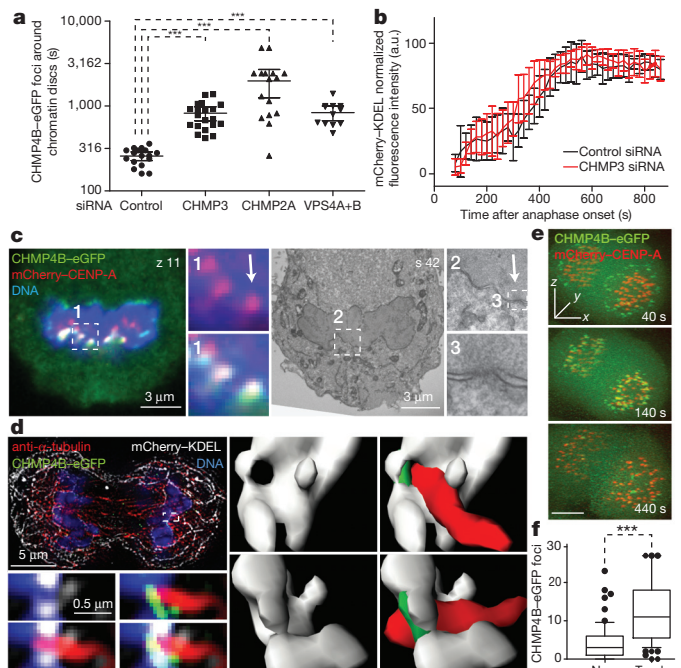


Figure 2 | ESCRT-III and VPS4 cooperate at sites of NE and MT intersection during nuclear envelope reassembly. **a**, Residence time of CHMP4B-eGFP around chromatin discs following indicated siRNA treatments. $n = 17$ cells for control siRNA; $n = 20$ cells for CHMP3 siRNA; $n = 16$ cells for CHMP2A; $n = 12$ cells for VPS4A + B siRNA. Bars, mean with 95% confidence intervals. $***P$ values ($P < 0.0001$) derived from unpaired t -test. **b**, Normalized fluorescence intensity of mCherry-KDEL at the NE in HeLa cells expressing CHMP4B-eGFP and mCherry-KDEL (a.u., arbitrary units). $n = 8$ DNA discs for control siRNA; $n = 8$ DNA discs for CHMP3 siRNA. Bars, mean and 95% confidence intervals. **c**, CLEM of an anaphase cell correlates CHMP4B-eGFP and mCherry-CENP-A foci (detected by light microscopy) with areas of unsealed NE (observed on EM sections). A confocal plane (z_{11}) with the respective electron micrographs is shown, including insets with increasing magnifications. Representative of 13 CHMP4B-eGFP and mCherry-CENP-A double-positive foci (Extended Data Fig. 4 and Methods). Label 's 42' refers to section number 42 within the transmission electron microscopy serial sections. **d**, A z-stack from SIM (left) and Imaris surface three-dimensional renderings (right) of a fixed anaphase HeLa cell stained as indicated. SIM image representative of at least ten captures. Imaris reconstruction was performed on four areas of intersection between CHMP4B, MTs and ER. **e**, Dynamic localization of ESCRT-III to kinetochore proximal regions in HeLa cells expressing CHMP4B-eGFP and mCherry-CENP-A. Scale bar, 5 μ m. Deconvolved wide-field images from live-cell imaging are representative of at least ten videos, where $t = 0$ represents onset of CHMP4B recruitment. **f**, Number of CHMP4B-eGFP foci appearing around chromatin in cells where mitotic slippage was induced in Taxol or nocodazole (Noc). $n = 73$ cells for nocodazole; $n = 69$ cells for Taxol. Whiskers illustrate the 10th–90th percentiles of samples. $***P < 0.0001$ derived from unpaired t -test.

were largely absent from nocodazole-treated cells (Fig. 2f and Supplementary Video 8).

Live-cell tracking of MTs using mCherry- α -tubulin showed a strong correlation between MT disassembly and CHMP4B-eGFP localization (Fig. 3a, b and Extended Data Fig. 6c). Importantly, knockdown of VPS4, CHMP3 or CHMP2A caused a specific delay in MT disassembly at CHMP4B-eGFP foci (Fig. 3c and Extended Data Fig. 6a, b). Together with the negative correlation between local intensities of CHMP4B and α -tubulin along individual MTs (Extended Data Fig. 6c), this suggested that ESCRT-III is dynamically required for complete MT severing. Moreover, CLEM experiments showed that CHMP3-depleted cells maintain a high number of gaps in the NE with MTs attached to the chromatin discs (Fig. 3d, e and Supplementary Video 9). The collective data raised the possibility that ESCRT-III

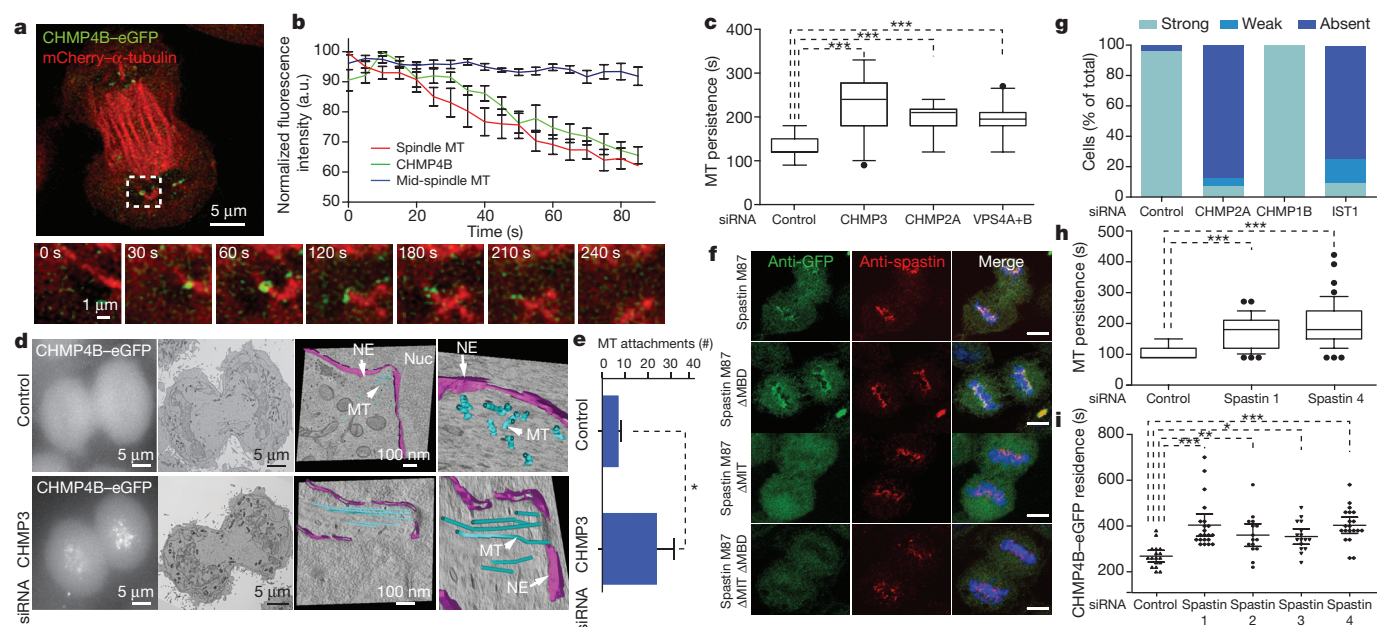


Figure 3 | ESCRT-III-dependent recruitment of spastin to the reforming NE mediates mitotic spindle disassembly. **a**, Tracking of CHMP4B association with a MT bundle over time. Deconvolved wide-field images representative of at least ten videos, with at least 30 events, were observed. **b**, Normalized fluorescence intensity of CHMP4B-eGFP and spindle MTs associated with CHMP4B foci. Normalized fluorescence intensity of mid-spindle MTs was used as control. $n = 5$. Bars, mean and s.e.m. **c**, Persistence of spindle MTs associated with CHMP4B foci. $n = 23$ MTs for control siRNA; $n = 26$ MTs for CHMP3 siRNA; $n = 18$ MTs for CHMP2A siRNA; $n = 22$ MTs for VPS4A+B siRNA. Whiskers illustrate the 5th–95th percentiles of samples. $***P < 0.0001$ derived from unpaired *t*-test. **d**, CLEM and EM tomography of anaphase cells shows persistent MT attachments to chromatin discs with unsealed NE in CHMP3 knockdown cells. Nuc, nucleus. Representative of three experiments ($n = 3$ cells for control siRNA; $n = 3$ cells for CHMP3 siRNA). **e**, Number of MT attachment points to chromatin discs scored from EM sections from **d**. $n = 3$ for control siRNA; $n = 3$ cells for CHMP3 siRNA. Bars, mean with s.d. $*P < 0.05$ derived from unpaired *t*-test. **f**, Confocal images of anaphase HeLa cells transiently transfected with GFP-spastin M87

constructs. Scale bars, 5 μ m. $n = 5$ cells for spastin M87; $n = 7$ cells for Δ MBD; $n = 15$ cells for spastin Δ MIT; $n = 3$ cells for spastin Δ MBD Δ MIT. **g**, Recruitment of spastin around anaphase chromatin in HeLa cells stably expressing mCherry-spastin M87 and CHMP4B-eGFP transfected with indicated siRNAs. $n = 46$ cells for control siRNA; $n = 14$ cells for CHMP2A siRNA; $n = 11$ cells for CHMP1B siRNA; $n = 34$ cells for IST1 siRNA. Results for CHMP2A and IST1 depletion are significantly different from control and CHMP1B depletion, $P < 0.001$. **h**, Time of disappearance of spindle MTs associated with CHMP4B foci. $n = 38$ MTs for control siRNA; $n = 67$ MTs for spastin siRNA 1; $n = 88$ MTs for spastin siRNA 4. Whiskers illustrate the 5th–95th percentiles of samples. $***P < 0.001$ derived from Dunnett's multiple comparison test. **i**, Residence time of CHMP4B-eGFP localization around anaphase chromatin discs upon treatment with indicated siRNAs. $n = 17$ cells for control siRNA; $n = 21$ cells for spastin siRNA 1; $n = 15$ cells for spastin siRNA 2; $n = 16$ cells for spastin siRNA 3; $n = 20$ cells for spastin siRNA 4. Bars, mean with 95% confidence intervals. $*P < 0.05$, $**P < 0.01$, $***P < 0.001$ derived from Dunnett's multiple comparison test.

could coordinate membrane sealing with disassembly of MTs during mitotic exit.

ESCRT-III is known to recruit the MT-severing AAA ATPase spastin during completion of cytokinesis^{7,20}. Confocal imaging, SIM analysis and live-cell microscopy showed that both endoplasmic reticulum-associated spastin M1 and cytosolic spastin M87²¹ co-localized with CHMP4B-eGFP on nuclear membranes during late anaphase (Fig. 3f and Extended Data Fig. 7a–c), in association with mitotic spindle MT bundles (Extended Data Fig. 7c). Deletion analyses showed that the ESCRT-III-interacting MIT domain²⁰ of spastin M87 is required for its nuclear membrane localization whereas the MT-binding domain (MBD) is dispensable, arguing for direct recruitment of spastin by ESCRT-III (Fig. 3f and Extended Data Fig. 7d, e). This notion was further supported by the finding that CHMP2A was essential for recruitment of spastin and its reported interactors, CHMP1B and IST1^{22,23} (Fig. 3g and Extended Data Fig. 7f–h). Interestingly, knockdown of IST1, but not CHMP1B, abolished spastin enrichment around chromatin discs (Fig. 3g and Extended Data Fig. 7f–h), indicating that IST1 serves as spastin recruiter to nuclear membranes.

To monitor whether spastin is required for the stability of MTs at ESCRT-III sites at the NE, we monitored MT persistence at CHMP4B-eGFP foci. As for CHMP2A knockdown, depletion of spastin resulted in a significant delay in MT disassembly following CHMP4B-eGFP enrichment (Fig. 3h and Extended Data Fig. 6b). Importantly, spastin depletion or overexpression of dominant-

negative spastin M87^{E442Q} prolonged the residence time of CHMP4B-eGFP around chromatin discs (Fig. 3i and Extended Data Fig. 8a, b), suggesting that ESCRT-III persistence at nuclear membrane foci is affected by the presence of MTs. Accordingly, CHMP4B-eGFP residence time almost doubled in the presence of Taxol (Extended Data Fig. 8c and Supplementary Video 10), arguing that ESCRT-III function at membrane foci cannot be completed until MTs penetrating the reassembling NE are removed.

We assessed nucleocytoplasmic compartmentalization in cells co-expressing histone 2B (H2B) fused to FRB (FK506 binding protein (FKBP)–rapamycin binding domain of mTOR) and mCherry-tagged maltose-binding protein (MBP) fused to FKBP. Addition of rapalog induces heterodimerization of FRB- and FKBP-fusions and traps soluble bulky MBP-mCherry on chromatin as it diffuses into the nucleus. Importantly, CHMP2A knockdown resulted in a highly significant increase in nuclear trapping rates compared with control cells (Fig. 4a), indicating that nuclear integrity is compromised upon ESCRT-III dysfunction.

Compromised NE integrity has been associated with DNA damage^{24,25}, and we found that knockdown of CHMP2A or VPS4 resulted in significantly increased DNA damage (Fig. 4b, c and Extended Data Fig. 9a). Importantly, DNA damage cluster markers (γ -H2AX and 53BP1) were closely associated with persistent CHMP4B-eGFP foci and enrichment of nuclear lamina markers (Fig. 4c) but not nuclear pore complexes (Extended Data Fig. 9b),

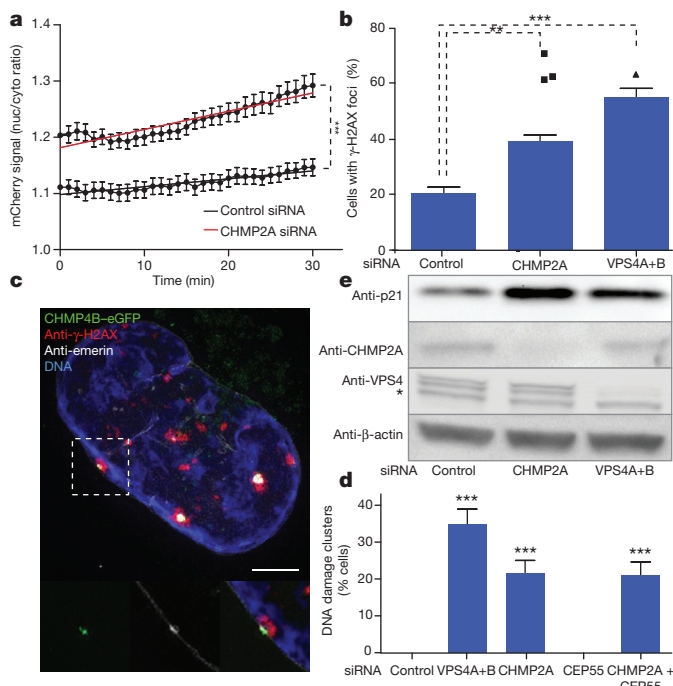


Figure 4 | ESCRT-III dysfunction compromises nuclear integrity and leads to DNA damage and cell cycle arrest. **a**, Nuclear/cytoplasmic (nuc/cyto) ratio of FKBP-MBP-mCherry in late cytokinetic HeLa cells expressing CHMP4B-eGFP, FKBP-MBP-mCherry and H2B-FRB. Nuclear/cytoplasmic ratio of FKBP-MBP-mCherry was plotted over time. Red and green lines represent the linear regression for control and CHMP2A siRNA-treated cells respectively. $n = 52$ cells for control siRNA; $n = 51$ cells for CHMP2A siRNA. Bars, mean and s.e.m. The difference between the slopes is highly significant ($***P < 0.0001$). **b**, Induction of γ -H2AX foci in hTERT RPE1 cells. Percentage of population was plotted. Bars, mean and s.e.m. $**P < 0.005$ and $***P < 0.001$ were derived from unpaired t -test. **c**, SIM of CHMP4B-eGFP HeLa cells depleted for CHMP2A show multiple structures where γ -H2AX, CHMP4B and emerin are highly associated. Scale bar, 5 μ m. Representative of $n = 38$ DNA damage structures, with high association of CHMP4B and DNA damage clusters (97.36%) and association of with nuclear lamina enrichments (100%) observed. **d**, Frequency of association of CHMP4B with 53BP1 or emerin within DNA damage structures induced by CHMP2A depletion in CHMP4B-eGFP HeLa cells. $n = 300$ cells for control siRNA; $n = 358$ cells for VPS4 siRNA; $n = 361$ cells for CHMP2A siRNA; $n = 300$ cells for CEP55 siRNA; $n = 325$ cells for CHMP2A + CEP55 siRNA. Bars, mean and s.e.m. VPS4, CHMP2A and CEP55 KD were highly significantly different from control and CEP55 KD ($***P < 0.0001$, unpaired t -test). **e**, Immunoblot showing levels of cellular p21 levels in hTERT RPE1 upon treatment with indicated siRNAs. Immunoblot is representative of four independent experiments. Asterisk indicates non-specific immunoreactivity.

suggestive of nuclear envelope perturbation. These clusters did not originate from untimely cytokinetic abscission in the presence of chromatin bridges, as impairment of abscission by CEP55 knockdown did not affect their formation (Fig. 4d and Extended Data Fig. 9c). The absence of CHMP4B from ionizing-radiation-induced DNA damage foci (Extended Data Fig. 9d) argues against a general role for ESCRT-III in DNA damage response and rather suggests that ESCRT-III dysfunction induces a condition permissive to DNA damage. Compromised genome integrity leads to p53-dependent cell cycle arrest, characterized by induction of the cyclin-dependent kinase inhibitor p21 (ref. 26). Indeed, elevation of p21 levels upon knockdown of CHMP2A or VPS4 (Fig. 4e) indicates the induction of cell cycle arrest and underscores the physiological relevance for ESCRT-III function during anaphase in maintaining cell fitness.

Collectively, our data reveal a novel role for ESCRT-III and spastin in coordination of NE reassembly and spindle disassembly during late anaphase. We propose that during NE reassembly, nuclear membranes encounter MTs associated with chromatin discs, precluding membrane closure (Extended Data Fig. 9e). To seal these holes, ESCRT-III is recruited by CHMP7 to sites of NE-MT intersection, with IST1 subsequently recruiting spastin to sever MTs. In concert with VPS4, ESCRT-III mediates constriction and sealing of the holes in the NE. Impairment of such sealing compromises nuclear integrity and nucleo-cytoplasmic compartmentalization, ultimately culminating in DNA damage²⁷. Together with the established function for ESCRT-III during cytokinetic abscission checkpoint signalling in the presence of pathological chromatin bridges^{28–30}, our results place ESCRT-III at centre stage for safeguarding the genome through mitotic exit.

Online Content Methods, along with any additional Extended Data display items and Source Data, are available in the online version of the paper; references unique to these sections appear only in the online paper.

Received 24 June 2014; accepted 13 March 2015.

Published online 3 June 2015.

- Guttinger, S., Laurell, E. & Kutay, U. Orchestrating nuclear envelope disassembly and reassembly during mitosis. *Nature Rev. Mol. Cell Biol.* **10**, 178–191 (2009).
- Burke, B. & Ellenberg, J. Remodelling the walls of the nucleus. *Nature Rev. Mol. Cell Biol.* **3**, 487–497 (2002).
- Babst, M., Katzmann, D. J., Estepa-Sabal, E. J., Meerloo, T. & Emr, S. D. Escrt-III: an endosome-associated heterooligomeric protein complex required for mvb sorting. *Dev. Cell* **3**, 271–282 (2002).
- von Schwedler, U. K. et al. The protein network of HIV budding. *Cell* **114**, 701–713 (2003).
- Carlton, J. G. & Martin-Serrano, J. Parallels between cytokinesis and retroviral budding: a role for the ESCRT machinery. *Science* **316**, 1908–1912 (2007).
- Jimenez, A. J. et al. ESCRT machinery is required for plasma membrane repair. *Science* **343**, 1247136 (2014).
- Guizetti, J. et al. Cortical constriction during abscission involves helices of ESCRT-III-dependent filaments. *Science* **331**, 1616–1620 (2011).
- Morita, E. et al. Human ESCRT and ALIX proteins interact with proteins of the midbody and function in cytokinesis. *EMBO J.* **26**, 4215–4227 (2007).
- Poser, I. et al. BAC TransgeneOmics: a high-throughput method for exploration of protein function in mammals. *Nature Methods* **5**, 409–415 (2008).
- Hanson, P. I., Roth, R., Lin, Y. & Heuser, J. E. Plasma membrane deformation by circular arrays of ESCRT-III protein filaments. *J. Cell Biol.* **180**, 389–402 (2008).
- Hetzler, M. W. The nuclear envelope. *Cold Spring Harb. Perspect. Biol.* **2**, a000539 (2010).
- Wollert, T., Wunder, C., Lippincott-Schwartz, J. & Hurley, J. H. Membrane scission by the ESCRT-III complex. *Nature* **458**, 172–177 (2009).
- Stauffer, D. R., Howard, T. L., Nyun, T. & Hollenberg, S. M. CHMP1 is a novel nuclear matrix protein affecting chromatin structure and cell-cycle progression. *J. Cell Sci.* **114**, 2383–2393 (2001).
- Buchkovich, N. J., Henne, W. M., Tang, S. & Emr, S. D. Essential N-terminal insertion motif anchors the ESCRT-III filament during MVB vesicle formation. *Dev. Cell* **27**, 201–214 (2013).
- Henne, W. M., Stenmark, H. & Emr, S. D. Molecular mechanisms of the membrane sculpting ESCRT pathway. *Cold Spring Harb. Perspect. Biol.* **5**, <http://dx.doi.org/10.1101/cshperspect.a016766> (2013).
- Horii, M. et al. CHMP7, a novel ESCRT-III-related protein, associates with CHMP4b and functions in the endosomal sorting pathway. *Biochem. J.* **400**, 23–32 (2006).
- Hill, C. P. & Babst, M. Structure and function of the membrane deformation AAA ATPase Vps4. *Biochim. Biophys. Acta* **1823**, 172–181 (2012).
- Haraguchi, T. et al. Live cell imaging and electron microscopy reveal dynamic processes of BAF-directed nuclear envelope assembly. *J. Cell Sci.* **121**, 2540–2554 (2008).
- Lu, L., Ladinsky, M. S. & Kirchhausen, T. Formation of the postmitotic nuclear envelope from extended ER cisternae precedes nuclear pore assembly. *J. Cell Biol.* **194**, 425–440 (2011).
- Yang, D. et al. Structural basis for midbody targeting of spastin by the ESCRT-III protein CHMP1B. *Nature Struct. Mol. Biol.* **15**, 1278–1286 (2008).
- Lumb, J. H., Connell, J. W., Allison, R. & Reid, E. The AAA ATPase spastin links microtubule severing to membrane modelling. *Biochim. Biophys. Acta* **1823**, 192–197 (2012).
- Agromayor, M. et al. Essential role of hIST1 in cytokinesis. *Mol. Biol. Cell* **20**, 1374–1387 (2009).
- Reid, E. et al. The hereditary spastic paraplegia protein spastin interacts with the ESCRT-III complex-associated endosomal protein CHMP1B. *Hum. Mol. Genet.* **14**, 19–38 (2005).
- Lattanzi, G., Marmiroli, S., Facchini, A. & Maraldi, N. M. Nuclear damages and oxidative stress: new perspectives for laminopathies. *Eur. J. Histochem.* **56**, e45 (2012).
- Liu, B. et al. Genomic instability in laminopathy-based premature aging. *Nature Med.* **11**, 780–785 (2005).

26. Abbas, T. & Dutta, A. p21 in cancer: intricate networks and multiple activities. *Nature Rev. Cancer* **9**, 400–414 (2009).
27. Hatch, E. & Hetzer, M. Breaching the nuclear envelope in development and disease. *J. Cell Biol.* **205**, 133–141 (2014).
28. Steigemann, P. *et al.* Aurora B-mediated abscission checkpoint protects against tetraploidization. *Cell* **136**, 473–484 (2009).
29. Carlton, J. G., Caballe, A., Agromayor, M., Kloc, M. & Martin-Serrano, J. ESCRT-III governs the Aurora B-mediated abscission checkpoint through CHMP4C. *Science* **336**, 220–225 (2012).
30. Thoresen, S. B. *et al.* ANCHR mediates Aurora-B-dependent abscission checkpoint control through retention of VPS4. *Nature Cell Biol.* **16**, 550–560 (2014).

Supplementary Information is available in the online version of the paper.

Acknowledgements We thank T. Høiby, T. Håve and K. W. Tan for assistance with generation of stable cell lines, M. Smestad and L. Hermansen for assistance with EM, A. Engen, A. Al-Kayssi and B. M. Furulund for assistance with cell cultures, E. Rønning and A. Gro Bergersen for technical support, and C. Bassols for IT support. We thank C. González, R. Syljuåsen, V. Nähse-Kumpf and E. Wenzel for discussions. We are grateful to A. A. Hyman for the gift of CHMP4B-eGFP BAC HeLa cells, and E. Reid for providing spastin constructs. We especially thank J. Carlton for sharing results before publication. The Core Facilities for Confocal Microscopy, Super-Resolution Microscopy and Electron Microscopy at Oslo University Hospital are acknowledged for providing access to relevant microscopes. M.V. is a PhD student and S.B.T. a postdoctoral fellow of the South-Eastern Norway Regional Health Authority. C.C. is a postdoctoral fellow and

C.R. a senior research fellow of the Norwegian Cancer Society. H.S. is the recipient of an Advanced Grant from the European Research Council. This work was partly supported by the Research Council of Norway through its Centres of Excellence funding scheme, project number 179571.

Author Contributions M.V. generated plasmid constructs and stable cell lines, performed confocal and live-cell imaging, cell transfections, image processing, data analyses, statistical analyses, and prepared figures; K.O.S. generated plasmid constructs and stable cell lines, performed live-cell and SIM imaging, image processing, developed algorithms for automated data analyses, performed data analyses, statistical analyses, and prepared figures; C.C. developed and co-supervised the project, generated plasmid constructs and stable cell lines, and performed live-cell imaging, image processing, data analyses and prepared figures; C.S.W., S.W.S. and A.B. performed EM and preparation of EM figures; L.C. performed confocal and live-cell imaging and cell transfections; S.B.T. performed confocal imaging and cell transfections; C.R. conceived and co-supervised the study, performed confocal microscopy, cell transfections, image processing and data analyses, and prepared figures; H.S. coordinated the study and oversaw experiments; M.V., C.C. and H.S. wrote the paper with input from all co-authors.

Author Information Reprints and permissions information is available at www.nature.com/reprints. The authors declare no competing financial interests. Readers are welcome to comment on the online version of the paper. Correspondence and requests for materials should be addressed to C.C. (coen.campsteijn@rr-research.no) or H.S. (stenmark@ulrik.uio.no).

METHODS

Antibodies. Rabbit anti-human CHMP4B antibody (western blot 1:2,000, immunofluorescence 1:1,000) and rabbit anti-CHMP3 (western blot 1:2,000, immunofluorescence 1:1,000) were produced as previously described^{31,32}. Rabbit anti-CHMP2A (Proteintech; western blot 1:500, immunofluorescence 1:100), rabbit anti-CHMP7 (Atlas Antibodies; Sigma-Aldrich; western blot 1:250), rabbit anti-CHMP1B (Fitzgerald; western blot 1:500), rabbit anti-IST1 (Proteintech; western blot 1:500, immunofluorescence 1:100), mouse anti-spastin (Santa Cruz Biotechnology sc-53443; western blot 1:400, immunofluorescence 1:50), rabbit anti-VPS4 (Sigma-Aldrich; western blot 1:500, immunofluorescence 1:200), rabbit anti-p21 (Santa Cruz Biotechnology H-164; western blot 1:700), mouse anti- γ -H2AX (Millipore 05-636; immunofluorescence 1:100), rabbit anti-53BP1 (Santa Cruz Biotechnology sc-22760; immunofluorescence 1:200), mouse anti-LAMP1 (DSHB; immunofluorescence 1:200), mouse anti-emerin (NeoMarkers MS-1751; immunofluorescence 1:100), mouse anti-Lamin A (Abcam ab8980; immunofluorescence 1:100), mouse anti-nuclear pore complex (pan NPC; Acris Antibodies; immunofluorescence 1:100), mouse anti-CEP55 (Abnova; western blot 1:300), mouse anti- α -tubulin (Sigma-Aldrich; western blot 1:10,000, immunofluorescence 1:800), sheep anti- α -tubulin (Cytoskeleton; immunofluorescence 1:100), mouse anti- β -actin (Sigma-Aldrich; western blot 1:30,000), mouse anti-Nup153 (Covance MMS-102P; immunofluorescence 1:200), rabbit anti-CHMP4A (Santa Cruz Biotechnology sc-67229; immunofluorescence 1:50), goat anti-V5 (Abcam; immunofluorescence 1:200), mouse anti-GFP (Living Colours; immunofluorescence 1:100), Rabbit anti-Flag (Cell Signaling Technology 2368; immunofluorescence 1:400), mouse anti-HA (Covance; immunofluorescence 1:100), goat anti-mCherry (Acris Antibodies; 1:200) were used as primary antibodies. Human anti-EEA1 serum³³ was a gift from B.-H. Toh. Rabbit anti-Hrs (immunofluorescence 1:100) was described in ref. 34. RFP-booster and GFP-booster (Chromotek) were used 1:200 for immunofluorescence. Secondary antibodies included anti-mouse, anti-rabbit and anti-goat Alexa Fluor 488 (Jackson), Alexa Fluor 555 (Molecular Probes), Alexa Fluor 568 (Molecular Probes), Alexa Fluor 647 (Jackson) and Cy5 (Jackson).

Cell culture. Cell lines were cultured in Dulbecco's modified Eagle's medium (DMEM; Gibco) supplemented with 10% fetal bovine serum (FBS), 5 U ml⁻¹ penicillin and 50 μ g ml⁻¹ streptomycin. For live-cell imaging, cells were seeded into Lab-Tek chambered coverslips (Nunc) or MatTek glass bottom microwell dishes (MatTek Corporation). For immunofluorescence studies, cells were grown on Precision cover glass (thickness 0.170 \pm 0.005 mm; Marienfeld). Samples were prepared on Precision cover glass and fixed with standard methods. Briefly, for SIM microscopy and α -tubulin stainings, microtubule integrity was preserved by fixing the cells with 4% EM grade formaldehyde (Polysciences) diluted in PEM buffer (80 mM K-Pipes, 5 mM EGTA, 1 mM MgCl₂ (pH 6.8)) for 5 min at 37°C. Cells were then permeabilized by treatment with PEM/0.15% Triton X-100 for 2 min. For confocal microscopy, Methanol fixation was performed for 10 min at -20°C. Primary and secondary antibodies were diluted in PBS/0.05% Saponin and incubated for 2–3 h for SIM or 1 h for confocal imaging. After antibody staining, samples were mounted on microscope slides (Menzel-Glaser) with Mowiol for standard confocal imaging. Vectashield (Biotek AS) or SlowFade Gold Antifade Reagent (Life Technologies) was used for SIM imaging.

Transient plasmid transfections. For transfection of eGFP-spastin constructs, cells were grown on Precision cover glass in 24-well plates and transfected with 0.5 μ g pcDNA3.1-HAeGFP-spastin M87 (full length), pcDNA3.1-HAeGFP-spastin M87 Δ MBD (deletion 270–328 counted from M1), pcDNA3.1-HAeGFP-spastin M87 Δ MIT (deletion 116–194 counted from M1) or pcDNA3.1-HAeGFP-spastin M87 Δ MBD/ Δ MIT (deletions 116–194 and 270–328 counted from M1) complexed with JetPEI (Polyplus) for 24 h.

siRNA treatments. All siRNAs were purchased from Ambion and contained the Silencer Select modification. Cells at 50% confluency where transfected using Lipofectamine RNAiMAX transfection reagent (Life Technologies) following the manufacturer's instructions. Cells were transfected with 50 nM siRNA targeting CHMP4B (CATCGAGTTCCAGCGGAG), CHMP3 (GGAAGAAGCAGA AATGGAA), CHMP1B (ACATGGAAGTTGCGAGGAT), IST1 1 (CCAAG TATAGCAAGGAATA), IST1 2 (GCAAATACGCCCTTCTCAT), CHMP7 1 (AGGTCTCTCCAGTCAATGA), CHMP7 2 (GCAATAGGCATTTCACCA), CHMP7 3 (GGATGAAGTTTCTCAGACT), CHMP2A 1 (AGGCAGAGAT CATGGATAT), CHMP2A 2 (AAGATGAAGAGGAGAGTGA), spastin 1 (pre-designed: GAACCTTGCTAACCTTATA; siRNA s13348), spastin 2 (pre-designed: GGAAGTCCATTGACCCAAA; siRNA s13349), spastin 3 (CCAATA TAATCATAATGTA) and spastin 4 (AAAACAGACTTAACAAAA), CEP55 (GGAGAAGAATGCTTATCAA), Hrs (CGACAAGAACCCACACGTC), Tsg101 (CCGTTTATAGTCAAGAAGTA), Alix (GCAGTGAGTTGTAA TGT), HD-PTP (GCAAACAGCGGATGAGCAA), BROX (GCAAAAGAAG TTCATCGAA) for 48 or 72 h. For VPS4 knockdown experiments, cells were

transfected with 25 nM of siRNA targeting VPS4A (CCGAGAAGCT GAAGGATTA), plus 25 nM of siRNA targeting VPS4B (CCAAAGAAG CACTGAAAGA) for 24 h. Non-targeting control Silencer Select siRNA (pre-designed, catalogue number 4390844) was used as control.

Confocal fluorescence microscopy. Fixed samples were imaged with a Zeiss LSM 710 or 780 confocal microscope (Carl Zeiss MicroImaging) equipped with an Ar-Laser Multiline (458/488/514 nm), a DPSS-561 10 (561 nm), a Laser diode 405-30 CW (405 nm) and a HeNe-laser (633 nm). The objective used was a Zeiss Plan-Apochromat \times 63/1.40 Oil DIC M27. Image processing was performed with basic software ZEN 2009 (Carl Zeiss MicroImaging) and ImageJ software (National Institutes of Health) which was used in CHMP4B depletion experiments (Extended Data Fig. 7e). The mean fluorescence intensity of spastin staining at anaphase chromatin discs was determined with the nuclear area as the defined region of interest (ROI). Here, intensity settings for the relevant channels were kept constant during imaging. Images shown in figures are representative of at least three independent experiments. For quantification of DNA damage structures induced by CHMP2A and VPS4 depletion (Fig. 4c), fixed hTERT RPE1 cells were immunolabelled for CHMP4B, γ -H2AX and DNA and imaged. Structures that showed high association of γ -H2AX with CHMP4B were manually scored. The frequency of association of CHMP4B with 53BP1 and emerin at DNA damage foci (Fig. 4c, explained in Methods) was manually scored on confocal images of CHMP2A-depleted hTERT RPE1 cells.

Live microscopy. Cells seeded in Lab-Tek four-well Chambered Coverglass (Nunc) were imaged on a DeltaVision microscope (Applied Precision) equipped with an Elite TruLight Illumination System, a CoolSNAP HQ2 camera and a \times 60 Plan Apochromat (1.42 numerical aperture) lens. For temperature control during live observation, the microscope stage was kept at 37°C by a temperature-controlled incubation chamber. Time-lapse images (14 z-sections 1 μ m apart for CHMP4B-eGFP HeLa cells; 6 z-sections 0.5 μ m apart for mCherry-KDEL/CHMP4B-eGFP HeLa cells, mCherry-NUP58/CHMP4B-GFP HeLa cells and IBB-eGFP/H2B-RFP transfected HeLa cells³⁵) were acquired every 20 s from anaphase onset, deconvolved using softWoRx software (Applied Precision, GE Healthcare) and processed with ImageJ for presentation and quantifications. Short-term, high-resolution live-cell imaging was performed on a Deltavision OMX V4 microscope equipped with three watercooled PCO.edge sCMOS cameras, a solid-state light source and a laser-based autofocus. To allow deep imaging with minimal spherical aberration, a \times 60 1.3 numerical aperture silicon oil immersion lens (Olympus) was used. Cells were imaged in Live Cell Imaging buffer (Invitrogen) supplemented with 20 mM glucose. Environmental control was provided by a heated stage and an objective heater (20-20 Technologies). Images were deconvolved using softWoRx software and processed in ImageJ/FIJI or Imaris.

Super-resolution imaging using structured illumination. SIM imaging was performed on a Deltavision OMX V4 microscope equipped with three water-cooled PCO.edge sCMOS cameras, 405 nm, 488 nm, 568 nm and 642 nm laserlines and a \times 60 1.42 numerical aperture Plan Apochromat lens (Olympus). z-Stacks covering the whole cell, with sections spaced 0.125 μ m apart, were recorded. For each z-section, 15 raw images (three rotations with five phases each) were acquired. Final super-resolution images were reconstructed using softWoRx software and processed in ImageJ/FIJI or Imaris.

High-content microscopy. For DNA damage experiments (Fig. 4b), Olympus ScanR system (illumination system with an UPLSAPO \times 40 objective) was used for imaging of a large number of cells in fixed samples that were immunolabelled for γ -H2AX, CHMP4B and DNA. Images were then processed with ImageJ for quantification.

Taxol treatments. HeLa cells stably expressing CHMP4B-eGFP were imaged live on a DeltaVision microscope every 20 s from anaphase onset. DMSO or 2 μ M Taxol in DMSO (Sigma-Aldrich) was added to cells in early anaphase (approximately 140 s after anaphase onset) during imaging.

Mitotic slippage assay. HeLa cells stably expressing CHMP4B-eGFP were synchronized in mitosis by incubating with 10 μ M Taxol (Sigma-Aldrich) or 10 μ M nocodazole (Calbiochem) for 2 h. Fields containing mitotic cells were selected on a DeltaVision microscope and mitotic slippage was induced by adding 10 μ M of the CDK1 inhibitor RO-3306 (Tocris). After addition of CDK1 inhibitor, cells were imaged live every minute.

DNase I treatment. Formaldehyde-fixed HeLa cells were subjected to DNase I (Sigma-Aldrich) treatment as previously described¹³. Cells were then immunolabelled for endogenous CHMP4B, α -tubulin and DNA.

Image processing. Image processing used ImageJ/FIJI software³⁶. For NE reformation assay and the nuclear pore deposition assay, mCherry-KDEL or mCherry-Nup58 fluorescence intensity was measured on a line manually drawn along the nucleus for each time point and normalized values plotted over time. For measuring residence time of CHMP4B-eGFP around chromatin, the presence of

CHMP4B foci around chromatin discs was manually scored over time and the total number of frames (seconds) positive for CHMP4B foci was plotted. For tracking of spindle MTs reaching CHMP4B foci (Fig. 3b), live HeLa cells stably co-expressing mCherry- α -tubulin and CHMP4B-eGFP were imaged every 5 s during anaphase using a Deltavision OMX V4 microscope. Five-pixel ROIs were selected at CHMP4B foci intersecting with spindle MTs, and fluorescence intensities of mCherry- α -tubulin and CHMP4B-eGFP were measured for each time point. Fluorescence intensity values were then normalized to 100 and data sets were aligned in time according to CHMP4B arrival at MTs. For control MTs, ROIs were selected at the spindle midzone. For time of spindle MTs persistence in siRNA KD experiments (Fig. 3c, h and Extended Data Fig. 6b), cells were imaged every 30 s during anaphase using a Deltavision OMX V4 microscope. For scoring the time of disappearance of spindle MTs at CHMP4B foci, only clear mid-spindle MT-CHMP4B structures were manually analysed. The time from CHMP4B onset on each analysed MT to the disappearance of the same MT was scored. For representative videos, time-lapse series were de-bleached using the 'correct bleaching' function in FIJI. Bitplane Imaris software was used to generate surface renderings of three-dimensional-SIM images. To track association of CHMP4B and CENP-A, time-lapse micrographs were segmented using the 'Spots' function in Imaris and analysed using the 'Colocalize Spots' function, with a distance threshold of 0.3 μ m. Nuclear import was assayed automatically using a customized ImageJ script. First, nuclei were segmented using the H2B channel of the images by median filtering and Otsu thresholding. The ImageJ function 'Analyse Particles' was then used to define ROIs. On the basis of these ROIs, the mean intensity of the nuclei was measured in the importin- β -binding domain of importin- α (IBB) channel. In parallel, a band-shaped ROI around the nuclei was used to measure the mean intensity of the cytoplasm as regularization factor. Nuclear import rates were determined by normalizing the mean intensity of the nuclear IBB signal to the overall IBB signal of the nucleus and cytoplasm. DNA damage was assessed by an ImageJ script that first generated ROIs by segmenting Hoechst-stained nuclei by Otsu thresholding and the ImageJ 'Analyse Particles' function. These ROIs were then used to segment and measure γ -H2AX-positive foci within spots. DNA damage was scored by counting the number of cells with large (≥ 20 pixels) DNA damage foci. Likewise, the mean intensity of these γ -H2AX foci was determined. To assess the number of CHMP4B foci in proximity to anaphase nuclei over time (Fig. 1b), nuclei were segmented using their H2B fluorescence signal by median filtering, Otsu thresholding and the 'Analyse Particles' function. Within these segmented nuclei, the number of CHMP4B foci was counted. To ease detection of these foci, we performed a 'Difference of Gaussian' filtering and then used the 'Find Maxima' function of ImageJ to detect nuclei. Counting of these foci was performed on maximum intensity projected images to find foci from all imaging planes. For each cell, anaphase onset was recorded and the measurements were aligned to this time point. Analysis of CHMP4B foci in CHMP7 knockdown cells (Fig. 1e) was used a similar procedure. Again, nuclei were segmented and used as a mask for spot analysis. Owing to different imaging modalities, these images showed more noise, which was enhanced by the 'Difference of Gaussian' filtering and skewed the scoring of spots. To avoid this limitation, we first subtracted the cytoplasmic background (cytoplasm mean intensity + 2 s.d.) before maximum detection. In this case, only single time points and a single, central plane in mid-anaphase (1–2 min after the beginning of furrow ingression) were chosen for measurement. Localization of membrane-defective CHMP4B to anaphase nuclei (Fig. 1d) was scored in the same manner, but a maximum intensity projection of all imaging planes was used. Temporal alignment was based on cell and chromatin shape. Post-processing of automatically measured image data used Python and the 'Pandas' data analysis package³⁷. Data points were plotted using Graphpad Prism.

Tubulin line plots analysis. To analyse the effects of CHMP4B presence on MT structure (Extended Data Fig. 6c), we measured α -tubulin intensity around CHMP4B spots using line plots. To this end, we chose MTs lying in a single plane and measured the fluorescence of both α -tubulin and CHMP4B in a two-pixel-wide line drawn along the MT. Measured values were transferred to Graphpad Prism for plotting and Spearman's correlation analysis.

Trapping of substrates by rapalog-mediated dimerization. The HeLa 'Kyoto' CHMP4B-eGFP BAC-tagged cell line was transduced with a lentivirus expressing H2B-FRB and FKBP-MBP-mCherry (which lacked a nuclear localization signal). These proteins were expressed as a single, T2A-cleaved open reading frame under control of the constitutive EF1 α promoter. Normally, we observed a diffuse localization of FKBP-MBP-mCherry in both the cytoplasm and nucleus. Addition of Rapalog caused trapping of the freely diffusible, but bulky FKBP-MBP-mCherry on chromatin. This was especially evident on metaphase chromatin, where we observed a rapid accumulation of mCherry at chromatin. Owing to the persistent permeability of the nucleus after anaphase³⁸, we decided to analyse nuclei of cells in late cytokinesis. We reasoned that these cells recently went through anaphase and would be challenged with the effects of ESCRT knockdown. Cells in late cytokin-

esis were selected on the basis of the presence of CHMP4B at the midbody. Rapalog (iDimerize Heterodimerizer, Clontech) was added to a final concentration of 1 μ M and cells were imaged for 30 min with 1 min time intervals. Nuclear leakage was assessed by measuring the fluorescence in the nucleus and cytoplasm within a manually placed circular ROI of 20-pixel diameter. The ratio of nuclear and cytoplasmic fluorescence was plotted and a linear regression line was fitted to the data points using Graphpad Prism software.

Stable cell lines. A stable HeLa 'Kyoto' cell line expressing CHMP4B-eGFP was obtained from A. Hyman⁹. All other stable cell lines were lentivirus-generated pools. To achieve low expression levels, the weak PGK promoter was used for transgene expression. For higher expression levels, CMV or EF1 α promoters were used. Third-generation lentivirus was generated using procedures and plasmids as previously described³⁹. Briefly, (eGFP/mCherry/LSSmKate1/Flag/V5 fusions of) transgenes were generated as Gateway ENTRY plasmids using standard molecular biology techniques. From these vectors, lentiviral transfer vectors were generated by recombination into lentiviral destination vectors (Addgene plasmids 19067, 19068, 41393; and vectors derived from pCDH-EF1 α -MCS-IRES-PURO (SystemBiosciences)) using Gateway LR reactions. VSV-G pseudotyped lentiviral particles were packaged using a third-generation packaging system⁴⁰ (Addgene plasmids 12251, 12253, 12259). Cells were then transduced with low virus titres (multiplicity of infection ≤ 1) and stable expressing populations were generated by antibiotic selection. Detailed cloning procedures are available from the authors. We used the following stable cell lines (listed here in order as background; new transgene (plasmids), respectively).

HeLa 'Kyoto'; HA-eGFP-VPS4A (pLenti-PGK_HA-eGFP-VPS4A_Puro).

HeLa 'Kyoto'; HA-CHMP4B (pLenti-PGK_HA-CHMP4B_Bsd).

HeLa 'Kyoto'; CHMP1A-V5 (pLenti-PGK_CHMP1A-V5_Puro).

HeLa 'Kyoto'; CHMP1B-FLAG (pLenti-PGK_CHMP1B-FLAG_Puro).

HeLa 'Kyoto'; IST1-mCherry (pLenti-PGK_IST1-mCherry_Puro).

HeLa 'Kyoto' CHMP4B-eGFP (BAC); mCherry- α -tubulin (pCDH-EF1 α _mCherry- α -Tubulin_Bsd).

HeLa 'Kyoto' CHMP4B-eGFP (BAC); H2B-mCherry (pCDH-EF1 α _H2B-mCherry_Bsd).

HeLa 'Kyoto' CHMP4B-eGFP (BAC); mCherry-KDEL (pCDH-EF1 α _mCherry-KDEL_Puro, derived from Addgene plasmid 36204).

HeLa 'Kyoto' CHMP4B-eGFP (BAC); mCherry-CENP-A (pLenti-PGK_mCherry-CENP-A_Bsd).

HeLa 'Kyoto' CHMP4B-eGFP (BAC); mCherry-NUP58 (pLenti-PGK_mCherry-NUP58_Puro).

HeLa 'Kyoto' CHMP4B-eGFP (BAC); mCherry-Spactin-M1 (pLenti-PGK_mCherry-spactin-M1_Puro).

HeLa 'Kyoto' CHMP4B-eGFP (BAC); mCherry-Spactin-M87 (pLenti-PGK_mCherry-spactin-M87_Puro).

HeLa 'Kyoto' CHMP4B-eGFP (BAC); mCherry-spactin-M87^{E442Q} (pCW57.1-TetON_mCherry-spactin-M87^{E442Q}_Puro).

HeLa 'Kyoto' CHMP4B-eGFP (BAC) mCherry-CENP-A (LSSmKate1- α -tubulin; pCDH-EF1 α _LSSmKate1- α -tubulin_Bsd, derived from Addgene plasmid 31902).

HeLa 'Kyoto' CHMP4B-eGFP (BAC); H2B-mCherry; CHMP2A wild type (pLenti-PGK_CHMP2Awt_Puro).

HeLa 'Kyoto' CHMP4B-eGFP (BAC); H2B-mCherry; CHMP2A siRNA1 resistant (pLenti-PGK_CHMP2Ares_Puro).

HeLa 'Kyoto' CHMP4B-eGFP (BAC); mCherry- α -tubulin; CHMP2A wild type (pLenti-PGK_CHMP2Awt_Puro).

HeLa 'Kyoto' CHMP4B-eGFP (BAC); mCherry- α -tubulin; CHMP2A siRNA1 resistant (pLenti-PGK_CHMP2Ares_Puro).

HeLa 'Kyoto'; H2B-mCherry; CHMP4B-eGFP siRNA resistant (pLenti-PGK_CHMP4B-eGFP_Puro).

HeLa 'Kyoto'; H2B-mCherry; CHMP4B(4DE (V3D, F4D, L7E, F8D))-eGFP siRNA resistant (pLenti-PGK_CHMP4B(4DE)-eGFP_Puro).

HeLa 'Kyoto' CHMP4B-eGFP (BAC); H2B-FRB FKBP-MBP-mCherry (pCDH_EF1 α _H2B-FRB-2A-FKBP-MBP-mCherry).

Protein blotting. Cells were lysed in 2 \times sample buffer (100 mM TrisHCl pH 6.8, 4% SDS, 20% glycerol, 200 mM DTT, bromophenol blue). The whole-cell lysate was subjected to SDS-polyacrylamide gel electrophoresis on a 4–20% gradient gel. Proteins were transferred to Immobilon-P membrane (Millipore). Immunodetection was performed using Supersignal West Dura Extended Duration Substrate (Pierce) followed by conventional film exposure and developing (Amersham Hyperfilm ECL, GE), or fluorescently labelled secondary antibodies and Odyssey developer. Western blots shown in figures are representative of at least three independent experiments.

CLEM. For CLEM using confocal microscopy, cells were grown on gridded coverslips (EMS) and fixed in 4% formaldehyde, 0.1% glutaraldehyde in 0.1 M PHEM and processed for EM as described below. For CLEM in combination with live-cell

imaging, HeLa CHMP4B-eGFP cells were grown on gridded glass-bottom dishes (MatTek) for 20 h and imaged every 20 s from the onset of anaphase. At the desired time point, cells were fixed in 2% glutaraldehyde in 0.1 M PHEM buffer. After 1 h the cells were washed in PHEM buffer and postfixed for 1 h with 2% OsO₄ and 1.5% K₄(Fe(CN)₆) in 0.1 M PHEM, followed by 0.5% tannic acid (30 min). After staining with 4% uranyl acetate in distilled H₂O (30 min) the coverslips were dehydrated in graded series of ethanol and embedded in Epon. Serial, semi-thin sections (120–150 nm) through the whole nucleus were cut (Leica EM FCS ultra-microtome) parallel to the substrate and placed on carbon/formvar-coated slot-grids (EMS) and contrasted with 1% Pb-citrate. Sections were observed at 80–120 kV on a JEOL JEM-1230 electron microscope and micrographs were recorded with a digital camera (Morada) using iTEM (SIS) software. Image processing was done with Adobe Photoshop CS2. First the image series were aligned in CS2, followed by serial reconstruction using three-dimensional modelling of the whole nucleus. This model was fitted onto a three-dimensional-reconstruction of confocal sections (600 nm in thickness, 22 sections in total) from the same nucleus using Imaris. For simpler alignment we used the maxcentre function in Imaris to mark CHMP4B-eGFP- and mCherry-CENP-A-containing spots and to correlate these with the appropriate EM sections.

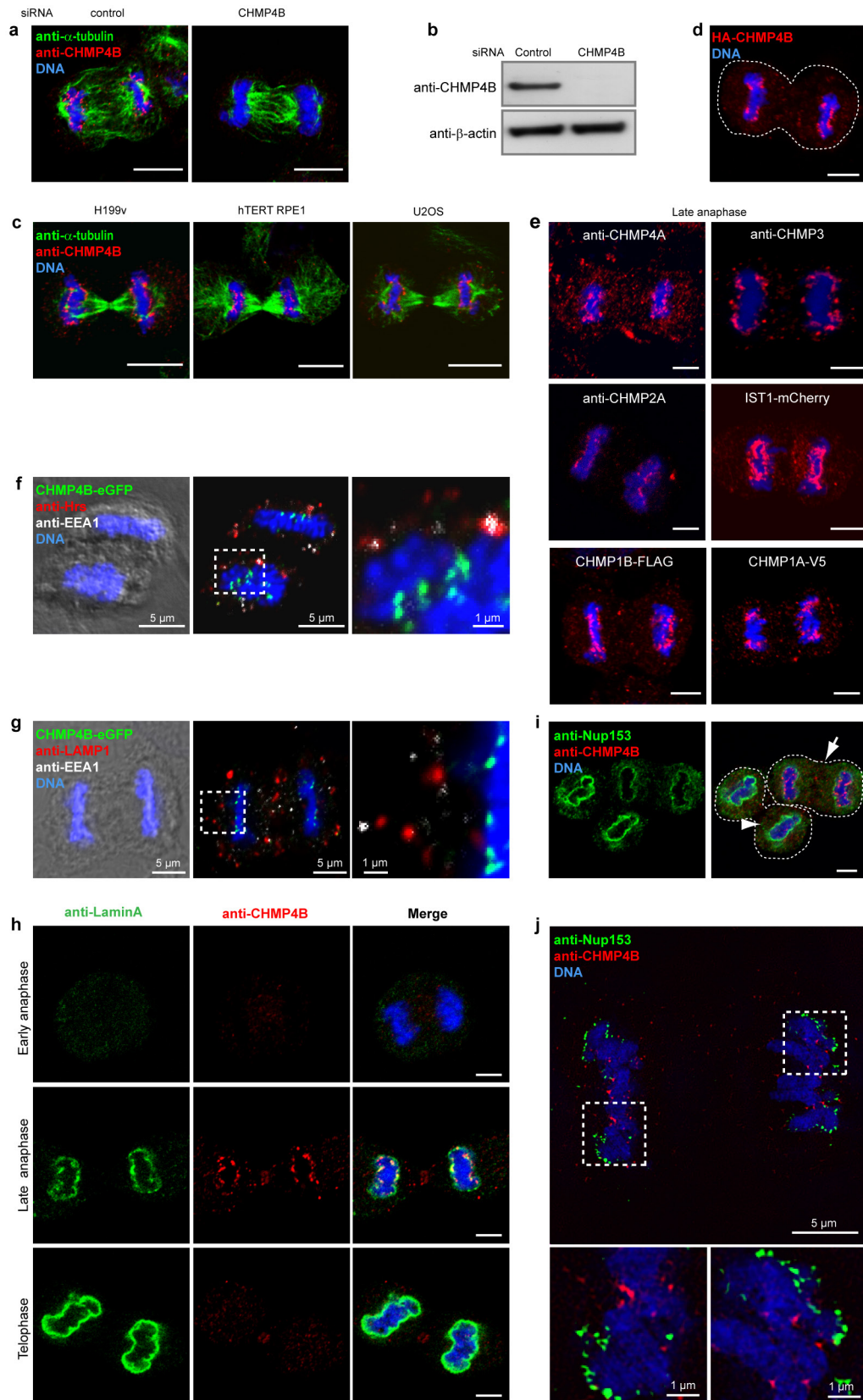
Quantification of MT attachment points to chromatin discs. Cells treated with control and CHMP3 siRNA (three cells per condition) were fixed at the same time point after anaphase onset and samples were processed for EM as described above. Semi-thin serial sections covering the whole-cell volume were inspected and gaps in the nuclear envelope with three or more MTs attached were scored.

Electron tomography. Semi-thin sections (160–200 nm) were cut parallel to the substrate and placed on carbon/formvar-coated slotgrids (EMS). Samples were observed on a FEI Tecnai microscope at 120 kV and image series were taken between –58° and 58° with 2° increments. Series were recorded with a FEI camera

at 1.9 nm pixel size. Tomograms were computed using weighted back-projection and the IMOD package⁴¹.

Sample sizes and statistical analyses. All data sets presented in this paper derive from at least three independent experiments. No statistical methods were used to predetermine sample size.

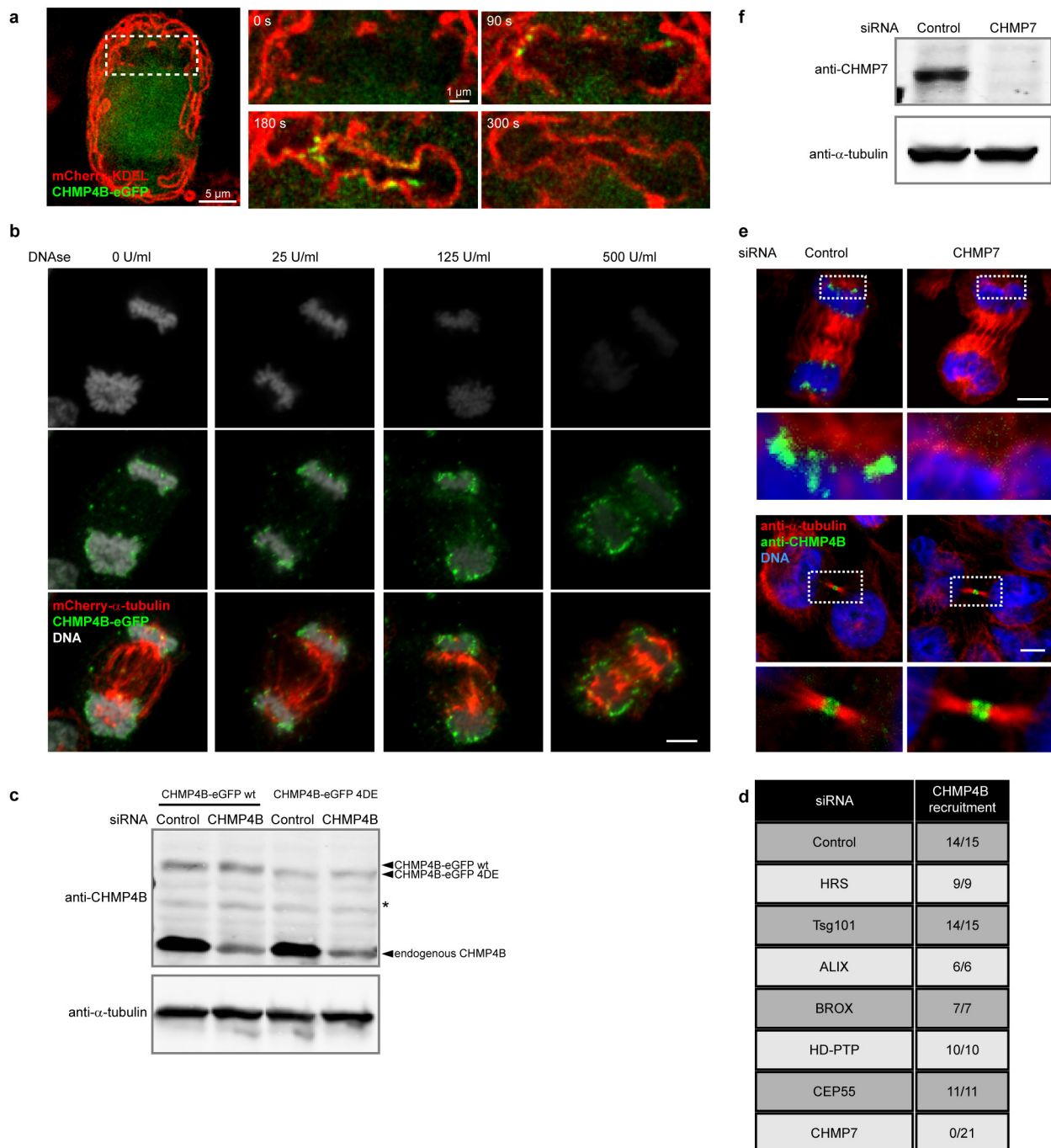
31. Bache, K. G. *et al.* The ESCRT-III subunit hVps24 is required for degradation but not silencing of the epidermal growth factor receptor. *Mol. Biol. Cell* **17**, 2513–2523 (2006).
32. Sagona, A. P. *et al.* PtdIns(3)P controls cytokinesis through KIF13A-mediated recruitment of FYVE-CENT to the midbody. *Nature Cell Biol.* **12**, 362–371 (2010).
33. Mu, F. T. *et al.* EEA1, an early endosome-associated protein. EEA1 is a conserved alpha-helical peripheral membrane protein flanked by cysteine “fingers” and contains a calmodulin-binding IQ motif. *J. Biol. Chem.* **270**, 13503–13511 (1995).
34. Raiborg, C., Bache, K. G., Mehlum, A., Stang, E. & Stenmark, H. Hrs recruits clathrin to early endosomes. *EMBO J.* **20**, 5008–5021 (2001).
35. Schmitz, M. H. *et al.* Live-cell imaging RNAi screen identifies PP2A-B55alpha and importin-beta1 as key mitotic exit regulators in human cells. *Nature Cell Biol.* **12**, 886–893 (2010).
36. Schindelin, J. *et al.* Fiji: an open-source platform for biological-image analysis. *Nature Methods* **9**, 676–682 (2012).
37. McKinney, W. Data structures for statistical computing in Python. In *Proc. 9th Python in Science Conference* 51–56 (2010).
38. Dultz, E., Huet, S. & Ellenberg, J. Formation of the nuclear envelope permeability barrier studied by sequential photoswitching and flux analysis. *Biophys. J.* **97**, 1891–1897 (2009).
39. Campeau, E. *et al.* A versatile viral system for expression and depletion of proteins in mammalian cells. *PLoS ONE* **4**, e6529 (2009).
40. Dull, T. *et al.* A third-generation lentivirus vector with a conditional packaging system. *J. Virol.* **72**, 8463–8471 (1998).
41. Kremer, J. R. *et al.* Computer visualization of three-dimensional image data using IMOD. *J. Struct. Biol.* **116**, 71–76 (1996).



Extended Data Figure 1 | ESCRT-III is transiently recruited around

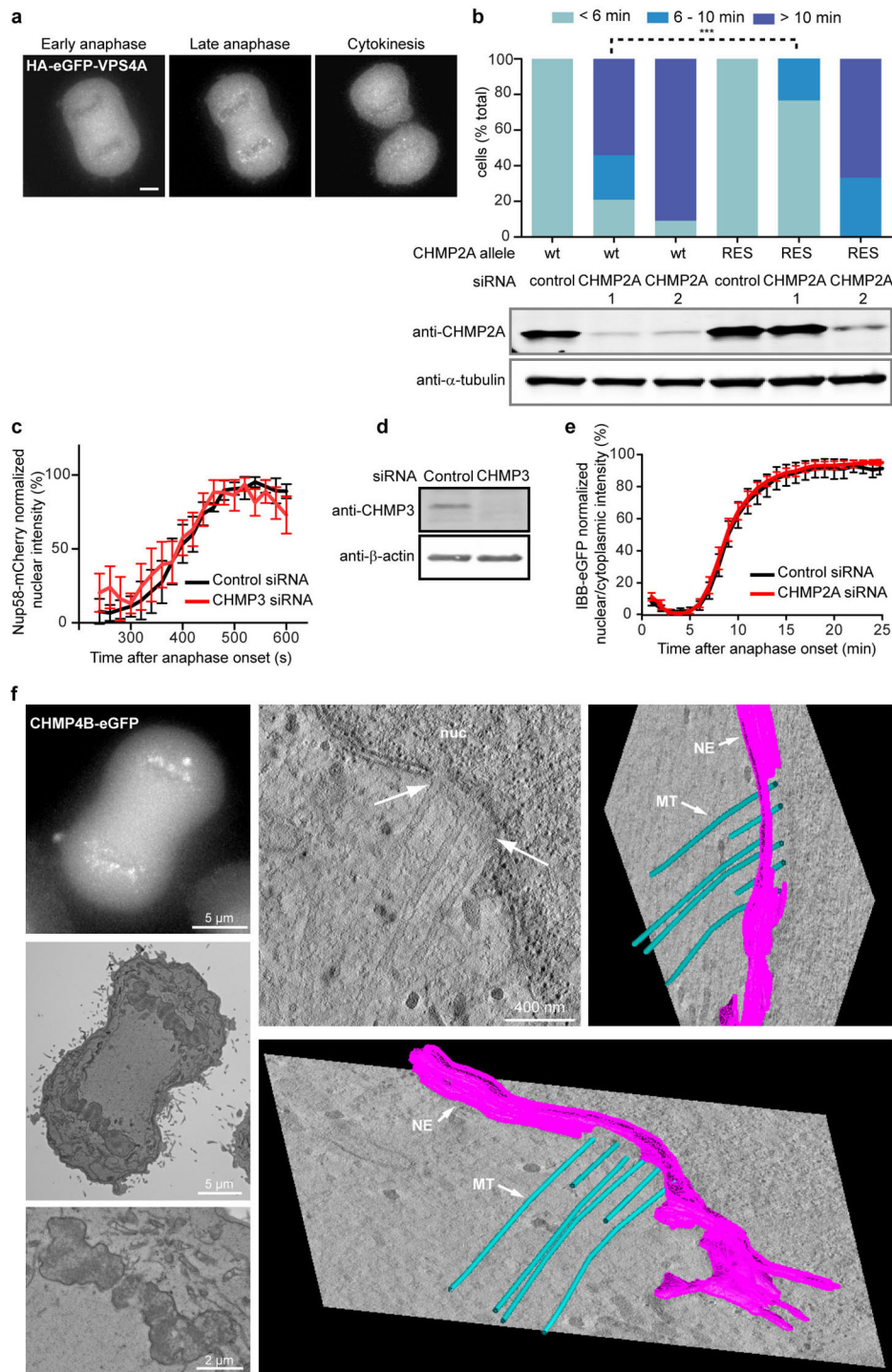
chromatin discs during nuclear envelope reformation. **a**, Confocal image of HeLa cells treated with control siRNA or CHMP4B targeting siRNA and stained as indicated. Scale bars, 10 μm . Image is representative of at least five captures. **b**, Immunoblot of whole-cell lysates probed for endogenous CHMP4B and β -actin. **c**, Confocal images of H199v, hTERT RPE1 and U2OS cells showing localization of endogenous CHMP4B around chromatin discs during late anaphase. Cells were co-stained for α -tubulin and DNA (Hoechst). Scale bars, 10 μm . Images are representative of at least three captures for each cell line. **d**, Confocal image of fixed HeLa cells stably expressing HA-CHMP4B. Anti-HA in red and DNA (Hoechst) labelled in blue. Scale bar, 5 μm . Image is representative of at least ten captures. **e**, Confocal images of late anaphase HeLa cells stained for endogenous proteins (CHMP4A, CHMP3, CHMP2 in red) or stably expressing tagged proteins (CHMP1B-Flag, CHMP1A-V5, IST1-mCherry in red) as indicated and DNA (Hoechst) shown in blue. Scale bars, 5

μm . Images are representative of at least three captures. **f**, Confocal image of HeLa cells labelled for CHMP4B-eGFP, the early endosome marker EEA1, the multivesicular endosome marker Hrs and DNA (Hoechst). Image is representative of five captures. **g**, As **f**, but stained for the late endosome marker LAMP1 instead of Hrs. Image is representative of five captures. **h**, Confocal images of fixed HeLa cells in different phases of mitotic exit, stained for lamin A, endogenous CHMP4B, and DNA (Hoechst). Scale bars, 5 μm . Images are representative of at least five captures for each stage. **i**, Confocal image of HeLa cells at different phases of mitotic exit stained as indicated. Note the different stage in nuclear pore reassembly in late anaphase (arrow) compared with telophase (arrowhead). Scale bar, 5 μm . Image is representative of at least ten captures. **j**, SIM reconstruction of HeLa cells (labelled as indicated) shows no co-localization between CHMP4B and nuclear pores (Nup153). Image is representative of five captures.



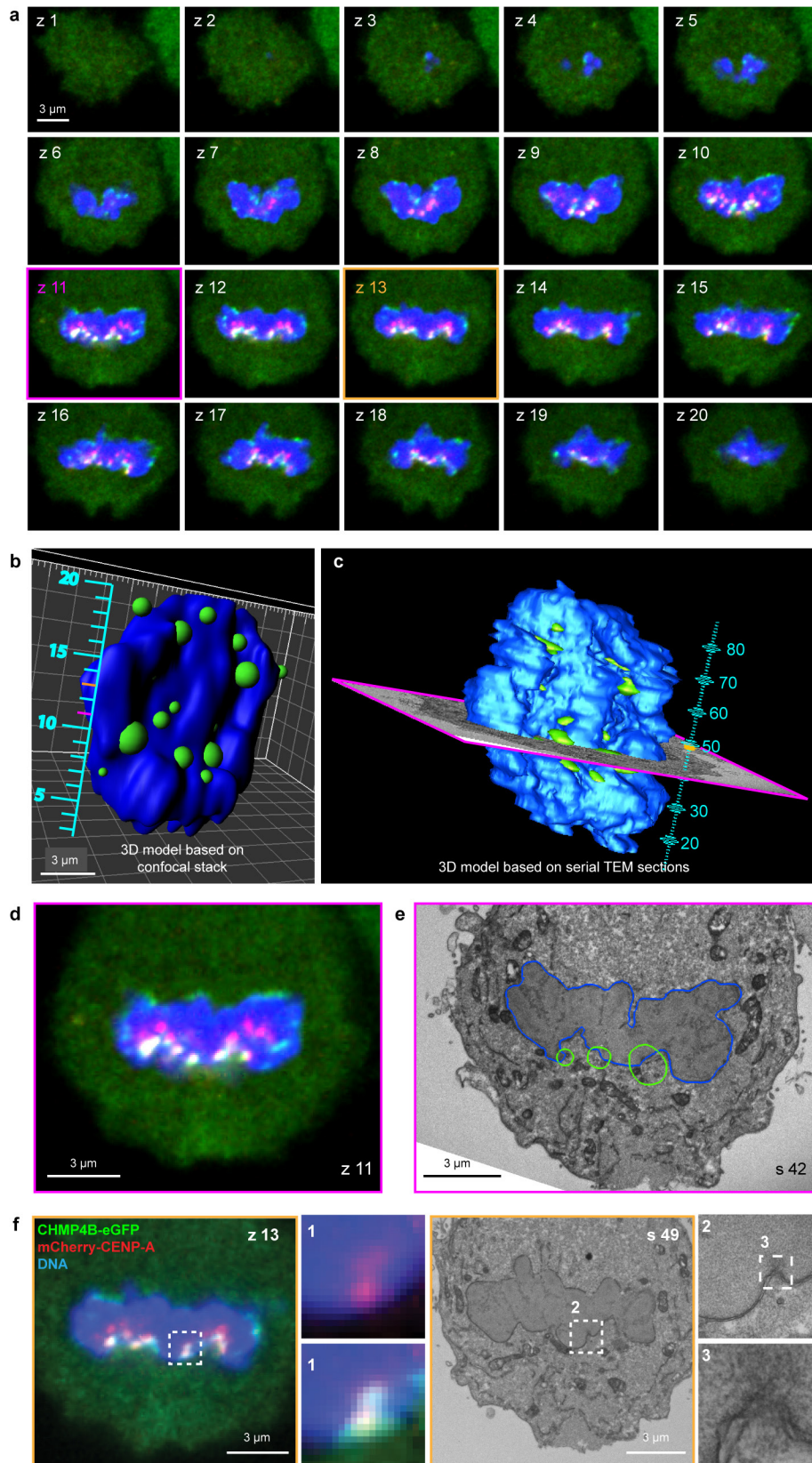
Extended Data Figure 2 | ESCRT-III is transiently recruited around chromatin discs during nuclear envelope reformation. **a**, Deconvolved wide-field live-cell imaging of HeLa cells stably expressing CHMP4B-eGFP and mCherry-KDEL, showing recruitment of CHMP4B only at sites where the reforming NE has engulfed the chromatin disc (see gallery). Images are representative of at least ten videos. **b**, HeLa cells stably expressing CHMP4B-eGFP and mCherry- α -tubulin were fixed and treated with increasing concentrations of DNase I. Cells were then labelled for GFP, mCherry and DNA and imaged with a confocal microscope. Scale bar, 5 μ m. Images are representative of at least three captures for each condition. **c**, Immunoblot showing endogenous CHMP4B knockdown in HeLa cells stably expressing WT CHMP4B-eGFP or a membrane binding defective mutant CHMP4B-

eGFP 4DE. Asterisk indicates non-specific immunoreactivity. **d**, Table showing frequency of cells where CHMP4B was recruited around anaphase chromatin under the indicated siRNA transfections. CHMP4B is not recruited upon CHMP7 depletion. This result is representative of knockdown experiments using three independent CHMP7-targeting siRNAs. **e**, Representative confocal images of HeLa cells transfected with the indicated siRNAs, fixed and immunolabelled for CHMP4B, α -tubulin and DNA. CHMP7 depletion affects CHMP4B recruitment around anaphase chromatin (upper panel), but does not affect CHMP4B recruitment at the midbody (lower panel). Scale bars, 5 μ m. Images are representative of 20 captures each for control and CHMP7 siRNAs. **f**, Immunoblot showing efficient endogenous CHMP7 knockdown in HeLa cells stably expressing CHMP4B-eGFP.



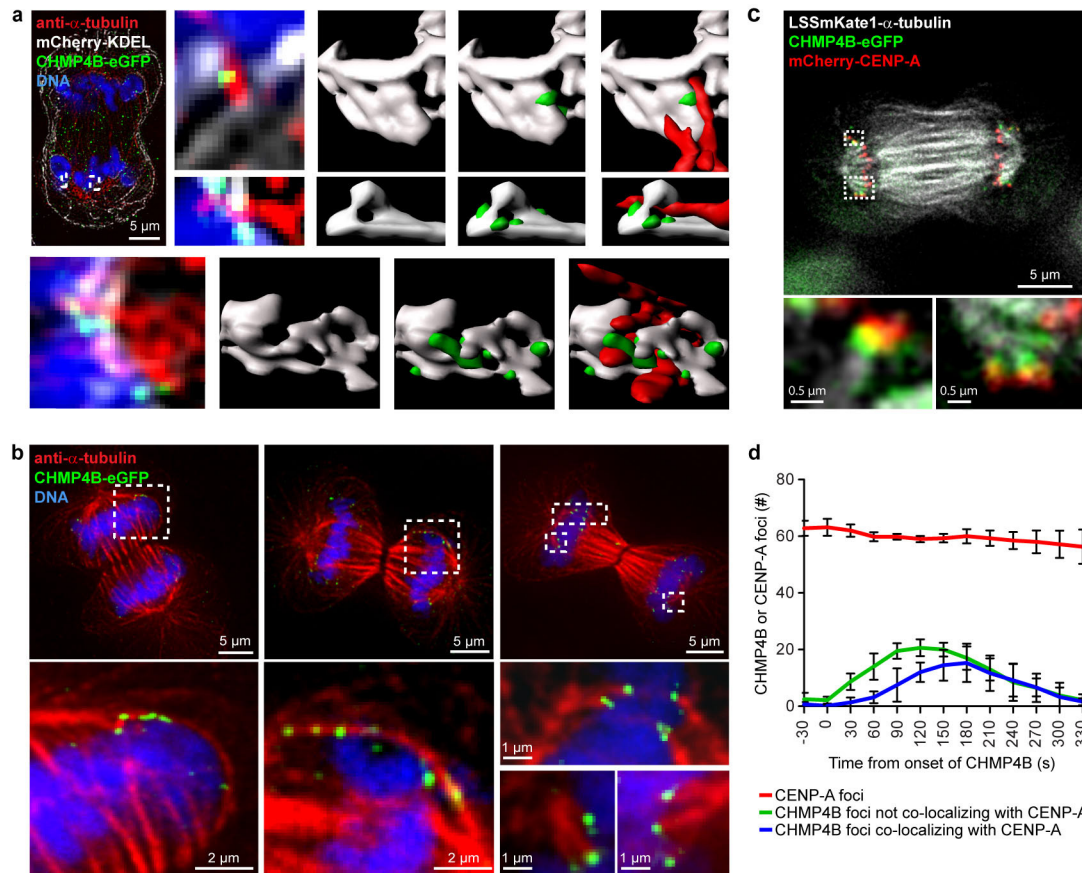
Extended Data Figure 3 | ESCRT-III and VPS4 cooperate at foci of NE-MT intersection during nuclear envelope reassembly. **a**, Deconvolved wide-field images of live HeLa cells stably expressing HA-eGFP-VPS4A followed through mitotic exit, showing transient localization around chromatin discs during late anaphase. Scale bar, 5 μ m. Gallery is representative of three videos. **b**, CHMP4B-eGFP/H2B-mCherry HeLa cells stably expressing untagged WT CHMP2A or untagged RES CHMP2A (CHMP2A allele resistant for CHMP2A siRNA 1) were transfected with the indicated siRNAs. Cells were then imaged live after anaphase onset and residence time (in minutes) of CHMP4B foci around chromatin was scored and plotted as a percentage of population. Immunoblot shows efficient depletion of CHMP2A in the non-resistant lines. $n = 21$ cells for WT/control siRNA; $n = 24$ cells for WT/CHMP2A siRNA 1; $n = 11$ cells WT/CHMP2A siRNA 2; $n = 18$ cells for RES/control siRNA; $n = 17$ cells for RES/CHMP2A siRNA 1; $n = 12$ cells for RES/CHMP2A siRNA 2. $***P = 0.0002$ was derived from an unpaired t -test. **c**, HeLa cells stably expressing CHMP4B-eGFP and Nup58-mCherry were transfected with the

indicated siRNAs for 48 h and imaged every 20 s after anaphase onset. Normalized fluorescence intensity of Nup58-mCherry at NE was plotted over time. $n = 8$ DNA discs for control siRNA; $n = 8$ DNA discs for CHMP3 siRNA. Bars, mean and 95% confidence intervals. **d**, Immunoblot showing efficient endogenous CHMP3 knockdown in HeLa cells stably expressing CHMP4B-eGFP and Nup58-mCherry. **e**, HeLa cells stably expressing IBB-eGFP and H2B-RFP were transfected with the indicated siRNAs. Cells were then imaged every 20 s after anaphase onset. The mean intensity of the nuclear IBB was normalized to the total cellular IBB signal (nucleus + cytoplasm) and plotted over time. $n = 37$ cells for control siRNA; $n = 32$ cells for CHMP2A siRNA. Bars, mean and 95% confidence intervals. **f**, Electron tomography and three-dimensional reconstruction of kinetochore MTs (light blue) intersecting the reforming NE (magenta), obtained from correlative live-cell imaging (inset) and transmission EM. Nuc, nucleus. The electron tomography image is representative of EM analysis of three anaphase cells.



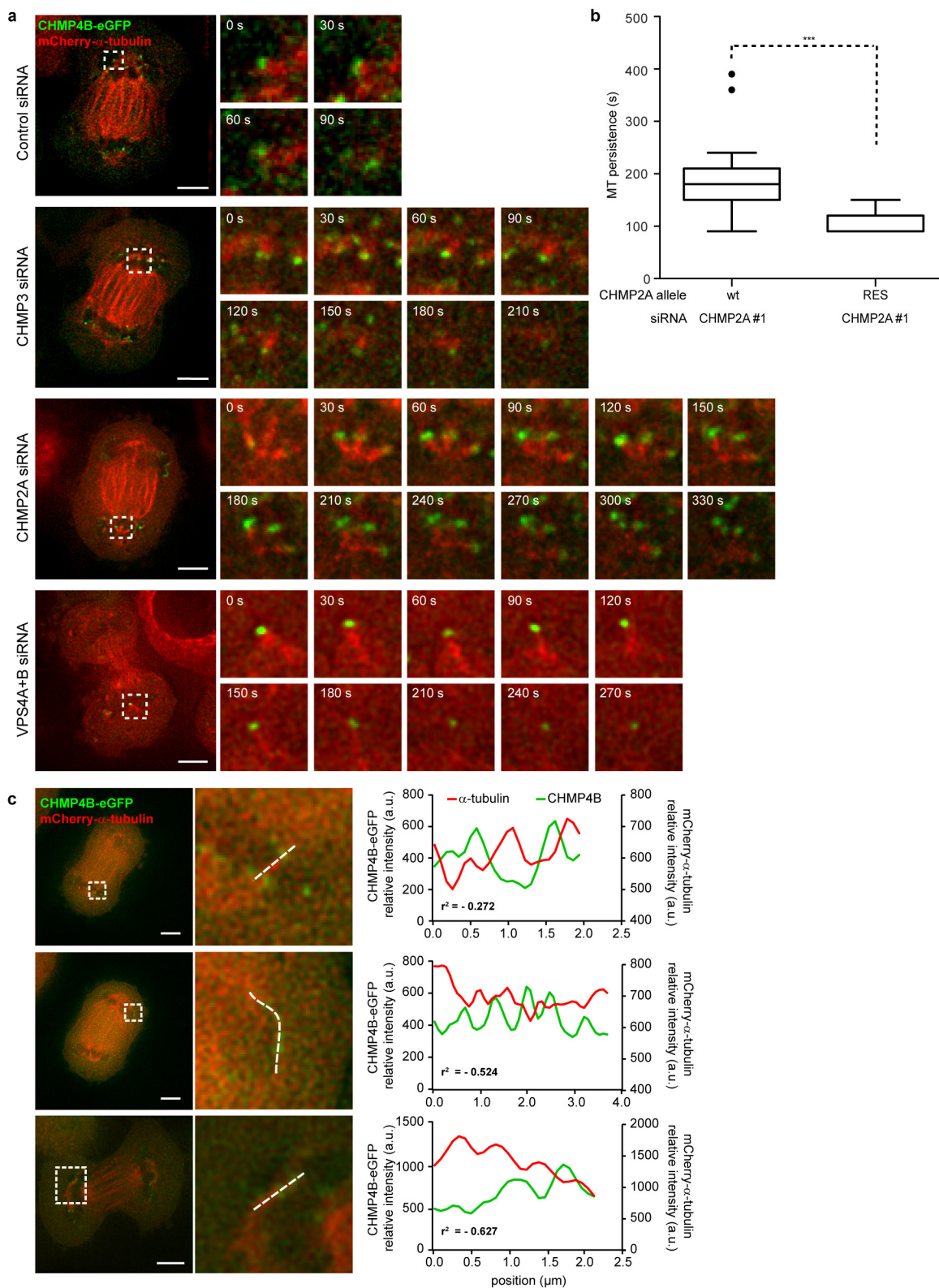
Extended Data Figure 4 | ESCRT-III and VPS4 cooperate at foci of the NE-MT intersection during nuclear envelope reassembly. CLEM of a whole nucleus from HeLa cells expressing CHMP4B-eGFP and mCherry-CENP-A by combination of a confocal stack and a complete serial EM reconstruction of the same structure. CLEM analysis is representative of three chromatin discs. **a**, Confocal stack; z_1 – z_{20} . Pink (z_{11}) and orange (z_{13}) highlighted confocal planes correspond to sections shown in Fig. 2c and in Extended Data Fig. 4f, respectively. **b**, The strongest CHMP4B-eGFP signals were annotated in an Imaris stack as centre of masses (green spheres in **b**; blue, DNA; pink and orange bars indicate sections shown in Fig. 2c) and then transferred manually

onto a three-dimensional reconstruction from serial EM sections ($n = 13$ CHMP4B-eGFP mCherry-CENP-A double-positive foci). **c**, Complete EM serial reconstruction. Bar index indicates corresponding EM sections. **d**, Immunofluorescence image corresponding to slice 11 through the three-dimensional model in **b**. **e**, Electron micrograph corresponding to slice 42 through the three-dimensional model in **c** (nucleus, blue outline; green circles, approximate positions of centre of masses from **b**). **f**, A confocal plane (z_{13}) with the respective electron micrographs is shown, including insets with increasing magnifications. CHMP4B and CENP-A foci (detected by light microscopy) correlate with unsealed NE (observed on EM sections).



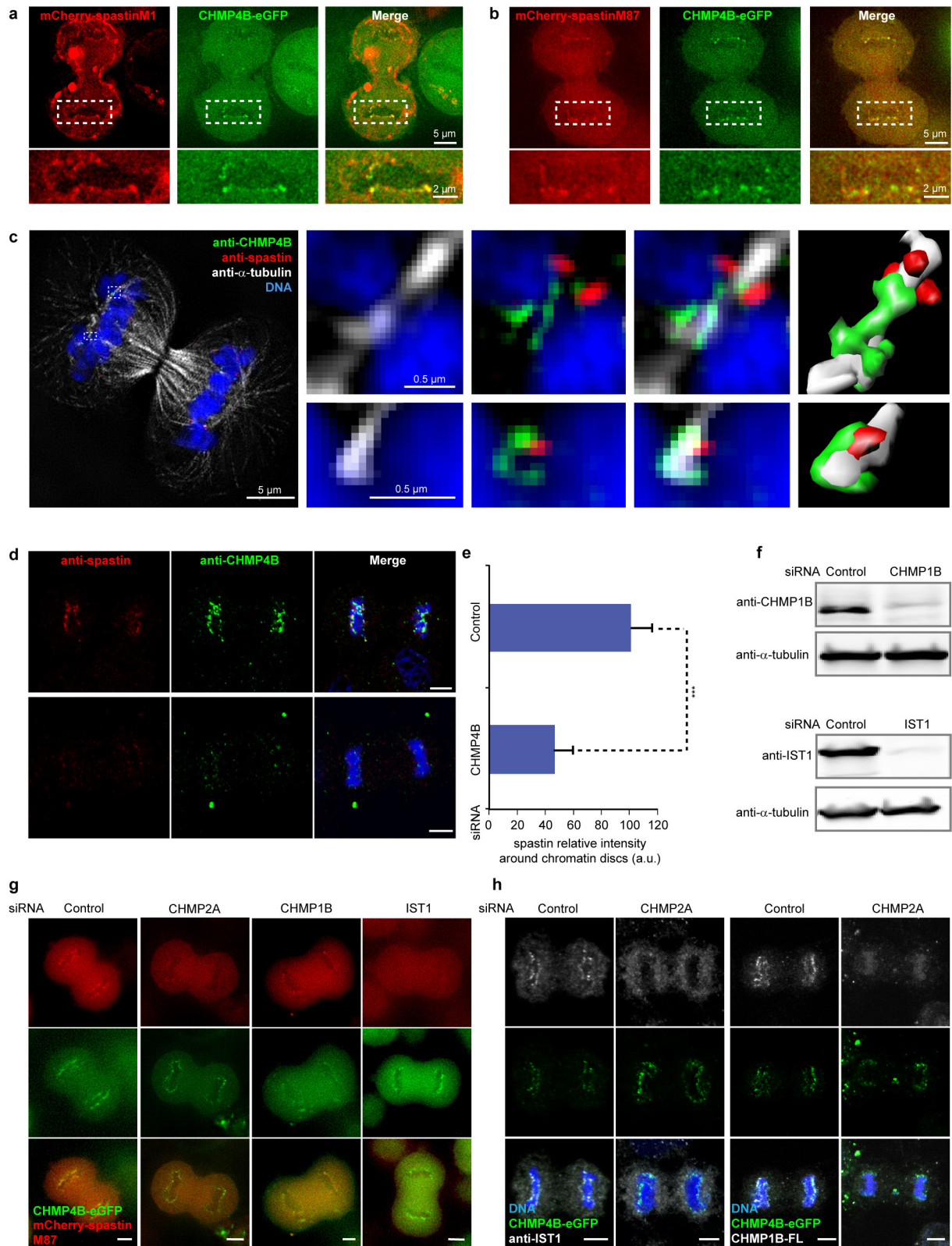
Extended Data Figure 5 | ESCRT-III and VPS4 cooperate at foci of the NE-MT intersection during nuclear envelope reassembly. **a**, Section from a SIM z-stack of a formaldehyde-fixed HeLa cell labelled as indicated. The Imaris surface three-dimensional renderings (three examples) illustrate holes in the NE with intersecting spindle MTs and CHMP4B localization within the NE holes. The SIM image is representative of at least ten captures. Imaris reconstruction was performed on four areas of intersection between CHMP4B, MTs and ER. **b**, Deconvolved wide-field images of fixed CHMP4B-eGFP HeLa cells labelled as indicated. Note CHMP4B foci localization in connection with polar MTs (left, middle and upper right panels) and to kinetochore MTs (lower

right panel). Images are representative of at least 20 videos. **c**, Deconvolved wide-field image from live HeLa cells stably expressing mCherry-CENP-A, CHMP4B-eGFP and LSSmKate1- α -tubulin, showing localization of CHMP4B on kinetochore MTs and in close proximity to kinetochores. Image is representative of five videos. **d**, HeLa cells stably expressing mCherry-CENP-A and CHMP4B-eGFP were imaged after anaphase onset. Number of CHMP4B foci not co-localizing or co-localizing with CENP-A, and total number of CENP-A foci, were quantified and plotted over time. Time = 0 equals onset of CHMP4B recruitment. $n = 6$ cells. Bars, mean and s.d.



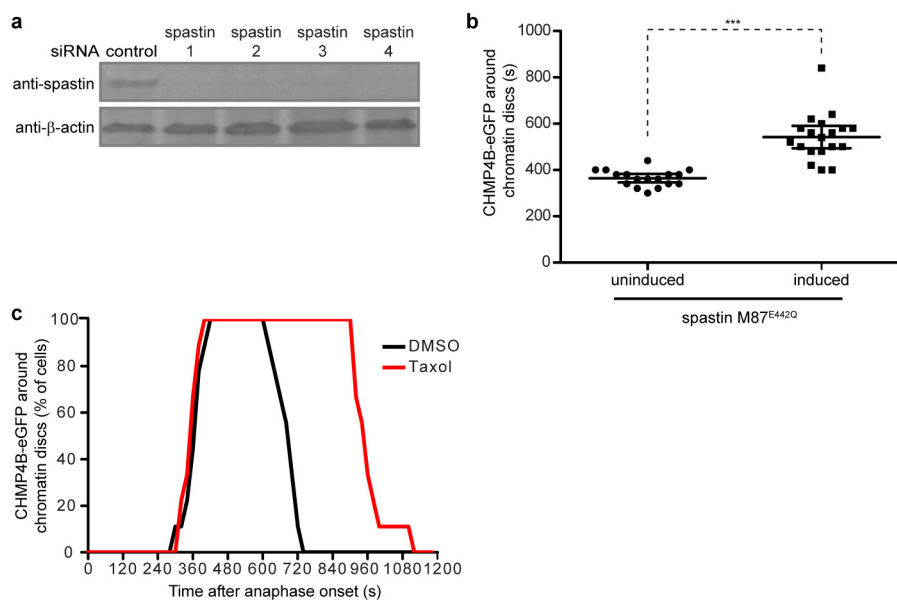
Extended Data Figure 6 | ESCRT-III and VPS4 cooperate at foci of the NE-MT intersection during nuclear envelope reassembly. **a**, HeLa cells stably expressing CHMP4B-eGFP and mCherry- α -tubulin were transfected with the indicated siRNAs and imaged every 30 s during mitotic exit. Microtubule bundles contacting CHMP4B foci around chromatin discs were tracked and shown in representative galleries. Time = 0 indicates CHMP4B enrichment on the MT bundle. Scale bars, 5 μ m. Images and galleries are representative of 23 events for control siRNA; 26 events for CHMP3 siRNA; 18 events for CHMP2A siRNA; 22 events for VPS4A+B siRNA. **b**, CHMP4B-eGFP/mCherry- α -tubulin HeLa cells stably expressing WT or siRNA 1 resistant CHMP2A were

transfected with CHMP2A siRNA 1 and imaged every 30 s during mitotic exit. Spindle MTs reaching CHMP4B were tracked and their time of disappearance after CHMP4B onset was scored and plotted. $n = 27$ MTs for WT CHMP2A; $n = 25$ MTs for RES CHMP2A. Tukey whiskers extend from the largest value within 1.5 IQR (interquartile range) of the upper quartile to the smallest value within 1.5 IQR of the lower quartile. *** $P < 0.0001$ derived from unpaired t -test. **c**, Deconvolved wide-field images of CHMP4B-eGFP/mCherry- α -tubulin HeLa cells where MT intensity around CHMP4B foci was measured using line plots. Measured values were plotted and Spearman's correlation analysed. Scale bars, 5 μ m.



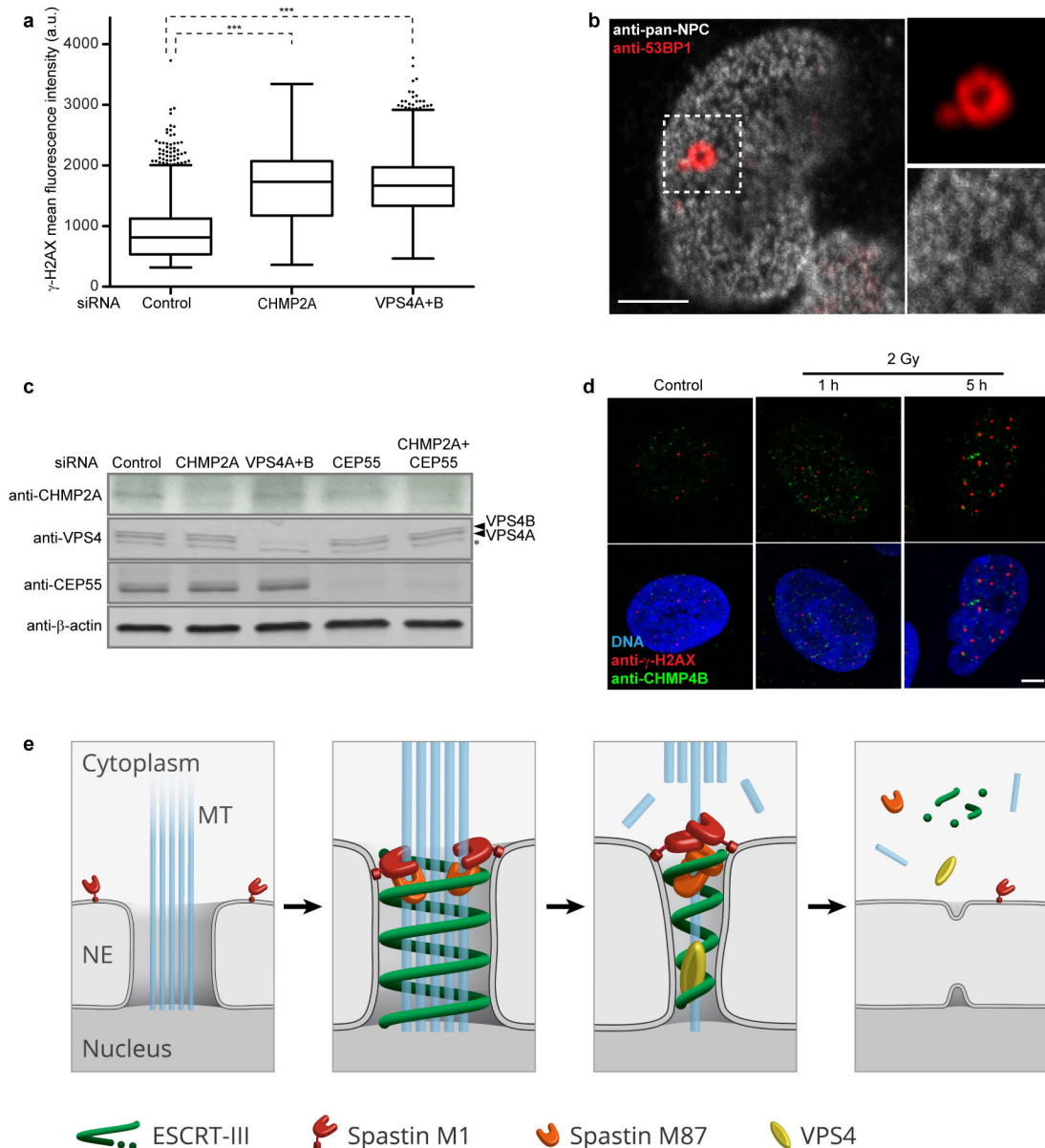
Extended Data Figure 7 | ESCRT-III-dependent recruitment of spastin to the reforming NE mediates mitotic spindle disassembly. **a**, Deconvolved wide-field image of live HeLa cells stably co-expressing mCherry-spastin M1 with CHMP4B-eGFP, illustrating co-localization. Image is representative of at least five videos. **b**, As in **a**, but instead co-expressing the mCherry-spastin M87 allele. Image is representative of at least five videos. **c**, A section from a SIM z-stack of a formaldehyde fixed HeLa cell labelled as indicated. The Imaris surface three-dimensional renderings (right) illustrate how CHMP4B and spastin embrace the spindle MT. SIM image is representative of five captures. **d**, ESCRT-III-dependent localization of spastin shown by confocal imaging of endogenous spastin (red), endogenous CHMP4B (green) and DNA (blue) after siRNA transfections as indicated. Scale bars, 5 μ m. Images are representative of 30 cells for control siRNA and 30 cells for CHMP4B siRNA. **e**, Quantification of endogenous spastin fluorescence intensity around anaphase chromatin in cells

treated and immunolabelled as in **d**. $n = 30$ cells for control siRNA; $n = 30$ cells for CHMP4B siRNA. Bars, mean and s.d. *** $P < 0.0001$ derived from unpaired *t*-test. **f**, Immunoblots show efficient knockdown of endogenous CHMP1B (upper panel) and endogenous IST1 (lower panel). **g**, Deconvolved wide-field images of live anaphase HeLa cells stably co-expressing mCherry-spastin M87 with CHMP4B-eGFP, transfected with the indicated siRNA. Scale bars, 5 μ m. Images are representative of 46 cells for control siRNA; 14 cells for CHMP2A siRNA; 11 cells for CHMP1B siRNA; 31 cells for IST1 siRNA. **h**, Confocal images of HeLa cells stably co-expressing CHMP1B-Flag with CHMP4B-eGFP, transfected with control or CHMP2A siRNA, fixed and stained for DNA, CHMP4B-eGFP and IST1 (left panel) or CHMP1B-Flag (CHMP1B-FL) (right panel). Scale bars, 5 μ m. Images are representative of at least five captures for each condition.



Extended Data Figure 8 | ESCRT-III-dependent recruitment of spastin to the reforming NE mediates mitotic spindle disassembly. **a**, Immunoblot of whole-cell lysates showing the efficiency of endogenous spastin depletion by the indicated siRNAs. **b**, Residence time of CHMP4B localization at anaphase chromatin discs is increased in HeLa cells expressing inducible spastin M87^{E442Q} allele in addition to CHMP4B-eGFP. $n = 17$ cells for control (non-

induced); $n = 19$ cells for induced spastin M87^{E442Q}. Bars, mean with 95% confidence intervals. *** $P < 0.0001$ derived from unpaired t -test. **c**, HeLa cells stably expressing CHMP4B-eGFP were imaged every 20 s after anaphase onset. Taxol or DMSO was added in early anaphase. The percentage of cells with CHMP4B localized at chromatin discs was plotted over time. $n = 9$ cells for DMSO; $n = 12$ cells for Taxol. $P < 0.0001$ derived from unpaired t -test.



Extended Data Figure 9 | ESCRT-III dysfunction compromises nuclear integrity and leads to DNA damage and cell cycle arrest. **a**, hTERT RPE1 cells were transfected with the indicated siRNAs. Cells were then fixed and labelled for γ -H2AX and DNA. Images were collected on a high-content ScanR microscope and the mean fluorescence intensity of γ -H2AX foci was measured and the percentage of the population plotted. $n = 3,414$ cells for control siRNA; $n = 2,320$ for CHMP2A siRNA; $n = 3,410$ for VPS4A+B siRNA. Tukey whiskers extend from the largest value within 1.5 IQR of the upper quartile to the smallest value within 1.5 IQR of the lower quartile. *** $P < 0.0001$ derived from unpaired t -test. **b**, Confocal image of HeLa cells depleted for CHMP2A fixed and labelled for nuclear pore complex (anti-pan NPC) and 53BP1. Scale bar, 5 μ m. Image is representative of six captures. **c**, Immunoblot showing efficient knockdown of CHMP2A, VPS4A, VPS4B and CEP55 in hTERT RPE1

cells. Asterisk indicates non-specific immunoreactivity. **d**, Confocal images of hTERT RPE1 cells that were fixed 1 h or 5 h after exposure to ionizing radiation. Cells are labelled for DNA, γ -H2AX and CHMP4B. Scale bar, 5 μ m. Images are representative of five captures for control; seven captures for 2 Gy, 1 h; eight captures for 2 Gy, 5 h. **e**, Model for coordination of spindle disassembly and nuclear envelope sealing by ESCRT-III, VPS4 and spastin. During anaphase, ESCRT-III is recruited by CHMP7 to sites where the reforming NE engulfs spindle MTs. ESCRT-III recruits spastin M1 that is embedded in the engulfing NE as well as cytosolic spastin M87, which together promote MT disassembly. As such, ESCRT-III, VPS4 and spastin cooperate to coordinate progressive membrane constriction while severing MTs. Only when the surface of the reforming nucleus is cleared from spindle MTs can NE sealing occur.

ESCRT-III controls nuclear envelope reformation

Yolanda Olmos¹, Lorna Hodgson², Judith Mantell^{2,3}, Paul Verkade^{2,3,4} & Jeremy G. Carlton¹

During telophase, the nuclear envelope (NE) reforms around daughter nuclei to ensure proper segregation of nuclear and cytoplasmic contents^{1–4}. NE reformation requires the coating of chromatin by membrane derived from the endoplasmic reticulum, and a subsequent annular fusion step to ensure that the formed envelope is sealed^{1,2,4,5}. How annular fusion is accomplished is unknown, but it is thought to involve the p97 AAA-ATPase complex and bears a topological equivalence to the membrane fusion event that occurs during the abscission phase of cytokinesis^{1,6}. Here we show that the endosomal sorting complex required for transport-III (ESCRT-III) machinery localizes to sites of annular fusion in the forming NE in human cells, and is necessary for proper post-mitotic nucleocytoplasmic compartmentalization. The ESCRT-III component charged multivesicular body protein 2A (CHMP2A) is directed to the forming NE through binding to CHMP4B, and provides an activity essential for NE reformation. Localization also requires the p97 complex member ubiquitin fusion and degradation 1 (UFD1). Our results describe a novel role for the ESCRT machinery in cell division and demonstrate a conservation of the machineries involved in topologically equivalent mitotic membrane remodelling events.

The ESCRT-III complex performs a topologically unique membrane fusion, allowing the release of enveloped retroviruses during viral budding, intraluminal vesicles during multivesicular body biogenesis, and daughter cells during the abscission phase of cytokinesis^{7–11}. We found that as well as localizing to the midbody during late cytokinesis, endogenous ESCRT-III components CHMP2A and CHMP2B encircled the forming daughter nuclei during telophase (Fig. 1a, b and Extended Data Fig. 1a). CHMP2A localization was sensitive to CHMP2A-targeting short interfering RNA (siRNA; Extended Data Fig. 1b) and was not continuous; instead we found that CHMP2A adopted a transient punctate localization around the decondensing nuclei during telophase (Extended Data Fig. 1c and Supplementary Video 1). By scoring localization in HeLa cells stably expressing mCherry-tubulin (cell cycle of 21.5 ± 1.7 h (mean \pm s.d.), $n = 93$), we estimate the duration of CHMP2A localization to be 96 ± 8.9 s. We found cells expressing green fluorescent protein (GFP)-tagged CHMP4B (ref. 12) also displayed a transient, punctate, juxta-nuclear localization during telophase with recruitment of GFP-CHMP4B lasting 225 ± 66 s ($n = 8$) and individual puncta lasting 75 ± 46 s ($n = 92$; Extended Data Fig. 1d and Supplementary Video 2). Telophase ESCRT-III localization was observed in other cell lines, including human diploid fibroblasts (Extended Data Fig. 1e). Using HeLa cells stably expressing a yellow fluorescent protein (YFP)-tagged nuclear envelope marker (lamin associated protein 2 β , YFP-LAP2 β)¹³, we determined that the juxta-nuclear localization corresponded to the forming nuclear envelope. Here, we observed colocalization with the lamin B receptor (LBR)¹⁴ (Fig. 1c) and demonstrated that CHMP2A localization occurred before appreciable formation of a nuclear lamina or nuclear pore complexes (Extended Data Fig. 1f, g). While mitotic chromatin association of ESCRT-III has been previously reported¹⁵, its function remains unknown. To investigate the role of ESCRT components at the NE, we used siRNA to deplete these proteins¹⁶. As described previously¹⁷,

depletion of ESCRT components produced aberrant nuclei, and these defects phenocopied those produced by depletion of proteins required for NE reformation¹⁸ (Extended Data Fig. 1h). NE reformation is thought to be a two-phase process, separable into membrane fusion events that create an expanding reticular network with subsequent annular fusion of holes within this network to create a sealed barrier¹. We next used correlative light-electron microscopy (Extended Data Fig. 2a–d) to examine telophase ESCRT-III NE localization. We found that at the stage of ESCRT-III recruitment, the NE had incompletely formed (Fig. 1d). Two populations of CHMP2A-positive membranes were found. First, isolated CHMP2A-decorated vesicles were observed in the cytoplasm, proximal to the forming NE ($5.7 \pm 4.2\%$ of total cellular gold, Extended Data Fig. 2e, i). Second, CHMP2A-decorated double-membrane sheets were observed to coat the chromatin ($51 \pm 1.7\%$ of total cellular gold was within 100 nm of the NE). On these sheets, CHMP2A localized to discrete regions, with intact NE being devoid of label, but with CHMP2A preferentially (Extended Data Fig. 2h) decorating nucleocytoplasmic channels (mean diameter 38.4 ± 12.5 nm (\pm s.e.m.), $n = 2$ from 17 determinations) between the forming double membranes of the NE (Fig. 1d, Extended Data Figs 2d–g and 3a–d and Supplementary Videos 3 and 4). These channels must be resolved through annular fusion, and given the observed localization and topological equivalence with cytokinetic abscission (Fig. 1e), we speculated that ESCRT-III might be involved in this process.

Requirements for CHMP2A localization to the telophase NE were revealed through depletion of partner ESCRT proteins, with CHMP4B and CHMP3, as for other ESCRT-dependent membrane remodelling events, having a major role in this recruitment (Fig. 2a). We used siRNA-resistant Flag-tagged CHMP2A expressed at near-endogenous levels to report localization in the presence of CHMP2A siRNA (Fig. 2b, c). Through introduction of mutations targeting known binding partners, we found, as for midbody recruitment and cytokinetic abscission (Extended Data Fig. 4a, b), and consistent with the previously determined telophase localization of GFP-CHMP4B (Extended Data Fig. 1d), that while CHMP2A^R-Flag localized to the forming NE, disrupting interaction with CHMP4 proteins by mutation of Arg24, Arg27 and Arg31 to Ala (CHMP2A^R-Flag(RRR/AAA))¹⁶ abolished this localization. Mutation of the amino-terminal CHMP2A α_0 helix¹⁹, or residues involved in the interaction with VPS4 (ref. 16) had no effect on NE localization (Fig. 2c and Extended Data Fig. 4a). These data indicate that CHMP2A is recruited to the forming NE through classical assembly of the ESCRT-III complex.

The p97 AAA-ATPase controls both phases of NE reformation; together with its adaptor protein p47, it regulates membrane delivery and NE expansion, whereas through its adaptors nuclear protein localization 4 (NPL4) and UFD1 it regulates annular fusion⁶. Through NPL4 and UFD1, the p97 complex extracts ubiquitinated aurora-B, a chromosomal passenger complex component, from chromatin to allow chromatin decondensation and membranation^{20,21}. Given our observed ESCRT-III localization (Fig. 1) and known interactions of ESCRT-III components with the chromosomal passenger complex¹³, we screened the ESCRT machinery for interaction with the p97

¹Division of Cancer Studies, Section of Cell Biology and Imaging, King's College London, London SE1 1UL, UK. ²School of Biochemistry, University of Bristol, Medical Sciences Building, University Walk, Bristol BS8 1TD, UK. ³Wolfson Bioimaging Facility, University of Bristol, Medical Sciences Building, University Walk, Bristol BS8 1TD, UK. ⁴School of Physiology & Pharmacology, University of Bristol, Medical Sciences Building, University Walk, Bristol BS8 1TD, UK.

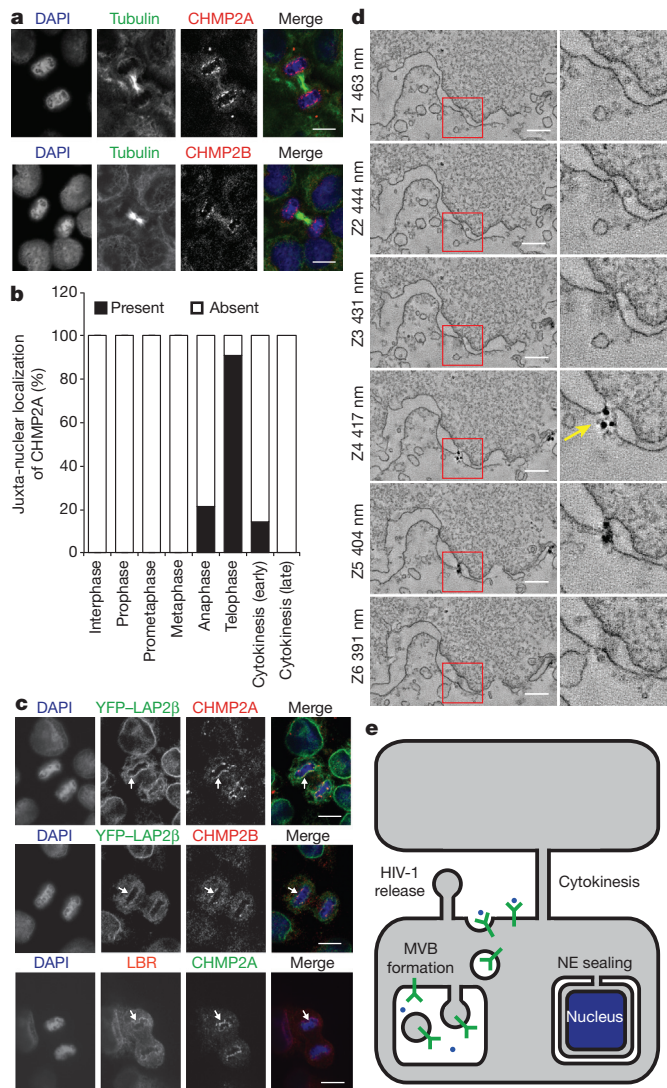


Figure 1 | ESCRT-III localizes to the forming nuclear envelope. **a**, HeLa cells stained with anti-tubulin, either anti-CHMP2A or anti-CHMP2B, and 4',6'-diamidino-2-phenylindole (DAPI). Scale bars, 10 μ m. Images representative of three acquired images in each case. **b**, Quantification of juxta-nuclear CHMP2A localization during mitosis from **a**, quantification from 20 cells in interphase, prophase, pro-metaphase and metaphase, 23 cells in anaphase, 24 cells in telophase, 36 cells in early cytokinesis and 20 cells in late cytokinesis. **c**, HeLa cells stained with DAPI, anti-CHMP2A or anti-CHMP2B, and either stably expressing YFP-LAP2 β or stained with anti-LBR. Arrows indicate regions of colocalization. Scale bars, 10 μ m. Images representative of two (anti-CHMP2B and YFP-LAP2 β , anti-LBR and anti-CHMP2A) or four (anti-CHMP2A and YFP-LAP2 β) acquired images. **d**, Tomographic slices of HeLa cells stained with fluoronogold anti-CHMP2A. Correlation depicted in Extended Data Fig. 2a–c; arrow indicates nucleo-cytoplasmic channel. Scale bars, 200 nm. Images representative of 25 gold-decorated nucleo-cytoplasmic channels and quantified in Extended Data Fig. 2h. **e**, Schematic depicting topological equivalence between annular fusion of the NE and ESCRT-dependent membrane fusion events. MVB, multivesicular body.

complex by yeast two-hybrid assay (Extended Data Fig. 5a–d). We found that CHMP2A bound specifically to UFD1 and confirmed this interaction by direct binding and co-precipitation assays (Fig. 3a, b and Extended Data Fig. 5e–h). We mapped the interaction with CHMP2A to the carboxy terminus of UFD1 (Extended Data Fig. 5f, g) and found that truncation of the C terminus of CHMP2A, or removal of the autoinhibitory helix (α 5), prevented interaction with UFD1 (Fig. 3a). We used siRNA targeting *UFD1* (also known as *UFD1L*) (Extended Data Fig. 6a); although its partner protein, p97,

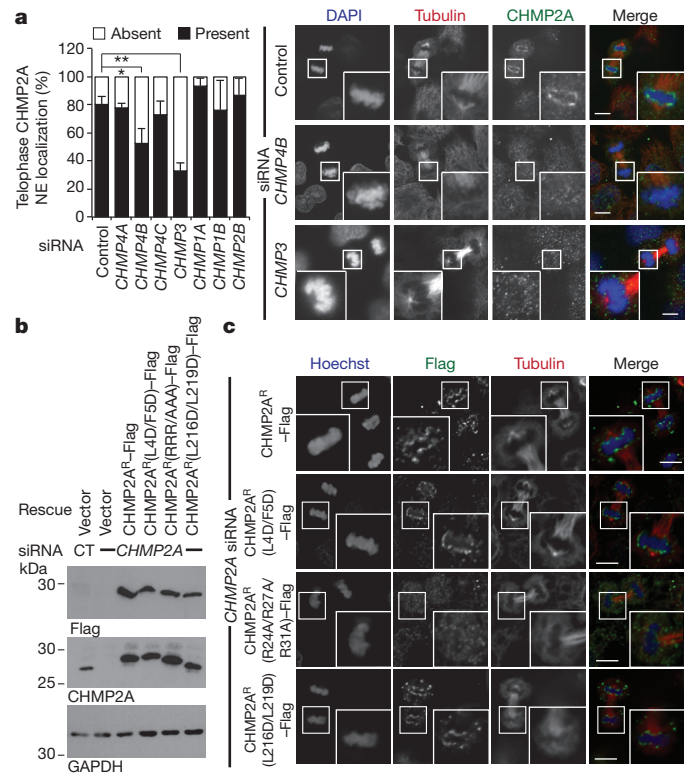


Figure 2 | Classical ESCRT interactions govern CHMP2A telophase NE localization. **a**, Immunofluorescence and quantification of NE localization in HeLa cells transfected with the indicated siRNA and stained with anti-CHMP2A, anti-tubulin and DAPI. Number of cells scored from 4 independent experiments: control, 58; CHMP4A, 59; CHMP4B, 55; CHMP4C, 53; CHMP3, 64; CHMP1A, 47; CHMP1B, 52; CHMP2B, 44. Data are mean \pm s.d. * P = 0.014, ** P = 0.0004 (two-tailed Student's t -test). Scale bars, 10 μ m. Images representative of 47 (control), 26 (CHMP4B siRNA) and 42 (CHMP3 siRNA) cells. **b**, Western blotting of lysates from siRNA-depleted HeLa cells stably expressing mCherry-tubulin and the indicated CHMP2A^R-Flag with anti-Flag, anti-CHMP2A or anti-GAPDH antisera. CT, control; kDa, kilodaltons. **c**, Immunofluorescence of CHMP2A^R-Flag recruitment to the telophase NE in CHMP2A-depleted cells. Scale bars, 10 μ m. Quantification in Extended Data Fig. 4a; images representative of 30 cells (control), 26 cells (L4D/F5D), 30 cells (RRR/AAA) and 26 cells (L216D/L219D).

was required for EGFR degradation²², we found cells depleted for UFD1 degraded EGFR normally (Extended Data Fig. 6b), allowed release of HIV-1-based lentivirus (Extended Data Fig. 6c), and completed cytokinesis normally as previously reported²¹ (Extended Data Fig. 6d). However, while cells depleted for UFD1 recruited CHMP2A to the midbody (Fig. 3d), recruitment of CHMP2A to the forming NE was impaired (Fig. 3c, d).

To examine mitotic roles for ESCRT-III in NE reformation, we imaged synchronized cultures of cells stably expressing both histone-2B-mCherry (H2B-mCh) and YFP-LAP2 β , and quantified the time taken to enclose the chromatin with YFP-LAP2 β -positive NE. We were surprised to find that cells lacking ESCRT-III, but not UFD1, enclosed their chromatin faster than control cells (Extended Data Fig. 7a–c). To explore the integrity of the nascent NE in CHMP2A-depleted cells, we followed a protocol similar to that recently described²³ and imaged synchronized cultures of HeLa cells stably expressing both H2B-mCh and GFP-tagged β -galactosidase (β Gal) fused to the nuclear localization signal (NLS) from Simian virus 40 (GFP-NLS- β Gal)²⁴. GFP-NLS- β Gal is released from the nucleus after NE breakdown at mitotic onset, and returned after formation of transport-competent nuclear pores during NE reformation (Extended Data Fig. 8a, b). We found that the rate of GFP-NLS- β Gal return to the nucleus was slower in ESCRT-III-depleted cells

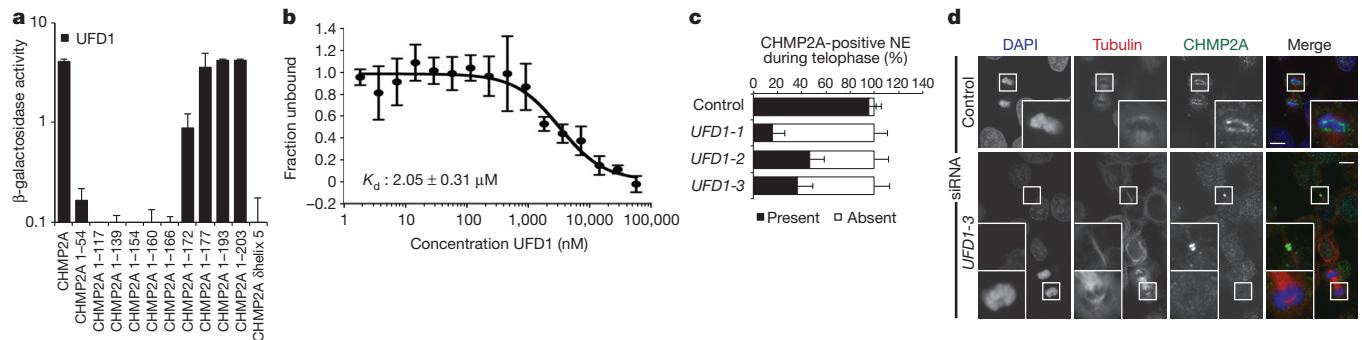


Figure 3 | UFD1 directs NE-localization of CHMP2A. **a**, β -galactosidase activity of yeast co-transformed with the indicated Gal4- and VP16-fused proteins ($n = 3$). **b**, Microscale thermophoresis experiments displaying interaction of histidine-tagged UFD1 with CHMP2A (fraction unbound displayed, $n = 5$). **c**, **d**, Immunofluorescence (**d**) and quantification (**c**) of NE

(Fig. 4a–c), despite the cells having enclosed their chromatin with NE membranes faster (Extended Data Fig. 7a). While nuclei were frequently malformed in ESCRT-III-depleted cells¹⁷ (Extended Data Fig. 1h), incorporation of nuclear pore complexes and import

localization (**c**: control, 35 cells; *UFD1-1*, 42 cells; *UFD1-2*, 25 cells; *UFD1-3*, 39 cells; data from 4 independent experiments) in HeLa cells transfected with the indicated siRNA and stained with anti-CHMP2A, anti-tubulin and DAPI. Scale bar, 10 μ m. Images representative of 23 cells (control), 34 cells (*UFD1-1*) 14 cells (*UFD1-2*) and 24 cells (*UFD1-3*). Data are mean \pm s.d.

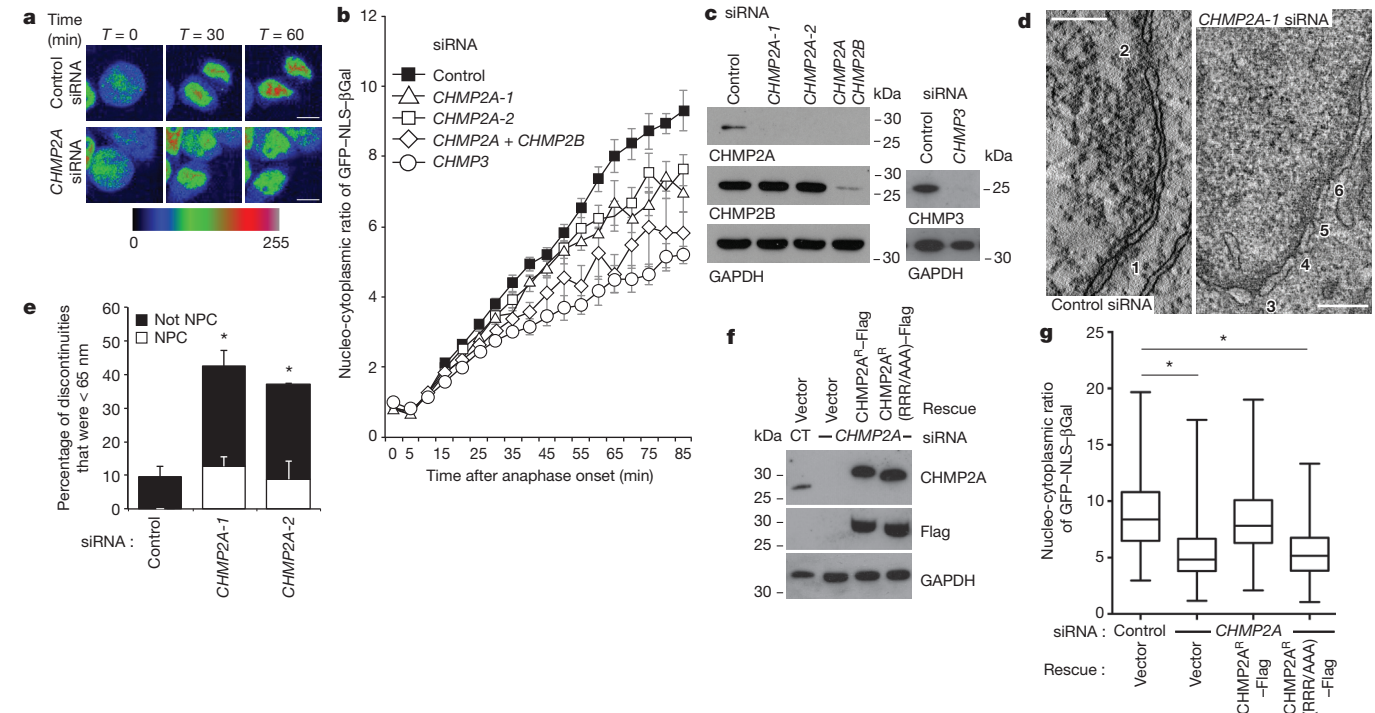


Figure 4 | ESCRT-III depletion disrupts nuclear envelope integrity.

a, Timelapse analysis of NE sealing in siRNA-transfected HeLa cells stably expressing H2B-mCh and GFP-NLS- β Gal. GFP signal presented according to pseudocolour scale at the indicated time points. Scale bars, 10 μ m. A single image was pseudocoloured for demonstrative purposes. **b**, Quantification of NE sealing from siRNA-treated cells in **a** (cells were quantified at each time point; control, 140 cells from 7 independent experiments; *CHMP2A-1*, 98 cells from 5 independent experiments, $P = 0.047$; *CHMP2A-2*, 80 cells from 4 independent experiments, $P = 0.023$; *CHMP2A* + *CHMP2B*, 60 cells from 3 independent experiments, $P = 0.006$; *CHMP3*, 34 cells from 3 independent experiments, $P = 0.002$. All values are mean \pm s.e.m.; two-tailed Student's t -test used to assess significance after 85 min). **c**, Western blotting of cell lysates from **b** with anti-CHMP2A, anti-CHMP2B, anti-CHMP3 or anti-GAPDH antisera. **d**, Z-slices extracted from a correlative tomographic reconstruction of the NE at 60 min after anaphase onset from the indicated siRNA-transfected mCherry-tubulin HeLa cells. The numbered circles correspond to discontinuities labelled in the 3D reconstructions in Extended Data Fig. 10a. Scale bars, 200 nm. Images representative of 6 (control) and 12 (*CHMP2A-1* siRNA) tomographic

reconstructions. **e**, The percentage of discontinuities smaller than 65 nm was scored. Discontinuities in this range that were not nuclear pore complexes (NPCs) as a percentage of total discontinuities (including NPCs) for n number of reconstructed tomograms: control, 9.4 ± 3.0 , $n = 6$; *CHMP2A-1*, 29.9 ± 4.7 , $P = 0.01$, $n = 12$; *CHMP2A-2*, 28.3 ± 2.0 , $P = 0.021$, $n = 2$. The increase in the percentage of non-NPC discontinuities was assessed by two-tailed Student's t -test (average diameter of non-NPC discontinuities was 38 ± 22 nm (*CHMP2A-1*) and 58 ± 19 nm (*CHMP2A-2*)). **f**, Western blotting of lysates from siRNA-treated HeLa cells stably expressing H2B-mCh, GFP-NLS- β Gal and siRNA-resistant *CHMP2A*^R-Flag with anti-CHMP2A, anti-Flag or anti-GAPDH antisera. **g**, Quantification of NE sealing from cells treated with siRNA as in **f** and imaged from 4 independent experiments (mean nucleocytoplasmic ratio given 85 min after anaphase onset \pm s.d., two-tailed Student's t -test was used to assess significance across 4 independent experiments (*); control, 8.9 ± 3.1 , $n = 174$; *CHMP2A* siRNA, 5.4 ± 2.6 , $n = 171$, $P = 0.0006$; *CHMP2A* siRNA + *CHMP2A*^R-Flag, 8.4 ± 3.3 , $n = 132$, not-significant; *CHMP2A* siRNA + *CHMP2A*^R(RRR/AAA)-Flag, 5.4 ± 2.2 , $n = 196$, $P = 0.0001$).

was compromised by treatments that prevent ESCRT-III assembly at the NE. Results were confirmed with a second reporter (GFP-NLS) (Extended Data Fig. 9c) and we demonstrated that nuclear retention of this probe was defective in post-mitotic ESCRT-III-depleted cells (Extended Data Fig. 9d, e). Using correlative live-cell electron tomography, we found that CHMP2A depletion resulted in the persistence of unsealed holes in the post-mitotic NE (Fig. 4d, e and Extended Data Fig. 10a, b). Paralleling CHMP2 requirements in lentiviral release and cytokinetic abscission (Extended Data Figs 6c and 9f), depletion of CHMP2B had minimal effect on NE integrity (Extended Data Fig. 9a, b), while co-depletion of CHMP2A and CHMP2B disrupted NE integrity to a greater extent than CHMP2A depletion alone (Fig. 4b). NE integrity could be rescued by stable expression of siRNA-resistant CHMP2A-Flag (CHMP2A^R-Flag), but, as with CHMP2A requirements in cytokinesis (Extended Data Fig. 4b) and HIV-1 release¹⁶, not by expression of CHMP2A^R-Flag(RRR/AAA) (Fig. 4f, g). We describe a novel localization and function of ESCRT-III in NE remodelling at sites of annular fusion, a process markedly similar to classical ESCRT-III-mediated membrane remodelling (Extended Data Fig. 10c). Localization is governed by classical ESCRT-III assembly mechanisms and also requires UFD1. An equivalent ESCRT-III-dependent membrane remodelling at the NE may allow viruses or megaRNPs to traverse this membrane^{25–27}, and in yeast, ESCRT-III has recently been shown to participate in surveillance and extraction of defective nucleoporins at the inner nuclear membrane²⁸, indicating additional ESCRT-III activities on this membrane may exist throughout the cell cycle. ESCRT-III is thus involved in regulating the quality of the NE, and gene expansion within the ESCRT machinery may have resulted from an evolutionary drive to accommodate open mitoses.

Online Content Methods, along with any additional Extended Data display items and Source Data, are available in the online version of the paper; references unique to these sections appear only in the online paper.

Received 24 June 2014; accepted 27 April 2015.

Published online 3 June 2015.

- Burke, B. The nuclear envelope: filling in gaps. *Nature Cell Biol.* **3**, E273–E274 (2001).
- Anderson, D. J. & Hetzer, M. W. Shaping the endoplasmic reticulum into the nuclear envelope. *J. Cell Sci.* **121**, 137–142 (2008).
- Schooley, A., Vollmer, B. & Antonin, W. Building a nuclear envelope at the end of mitosis: coordinating membrane reorganization, nuclear pore complex assembly, and chromatin de-condensation. *Chromosoma* **121**, 539–554 (2012).
- Burke, B. & Ellenberg, J. Remodelling the walls of the nucleus. *Nature Rev. Mol. Cell Biol.* **3**, 487–497 (2002).
- Lu, L., Ladinsky, M. S. & Kirchhausen, T. Formation of the postmitotic nuclear envelope from extended ER cisternae precedes nuclear pore assembly. *J. Cell Biol.* **194**, 425–440 (2011).
- Hetzer, M. *et al.* Distinct AAA-ATPase p97 complexes function in discrete steps of nuclear assembly. *Nature Cell Biol.* **3**, 1086–1091 (2001).
- McCullough, J., Colf, L. A. & Sundquist, W. I. Membrane fission reactions of the mammalian ESCRT pathway. *Annu. Rev. Biochem.* **82**, 663–692 (2013).
- Carlton, J. G., Agromayor, M. & Martin-Serrano, J. Differential requirements for Alix and ESCRT-III in cytokinesis and HIV-1 release. *Proc. Natl Acad. Sci. USA* **105**, 10541–10546 (2008).
- Carlton, J. G. & Martin-Serrano, J. Parallels between cytokinesis and retroviral budding: a role for the ESCRT machinery. *Science* **316**, 1908–1912 (2007).
- Elia, N., Sougrat, R., Spurlin, T. A., Hurley, J. H. & Lippincott-Schwartz, J. Dynamics of endosomal sorting complex required for transport (ESCRT) machinery during cytokinesis and its role in abscission. *Proc. Natl Acad. Sci. USA* **108**, 4846–4851 (2011).
- Morita, E. *et al.* Human ESCRT and ALIX proteins interact with proteins of the midbody and function in cytokinesis. *EMBO J.* **26**, 4215–4227 (2007).
- Jouvenet, N., Zhadina, M., Bieniasz, P. D. & Simon, S. M. Dynamics of ESCRT protein recruitment during retroviral assembly. *Nature Cell Biol.* **13**, 394–401 (2011).
- Carlton, J. G., Caballe, A., Agromayor, M., Kloc, M. & Martin-Serrano, J. ESCRT-III governs the Aurora B-mediated abscission checkpoint through CHMP4C. *Science* **336**, 220–225 (2012).
- Clever, M., Funakoshi, T., Mimura, Y., Takagi, M. & Imamoto, N. The nucleoporin ELYS/Mel28 regulates nuclear envelope subdomain formation in HeLa cells. *Nucleus* **3**, 187–199 (2012).
- Stauffer, D. R., Howard, T. L., Nyun, T. & Hollenberg, S. M. CHMP1 is a novel nuclear matrix protein affecting chromatin structure and cell-cycle progression. *J. Cell Sci.* **114**, 2383–2393 (2001).
- Morita, E. *et al.* ESCRT-III protein requirements for HIV-1 budding. *Cell Host Microbe* **9**, 235–242 (2011).
- Morita, E. *et al.* Human ESCRT-III and VPS4 proteins are required for centrosome and spindle maintenance. *Proc. Natl Acad. Sci. USA* **107**, 12889–12894 (2010).
- Asencio, C. *et al.* Coordination of kinase and phosphatase activities by Lem4 enables nuclear envelope reassembly during mitosis. *Cell* **150**, 122–135 (2012).
- Buchkovich, N. J., Henne, W. M., Tang, S. & Emr, S. D. Essential N-terminal insertion motif anchors the ESCRT-III filament during MVB vesicle formation. *Dev. Cell* **27**, 201–214 (2013).
- Ramadan, K. *et al.* Cdc48/p97 promotes reformation of the nucleus by extracting the kinase Aurora B from chromatin. *Nature* **450**, 1258–1262 (2007).
- Dobrynin, G. *et al.* Cdc48/p97-Ufd1-Npl4 antagonizes Aurora B during chromosome segregation in HeLa cells. *J. Cell Sci.* **124**, 1571–1580 (2011).
- Ritz, D. *et al.* Endolysosomal sorting of ubiquitylated caveolin-1 is regulated by VCP and UBXD1 and impaired by VCP disease mutations. *Nature Cell Biol.* **13**, 1116–1123 (2011).
- Anderson, D. J. & Hetzer, M. W. Reshaping of the endoplasmic reticulum limits the rate for nuclear envelope formation. *J. Cell Biol.* **182**, 911–924 (2008).
- Sorg, G. & Stamminger, T. Mapping of nuclear localization signals by simultaneous fusion to green fluorescent protein and to β -galactosidase. *Biotechniques* **26**, 858–862 (1999).
- Lee, C.-P. *et al.* The ESCRT machinery is recruited by the viral BFRF1 protein to the nucleus-associated membrane for the maturation of Epstein–Barr Virus. *PLoS Pathog.* **8**, e1002904 (2012).
- Pawliczek, T. & Crump, C. M. Herpes simplex virus type 1 production requires a functional ESCRT-III complex but is independent of TSG101 and ALIX expression. *J. Virol.* **83**, 11254–11264 (2009).
- Speese, S. D. *et al.* Nuclear envelope budding enables large ribonucleoprotein particle export during synaptic Wnt signaling. *Cell* **149**, 832–846 (2012).
- Webster, B. M., Colombi, P., Jäger, J. & Lusk, C. P. Surveillance of nuclear pore complex assembly by ESCRT-III/Vps4. *Cell* **159**, 388–401 (2014).

Supplementary Information is available in the online version of the paper.

Acknowledgements J.G.C. is a Wellcome Trust Research Career Development Fellow. We acknowledge the Nikon Imaging Centre at KCL and the NIHR Comprehensive Biomedical Research Centre at Guy's and St Thomas' NHS Foundation Trust for access to core equipment. We thank the staff of the Wolfson Bioimaging Facility for their support. We thank J. Martin-Serrano for gifts of plasmids and cells.

Author Contributions J.G.C. conceived the study. P.V., L.H. and J.M. designed, performed and analysed electron microscopy experiments. J.G.C. and Y.O. designed, performed and analysed data from other experiments. J.G.C. wrote the manuscript with assistance from all other authors.

Author Information Reprints and permissions information is available at www.nature.com/reprints. The authors declare no competing financial interests. Readers are welcome to comment on the online version of the paper. Correspondence and requests for materials should be addressed to J.G.C. (jeremy.carlton@kcl.ac.uk).

METHODS

Cell culture. HeLa and 293T cells were gifts from J. Martin-Serrano and were cultured in DMEM containing 10% FBS, penicillin (100 U ml^{-1}) and streptomycin (0.1 mg ml^{-1}). GP2-293 cells were obtained from Clontech and were cultured similarly. BJ fibroblasts were obtained from the ATCC and cultured in 4:1 DMEM:199 Media, supplemented with 15% FCS, penicillin (100 U ml^{-1}) and streptomycin (0.1 mg ml^{-1}). Stable cell lines were generated by transduction using MLV-based retroviruses as described previously⁹, and selected using Puromycin (200 ng ml^{-1}), G418 ($500 \text{ } \mu\text{g ml}^{-1}$) or hygromycin ($200 \text{ } \mu\text{g ml}^{-1}$) as necessary. Cells were sorted to monoclonality by limiting dilution or FACS. HeLa cells stably expressing mCherry-tubulin²⁹ or GFP-CHMP4B (ref. 12) have been described previously and were gifts from J. Martin-Serrano. MycoSensor (Agilent) was used to screen for contamination.

Plasmids. Plasmids encoding *TSG101*, *EAP20* (also known as *VPS25*), *EAP30* (*SNF8*), *EAP45* (*VPS36*), *CHMP1A*, *CHMP1B*, *CHMP2A*, *CHMP2B*, *CHMP3*, *CHMP4A*, *CHMP4B*, *CHMP4C*, *CHMP5*, *VPS4A*, *LIP5* (*VTA1*), *UBPY*, *CEP55*, *TAL*, *LAP2B* (*TMPO*) and *ALG2* were gifts from J. Martin-Serrano and have been described previously^{8,9,13,30}. Coding sequences for *p97* (also known as *VCP*), *p47* (*NSFL1C*), *NPL4* (*NPOC4*), *UFD1*, *CHMP7*, *VPS4B* and *SPARTIN* (*SPG20*) were amplified from IMAGE clones (6502535, 3635947, 5017718, 3507963, 5551762, 6042862 and 5313378), respectively, and were cloned into mammalian expression (pCR3.1-YFP) and yeast two-hybrid plasmids (pHB18 and pGBKT7). A plasmid encoding HD-PTP was a gift from P. Woodman and was cloned similarly. siRNA-resistant *CHMP2A* constructs were created by introducing Gln132Gln, Ala133Ala, Glu134Glu, Ile135Ile and Asp137Asp silent mutations in the *CHMP2A* coding sequence by PCR. 5' EcoRI and 3' NotI sites were added to facilitate cloning. Additional *CHMP2A* truncations, mutations and deletions were created by standard PCR procedures. *UFD1* and its deletions were cloned with 5' and 3' NotI sites into relevant expression vectors. *CHMP2A* constructs were subcloned into pGBKT7 and *UFD1* constructs were cloned into pHB18 for yeast two-hybrid analysis. For recombinant protein expression, *CHMP2A* was cloned into pGEX (GE Healthcare) and *UFD1* constructs were cloned into pET28a (Novagen). For glutathione S-transferase (GST)-pulldown experiments, constructs were cloned into pCAGGS-GST-EcoRI-NotI-XhoI (a gift from J. Martin-Serrano). A lentiviral expression vector (pLVXP) was a gift from M. Dodding and modified to express a GFP-EcoRI-NotI-XhoI polylinker by replacing its SnaBI/XbaI fragment with a GFP-EcoRI-XhoI-NotI-STOP-XbaI fragment, obtained by PCR from pCR3.1-GFP-EcoRI-XhoI-NotI (a gift from J. Martin-Serrano). SnaBI/XhoI fragments of pHM840 (encoding GFP-NLS-βGal and obtained from T. Stamminger via Addgene) were cloned into the SnaBI/XhoI sites of pLVXP-GFP-ENX to produce pLVXP-GFP-NLS-βGal. pLVXP-GFP-NLS was obtained by amplifying GFP using primers to incorporate a C-terminal SV40 NLS.

A SnaBI/NotI fragment from pH2B-mCherry-IRES-Neo3 (a gift from U. Eggert) was subcloned into SnaBI/NotI sites of pLHCX-MCS (a modified version of pLHCX containing a HindIII/MluI/SalI/XhoI/NotI/HpaI/BamHI/NsiI/ClaI MCS; a gift from T. Ng) to create pLHCX-H2B-mCh. *LAP2B* residues 244–454 were amplified with in-frame NotI sites and cloned into the NotI site of pMSCVneo-YFP-EXN to create pMSCVneo-YFP-LAP2β. siRNA-resistant *CHMP2A* constructs were cloned with C-terminal Flag extensions into EcoRI and NotI sites of pCR3.1-EXN and subcloned into pNG72-ENX (gifts from J. Martin-Serrano).

For retroviral transduction, above constructs within pMSCVneoYFP-EXN, pNG72 or pLHCX-MCS retroviral packaging vectors were transfected with pVSVG into GP2-293 cells (all from Clontech). Supernatants were collected, clarified by centrifugation (200g, 5 min), filtered (0.45 μm) and used to infect target cells in the presence of $8 \text{ } \mu\text{g ml}^{-1}$ polybrene (Millipore) at multiplicity of infection (MOI) < 1. For lentiviral transduction, 293T cells were transfected with pCMV8.91, pVSVG and with pLVXP-GFP-NLS-βGAL or pLVXP-GFP-NLS. Supernatants were collected, clarified by centrifugation (200g, 5 min), filtered (0.45 μm) and used to infect target cells in the presence of $8 \text{ } \mu\text{g ml}^{-1}$ polybrene (Millipore) at MOI < 1. In both cases, antibiotic selection was applied after 48 h.

Antibodies. Antibodies against HSP90 (H114) were from Santa Cruz Biotechnology, TSG101 (T5701) was from Sigma, GAPDH (MAB374) was from Millipore, tubulin (DM1A) was from Sigma, CHMP2A (104771-AP) was from Proteintech, CHMP2B (ab33174) was from Abcam, CHMP4B (sc82556) was from Santa Cruz, CHMP3 (sc67228) was from Santa Cruz, UFD1 (106151-AP) was from Proteintech, anti-p24 Gag (183-H12-5C) was from the NIH AIDS Research and Reference Reagent Program, EGFR (2232) was from Cell Signaling Technology, GFP (7.1/13.1) was from Roche, LBR (SAB10400151) was from Sigma, Lamin A/C (MAB3538) was from Millipore, mAb414 was from Covance, DYKDDDDK-Tag (Flag) was from Cell Signaling Technology. Alexa-conjugated secondary antibodies were from Invitrogen and horseradish peroxidase (HRP)-conjugated secondary antibodies were from Millipore.

SDS-PAGE and western blotting. Cell lysates were denatured in Laemmli buffer and resolved using SDS-PAGE gels. Resolved proteins were transferred onto nitrocellulose by western blotting and were probed with the indicated antisera in 5% milk. HRP-conjugated secondary antibodies were incubated with ECL Prime enhanced chemiluminescent substrate (GE Healthcare) and visualized by exposure to autoradiography film.

Transient transfection of cDNA. HeLa cells were transfected using Lipofectamine-2000 (Life Technologies) according to the manufacturer's instructions. GP2-293 and 293T cells were transfected using linear 25-kDa polyethylenimine (PEI, Polysciences, Inc.).

siRNA transfections. Cells were seeded at a density of 1×10^5 cells per ml (HeLa, BJ) or 2.6×10^5 cells per ml (293T) and were transfected with siRNA at 100 nM, 2 h after plating using Dharmafect-1 (Dharmacon). To minimize toxicity associated with CHMP2A and UFD1 depletion, single transfections were performed for 72 h. The following targeting sequences that have already been demonstrated to achieve potent and specific suppression of the targeted *CHMP* were used: control, Dharmacon non-targeting control D-001810-01. *CHMP2A-1*: AGGCAGAGAU CAUGGAUAUdTdT¹⁶; *CHMP2A-2*: AAGAUGAAGAGGAGAGUGAdTdT¹⁷; *CHMP2B*: UCGAGCAGCUUAGAGAAAdTdT¹⁷; *CHMP3*: GGAAGAAGCA GAAUGGAAdTdT¹⁷; *CHMP4A*: Q-SI04268845 (ref. 13), *CHMP4B*: Q-SI0032 5199 (ref. 13); *CHMP4C*: Q-SI04279674 (ref. 13); *CHMP1A*: CCAAGAAGG CGGAGAAGGAAdTdT¹⁷; *CHMP1B*: UGGACAAUUCGAGCACCAdTdT¹⁷; *UFD1-1*: GAGGCAGAUUCGUCGUUdTdT; *UFD1-2*: MQ-017918-03-0002; *UFD1-3*: GUGGCCACCUACUCCAAAUdTdT³¹; *LEM4*: GAGAAGACGCUGA GAAAUUdTdT¹⁸. *UFD1-2* was excluded from much of the analysis owing to toxicity and morphological changes specific to this oligonucleotide.

Yeast two-hybrid assays. Yeast Y190 cells were co-transformed with plasmids encoding the indicated proteins fused to the VP16 activation domain (pHB18) or the Gal4 DNA-binding domain (pGBKT7). Co-transformants were selected on SD-Leu-Trp agar for 3 days at 30 °C, collected, and *LacZ* activity was measured using a liquid β-galactosidase assay using chlorophenolred-β-D-galactopyranoside (Roche) as a substrate. Average β-galactosidase activities presented.

Lentiviral release. 293T cells were transfected with siRNA as described above, except that the second transfection contained additionally 300 ng of HIV-1 pCMVd8.91 (a gift from T. Ng), 100 ng of pLenti-SEW (a packaging vector encoding GFP, a gift from A. Ridley) and 100 ng pVSVG. After 48 h, virions were collected from 293T supernatants by filtration (0.45 μm) and centrifugation through 20% sucrose (21,000g, 120 min), lysed, resolved by SDS-PAGE and examined by western blotting. Additionally, HeLa cells were infected with 50 μl of viral supernatant and GFP-expression in these cells was measured by western blotting. Virion release was calculated by quantifying $\text{Gag}^{\text{virion}}/\text{Gag}^{\text{cellular}}$ as determined densitometry using ImageJ.

Co-precipitation assays. 293T cells were co-transfected equal quantities of the indicated pCAGGS-GST construct and the relevant pCR3.1-YFP construct for 48 h. Cells were collected and lysed in 1 ml of 50 mM Tris-HCl, pH 7.4, 150 mM NaCl, 5 mM EDTA, 5% glycerol, 1% Triton X-100, a protease inhibitor mixture (complete mini-EDTA-free, Roche). Clarified lysates were incubated with glutathione-Sepharose beads (Amersham Biosciences) for 3 h at 4 °C and washed three times with wash buffer (50 mM Tris-HCl, pH 7.4, 150 mM NaCl, 5 mM EDTA, 5% glycerol, 0.1% Triton X-100). Bead-bound proteins were recovered in Laemmli sample buffer, resolved by SDS-PAGE and examined by western blotting.

Production of recombinant proteins. BL21(DE3) *Escherichia coli*-expressing plasmids encoding GST-tagged or His-tagged proteins were collected in bacterial lysis buffer (20 mM Hepes, pH 7.4, 500 mM NaCl, supplemented with complete mini, EDTA-free protease inhibitor (Roche) and 1 mM phenylmethylsulfonyl fluoride (PMSF); buffers for His-tagged protein purification were supplemented with 20 mM imidazole. Cells were lysed by addition of lysisosyme (1 mg ml^{-1} , 15 min), Triton X-100 (0.25%, 15 min) and were snap-frozen in liquid nitrogen. Cells were thawed on ice, clarified through addition of DNase1 ($20 \text{ } \mu\text{g ml}^{-1}$) and soluble proteins were collected by centrifugation at 28,000g for 30 min. Proteins were immobilised on Glutathione Sepharose 4β or Ni-NTA-sepharose resin, washed in wash buffer (20 mM Hepes, pH 7.4, 150 mM NaCl), containing 20 mM imidazole if required. Proteins were eluted from Glutathione Sepharose 4β resin in wash-buffer supplemented with 10 mM reduced glutathione (pH 8), or were eluted from Ni-NTA sepharose with a step gradient of imidazole. CHMP2A was cleaved from the GST using AcTEV protease (Life Technologies). Protein concentrations were measured using the Qubit assay system (Life Technologies).

Microscale thermophoresis. Measurements were performed using a Monolith NT.115 instrument (Nanotemper). In brief, recombinant CHMP2A was labelled with Alexa-647 using an NHS Amine-reactive labelling kit (Nanotemper), labelling was verified by infrared imaging (Licor). 360 nM Alexa-647 CHMP2A was combined with serial dilutions of GST, His-UFD1 or His-UFD1(1–257) (maximally 52.8 μM). Interactions were performed in 150 mM NaCl, 20 mM Hepes,

0.04% Tween-20, pH 7.4. Temperature jump and thermophoresis experiments were conducted using 100% LED illumination and 40% infrared laser power and were analysed using Nanotemper's analysis suite. Binding curves could only be generated for the CHMP2A:UFD1 interaction, affinities were calculated by the software and averaged.

Fixed cell imaging. Cells were imaged using Nikon Eclipse microscopes teamed with widefield (Ti-E) and confocal (A1R or Spinning Disc) imaging systems. Widefield image stacks were iteratively deconvolved using Autoquant. Images were processed in NIS Elements and exported to Photoshop for assembly. HeLa cells were fixed in methanol (for CHMP2A staining) or 4% paraformaldehyde (PFA) and subject to processing for immunofluorescence as described previously⁹. For multinucleation and midbody arrest assays, at least 300 cells per experiment were quantified. For telophase NE localization, between 10 and 20 telophase cells per experiment were scored. For fixed cell microscopical analysis, we scanned multiple coverslips and experiments before acquiring two to three representative images for presentation in figures.

Live cell imaging. HeLa cells stably expressing the indicated proteins were plated in Stickyslides (Ibidi) adhered to a glass number 1 coverslip and transfected with the indicated siRNA. Cells were synchronised using a double thymidine block, and 48 h after siRNA transfection (10.5 h after release from the second thymidine block), cells were transferred to a Nikon inverted spinning disc confocal microscope with attached environmental chamber and imaged live for 4 h using a 20× dry objective and a 1.5× magnification lens. For mitotic rim formation, three coordinates per condition were selected and frames were acquired every 1 min, rim formation was scored through manual analysis of individual frames. For nuclear accumulation of GFP-NLS and GFP-NLS-βGal, frames were acquired every 1 min. The ratio of background-corrected, area-normalized, GFP-positive pixel intensities within the cytoplasm and mCh-H2B demarcated nuclei at the indicated intervals were obtained using NIS-elements. We excluded 2 out of 98 cells from CHMP2A-1 analysis, 2 out of 60 cells from UFD1-1 analysis and 2 out of 60 cells from UFD1-3 analysis as these gave anomalous *N/C* (nuclear/cytoplasmic) ratios >10× s.d. from the mean. For imaging of GFP-CHMP4B recruitment to the telophase NE, cells were imaged using a 100× oil-immersion objective and confocal slices were acquired every 30 s using a spinning disc confocal microscope. For analysis of nuclear retention, siRNA-treated HeLa cells stably expressing GFP-NLS and mCh-H2B were imaged live using a Nikon A1R confocal microscope. Between 1 and 2 h after anaphase onset, cells were subject to photo-ablation of cytosolic GFP-NLS signal by point bleaching and the recovery of cytoplasmic fluorescence from the nuclear pool was quantified for 10 min after bleaching.

Correlative light electron microscopy. Around 500,000 HeLa cells were seeded in a 3.5-cm Mattek gridded dish (P35G-2-14-C-GRID). The next morning, cells were fixed in phosphate buffer containing 1% PFA for 3 min. Cells were permeabilized with 0.1% saponin in PHEM (60 mM PIPES, 25 mM HEPES, 10 mM EGTA, 2 mM MgCl₂, pH 6.9) and processed for immunofluorescence using anti-CHMP2A primary and goat anti-rabbit Alexa-594-conjugated fluoronano-

gold (Nanoprobes) and DAPI. Cells were subjected to a subsequent 10-min 3% PFA fixation and quenching before imaging on a Leica SP5 or SP8 confocal microscope.

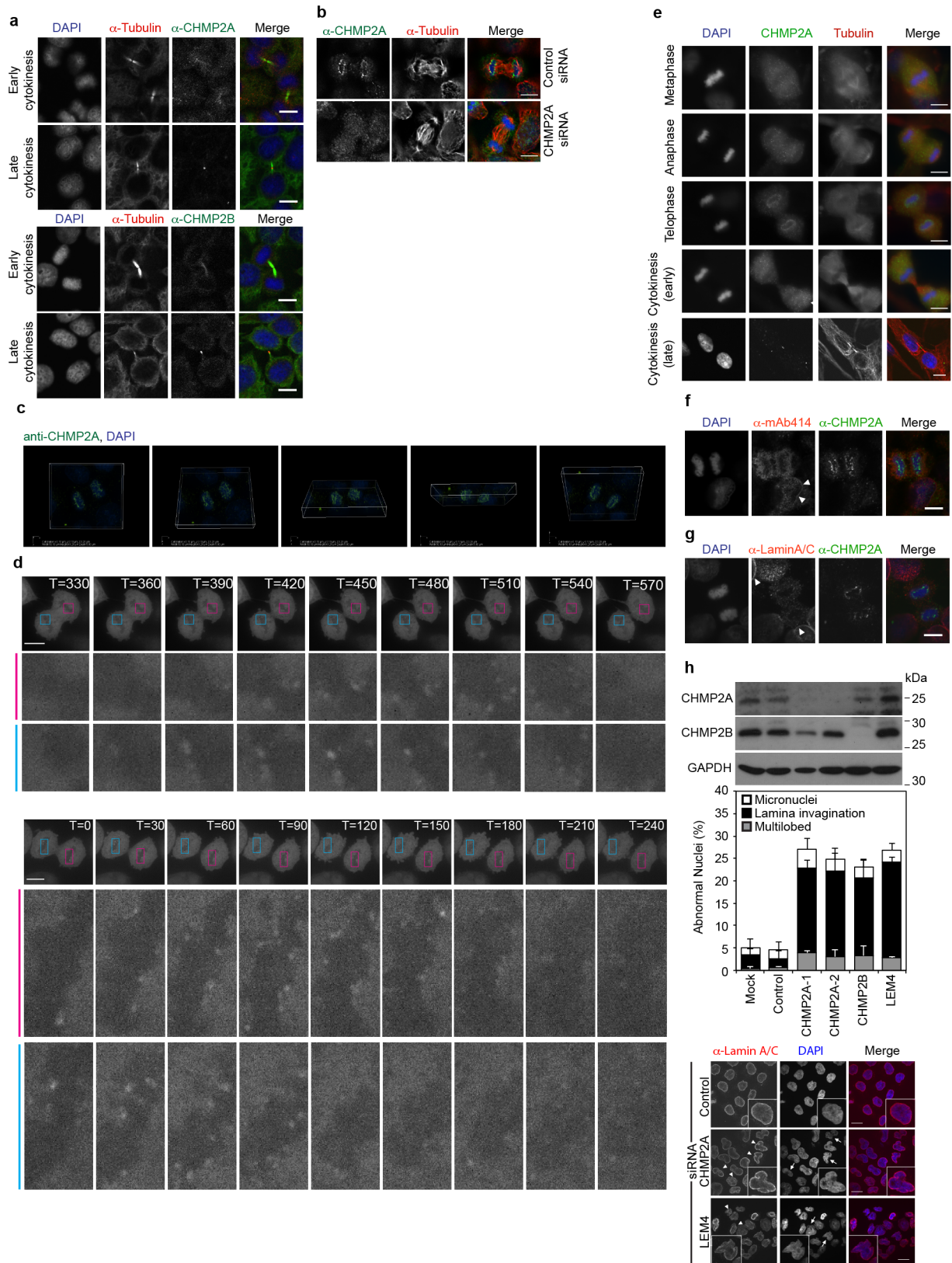
After fluorescent imaging, cells were postfixed in glutaraldehyde, subjected to silver enhancement (Aurion RGENT SE-EM), stained with OsO₄ and uranyl acetate, dehydrated through ethanol and embedded in Epon. Blocks were trimmed to the region identified by confocal imaging and 300-nm serial sections were cut using a diamond knife³². For retracing of the cells of interest, sections were imaged on a FEI Tecnai12 and subsequently double tilt series of regions of interest were acquired on a FEI Tecnai20. Tilt series were reconstructed using iMOD and selected frames and movies were extracted using ImageJ.

For quantification of holes remaining in the NE after CHMP2A depletion, tomograms were acquired by CLEM as described above. Discontinuities in the NE were scored as being NPC or non-NPC on the basis of cross-sectional morphology. Internal diameters of these discontinuities were measured from reconstructed tomograms using FIJI. Discontinuities were segregated by size and whether they were identifiable as NPCs or not. A threshold was set at 65 nm (>2 s.d. smaller than the measured control NPC diameter) and the percentage of discontinuities smaller than this was displayed. At least 50 discontinuities were analysed per treatment across multiple cells from the indicated number of tomograms.

Statistical analysis. Variance was analysed using an *F*-test, and type-relevant two-tailed Student's *t*-tests were used to assess significance between test samples and controls. No statistical methods were used to predetermine sample size. The experiments were not randomized, and the investigators were not blinded to allocation during experiments and outcome assessment.

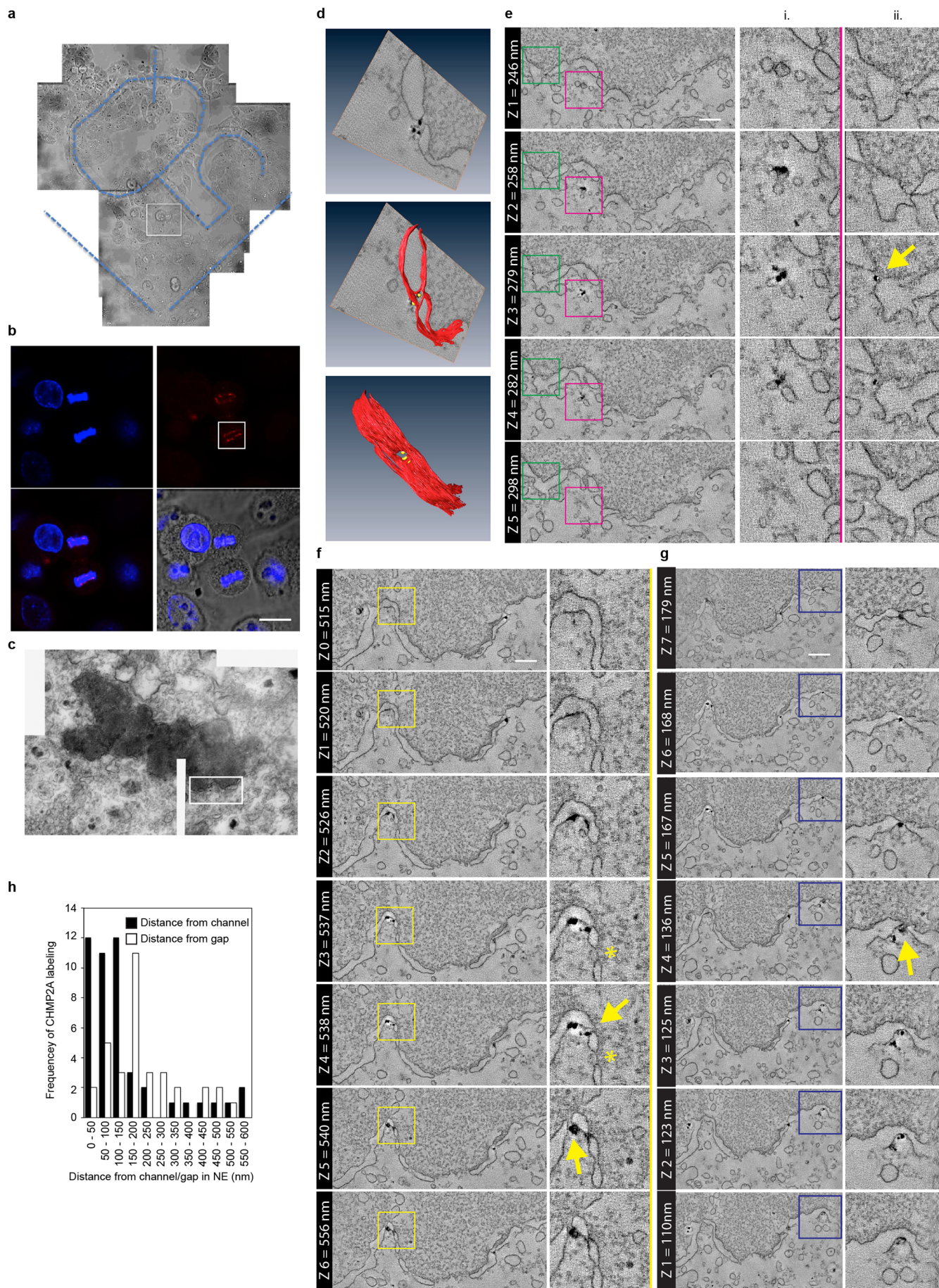
ImageStream analysis. siRNA-treated HeLa cells in 6-well dishes were detached, fixed in 4% PFA, permeabilized with 0.1% Triton X-100 and stained in suspension with mAb414, Alexa-594-conjugated secondary antibodies and DAPI (at 0.1 µg ml⁻¹). In-focus, single-cellular populations were acquired and a mask was applied to the DAPI channel and duplicated then dilated by three pixels to encompass the mAb414 signal surrounding the nuclei. The difference in the mAb414 signal captured by these masks was given as the nuclear envelope mAb414 and presented as a histogram. Representative images of average mAb414 intensity were extracted for presentation.

29. Agromayor, M. *et al.* Essential role of H1ST1 in cytokinesis. *Mol. Biol. Cell* **20**, 1374–1387 (2009).
30. Martin-Serrano, J., Yarovoy, A., Perez-Caballero, D., Bieniasz, P. D. & Yarovoy, A. Divergent retroviral late-budding domains recruit vacuolar protein sorting factors by using alternative adaptor proteins. *Proc. Natl Acad. Sci. USA* **100**, 12414–12419 (2003).
31. Meerang, M. *et al.* The ubiquitin-selective segregase VCP/p97 orchestrates the response to DNA double-strand breaks. *Nature Cell Biol.* **13**, 1376–1382 (2011).
32. van Weering, J. R. T. *et al.* Intracellular membrane traffic at high resolution. *Methods Cell Biol.* **96**, 619–648 (2010).



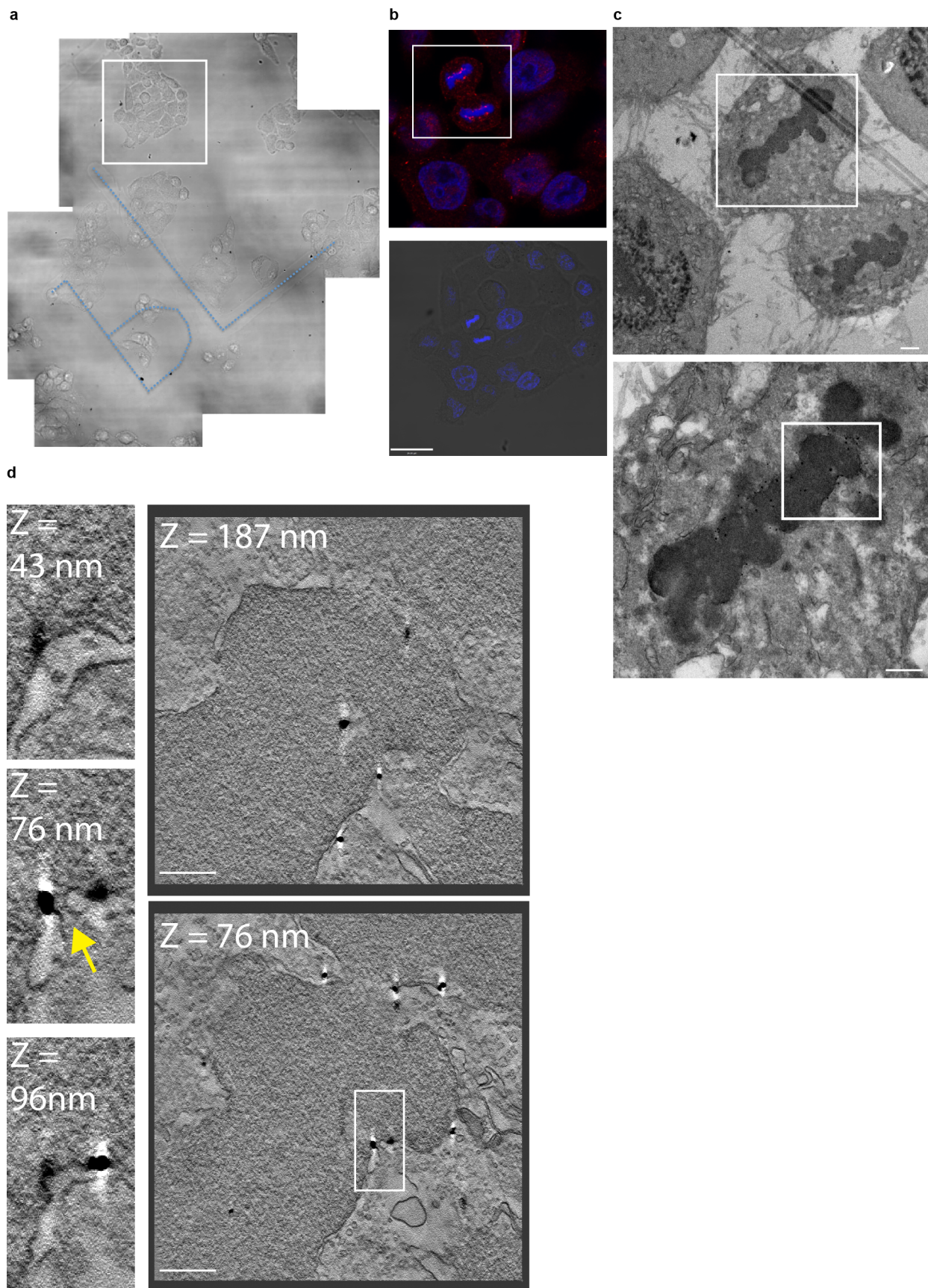
Extended Data Figure 1 | Localization of ESCRT components during the cell cycle. **a, b**, Immunofluorescence analysis of HeLa cells stained with anti-tubulin, anti-CHMP2A or anti-CHMP2B and DAPI (**a**). Images in **a** are representative of two acquired images per field of view. Cells in **b** were treated with control or *CHMP2A*-targeting siRNA; images representative of four (control) or two (*CHMP2A* siRNA) acquired images. **c**, Deconvolved projections of HeLa cells stained with anti-CHMP2A and DAPI, corresponding to stills from Supplementary Video 1. Images representative of two deconvolved image series. **d**, HeLa cells stably expressing GFP-CHMP4B were imaged live during the anaphase to telophase transition. Telophase frames at 30-s intervals are presented, corresponding to stills from Supplementary Video 2. Images representative of four acquisitions. **e**, Immunofluorescence analysis of human diploid fibroblasts stained with anti-CHMP2A, anti-tubulin and

DAPI, images representative of three acquired cells per cell cycle phase. **f, g**, Immunofluorescence analysis of HeLa cells stained with anti-CHMP2A, DAPI and either anti-mAb414 (**f**) or anti-LaminA/C (**g**), images representative of five acquired cells. Arrowheads indicate regions of formed nuclear pores or lamina as indicated. **h**, Quantification of abnormal nuclei (the presence of multiple lobes, micronuclei, lamina ingression or invagination) in HeLa cells transfected with the indicated siRNA and stained with anti-LaminA/C (1,300 cells over 5 experiments quantified per treatment; data are mean \pm s.d.). Images representative of three (control, *CHMP2A* siRNA) or two (*LEM4* siRNA) acquired fields of view and resolved cell lysates were examined by western blotting with anti-CHMP2A, anti-CHMP2B or anti-GAPDH antisera as indicated. Scale bars, 10 μ m.



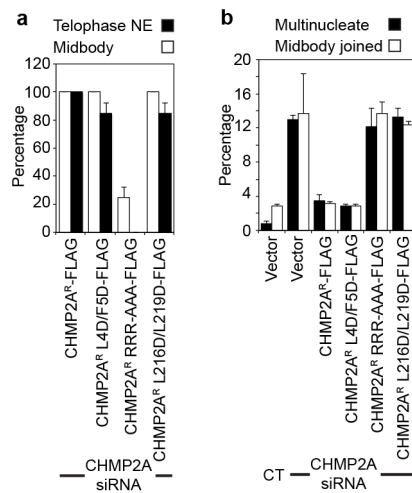
Extended Data Figure 2 | Correlative light and electron microscopy (CLEM) of endogenous CHMP2A localization in telophase NE. **a–c**, Phase-contrast (**a**), correlative immunofluorescence (**b**) and transmission electron microscopy of HeLa cells stained with anti-CHMP2A, detected by Alexa-594-fluoronanogold and DAPI. Boxed region in **a** is shown in **b**; boxed region in **b** is shown in **c**. In all cases, images representative of three cells prepared for CLEM. **d**, 3D rendering of tomographic reconstruction of forming NE from boxed region in **c** and Fig. 1d; a single example of a nucleo-cytoplasmic channel was selected for 3D rendering. **e–g**, Z-slices extracted from tomographic reconstructions of forming NE depicting CHMP2A localization to isolated vesicles (**e**, i) and nucleo-cytoplasmic channels (arrows in **e**, ii, **f**, **g**) at the

indicated Z-heights. Localization of CHMP2A to nucleo-cytoplasmic channels was observed in three independent cells; data from a second cell are presented in Extended Data Fig. 3. Note CHMP2A localization to nucleo-cytoplasmic channels is distinct from nuclear pores (asterisk in **f**). **h**, Quantification of CHMP2A labelling from two independently prepared cells. Channels were defined as discontinuities up to 80 nm, and gaps were defined as discontinuities over 80 nm. Distances of the gold-particles from channels or gaps were measured on the tomograms in three-dimensions and plotted as a histogram. Most (74.4%) of the gold label was found within 150 nm of nucleo-cytoplasmic channels, and most (70.6%) of the gold label was found more than 150 nm from the larger gaps in the NE. Scale bars, 10 μ m (**b**) and 200 nm (**f**, **g**).

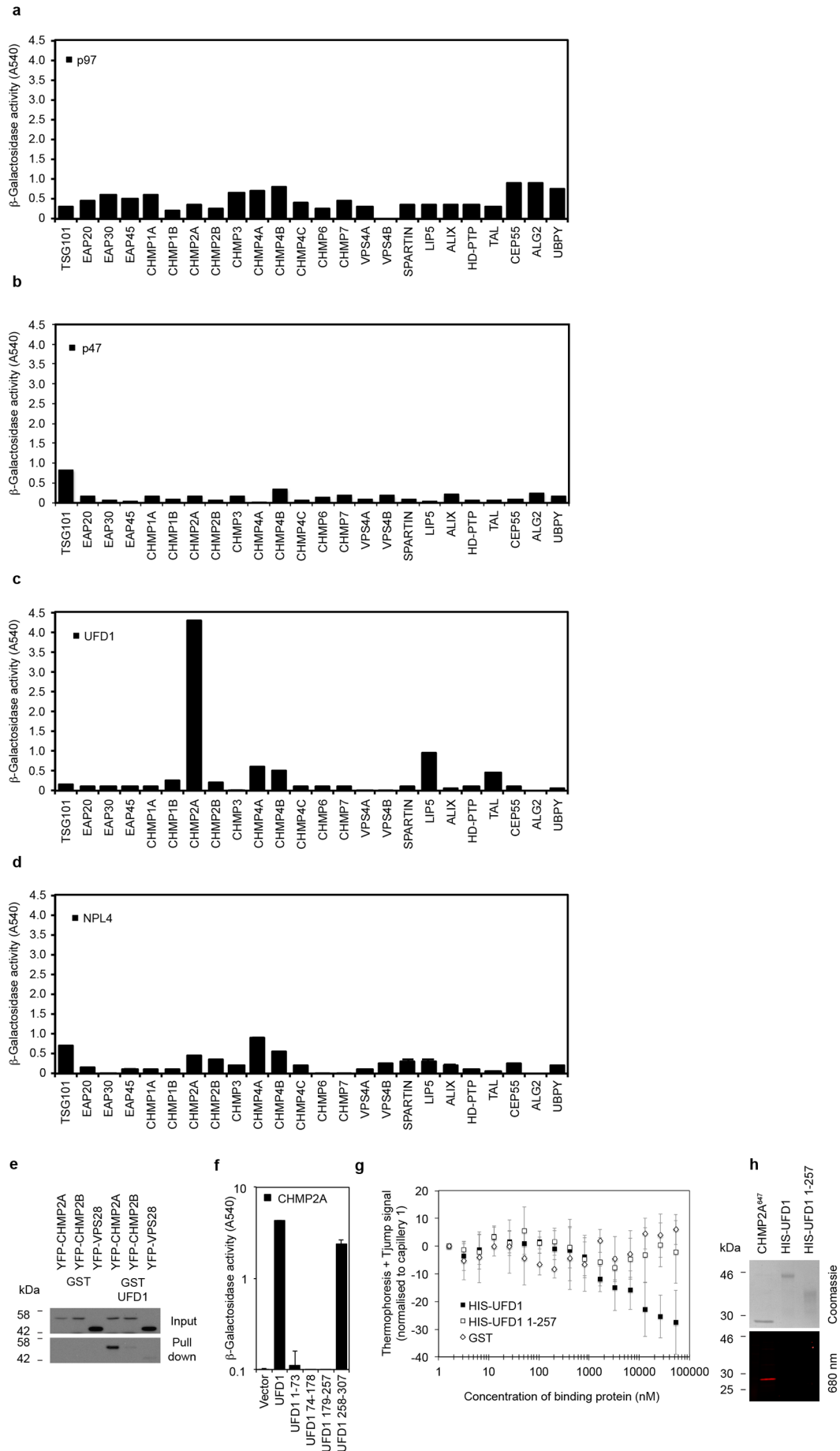


Extended Data Figure 3 | CLEM of endogenous CHMP2A localization in telophase NE. **a–c**, Phase-contrast (**a**), correlative immunofluorescence (**b**) and transmission electron microscopy (**c**) of a second HeLa cell stained with anti-CHMP2A, detected by Alexa-594-fluoronanogold and DAPI. Boxed region in **a** is shown in **b**; boxed region in **b** is shown in **c**. **d**, Z-slices extracted from tomographic reconstruction of forming NE from boxed region in

c depicting CHMP2A-localization to nucleo-cytoplasmic channels at the indicated Z-heights. Arrow indicates nucleo-cytoplasmic channel. Images in all cases representative of 3 cells processed for CLEM, quantification of gold localization given in Extended Data Fig. 2H. Scale bars, 24 μm (**b**), 1 μm (**c**) and 200 nm (**d**).

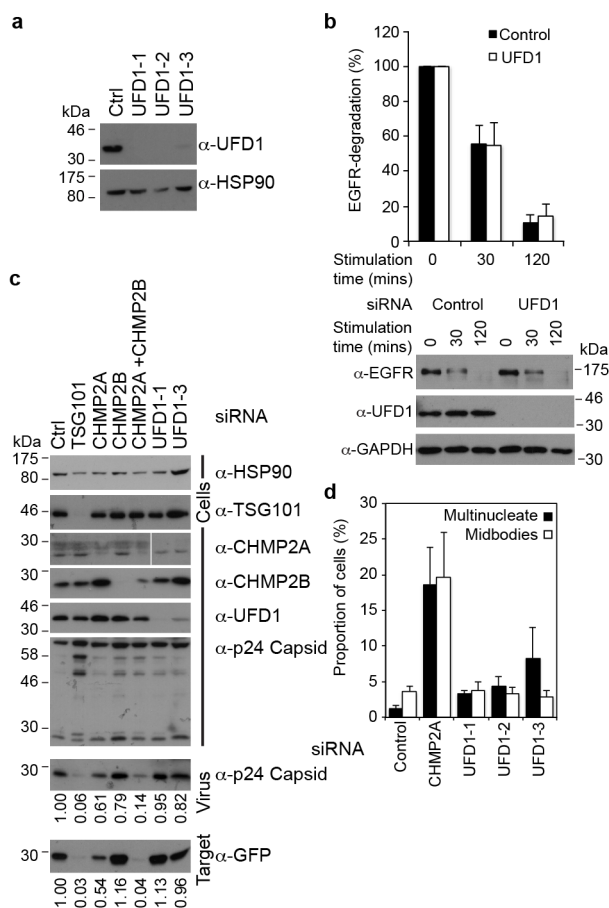


Extended Data Figure 4 | Mitotic defects in cells reliant on mutated forms of CHMP2A. **a**, Quantification of CHMP2A recruitment to the telophase NE or the midbody from Fig. 2c ($n = 3$, 10 cells (midbody or telophase) scored per experiment). **b**, Quantification of cytokinetic failure from cells treated with the indicated siRNA (300 cells were quantified per experiment, from three independent experiments). Data are mean \pm s.d.



Extended Data Figure 5 | Screening for ESCRT-p97 complex interactions. **a–d**, β -galactosidase activity of yeast co-transformed with the indicated Gal4 (ESCRT)- and VP16-fused proteins ($n = 2$). **e**, Resolved cell lysates and glutathione-bound fractions from 293T cells transfected with the indicated fusion proteins were examined by western blotting with anti-GFP ($n = 3$). **f**, β -galactosidase activity of yeast co-transformed with the indicated Gal4- and VP16-fused proteins ($n = 3$). **g**, Microscale thermophoresis experiments

detailing binding of CHMP2A to GST ($n = 4$), His-UFD1 ($n = 5$) or His-UFD1(1–257) ($n = 4$). As no reduction in thermophoresis signal was observed for GST or His-UFD1(1–257) across the concentration range, we present here the average thermophoresis signal change at equivalent protein concentrations for these three proteins, normalized to zero at the concentration in capillary 1. **h**, Alexa-647-labelled CHMP2A, His-UFD1 and His-UFD1(1–257) were examined by infrared imaging or Coomassie staining. Data are mean \pm s.d.



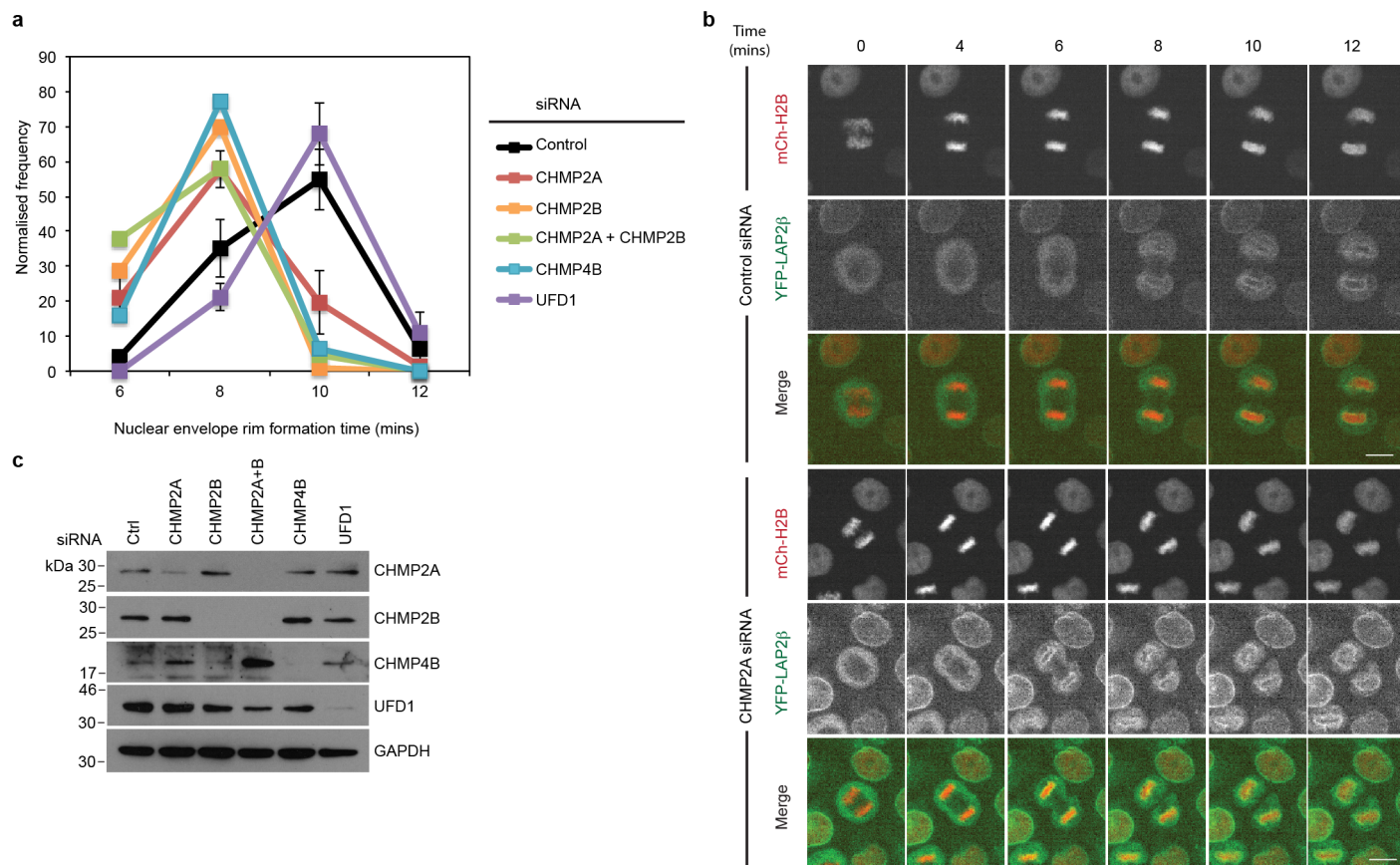
Extended Data Figure 6 | UFD1 depletion does not affect ESCRT-dependent receptor degradation, lentivirus release or cytokinetic abscission.

a, Resolved cell lysates of HeLa cells transfected with the indicated siRNA were examined by western blotting with anti-UFD1 or anti-HSP90 antisera.

b, Resolved lysates of human diploid fibroblasts transfected with the indicated siRNA and treated for the indicated times with epidermal growth factor (20 ng ml^{-1}) were examined by western blotting with anti-EGFR, anti-UFD1 and anti-GAPDH antisera. EGFR degradation was quantified by densitometry ($n = 3$).

c, Resolved cell lysates from 293T cells transfected with the indicated HIV-1 based lentiviral plasmids, a virally packaged GFP-plasmid, and the indicated siRNA were examined by western blotting with anti-p24 capsid, -HSP90, -TSG101, -CHMP2A, -CHMP2B and -UFD1 antibodies. Viral supernatants were collected and used to infect target HeLa cells. Resolved virions present in the 293T supernatant were examined by western blotting with anti-p24 capsid. Resolved lysates of infected HeLa cells were examined by western blotting with anti-GFP. Virion release was the ratio of released to cellular p24 capsid, as quantified by densitometry ($n = 2$); infectivity was quantified as GFP signal in target cells, as quantified by densitometry ($n = 2$).

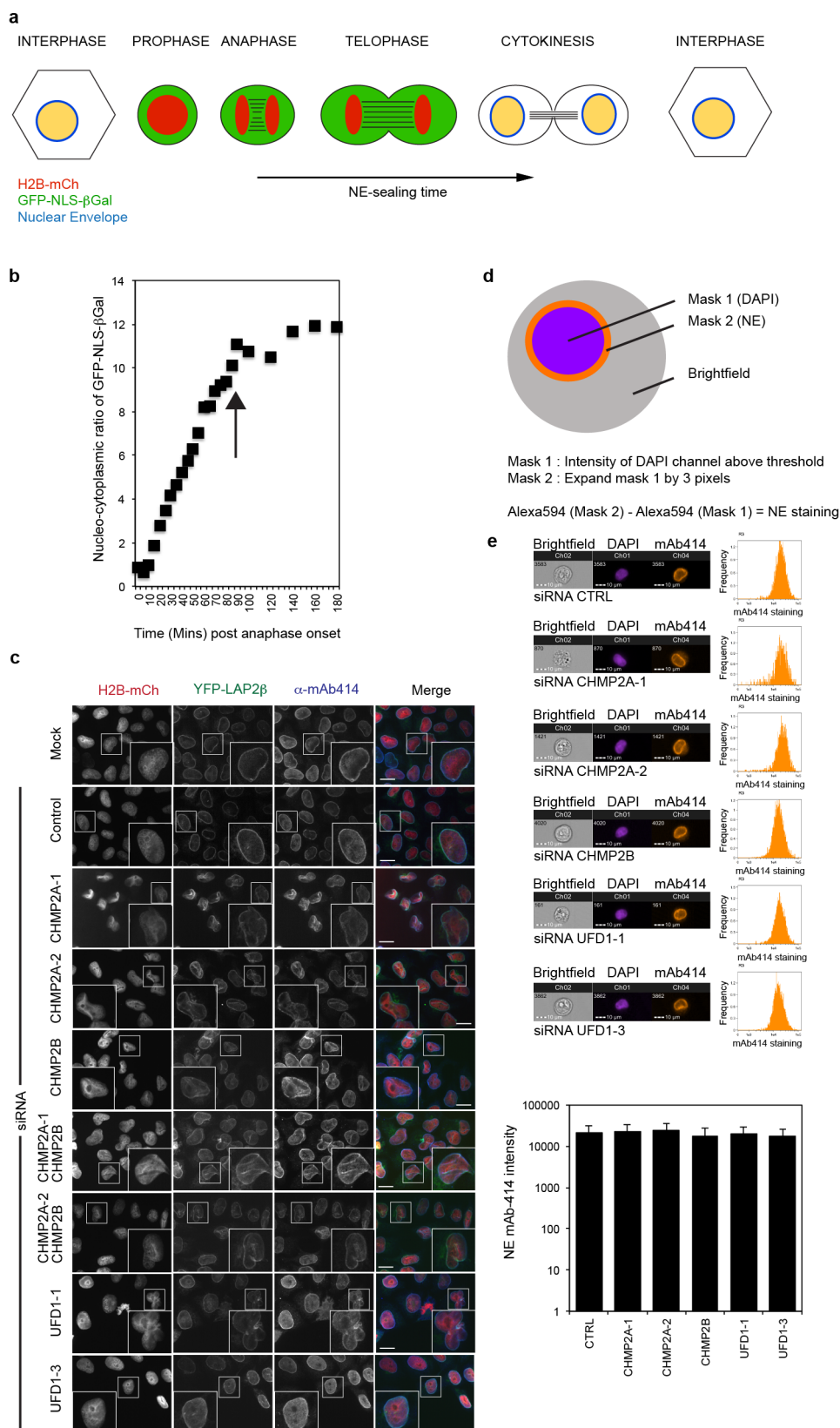
d, siRNA-transfected HeLa cells were fixed and stained with anti-tubulin. Multinucleate cells ($n = 5$) or cells connected by midbodies ($n = 5$) were scored visually, 300 cells scored per experiment. Data are mean \pm s.d.



Extended Data Figure 7 | ESCRT depletion impairs NE-rim formation.

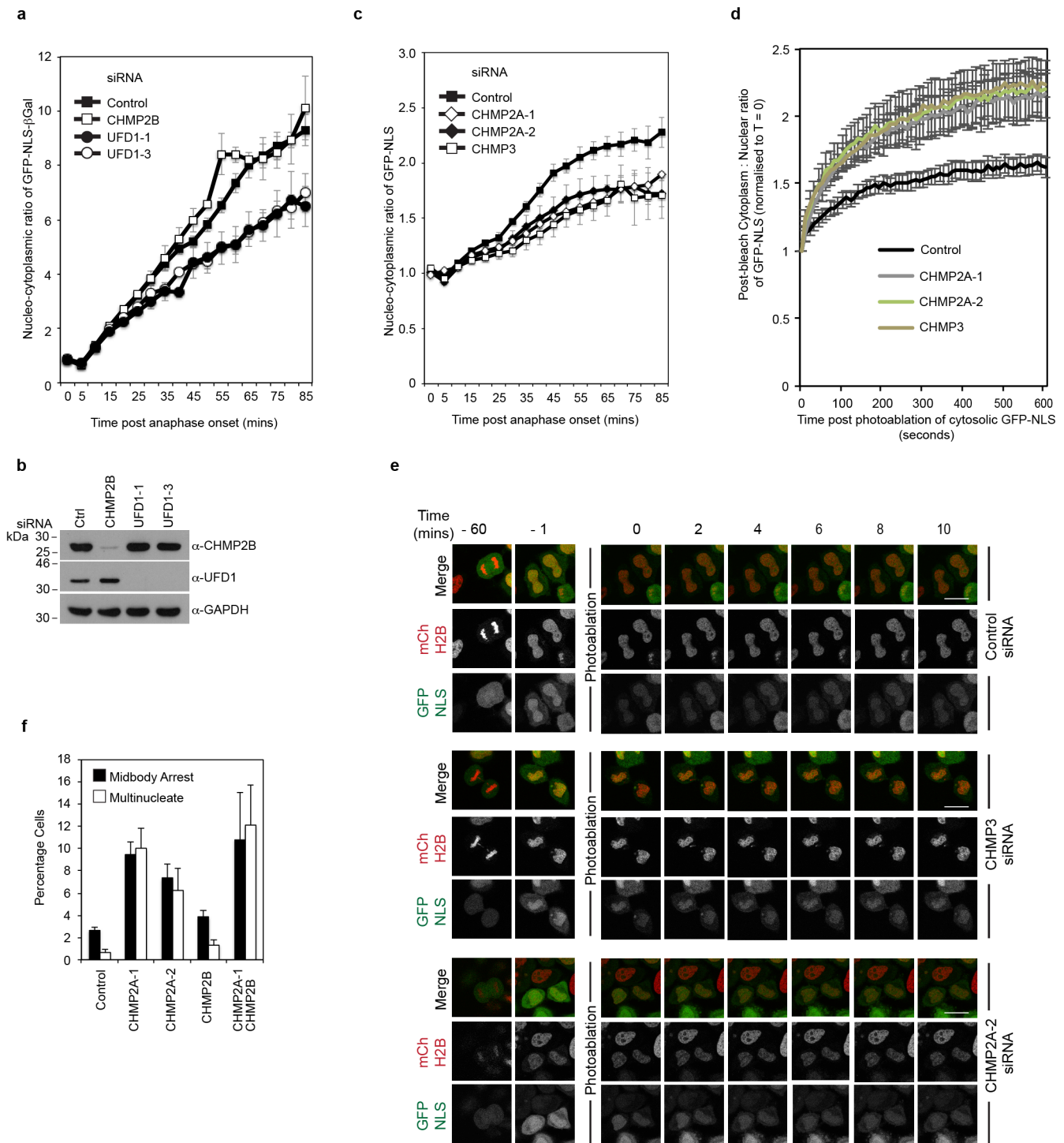
a, b, Timelapse microscopy analysis and quantification of NE-rim formation in HeLa cells stably expressing YFP-LAP2 β and mCh-H2B and treated with the indicated siRNA. Scale bars, 10 μ m. Time for rim formation post anaphase onset given (mins) (control, 8.53 ± 0.09 , 226 cells analysed over 8 independent experiments; CHMP2A-1, 7.60 ± 0.09 , 205 cells analysed over 7 independent experiments; CHMP2A-2, 6.86 ± 0.12 , 37 cells analysed over 2 independent

experiments; CHMP2B, 6.92 ± 0.09 , 79 cells analysed over 4 independent experiments; CHMP2A and CHMP2B, 6.84 ± 0.13 , 50 cells analysed over 2 independent experiments; CHMP4B, 7.07 ± 0.14 , 44 cells analysed over 2 independent experiments; UFD1, 9.2 ± 0.18 , 39 cells analysed over 3 independent experiments). Data are mean \pm s.e.m. (in minutes). Images representative of the indicated number of cell analysed. **c**, Resolved cell lysates from **a** were analysed by western blotting with the indicated antisera.



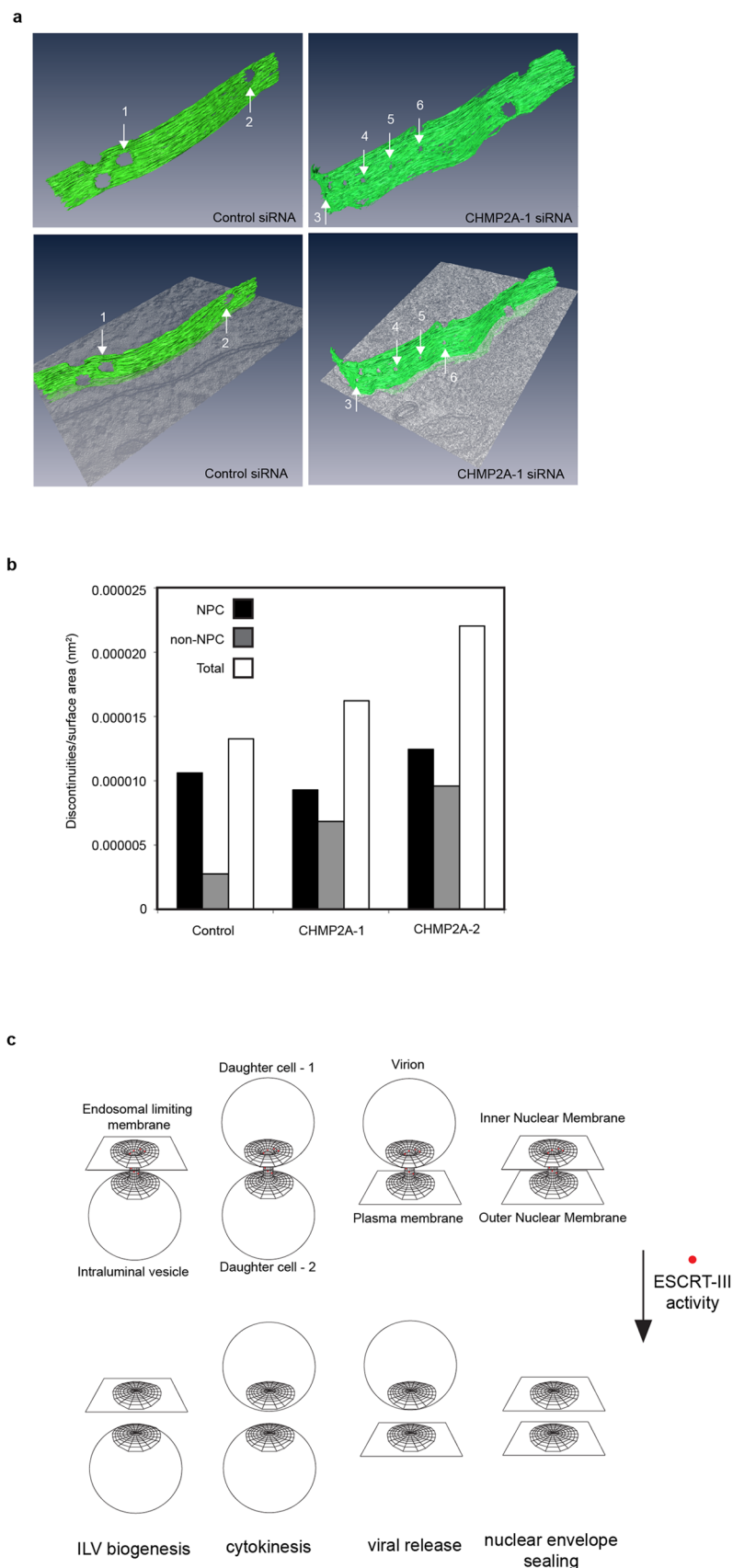
Extended Data Figure 8 | ESCRT depletion does not impair nuclear pore formation. **a**, Schematic of nuclear envelope integrity assay. **b**, Control-siRNA-treated HeLa cells reporting nucleo-cytoplasmic partitioning using the GFP-NLS- β Gal assay, average NE compartmentalization from 20 cells presented. Nucleo-cytoplasmic partitioning stabilizes at 85 min (indicated by arrow). **c**, Immunofluorescence analysis of HeLa cells stably expressing YFP-LAP2 β , transfected with the indicated siRNA then stained with anti-mAb414 and DAPI ($n = 3$). Scale bars, 10 μ m. **d**, Mask used to quantify nuclear pore

formation by image-based flowcytometry (Imagestream). **e**, Imagestream analysis of HeLa cells transfected with the indicated siRNA, then stained with anti-mAb414 and DAPI. Nuclear pore intensity quantified by mask described in **d**. Representative images from two independent experiments, histogram and population averages displayed, graphical quantification of NPC intensity from the indicated number of gated cells (control, 3,045; CHMP2A-1, 1,256; CHMP2A-2, 2,152; CHMP2B, 5,237; UFD1-1, 4,146; UFD1-3, 4,325). Data are mean \pm s.d.



Extended Data Figure 9 | Requirements for nucleo-cytoplasmic compartmentalization. **a**, Quantification of NE sealing from siRNA-treated cells as in Fig. 4b (control, 140 cells from 7 independent experiments; UFD1-1, 60 cells from 3 independent experiments, $P = 0.044$; UFD1-3, 60 cells from 3 independent experiments, $P = 0.021$; CHMP2B 40 cells from 2 independent experiments; two-tailed Student's t -test was used to assess significance at the 85-min time point). **b**, Resolved cell lysates from **a** were analysed by western blotting with the indicated antisera. **c**, NE integrity assay as performed with cells stably expressing mCh-H2B and GFP-NLS and transfected with the indicated siRNA. Differences in nucleo-cytoplasmic partitioning was assessed after plateau at the 65-min time point using a two-tailed Student's t -test (control, 79 cells from 4 independent experiments, $P = 0.048$; CHMP2A-1, 60 cells from 3 independent experiments, $P = 0.048$; CHMP2A-2, 52 cells from 3 independent experiments, $P = 0.011$; CHMP3, 28 cells from 3 independent experiments,

$P = 0.028$). **d**, **e**, HeLa cells stably expressing mCh-H2B and GFP-NLS were transfected with the indicated siRNA and imaged live. 60 min after anaphase onset, cytoplasmic signal was photo-ablated ($T = 0$) and recovery of cytoplasmic signal from the nuclear pool was calculated for the indicated conditions (cytoplasmic:nuclear ratio of GFP-NLS was normalized to $T = 0$; control, 21 cells from 4 independent experiments; CHMP2A-1, 24 cells from 4 independent experiments, $P = 0.04$; CHMP2A-2, 23 cells from 4 independent experiments, $P = 0.05$; CHMP3, 15 cells from 3 independent experiments, $P = 0.004$, two-tailed Student's t -test was used to assess significance after 10 min). Scale bars, 10 μ m. **f**, Scoring of multinucleate and midbody-connected HeLa cells transfected with the indicated siRNA and stained with anti-tubulin and DAPI (300 cells analysed per condition, $n = 4$). Data are mean \pm s.e.m. (**a**, **c**, **d**) and mean \pm s.d. (**f**).



Extended Data Figure 10 | Effect of CHMP2A depletion on NE discontinuities. **a**, Presentation of reconstructed tomograms from Fig. 4d. **b**, CHMP2A-depleted cells exhibited more non-NPC discontinuities per unit area, while the number of NPC per unit area was constant. Tomograms as

described in Fig. 4d, e were scored for discontinuities. The internal diameter of NPCs was slightly reduced in CHMP2A-depleted cells (control, 84 ± 7.6 nm, CHMP2A-1, 74 ± 8.8 nm; CHMP2A-2, 74 ± 5.7 nm). **c**, Schematic depicting topological equivalent of ESCRT-III-dependent membrane fusion events.

Histone H3.3 is required for endogenous retroviral element silencing in embryonic stem cells

Simon J. Elsässer^{1,2*}, Kyung-Min Noh³, Nichole Diaz³, C. David Allis³ & Laura A. Banaszynski^{3,4*}

Transposable elements comprise roughly 40% of mammalian genomes¹. They have an active role in genetic variation, adaptation and evolution through the duplication or deletion of genes or their regulatory elements^{2–4}, and transposable elements themselves can act as alternative promoters for nearby genes, resulting in non-canonical regulation of transcription^{5,6}. However, transposable element activity can lead to detrimental genome instability⁷, and hosts have evolved mechanisms to silence transposable element mobility appropriately^{8,9}. Recent studies have demonstrated that a subset of transposable elements, endogenous retroviral elements (ERVs) containing long terminal repeats (LTRs), are silenced through trimethylation of histone H3 on lysine 9 (H3K9me3) by ESET (also known as SETDB1 or KMT1E)¹⁰ and a co-repressor complex containing KRAB-associated protein 1 (KAP1; also known as TRIM28)¹¹ in mouse embryonic stem cells. Here we show that the replacement histone variant H3.3 is enriched at class I and class II ERVs, notably those of the early transposon (ETn)/MusD family and intracisternal A-type particles (IAPs). Deposition at a subset of these elements is dependent upon the H3.3 chaperone complex containing α -thalassaemia/mental retardation syndrome X-linked (ATRX)¹² and death-domain-associated protein (DAXX)^{12–14}. We demonstrate that recruitment of DAXX, H3.3 and KAP1 to ERVs is co-dependent and occurs upstream of ESET, linking H3.3 to ERV-associated H3K9me3. Importantly, H3K9me3 is reduced at ERVs upon H3.3 deletion, resulting in derepression and dysregulation of adjacent, endogenous genes, along with increased retrotransposition of IAPs. Our study identifies a unique heterochromatin state marked by the presence of both H3.3 and H3K9me3, and establishes an important role for H3.3 in control of ERV retrotransposition in embryonic stem cells.

Deposition of the histone variant H3.3 has been linked to regions of high nucleosome turnover and has been traditionally associated with gene activation. However, we and others have demonstrated that H3.3 is incorporated into both facultative and constitutive heterochromatin^{12,15,16}. Here, we used chromatin immunoprecipitation followed by sequencing (ChIP-seq) to identify 79,532 regions of H3.3 enrichment across the entire mouse genome, including repetitive regions (see later and Methods for details of data analysis), and performed a hierarchical clustering of H3.3 with various chromatin modifications. Consistent with deposition at euchromatin and heterochromatin, we observe H3.3 associated with both active (for example, H3K4me3, H3K27ac, H3K4me1) and repressed (for example, H3K9me3, H3K27me3, H4K20me3) chromatin states (Fig. 1a). While most H3.3 peaks localized to genic regions and intergenic regulatory regions such as enhancers¹², 23% (18,606/79,532) intersected with H3K9me3 peaks indicative of heterochromatic regions. Of these, 59% (11,010/18,606) localized to interspersed repeats (longer than 1 kb) and only 9% (1,747/18,606) fell within genic regions (Fig. 1b). Sequential ChIP-seq

(re-ChIP) demonstrated co-enrichment of H3.3 and H3K9me3 at these regions (Fig. 1c).

To identify repeat families that were associated with H3.3, we mapped our H3.3 ChIP-seq data to a comprehensive database of murine repetitive sequences^{17–19}. Unbiased hierarchical clustering demonstrated a striking correlation between H3.3, H3K9me3 and H3.3–H3K9me3 re-ChIP over class I and II ERVs, as well as enrichment of known silencing factors KAP1 and ESET (Fig. 1d and Extended Data Fig. 1). Class III ERVs and non-LTR long interspersed nuclear elements (LINEs) and short interspersed nuclear elements (SINEs) carry little H3.3 and H3K9me3 but higher levels of H3K9me2. However, the promoter/5' untranslated region (UTR) of intact LINE1 elements are enriched with H3.3, H3K9me3, KAP1 and ESET (Fig. 1d and Extended Data Fig. 1), suggesting a related mechanism of repression. Analysing individual well-annotated integration sites of ERVs^{5,20}, we found that IAP and ETn/MusD ERVs, the most active transposons in the mouse genome^{21–23}, are significantly enriched in H3.3 and H3K9me3 (Extended Data Fig. 2a–c), with 94% of IAP and 53% of ETn ERVs enriched with both H3.3 and H3K9me3 (Extended Data Fig. 2d).

Repetitive regions provide a challenge to next-generation sequencing analysis due to the ambiguity arising from mapping short reads to non-unique sequences. Standard ChIP-seq alignments disregard reads that map to more than a single location in the genome, leaving gaps wherever the underlying sequence is non-unique (Fig. 1e). To include interspersed repeats, we allowed random assignment of ambiguously mappable reads to one of the best matches²⁴ (Fig. 1e), effectively averaging counts over multiple occurrences of the same exact read match. As exemplified by ETn and IAP insertions downstream of the *Vnn3* transcription start site, H3K9me3 is broadly enriched over the non-unique ERV sequence, whereas H3.3 appears to be more confined over 3' and 5' regions of the repeats (Fig. 1e). Neither ChIP-seq using an antibody recognizing only the canonical H3 isoforms (H3.1/2) nor an antibody recognizing all H3 isoforms (total H3; H3.3 constitutes ~10% of total H3 in embryonic stem (ES) cells) show enrichment at the corresponding regions (Fig. 1e), and H3.3 enrichment was lost in ES cells lacking H3.3 (Extended Data Fig. 3)¹⁶. We were further able to detect both H3.3 and H3K9me3 in the uniquely mappable flanking sites of IAP and ETn ERVs, (Extended Data Fig. 4a, b). In addition to full ERVs, we found single (so-called 'orphan') LTRs to be enriched in both H3.3 and H3K9me3 (Extended Data Fig. 4c), suggesting that the LTR sequence itself is sufficient for the nucleation of H3.3 and heterochromatin factors.

H3.3 deposition has been linked to dynamic chromatin regions with high levels of nucleosome turnover and DNA accessibility. As H3.3 enrichment at ETn and IAP ERVs was comparable to levels found at active promoters in ES cells (Extended Data Figs 2a and 5a; compare also to *Rps12* enrichment in Fig. 1e), we tested whether ERVs were nucleosome-depleted in ES cells. Surprisingly, we found that ERVs

¹MRC Laboratory of Molecular Biology, Francis Crick Ave, Cambridge CB2 0QH, UK. ²Science for Life Laboratory, Division of Translational Medicine and Chemical Biology, Department of Medical Biochemistry and Biophysics, Karolinska Institutet, S-171 21 Stockholm, Sweden. ³Laboratory of Chromatin Biology and Epigenetics, The Rockefeller University, 1230 York Avenue, New York, New York 10065, USA. ⁴Cecil H. and Ida Green Center for Reproductive Biology Science and Children's Medical Center Research Institute, UT Southwestern Medical Center, 5323 Harry Hines Boulevard, Dallas, Texas 75390, USA.

*These authors contributed equally to this work.

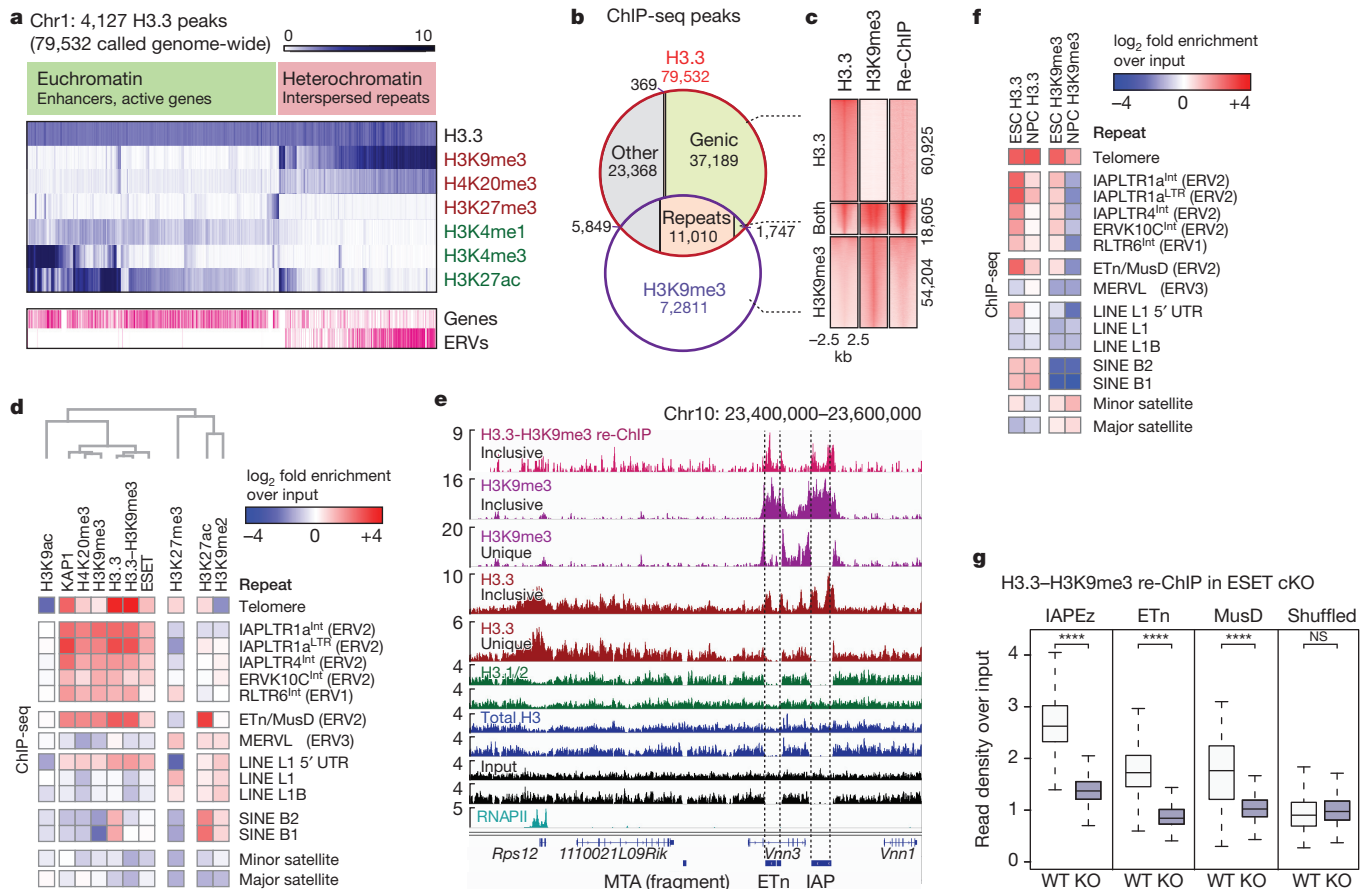


Figure 1 | H3.3 is co-enriched with H3K9me3 at class I and II ERV-associated heterochromatin. **a**, Hierarchical (Spearman rank) clustering of H3.3 peaks on chromosome 1 with histone modifications associated with active (green) or repressed (red) chromatin states. Annotated genes and ERVs are shown. **b**, Venn diagram of H3.3 and H3K9me3 peaks demonstrating overlap at repetitive elements. **c**, ChIP-seq density heat maps for peaks classified as H3.3 only ($n = 60,925$) and H3K9me3 only ($n = 18,605$), or H3K9me3 only ($n = 54,204$). Colour intensity represents normalized and globally scaled tag counts. **d**, ChIP-seq enrichment of H3.3 and heterochromatic histone modifications and factors mapped to the repetitive genome. Data are

represented in a hierarchically (Spearman rank) clustered heat map of \log_2 fold enrichment (red) or depletion (blue) over a matched input. See Extended Data Fig. 1 for complete heat map. **e**, Genome browser ChIP-seq representations in ES cells. Read counts are normalized to total number of reads for each data set and exclude ('unique') or include ('inclusive') repetitive reads. MTA, MT subfamily A. **f**, ChIP-seq enrichment of H3.3 and H3K9me3 at various repeat regions in ES cells (ESCs) and NPCs. Data are represented as in **d**. **g**, Levels of co-enriched H3.3-H3K9me3 in control and ESET conditional knockout (cKO) ES cells. IAPez, IAP subfamily Ez; WT, wild type. **** $P < 0.0001$, one-sided Wilcoxon signed rank test. NS, not significant.

showed low DNA accessibility compared to promoters of highly expressed genes with comparable H3.3 enrichment, as measured by DNase and MNase digestion²⁵, and showed no signs of transcription as judged by RNA polymerase (Pol) II occupancy¹² (Extended Data Fig. 5a). Notably, we find that newly synthesized H3.3 (ref. 26) is rapidly incorporated at IAPs, despite the high levels of H3K9me3 and silent state (Extended Data Fig. 5b). Overall, our data suggest that a substantial fraction of H3.3 resides at ERVs in ES cells and constitutes a unique chromatin state fundamentally distinct from previously described combinations of histone variants and modifications.

Previous studies have demonstrated that silencing of ERVs via H3K9me3 is unique to the pluripotent or embryonic state, with adult somatic tissues showing dependence upon DNA methylation for ERV repression. Concomitant with loss of H3K9me3, H3.3 enrichment is lost from IAP and ETn ERVs upon differentiation from ES cells to neuronal precursor cells (NPCs) (Fig. 1f and Extended Data Fig. 6a, b). These data indicate that, like H3K9me3, H3.3 may have a role in the embryonic establishment, but not the somatic maintenance, of this silenced chromatin state. Unlike H3K9me3, H3.3 is retained at telomeres upon differentiation (Fig. 1f), suggesting uncoupled or alternative mechanisms of repression from those functioning at ERVs.

H3K9me3 is facilitated by two histone methyltransferases—ESET and SUV39h1/2—that display distinct properties and regions

of genomic activity. Previous studies demonstrate that ESET has a critical role in the establishment of H3K9me3 at a large number of ERVs¹⁰, while SUV39h1/2 is involved in the maintenance and spreading of H3K9me3 at a subset of repeat elements²⁷. To elucidate which methyltransferase was responsible for establishing H3.3/H3K9me3 heterochromatin, we analysed the effect of ESET and SUV39h1/2 knockout on H3K9me3 levels at H3.3-containing ERVs. We found that ESET was required for H3K9me3 at all H3.3-containing classes of repeats (Fig. 1g and Extended Data Fig. 6c). SUV39h1/2 deletion resulted in a small decrease of H3K9me3 at IAP and ETn/MusD elements, but greatly decreased H3K9me3 at intact LINE elements, including their 5' UTR (Extended Data Fig. 6c). In conclusion, the co-occurrence of H3.3 and H3K9me3 facilitated by ESET methyltransferase activity defines a novel class of heterochromatin that functions at ERVs and intact LINE1 5' ends.

The histone variant H3.3 is incorporated at distinct regions of chromatin by either the HIRA or ATRX-DAXX histone chaperone complexes^{12–14}. We and others previously demonstrated that HIRA is responsible for H3.3 enrichment at genic regions, while the ATRX-DAXX complex facilitates H3.3 deposition at simple repeat regions such as telomeres^{12,13,15}. Using ChIP-seq, we found that DAXX and ATRX were responsible for H3.3 incorporation at regions enriched with both H3.3 and H3K9me3, whereas HIRA facilitated deposition at

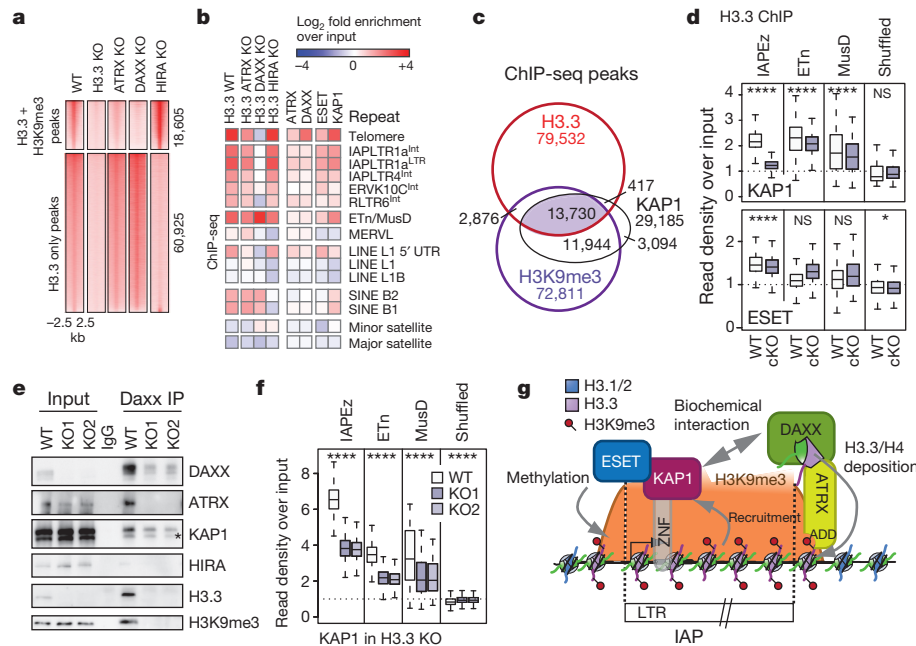


Figure 2 | DAXX-ATRAX is responsible for H3.3 deposition at a subset of ERVs and co-localizes with ERV-specific heterochromatic factors. **a**, ChIP-seq density heat maps for peaks classified as both H3.3 and H3K9me3 ($n = 18,605$) or H3.3 only ($n = 60,925$). Colour intensity represents normalized and globally scaled tag counts. WT, wild type. **b**, ChIP-seq enrichment of H3.3 chaperones and chaperone-dependent H3.3 deposition at repetitive regions. Data are represented in a heat map of \log_2 fold enrichment (red) or depletion (blue) over a matched input. **c**, Venn diagram of H3.3, H3K9me3 and KAP1 peaks demonstrating substantial overlap in ES cells. **d**, Levels of H3.3 in control and KAP1 conditional knockout (cKO; top) and control and ESET cKO (bottom) ES cells. **** $P < 0.0001$, * $P < 0.05$, one-sided Wilcoxon signed rank

test. NS, not significant. **e**, Immunoblotting of DAXX immunoprecipitated from wild-type or H3.3-null nuclear extracts showing co-immunoprecipitation with ATRX, H3.3, H3K9me3 and KAP1 independent of H3.3 (1% input). Asterisk denotes cross-reacting band. **f**, Levels of KAP1 in control and H3.3-knockout ES cells. Data are presented as in **d**. **g**, Model of corepressor complex function at IAPs: KAP1 recognizes ERVs through sequence-specific KRAB zinc finger (ZNF) DNA-binding proteins and recruits DAXX-ATRAX independently of its interaction with ESET. DAXX-ATRAX deposit H3.3 at IAPs, facilitating efficient KAP1 association with chromatin. ESET is then recruited, resulting in H3K9me3-mediated silencing of ERVs.

regions enriched with H3.3 alone (Fig. 2a). ATRX and DAXX deletion, but not HIRA, attenuated H3.3 enrichment at telomeres as well as at IAP ERVs, but not at ETn/MusD ERVs (Fig. 2b and Extended Data Fig. 7a, b), indicating that ATRX-DAXX is required for H3.3 enrichment at specific subclasses of ERVs. ChIP-seq analysis at repeats demonstrated that both DAXX and ATRX co-occupied class I and II ERVs enriched with KAP1 and ESET, as well as telomeres (Fig. 2b). To

understand further the relationship between the corepressor KAP1 and ATRX-DAXX-dependent H3.3 deposition at ERVs, we mapped genome-wide enrichment of KAP1 and found that almost half (13,730/29,185) of the KAP1 peaks coincided with shared H3.3/H3K9me3 peaks (Fig. 2c). We therefore wanted to determine whether KAP1 had a role in targeting H3.3 deposition via recruitment of ATRX-DAXX. Indeed, H3.3 enrichment was reduced at IAP ERVs in the absence of KAP1 but was independent of ESET (Fig. 2d and Extended Data Fig. 7c–e), suggesting a novel role for KAP1 in recruitment of ATRX-DAXX.

To determine whether KAP1 and ATRX-DAXX associated biochemically, we prepared nuclear extracts from ES cells. We found that DAXX co-immunoprecipitated its known complex member ATRX as well as its substrate H3.3 (Fig. 2e). Of note, DAXX-associated histone was enriched with H3K9me3 (Fig. 2e). In addition, DAXX co-immunoprecipitated KAP1 (Fig. 2e), suggesting that DAXX-ATRAX and KAP1 can form a biochemical complex. HIRA was not co-immunoprecipitated, demonstrating the specificity of the interaction. Given the requirement of H3.3 for DAXX folding²⁸, we repeated DAXX immunoprecipitation from two independent ES cell lines lacking H3.3 (Fig. 2e)¹⁶. While overall nuclear DAXX levels were reduced in the absence of H3.3 (Fig. 2e and Extended Data Fig. 7f), in agreement with a co-folding mechanism, the low levels of remaining DAXX maintained association with KAP1 (Fig. 2e), suggesting an interaction independent of the H3.3 substrate.

We next wanted to determine whether the loss of H3.3 affected KAP1 or DAXX targeting to ERVs. Intriguingly, both KAP1 and DAXX recruitment to ERVs was reduced in the absence of H3.3, and telomere association was lost (Fig. 2f and Extended Data Fig. 7g). We cannot distinguish, however, if reduced enrichment of DAXX at chromatin is a result of KAP1 impairment or a direct

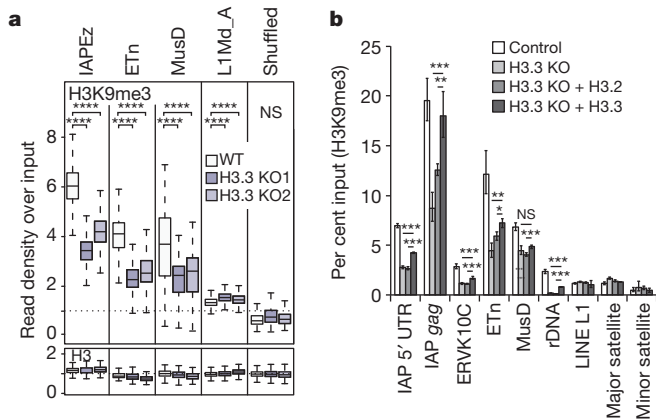


Figure 3 | H3.3 is required for the maintenance of H3K9me3 at specific class I and II ERVs. **a**, Levels of H3K9me3 and total H3 in control and H3.3 knockout (KO) ES cells. **** $P < 0.0001$, one-sided Wilcoxon signed rank test. NS, not significant. **b**, ChIP with quantitative polymerase chain reaction (qPCR) analysis of H3K9me3 enrichment at various repeat regions in control ES cells and H3.3-KO ES cells exogenously expressing either H3.2 or H3.3. rDNA, ribosomal DNA. Error bars represent standard deviation (s.d.) from one experiment ($n = 3$). Data are representative of three independent ChIP experiments. * $P < 0.05$, ** $P < 0.01$, *** $P < 0.001$, t -test.

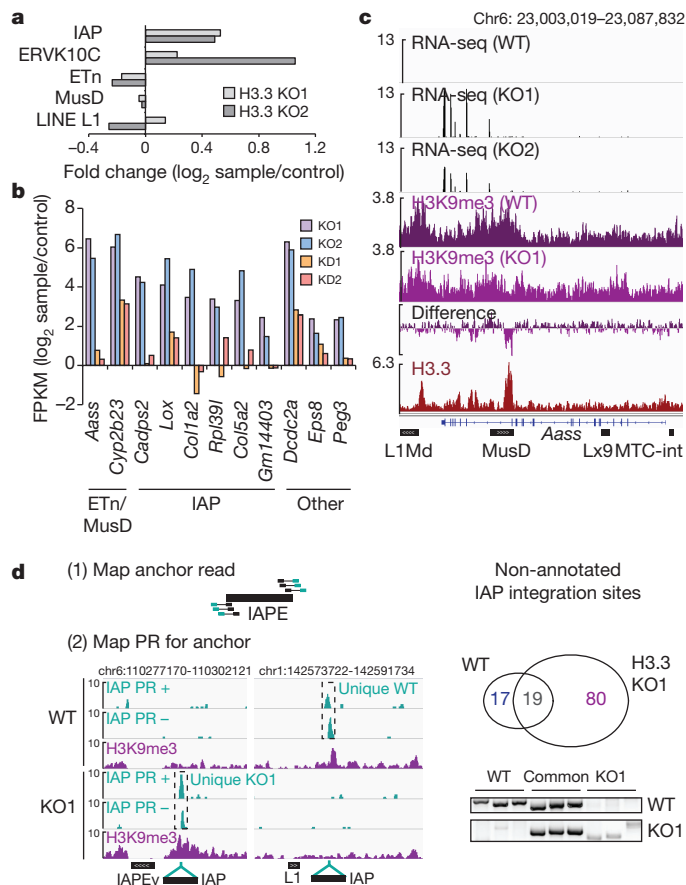


Figure 4 | Loss of H3.3 leads to ERV derepression. **a**, RNA-seq analysis of repeat transcripts. Data are represented as log₂ change in transcript over control for H3.3 KO1 and KO2 ES cells. **b**, RNA-seq analysis of transcripts with nearby ERVs that are significantly upregulated in H3.3 KO1 and KO2 ($q < 0.05$) (see Extended Data Fig. 10a). Data are represented as in **a**. Nearby ERV classes are indicated. FPKM, fragments per kilobase of transcript per million fragments mapped. **c**, Representative example of an upregulated transcript in the absence of H3.3. RNA-seq tracks (black) show all reads mappable to the genome (without restriction to known transcripts). H3K9me3 (purple and violet) and H3.3 (red) tracks show inclusive reads as standardized read densities. The relative H3K9me3 difference between wild type (WT) and knockout (KO) is shown in a separate track ('difference'). **d**, Paired-end-based *de novo* discovery of non-annotated IAP integration sites in control and H3.3 KO1 ES cells (for details see Methods). Venn diagram and PCR genotyping validation of non-annotated IAP integration sites in control and H3.3 KO1 ES cells. PR, paired read.

consequence of reduced DAXX protein stability in the absence of H3.3. Together, these data suggest that H3.3, DAXX and KAP1 are cooperative in their function related to ERV silencing (Fig. 2g). Intriguingly, while H3.3 enhances KAP1 and DAXX recruitment to ETn/MusD elements (Fig. 2f and Extended Data Fig. 7g), the variant remains enriched at these elements in the absence of the corepressor complex (Fig. 2b, d and Extended Data Fig. 7c–e).

As we observed a positive correlation between H3K9me3 and H3.3 enrichment at IAP ERVs (Extended Data Figs 4a and 8a), we next tested whether there was a functional link between H3.3 deposition and H3K9me3 establishment at specific subclasses of ERVs. Although global levels of H3K9me3 were not affected by the loss of H3.3 (Extended Data Fig. 8b), we found that H3K9me3 was reduced specifically at peaks enriched with both H3.3 and H3K9me3, concomitant with a reduction of KAP1 occupancy (Extended Data Fig. 8c). Indeed, H3K9me3 levels were reduced up to 50% at IAP, ETn and MusD repeats in the absence of H3.3 (Fig. 3a). Importantly, nucleosome density was not reduced, as evidenced by the overall maintenance of total H3 (Fig. 3a). Intriguingly, H3K9me3 levels were reduced at ETn/MusD elements in the absence of

DAXX, ATRX, KAP1 or ESET (Extended Data Fig. 8d–h), whereas H3.3 enrichment at these elements was independent of the corepressor complex (Fig. 2 and Extended Data Fig. 7), suggesting a multifaceted mechanism in which both H3.3 deposition and corepressor complex recruitment contribute to ERV silencing.

Intriguingly, ERVs retained H3.3 to a larger extent than other regions in ES cells RNA interference (RNAi)-depleted of H3.3 (H3.3 knockdown¹⁶; Extended Data Fig. 9a–c), suggesting they may act as 'sinks' for the remaining low levels of H3.3 present in H3.3-knockdown ES cells. Furthermore, exogenously expressed H3.3, but not H3.2, in both H3.3-knockout and H3.3-knockdown ES cells was focally enriched at IAP ERVs (Extended Data Fig. 9d–f). Importantly, exogenous expression of H3.3, but not H3.2, was able partially to rescue the loss of H3K9me3 at specific repeat regions (Fig. 3b). Together, these data suggest a direct and variant-specific role for H3.3 in establishing H3K9me3 chromatin at a subset of ERVs that cannot be compensated by the canonical H3.1/2 isoforms.

As H3K9me3 is known to be required for silencing of ERVs¹⁰, we tested whether loss of H3.3 would cause a derepression of ERVs concomitant with a reduction of H3K9me3 levels. RNA-sequencing (RNA-seq) demonstrated a moderate increase in global transcripts from IAPs, but not ETn/MusD ERVs (Fig. 4a). Since ERVs have recently been shown to control expression of nearby genes^{5,6}, we next tested whether endogenous genes that were deregulated in H3.3-knockout ES cells were proximal to ERVs. While the majority of ERVs are neutral to neighbouring genes, a number of genes in the vicinity of ERVs were highly upregulated (Fig. 4b and Extended Data Fig. 10a), including the known gene *Cyp2b23* and a new putative chimaeric transcript originating from a MusD element within the *Aass* gene (Fig. 4c). Notably, the same set of transcripts was upregulated in H3.3-depleted ES cells, albeit at a lower level (Fig. 4b), suggesting that the remaining H3.3 is partially functional in maintaining silent ERVs.

We hypothesized that ERV desilencing should result in increased ERV mobility. Paired-end sequencing of genomic DNA identified 80 non-annotated IAP integrations unique to H3.3-knockout ES cells, and only 17 unique to wild-type ES cells (Fig. 4d and Extended Data Fig. 10b). As derepressed IAPs have been shown to cause chromosome rearrangements, we analysed H3.3-knockout ES cells for increased genome instability. Indeed, karyotypic analysis of H3.3-knockout ES cells showed a number of chromosomal abnormalities not observed in the wild-type control (Extended Data Fig. 10c). Despite these observations, we cannot exclude that genomic instability in H3.3-knockout ES cells might result from a loss of function unrelated to retrotransposon silencing^{29,30}.

We have uncovered an unexpected role for the histone variant H3.3 in the establishment of heterochromatin. We demonstrate a hierarchy for deposition of H3.3, favouring DAXX–ATRX-mediated chromatin assembly at ERVs over transcription-associated deposition. We propose a model in which H3.3-containing chromatin facilitates the recruitment of KAP1 to ERVs, which in turn recruits DAXX–ATRX for the maintenance of H3.3 chromatin, thus creating a positive feedback or propagation loop. This mechanism acts synergistically with ESET-mediated H3K9me3 in maintaining a silent chromatin state at ERVs. Our data also indicate an H3.3-independent function of DAXX–ATRX in maintaining H3K9me3, possibly related to an architectural role in a larger corepressor complex with KAP1 and ESET. Our findings solidify an emerging understanding of the importance of the histone variant H3.3 in the establishment of silenced chromatin states and in maintenance of genome stability.

Online Content Methods, along with any additional Extended Data display items and Source Data, are available in the online version of the paper; references unique to these sections appear only in the online paper.

Received 23 June 2014; accepted 19 February 2015.

Published online 4 May 2015.

1. Waterston, R. H. *et al.* Initial sequencing and comparative analysis of the mouse genome. *Nature* **420**, 520–562 (2002).

2. Longo, M. S., Carone, D. M., Green, E. D., O'Neill, M. J. & O'Neill, R. J. Distinct retroelement classes define evolutionary breakpoints demarcating sites of evolutionary novelty. *BMC Genomics* **10**, 334 (2009).
3. Lee, J., Han, K., Meyer, T. J., Kim, H. S. & Batzer, M. A. Chromosomal inversions between human and chimpanzee lineages caused by retrotransposons. *PLoS ONE* **3**, e4047 (2008).
4. Feschotte, C. & Gilbert, C. Endogenous viruses: insights into viral evolution and impact on host biology. *Nature Rev. Genet.* **13**, 283–296 (2012).
5. Karimi, M. M. *et al.* DNA methylation and SETDB1/H3K9me3 regulate predominantly distinct sets of genes, retroelements, and chimeric transcripts in mESCs. *Cell Stem Cell* **8**, 676–687 (2011).
6. Rowe, H. M. *et al.* TRIM28 repression of retrotransposon-based enhancers is necessary to preserve transcriptional dynamics in embryonic stem cells. *Genome Res.* **23**, 452–461 (2013).
7. Robberecht, C., Voet, T., Zamani Esteki, M., Nowakowska, B. A. & Vermeesch, J. R. Nonallelic homologous recombination between retrotransposable elements is a driver of *de novo* unbalanced translocations. *Genome Res.* **23**, 411–418 (2013).
8. Maksakova, I. A., Mager, D. L. & Reiss, D. Keeping active endogenous retroviral-like elements in check: the epigenetic perspective. *Cell. Mol. Life Sci.* **65**, 3329–3347 (2008).
9. Gifford, W. D., Pfaff, S. L. & Macfarlan, T. S. Transposable elements as genetic regulatory substrates in early development. *Trends Cell Biol.* **23**, 218–226 (2013).
10. Matsui, T. *et al.* Proviral silencing in embryonic stem cells requires the histone methyltransferase ESET. *Nature* **464**, 927–931 (2010).
11. Rowe, H. M. *et al.* KAP1 controls endogenous retroviruses in embryonic stem cells. *Nature* **463**, 237–240 (2010).
12. Goldberg, A. D. *et al.* Distinct factors control histone variant H3.3 localization at specific genomic regions. *Cell* **140**, 678–691 (2010).
13. Lewis, P. W., Elsaesser, S. J., Noh, K. M., Stadler, S. C. & Allis, C. D. Daxx is an H3.3-specific histone chaperone and cooperates with ATRX in replication-independent chromatin assembly at telomeres. *Proc. Natl Acad. Sci. USA* **107**, 14075–14080 (2010).
14. Drané, P., Ouarrhni, K., Depaux, A., Shuaib, M. & Hamiche, A. The death-associated protein DAXX is a novel histone chaperone involved in the replication-independent deposition of H3.3. *Genes Dev.* **24**, 1253–1265 (2010).
15. Wong, L. H. *et al.* Histone H3.3 incorporation provides a unique and functionally essential telomeric chromatin in embryonic stem cells. *Genome Res.* **19**, 404–414 (2009).
16. Banaszynski, L. A. *et al.* Hira-dependent histone H3.3 deposition facilitates PRC2 recruitment at developmental loci in ES cells. *Cell* **155**, 107–120 (2013).
17. Mikkelsen, T. S. *et al.* Genome-wide maps of chromatin state in pluripotent and lineage-committed cells. *Nature* **448**, 553–560 (2007).
18. Day, D. S., Luquette, L. J., Park, P. J. & Kharchenko, P. V. Estimating enrichment of repetitive elements from high-throughput sequence data. *Genome Biol.* **11**, R69 (2010).
19. Jurka, J., Kohany, O., Pavlicek, A., Kapitonov, V. V. & Jurka, M. V. Clustering, duplication and chromosomal distribution of mouse SINE retrotransposons. *Cytogenet. Genome Res.* **110**, 117–123 (2005).
20. Rebollo, R. *et al.* Epigenetic interplay between mouse endogenous retroviruses and host genes. *Genome Biol.* **13**, R89 (2012).
21. Ribet, D. *et al.* An infectious progenitor for the murine IAP retrotransposon: emergence of an intracellular genetic parasite from an ancient retrovirus. *Genome Res.* **18**, 597–609 (2008).
22. Dewannieux, M., Dupressoir, A., Harper, F., Pierron, G. & Heidmann, T. Identification of autonomous IAP LTR retrotransposons mobile in mammalian cells. *Nature Genet.* **36**, 534–539 (2004).
23. Zhang, Y., Maksakova, I. A., Gagnier, L., van de Lagemaat, L. N. & Mager, D. L. Genome-wide assessments reveal extremely high levels of polymorphism of two active families of mouse endogenous retroviral elements. *PLoS Genet.* **4**, e1000007 (2008).
24. Treangen, T. J. & Salzberg, S. L. Repetitive DNA and next-generation sequencing: computational challenges and solutions. *Nature Rev. Genet.* **13**, 36–46 (2012).
25. Chen, P. *et al.* H3.3 actively marks enhancers and primes gene transcription via opening higher-ordered chromatin. *Genes Dev.* **27**, 2109–2124 (2013).
26. Yildirim, O. *et al.* A system for genome-wide histone variant dynamics in ES cells reveals dynamic MacroH2A2 replacement at promoters. *PLoS Genet.* **10**, e1004515 (2014).
27. Bulut-Karslioglu, A. *et al.* Suv39h-dependent H3K9me3 marks intact retrotransposons and silences LINE elements in mouse embryonic stem cells. *Mol. Cell* **55**, 277–290 (2014).
28. DeNizio, J. E., Elsasser, S. J. & Black, B. E. DAXX co-folds with H3.3/H4 using high local stability conferred by the H3.3 variant recognition residues. *Nucleic Acids Res.* **42**, 4318–4331 (2014).
29. Adam, S., Polo, S. E. & Almouzni, G. Transcription recovery after DNA damage requires chromatin priming by the H3.3 histone chaperone HIRA. *Cell* **155**, 94–106 (2013).
30. Frey, A., Listovsky, T., Guilbaud, G., Sarkies, P. & Sale, J. E. Histone H3.3 is required to maintain replication fork progression after UV damage. *Curr. Biol.* **24**, 2195–2201 (2014).

Acknowledgements This work was supported by the Rockefeller University Fund and the Tri-Institutional Stem Cell Initiative. S.J.E. acknowledges funding from EMBO ALTF 1232-2011 and the Cambridge University Herchel Smith Fund. We thank D. Pickett, D. Trono and D. Shinkai for cell lines. We thank A. Goldberg and C. Li for technical assistance and members of the Allis laboratory for helpful discussions.

Author Contributions S.J.E. and L.A.B. contributed equally to this project. S.J.E. and L.A.B. conceived, performed and interpreted most experiments with guidance from C.D.A. K.-M.N. and N.D. contributed to experiments. S.J.E. and L.A.B. wrote the manuscript with input from all authors.

Author Information The ChIP-seq and RNA-seq data sets have been deposited in the Gene Expression Omnibus under accession number GSE59189. Reprints and permissions information is available at www.nature.com/reprints. The authors declare no competing financial interests. Readers are welcome to comment on the online version of the paper. Correspondence and requests for materials should be addressed to S.J.E. (simon.elsasser@scilifelab.se), C.D.A. (alliscd@rockefeller.edu) or L.A.B. (laura.banaszynski@utsouthwestern.edu).

METHODS

ES cell culture. ES cells were cultured under standard conditions (KO-DMEM, 2 mM Glutamax, 15% ES grade fetal bovine serum, 0.1 mM 2-mercaptoethanol and leukaemia inhibitory factor (LIF)). H3.3-knockout/knockdown ES cells were C57BL/6J background. H3.3-knockout ES cells were a mixed 129×C57BL/6J background. Generation of H3.3-knockout/knockdown and H3.3-knockout ES cells were previously described¹⁶. For early passages, cells were maintained on an irradiated feeder layer. To remove feeders, cells were passaged at least two passages off of feeders onto gelatin-coated plates. ES cells were routinely tested for mycoplasma. **ChIP.** Native ChIP assays (H3K9me3, H3.3-HA) were performed with approximately 2×10^7 ES cells per experiment. Cells were subject to hypotonic lysis and treated with micrococcal nuclease to recover mono- to tri-nucleosomes. Nuclei were lysed by brief sonication and dialysed into N-ChIP buffer (10 mM Tris pH 7.6, 1 mM EDTA, 0.1% SDS, 0.1% Na-Deoxycholate, 1% Triton X-100) for 2 h at 4 °C. Soluble material was recovered (~70%) and incubated with 3–5 µg of antibody bound to 75 µl protein A Dynal magnetic beads (Invitrogen) and incubated overnight at 4 °C, with 5% kept as input DNA. Magnetic beads were washed, chromatin was eluted, and ChIP DNA was dissolved in 10 mM Tris pH 8.

Crosslinking ChIP assays (H3gen, H3.1/2, H3.3, H3K9me3, DAXX, KAP1) were performed with approximately 2×10^7 ES cells per experiment. Cells were crosslinked with 1% paraformaldehyde (PFA) for 10 min at room temperature and quenched by glycine at a final concentration of 0.125 M. Chromatin was sonicated to an average size of 0.3–0.7 kb using a Biorupter (Diagenode). Purified nuclei were resuspended in X-ChIP buffer (10 mM Tris pH 8, 100 mM NaCl, 1 mM EDTA, 0.5 mM EGTA, 0.1% Na-Deoxycholate, 0.5% N-lauroylsarcosine) and incubated with 3–5 µg of antibody bound to 75 µl protein A Dynal magnetic beads (Invitrogen) and incubated overnight at 4 °C, with 5% kept as input DNA. Magnetic beads were washed, chromatin was eluted, and ChIP DNA was dissolved in 10 mM Tris pH 8.

Antibodies. H3 general (ab1791, Abcam), H3.3 (09-838, Millipore), H3.1/2 (ABE154, Millipore), H4 (rabbit antiserum), H3K9me3 (ab8898, Abcam), HIRA (mouse monoclonal WC15 and WC119), DAXX (sc-7152, Santa Cruz Biotechnology), ATRX (sc-15408, Santa Cruz Biotechnology), KAP1 (ab22553, Abcam; ab10483, Abcam), tubulin (TUB2.1, Sigma), lamin (ab26300, Abcam), normal rabbit IgG (12-370, Millipore).

Nuclear extract preparation. ES cells were harvested from 60 15-cm dishes at 80% confluency. Cell pellets were resuspended in 150 ml hypotonic lysis buffer (20 mM HEPES pH 7.9, 10 mM KCl, 5 mM MgCl₂, 0.5 mM EGTA, 0.1 mM EDTA, 5 mM 2-mercaptoethanol, 0.4 mM PMSF) and homogenized (dounce 10× A, 5× B). Cell lysis was confirmed by trypan blue staining. Nuclei were harvested for 5 min at 1,900g at 4 °C. Nuclei were resuspended in 45 ml buffer (20 mM HEPES pH 7.9, 110 mM KCl, 2 mM MgCl₂, 0.1 mM EDTA, 5 mM 2-mercaptoethanol, 0.4 mM PMSF, 1× complete protease inhibitor cocktail (Roche)). One-tenth volume saturated (NH₄)₂SO₄ pH 7.5 (final concentration ~400 mM) was added and lysates were incubated for 20 min at 4 °C rotating. Lysates were clarified for 90 min at 35,000 r.p.m. at 4 °C. Protein complexes were precipitated by slow addition of (NH₄)₂SO₄ to 60% saturation and collected for 10 min at 13,000 r.p.m. at 4 °C. Precipitated complexes were resuspended by dialysis in immunoprecipitation buffer (20 mM HEPES pH 7.9, 200 mM KCl, 0.01% NP-40, 5 mM 2-mercaptoethanol, 0.4 mM PMSF) and concentration was determined by Bradford assay.

Immunoprecipitation. Five micrograms antibody bound to 25 µl Dynabeads was incubated with 1 mg of ES cell nuclear extract for 3 h at 4 °C. Beads were washed four times with 1 ml buffer (20 mM HEPES pH 7.9, 400 mM KCl, 0.01% NP-40, 5 mM 2-mercaptoethanol, 0.4 mM PMSF) and eluted in 1× SDS loading buffer.

Data sets. The following published next-generation sequencing data sets were meta-analysed in this study: (1) ChIP-RNA Pol II (CTD4H8), H3.3-HA in HIRA wild-type, HIRA-null, C57BL/6J ES cells and NPCs¹²; ATRX²¹; ESET³²; H3K9me3 and SUV39h1/2 (ref. 27); H4K20me3 (ref. 17); H3K9me2 (ref. 33); H3K4me1, H3K4me3, H3K27me3, H3K27ac, H3.3-HA from C57BL/6J ES cells¹⁶; (2) DNase I Hypersensitivity (ENCODE U Wash), MNase accessibility²⁵; and (3) RNA-seq in H3.3B-HA and H3.3-knockout/knockdown C57BL/6J ES cells¹⁶.

Data sets used for individual figure panels are described in Supplementary Table 1.

ChIP-seq analysis. ChIP-seq libraries were prepared according to the Illumina protocol and sequenced with HiSeq 2000. Raw reads in FASTQ format were aligned to the mouse genome version mm9 with Bowtie³⁴ using “-m 1 --best” parameters for unique alignments and “-M 1 --best” parameters for inclusive alignment of non-unique reads. The former parameters instruct Bowtie to report a maximum of one match per read and discard any read that cannot be mapped to a unique best match. The “-M 1 --best” parameters ensure that only one alignment is reported for each read. This is either the single best alignment or, if more than one equivalent best alignment is found, one of those matches selected randomly. Input DNA mapped using the latter parameters extends evenly over the repeat

classes analysed in this study (namely IAP, ETn, MusD and L1 elements), confirming a proportional representation of those repetitive sequences relative to the unique genome (Extended Data Fig. 2a, b).

Bowtie SAM output files were converted to sorted BAM files using SAMtools³⁵. For unique alignments, duplicate reads were filtered using the rmdup function of SAMtools. Wig files were created from BAM files using IGVTools count function (The Broad Institute) and scaled to a genome-wide average read density of 1 using java-genomic-toolkit wigmath.Scale function (as a reference, 17.5 Mio mapped reads at a fragment size of 150 bp yield an average genome-wide read density of 1 for mm9). Figures of these continuous tag counts over selected genomic intervals were created in the IGV browser (The Broad Institute).

Repetitive genome ChIP-seq analysis. The current build of rodent repeat sequences was downloaded from Repbase (<http://www.girinst.org/repbase/>) and filtered for *Mus musculus* sequences. A Bowtie index was created with Bowtie-build. Raw ChIP-seq FASTQ reads were mapped to the repetitive sequence database using Bowtie “-best” and “-k 1” options. A table of mapped short read counts per repetitive element were extracted from bam file using SAMtools idxstats function. Further analysis was performed with R and visualized as heat maps using GENE-E. Mapped read counts were expressed as a fraction of total mapped repetitive reads for each sample. For enrichment analysis, normalized read counts of ChIP samples were divided by normalized read counts of a matched input sample and expressed as log₂ fold enrichment. In addition, the following quality controls were performed: read distribution across the repetitive sequence was inspected using IGV genome browser for each repeat family to confirm coverage of the whole repetitive sequence. To avoid over- or underestimating fold enrichments due to low sequence representation, repetitive sequences with consistently less than ~100 mapped reads per sample or control were excluded from analysis.

Peak calling. Peaks were called for H3.3, H3K9me3 and total H3 ChIP-seq data sets from control C57BL/6J ES cells¹⁶, including non-unique reads. MACS ChIP-seq peak finding was performed against a matched input using cut-off values “-pvalue 1e-6 --mfold 10,50”. 79,532, 72,811 and 29,189 peaks were called for H3.3, H3K9me3 and KAP1, respectively. For total H3, only 996 peaks were called with the same parameters.

Enrichment analysis over H3.3 peaks. For Fig. 1a, enrichment of H3.3 and histone modifications over H3.3 peaks were calculated as follows: average ChIP-seq read densities over the peak interval defined in the MACS³⁶ bed output file were extracted from normalized wig files using the java-genomics-toolkit ngs.IntervalStats function (T. Palpant; <http://palpant.us/java-genomics-toolkit/>). ChIP-seq enrichment for each interval was normalized subsequently, dividing the mean read density of the ChIP-seq sample by the corresponding density of the matched input sample. Data were visualized in a heat map as log₂ fold enrichment over input and clustered with GENE-E (The Broad Institute).

Enrichment analysis over repetitive and unique genomic regions. For Figs 1g, 2d, f, 3a and Extended Data Figs 2a–c, 5, 6, 8d, 9c, f, intervals were derived from following sources: Transcription start sites (TSSs) of ~2,000 highly active genes previously shown to be enriched in H3.3 were defined as intervals from –1 kb to +1 kb around their annotated TSS. H3K27me3-containing promoters (K27pro) were previously characterized¹⁶. Curated sets of IAP, IAPd, RLTR10, ETn, MusD, ERGLN, ERVK10C⁶ and L1Md_A²⁷ repeat locations were used. Additional intact IAP elements were identified using the BLAT function of USCS and combined with the existing IAP data set. Intact LINE L1Md_F promoters/5' UTRs were identified in the reference genome using BLAT with the RepBase sequence L1MM_F_L1.

Enrichments over these intervals were calculated as described earlier from normalized ChIP and input wig files using wigmath.IntervalStats. Log₂ fold enrichments over individual intervals were summarized using R in boxplots (Tuckey box-and-whisker plots using R boxplot defaults). Specifically, the box indicates median, as well as upper and lower quartiles of the data. Whiskers extend to the most extreme datapoint within 1.5-times the interquartile range (IQR). Outliers are not shown. Significance levels were calculated using Wilcoxon tests: not significant, $P > 0.05$; * $P < 0.05$; ** $P < 0.01$; *** $P < 0.001$; **** $P < 0.0001$.

Peak profile heat maps. For Figs 1c, 2a and Extended Data Figs 8c, 9e, peak profile heat maps were calculated using ngsplot³⁷ over a 5-kb window around the MACS peak centres (parameters: -SC global -I 0 -L 2500 -MQ 0 -RB 0.05) from BAM files using the inclusive mapping procedure. Data sets are normalized to total read counts and all maps are represented on the same global scale.

Analysis regions flanking repetitive elements. For Extended Data Fig. 4, profiles were calculated from uniquely mapped reads only, that is, non-unique reads and PCR duplicates were discarded before calculating the coverage using IGVtools count function (see earlier). Profiles over flanking regions were aggregated using the sitepro function from the CEAS suite³⁸ with the following modifications: profiles were not centred over the element but instead separately collected for the 3' and 5' flanking regions. The mean of the profiles in two, 5' and 3', 500

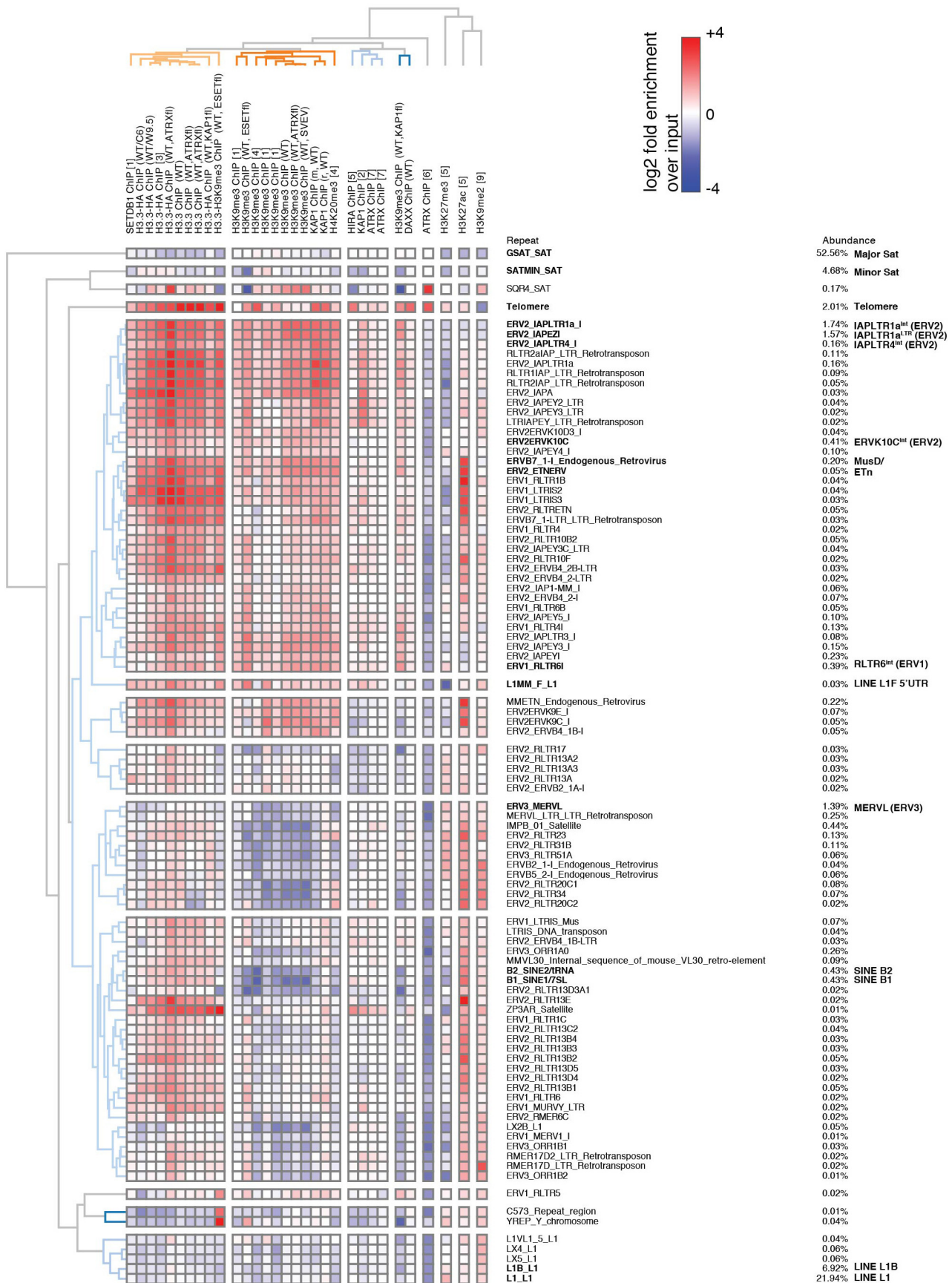
bp windows was extracted for each interval as an approximation of enrichment over the central, repetitive, interval. Profiles were either visualized as heat map (using GENE-E), or averaged into a single plot (CEAS sitepro). Wig files were normalized to a global average of 1, thus the ordinate of the profile plot represents fold enrichment/depletion over a random genome-wide distribution of reads.

RNA-seq preparation and analysis. RNA was isolated using QIAGEN RNeasy. Libraries were prepared according to the Illumina TruSeq protocol and were sequenced on the HiSeq 2000. Resulting reads (101 nucleotides) were aligned to the mouse genome (mm9) using TopHat³⁹. Gene expression level measured as FPKM was determined by the maximum likelihood estimation method implemented in the Cufflinks software package with annotated transcripts as references. Differential expression was analysed using the Student's *t*-test in the program Cuffdiff⁴⁰ with *P* values corrected for multiple testing.

De novo mapping of unannotated ERVs. Genomic DNA from H3.3 wild-type and KO1 ES cells was sheared to an average of 500 bp. Illumina paired-end sequencing was performed with 50 bp read lengths. ERVs were mapped to the reference genome in a two-step procedure. First, all reads were mapped to a genome consisting of all RepBase sequences belonging to specific ERV class (for example, IAPs), using Bowtie2. Next, unpaired read pairs (where one mate matched an ERV sequence but the other could not be aligned) were extracted using samtools and mapped to the mm9 reference genome using Bowtie (allowing only for uniquely mappable reads). This strategy allowed us to anchor each ERV integration site with up to 10 uniquely mappable reads on either side of the repetitive sequence. Plus/minus-strand-specific wig coverage tracks were created using IGVTools, extending reads to 500 bp. We took advantage of the fact that left-hand anchor reads mapped exclusively to the plus strand and right-hand anchor reads to the minus strand. Thus, while existing ERVs were demarcated by a plus peak on the left and minus peaks on the right of the repeat sequence, non-annotated integration sites were characterized by a plus peak directly overlapping with a minus peak at the insertion site. Plus and minus peaks were identified separately

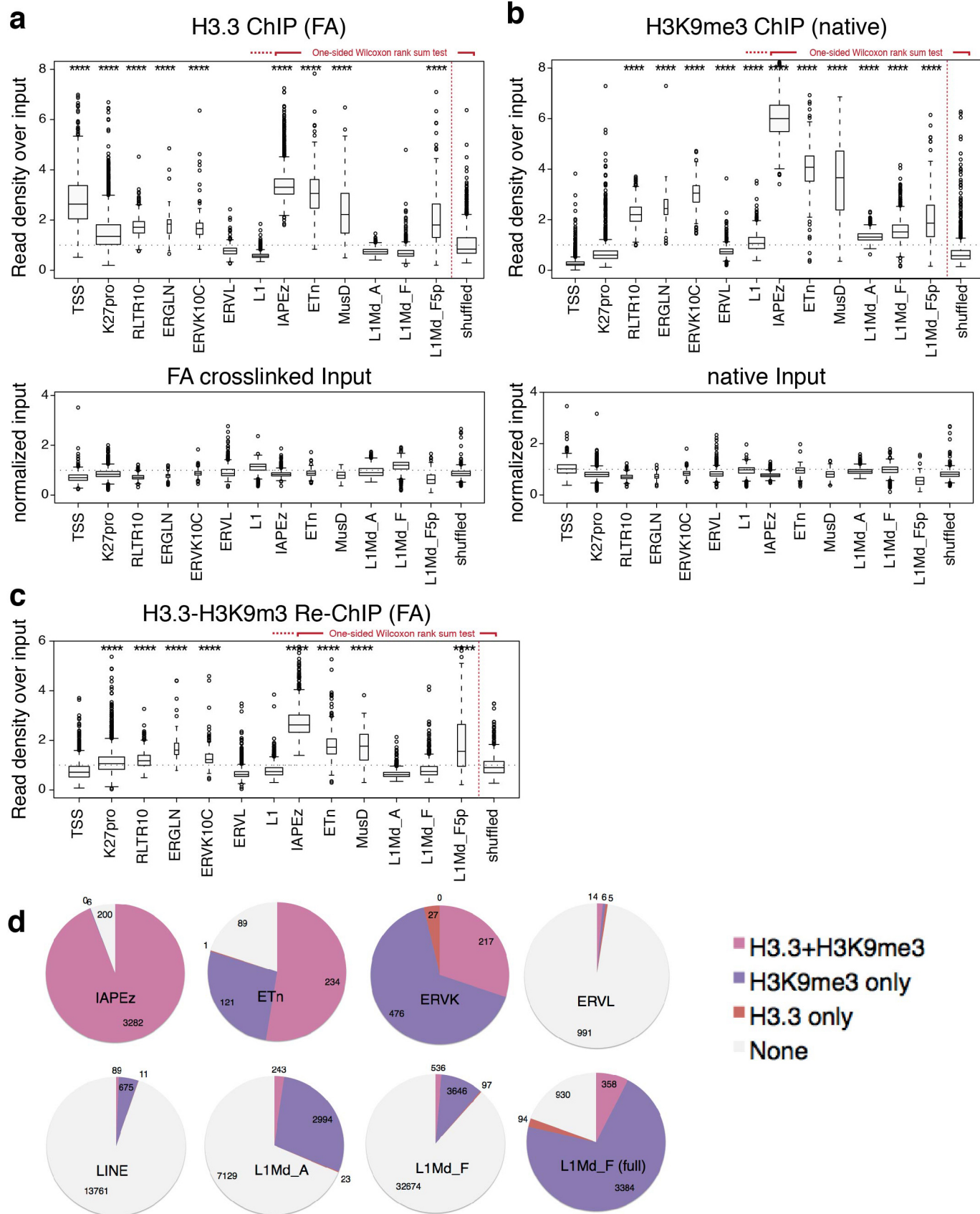
using the FindOutlierRegion of Java genomics toolkit on split plus and minus wig files. Peak intervals were then intersected to find overlapping plus/minus peaks. Wild-type and KO1 ES cell peaks were intersected and new integration sites were only called if a plus/minus peak did not overlap with a minus or plus peak in the respective control data set. IAP integration sites were validated by genotyping, using primer pairs spanning a ~300 bp region between the IAP LTR and the unique flanking region.

31. Sarma, K. *et al.* ATRX directs binding of PRC2 to Xist RNA and Polycomb targets. *Cell* **159**, 869–883 (2014).
32. Bilodeau, S., Kagey, M. H., Frampton, G. M., Rahl, P. B. & Young, R. A. SetDB1 contributes to repression of genes encoding developmental regulators and maintenance of ES cell state. *Genes Dev.* **23**, 2484–2489 (2009).
33. Das, P. P. *et al.* Distinct and combinatorial functions of Jmjd2b/Kdm4b and Jmjd2c/Kdm4c in mouse embryonic stem cell identity. *Mol. Cell* **53**, 32–48 (2014).
34. Langmead, B., Trapnell, C., Pop, M. & Salzberg, S. L. Ultrafast and memory-efficient alignment of short DNA sequences to the human genome. *Genome Biol.* **10**, R25 (2009).
35. Li, H. *et al.* The Sequence Alignment/Map format and SAMtools. *Bioinformatics* **25**, 2078–2079 (2009).
36. Liu, T. Use model-based analysis of ChIP-Seq (MACS) to analyze short reads generated by sequencing protein–DNA interactions in embryonic stem cells. *Methods Mol. Biol.* **1150**, 81–95 (2014).
37. Shen, L., Shao, N., Liu, X. & Nestler, E. ngs.plot: Quick mining and visualization of next-generation sequencing data by integrating genomic databases. *BMC Genomics* **15**, 284 (2014).
38. Shin, H., Liu, T., Manrai, A. K. & Liu, X. S. CEAS: *cis*-regulatory element annotation system. *Bioinformatics* **25**, 2605–2606 (2009).
39. Trapnell, C., Pachter, L. & Salzberg, S. L. TopHat: discovering splice junctions with RNA-Seq. *Bioinformatics* **25**, 1105–1111 (2009).
40. Trapnell, C. *et al.* Differential analysis of gene regulation at transcript resolution with RNA-seq. *Nature Biotechnol.* **31**, 46–53 (2013).



Extended Data Figure 1 | H3.3 and H3K9me3 correlate within the mouse repetitive ES cell genome. Related to Fig. 1. Hierarchically (Spearman rank) clustered heat map showing occupancy of histone H3.3 and known heterochromatic histone modification and factors over a comprehensive set of

mouse repetitive sequences (see Methods for details). Published data sets used are listed in the Methods section. Data are represented as log₂ fold enrichment over matched inputs for each ChIP data set. Repeats with less than 0.01% abundance are omitted.



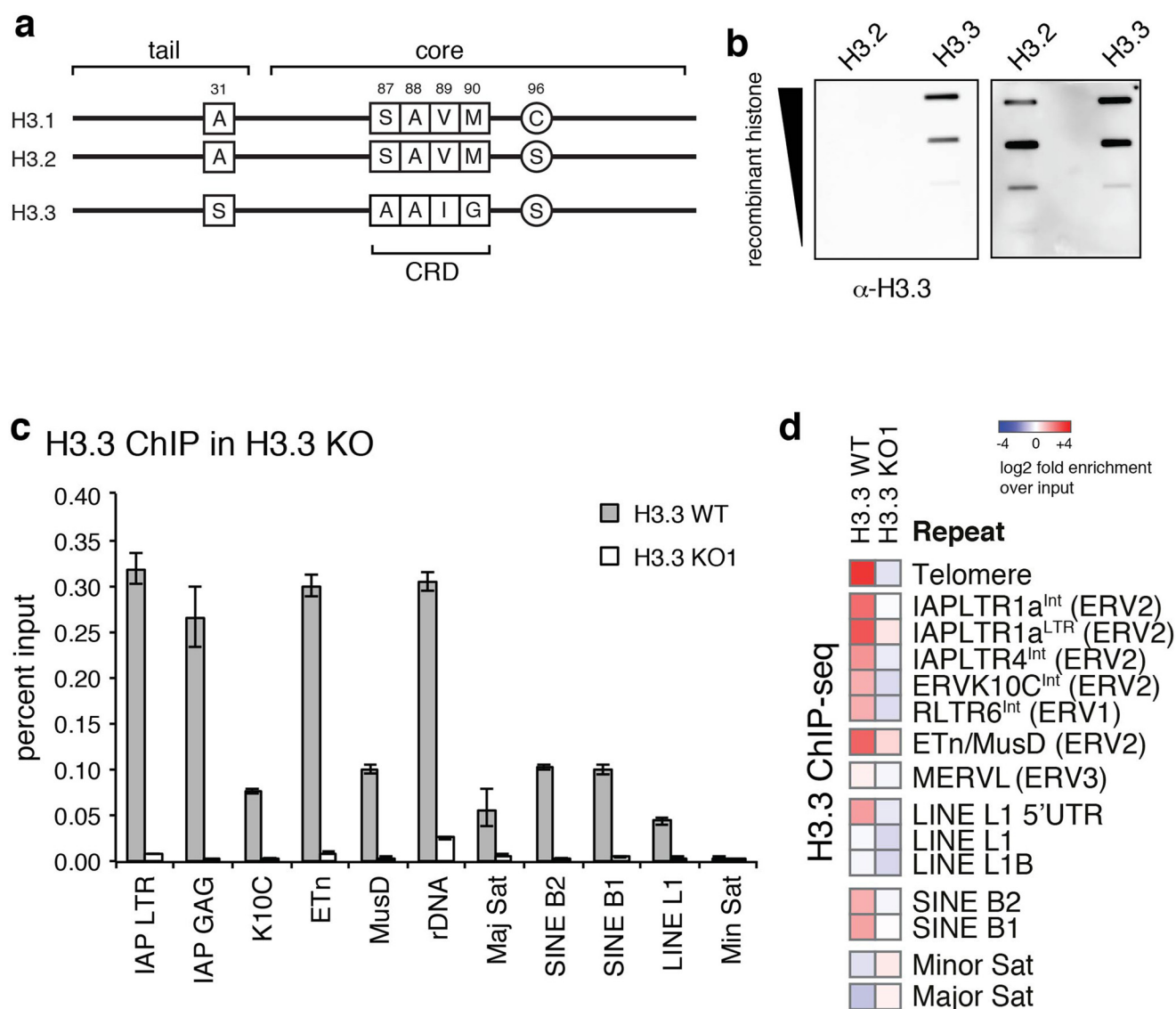
Distribution of H3.3 and H3K9me3 peaks amongst interspersed repeats

Extended Data Figure 2 | H3.3 and H3K9me3 co-occupy class I and II

ERVs. Related to Fig. 1. **a**, Direct comparison of H3.3 enrichment at genic and repetitive sites. Box plot (top) showing enrichment of H3.3 over sets of intervals either representing genic or repetitive elements⁵ annotated in the reference genome, using inclusive read mapping. H3.3 ChIP was performed using an H3.3 antibody and formaldehyde (FA) crosslinking in H3.3 wild-type (WT) cell line. H3.3 enrichment is shown as standardized ChIP-seq read density divided by the standardized input read density on a per-interval basis. The width of the box is proportional to the number of intervals in each group. TSS, transcription start sites of highly active genes; K27pro, bivalent promoters¹⁶. Box plot (bottom) shows the input read density (standardized by scaling to a genome-wide mean of 1), confirming the even representation of unique and repetitive sequences resulting from the inclusive mapping procedure (see Methods for details). Result of one-sided Wilcoxon rank sum test against a set of randomly selected genomic intervals (shuffled) is indicated (**** $P < 0.0001$).

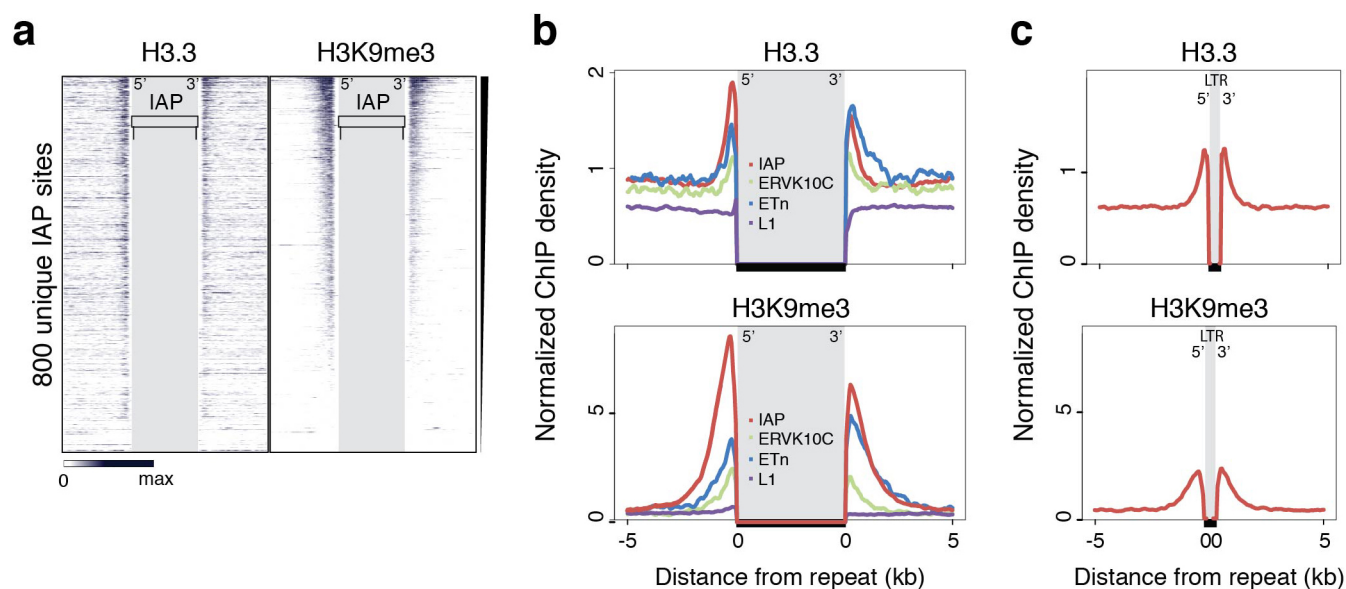
b, H3K9me3 enrichment at genic and repetitive sites. H3K9me3 ChIP was

performed using MNase digestion under native conditions. Box plot (top) showing enrichment of H3K9me3 over sets of intervals either representing genic or repetitive elements analogous to **a**. Box plot (bottom) shows the input read density analogous to **a**. Result of one-sided Wilcoxon rank sum test against a set of randomly selected genomic intervals (shuffled) is indicated (**** $P < 0.0001$). **c**, Sequential H3.3 and H3K9me3 (re)-ChIP at genic and repetitive sites. Boxplots showing enrichment of Re-ChIP inclusive read mapping relative to an input control. Result of one-sided Wilcoxon rank sum test against a set of randomly selected genomic intervals (shuffled) is indicated (**** $P < 0.0001$). **d**, Co-occupancy of H3.3 and H3K9me3 at specific classes of ERVs. H3.3 and H3K9me3 peak intervals were independently intersected with annotated ERVs⁵ and their co-occurrences within the same ERV were evaluated. L1Md_F (full) is a subset of L1Md_F, comprising only full length repeats (>5 kb). All pie charts include total number of intervals for each family that had none, (at least) one H3.3 peak (H3.3 only), or H3K9me3 peak(s) (H3K9me3 only), or at least one of each (H3.3+H3K9me3).



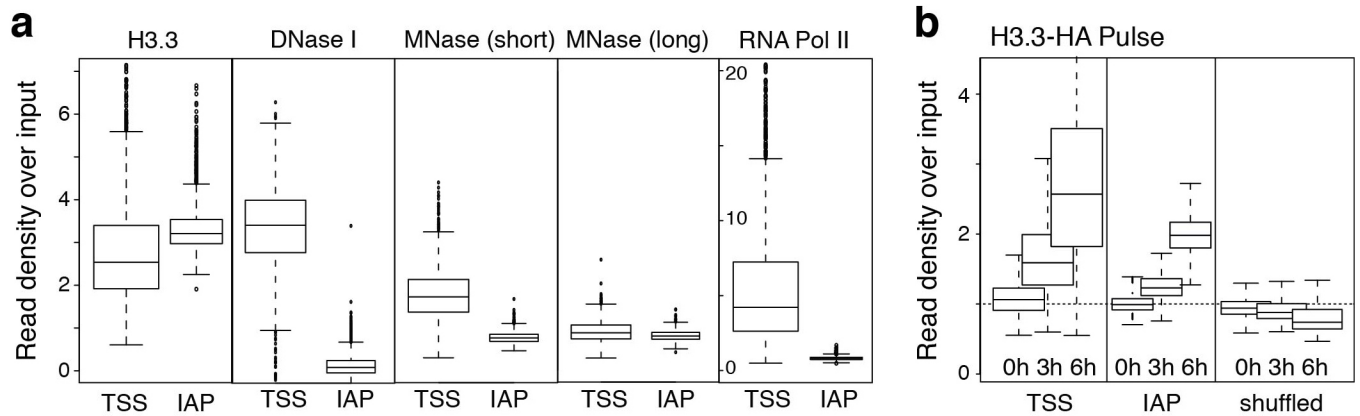
Extended Data Figure 3 | Generation of H3.3-isoform-specific antibodies. Related to Fig. 1. **a**, Schematic of amino acid sequence differences for the canonical histones H3.1 and H3.2 versus the histone variant H3.3. H3.3 differs from H3.2 or H3.1 at only 4 or 5 amino acids, positions 31, 87, 89, 90 and 96, as indicated. **b**, Immunoblot against recombinant histones using the final purified antibody (Millipore 09-838), confirming specificity of the H3.3-isoform-

specific antibody. **c**, ChIP-qPCR analysis of H3.3 enrichment at various repeat regions in control and H3.3-knockout ES cells. Error bars represent s.d. from one experiment ($n = 3$). **d**, ChIP-seq enrichment of H3.3 at repetitive regions of the mouse genome in control and H3.3-knockout ES cells. Data are represented in a heat map of log₂ fold enrichment (red) or depletion (blue) over a matched input.



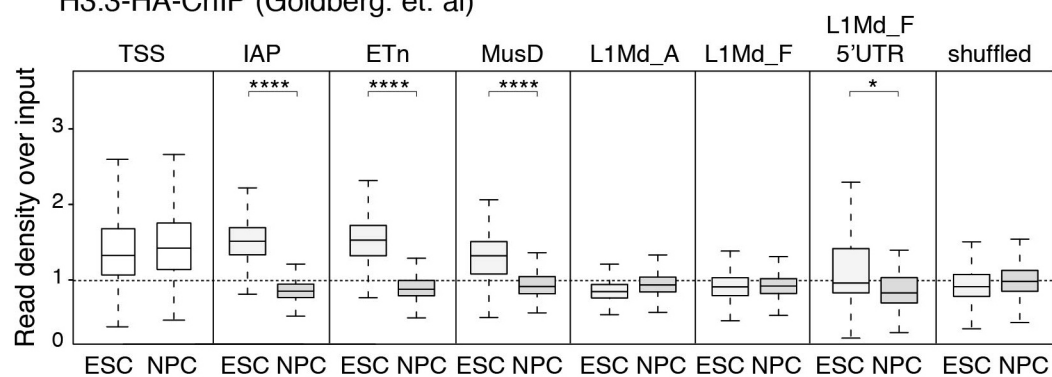
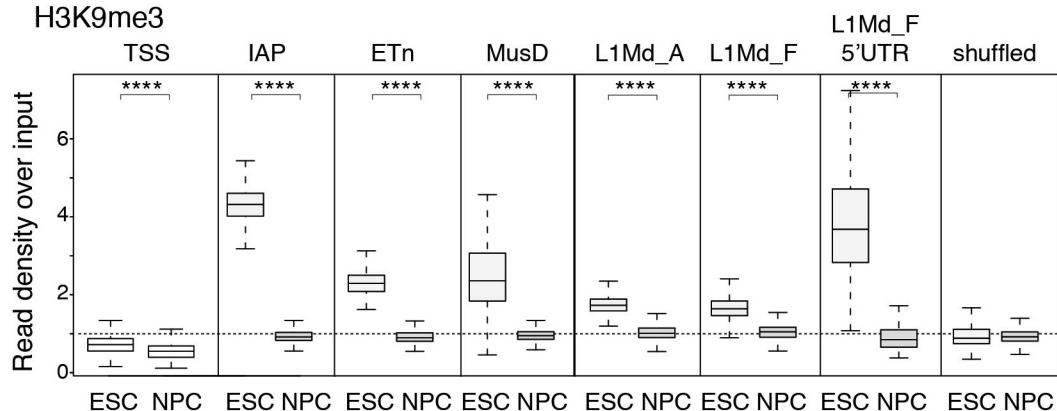
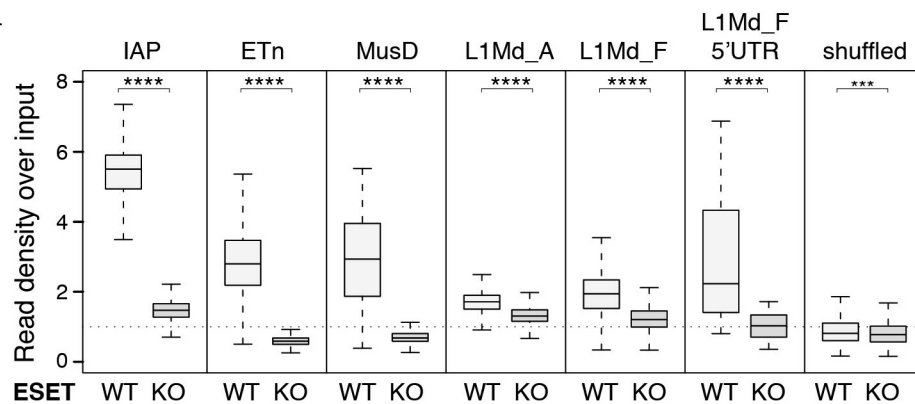
Extended Data Figure 4 | H3.3 is enriched in regions flanking ERVs and orphan LTRs. Related to Fig. 1. **a**, ChIP-seq density heat maps for unique sites flanking full-length IAP ERVs ($n = 800$) rank ordered by H3K9me3 enrichment. Colour intensity represents normalized and globally scaled tag counts. **b**, H3.3 (top) and H3K9me3 (bottom) enrichment over regions flanking IAP, ERVK10C, ETn ERVs and L1 elements. H3.3 ChIP-seq was performed with FA crosslinking, H3K9me3 ChIP-seq under native conditions. Average profiles were aligned and aggregated at the 5' and 3' boundaries of hundreds of

annotated elements from standardized unique read count coverage tracks. The profiles are directional with the 5' ends on the left and 3' end on the right. **c**, H3.3 (top) and H3K9me3 (bottom) enrichment over regions flanking single (so-called orphan) IAP LTRs, ~500 bp. Orphan LTRs are the result of a recombination event between two LTRs—usually the 3' and 5' LTRs of the same ERV—effectively deleting the internal coding sequence. Approximately 600 full-length LTRs (~500 bp) enriched in H3.3 and H3K9me3 were identified in the mouse genome and aggregated for the profiles.

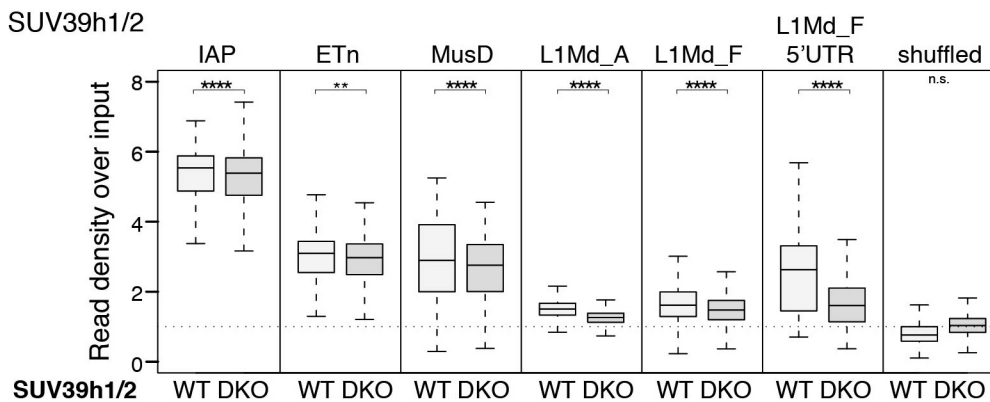


Extended Data Figure 5 | H3.3 at IAPs is not associated with transcription, DNase I or MNase sensitivity. Related to Fig. 1. **a**, Direct comparison of chromatin properties at TSSs of highly expressed genes and IAP ERVs. Box plots showing (from left to right) comparable enrichment of H3.3; DNase I sensitivity; MNase sensitivity; elongating RNAP2 occupancy. MNase data sets are from a recent study, showing H3.3 localizing to MNase hypersensitive regions such as active promoters²⁵. In this study, MNase sensitivity was assessed

by sequencing nucleosomes released under mild ('short') or extensive ('long') MNase digestion conditions; MNase hypersensitive sites were shown to be specifically enriched by mild MNase digestion, whereas long digestion released chromatin more evenly²⁵. **b**, Comparison of kinetics of H3.3 incorporation²⁶ at the TSS of highly expressed genes and IAP ERVs; as control, a randomized set of intervals is shown.

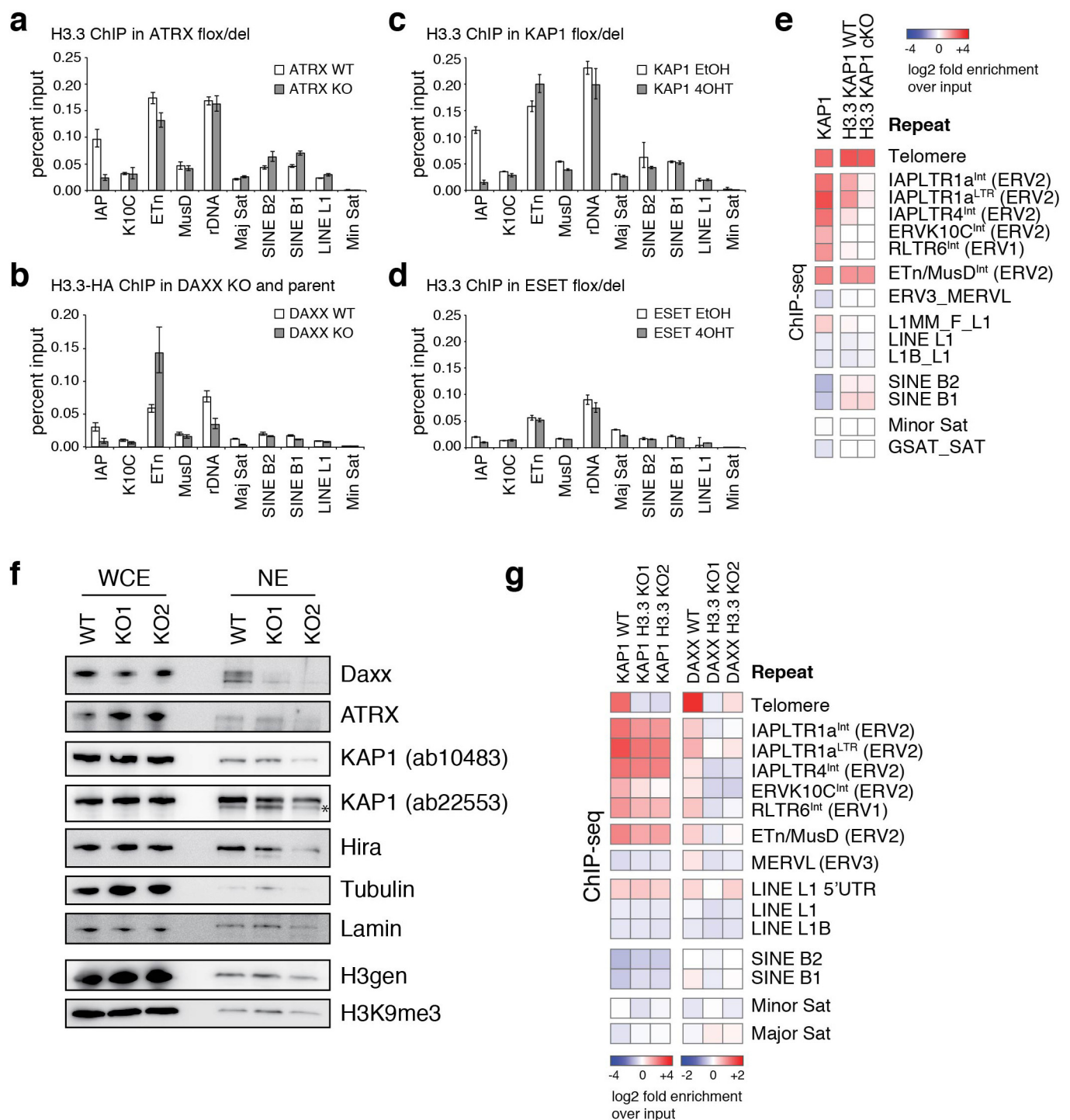
a H3.3-HA-ChIP (Goldberg. et. al)**b** H3K9me3**c** ESET

SUV39h1/2



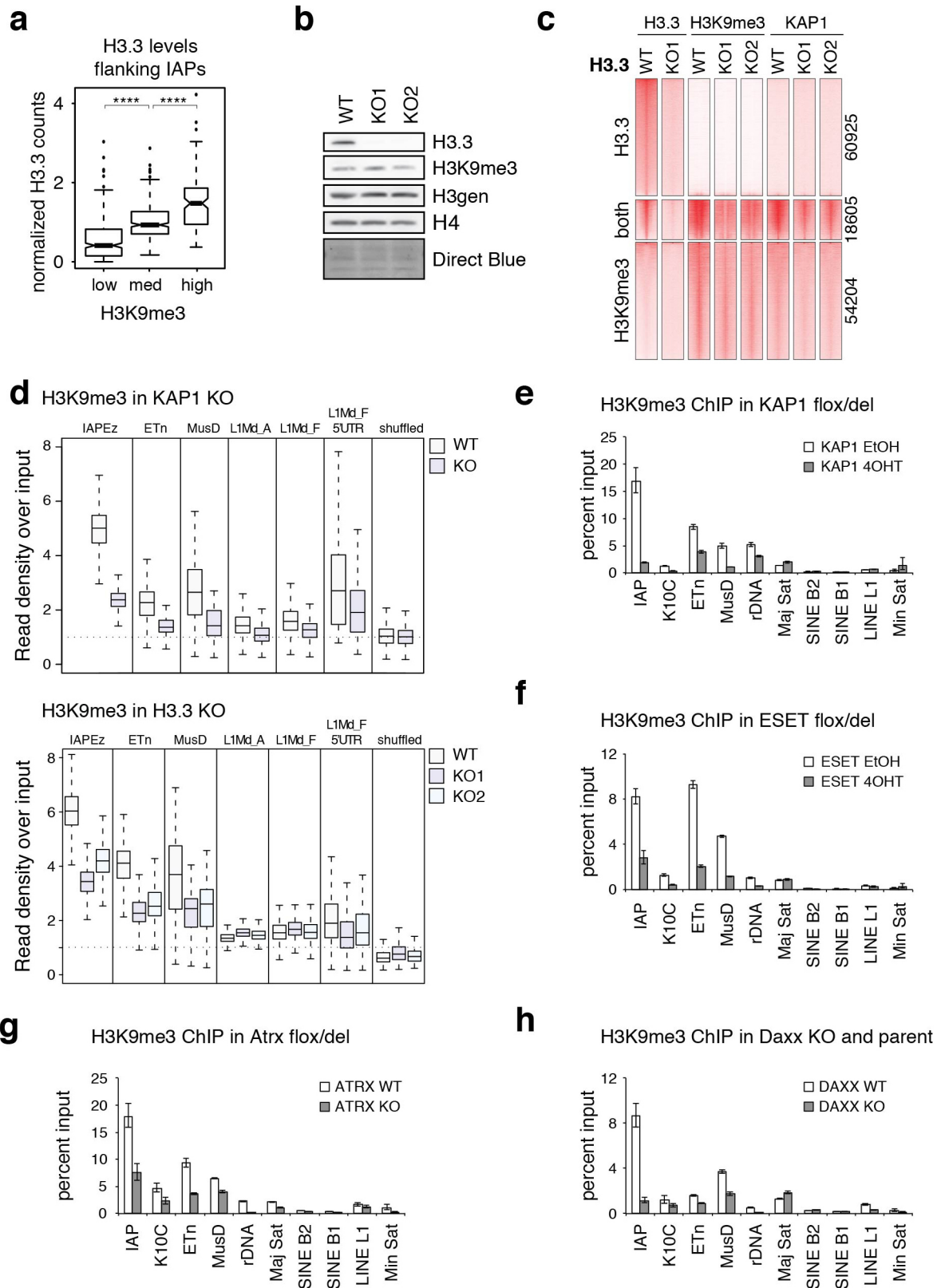
Extended Data Figure 6 | H3.3 and ESET-dependent H3K9me3 enrichment at IAPs is lost upon differentiation. Related to Fig. 1. **a, b**, Comparison of H3.3 (**a**) and H3K9me3 (**b**) enrichment at the TSS of highly expressed genes and various repeat classes in ES cells and NPCs using inclusive read mapping. H3.3 ChIP was performed using a genomic knock-in tagged H3.3B-HA and FA crosslinking¹². H3K9me3 ChIP was performed using FA crosslinking¹⁷. Enrichment is shown as standardized ChIP-seq read density divided by the

standardized input read density on a per interval basis. Result of one-sided Wilcoxon signed rank test (NPCs versus ES cells) are shown (**** $P < 0.0001$; *** $P < 0.0005$; ** $P < 0.005$; * $P < 0.05$; no annotation = not significant). **c**, Levels of H3K9me3 enrichment in control and ESET-knockout ES cells (top) or control and SUV39h1/2-knockout ES cells²⁷ (bottom) at various repeat classes. DKO, double knockout. Data are represented as in **a** and **b**.



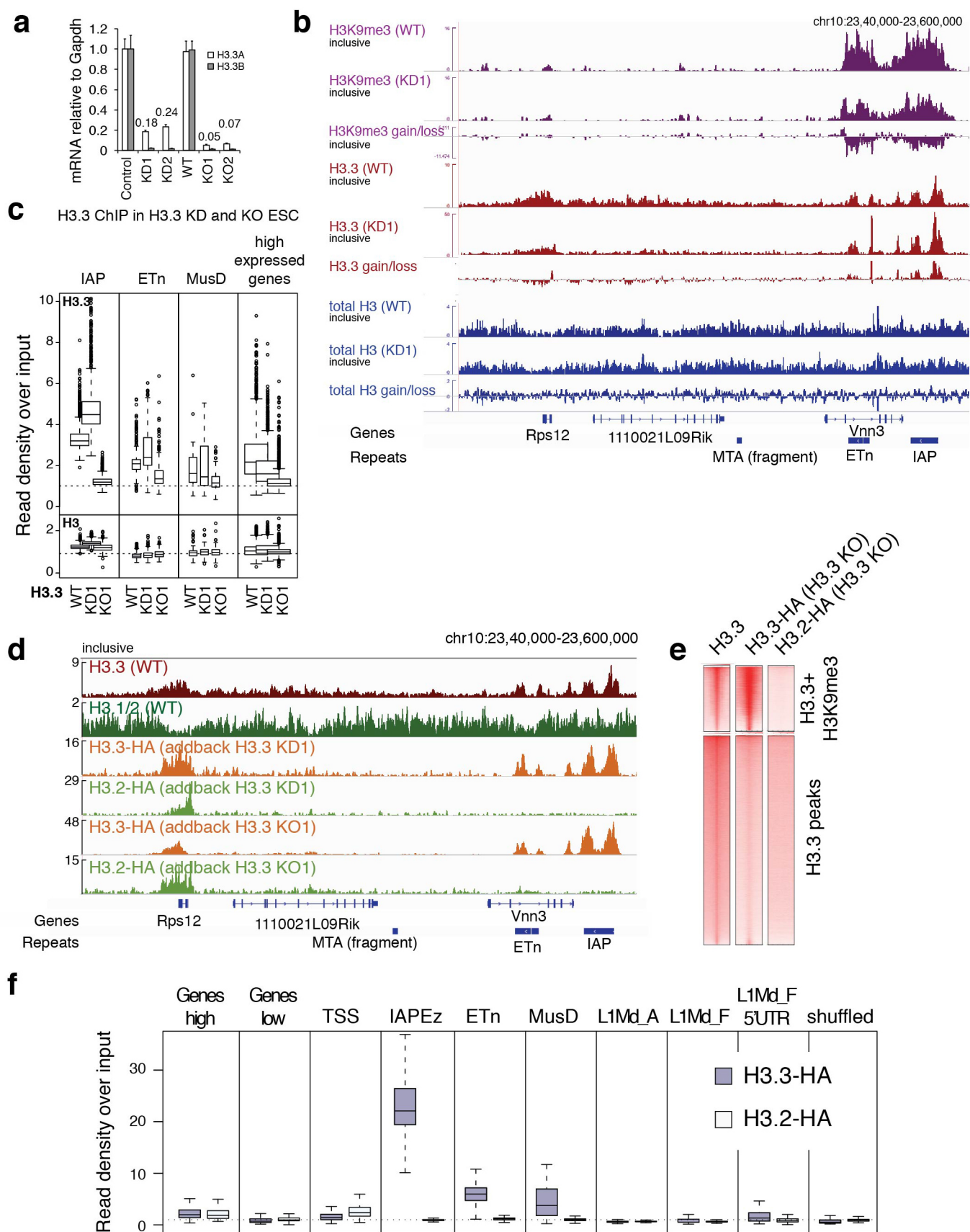
Extended Data Figure 7 | Contribution of DAXX, ATRX, KAP1 and ESET to H3.3 enrichment at ERVs. Related to Fig. 2. **a–d**, ChIP-qPCR analysis of H3.3 enrichment at various repeat regions in control and ATRX-knockout (**a**), DAXX-knockout (**b**), KAP1-knockout (**c**) and ESET-knockout (**d**) ES cells. Error bars represent s.d. from one experiment ($n = 3$). Data are representative of two independent ChIP experiments. **e**, ChIP-seq enrichment of KAP1 and H3.3 in control and KAP1-knockout ES cells at repetitive regions of the mouse

genome. Data are represented in a heat map of \log_2 fold enrichment (red) or depletion (blue) over a matched input. **f**, Loss of H3.3 reduces nuclear DAXX levels. Immunoblot from whole-cell extracts (WCE) or nuclear extracts (NE) in the presence and absence of H3.3. Asterisk denotes cross-reacting band. **g**, ChIP-seq enrichment of KAP1 and DAXX in control and H3.3-knockout ES cells. Data are represented as in **e**. Note the different colour scale used for KAP1 and DAXX.



Extended Data Figure 8 | Effects of H3.3 and corepressor complex depletion on H3K9me3 heterochromatin. Related to Fig. 3. **a**, Positive correlation of H3.3 and H3K9me3 at IAP ERVs. H3.3 ChIP-seq enrichment at 800 unique IAP flanking regions (see Fig. 1e) was binned into three groups by their H3K9me3 ChIP-seq enrichment (low, medium and high). Wilcoxon rank sum test (**** $P < 0.0001$). **b**, Immunoblot from ES cell whole-cell lysates in the presence and absence of H3.3. **c**, H3.3, H3K9me3 and KAP1 ChIP-seq density heat maps for peaks classified as H3.3 only ($n = 60,925$), both H3.3 and H3K9me3 ($n = 18,605$), or H3K9me3 only ($n = 54,204$) in control and H3.3-

knockout ES cell. Five-kilobase intervals around peak centres are shown. Colour intensity represents normalized and globally scaled tag counts. **d**, Levels of H3K9me3 at IAP, ETn, MusD ERVs and LINE elements in control and KAP1-knockout ES cells (top) and control and H3.3-knockout ES cells (bottom). Box plots show enrichment over matched input. **e–h**, ChIP-qPCR analysis of H3K9me3 at various repeat regions in control and KAP1-knockout (**e**), ESET-knockout (**f**), ATRX-knockout (**g**) and DAXX-knockout (**h**) ES cells. Error bars represent s.d. from one experiment ($n = 3$). Data are representative of two independent ChIP experiments.

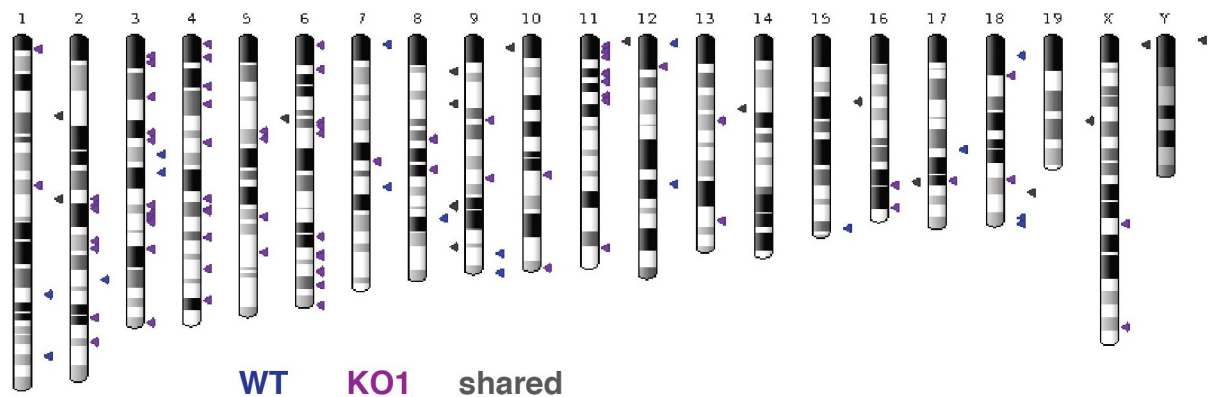
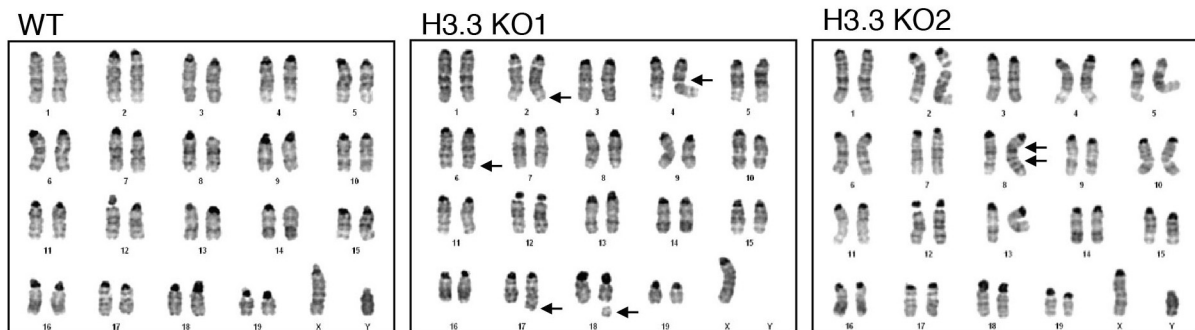


Extended Data Figure 9 | Global effects of H3.3 depletion. Related to Fig. 3. **a**, H3.3 transcript levels in control, H3.3-knockdown and H3.3-knockout ES cells. Data are represented as mean expression relative to *Gapdh* \pm s.d. ($n = 3$). **b**, Relative gain/loss upon H3.3 knockdown of H3K9me3, H3.3 and total H3 are shown over a section of chromosome 10 containing the highly transcribed *Rps12* gene and several ERVs. Gain/loss tracks are calculated by subtracting the respective control from H3.3 KD1 tracks, both standardized to a global mean of 1. Note that H3.3 ChIP-seq data in KD1 cells represents the remaining 10% H3.3. The global loss of H3.3 is not directly apparent from the track due to the necessary normalization of the data. The H3.3 difference track thus does not indicate the global loss of H3.3 but merely represent the relative redistribution of the remaining H3.3 from active genes (*Rps12*) towards repetitive sequences. **c**, Levels of H3.3 and H3 and IAP, ETn, MusD, and the TSS of highly expressed genes in control, H3.3-knockdown and H3.3-knockout ES cells. Box plots show

enrichment over matched input. **d**, Incorporation of exogenous, constitutively expressed, H3.3 and H3.2 added back into H3.3-knockdown or H3.3-knockout ES cells. H3.2 cannot substitute for H3.3 at repetitive ERVs but is efficiently incorporated at sites of active transcription. ChIP-seq was performed on lentivirally integrated H3.3-haemagglutinin (HA) and H3.2-HA in H3.3 KD1 and H3.3 KO1. **e**, ChIP-seq density heat maps for peaks classified as enriched with both H3.3 and H3K9me3 ($n = 18,605$) or H3.3 only ($n = 60,925$). Colour intensity represents tag counts scaled and normalized globally. Five-kilobase intervals around peak centres are shown. **f**, Quantification of H3.3-HA and H3.2-HA add-back in H3.3-knockout enrichment at low and highly expressed genes, as well as the TSS (± 1 kb) of the latter, IAP, ETn and MusD ERVs, and full-length LINE elements and their 5' promoter regions. Data are represented as enrichment over input.

a

Gene	Location	Element(s) upstream of one or more exons	distance (kb)
Aass	chr6:23072172-23132986	ETnERV2-int,RLTR13D6,RLTRETN_Mm	1
Dcdc2a	chr13:25056003-25210706	(TG)n,B3A	5
Cyp2b23	chr7:26665226-26686430	ETnERV-int,ETnERV2-int,L1_Mm,Lx4A,MMETn-int,RLTR1B,RLTR9D,RMER16	4
Cadps2	chr6:23262773-23839421	IAPEz-int,IAPLTR2_Mm,RLTR44-int,RLTR44E	31
Lox	chr18:52517237-52529708	IAPLTR2a	12
Col1a2	chr6:4505696-4541543	IAPEz-int,IAPLTR1_Mm	137
Rpl39l	chr16:10170227-10174911	IAPLTR2b,LTRIS2,RLTR41,RLTR44-int,RLTRETN_Mm	9
Col5a2	chr1:45374330-45503282	IAP-d-int,IAPEz-int,IAPLTR2_Mm,RLTR10D,RLTR45-int	55
Gm14403	chr2:177498225-177512311	.,B2_Mm1t,IAPEz-int,IAPLTR1_Mm,IAPLTR2b,LTRIS3,MuRRS4-int,RLTR41	7
Eps8	chr6:137477244-137649285	LTRIS2	6
Peg3	chr7:6705959-6730419	Imprinted DMR	1

b**c**

Extended Data Figure 10 | ERV reactivation upregulates adjacent genes and may be linked to unbalanced chromosomal translocations. Related to Fig. 4. **a**, Repetitive elements associated with genes in Fig. 4b. Elements that were found either within or nearby the transcription unit are listed and the closest distance of an ERV to an exon is given (accounting for the possibility that ERVs could initiate a partial transcript from an alternative start site). **b**, Newly annotated sites of IAP integration in wild-type and H3.3 KO1 are indicated on karyogram. **c**, Karyotype analysis of wild-type and H3.3-knockout ES cells.

Abnormal karyotype is indicated by arrows. All analysed cells in H3.3 KO1 had a small reciprocal translocation between chromosomes 2q and 6q and an unbalanced translocation between chromosomes 6 and 17 resulting in partial gain of chromosomal segment 6qD to 6qG and partial loss of chromosomal segment 17qE2 to 17qE5. Approximately 45% of the cells had chromosomal breaks or gaps (1–2 per cell). Approximately 45% of the H3.3 KO2 ES cells had a duplication of the segment 8qC to 8qD resulting in partial gain of this segment.

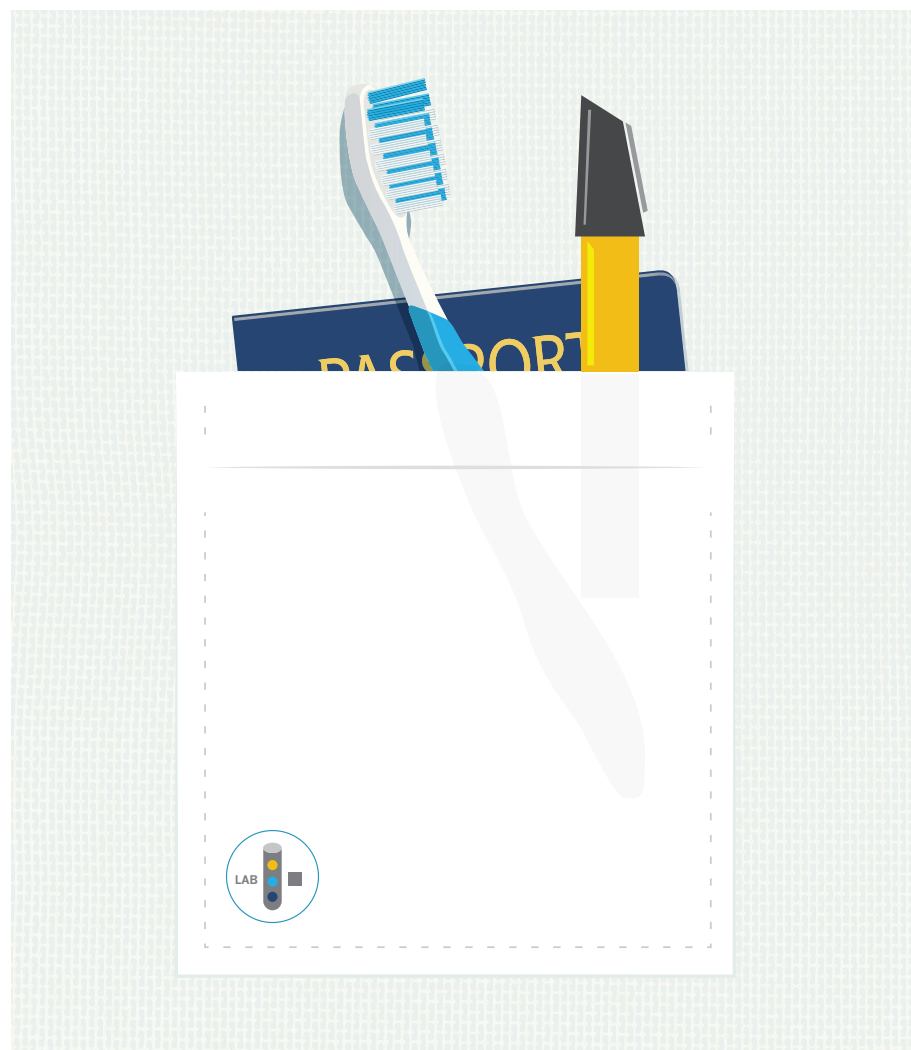
CAREERS

CREATIVE FUNDING Researcher sells discount cards to finance lab **p.247**

UNCONVENTIONAL PATHS Tales of an academic entrepreneur go.nature.com/iehyjn

NATUREJOBS For the latest career listings and advice www.naturejobs.com

ADAPTED FROM STEVEGRAHAM/GETTY



MOBILITY

A strategic move

Short-term upheaval can yield widespread collaborations and long-term resources.

BY JULIE GOULD

Ecologist Roberto Salguero-Gomez has moved countries six times in the past dozen years. Each move represented the next step in his academic career: he stacked up degrees in his native Spain, the United

Kingdom and the United States before gaining his first postdoctoral position in Germany and then moving to his current postdoc job at the University of Queensland in Brisbane, Australia. Along the way, he put in stints as a research assistant in Austria and Spain.

From the moment he arrived at his latest

post, Salguero-Gomez devoted most of his time to writing proposals to extend his stay in the country, and so recoup the effort of his move. His persistence paid off with a three-year fellowship from the Australian Research Council. Although he still has more than 18 months before his contract runs out, he is intent on pursuing a position in Europe next. “In the last year, I have applied for 22 jobs across the world, most of which I have not heard back from,” he says. Such globe-spanning searches, he says, are the nature of scientific research.

Indeed, mobility is the reality for many early-career scientists. In 2012, *Nature* conducted an international poll on attitudes towards researcher mobility. It found that those who had received their PhDs recently (in the past 2 years) were particularly open to moving internationally; only 10% said that they were “not interested”, compared with 40% of those who earned their doctorate at least 16 years ago. Recent graduates were also more likely to be living outside their country of upbringing (see *Nature* **490**, 326–329; 2012).

Salguero-Gomez criss-crossed the planet because he thought it would make him more successful. Data largely support that stance. In 2012, Paula Stephan, an economist at Georgia State University in Atlanta, and her colleagues published a study of scientists from 16 countries. The survey, termed GlobSci, found that those who left their country of origin outperformed non-mobile scientists, as measured by the impact factor of journals that included their work (C. Franzoni, G. Scellato and P. Stephan *Nature Biotechnol.* **30**, 1250–1253; 2012).

But not all moves bring equal benefits, says Stephan. Her work suggests that the biggest career boosts come from relocating for a post-doc position or to gain a specific skill. And, not surprisingly, those who have a position lined up will find getting a work permit much easier, adds Rachel Banks, director of public policy at NAFSA: Association of International Educators, headquartered in Washington DC.

In his quest to determine whether his mobile lifestyle was beneficial for his career, Salguero-Gomez read many opinion pieces, but he struggled to find concrete data on the subject. He has since developed his own survey to explore whether mobility confers greater productivity (calculated by the number of one’s publications) and what cost it imposes on happiness (measured by perceptions of work–life balance).

His preliminary results, he says, show that researchers who travelled during the master’s and PhD stages of their careers have ►

► published fewer papers compared with their non-mobile counterparts, and that those who moved during a first and second postdoc stint have published more.

ECONOMIC ADVANTAGE

The clearest-cut cases of mobility benefits involve scientists who relocate from economically disadvantaged nations. In 2001, Fernando Colchero moved from Mexico to the United States to start his PhD at Columbia University in New York City. It turned out to be a fairly bumpy ride — a year into his programme, he found himself relocating again to follow his supervisor to Duke University in Durham, North Carolina. Soon after, a collaboration he had been developing for his PhD research on tigers in India fell through, and he switched supervisors entirely. He finally finished his PhD in 2008, two years later than he had hoped. The setbacks were frustrating, but Colchero reckons that overall, he still came out ahead. “The direction my career took was only possible because I left Mexico.”

In 2008, he and his wife accepted postdoc positions at the Max Planck Institute for Demographic Research in Rostock, Germany. This move, he says, was less challenging than his first — he was used to acclimatizing to a different culture and had no teaching responsibilities;



OWEN JONES

Julia Barthold conducts field work on a nest-box study at the University of Southern Denmark in Odense.

as a result, he was able to focus on experiments, and his research output soared. His next move took him to the University of Southern Denmark in Odense, where he now works as an assistant professor, and he hopes to attain a tenure-track position soon. Although he would like to remain in Denmark, he is applying to positions outside the country, just in case.

NETWORK CONNECTIONS

PhD students and postdocs generally move abroad in search of opportunities, but developing networks in unfamiliar countries takes time and energy. In 2012, economist Guiseppe Scellato at the Polytechnic University of Turin in Italy worked with his colleagues to build on data from their initial GlobSci survey. They showed that mobile scientists develop broad networks that span continents and age groups, which could ultimately benefit their careers (G. Scellato, C. Franzoni and P. Stephan *Natl Bur. Econ. Res. Working Pap. Ser.* 18613; 2012).

Duan Biggs, a postdoc in ecology and environmental science at the University of Queensland, spent a year doing research in Chile so that he could learn Spanish. Like Colchero, Biggs faced some initial setbacks. Thanks to communication snags and issues getting in touch with the right people, it took him a long time to get access to his lab after typical work hours, and language-barrier problems prolonged his apartment search for two months. “But looking back, moving abroad was a really fantastic decision,” he says. “My scientific capacity and career really took off.” He is forming collaborations with researchers across South America, his native South Africa and Australia.

Many scientists go through an unstable period as they search for a home, adapt to a culture and, sometimes, learn another language. Just the prospect of shifting countries can be unsettling. “The toughest thing about moving abroad is making the decision,” says Owen Jones, an evolutionary biologist at the University of Southern Denmark, who held

three consecutive UK postdoc positions from March 2005 to December 2009. But moving away from one social network and forming another has benefits, he says. “Because I’ve also changed research fields a lot, I have a very broad network, which means forming collaborations is much easier.”

Being able to adapt to an unfamiliar situation is a key survival skill for the mobile academic (see ‘How to cope with relocation’). “Some days will be tough and you won’t be happy about your decision to move,” says Jones. “You will probably have misconceptions about what things will be like.” He experienced this when he moved to Germany after being told he could get along fine speaking only English. That might have been true in a big city such as Berlin, he says, but when he moved to the small town of Rostock, he was forced to learn German.

Jones’s partner, Julia Barthold, a recent PhD graduate who models animal populations, has moved several times for scientific posts. A part-time research assistant at Max Planck, Rostock, she is seeking work in the private sector and the couple are considering their next move. They have also postponed having children. “Moving to Denmark with Owen was strategic: they’ve got a great social system that supports young families,” she says. But the pair recently learned that Owen’s position is not as permanent as they thought, and they are weighing the personal costs of another move against the professional benefits. “We’ve become a nomadic team — entirely self-reliant and self-contained,” she says. “It’s difficult to build networks of friends and maintain them if you’re moving every year.”

HOME FIRES BURNING

Claudio Quilodrán is maintaining his connections in Chile while he works towards his PhD at the University of Geneva in Switzerland. He is carrying out his ideal project: investigating the biodiversity lost as a result of invasive species and cross-species breeding. But he knows that his time abroad is limited. A condition of his

SURVIVAL STRATEGIES

How to cope with relocation

No matter where a researcher ends up, there are a few strategies that can help to settle into an unfamiliar environment.

● **Follow the subject.** Biologist Sara Sandin moved to Nanyang Technological University in Singapore because the research field in which she specialized was getting a lot of funding there. “Think about what you want to do your research in first,” she says, “then find out where the best people in that field are — and speak to them.”

● **Get a job first.** If you have the acceptance letter before going through work-permit and visa applications, the processes will be much smoother.

● **Keep home networks.** You never know where your career path might lead you, and you could end up on a path that returns you to your country of origin. Stay in touch with previous supervisors and colleagues so that you maintain options that could bring future jobs with them.

● **Plan ahead.** If you know what field you want to work in, do some research to find out where the best opportunities for work are. If they are in a country where the language is unfamiliar, take time to learn it in advance. **J.G.**

scholarship from Chile is that he move back within two years of finishing his PhD — and he wants to make sure his South American connections stay strong. “Every time I go home to visit family, I also make sure I visit my old MSc professor,” he says.

Roving scientists may really reap their rewards when they come home, says Stephan — as can the country to which they return. “Returnees are likely to continue to collaborate with scientists in the country where they trained and thus provide a means of diffusion of knowledge in the home country,” she says. They also train new generations of scientists, passing on knowledge gained from different countries and cultures.

That rings true for Mehmet Somel. He moved from Ankara, Turkey, to the University of Leipzig, Germany, for his PhD, and then to postdoc positions at the CAS-MPG Partner Institute for Computational Biology in Shanghai, China, and the University of California, Berkeley. Now, he has returned to Ankara as an evolutionary biologist at the Middle East Technical University, from which he earned his undergraduate and master’s degrees. “Biology in Turkey is relatively underdeveloped compared to other disciplines, especially evolutionary genetics,” he says. “I wouldn’t have been able to get the training and tools I needed to contribute without going abroad.”

The benefits of working abroad in three highly diverse cultures continue to accrue. “I am still collaborating with nearly all the people that I worked with,” Somel says. Not only that, but he had the opportunity to see how different laboratories were managed. “I could take away what I learned from each one and apply them to my lab in Ankara.”

But not everyone returns. Colchero opted to move from Mexico to the United States because that was where he could pursue the studies that most interested him. He has considered moving back to Mexico at several points in his career, but it is looking less likely, he says. “The economic climate has made it almost impossible to get a job in academia. So we’ve decided not to return.” His is a common tale: a 2011 study found that although one in eight of the world’s most highly cited scientists from 1981 to 2003 were born in developing countries, 80% of this fraction worked in developed countries, mostly the United States (B. A. Weinberg *J. Dev. Econ.* **95**, 95–104; 2010).

Every researcher who relocates recounts a different experience, and the choice of whether to move comes down to weighing the odds. For Biggs, the pluses win out: being mobile as a researcher might affect one’s productivity in the short term, he says, “but when you’re looking longer term, you know that it will benefit you in the end.” ■

Julie Gould is the editor of *Naturejobs*.

TURNING POINT

Kai Landskron

Like many researchers, chemist Kai Landskron struggles to piece together enough funding to keep graduate students in his lab at Lehigh University in Bethlehem, Pennsylvania. In March, he started an unconventional crowdfunding campaign — selling discount cards on his lab webpage that are valid at more than 100,000 restaurants, cinemas and shops.

How would you describe the current US funding climate?

Securing funding for research is the most difficult — and most frustrating — part of a job that I otherwise love. The funding climate is very bad. I think that the effort needed to obtain research funding is no longer proportionate to the money that you get, and I believe that this is true for many people. I have enough funding from the US National Science Foundation, the US Department of Energy and Lehigh University to work until the end of 2018. It is enough to support five postdocs and graduate students — the size of my lab for the past four years.

What projects will donors be supporting?

My group is developing nanoporous materials for use in greenhouse-gas reduction, catalytic converters, air and water purification and energy storage.

How much of your time do you spend writing grant applications?

More than half. I have applied for five to ten grants each year, including federal, state and private-foundation grants — basically, any opportunity that presents itself. I have more publications than one might expect relative to the number of personnel and dollars I have.

How did you decide to sell discount cards?

I wanted to pursue a crowdfunding model, but I did not want to use a platform such as Kickstarter. Instead, I wanted to use my own university website as the crowdfunding platform.

Why?

Kickstarter allows technology projects if they create a consumer product, but that is not a typical outcome of basic scientific research. And often, crowdfunding campaigns offer perks for different levels of donations. In researching my options, I found these discount cards, which are valued at US\$10. But, depending on how often one uses them, they can actually save the cardholder more than \$10, and they ship easily and inexpensively. Supporters can also give a charitable donation. Often, funding organizations



and the public seem to expect science to refund society immediately. That is difficult to achieve, because scientific research is a long-term endeavour. But with this card, I can return the value to society — or at least to the donor.

How many have you sold so far?

Not very many. Fewer than 50. But I have had a few people also give donations.

What is the campaign’s biggest challenge?

Getting the word out. I am hopeful that talking to the press will work as an advertisement that could spread further through social media.

What do your colleagues think of the idea?

The feedback has been positive — basically, people are saying that I’m showing ingenuity. One colleague in my department has changed his website to be able to receive donations, too.

Would you contemplate moving to another country, where funding might be better?

That is a complicated question in several ways. I am settled here for personal and professional reasons. And leaving is a complex decision that would involve more than solely funding concerns. I have colleagues in other countries who say it is not easy to find funding where they are either. But if funding in another country were dramatically improved, for example, I would consider it.

What is the outlook for your future funding?

To me, the tunnel seems to be getting darker rather than brighter. That is something that scares me. I’ve got 25 years ahead of me. If it gets even worse than now, that is a scary prospect. ■

INTERVIEW BY VIRGINIA GEWIN

This interview has been edited for length and clarity.

JIFFY

Nothing will come of nothing.

BY GEORGE ZEBROWSKI AND
CHARLES PELLEGRINO

“The box flickers from absolute zero to normal, back and forth,” Cora said.

“It’s only the instruments,” her thesis adviser said, and laughed. “We’d all be dead if they were measuring anything outside themselves.”

“Not if it’s far enough below the jiffy point,” she said.

“Is this April first?” he asked, chuckling, well aware that they were looking far below the travel time of light across the diameter of a proton, below one billion-trillionth of a second, below an instant called a jiffy. His neck tingled as he gazed into the black box.

“The meter flickers at the lowest limit of detection,” Cora said as Professor Draud glimpsed the jitter. It had to be one of those irreproducible results, seen by one observer and not another, probably not there at all. Near the theoried bottom of time-framing, with a jiffy measuring the travel time of light across a proton, and if one imagined the proton as the diameter of Earth, one would notice a passage of time smaller than light’s sprint across the eye of a flea on a jiffy-sized Earth.

“There!” Cora shouted. “Duration is up.”

“If it’s really there,” he said, as if that would stop the absurdity.

Now you see it, now you don’t, went on for an hour. Their necks tingled in unison and Cora imagined that all the errant twinges she had ever felt in her body had registered cosmic rays, neutrinos, irrational stray thoughts from previous boyfriends, tachyons allegedly travelling back in time, or even her cat’s psychotic proings. But this ambiguous nonsense about absolute zero spilling out of a black box from the realm of manifold space-time was a perversity worthy of money-hungry sci-fi writers.

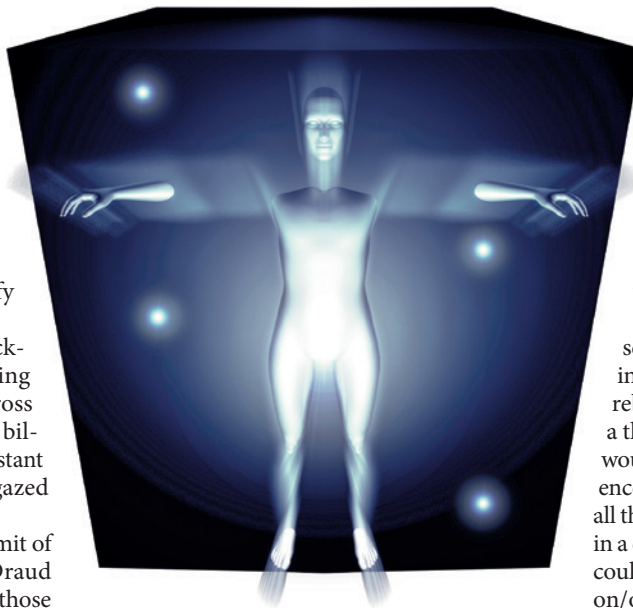
“Can our equipment be measuring this?” he asked.

“Well, it’s doing it,” she replied, enhancing the resolution.

Unlike most of his colleagues, Professor Draud encouraged students to lead him, if and when they could.

The view through the black box was impossible. “Two

flea eyes at least, and growing,” he muttered, no longer in denial.



“Still not large enough or fast enough to be noticed by the rest of the Universe,” Cora added.

“But if it keeps expanding?”

“If it’s everywhere at once, then there are three possible outcomes — all different levels of bad.”

“And least bad?” he asked.

“Another cosmic crunch, and maybe another inflationary universe afterwards.”

Was that really it? The true default condition outside the multiverse? Untypically, Draud seized on the idea of an exterior infinity. Jean-Paul Sartre’s nothingness was leaking into being. Outside the multiverses that bubbled into existence, the norm was absolute zero, which the bubbles resisted.

Cora interrupted his wild thoughts. “When I began this, I was a little afraid, certain that I would get no interesting results.”

He cringed inwardly at the strangeness on the bench before them. “Three flea-eye diameters now,” he said.

They set up a fresh box with two monitors, like gamblers hoping that a new deck of cards would defeat the cheater in the game. But it all came back with the same vision of the entire brane of existence coming to a particle stop, all the granularity of the periodic table suddenly stilled, leaving a timeless existent. They stared as if blinded, expecting it all to wink out in a grotesque spasm of decay.

“Can it be happening everywhere throughout the Universe?” Draud asked, eager to deny that much. Nothing in physics

had ever been local. Even in the quantum realm of imagined fleas on a proton as large as Earth, the laws of physics were not suggestions, but obligatory.

“From the very first jiffy of the entire visible Universe, it’s all been running down from energy into matter, and towards the zero point...”

Draud said, remembering an errant wish to have fathered a child.

“Six flea eyes!” he announced, suddenly seeing himself as a fearful inflation in an infinite series of cosmic doomsdays and rebirths. If the anomaly lurched beyond a thousand flea-leaps, quarks and gluons would phase into instantaneous non-existence, with every living creature throughout all the galaxies suddenly gone, all choice lost in a death unlike any that had ever been and could only be imagined, yet as simple as an on/off switch. No rending and tearing of flesh, but the truest of evils, nothingness itself, to which all lesser evils were beholden, to be feared but never experienced.

Student Draud had sometimes longed for a path along which science never became his life. What joyful memories would comfort him now?

“It’s still increasing!” he shouted. How many times had his life gone wrong, how often right?

Did having progeny have anything to do with fathering universes? Were there intelligences who could do that?

As Cora stared at him, the black behind his eyes fragmented her loveliness into chaos, mocking the logic that insisted on the impossibility, of non-existence, the much denied zero-point field...

They teetered between everything and nothing, an ancient undefeated void at their throats, and he felt the onset of the distinguished moment, so much greater than the usual dying, unequalled except by the lost strangeness of birth. ■

George Zebrowski is the Campbell Award winning novelist of *Brute Orbits* and the classic *Macrolife*. All his fiction is available from Gollancz’s *SF Gateway* (www.sfgateway.com) and *Open Road* (www.openroadmedia.com). **Charles Pellegrino**’s many books of history and archaeology include *Her Name Titanic* and *To Hell and Back: The Last Train From Hiroshima*. His science-fiction novels include *Dust* and *The Killing Star* (with George Zebrowski).

ILLUSTRATION BY JACEY

